1

Electric Energy and Electric Generators

1.1   Introduction

Energy is defined as the capacity of a body to do mechanical work. Intelligent harnessing and control of energy determines essentially the productivity and, subsequently, the lifestyle advancement of society.

Energy is stored in nature in quite a few forms, such as fossil fuels (coal, petroleum, and natural gas), solar radiation, and in tidal, geothermal, and nuclear forms.

Energy is not stored in nature in electrical form. However, electric energy is easy to transmit at long distances and complies with customer's needs through adequate control. More than 30% of energy is converted into electrical energy before usage, most of it through electric generators that convert mechanical energy into electric energy. Work and energy have identical units. The fundamental of energy unity is a joule, which represents the work of a force of a Newton in moving a body through a distance of 1 m along the direction of force (1 J = 1 N × 1 m). Electric power is the electric energy rate; its fundamental unit is a watt (1 W = 1 J/sec). More commonly, electric energy is measured in kilowatthours (kWh):

$$1\ kWh = 3.6 \times 10^6\ J \tag{1.1}$$

Thermal energy is usually measured in calories. By definition, 1 cal is the amount of heat required to raise the temperature of 1 g of water from 15 to 16°C. The kilocalorie is even more common (1 kcal = 10^3 cal).

As energy is a unified concept, as expected, the joule and calorie are directly proportional:

$$1\ cal = 4.186\ J \tag{1.2}$$

A larger unit for thermal energy is the British thermal unit (Btu):
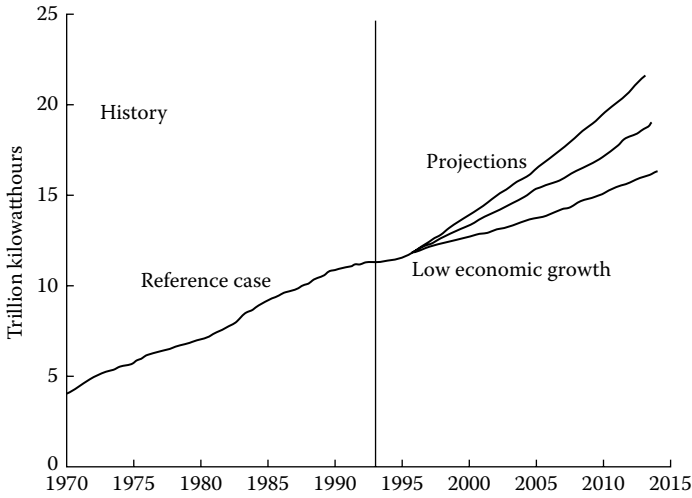
$$1\ BTU = 1,055\ J = 252\ cal \tag{1.3}$$

FIGURE 1.1 Typical annual world energy requirements.

A still larger unit is the quad (quadrillion Btu):

$$1 \, quad = 10^{15} \, BTU = 1.055 \times 10^{18} \, J \tag{1.4}$$

In the year 2000, the world used about 16×10^{12} kWh of energy, an amount above most projections (Figure 1.1). An annual growth of 3.3 to 4.3% was typical for world energy consumption in the 1990 to 2000 period. A slightly lower rate is forecasted for the next 30 years.

Besides annual energy usage (and growth rate), with more than 30 to 40% of total energy being converted into electrical energy, it is equally important to evaluate and predict the electric power peaks for each country (region), as they determine the electric generation reserves. The peak electric power in the United States over several years is shown in Figure 1.2. Peak power demands tend to be more dynamic than energy needs; thus, electric energy planning becomes an even more difficult task.

Implicitly, the transients and stability in the electric energy (power) systems of the future tend to be more severe.

To meet these demands, we need to look at the main energy sources: their availability, energy density, the efficiency of the energy conversion to thermal to mechanical to electrical energy, and their secondary ecological effects (limitations).

1.2 Major Energy Sources

With the current annual growth in energy consumption, the fossil fuel supplies of the world will be depleted in, at best, a few hundred years, unless we switch to other sources of energy or use energy conservation to tame energy consumption without compromising quality of life.

The estimated world reserves of fossil fuel [1] and their energy density are shown in Table 1.1. With a doubling time of energy consumption of 14 years, if only coal would be used, the whole coal reserve would be depleted in about 125 years. Even if the reserves of fossil fuels were large, their predominant or exclusive usage is not feasible due to environmental, economical, and even political reasons.

Alternative energy sources are to be used increasingly, with fossil fuels used slightly less, gradually, and more efficiently than today.

The relative cost of electric energy in 1991 from different sources is shown in Table 1.2.

Wind energy conversion is becoming cost-competitive, while it is widespread and has limited environmental impact. Unfortunately, its output is not steady, and thus, very few energy consumers rely solely
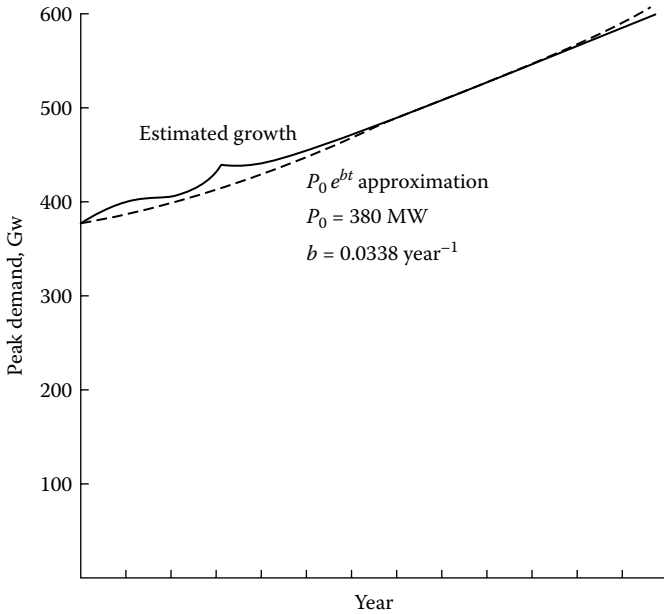
FIGURE 1.2 Peak electric power demand in the United States and its exponential predictions.

TABLE 1.1 Estimated Fossil Fuel Reserves

Fuel	Estimated Reserves	Energy Density in Watthours (Wh)
Coal	7.6×10^{12} metric tons	937 per ton
Petroleum	2×10^{12} barrels	168 per barrel
Natural gas	10^{16} ft^3	0.036 per ft^3

TABLE 1.2 Cost of Electric Energy

Energy Source	Cents/kWh
Gas (in high-efficiency combined cycle gas turbines)	3.4–4.2
Coal	5.2–6
Nuclear	7.4–6.7
Wind	4.3–7.7

on wind to meet their electric energy demands. As, in general, the electric power plants are connected in local or regional power grids with regulated voltage and frequency, connecting large wind generator parks to them may produce severe transients that have to be taken care of by sophisticated control systems with energy storage elements, in most cases.

By the year 2005, more than 20,000 megawatts (MW) of wind power generators will be in place, with much of it in the United States. The total wind power resources of the planet are estimated at 15,000 terra watthours (TWh), so much more work in this area is to be expected in the near future.

Another indirect means of using solar energy, besides wind energy, is to harness energy from the stream-flow part of the hydrological natural cycle. The potential energy of water is transformed into kinetic energy by a hydraulic turbine that drives an electric generator. The total hydropower capacity of the world is about 3×10^{12} W. Only less than 9% of it is used today, because many regions with the greatest potential have economic problems.

Despite initial high costs, the costs of generating energy from water are low, resources are renewable, and there is limited ecological impact. Therefore, hydropower is up for a new surge.

Tidal energy is obtained by filling a bay, closed by a dam, during periods of high tides and emptying it during low-tide time intervals. The hydraulic turbine to be used in tidal power generation should be reversible so that tidal power is available twice during each tidal period of 12 h and 25 min.

Though the total tidal power is evaluated at 64×10^{12} W, its occurrence in short intervals requires large rating turbine-generator systems which are still expensive. The energy burst cannot be easily matched with demand unless large storage systems are built. These demerits make many of us still believe that the role of tidal energy in world demand will be very limited, at least in the near future. However, exploiting submarine currents energy in windlike low-speed turbines may be feasible.

Geothermal power is obtained by extracting the heat inside the earth. With a 25% conversion ratio, the useful geothermal electric power is estimated to 2.63×10^{10} MWh.

Fission and fusion are two forms of nuclear energy conversion that produce heat. Heat is converted to mechanical power in steam turbines that drive electric generators to produce electrical energy.

Only fission-splitting nuclei of a heavy element such as uranium 235 are used commercially to produce a good percentage of electric power, mostly in developed countries. As uranium 235 is in scarce supply, uranium 238 is converted into fissionable plutonium by absorbing neutrons. One gram of uranium 238 will produce about 8×10^{10} J of heat. The cost of nuclear energy is still slightly higher than that of coal or gas (Table 1.2). The environmental problems with disposal of expended nuclear fuel by-products or with potential reactor explosions make nuclear energy tough for the public to accept.

Fusion power combinations of light nuclei, such as deuterium and tritium, at high temperatures and pressures, are scientifically feasible but not yet technically proven for efficient energy conversion.

Solar radiation may be used either through heat solar collectors or through direct conversion to electricity in photovoltaic cells. From an average of 1 kW/m^2 of solar radiation, less than 180 W/m^2 could be converted to electricity with current solar cells. Small energy density and nonuniform availability (mainly during sunny days) lead to a higher cents/kWh rate than that of other sources.

1.3   Electric Power Generation Limitations

Factors limiting electric energy conversion are related to the availability of various fuels, technical constraints, and ecological, social, and economical issues.

Ecological limitations include those due to excess low-temperature heat and carbon dioxide (solid particles) and oxides of sulfur nitrogen emissions from fuel burning.

Low-temperature heat exhaust is typical in any thermal energy conversion. When too large, this heat increases the earth's surface temperature and, together with the emission of carbon dioxide and certain solid particles, has intricate effects on the climate. Global warming and climate changes appear to be caused by burning too much fossil fuel. Since the Three Mile Island and Chernobyl incidents, safe nuclear electric energy production has become not only a technical issue, but also an ever-increasing social (public acceptance) problem.

Even hydro- and wind-energy conversion pose some environmental problems, though much smaller than those from fossil or nuclear fuel–energy conversion. We refer to changes in flora and fauna due to hydro–dams intrusion in the natural habitat. Big windmill farms tend to influence the fauna and are sometimes considered "ugly" to the human eye.

Consequently, in forecasting the growth of electric energy consumption on Earth, we must consider all of these complex limiting factors.

Shifting to more renewable energy sources (wind, hydro, tidal, solar, etc.), while using combined heat–electricity production from fossil fuels to increase the energy conversion factor, together with intelligent energy conservation, albeit complicated, may be the only way to increase material prosperity and remain in harmony with the environment.
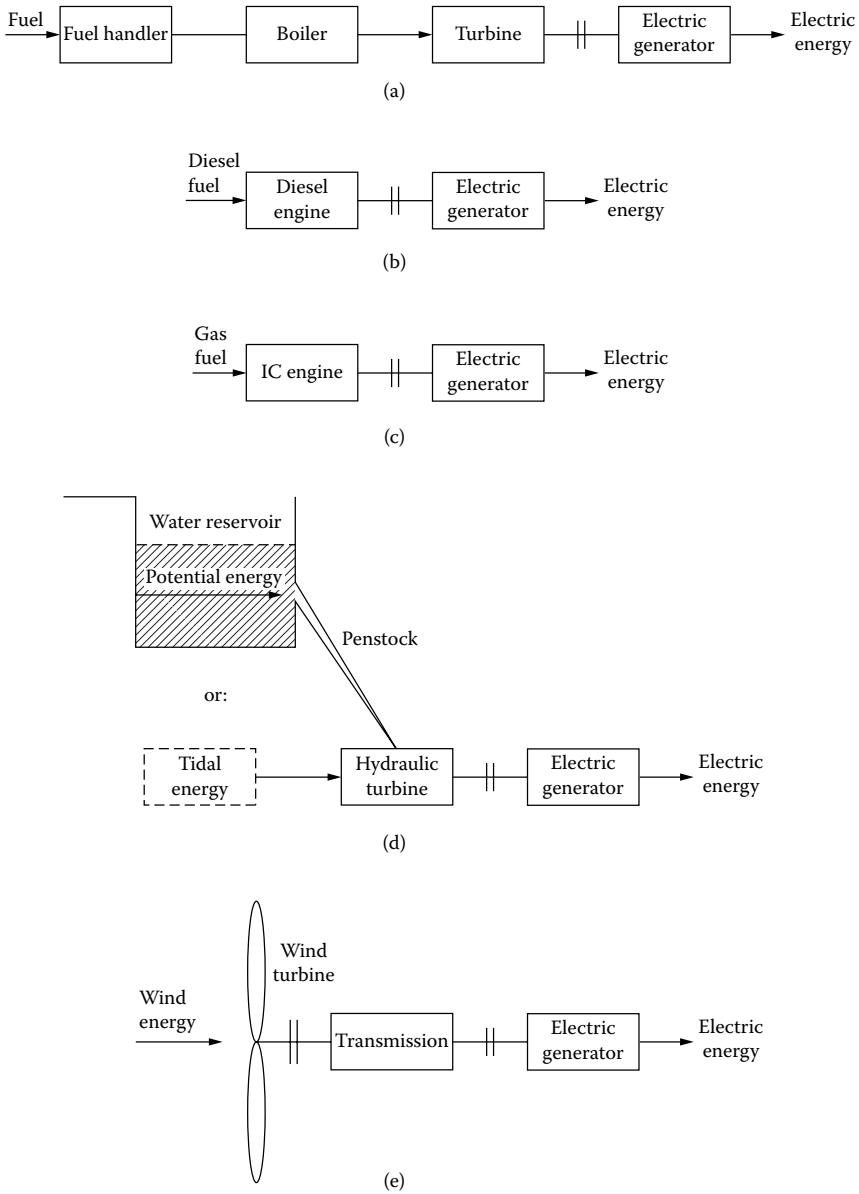
FIGURE 1.3 The most important ways to produce electric energy: (a) fossil fuel thermoelectric energy conversion, (b) diesel-engine electric generator, (c) IC engine electric generator, (d) hydro turbine electric generator, and (e) wind turbine electric generator.

1.4 Electric Power Generation

Electric energy (power) is produced by coupling a prime mover that converts the mechanical energy (called a turbine) to an electrical generator, which then converts the mechanical energy into electrical energy (Figure 1.3a through Figure 1.3e). An intermediate form of energy is used for storage in the electrical generator. This is the so-called magnetic energy, stored mainly between the stator (primary) and rotor (secondary). The main types of "turbines" or prime movers are as follows:

- Steam turbines
- Gas turbines
- Hydraulic turbines
- Wind turbines
- Diesel engines
- Internal combustion (IC) engines

The self-explanatory Figure 1.3 illustrates the most used technologies to produce electric energy. They all use a prime mover that outputs mechanical energy. There are also direct electric energy production methods that avoid the mechanical energy stage, such as photovoltaic, thermoelectric, and electrochemical (fuel cells) technologies. As they do not use electric generators, and still represent only a tiny part of all electric energy produced on Earth, discussion of these methods falls beyond the scope of this book.

The steam (or gas) turbines in various configurations make use of practically all fossil fuels, from coal to natural gas and oil and nuclear fuel to geothermal energy inside the earth.

Usually, their efficiency reaches 40%, but in a combined cycle (producing heat and mechanical power), their efficiency recently reached 55 to 60%. Powers per unit go as high 100 MW and more at 3000 (3600 rpm) but, for lower powers, in the MW range, higher speeds are feasible to reduce weight (volume) per power.

Recently, low-power high-speed gas turbines (with combined cycles) in the range of 100 kW at 70,000 to 80,000 rpm became available. Electric generators to match this variety of powers and speeds were also recently produced. Such electric generators are also used as starting motors for jet engines.

High speed, low volume and weight, and reliability are key issues for electric generators on board aircraft. Power ranges are from hundreds of kilowatts to 1 MW in large aircraft. On ships or trains, electric generators are required either to power the electric propulsion motors or for multiple auxiliary needs. Diesel engines (Figure 1.3b) drive the electric generators on board ships and trains.

In vehicles, electric energy is used for various tasks for powers up to a few tens of kilowatts, in general. The internal combustion (or diesel) engine drives an electric generator (alternator) directly or through a belt transmission (Figure 1.3c). The ever-increasing need for more electric power in vehicles to perform various tasks — from lighting to engine start-up and from door openers to music devices and windshield wipers and cooling blowers — poses new challenges for creators of electric generators of the future.

Hydraulic potential energy is converted to mechanical potential energy in hydraulic energy turbines. They, in turn, drive electric generators to produce electric energy. In general, the speed of hydraulic turbines is rather low — below 500 rpm, but in many cases, below 100 rpm.

The speed depends on the water head and flow rate. High water head leads to higher speed, while high flow rate leads to lower speeds. Hydraulic turbines for low, medium, and high water heads were perfected in a few favored embodiments (Kaplan, Pelton, Francis, bulb type, Strafflo, etc.).

With a few exceptions — in Africa, Asia, Russia, China, and South America — many large power/unit water energy reservoirs were provided with hydroelectric power plants with large power potentials (in the hundreds and thousands of megawatts). Still, by 1990, only 15% of the world's 624,000 MW reserves were put to work. However, many smaller water energy reservoirs remain untapped. They need small
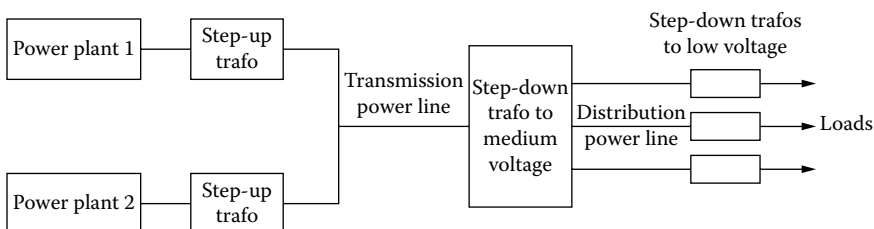

FIGURE 1.4 Single transmission in a multiple power plant — standard power grid.

TABLE 1.3 World Hydro Potential by Region (in TWh)

	Gross	Economic	Feasible
Europe	5,584	2,070	1,655
Asia	13,399	3,830	3,065
Africa	3,634	2,500	2,000
America	11,022	4,500	3,600
Oceania	592	200	160
Total	34,231	13,100	10,480

TABLE 1.4 Proportion of Hydro Already Developed

Africa	6%
South and Central America	18%
Asia	18%
Oceania	22%
North America	55%
Europe	65%

Source: Adapted from World Energy Council.

hydrogenerators with power below 5 MW at speeds of a few hundred revolutions per minute. In many locations, tens of kilowatt microhydrogenerators are more appropriate [2–5].

The time for small and microhydroenergy plants has finally come, especially in Europe and North America, where there are less remaining reserves. Table 1.3 and Table 1.4 show the world use of hydro energy in tWh in 1997 [6,7].

The World Energy Council estimated that by 1990, of a total electric energy demand of 12,000 TWh, about 18.5% was contributed by hydro. By 2020, the world electric energy demand is estimated to be 23,000 TWh. From this, if only 50% of all economically feasible hydroresources were put to work, in 2020, hydro would contribute 28% of total electric energy demands.

These numbers indicate that a new era of dynamic hydroelectric power development is to come soon, if the world population desires more energy (prosperity for more people) with a small impact on the environment (constant or less greenhouse emission effects).

Wind energy reserves, though discontinuous and unevenly distributed, mostly around shores, are estimated at four times the electric energy needs of today.

To its uneven distribution, its discontinuity, and some surmountable public concerns about fauna and human habitats, we have to add the technical sophistication and costs required to control, store, and distribute wind electric energy. These are the obstacles to the widespread use of wind energy, from its current tiny 20,000 MW installation in the world. For comparison, more than 100,000 MW of hydropower reserves are tapped today in the world. But ambitious plans are in the works, with the European Union planning to install 10,000 MW between 2000 and 2010.

The power per unit for hydropower increased to 4 MW and, for wind turbines, it increased up to 5 MW. More are being designed, but as the power per unit increases, the speed decreases to 10 to 24 rpm or less. This poses an extraordinary problem: either use a special transmission and a high-speed generator or build a direct-driven low-speed generator. Both solutions have merits and demerits.

The lowest speeds in hydrogenerators are, in general, above 50 rpm, but at much higher powers and, thus, much higher rotor diameters, which still lead to good performance.

Preserving high performance at 1 to 5 MW and less at speeds below 30 rpm in an electric generator poses serious challenges, but better materials, high-energy permanent magnets, and ingenious designs are likely to facilitate solving these problems.
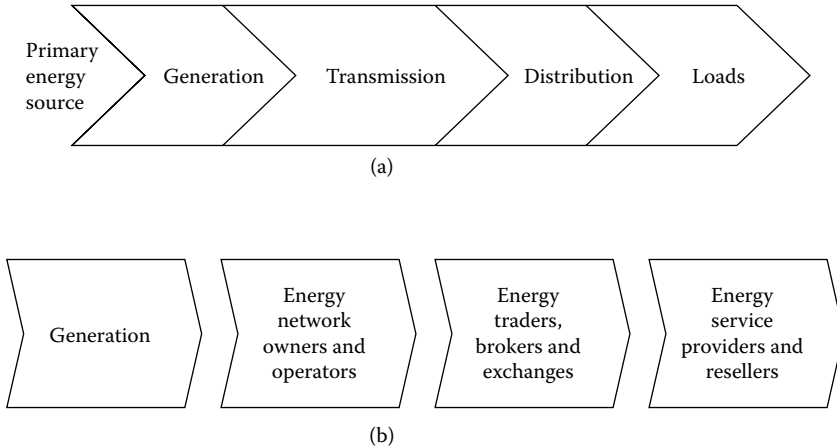
FIGURE 1.5 (a) Standard value chain power grid and (b) unbundled value chain.

It is planned that wind energy will produce more than 10% of electric energy by 2020. This means that wind energy technologies and businesses are apparently entering a revival — this time with sophisticated control and flexibility provided by high-performance power electronics.

1.5 From Electric Generators to Electric Loads

Electric generators traditionally operate in large power grids — with many of them in parallel to provide voltage and frequency stability to changing load demands — or they stand alone.

The conventional large power grid supplies most electric energy needs and consists of electric power plants, transmission lines, and distribution systems (Figure 1.4).

Multiple power plants, many transmission power lines, and complicated distribution lines constitute a real regional or national power grid. Such large power grids with a pyramidal structure — generation to transmission to distribution and billing — are now in place, and to connect a generator to such a system implies complying with strict rules. The rules and standards are necessary to provide quality power in terms of continuity, voltage and frequency constancy, phase symmetry, faults treatment, and so forth. The thoughts of the bigger the unit, the more stable the power supply seem to be the driving force behind building such huge "machine systems." The bigger the power or unit, the higher the energy efficiency, was for decades the rule that led to steam generators of up to 1500 MW and hydrogenerators up to 760 MW.

However, investments in new power plants, redundant transmission power lines, and distribution systems, did not always keep up with ever-increasing energy demands. This is how blackouts developed. Aside from extreme load demands or faults, the stability of power grids is limited mainly by the fact that existing synchronous electric generators work only at synchronism, that is, at a speed n_1 rigidly related to frequency f_1 of voltage $f_1 = n_1 \times p_1$. Standard power grids are served exclusively by synchronous generators and have a pyramidal structure (Figure 1.5a and Figure 1.5b) called utility. Utilities still run, in most places, the entire process from generation to retail settlement.

Today, the electricity market is deregulating at various paces in different parts of the world, though the process must be considered still in its infancy.

The new unbundled value chain (Figure 1.5b) breaks out the functions into the basic types: electric power plants; energy network owners and operators; energy traders, breakers, and exchanges; and energy service providers and retailers [8,9]. The hope is to stimulate competition for energy cost reduction while also improving the quality of power delivered to end users, by developing and utilizing sustainable technologies that are more environmentally friendly. Increasing the number of players requires clear rules
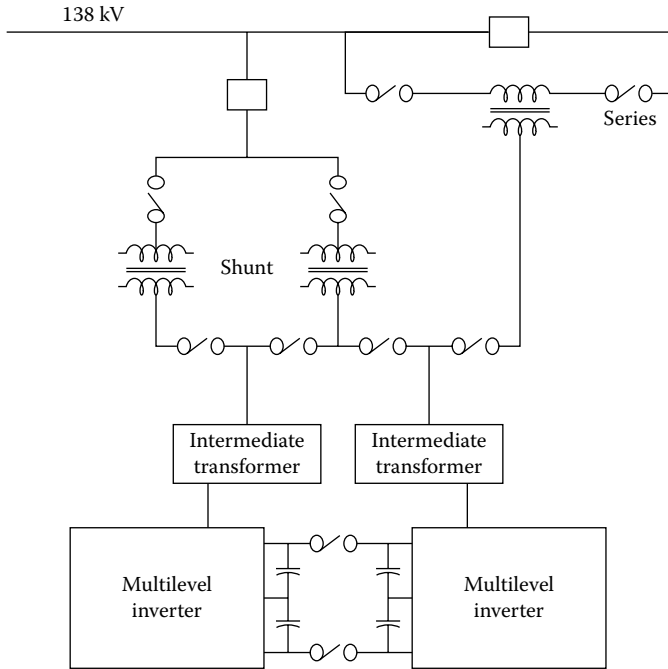
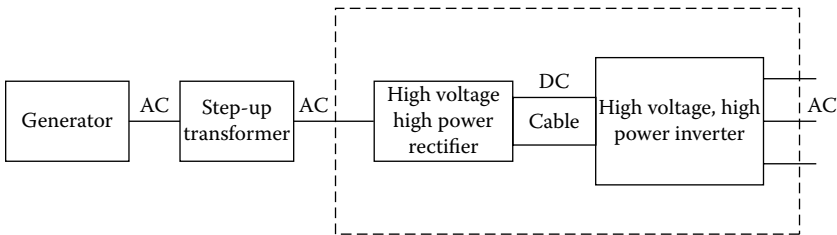**FIGURE 1.6** FACTS: series parallel compensator.

FIGURE 1.7 AC–DC–AC power cable transmission system.

of the game to be set. Also, the transient stresses on such a power grid, with many energy suppliers entering, exiting, or varying their input, are likely to be more severe. To counteract such a difficulty, more flexible power transmission lines were proposed and introduced in a few locations (mostly in the United States) under the logo "FACTS" (flexible alternating current [AC] transmission systems) [10].

FACTS introduces controlled reactive power capacitors in the power transmission lines in parallel for higher voltage stability (short-term voltage support), and in series for larger flow management in the long term (Figure 1.6). Power electronics at high power and voltage levels is the key technology to FACTS. FACTS also includes the AC–DC–AC power transmission lines to foster stability and reduce losses in energy transport over large distances (Figure 1.7).

The direct current (DC) high-voltage large power bus allows for parallel connection of energy providers with only voltage control; thus, the power grid becomes more flexible. However, this flexibility occurs at the price of full-power high-voltage converters that take advantage of the selective catalytic reduction (SCR) technologies.

Still, most electric generators are synchronous machines that need tight (rigid) speed control to provide constant frequency output voltage. To connect such generators in parallel, the speed controllers (governors) have to allow for a speed drop in order to produce balanced output of all generators. Of course, frequency also varies with load, but this variation is limited to less than 0.5 Hz.
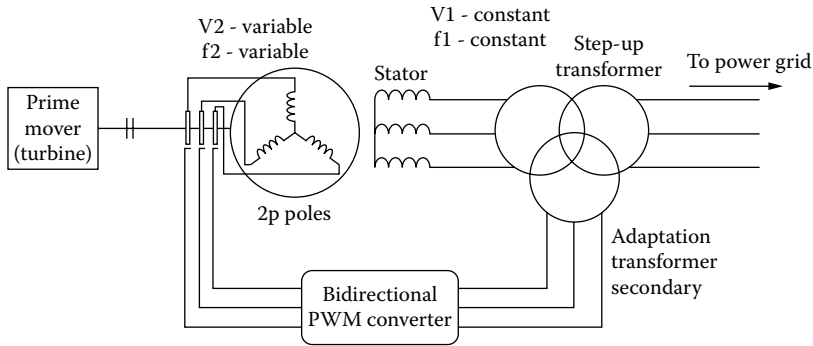
FIGURE 1.8 Variable-speed constant voltage and frequency generator.

Variable-speed constant voltage and frequency generators with decoupled active and reactive power control would make the power grids naturally more stable and more flexible.

The doubly fed induction generator (DFIG) with three-phase pulse-width modulator (PWM) bidirectional converter in the three-phase rotor circuit supplied through brushes and slip rings does just that (Figure 1.8). DFIG works as a synchronous machine. Fed in the rotor in AC at variable frequency f_2, and operating at speed n, it delivers power at the stator frequency f_1:

$$f_1 = np_1 + f_2 \tag{1.5}$$

where $2p_1$ is the number of poles of stator and rotor windings.

The frequency f_2 is considered positive when the phase sequence in the rotor is the same as that in the stator and negative otherwise. In the conventional synchronous generator, $f_2 = 0$ (DC). DFIG is capable of working at $f_2 = 0$ and at $f_2 <> 0$. With a bidirectional power converter, DFIG may work both as motor and generator with f_2 negative and positive — that is, at speeds lower and larger than that of the standard synchronous machine. Starting is initiated from the rotor, with the stator temporarily short-circuited, then opened. Then, the machine is synchronized and operated as a motor or a generator. The "synchronization" is feasible at all speeds within the design range (±20%, in general). So, not only the generating mode but also the pumping mode are available, in addition to flexibility in fast active and reactive power control.

Pump storage is used to store energy during off-peak hours and is then used for generation during peak hours at a total efficiency around 70% in large head hydropower plants.

DFIG units up to 400 MW with about ±5% speed variation were put to work in Japan, and more recently (in 300 MW units) in Germany. The converter rating is about equal to the speed variation range, which noticeably limits the costs. Pump storage plants with conventional synchronous machines working as motors have been in place for a few decades. DFIG, however, provides the optimum speed for pumping, which, for most hydroturbines, is different than that for generating.

While fossil-fuel DFIGs may be very good for power grids because of stability improvements, they are definitely the solution when pump storage is used and for wind generators above 1 MW per unit.

Will DFIG gradually replace the omnipresent synchronous generators in bulk electric energy conversion? Most likely, yes, because the technology is currently in use up to 400 MW/unit.

At the distribution (local) stage (Figure 1.5b), a new structure is gaining ground: the distributed power system (DPS). This refers to low-power energy providers that can meet or supplement some local power needs. DPS is expected to either work alone or be connected at the distribution stage to existing systems. It is to be based on renewable resources, such as wind, hydro, and biomass, or may integrate gas turbine generators or diesel engine generators, solar panels, or fuel cells. Powers in the orders of 1 to 2 MW, possibly up to 5 MW, per unit energy conversion are contemplated.

DPSs are to be provided with all means of control, stability, and power quality, that are so typical to conventional power grids. But, there is one big difference: they will make full use of power electronics to provide fast and robust active and reactive power control.

Here, besides synchronous generators with electromagnetic excitation, permanent magnet (PM) synchronous as well as cage-rotor induction generators and DFIGs, all with power electronics control for variable speed operation, are already in place in quite a few applications. But, their widespread usage is only about to take place.

Stand-alone electric power generation directly ties the electric energy generator to the load. Stand-alone systems may have one generator only (such as on board trains and standby power groups for automobiles) or may have two to four such generators, such as on board large aircraft or vessels. Stand-alone gas-turbine residential generators are also investigated for decentralized electricity production.

Stand-alone generators and their control are tightly related to application, from design to the embodiment of control and protection. Vehicular generators have to be lightweight and efficient, in this order. Standby (backup) power groups for hospitals, banks, telecommunications, and so forth, have to be quickly available, reliable, efficient, and environmentally friendly.

Backup power generators are becoming a must in public buildings, as all now use clusters of computers. Uninterruptible power supplies (UPSs) that are battery or fuel cell based, all with power electronics controls, are also used at lower powers. They do not include electric generators and, therefore, fall beyond the scope of our discussion.

Electric generators or motors are also used for mechanical energy storage, "inertial batteries" (Figure 1.9) in vacuum, with magnetic suspension to enable the storage of energy for minutes to hours. Speeds up to 1 km/sec (peripheral speed with composite material flywheels) at costs of $400 to $800 per kilowatt ($50 to $100 per kilowatt for lead acid batteries) for an operation life of over 20 years (3 to 5 years for lead acid batteries) [11] are feasible today.

PM synchronous generators or motors are ideal for uses at rotational speeds preferably around 40 krpm, for the 3 to 300 kW range and less for the megawatt range.
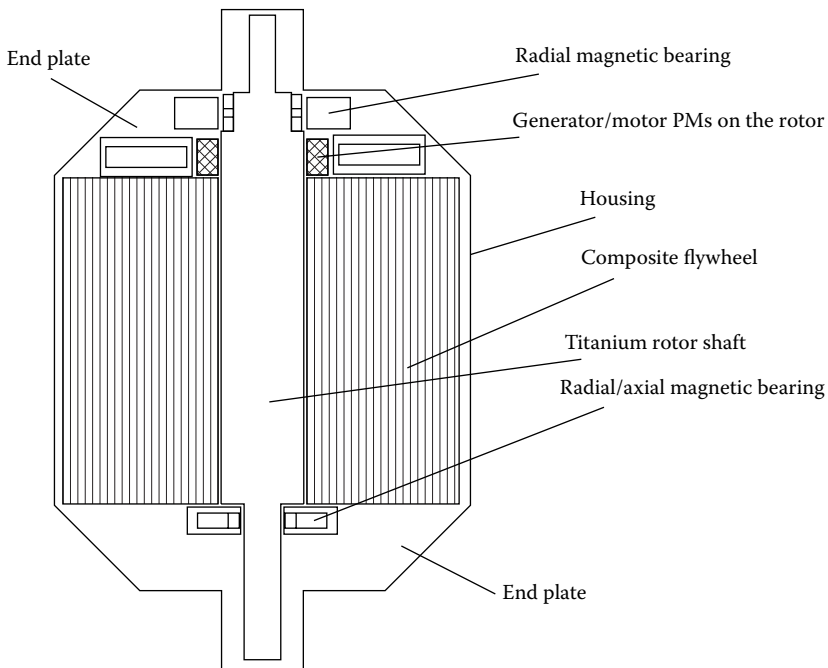

FIGURE 1.9 Typical flywheel battery.

Satellites, power quality (for active power control through energy storage), hybrid buses, trains (to store energy during braking), and electromagnetic launchers, are typical applications for storage generator and motor systems. The motoring mode is used to reaccelerate the flywheel (or charge the inertial battery) via power electronics.

Energy storage up to 500 MJ (per unit) is considered practical for applications that (at 50 Wh/kg density or more) need energy delivered in seconds or minutes at a time, for the duration of a power outage. As most (80%) power line disturbances last for less than 5 sec, flywheel batteries can fill up this time with energy as a standby power source. Though very promising, electrochemical and superconducting coil energy storage fall beyond the scope or our discussion here.

1.6   Summary

The above introductory study leads to the following conclusions:

- Electric energy demand is on the rise (at a rate of 2 to 3% per annum), but so are the environmental and social constraints on the electric energy technologies.
- Renewable resource input is on the rise — especially wind and hydro, at powers of up to a few megawatts per unit.
- Single-value power grids will change to bundled valued chains as electric energy opens to markets.
- Electric generators should work at variable speeds, but provide constant voltage and frequency output via power electronics with full or partial power ratings, in order to tap more energy from renewable resources and provide faster and safer reactive power control.
- The standard synchronous generator, working at constant speed for constant frequency output, is challenged by the doubly fed induction generator at high to medium power (from hundreds of megawatts to 1 to 2 MW) and by the PM synchronous generator and the induction generator with full power bidirectional power electronics in the stator up to 1 MW.
- Most variable-speed generators with bidirectional power electronics control will also allow motoring (or starting) operation in both conventional or distributed power grids and in stand-alone (or vehicular) applications.
- Home and industrial combined heat and electricity generation by burning gas in high-speed gas turbines requires special electric generators with adequate power electronics digital control.
- In view of such a wide power and unit and applications range, a classification of electric generators seems to be in order. This is the subject of Chapter 2.

References

1. B. Sadden, Hydropower development in southern and southeastern Asia, *IEEE Power Eng. Rev.*, 22, 3, March, 2002, pp. 5–11.
2. J.A. Veltrop, Future of dams, *IEEE Power Eng. Rev.*, 22, 3, March, 2002, pp. 12–18.
3. H.M. Turanli, Preparation for the next generation at Manitoba Hydro, *IEEE Power Eng. Rev.*, 22, 3, March, 2002, pp. 19–23.
4. O. Unver, Southeastern Anatolia development project, *IEEE Power Eng. Rev.*, 22, 3, March, 2002, pp. 10–11, 23–24.
5. H. Yang, and G. Yao, Hydropower development in Southern China, *IEEE Power Eng. Rev.*, 22, 3, March, 2002, pp. 16–18.
6. T.J. Hammons, J.C. Boyer, S.R. Conners, M. Davies, M. Ellis, M. Fraser, E.A. Nolt, and J. Markard, Renewable energy alternatives for developed countries, *IEEE Trans.*, EC-15, 4, 2000, pp. 481–493.
7. T.J. Hammons, B.K. Blyden, A.C. Calitz, A.G. Gulstone, E.I. Isekemanga, R. Johnstone, K. Paleku, N.N. Simang, and F. Taher, African electricity infrastructure interconnection and electricity exchanges, *IEEE Trans.*, EC-15, 4, 2000, pp. 470–480.

8. C. Lewiner, Business and technology trends in the global utility industries, *IEEE Power Eng. Rev.*, 21, 12, 2001, pp. 7–9.

9. M. Baygen, A vision of the future grid, *IEEE Power Eng. Rev.*, 21, 12, 2001, pp. 10–12.

10. A. Edris, FACTS technology development: an update, *IEEE Power Eng. Rev.*, 20, 3, 2000, pp. 4–9.

11. R. Hebner, J. Beno, and A. Walls, Flywheel batteries come around again, *IEEE-Spectrum*, 39, 4, 2002, pp. 46–51.

2

Principles of Electric Generators

The extremely large power/unit span, from milliwatts to hundreds of megawatts (MW) and more, and the wide diversity of applications, from electric power plants to car alternators, should have led to numerous electric generator configurations and controls. And, so it did. To bring order to our presentation, we need some classifications.

2.1   The Three Types of Electric Generators

Electric generators may be classified many ways, but the following are deemed as fully representative:

- By principle
- By application domain

The application domain implies the power level. The classifications by principle unfolded here include commercial (widely used) types together with new configurations, still in the laboratory (although advanced) stages.

   By principle, there are three main types of electric generators:

- Synchronous (Figure 2.1)
- Induction (Figure 2.2)
- Parametric, with magnetic anisotropy and permanent magnets (Figure 2.3)

Parametric generators have in most configurations doubly salient magnetic circuit structures, so they may be called also doubly salient electric generators.
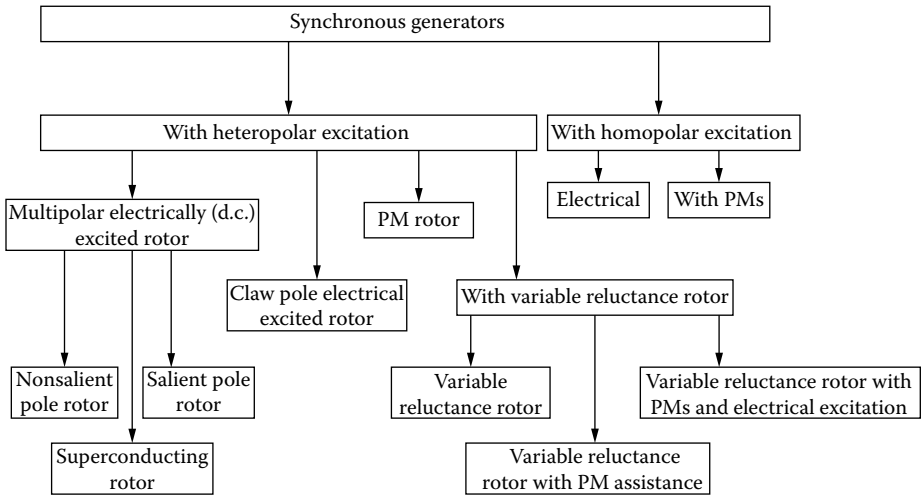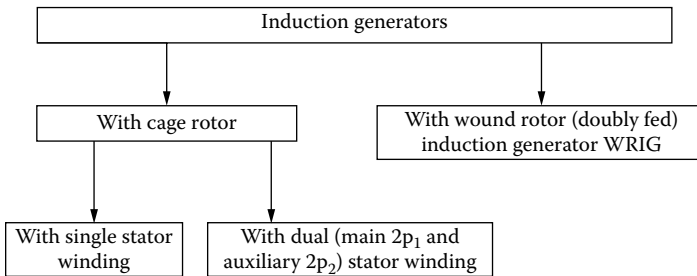
FIGURE 2.1   Synchronous generators.

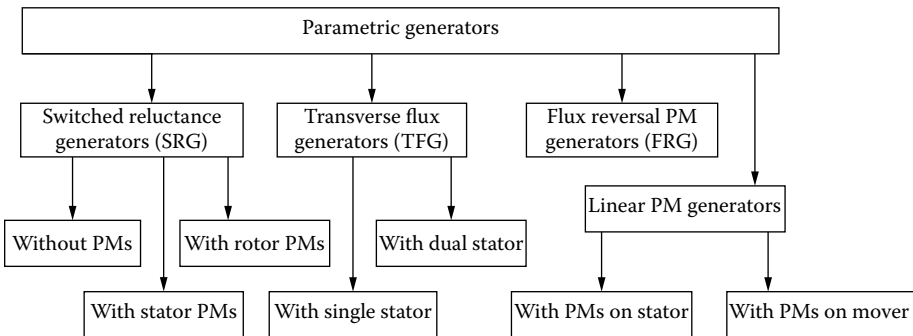**FIGURE 2.2**   Induction generators.

FIGURE 2.3   Parametric generators.

Synchronous generators [1–4] generally have a stator magnetic circuit made of laminations provided with uniform slots that house a three-phase (sometimes a single or a two-phase) winding and a rotor. It is the rotor design that leads to a cluster of synchronous generator configurations as seen in Figure 2.1.

They are all characterized by the rigid relationship between speed n, frequency f_1, and the number of poles $2p_1$:

$$n = {f \Big/ p_1} \tag{2.1}$$

Those that are direct current (DC) excited require a power electronics excitation control, while those with permanent magnets (PMs) or variable reluctance rotors have to use full-power electronics in the stator to operate at adjustable speeds. Finally, even electrically excited, synchronous generators may be provided with full-power electronics in the stator when they work alone or in power grids with DC high-voltage cable transmission lines.

Each of these configurations will be presented, in terms of its principles, later in this chapter.

For powers in the MW/unit range and less, induction generators (IGs) were also introduced. They are as follows (Figure 2.2):

- With cage rotor and single stator-winding
- With cage rotor and dual (main and additional) stator-winding with different number of poles
- With wound rotor

Pulse-width modulator (PWM) converters are connected to the stator (for the single stator-winding and, respectively, to the auxiliary stator-winding in the case of dual stator-winding).

The principle of the IG with single stator-winding relies on the following equation:

$$f_1 = p_1 n + f_2 \tag{2.2}$$

where

$\quad f_1 > 0$ = stator frequency
$\quad f_2 <> 0$ = slip (rotor) frequency
$\quad\quad n$ = rotor speed (rps)

The term f_2 may be either positive or negative in Equation 2.2, even zero, provided the PWM converter in the wound rotor is capable of supporting a bidirectional power flow for speeds n above f_1/p_1 and below f_1/p_1.

Notice that for $f_2 = 0$ (DC rotor excitation), the synchronous generator operation mode is reobtained with the doubly fed IG.

The slip S definition is as follows:

$$S = \frac{f_2}{f_1} <> 0 \tag{2.3}$$

The slip is zero, as $f_2 = 0$ (DC) for the synchronous generator mode.

For the dual stator-winding, the frequency–speed relationship is applied twice:

$$f_1 = p_1 n + f_2 ; p_2 > p_1$$
$$f_1' = p_2 n + f_2' \tag{2.4}$$

So, the rotor bars experience, in principle, currents of two distinct (rather low) frequencies f_2 and f_2'. In general, $p_2 > p_1$ to cover lower speeds.

The PWM converter feeds the auxiliary winding. Consequently, its rating is notably lower than that of the full power of the main winding, and it is proportional to the speed variation range.

As it may also work in the pure synchronous mode, the doubly fed IG may be used up to the highest levels of power for synchronous generators (400 MW units have been in use for some years in Japan) and a 2×300 MW pump storage plant is now commissioned in Germany.

On the contrary, the cage-rotor IG is more suitable for powers in the MW and lower power range.

Parametric generators rely on the variable reluctance principle, but may also use PMs to enhance the power and volume and to reduce generator losses.

There are quite a few configurations that suit this category, such as the switched reluctance generator (SRG), the transverse flux PM generator (TFG), and the flux reversal generator (FRG). In general, the principle on which they are based relies on coenergy variation due to magnetic anisotropy (with or without PMs on the rotor or on the stator), in the absence of a pure traveling field with constant speed (f_1/p), so characteristic for synchronous and IGs (machines).

2.2   Synchronous Generators

Synchronous generators (classifications are presented in Figure 2.1) are characterized by an uniformly slotted stator laminated core that hosts a three-, two-, or one-phase alternating current (AC) winding and a DC current excited, or PM-excited or variable saliency, rotor [1–5].

As only two traveling fields — of the stator and rotor — at relative standstill interact to produce a rippleless torque, the speed n is rigidly tied to stator frequency f_1, because the rotor-produced magnetic field is DC, typically heteropolar in synchronous generators.

They are built with nonsalient pole, distributed-excitation rotors (Figure 2.4) for $2p_1 = 2,4$ (that is, high speed or turbogenerators) or with salient-pole concentrated-excitation rotors (Figure 2.5) for $2p_1 > 4$ (in general, for low-speed or hydrogenerators).

As power increases, the rotor peripheral speed also increases. In large turbogenerators, it may reach more than 150 m/sec (in a 200 MVA machine $D_r = 1.2$ m diameter rotor at $n = 3600$ rpm, $2p_1 = 2$, $U = \pi D_r n = \pi \times 1.2 \times 3600/60 > 216$ m/sec). The DC excitation placement in slots, with DC coil end connections protected against centrifugal forces by rings of highly resilient resin materials, thus becomes necessary. Also, the DC rotor current airgap field distribution is closer to a sinusoid. Consequently, the
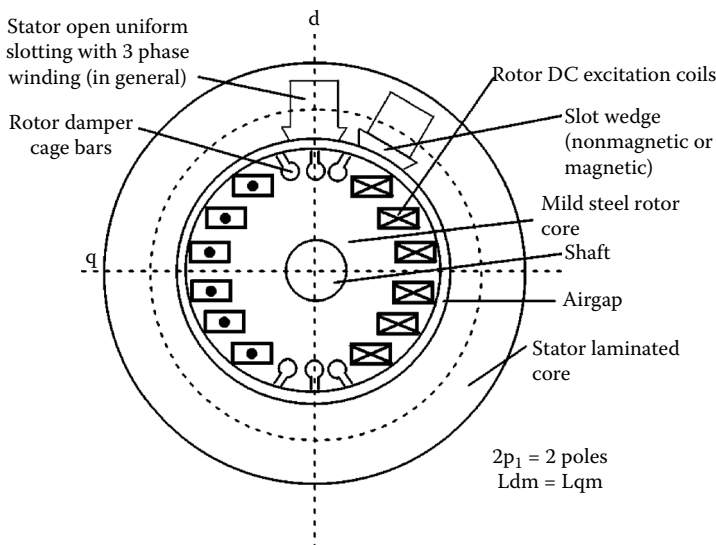

FIGURE 2.4   Synchronous generator with nonsalient pole heteropolar DC distributed excitation.
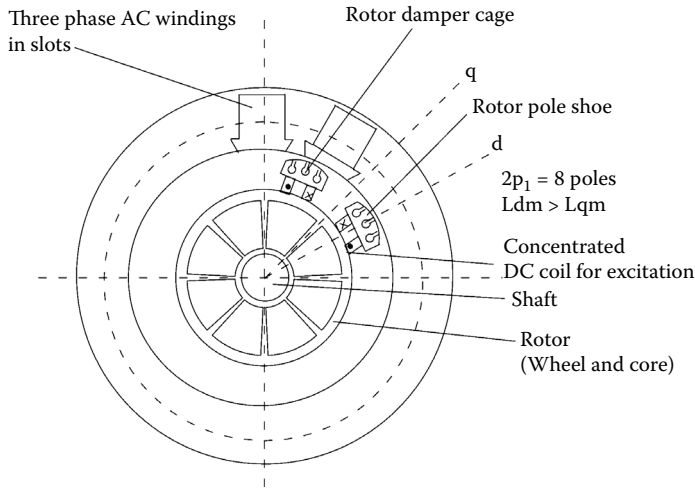
FIGURE 2.5 Synchronous generator with salient pole heteropolar DC concentrated excitation.

harmonics content of the stator-motion-induced voltage (electromagnetic force or no load voltage) is smaller, thus complying with the strict rules (standards) of large commercial power grids.

The rotor body is made of solid iron for better mechanical rigidity and heat transmission.

The stator slots in large synchronous generators are open (Figure 2.4 and Figure 2.5), and they are provided, sometimes, with magnetic wedges to further reduce the field space harmonics and thus reduce the electromagnetic force harmonics content and additional losses in the rotor damper cage. When $n = f_1/p_1$ and for steady state (sinusoidal symmetric stator currents of constant amplitude), the rotor damper cage currents are zero. However, should any load or mechanical transient occur, eddy currents show up in the damper cage to attenuate the rotor oscillations when the stator is connected to a constant frequency and voltage (high-power) grid.

The rationale neglects the stator magnetomotive force space harmonics due to the placement of windings in slots and due to slot openings. These space harmonics induce voltages and thus produce eddy currents in the rotor damper cage, even during steady state.

Also, even during steady state, if the stator phase currents are not symmetric, their inverse components produce currents of $2f_1$ frequency in the damper cage. Consequently, to limit the rotor temperature, the degree of current (load) unbalance permitted is limited by standards. Nonsalient pole DC excited rotor synchronous generators are manufactured for $2p_1 = 2, 4$ poles high-speed turbogenerators that are driven by gas or steam turbines.

For lower-speed synchronous generators with a large number of poles ($2p_1 > 4$), the rotors are made of salient rotor poles provided with concentrated DC excitation coils. The peripheral speeds are lower than those for turbogenerators, even for high-power hydrogenerators (for 200 MW 14 m rotor diameter at 75 rpm, and $2p_1 = 80$, $f_1 = 50$ Hz, the peripheral speed $U = \pi \times D_r \times n = \pi \times 14 \times 75/60 > 50$ m/sec). About 80 m/sec is the limit, in general, for salient pole rotors. Still, the excitation coils have to be protected against centrifugal forces.

The rotor pole shoes may be made of laminations, in order to reduce additional rotor losses, but the rotor pole bodies and core are made of mild magnetic solid steel.

With a large number of poles, the stator windings are built for a smaller number of slot/pole couplings: between 6 and 12, in many cases. The number of slots per pole and phase, q, is thus between two and four. The smaller the value of q, the larger the space harmonics present in the electromagnetic force. A fractionary q might be preferred, say 2.5, which also avoids the subharmonics and leads to a cleaner (more sinusoidal) electromagnetic force, to comply with the current standards.

The rotor pole shoes are provided with slots that house copper bars short-circuited by copper rings to form a rather complete squirrel cage. A stronger damper cage was thus obtained.
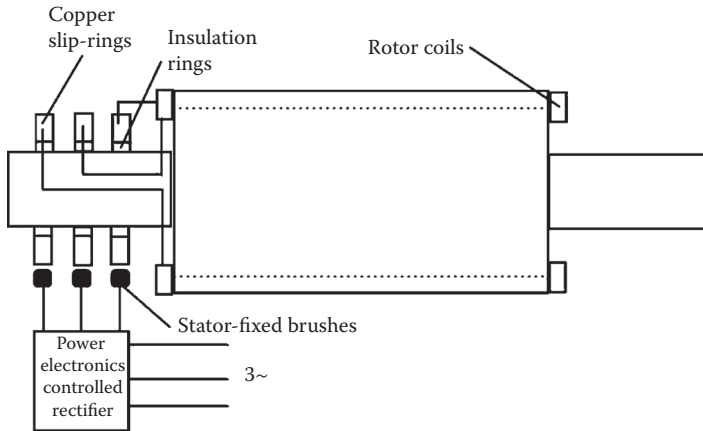
FIGURE 2.6 Slip-ring-brush power electronics rectifier DC excitation system.

DC excitation power on the rotor is transmitted by either:

- Copper slip-rings and brushes (Figure 2.6)
- Brushless excitation systems (Figure 2.7)

The controlled rectifier, with power around 3% of generator rated power, and with a sizable voltage reserve to force the current into the rotor quickly, controls the DC excitation currents according to the needs of generator voltage and frequency stability.

Alternatively, an inverted synchronous generator (with its three-phase AC windings and diode rectifier placed on the rotor and the DC excitation in the stator) may play the role of a brushless exciter (Figure 2.7). The field current of the exciter is controlled through a low-power half-controlled rectifier. Unfortunately, the electrical time constant of the exciter generator notably slows the response in the main synchronous generator excitation current control. Still another brushless exciter could be built around
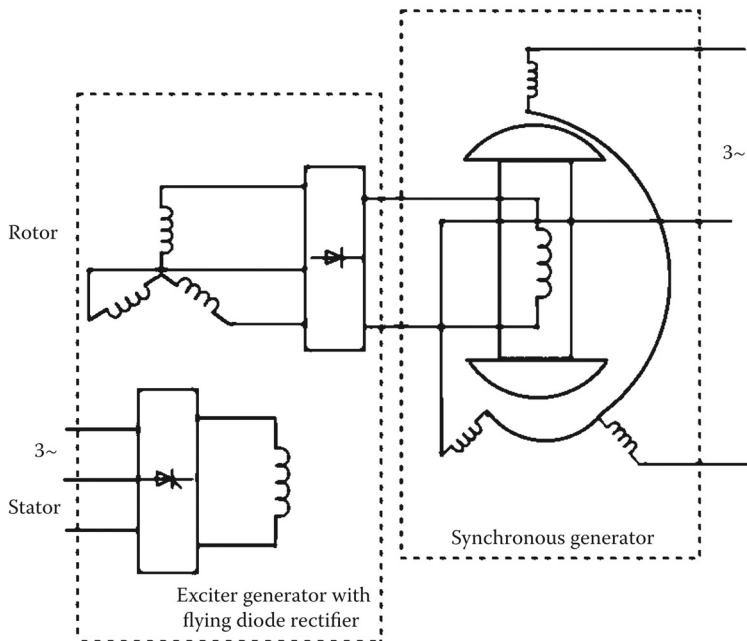

FIGURE 2.7 Brushless exciter with "flying diode" rectifier for synchronous generators.
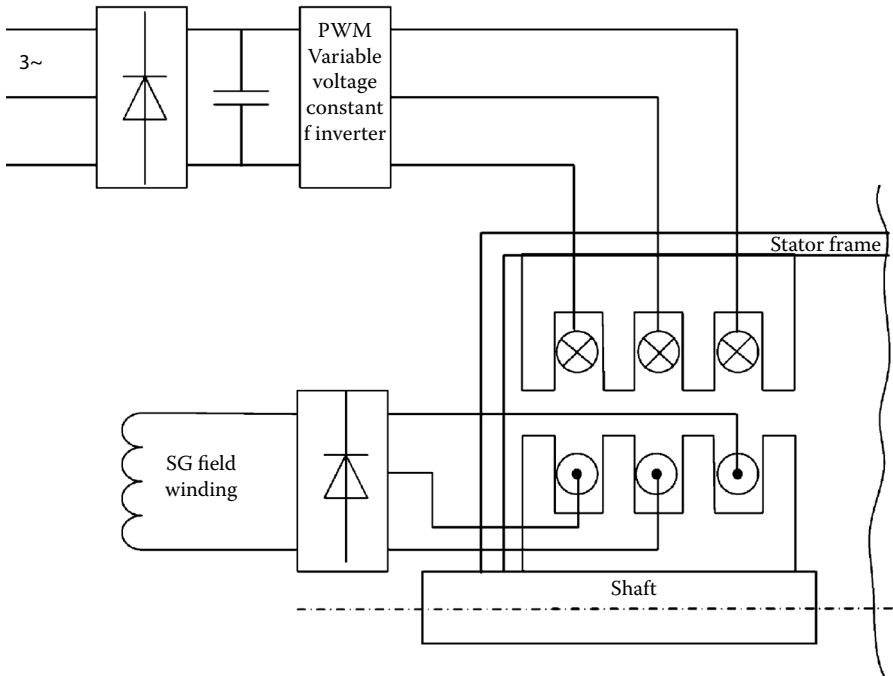
FIGURE 2.8 Rotating transformer with inverter in the rotor as brushless exciter.

a single-phase (or three-phase) rotating transformer working at a frequency above 300 Hz to cut its volume considerably (Figure 2.8). An inverter is required to feed the transformer, primarily at variable voltage but constant frequency. The response time in the generator's excitation current control is short, and the size of the rotating transformer is rather small. Also, the response in the excitation control does not depend on speed and may be used from a standstill.

Claw-pole (Lundell) synchronous generators are now built mainly for use as car alternators. The excitation winding power is reduced considerably for the multiple rotor construction ($2p_1 = 10, 12, 14$) to reduce external diameter and machine volume.

The claw-pole solid cast iron structure (Figure 2.9) is less costly to manufacture, while the single ring-shape excitation coil produces a multipolar airgap field (though with a three-dimensional field path) with reduced copper volume and DC power losses.

The stator holds a simplified three-phase single-layer winding with three slots per pole, in general. Though slip-rings and brushes are used, the power transmitted through them is small (in the order of 60 to 200 W for car and truck alternators); thus, low-power electronics are used to control the output. The total cost of the claw-pole generator for automobiles, including field current control and the diode full-power rectifier, is low, and so is the specific volume.

However the total efficiency, including the diode rectifier and excitation losses, is low at 14 V DC output: below 55%. To blame are the diode losses (at 14 V DC), the mechanical losses, and the eddy currents induced in the claw poles by the space and time harmonics of the stator currents magnetomotive force. Increasing the voltage to 42 V DC would reduce the diode losses in relative terms, while the building of the claw poles from composite magnetic materials would notably reduce the claw-pole eddy current losses. A notably higher efficiency would result, even if the excitation power might slightly increase, due to the lower permeability ($500 \mu_0$) of today's best composite magnetic materials. Also, higher power levels might be obtained.

The concept of a claw-pole alternator may be extended to the MW range, provided the number of poles is increased (at 50/60 Hz or more) in variable speed wind and microhydrogenerators with DC-controlled output voltage of a local DC bus.
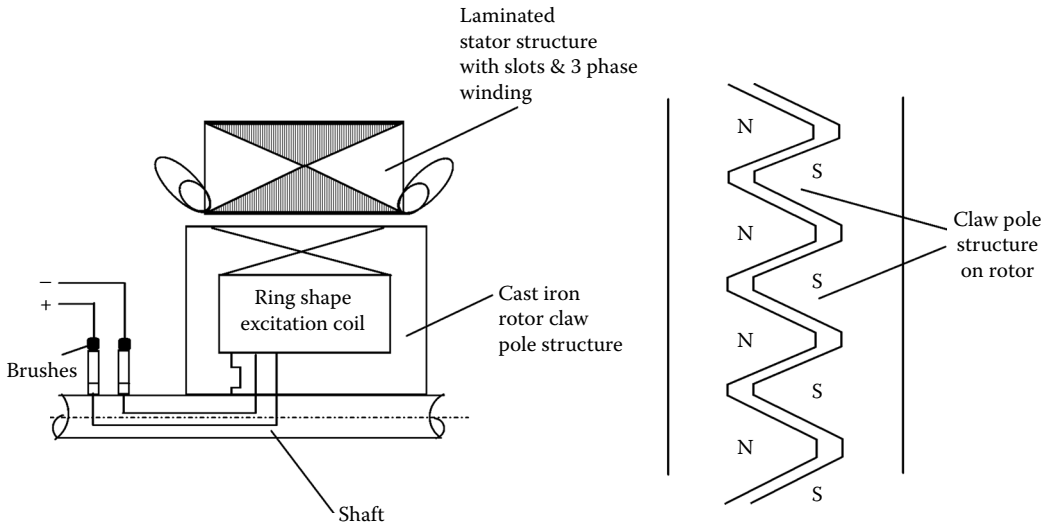
FIGURE 2.9   The claw-pole synchronous generator.

Though the claw-pole synchronous generator could be built with the excitation on the stator, to avoid brushes, the configuration is bulky, and the arrival of high-energy PMs for rotor DC excitation has put it apparently to rest.

2.3   Permanent Magnet Synchronous Generators

The rapid development of high-energy PMs with a rather linear demagnetization curve led to widespread use of PM synchronous motors for variable speed drives [6–10]. As electric machines are reversible by principle, the generator regime is available, and, for direct-driven wind generators in the hundreds of kilowatt or MW range, such solutions are being proposed. Super-high-speed gas-turbine-driven PM synchronous generators in the 100 kW range at 60 to 80 krpm are also introduced. Finally, PM synchronous generators are being considered as starter generators for the cars of the near future.

There are two main types of rotors for PM synchronous generators:

- With rotor surface PMs (Figure 2.10) — nonsalient pole rotor (SPM)
- With interior PMs (Figure 2.11a through Figure 2.11c) — salient pole rotor (IPM)

The configuration in Figure 2.10 shows a PM rotor made with parallelepipedic PM pieces such that each pole is patched with quite a few of them, circumferentially and axially.

The PMs are held tight to the solid (or laminated) rotor iron core by special adhesives, and a highly resilient resin coating is added for mechanical rigidity.

The stator contains a laminated core with uniform slots (in general) that house a three-phase winding with distributed (standard) coils or with concentrated (fractionary) coils.

The rotor is practically isotropic from the magnetic point of view. There is some minor difference between the d and the q axis magnetic permeances, because the PM recoil permeability ($\mu_{rec} = (1.04 - 1.07)\ \mu_0$ at 20°C) increases somewhat with temperature for NeFeB and SmCo high-energy PMs.

So, the rotor may be considered as magnetically nonsalient (the magnetization inductances L_{dm} and L_{qm} are almost equal to each other).

To protect the PMs, mechanically, and to produce reluctance torque, the interior PM pole rotors were introduced. Two typical configurations are shown in Figure 2.11a through Figure 2.11c.

Figure 2.11a shows a practical solution for two-pole interior PM (IPM) rotors. A practical $2p_1 = 4,6,\ldots$ IPM rotor as shown in Figure 2.11b has an inverse saliency: $L_{dm} < L_{qm}$, as is typical with IPM machines.
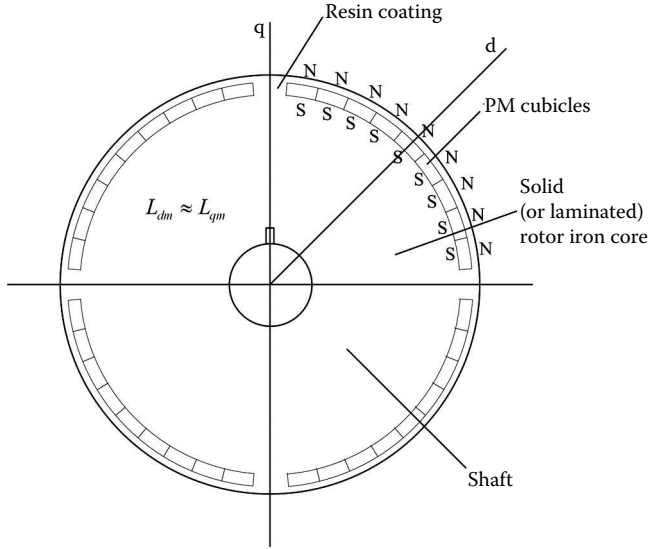
FIGURE 2.10 Surface PM rotor ($2p_1$ = four poles).

Finally, a high-saliency rotor ($L_{dm} > L_{qm}$), obtained with multiple flux barriers and PMs acting along axis *q* (rather than axis *d*), is presented in Figure 2.11c. It is a typical IPM machine but with large magnetic saliency. In such a machine, the reluctance torque may be larger than the PM interactive torque. The PM field first saturates the rotor flux bridges and then overcompensates the stator-produced field in axis *q*. This way, the stator flux along the *q* axis decreases with current in axis *q*. For flux weakening, the I_d current component is reduced. A wide constant power (flux weakening) speed range of more than 5:1 was obtained this way. Starters/generators on cars are a typical application for this rotor.

As the PM's role is limited, lower-grade (lower B_r) PMs, at lower costs, may be used.

It is also possible to use the variable reluctance rotor with high magnetic saliency (Figure 2.11a) without permanent magnets. With the reluctance generator, either power grid or stand-alone mode operation is feasible. For stand-alone operation, capacitor self-excitation is needed. The performance is moderate, but the rotor cost is also moderate. Standby power sources would be a good application for reluctance synchronous generators with high saliency $L_{dm}/L_{qm} > 4$.

PM synchronous generators are characterized by high torque (power) density and high efficiency (excitation losses are zero). However, the costs of high-energy PMs are still up to $100 per kilogram. Also, to control the output, full-power electronics are needed in the stator (Figure 2.12).

A bidirectional power flow pulse-width modulator (PWM) converter, with adequate filtering and control, may run the PM machine either as a motor (for starting the gas turbine) or as a generator, with controlled output at variable speed. The generator may work in the power-grid mode or in stand-alone mode. These flexibility features, together with fast power-active and power-reactive decoupled control at variable speed, may make such solutions a way of the future, at least in the tens and hundreds of kilowatts range.

Many other PM synchronous generator configurations were introduced, such as those with axial airgap. Among them, we will mention one that is typical in the sense that it uses the IPM reluctance rotor (Figure 2.11c), but it adds an electrical excitation. (Figure 2.13) [11].

In addition to the reluctance and PM interaction torque, there will be an excitation interaction torque. The excitation current may be positive or negative to add or subtract from I_d current component in the stator. This way, at low speeds, the controlled positive field current will increase and control the output voltage, while at high speeds, a negative field current will suppress the electromagnetic torque, when needed, to keep the voltage constant.

For DC-controlled output only a diode rectifier is necessary, as the output voltage is regulated via DC current control in four quadrants. A low-power four-quadrant chopper is needed. For wide speed
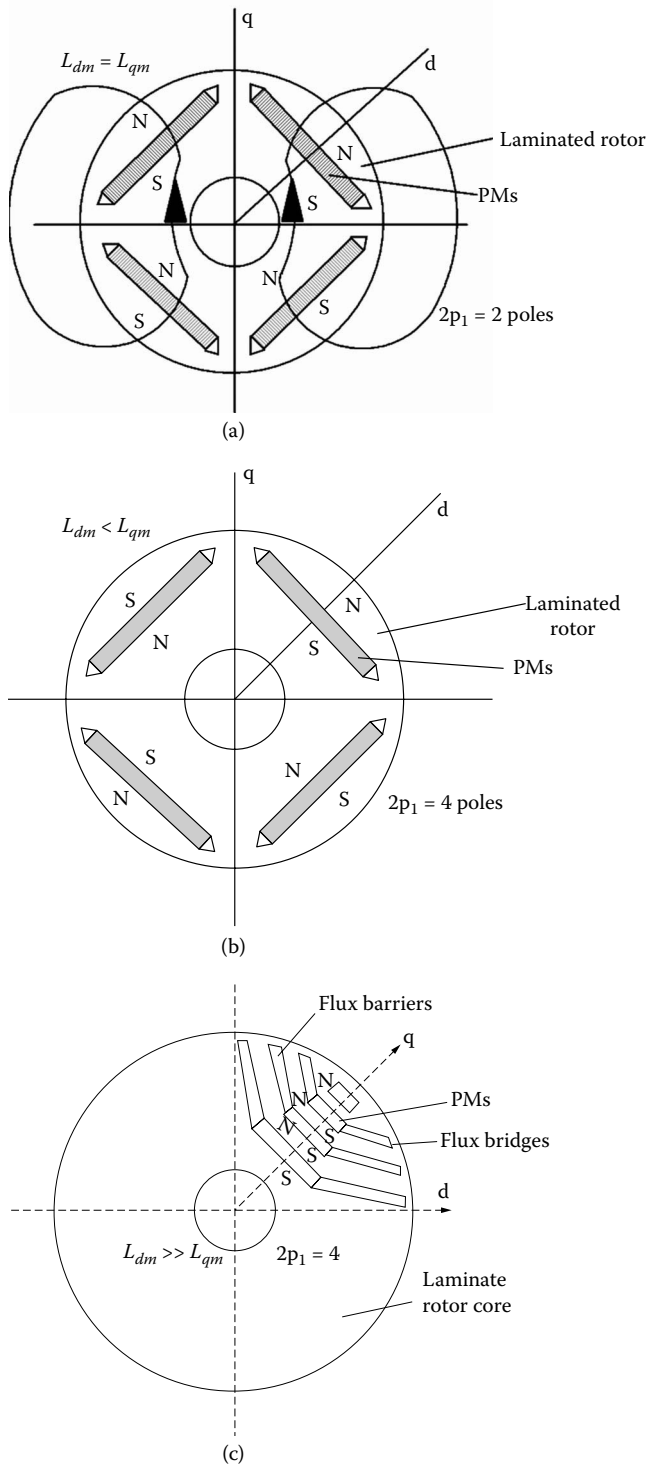
(a)

(b)

(c)

FIGURE 2.11 Interior PM rotors: (a) $2p_1 = 2$ poles, (b) $2p_1 = 4$, and (c) with rotor flux barriers (IPM – reluctance).
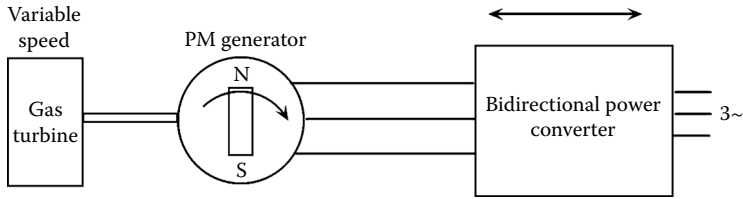
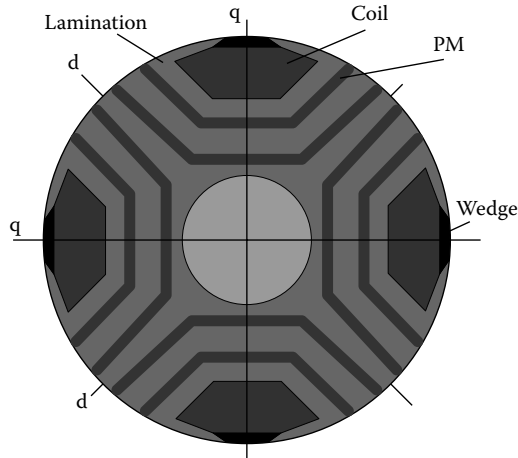**FIGURE 2.12** Bidirectional full-power electronics control.

FIGURE 2.13 Biaxial excitation PM reluctance rotor generator (biaxial excitation generator for automobiles [BEGA]).

range applications such a hybrid excitation rotor may be a competitive solution. The rotor is not very rugged mechanically, but it can easily handle peripheral speeds of up to 50 m/sec (10,000 rpm for 0.1 m diameter rotor).

2.4 The Homopolar Synchronous Generator

Placing both the DC excitation coils and the three-phase AC winding on the stator characterizes the so-called homopolar (or inductor) synchronous machine (generator and motor; see Figure 2.14a through Figure 2.14c).

The rather rugged rotor with solid (even laminated) salient poles and solid core is an added advantage. The salient rotor poles (segments) and interpoles produce a salient magnetic structure with a notable saliency ratio, especially if the airgap is small.

Consequently, the magnetic field produced by the DC field current closes paths, partially axially and partially circumferentially, through stator and rotor, but it is tied (fixed) to the rotor pole axis.

It is always maximum in the axis of rotor poles and small, but of the same polarity, in the axis of interpoles. An AC airgap magnetic component is present in this homopolar distribution. Its peak value is ideally 50% of maximum airgap field of the DC excitation current. Fringing reduces it 35 to 40% (Figure 2.14a through Figure 2.14c), at best.

The machine is a salient pole machine with doubled airgap, but it behaves as a nonsalient pole rotor one and with rotor excitation.

So, for the same airgap flux density fundamental B_{g1} (Figure 2.14a through Figure 2.14c), the same mechanical airgap, the DC magnetomotive force of the field winding is doubled, and the power loss quadruples. However, the ring-shaped coil reduces the copper weight and losses (especially when the
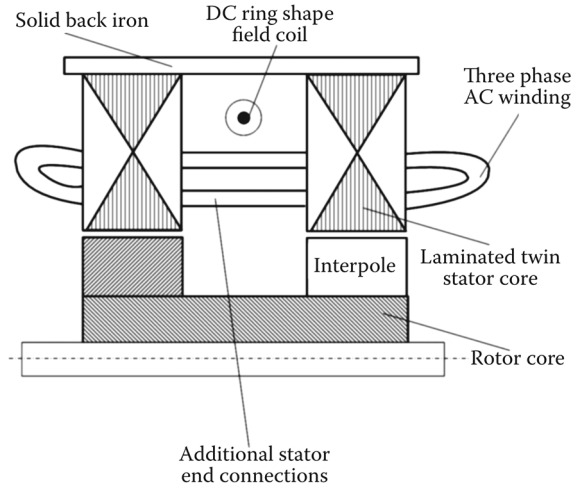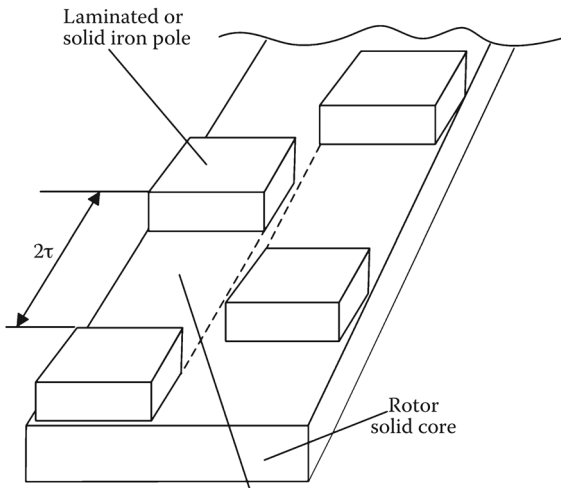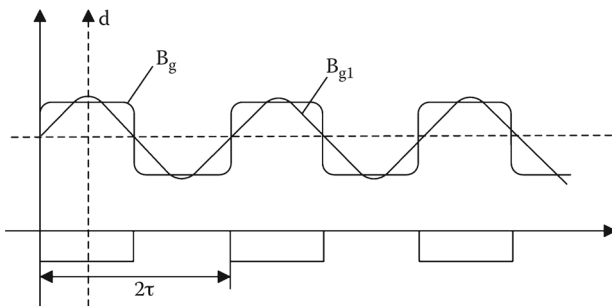
FIGURE 2.14 The homopolar synchronous generator: (a) and (b) the geometry and (c) airgap excitation field distribution.

FIGURE 2.15 Cage-rotor induction generator: (a) at power grid: $V_1 = ct$, $f_1 = ct$, and (b) stand-alone (capacitor excited): V_1, f_1, variable with speed and load.

number of poles increases) in comparison with a multipolar heteropolar DC rotor excitation system. The blessing of circularity comes into place here. We also have to note the additional end connection in the middle of the stator AC three-phase winding, between the two slotted laminated cores.

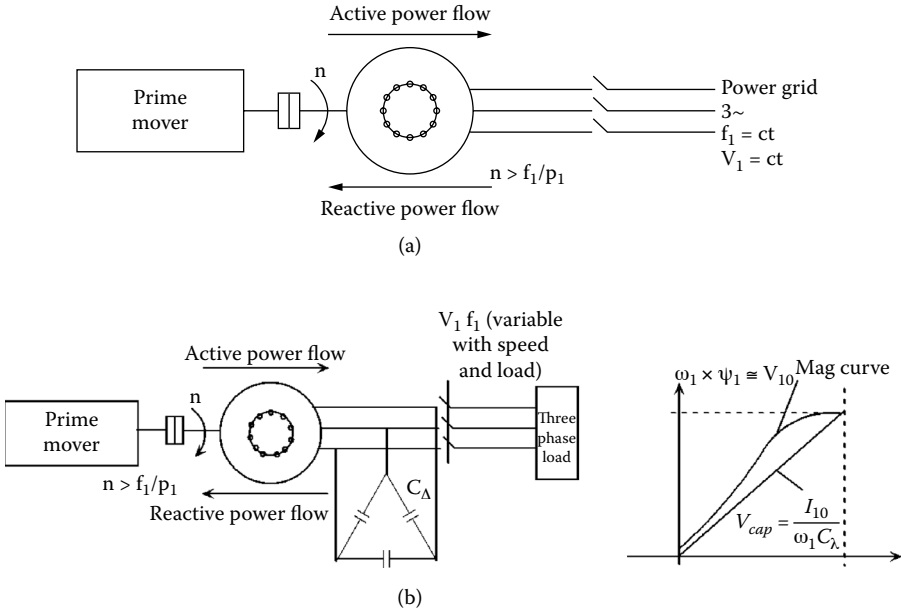The rotor mechanical ruggedness is superior only with solid iron poles when made in one piece. Unfortunately, stator magnetomotive force and slot space harmonics induce eddy currents in the rotor solid poles, notably reducing the efficiency, typically below 90% in a 15 kW, 15,000 rpm machine.

2.5 Induction Generator

The cage-rotor induction machine is known to work as a generator, provided the following:

- The frequency f_1 is smaller than $n \times p_1$ (speed $\times$ pole pairs): $S < 0$ (Figure 2.15a).
- There is a source to magnetize the machine.

An induction machine working as a motor, supplied to fixed frequency and voltage f_1, V_1 power grid becomes a generator if it is driven by a prime mover above no load ideal speed f_1/p_1:

$$n > \frac{f_1}{p_1} \tag{2.5}$$

Alternatively, the induction machine with the cage rotor may self-excite on a capacitor at its terminals (Figure 2.15b).

For an IG connected to a strong (constant frequency and voltage) power grid, when the speed n increases (above f_1/p_1), the active power delivered to the power grid increases, but so does the reactive power drawn from the power grid.

Many existing wind generators use such cage-rotor IGs connected to the power grid. The control is only mechanical. The blade pitch angle is adjusted according to wind speed and power delivery requirements. However, such IGs tend to be rigid, as they are stable only until n reaches the following value:

$$n_{\max} = \frac{f_1}{p_1}\left(1+\left|S_K\right|\right) \tag{2.6}$$

where S_K is the critical sleep, which decreases with power and is, anyway, below 0.08 for IGs in the hundreds of kilowatts. Additional parallel capacitors at the power grid are required to compensate for the reactive power drained by the IG.

Alternatively, the reactive power may be provided by parallel (plus series) capacitors (Figure 2.15b). In this case, we have a self-excitation process that requires some remanent flux in the rotor (from previous operation) and the presence of magnetic saturation (Figure 2.15b). The frequency f_1 of self-excitation voltage (under no load) depends on the capacitor value and on the magnetization curve of the induction machine $\Psi_1(I_{10})$:

$$V_{10} \approx \psi_1(I_{10})\cdot 2\cdot\pi\cdot f_1 \approx V_{C_Y} = I_{10}\frac{3}{C_\Delta\cdot 2\cdot\pi\cdot f_1} \tag{2.7}$$

The trouble is that on load, even if the speed is constant through prime mover speed control, the output voltage and frequency vary with load. For constant speed, if frequency reduction under a load of 1 Hz is acceptable, voltage control suffices. A three-phase AC chopper (Variac™) supplying the capacitors would do it, but the harmonics introduced by it have to be filtered out. In simple applications, a combination of parallel and series capacitors would provide constant (with 3 to 5% regulation) voltage up to rated load.

Now, if variable speed is to be used, then, for constant voltage and frequency, PWM converters are needed. Such configurations are illustrated in Figure 2.16a and Figure 2.16b. A bidirectional power flow PWM converter (Figure 2.16a) provides both generating and motoring functions at variable speed. The capacitor in the DC line of the converter may lead not only to active, but also to reactive, power delivery. Connection to the power grid without large transients is implicit, and so is fast, decoupled, active, and reactive power control.

The stand-alone configuration in Figure 2.16b is less expensive, but it provides only unidirectional power flow. A typical V_1/f_1 converter for drives is used. It is possible to inverse the connections, that is, to connect the diode rectifier and capacitors to the grid and the converter to the machine. This way, the system works as a variable speed drive for pumping and so forth, if a local power grid is available. This commutation may be done automatically, but it would take 1 to 2 min. For variable speed, in a limited range, an excitation capacitor in two stages would provide the diode rectifier with only slightly variable DC link voltage. Provided the minimum and maximum converter voltage limits are met, the former would operate over the entire speed range. Now, the converter is V_1/f_1 controlled for constant voltage and frequency.

A transformer (Y, Y_0) may be needed to accommodate unbalanced (or single-phase) loads.

The output voltage may be close-loop controlled through the PWM converter. On the other end, the bidirectional PWM converter configuration may be provided with a reconfigurable control system so as to work not only on the power grid, but also to separate itself smoothly to operate as a stand-alone or to wait on standby and then be reconnected smoothly to the power grid. Thus, multifunctional power generation at variable speed is produced. As evident in Figure 2.16a and Figure 2.16b, full-power electronics are required. For a limited speed range, say up to 25%, it is possible to use two IGs with cage-rotor and different pole numbers $(2p_2/2p_1 = 8/6, 5/4, 4/3....)$. The one with more poles $(2p_2 > 2p_1)$ is rated at 25% of rated power and is fed from a bidirectional power converter sized also at about 25%. The scheme works at the power grid (Figure 2.17).

The soft-starter reduces the synchronization transients and disconnects the 100% IG when the power required is below 25%. Then, the 25% IG remains alone at work, at variable speed $(n < f_1/p_1)$, to tap the energy available from (for example) low-speed wind or from a low-head microhydroturbine. Also, above 25% load, when the main (100%) IG works, the 25% IG may add power as generator or work in motoring
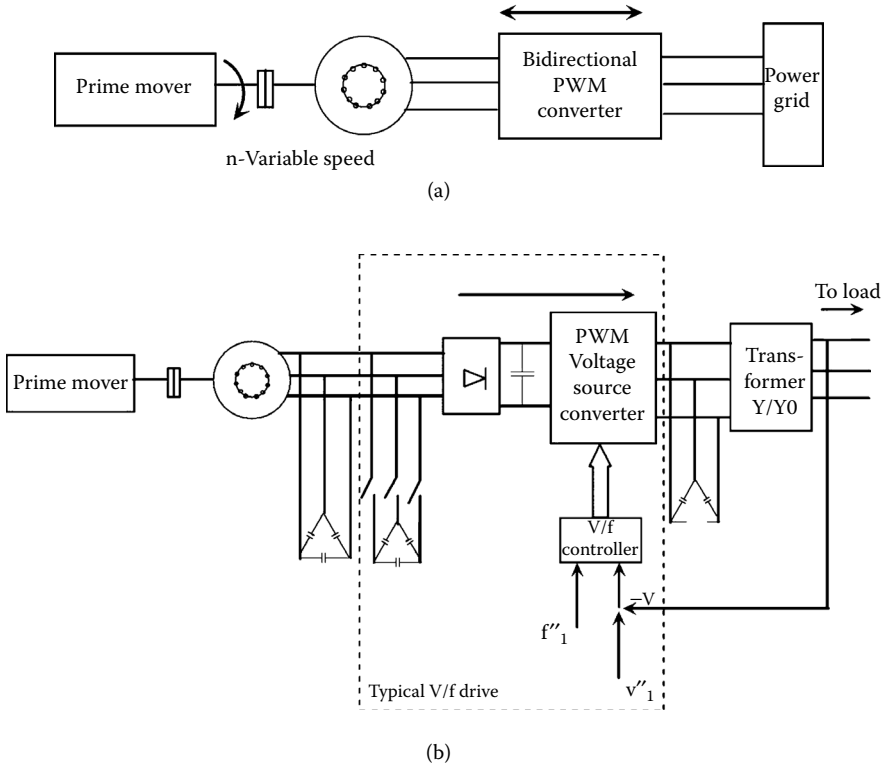
FIGURE 2.16 Cage-rotor induction generators for variable speed: (a) at power grid $V_1 = ct.$, $f_1 = ct.$, and (b) standalone $V_1'' = ct.$, $f_1'' = ct.$ (controlled).
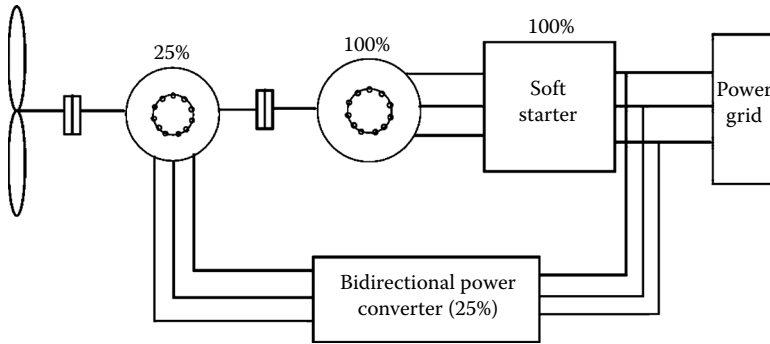
FIGURE 2.17 Dual-induction generator system for limited speed variation range.

for better dynamics and stability. Now, we may imagine a single rotor-stator IG with two separate stator windings ($2p_2 > 2p_1$) to perform the same task.

The reduction in rating, from 100% to 25%, of the bidirectional PWM converter is noteworthy.

The main advantage of the dual IG or dual-stator winding IG is lower cost, although the cost is for lower performance (low-speed range above f_1/p_1).

2.6 The Wound Rotor (Doubly Fed) Induction Generator (WRIG)

It all started between 1907 and 1913, with the Scherbius and Kraemer cascade configurations, which are both slip-power recovery schemes of wound-rotor induction machines. Leonhard analyzed it pertinently
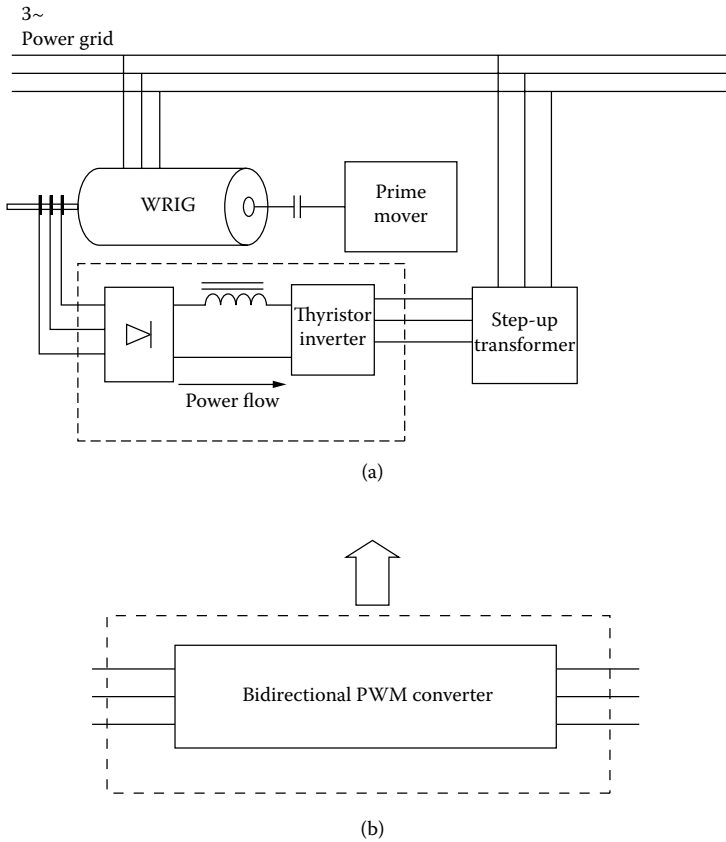
FIGURE 2.18 Wound rotor induction generator (WRIG): (a) with diode rectifier (slip recovery system), and (b) with bidirectional pulse-width modulator (PWM) converter.

in 1928, but adequate power electronics for it were not available by then. A slip recovery scheme with thyristor power electronics is shown in Figure 2.18a. Unidirectional power flow, from IG rotor to the converter, is only feasible because of the diode rectifier. A step-up transformer is necessary for voltage adaption, while the thyristor inverter produces constant voltage and frequency output. The principle of operation is based on the frequency theorem of traveling fields.

$$f_1 = np_1 + f_2; f_2 \lessgtr 0 \text{ , and variable } f_1 = ct \tag{2.8}$$

Negative frequency means that the sequence of rotor phases is different from the sequence of stator phases. Now if f_2 is variable, n may also be variable, as long as Equation 2.8 is fulfilled.

That is, constant frequency f_1 is provided in the stator for adjustable speed. The system may work at the power grid or even as a stand-alone, although with reconfigurable control. When $f_2 > 0$, $n < f_1/p_1$, we have subsynchronous operation. The case for $f_2 < 0$, $n > f_1/p_1$ corresponds to hypersynchronous operation. Synchronous operation takes place at $f_2 = 0$, which is not feasible with the diode rectifier current source inverter, but it is feasible with the bidirectional PWM converter.

The slip recovery system can work as a subsynchronous ($n < f_1/p$) motor or as a supersynchronous ($n > f_1/p$) generator. The WRIG with bidirectional PWM converter may work as a motor and generator for both subsynchronous and supersynchronous speed. The power flow directions for such a system are shown in Figure 2.19a and Figure 2.19b.

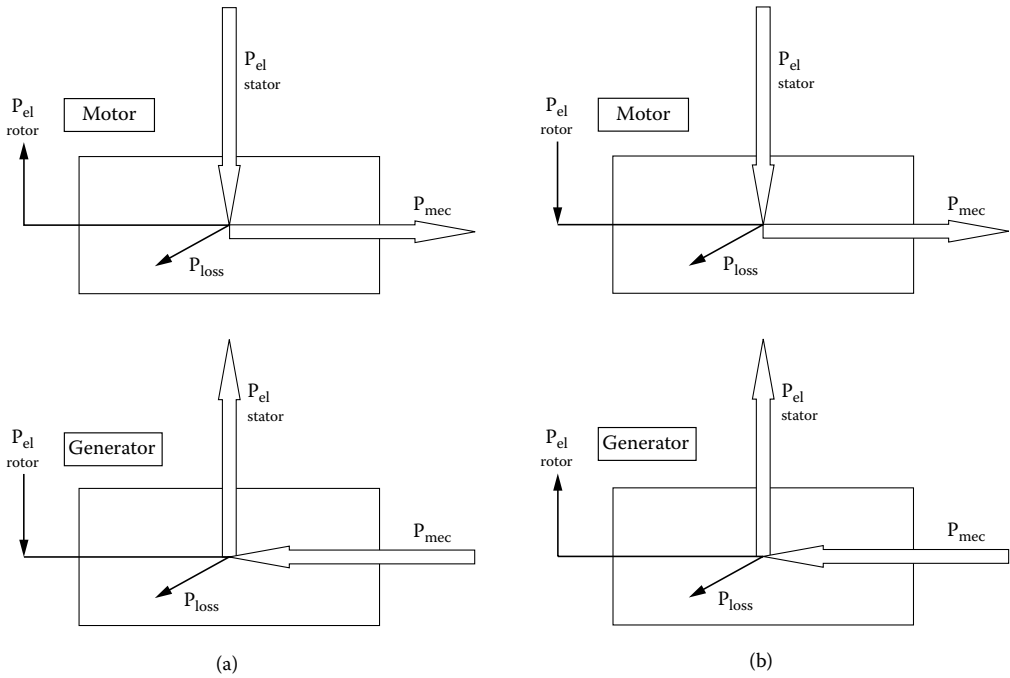The converter rating is commensurable to speed range, that is, to maximum slip S_{max}:

FIGURE 2.19 Operation modes of wound rotor induction generator (WRIG) with bidirectional pulse-width modulator (PWM) converter (in the rotor): (a) $S < 0$ and (b) $S > 0$.

$$KVA_{rating} = K\,\frac{f_{2\max}}{f_1}\times 100\big[\,\%\,\big] \tag{2.9}$$

$K = 1–1.4$ depending on the reactive power requirements from the converter

Notice that, being placed in the rotor circuit, through slip-rings and brushes, the converter rating is around $|S_{max}|$ in percent. The larger the speed range, the larger the rating and the costs of the converter. Also, the fully bidirectional PWM converter — as a back-to-back voltage source multilevel PWM converter system — may provide fast and continuous decoupled active and reactive power control operation, even at synchronism ($f_2 = 0$, DC rotor excitation). And, it may perform the self-starting as well. The self-starting is done by short-circuiting the stator, previously disconnected from the power grid, and supplying the rotor through the PWM converter in the subsynchronous motoring mode. The rotor accelerates up to a prescribed speed corresponding to $f_2 > f_1(1 - S_{max})$. Then, the stator winding is opened and, with the rotor freewheeling, the stator no load voltage, sequence and frequency are adjusted to coincide with that of the power grid, by adequate PWM converter control. Finally, the stator winding is connected to the power grid without notable transients.

This kind of rotor-starting procedure requires $f_2 \approx (0.8 - 1)f_1$, which means that the standard cyclo-converter is out of the question. So, it is only the back-to-back voltage PWM multilevel converter or the matrix converter that is suitable for full exploitation of motoring/generating at sub- and supersynchronous speeds, so typical in pump storage applications.

2.7 Parametric Generators

Parametric generators exploit the magnetic anisotropy of both stator and rotor. PMs may be added on the stator or on the rotor. Single magnetic saliency with PMs on the rotor is also used in some configurations. Parametric generators use nonoverlapping (concentrated) windings to reduce end-connection
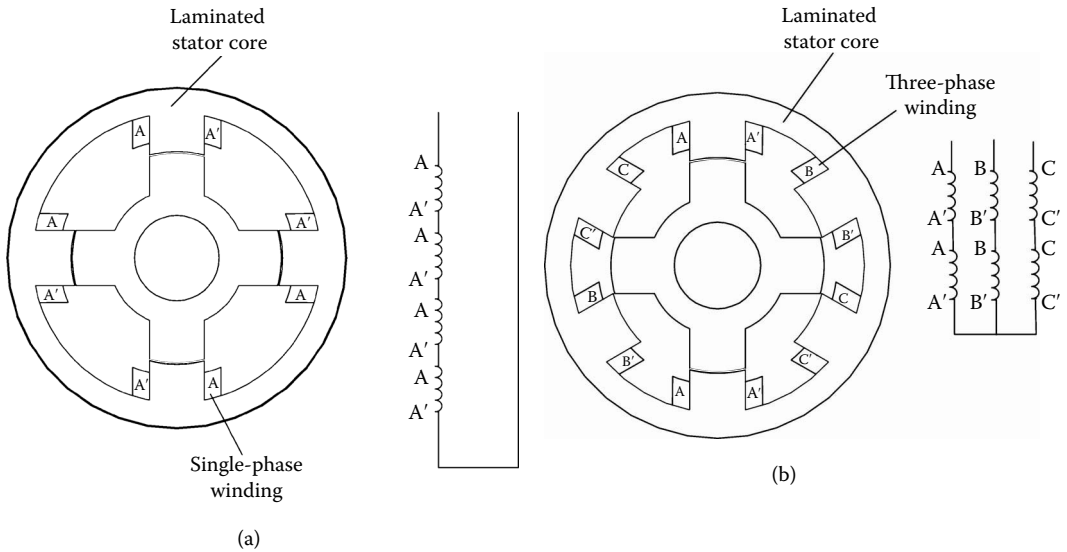
FIGURE 2.20 Switched reluctance generators (SRGs): (a) single-phase: 4/4 (4 × 4 poles) and (b) three-phase: 6/4 (6 × 4 poles).

copper losses on the stator. As the stator magnetomotive force does not produce a pure traveling field, there are core losses both in the stator and in the rotor. The simplicity and ruggedness of such generators make them adequate for use in some applications.

Among parametric generators, some of the most representative are detailed here:

- The switched reluctance generators (SRGs):
  - Without PMs
  - With PMs on the stator or on the rotor
- The transverse flux generators (TFGs):
  - With rotor PMs
  - With stator PMs
- The flux reversal generators (FRGs):
  - With PMs on the stator
  - With PMs on the rotor (and flux concentration)
- The linear motion alternators (LMAs):
  - With coil mover and PMs on the stator
  - With PM mover, tubular or flat (with PM flux concentration)
  - With iron mover and PMs on the stator

The SRG [12] has a double saliency magnetic laminated structure — on the stator and rotor — and concentrated coils on the stator (Figure 2.20a and Figure 2.20b). The stator phases are PWM voltage fed as long as the rotor poles are approaching them, one at a time, for the three-phase configuration. The phase inductances vary with rotor position (Figure 2.21a and Figure 2.21b) and, at least for the three-phase configuration, there is little magnetic coupling between phases.

Eventually, each phase is turned on around point A (in Figure 2.21a and Figure 2.21b); then it magnetizes the phase, and the dL/dθ effect produces a motion-induced voltage (electromagnetic force) which, in interaction with the phase current, produces torque. The phase is turned off around point B, when the next phase is turned on. The current polarity is not relevant; thus, positive current is flowed through voltage PWM. The maximum voltage is applied until the phase current magnetizes to maximum admitted current.
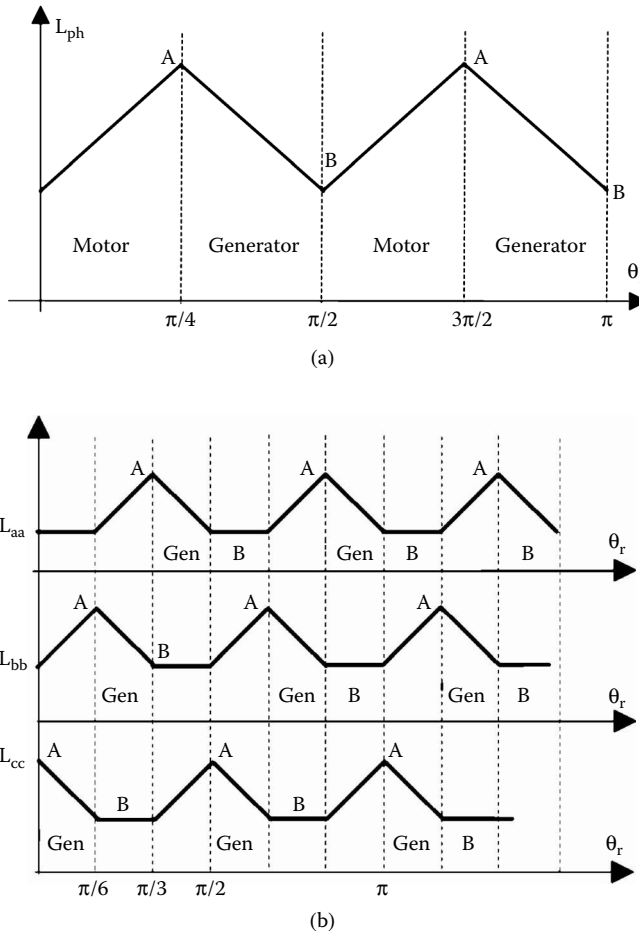
FIGURE 2.21 Phase inductance vs. rotor position: (a) the single-phase 4/4 switched reluctance generator (SRG) and (b) the three-phase 6/4 SRG.

As part of the AB interval available for generating is lost to the magnetization process, the latter takes up around 30% of energy available per cycle. For the single-phase machine, the torque, as expected, has notches, as only the negative slopes of the inductance are adequate for generating.

It is machine simplicity and ruggedness that characterize SRGs. High speed is feasible. Rotor higher temperature due to the local environment is also acceptable, because there are no PMs or windings on the rotor. PMs may be added on the rotor (Figure 2.22a and Figure 2.22b) [13,14]. In this situation, the current polarity has to change, and the torque production relies heavily on phase interaction through PMs. The reluctance torque is small.

Alternatively, PMs may be placed on the stator (Figure 2.22c) [15] with some PM flux concentration. Again, the reluctance torque is reduced, and PM torque prevails. The PM flux polarity in one phase does not change sign, so we may call it a homopolar PM excitation.

Other SRG configurations with homopolar excitation flux were proposed but did not reach very far in the markets.

2.7.1 The Flux Reversal Generators

In these configurations, reliance is on PM flux switch (reversal) in the stator-concentrated coils (Figure 2.23a [16]). The PM flux linkage in the stator coils of Figure 2.23a changes sign when the rotor moves

(a)

(b)

(c)

FIGURE 2.22 Permanent magnet (PM)-assisted switched reluctance generators (SRGs): (a) with long PMs on the rotor, (b) with short PMs on the rotor, and (c) with PMs on the stator.

(a)

(b)

FIGURE 2.23 Flux reversal generators (FRGs) with stator permanent magnets (PMs): (a) the single-phase 4/2 flux–switch alternator and (b) the three-phase 6/8 FRG.

FIGURE 2.24 Three-phase flux reversal generator (FRG) with stator permanent magnet (PM) flux concentration.
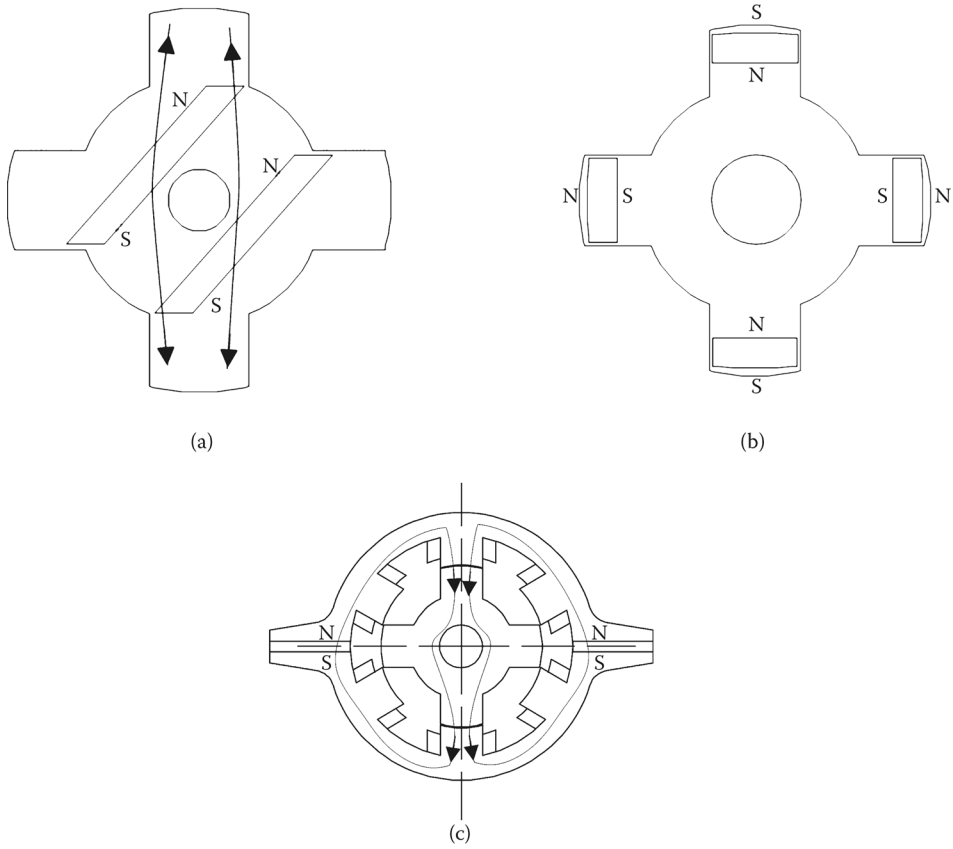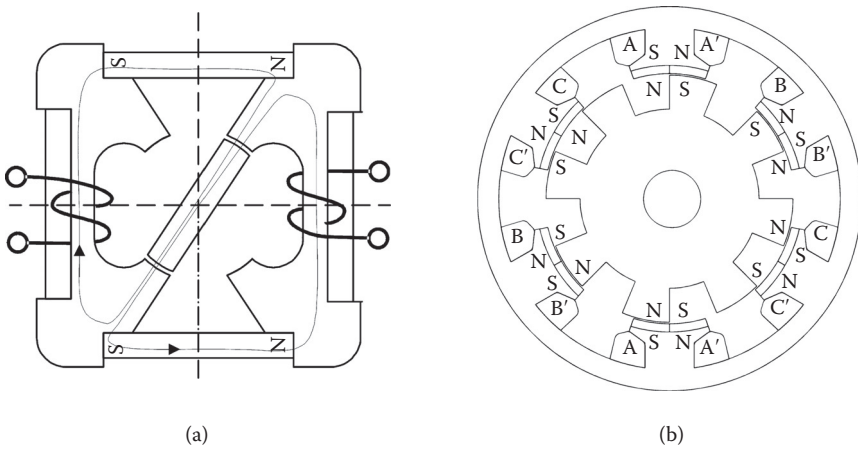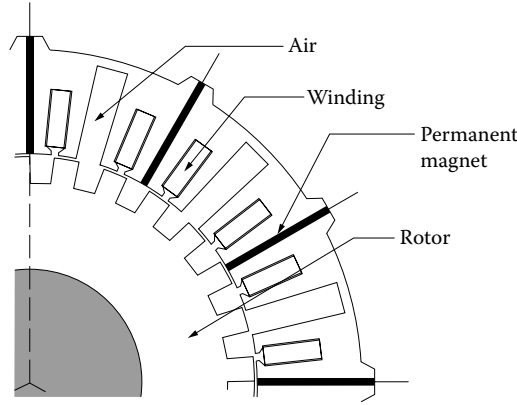
90° (mechanical) and does the same, for each phase in Figure 2.23b for the three-phase FRG, when the rotor moves 22.5° mechanical degrees.

In general, it is π/N_r (which corresponds to electrical radius). The electrical and mechanical radians are related as follows:

$$\alpha_{el} = N_r \alpha_{mec}, f_1 = N_r \cdot n \tag{2.10}$$

So, the frequency of the electromagnetic force f_1 is as if the number of pole pairs on the rotor was N_r.

The three-phase FRG configuration [17] makes better use of the stator and rotor core, and the manufacturing process is easier than that for the single-phase configuration, as the coils are inserted by conventional technology. Premade stator poles, with coils on, may be mounted inside the stator back iron, as done with rotor poles in salient poles in hydrogenerators. The main problem is the large flux fringing due to the juxtaposition of the North and South Poles (there could be 2,4,6,… of them on a stator pole). This reduces the useful flux to about 0.3 to 0.4 of its ideal value (in homopolar stator excitation, this is normal). PM flux concentration should provide better torque density for the same power factor. A three-phase configuration as described is shown on Figure 2.24.

It is evident that the manufacturing of a stator is a bit more complicated, and usage of the stator core is partial but still, PM flux concentration may increase the torque density without compromising the power factor too much. The phases are magnetically independent, and thus, high fault tolerance is expected.

For a better core utilization, the PMs with flux concentration may be placed on the rotor. An interior stator is added to complete the magnetic circuit (Figure 2.25).

The second (interior) windingless stator poses some manufacturing problems (the rotor also), but the higher torque/volume at an acceptable power factor may justify it. The power factor is mentioned here because it influences the converter kilo volt amps (KVAs) through reactive power demands.

FRGs are, in general, meant for mainly very low-speed applications, such as direct-driven wind generators on vessel generator/motors, and so forth.

2.7.2 The Transverse Flux Generators (TFGs)

TFGs are built in single-phase configurations with ring-shaped stator coils and surface PMs on the rotor (Figure 2.26) or with PM rotor flux concentration (Figure 2.27) [17,18].

The double-sided (dual-stator) configuration in Figure 2.27 takes advantage of PM flux concentration on the rotor. In general, TFGs are characterized by moderately low winding losses, due to the blessing of the ring-shaped coil.
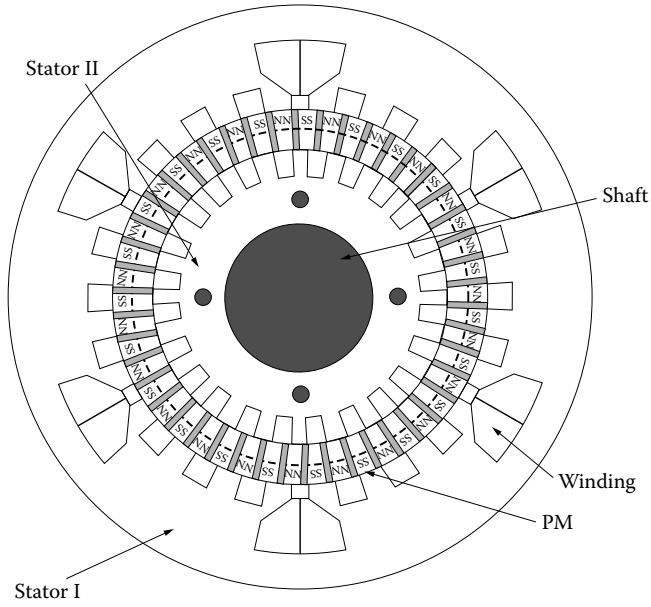
FIGURE 2.25 Flux reversal generator (FRG) with rotor permanent magnet (PM) flux concentration.
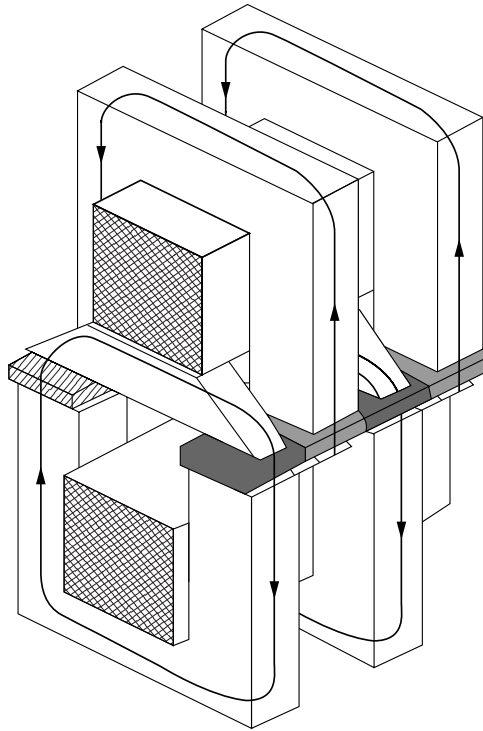
FIGURE 2.26 Double-sided transverse flux generator (TFG) with surface PM rotor.
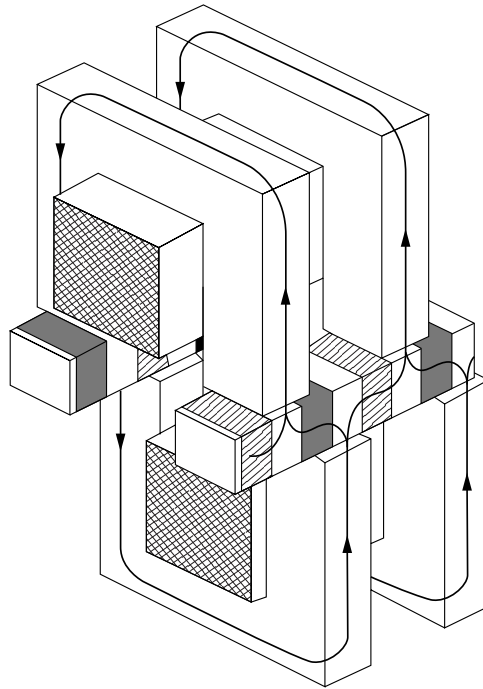
FIGURE 2.27 Double-sided transverse flux generator (TFG) with rotor PM flux concentration.

A three-phase machine is built by adding axially three single-phase units, properly displaced tangentially by 2/3 of a pole with each other. It is evident that the stators could best be built from magnetic composite materials. However, this solution would reduce torque density, because the permeability of such materials is below 500 μ_0 under some magnetic saturation. The core losses would be reduced if frequency goes above 600 Hz with magnetic composite materials (magnetic powder).

The stator-PM TFG (originally called the axial flux circumferential current PM machine [AFCC] [19]) imposes the use of composite magnetic materials both on the stator and on the rotor due to its intricated geometry. Again, it is essentially a single-phase machine. PM flux concentration occurs along the axial direction. Good usage of PMs and cores is inherent in the axial-airgap stator PM FRG shown in Figure 2.28a and Figure 2.28b.

FRGs need more PMs than usual, but the torque density is rather good, and compact geometries are very likely. The large number of poles on the rotor in most TFGs leads to a good frequency, unless speed is not very low.

The rather high torque density (in Nm/m³, or [6 to 9] N/cm² of rotor shear stress) is inherent, as the number of PM flux reversals (poles) in the stator ring-shaped coils is large per one revolution. This effect may be called torque magnification [11].

2.7.3 Linear Motion Alternators

The microphone is the classical example of a linear motion alternator (LMA) with moving coil. The loudspeaker illustrates its motoring operation mode.

Though there are many potential LMA configurations (or actuators), they all use PMs and fall into three main categories [20]:

- With moving coil (and stator PMs) — Figure 2.29a
- With moving PMs (and stator coil) — Figure 2.29b
- With moving iron (and stator PMs) — Figure 2.29c
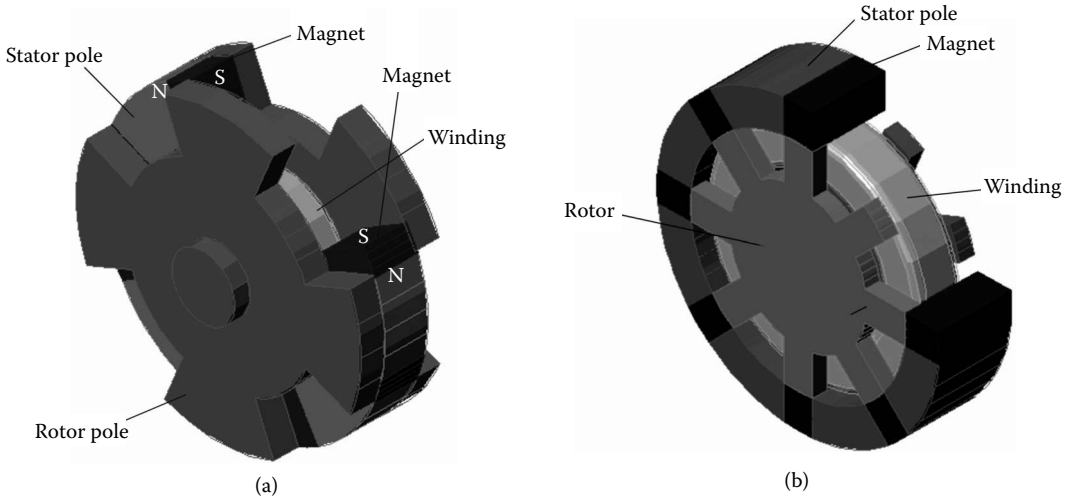
FIGURE 2.28 TFG with stator — permanent magnet (PM) flux concentration: (a) with axial airgap and (b) with radial airgap.

In essence, the PM flux linkage in the coil changes sign when the mover travels the excursion length l_{stroke} which serves as a kind of pole pitch. So they are, in a way, single-phase flux reversal machines. The average speed U_{av} is as follows:

$$U_{av} = 2 \cdot l_{stroke} \cdot f_1 \tag{2.11}$$

where f_1 = the frequency of mechanical oscillations.

To secure high efficiency, beryllium-copper flexured springs (Figure 2.30) are used to store the kinetic energy of the mover at excursion ends. They also serve as linear bearings. The proper frequency of these mechanical springs f_m should be equal to electrical frequency:

$$f_e = f_m = \frac{1}{2\pi}\sqrt{\frac{K}{m}} \tag{2.12}$$

where

   K = spring rigidity coefficient
   m = moving mass

The current is in phase with speed for best operation.

The strokes involved in LMAs are in the order of 0.5 to 100 mm or so. Their power, in general, is limited to 10 to 50 kW at 50 (60) Hz.

They are basically synchronous single-phase machines with harmonic motion and linear flux to position ideal variation.

Further increasing the power and volume requires — if average speed U_s is limited — configurations with PM flux concentration and three phases. Such a single-phase flat configuration, with moving PMs, is shown in Figure 2.31 [26].

Again, it is a single-phase device, and the PM flux reverses polarity when the mover advances one "small," stator, pole (tooth). The two twin stators are displaced by one stator tooth also, to provide for optimal magnetic circuit completion. Large airgap PM flux densities of up to 1.25 T may be obtained under the stator teeth with 0.65 T left for armature reaction, to secure both high-force (power) density and a satisfactory power factor (or reasonable $IX/E = 0.5$ ratio; X = machine reactance). The PM height
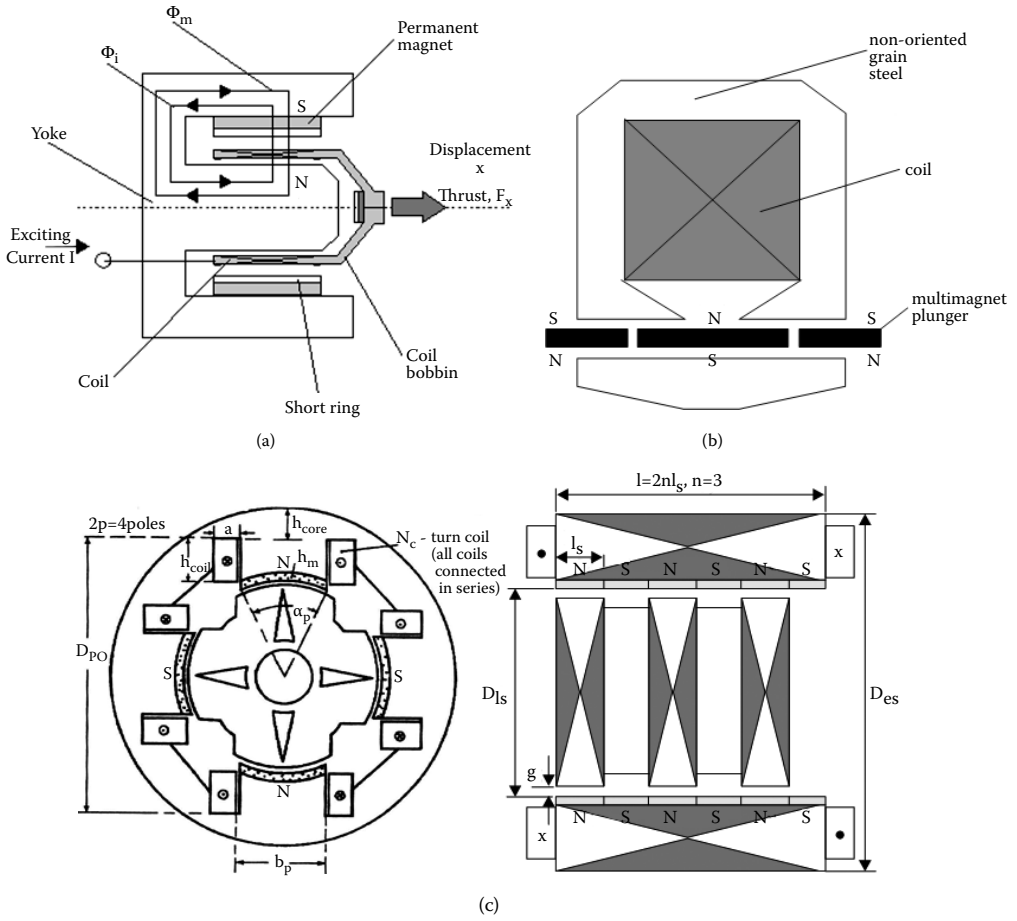
FIGURE 2.29 Commercial linear motion alternators: (a) with moving coil, (b) with moving permanent magnets (PMs), and (c) with moving iron.
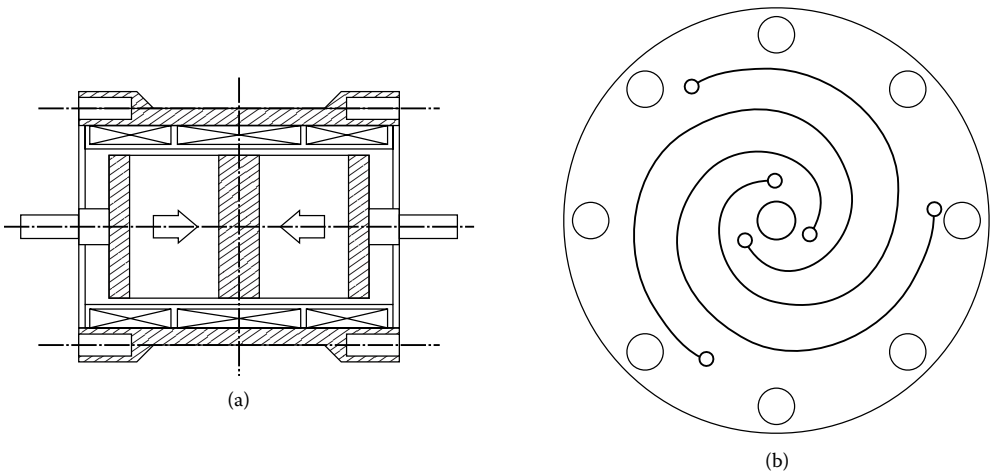
FIGURE 2.30 (a) Tubular linear motion alternator (LMA) and (b) with plunger supported on flexural springs.
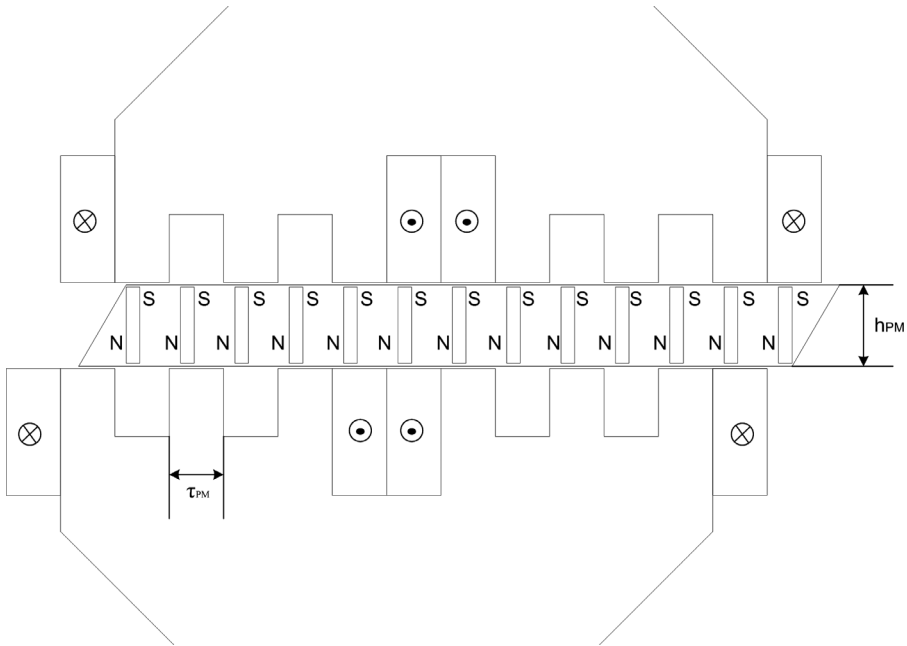
FIGURE 2.31   Flux reversal linear motion alternator (LMA) with mover permanent magnet (PM) concentration.

h_{PM} per pole pitch τ_{PM} is h_{PM}/τ_{PM} 1.5 − 2.5, as all PMs are active all the time, and full use of both stator and mover cores and copper is made.

Note that there are also LMAs that exploit progressive (rather than oscillatory) linear motion. Applications include auxilliary power LMAs on magnetically levitated vehicles (MAGLEVs) and plasma magnetohydrodynamic (MHD) linear motion DC generators with superconducting excitation (see Chapter 12 in *Variable Speed Generators*).

2.8   Electric Generator Applications

The application domains for electric generators embrace almost all industries, traditional and new, with powers from milliwatts to hundreds of megawatts per unit, and more [20–25].

Table 2.1 summarizes our view of electric generator main applications and the competitive types that may suit each person and need.

2.9   Summary

In this chapter, we presented some representative, in use and newly proposed, types of electric generators by principle, configuration, and application.

A few concluding remarks are in order:

- The power per unit range varies from a few milliwatts to a few hundred megawatts (even 1500 MVA) per unit.
- Large power generators, those above a few megawatts, are electrically excited on the rotor, either by DC, as in conventional synchronous generator (SG), or in three-phase AC, as in the wound rotor (doubly fed) induction generator (WRIG).
- While the conventional DC rotor-excited SGs require tightly controlled constant speed to produce constant frequency output, the WRIG may work with adjustable speed.

TABLE 2.1   Electric Generator Applications

Application	Large power systems (gas, coal, nuclear, hydrogen)	Distributed power systems (wind, hydro)	Standby diesel-driven EGs	Automotive starter-generators	Diesel locomotives
Suitable generator	Excited rotor synchronous generators, doubly fed induction generators (up to hundreds of MW/unit)	Excited rotor synchronous generators, cage-rotor induction generators, PM synchronous generators, parametric generators (up to 10 MW power/unit)	PM synchronous generators, cage-rotor induction generators	IPM synchronous generators, induction generators, transverse flux generators	Excited-rotor synchronous generators
Application	Home electricity production	Spacecraft applications	Aircraft applications	Ship applications	
Suitable generator	PM synchronous generators and LMAs	Linear motion alternators (LMAs)	PM synchronous, cage-rotor induction, or doubly fed induction generators (up to 500 kW/unit)	Excited synchronous generators (power in the order of a few MWs)	
Application	Small-power telemetry-based vibration monitoring	Inertial batteries	Super-high-speed gas-turbine generators		
Suitable generator	LMAs: 20–50 mW to 5 W	Axial-airgap PM synchronous generators up to hundreds of MJ/unit	PM synchronous generators up to 150 kW and 80,000 rpm (higher powers at lower speeds)		

- The rating of the rotor-connected PWM converter in WRIG is about equal to the adjustable speed range (slip), in general, around 20%. This implies reasonable costs for a more flexible generator with fast active and reactive power (or frequency and voltage) control.
- WRIG seems the way of the future in electric generation at adjustable speed for powers above a few megawatts, in general, per unit.
- PM synchronous generators are emerging for kilowatts, tenth of a kilowatt, and even hundreds of kilowatts or 1–3 MW/unit in special applications, such as automotive starter-alternators or super-high-speed gas turbine generators or direct-driven wind generators, respectively.
- Linear motion alternators are emerging for power operation up to 15 kW, even 50 kW for home or special series hybrid vehicles, with linear gas combustion engines and electric propulsion.
- Parametric generators are being investigated for special applications: switched reluctance generators for aircraft jet engine starter-alternators and transverse flux PM generators/motors for hybrid or electrical bus propulsion or direct-driven wind generators.
- Electric generators are driven by different prime movers that have their own characteristics, performance levels, and mathematical models, which, in turn, influence the generator operation, because at least speed control is enacted upon the prime mover. The next chapter discusses in some detail most used prime movers with their characteristics, mathematical models, and speed control methods.

References

1. T. Bödefeld, and H. Sequenz, *Elektrische Maschinen*, Springer, Vienna, 1938 (in German).
2. C. Concordia, *Synchronous Machines, Theory and Performance*, John Wiley & Sons, New York, 1951.
3. R. Richter, *Electrical Machines, vol. 2, Synchronous Machines*, Verlag Birkhäuser, Basel, 1963 (in German).
4. M. Kostenko, and L. Piotrovski, *Electrical Machines, vol. 2, AC Machines*, Mir Publishers, Moscow, 1974.
5. J.H. Walker, *Large Synchronous Machines*, Clarendon Press, Oxford, 1981.
6. T.J.E. Miller, *Brushless PM and Reluctance Motor Drives*, Clarendon Press, Oxford, 1989.
7. S.A. Nasar, I. Boldea, and L. Unnewher, *Permanent Magnet, Reluctance and Selfsynchronous Motors*, CRC Press, Boca Raton, FL, 1993.
8. D.C. Hanselman, *Brushless PM Motor Design*, McGraw-Hill, New York, 1994.
9. D.R. Hendershot Jr., and T.J.E. Miller. *Design of Brushless PM Motors*, Magna Physics Publishing and Clarendon Press, Oxford, 1994.
10. J. Gieras, F. Gieras, and M. Wing, *PM Motor Technologies*, 2nd ed., Marcel Dekker, New York, 2002.
11. I. Boldea, S. Scridon, and L. Tutelea, BEGA: Biaxial Excitation Generator for Automobiles, Record of OPTIM-2000, Poiana Brasov, Romania, vol. 2, pp. 345–352.
12. T. Miller, *Switched Reluctance Motors and Their Control*, Oxford University Press, Oxford, U.K., 1993.
13. Y. Liuo, and T.A. Lipo, A new doubly salient PM motor for adjustable speed drives, *EMPS*, 22, 3, 1994, pp. 259–270.
14. M. Radulescu, C. Martis, and I. Husain, Design and performance of small doubly salient rotor PM motor, *EPCS* (former *EMPS*), vol. 30, 2002, pp. 523–532.
15. F. Blaabjerg, I. Christensen, P.O. Rasmussen, and L. Oestergaard, New advanced control methods for doubly salient PM motor, Record of IEEE-IAS-1996, pp. 786–793.
16. S.E. Rauch, and L.J. Johnson, Design principles of flux switch alternator, *AIEE Trans.*, 74, III, 1955, pp. 1261–1268.
17. H. Weh, H. Hoffman, and J. Landrath, New permanent excited synchronous machine with high efficiency at low speeds, In *Proceedings of the ICEM-1988*, Pisa, Italy, pp. 1107–1111.
18. G. Henneberger, and I.A. Viorel, Variable reluctance electric machines, Shaker Verlag, Aachen, 2001, Chapter 6.

19. L. Luo, S. Huang, S. Chen, T.A. Lipo, Design and experiments of novel axial flux circumferentially current PM (AFCC) machine with radial airgap, Record of IEEE-IAS-2001.

20. I. Boldea, and S.A. Nasar, Linear Electric Actuators and Generators, Cambridge University Press, London; New York, 1997.

21. J. Wang, W. Wang, G.W. Jewell, and D. Howe, Design and experimental characterisation of a linear reciprocating generator, *Proc. IEE*, vol. 145-EPA, 6, 1998, pp. 509–518.

22. L.M. Hansen, P.H. Madsen, F. Blaabjerg, H.C. Christensen, U. Lindhard, and K. Eskildsen, Generators and power electronics technology for wind turbines, Record of IEEE-IECON-2001, pp. 2000–2005.

23. I. Boldea, I. Serban, and L. Tutelea, Variable speed generators and their control, J. Elec. Eng., vol. 2, no. 1, 2002 (www.jee.ro).

24. K. Kudo, "Japanese experience with a converter fed variable speed pumped storage system, *Hydropower & Dams*, March 1994.

25. T. Kuwabata, A. Shibuya, and M. Furuta, Design and dynamic response characteristics of 400 MW adjustable speed pump storage unit for Ohkawachi Power Station, *IEEE Trans.*, EC-11, 2, 1996, pp. 376–384.

26. T.-H. Kim, H.-W. Lee, Y.H. Kim, J. Lee, and I. Boldea, Development of a flux concentration-type linear oscillatory actuator, *IEEE Trans.*, MAG – 40, 4, 2004, pp. 2092–2094.

3

Prime Movers

3.1 Introduction

Electric generators convert mechanical energy into electrical energy. The mechanical energy is produced by prime movers. Prime movers are mechanical machines. They convert primary energy of a fuel or fluid into mechanical energy. They are also called turbines or engines. The fossil fuels commonly used in prime movers are coal, gas, oil, or nuclear fuel.

Essentially, the fossil fuel is burned in a combustor; thus, thermal energy is produced. Thermal energy is then taken by a working fluid and turned into mechanical energy in the prime mover.

Steam is the working fluid for coal or nuclear fuel turbines. In gas turbines or in diesel or internal combustion engines, the working fluid is the gas or oil in combination with air.

On the other hand, the potential energy of water from an upper-level reservoir may be turned into kinetic energy that hits the runner of a hydraulic turbine, changes momentum and direction, and produces mechanical work at the turbine shaft as it rotates against the "braking" torque of the electric generator under electric load.

Wave energy is similarly converted into mechanical work in special tidal hydraulic turbines. Wind kinetic energy is converted by wind turbines into mechanical energy.

A complete classification of prime movers is difficult due to the many variations in construction, from topology to control. However, a simplified prime mover classification is described in Table 3.1.

TABLE 3.1   Prime Mover Classification

Fuel	Working Fluid	Power Range	Main Applications	Type	Observation
Coal or nuclear fuel	Steam	Up to 1500 MW/unit	Electric power systems	Steam turbines	High speed
Gas or oil	Gas (oil) + air	From watts to hundreds of MW/unit	Large and distributed power systems, automotive applications (vessels, trains, highway and off-highway vehicles), autonomous power sources	Gas turbines, diesel engines, internal combustion engines, Stirling engines	With rotary but also linear reciprocating motion
Water energy	Water	Up to 1000 MW/unit	Large and distributed electric power systems, autonomous power sources	Hydraulic turbines	Medium and low speeds, >75 rpm
Wind energy	Air	Up to 5 MW/unit	Distributed power systems, autonomous power sources	Wind or wave turbines	Speed down to 10 rpm
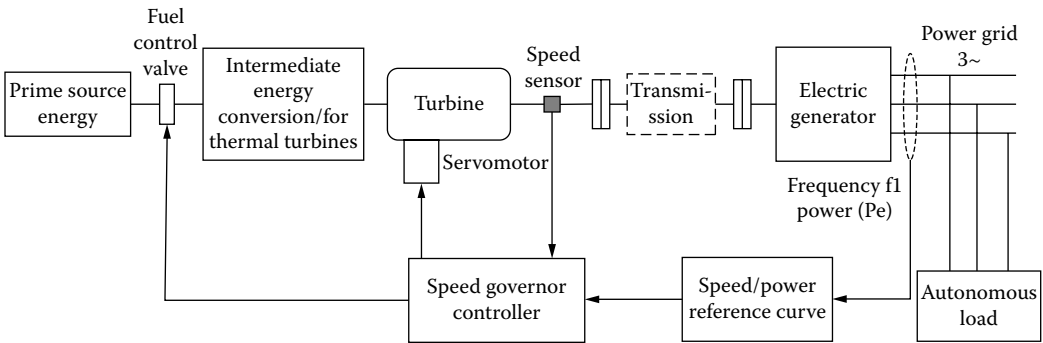
FIGURE 3.1   Basic prime-mover generator system.

In general, a prime mover or turbine drives an electric generator directly, or through a transmission (at power less than a few megawatts [MW]), Figure 3.1, [1–3]. The prime mover is necessarily provided with a so-called speed governor (in fact, a speed control and protection system) that properly regulates the speed, according to electric generator frequency/power curves (Figure 3.2).

Notice that the turbine is provided with a servomotor that activates one or a few control valves that regulate the fuel (or fluid) flow in the turbine, thus controlling the mechanical power at the turbine shaft. The speed at the turbine shaft is measured precisely and compared with the reference speed. The speed controller then acts on the servomotor to open or close control valves and control speed as required. The reference speed is not constant. In alternating current (AC) power systems, with generators in parallel, a speed drop of 2 to 3% is allowed, with power increased to the rated value [1–3].

The speed drop is required for two reasons:

- With a few generators of different powers in parallel, fair (proportional) power load sharing is provided.
- When power increases too much, the speed decreases accordingly, signaling that the turbine has to be shut off.

In Figure 3.2, at point A at the intersection between generator power and turbine power, speed is statically stable, as any departure from this point would provide the conditions (through motion equation) to return to it.
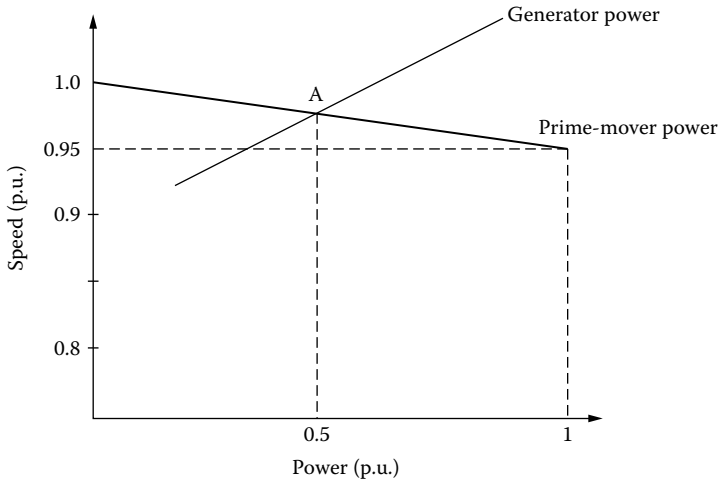
FIGURE 3.2 The reference speed (frequency)/power curve.

With synchronous generators operating in a constant voltage and frequency power system, the speed drop is very small, which implies strong strains on the speed governor due to inertia and so forth. It also leads to slower power control. On the other hand, the use of doubly fed induction generators, or of AC generators with full power electronics between them and the power system, would allow for speed variation (and control) in larger ranges ($\pm 20\%$ and more). That is, a smaller speed reference for lower power. Power sharing between electric generators would then be done through power electronics in a much faster and more controlled manner. Once these general aspects of prime mover requirements are clarified, we will deal in some detail with prime movers in terms of principles, steady-state performance, and models for transients. The main speed governors and their dynamic models are also included for each main type of prime mover investigated here.

3.2   Steam Turbines

Coal, oil, and nuclear fuels are burned to produce high pressure, high temperature, and steam in a boiler. The potential energy in the steam is then converted into mechanical energy in the so-called axial-flow steam turbines.

The steam turbines contain stationary and rotating blades grouped into stages: high pressure (HP), intermediate pressure (IP), low pressure (LP), and so forth. The high-pressure steam in the boiler is let to enter — through the main emergency stop valves (MSVs) and the governor valves (GVs) — the stationary blades, where it is accelerated as it expands to a lower pressure (Figure 3.3). Then the fluid is guided into the rotating blades of the steam turbine, where it changes momentum and direction, thus exerting a tangential force on the turbine rotor blades. Torque on the shaft and, thus, mechanical power, are produced. The pressure along the turbine stages decreases, and thus, the volume increases. Consequently, the length of the blades is lower in the high-pressure stages than in the lower-power stages.

The two, three, or more stages (HP, IP, and LP) are all, in general, on the same shaft, working in tandem. Between stages, the steam is reheated, its enthalpy is increased, and the overall efficiency is improved — up to 45% for modern coal-burn steam turbines.

Nonreheat steam turbines are built below 100 MW, while single-reheat and double-reheat steam turbines are common above 100 MW, in general. The single-reheat tandem (same-shaft) steam turbine is shown in Figure 3.3. There are three stages in Figure 3.3: HP, IP, and LP. After passing through the MSVs and GVs, the high-pressure steam flows through the high-pressure stage where it experiences a partial expansion. Subsequently, the steam is guided back to the boiler and reheated in the heat exchanger to increase its enthalpy. From the reheater, the steam flows through the reheat emergency stop valve
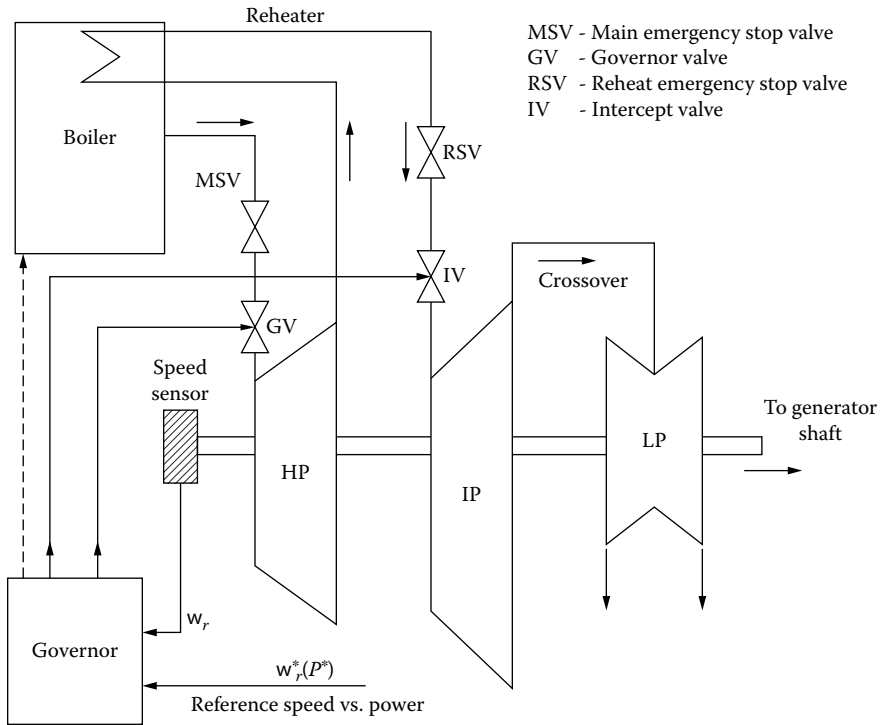
FIGURE 3.3 Single-reheat tandem-compound steam turbine.

(RSV) and intercept valve (IV) to the intermediate-pressure stage of the turbine, where again it expands to do mechanical work. For final expansion, the steam is headed to the crossover pipes and through the low pressure stage where more mechanical work is done. Typically, the power of the turbine is divided as follows: 30% in the HP, 40% in the IP, and 30% in the LP stages. The governor controls both the GV in the HP stage and the IV in the IP stage to provide fast and safe control.

During steam turbine starting — toward synchronous generator synchronization — the MSV is fully open, while the GV and IV are controlled by the governor system to regulate the speed and power. The governor system contains a hydraulic (oil) or an electrohydraulic servomotor to operate the GV and IV and to control the fuel and air mix admission and its parameters in the boiler. The MSV and RSV are used to quickly and safely stop the turbine under emergency conditions.

Turbines with one shaft are called tandem compound, while those with two shafts (eventually at different speeds) are called cross-compound. In essence, the LP stage of the turbine is attributed to a separate shaft (Figure 3.4). Controlling the speeds and powers of two shafts is difficult, though it adds flexibility. Also, shafts are shorter. Tandem-compound (single-shaft) configurations are more often used.

Nuclear units generally have tandem-compound (single-shaft) configurations and run at 1800 (1500) rpm for 60 (50) Hz power systems. They contain one HP and three LP stages (Figure 3.5). The HP exhaust passes through the moisture reheater (MSR) before entering the LP 1,2,3 stages in order to reduce steam moisture losses and erosion. The HP exhaust is also reheated by the HP steam flow.

The governor acts upon the GV and the IV 1,2,3 to control the steam admission in the HP and LP 1,2,3 stages, while the MSV and the RSV 1,2,3 are used only for emergency tripping of the turbine. In general, the GVs (control) are of the plug-diffuser type, while the IVs may be either the plug or the butterfly type (Figure 3.6a and Figure 3.6b, respectively). The valve characteristics are partly nonlinear, and, for better control, they are often "linearized" through the control system.
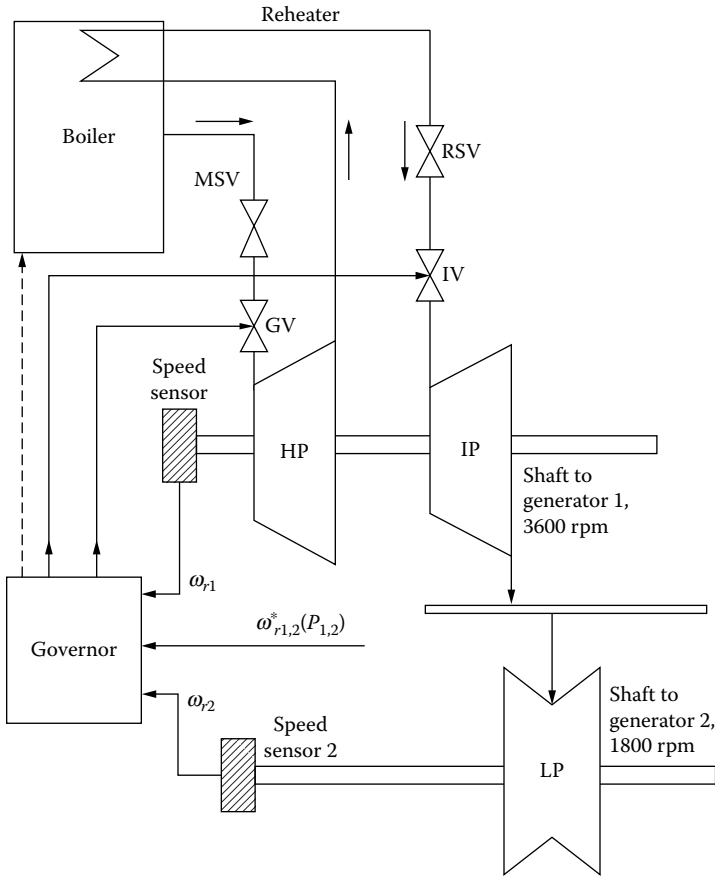
FIGURE 3.4 Single-reheat cross-compound (3600/1800 rpm) steam turbine.

3.3 Steam Turbine Modeling

The complete model of a multiple-stage steam turbine is rather involved. This is why we present here first the simple steam vessel (boiler, reheated) model (Figure 3.7), [1–3], and derive the power expression for the single-stage steam turbine.

The mass continuity equation in the vessel is written as follows:

$$\frac{dW}{dt} = V\frac{d\rho}{dt} = Q_{input} - Q_{output} \tag{3.1}$$

where

V = the volume (m³)
Q = the steam mass flow rate (kg/sec)
ρ = the density of steam (kg/m³)
W = the weight of the steam in the vessel (kg).

Let us assume that the flow rate out of the vessel Q_{output} is proportional to the internal pressure in the vessel:

$$Q_{output} = \frac{Q_0}{P_0} P \tag{3.2}$$

where

P = the pressure (KPa)

P_0 and Q_0 = the rated pressure and flow rate out of the vessel
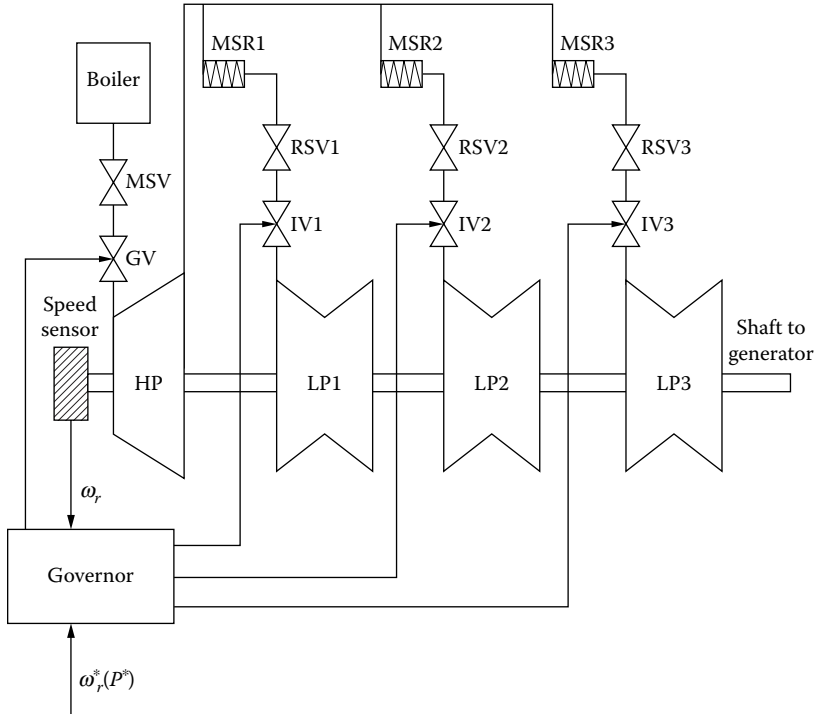
FIGURE 3.5 Typical nuclear steam turbine.
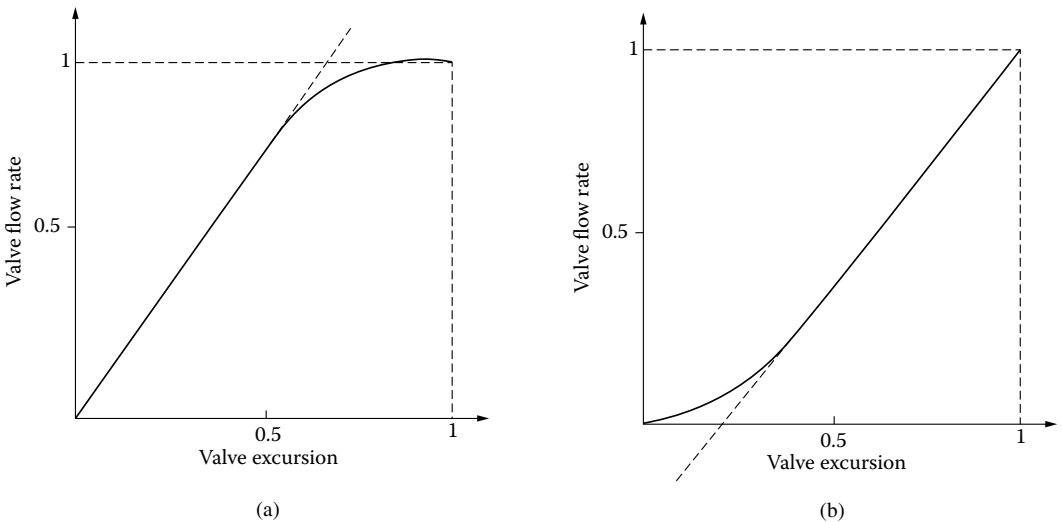
FIGURE 3.6 Steam valve characteristics: (a) plug-diffuser valve and (b) butterfly-type valve.
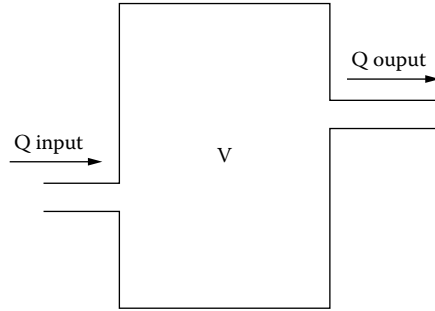
FIGURE 3.7 The steam vessel.

As the temperature in the vessel may be considered constant,

$$\frac{d\rho}{dt} = \frac{\partial \rho}{\partial P} \cdot \frac{dP}{dt} \tag{3.3}$$

Steam tables provide $(\partial \rho / \partial P)$ functions.

Finally, from Equation 3.1 through Equation 3.3, we obtain the following:

$$Q_{input} - Q_{output} = T_V \frac{dQ_{output}}{dt} \tag{3.4}$$

$$T_V = \frac{P_0}{Q_0} V \cdot \frac{\partial \rho}{\partial P} \tag{3.5}$$

T_V is the time constant of the steam vessel. With $d/dt = s$, the Laplace form of Equation 3.4 can be written as follows:

$$\frac{Q_{output}}{Q_{input}} = \frac{1}{1 + T_V \cdot s} \tag{3.6}$$

The first-order model of the steam vessel has been obtained. The shaft torque T_m in modern steam turbines is proportional to the flow rate:

$$T_m = K_m \cdot Q \tag{3.7}$$

So the power P_m is:

$$P_m = T_m \cdot \Omega_m = K_m Q \cdot 2\pi n_m \tag{3.8}$$

Example 3.1

The reheater steam volume of a steam turbine is characterized by $Q_0 = 200$ kg/sec, $V = 100$ m³, $P_0 = 4000$ kPa, and $\partial \rho / \partial P = 0.004$.

Calculate the time constant T_R of the reheater and its transfer function.

We use Equation 3.4 and Equation 3.5 and, respectively, Equation 3.6:
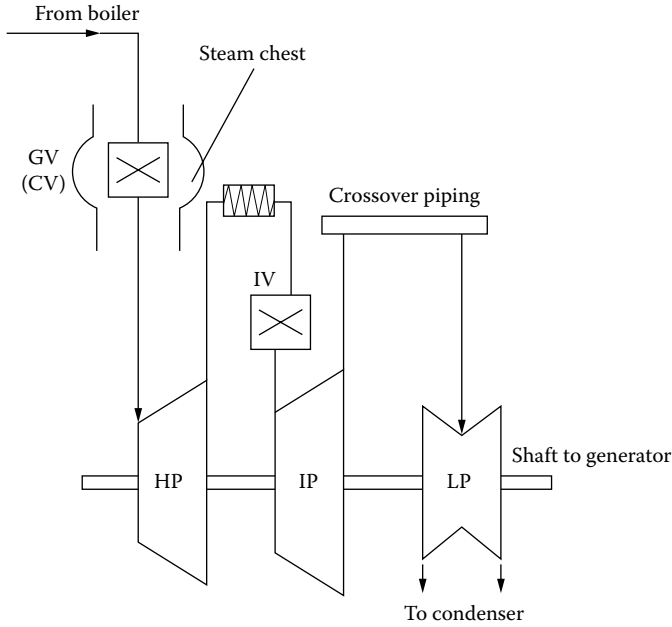
FIGURE 3.8 Single-reheat tandem-compound steam turbine.

$$T_R = \frac{P_0}{Q_0} V \cdot \frac{\partial \rho}{\partial P} = \frac{4000}{200} \times 100 \times 0.004 = 8.0 \text{ sec}$$

$$\frac{Q_{output}}{Q_{input}} = \frac{1}{1 + 8 \cdot s}$$

Now consider the rather complete model of a single-reheat, tandem-compound steam turbine (Figure 3.3). We will follow the steam journey through the turbine, identifying a succession of time delays/time constants.

The MSV and RSV are not shown in Figure 3.8, as they intervene only in emergency conditions.

The GVs modulate the steam flow through the turbine to provide for the required (reference) load (power)/frequency (speed) control. The GV has a steam chest where substantial amounts of steam are stored; and it is also found in the inlet piping. Consequently, the response of steam flow to a change in a GV opening exhibits a time delay due to the charging time of the inlet piping and steam chest. This time delay is characterized by a time constant T_{CH} in the order of 0.2 to 0.3 sec.

The IVs are used for rapid control of mechanical power (they handle 70% of power) during overspeed conditions; thus, their delay time may be neglected in a first approximation.

The steam flow in the IP and LP stages may be changed with an increase in pressure in the reheater. As the reheater holds a large amount of steam, its response-time delay is larger. An equivalent larger time constant T_{RM} of 5 to 10 sec is characteristic of this delay [4].

The crossover piping also introduces a delay that may be characterized by another time constant T_{CO}.

We should also consider that the HP, IP, and LP stages produce F_{HP}, F_{IP}, and F_{LP} fractions of total turbine power such that

$$F_{HP} + F_{IP} + F_{LP} = 1 \tag{3.9}$$
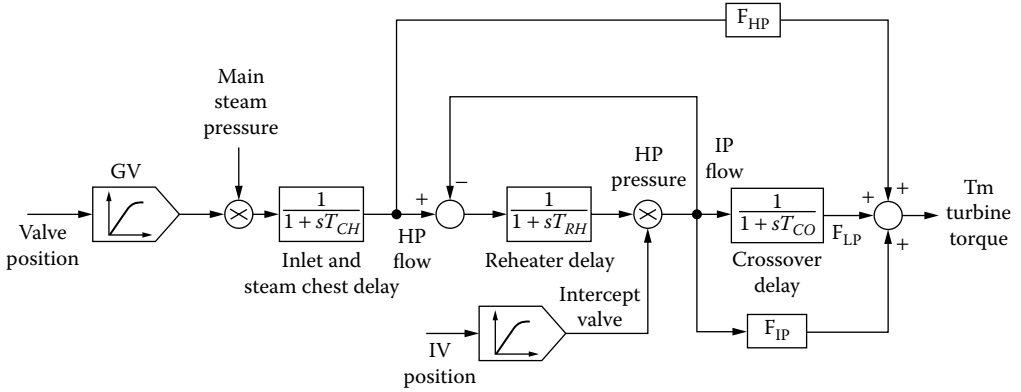
FIGURE 3.9 Structural diagram of single-reheat tandem-compound steam turbine.
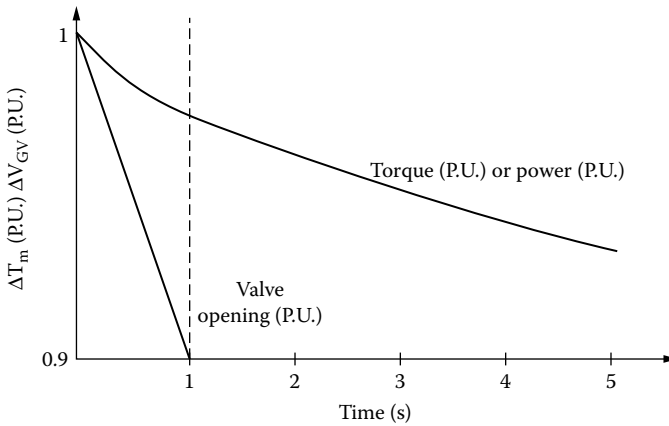
FIGURE 3.10 Steam turbine response to 0.1 (P.U.) 1 sec ramp change of GV opening.

We may integrate these aspects of a steam turbine model into a structural diagram as shown in Figure 3.9.

Typically, as already stated: $F_{HP} = F_{IP} = 0.3$, $F_{LP} = 0.4$, $T_{CH} \approx 0.2–0.3$ sec, $T_{RH} = 5–9$ sec, and $T_{CO} = 0.4–0.6$ sec.

In a nuclear-fuel steam turbine, the IP stage is missing ($F_{IP} = 0$, $F_{LP} = 0.7$), and T_{RH} and T_{CH} are notably smaller. As T_{CH} is largest, reheat turbines tend to be slower than nonreheat turbines. After neglecting T_{CO} and considering GV as linear, the simplified transfer function may be obtained:

$$\frac{\Delta Tm}{\Delta V_{GV}} \approx \frac{\left(1 + sF_{HP}T_{RH}\right)}{\left(1 + sT_{CH}\right)\left(1 + sT_{RH}\right)} \tag{3.10}$$

The transfer function in Equation 3.10 clearly shows that the steam turbine has a straightforward response to GV opening.

A typical response in torque (in per unit, P.U.) — or in power — to 1 sec ramp of 0.1 (P.U.) change in GV opening is shown in Figure 3.10 for $T_{CH} = 8$ sec, $F_{HP} = 0.3$, and $T_{CH} = T_{CO} = 0$.

In enhanced steam turbine models involving various details, such as IV, more rigorous representation counting for the (fast) pressure difference across the valve may be required to better model various intricate transient phenomena.
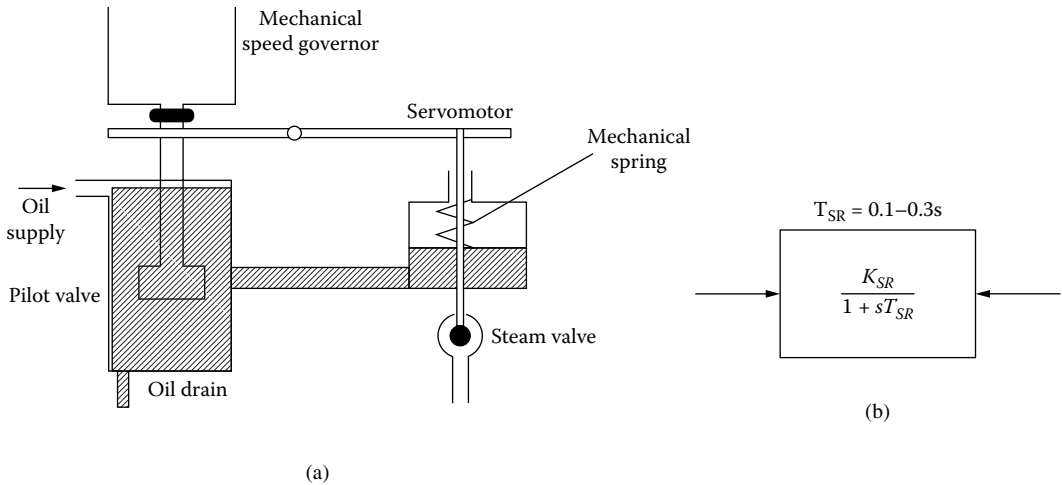
FIGURE 3.11 Speed relay: (a) configuration and (b) transfer function.

3.4   Speed Governors for Steam Turbines

The governor system of a turbine performs a multitude of functions, including the following [1–4]:

- Speed (frequency)/load (power) control: mainly through GVs
- Overspeed control: mainly through the IV
- Overspeed trip: through MSV and RSV
- Start-up and shutdown control

The speed/load (frequency/power) control (Figure 3.2) is achieved through the control of the GV to provide linearly decreasing speed with load, with a small speed drop of 3 to 5%. This function allows for paralleling generators with adequate load sharing. Following a reduction in electrical load, the governor system has to limit overspeed to a maximum of 120%, in order to preserve turbine integrity. Reheat-type steam turbines have two separate valve groups (GV and IV) to rapidly control the steam flow to the turbine.

The objective of the overspeed control is set to about 110 to 115% of rated speed to prevent overspeed tripping of the turbine in case a load rejection condition occurs.

The emergency tripping (through MSV and RSV — Figure 3.3 and Figure 3.5) is a protection solution in case normal and overspeed controls fail to limit the speed to below 120%.

A steam turbine is provided with four or more GVs that admit steam through nozzle sections distributed around the periphery of the HP stage. In normal operation, the GVs are open sequentially to provide better efficiency at partial load. During the start-up, all the GVs are fully open, and stop valves control steam admission.

Governor systems for steam turbines evolve continuously. Their evolution mainly occurred from mechanical-hydraulic systems to electrohydraulic systems [4].

In some embodiments, the main governor systems activate and control the GV, while an auxiliary governor system operates and controls the IV [4]. A mechanical-hydraulic governor generally contains a centrifugal speed governor (controller), that has an effect that is amplified through a speed relay to open the steam valves. The speed relay contains a pilot valve (activated by the speed governor) and a spring-loaded servomotor (Figure 3.11a and Figure 3.11b).

In electrohydraulic turbine governor systems, the speed governor and speed relay are replaced by electronic controls and an electric servomotor that finally activates the steam valve.

In large turbines an additional level of energy amplification is needed. Hydraulic servomotors are used for the scope (Figure 3.12). By combining the two stages — the speed relay and the hydraulic servomotor — the basic turbine governor is obtained (Figure 3.13).
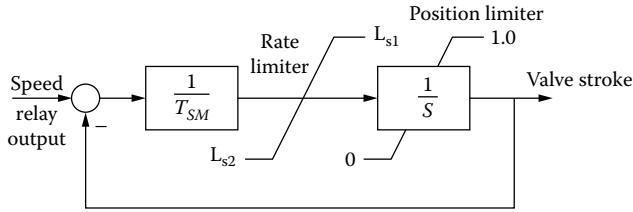
FIGURE 3.12 Hydraulic servomotor structural diagram.
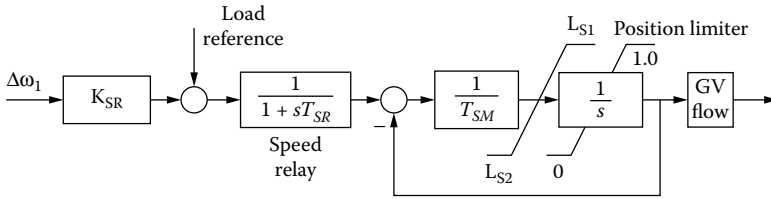
FIGURE 3.13 Basic turbine governor.
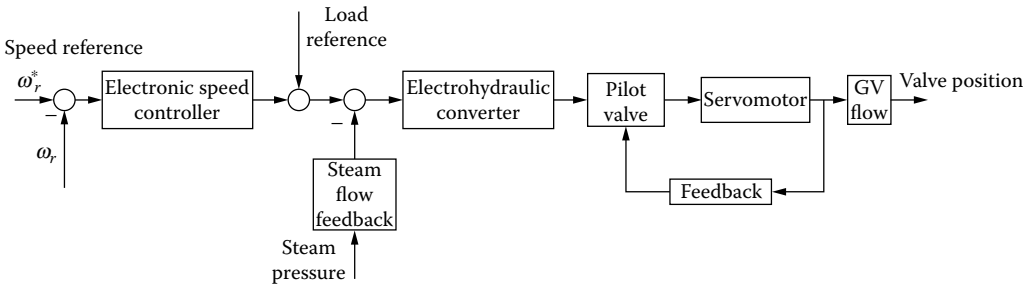
FIGURE 3.14 Generic electrohydraulic governing system.

For a speed drop of 4% at rated power, $K_{SR} = 25$ (Figure 3.12). A similar structure may be used to control the IV [2].

Electrohydraulic governor systems perform similar functions, but by using electronics control in the lower power stages, they bring more flexibility, and a faster and more robust response. They are provided with acceleration detection and load power unbalance relay compensation. The structure of a generic electrohydraulic governor system is shown in Figure 3.14. Notice the two stages in actuation: the electrohydraulic converter plus the servomotor, and the electronic speed controller.

The development of modern nonlinear control (adaptive, sliding mode, fuzzy, neural networks, H_∞, etc.) [5] led to the recent availability of a wide variety of electronic speed controllers or total steam turbine-generator controllers [6]. These, however, fall beyond the scope of our discussion here.

3.5 Gas Turbines

Gas turbines burn gas, and that thermal energy is then converted into mechanical work. Air is used as the working fluid. There are many variations in gas turbine topology and operation [1], but the most used one seems to be the open regenerative cycle type (Figure 3.15).

The gas turbine in Figure 3.14 consists of an air compressor (C) driven by the turbine (T) and the combustion chamber (CH). The fuel enters the combustion chamber through the GV, where it is mixed with the hot-compressed air from the compressor. The combustion product is then directed into the turbine, where it expands and transfers energy to the moving blades of the gas turbine. The exhaust gas heats the air from the compressor in the heat exchanger. The typical efficiency of a gas turbine is 35%.
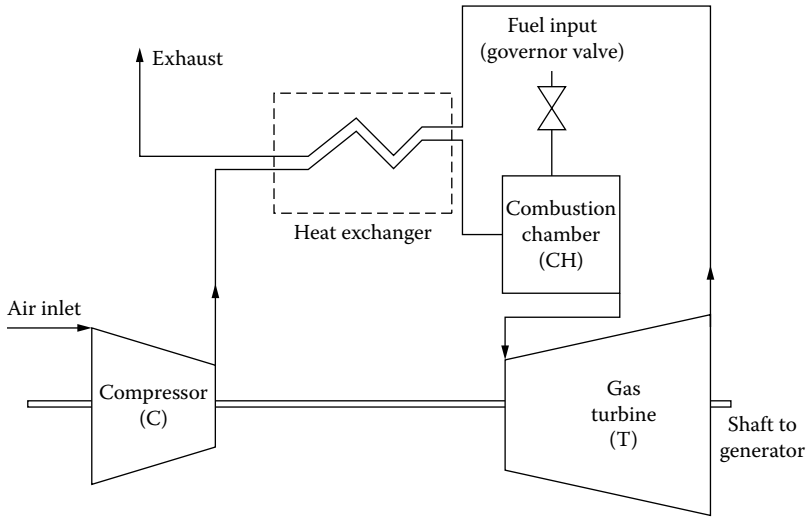
FIGURE 3.15 Open regenerative cycle gas turbine.

More complicated cycles, such as compressor intercooling and reheating or intercooling with regeneration and recooling, are used for further (slight) improvements in performance [1].

The combined- and steam-cycle gas turbines were recently proven to deliver an efficiency of 55% or even slightly more. The generic combined-cycle gas turbine is shown in Figure 3.16.

The exhaust heat from the gas turbine is directed through the heat recovery boiler (HRB) to produce steam, which, in turn, is used to produce more mechanical power through a steam turbine section on the same shaft. With the gas exhaust exiting the gas turbine above 500°C and supplementary fuel burning, the HRB temperature may rise further than the temperature of the HP steam, thus increasing efficiency. Additionally, some steam for home (office) heating or process industries may be delivered.

Already in the tens of MW, combined-cycle gas turbines are becoming popular for cogeneration in distributed power systems in the MW or even tenths and hundreds of kilowatts per unit. Besides efficiency, the short construction time, low capital cost, low SO_2 emission, little staffing necessary, and easy fuel (gas) handling are all main merits of combined-cycle gas turbines. Their construction at very high speeds (tens of krpm) up to the 10 MW range, with full-power electronics between the generator and the distributed power grid, or in stand-alone operation mode at 50(60) Hz, make the gas turbines a way of the future in this power range.

3.6 Diesel Engines

Distributed electric power systems, with distribution feeders at approximately 12 kV, standby power sets ready for quick intervention in case of emergency or on vessels, locomotives, or series or parallel hybrid vehicles, and power-leveling systems in tandem with wind generators, all make use of diesel (or internal combustion) engines as prime movers for their electric generators. The power per unit varies from a few tenths of a kilowatt to a few megawatts.

As for steam or gas turbines, the speed of a diesel-engine generator set is controlled through a speed governor. The dynamics and control of fuel–air mix admission are very important to the quality of the electric power delivered to the local power grid or to the connected loads, in stand-alone applications.

3.6.1 Diesel-Engine Operation

In four-cycle internal combustion engines [7], and the diesel engine is one of them, with the period of one shaft revolution $T_{REV} = 1/n$ (n is the shaft speed in rev/sec), the period of one engine power stroke T_{PS} is
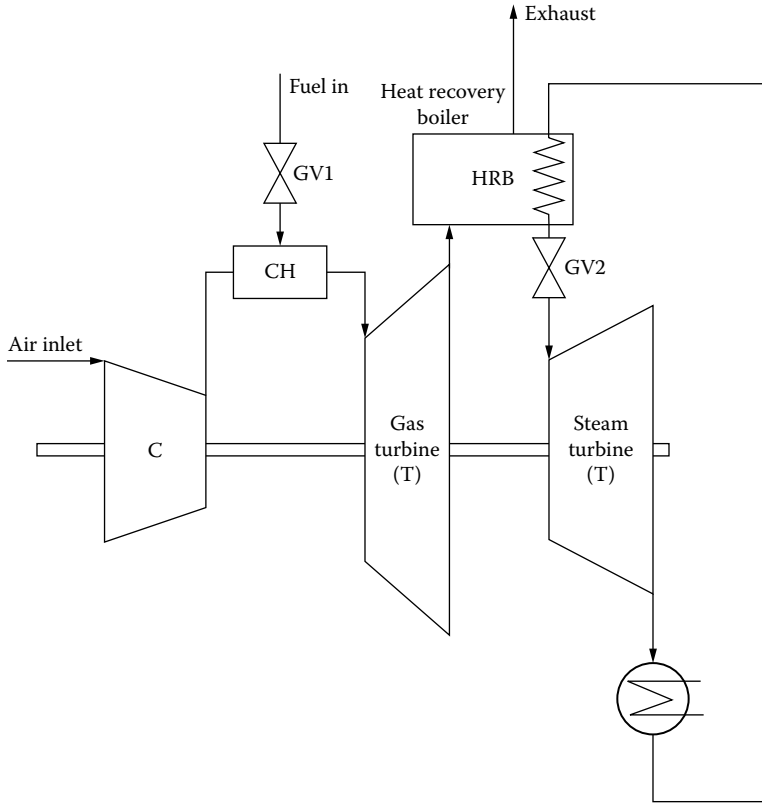
FIGURE 3.16 Combined-cycle unishaft gas turbine.

$$T_{PS} = 2T_{REV} \qquad (3.11)$$

The frequency of power stroke f_{PS} is as follows:

$$f_{PS} = \frac{1}{T_{PS}} \qquad (3.12)$$

For an engine with N_c cylinders, the number of cylinders that fire each revolution, N_f, is

$$N_f = \frac{N_c}{2} \qquad (3.13)$$

The cylinders are arranged symmetrically on the crankshaft, so that the firing of the N_f cylinders is uniformly spaced in angle terms. Consequently, the angular separation (θ_c) between successive firings in a four-cycle engine is as follows:

$$\theta_c = \frac{720^0}{N_c} \qquad (3.14)$$

The firing angles for a twelve-cylinder diesel engine are illustrated in Figure 3.17a, while the two-revolution sequence is intake (I), compression (C), power (P), and exhaust (E) (Figure 3.17b). The twelve-
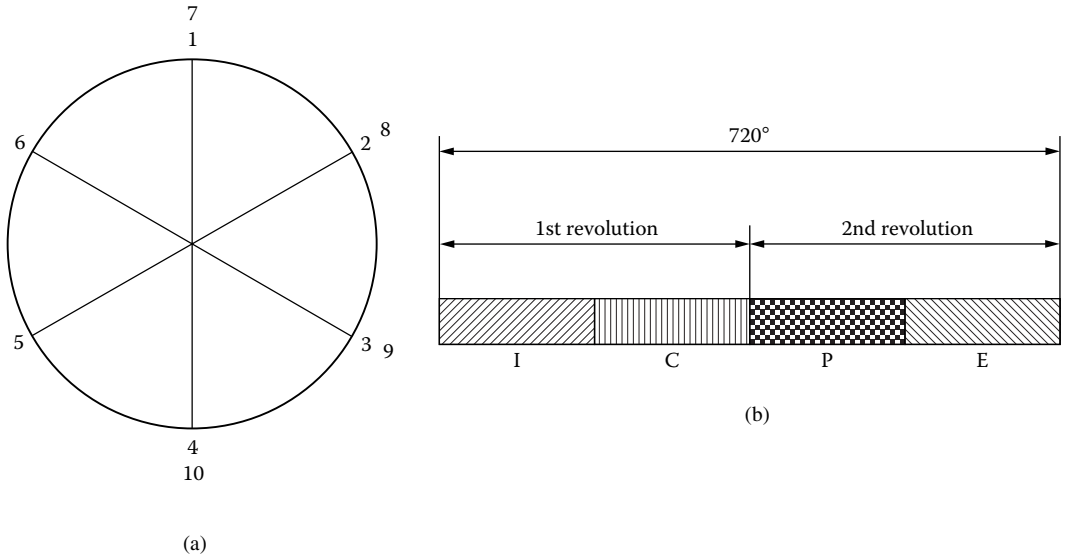
FIGURE 3.17 Twelve-cylinder four-cycle diesel engine: (a) configuration and (b) sequence.
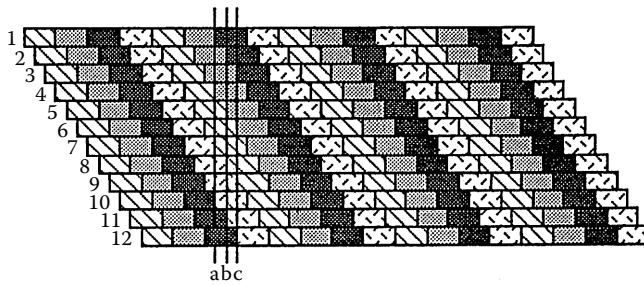
FIGURE 3.18 Twelve-cylinder engine timing.

cylinder timing is shown in Figure 3.18. There are three cylinders out of twelve firing simultaneously at steady state. The resultant shaft torque of one cylinder varies with shaft angle, as shown in Figure 3.19. The compression torque is negative, while during the power cycle, it is positive. With twelve cylinders, the torque will have much smaller pulsations, with twelve peaks over 720° (period of power engine stroke) — see Figure 3.20. Any misfire in one or a few of the cylinders would produce severe pulsations in the torque that would reflect as a flicker in the generator output voltage [8].

Large diesel engines generally have a turbocharger (Figure 3.21) that notably influences the dynamic response to perturbations by its dynamics and inertia [9]. The turbocharger is essentially an air compressor that is driven by a turbine that runs on the engine exhaust gas. The compressor provides compressed air to the engine cylinders. The turbocharger works as an energy recovery device with about 2% power recovery.

3.6.2 Diesel-Engine Modeling

A diagram of the general structure of a diesel engine with turbocharger and control is presented in Figure 3.22.

The following are the most important components:

- The actuator (governor) driver that appears as a simple gain K_3.
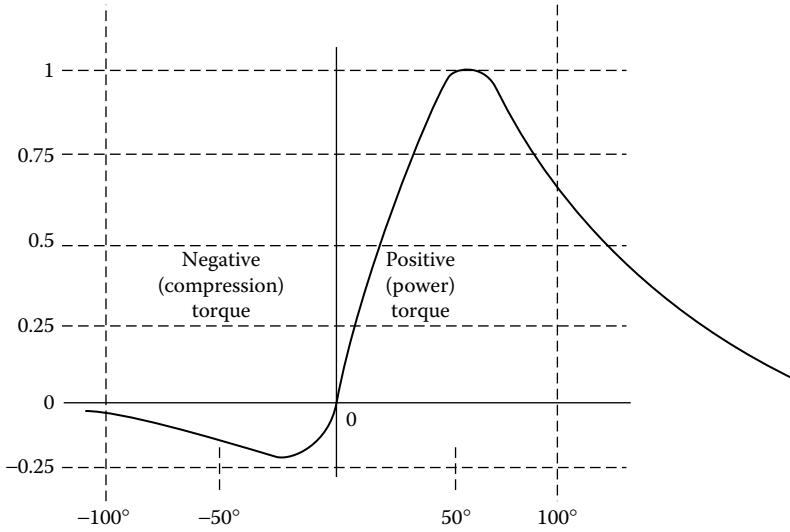
FIGURE 3.19 P.U. torque/angle for one cylinder.
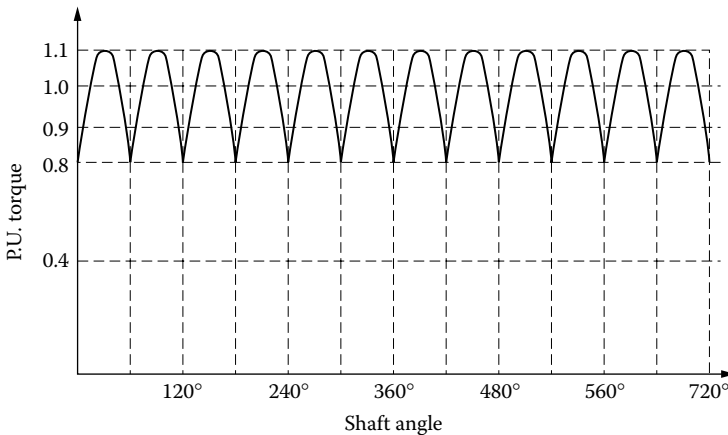
FIGURE 3.20 P.U. torque vs. shaft angle in a 12-cylinder ICE (internal combustion engine).

- The actuator (governor) fuel controller that converts the actuator's driver into an equivalent fuel flow, Φ. This actuator is represented by a gain K_2 and a time constant (delay) τ_2, which is dependent on oil temperature, and an aging-produced backlash.
- The inertias of engine J_E, turbocharger J_T, and electric generator (alternator) J_G.
- The flexible coupling that mechanically connects the diesel engine to the alternator (it might also contain a transmission).
- The diesel engine is represented by the steady-state gain K_1 — constant for low fuel flow Φ and saturated for large Φ, multiplied by the equivalence ratio factor (erf) and by a time constant τ_1.
- The erf depends on the engine equivalence ratio (eer), which, in turn, is the ratio of fuel/air normalized by its stoichiometric value. A typical variation of erf with eer is shown in Figure 3.22. In essence, erf is reduced, because when the ratio of fuel/air increases, incomplete combustion occurs, leading to low torque and smoky exhaust.
- The dead time of the diesel engine is composed of three delays: the time elapsed until the actuator output actually injects fuel into the cylinder, fuel burning time to produce torque, and time until all cylinders produce torque at the engine shaft:
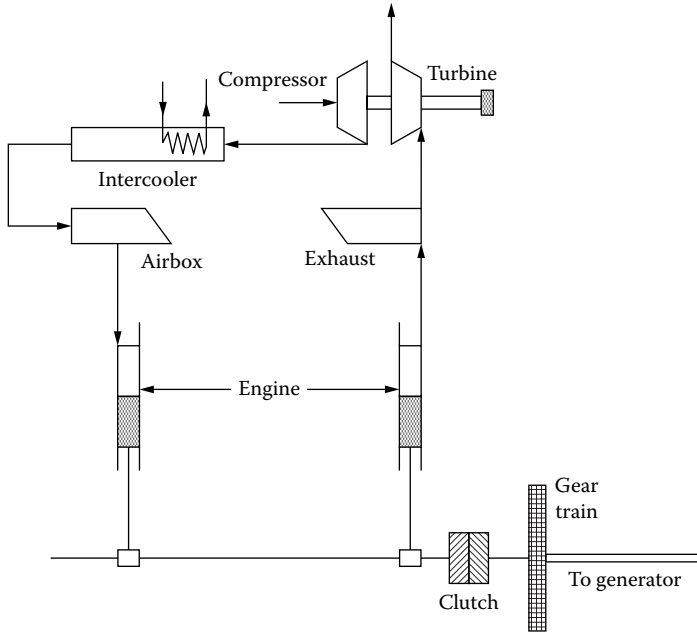
FIGURE 3.21 Diesel engine with turbocharger.
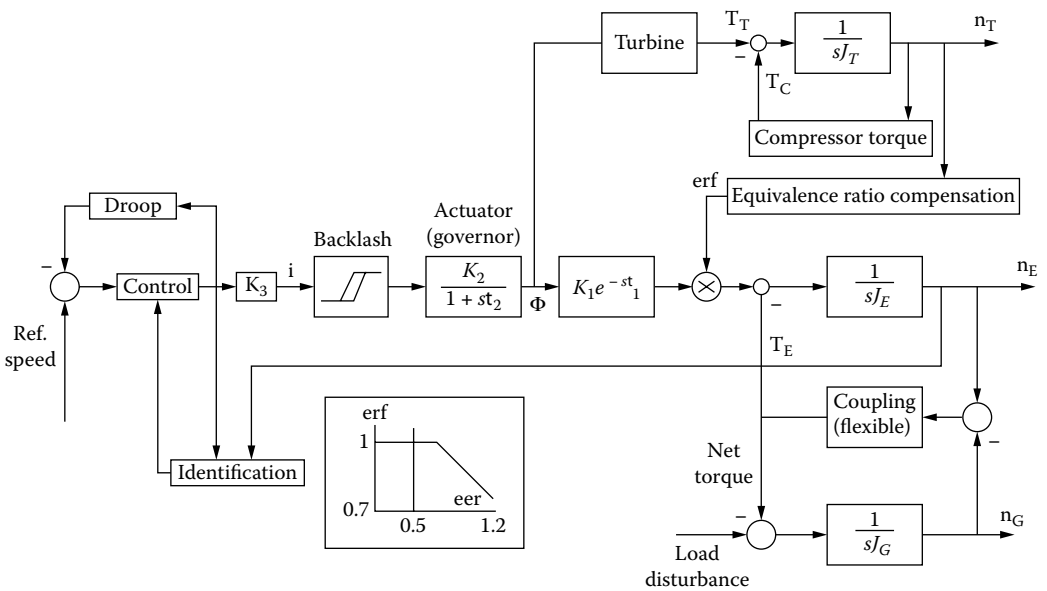
FIGURE 3.22 Diesel engine with turbocharger and controller.

$$\tau_1 \approx A + \frac{B}{n_E} + \frac{C}{n_E^2} \tag{3.15}$$

where n_E is the engine speed.

The turbocharger acts upon the engine in the following ways:

- It draws energy from the exhaust to run its turbine; the more fuel in the engine, the more exhaust is available.
- It compresses air at a rate that is a nonlinear function of speed; the compressor is driven by the turbine, and thus, the turbine speed and ultimate erf in the engine are influenced by the airflow rate.
- The turbocharger runs freely at high speed, but it is coupled through a clutch to the engine at low speeds, to be able to supply enough air at all speeds; thus, the system inertia changes at low speeds, by including the turbocharger inertia.

Any load change leads to transients in the system pictured in Figure 3.22 that may lead to oscillations due to the nonlinear effects of fuel–air flow — equivalence ratio factor — inertia. As a result, there will be either too little or too much air in the fuel mix. In the first case, smoky exhaust will be apparent. In the second situation, not enough torque will be available for the electric load, and the generator may pull out of synchronism. This situation indicates that proportional integral (PI) controllers of engine speed are not adequate, and nonlinear controllers (adaptive, variable structure, etc.) are required [10].

A higher-order model may be adopted both for the actuator [11, 12] and for the engine [13] to better simulate in detail the diesel-engine performance for transients and control.

3.7 Stirling Engines

Stirling engines are part of the family of thermal engines: steam turbines, gas turbines, spark-ignited engines, and diesel engines. They were already described briefly in this chapter, but it is time now to dwell a little on the thermodynamic engine cycles to pave the way for our discussion on Stirling engines.

3.7.1 Summary of Thermodynamic Basic Cycles

The steam engine, invented by James Watt, is a continuous combustion machine. Subsequently, the steam is directed from the boiler to the cylinders (Figure 3.23a and Figure 3.23b). The typical four steps of the steam engine (Figure 3.23a) are as follows:

- Isochoric compression (1–1′) followed by isothermal expansion (1′–2): The hot steam enters the cylinder through the open valve at constant volume; it then expands at constant temperature.
- Isotropic expansion: Once the valve is closed, the expansion goes on until the maximum volume is reached (3).
- Isochoric heat regeneration (3–3) and isothermal compression (3′–4): The pressure drops at constant volume, and then the steam is compressed at constant temperature.
- Isentropic compression takes place after the valve is closed and the gas is mechanically compressed. An approximate formula for thermal efficiency η_{th} is as follows [13]:

$$\eta_{th} = 1 - \frac{\rho^{K-1}(K-1)(1+\ln\rho)}{\varepsilon^{K-1}(x-1)+(K-1)\ln\rho} \tag{3.16}$$

where

$\varepsilon = V_3/V_1$ is the compression ratio
$\rho = V_2/V_1 = V_3/V_4$ is the partial compression ratio
$x = p_1'/p_1$ is the pressure ratio
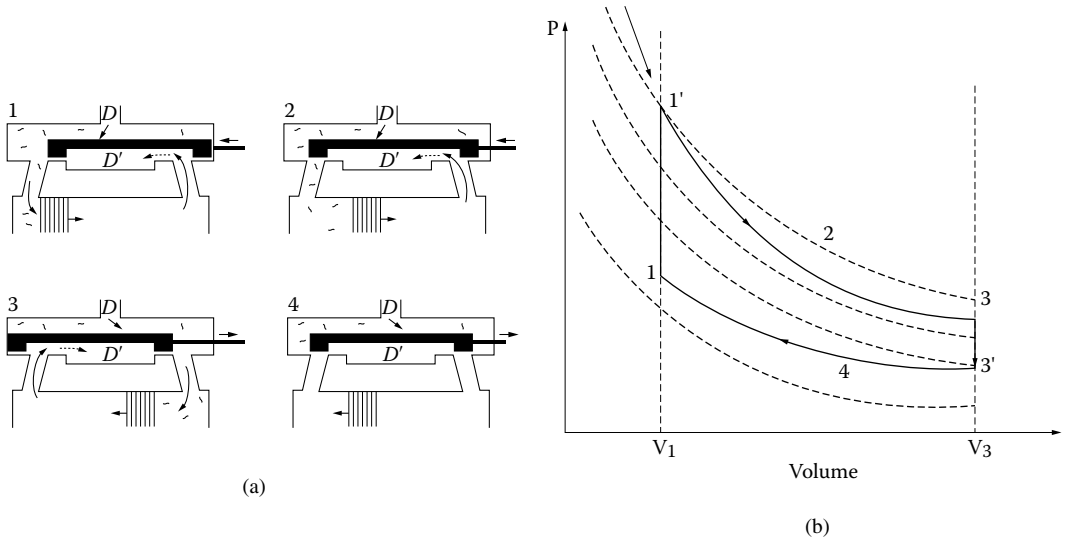
FIGURE 3.23   The steam engine "cycle": (a) the four steps and (b) PV diagram.
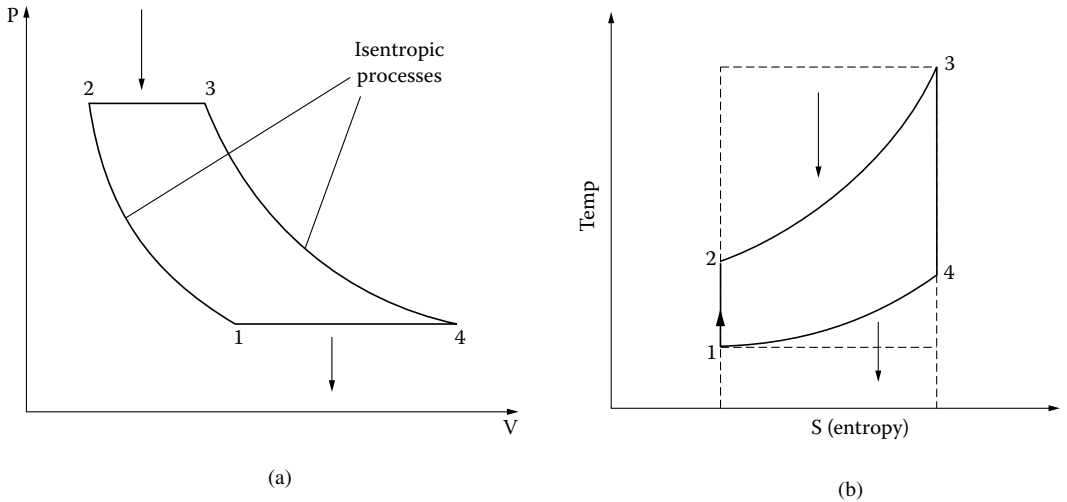
FIGURE 3.24   Brayton cycle for gas turbines: (a) PV diagram and (b) TS diagram.

For $\rho = 2$, $x = 10$, $K = 1.4$, and $\varepsilon = 3$, $\eta_{th} = 31\%$.

The gas turbine engine fuel is also continuously combusted in combination with precompressed air. The gas expansion turns the turbine shaft to produce mechanical power. The gas turbines work on a Brayton cycle (Figure 3.24a and Figure 3.24b). The four steps of a Brayton cycle are as follows:

- Isentropic compression
- Isobaric input of thermal energy
- Isentropic expansion (work generation)
- Isobaric thermal energy loss

Similarly, with $T_1/T_4 = T_2/T_3$ for the isentropic steps, and the injection ratio $\rho = T_3/T_2$, the thermal efficiency η_{th} is as follows:

$$\eta_{th} \approx 1 - \frac{1}{\rho}\frac{T_4}{T_2} \qquad (3.17a)$$

With ideal, complete, heat recirculation:

$$\eta_{th} \approx 1 - \frac{1}{\rho} \qquad (3.17b)$$

Gas turbines are more compact than other thermal machines; they are easy to start and have low vibration, but they also have low efficiency at low loads (ρ small) and tend to have poor behavior during transients.

The spark-ignition (Otto) engines work on the cycle shown in Figure 3.25a and Figure 3.25b. The four steps are as follows:

- Isentropic compression
- Isochoric input of thermal energy
- Isentropic expansion (kinetic energy output)
- Isochoric heat loss

The ideal thermal efficiency η_{th} is

$$\eta_{th} = 1 - \frac{1}{\varepsilon^{K-1}}; \varepsilon = V_1 / V_2 \qquad (3.18)$$

where

$$\frac{T_4}{T_3} = \frac{T_1}{T_2} = \left(\frac{V_3}{V_4}\right)^{K-1} = \frac{1}{\varepsilon^{K-1}} \qquad (3.19)$$

for isentropic processes. With a high compression ratio (say $\varepsilon = 9$) and the adiabatic coefficient K = 1.5, $\eta_{th} = 0.66$.
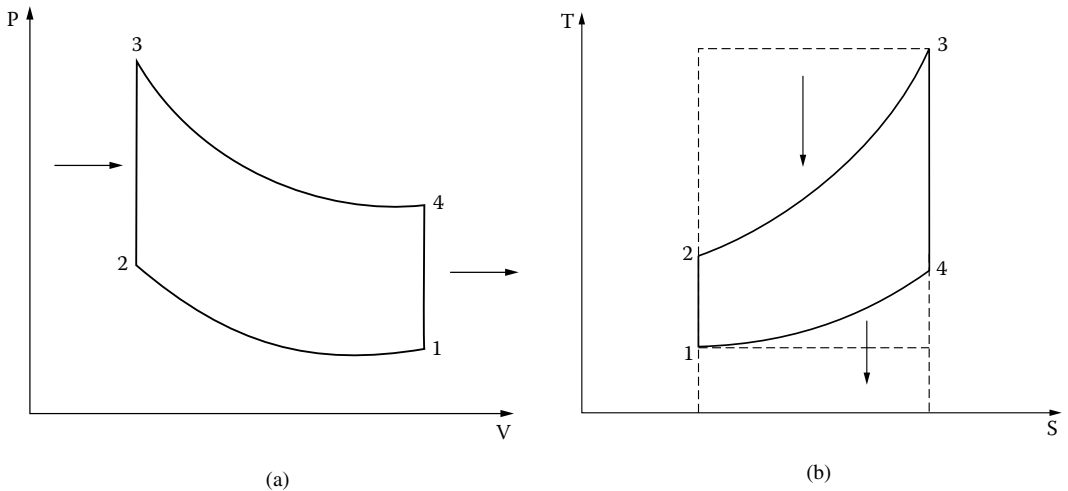
FIGURE 3.25 Spark-ignition engines: (a) PV diagram and (b) TS diagram.
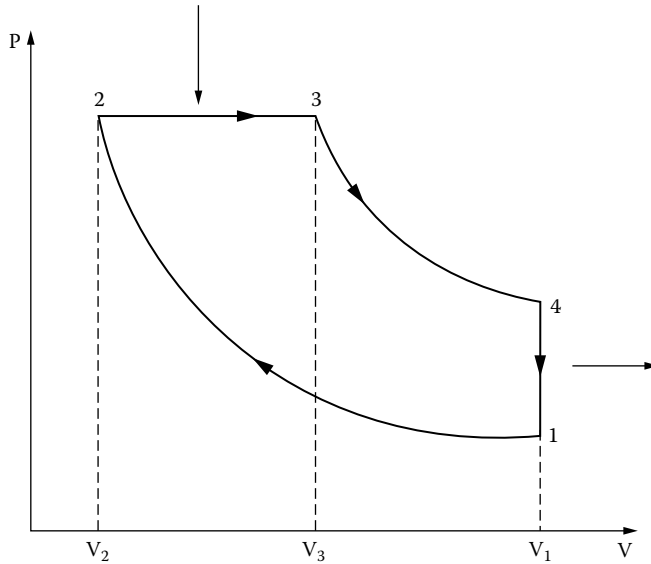
FIGURE 3.26 The diesel-engine cycle.

The diesel-engine cycle is shown in Figure 3.26. During the downward movement of the piston, an isobaric state change takes place by controlled injection of fuel:

$$\rho = \frac{V_3}{V_2} = \frac{T_3}{T_2};$$

$$\eta_{th} = 1 - \frac{1}{\varepsilon^{K-1}} \cdot \frac{1}{K} \frac{\rho^K - 1}{\rho - 1}$$

(3.20)

Efficiency decreases when load ρ increases, in contrast to spark-ignition engines for the same ε. Lower compression ratios (ε) than those for spark-ignition engines are characteristic of diesel engines so as to obtain higher thermal efficiency.

3.7.2 The Stirling-Cycle Engine

The Stirling engine (developed in 1816) is a piston engine with continuous heat supply (Figure 3.27a through Figure 3.27c). In some respects, the Stirling cycle is similar to the Carnot cycle (with its two isothermal steps). It contains two opposed pistons and a regenerator in between. The regenerator is made in the form of strips of metal. One of the two volumes is the expansion space kept at a high temperature $T_{\max}$, while the other volume is the compression space kept at a low temperature $T_{\min}$. Thermal axial conduction is considered negligible. Suppose that the working fluid (all of it) is in the cold compression space.

During compression (steps 1 to 2), the temperature is kept constant because heat is extracted from the compression space cylinder to the surroundings.

During the transfer step (steps 2 to 3), both pistons move simultaneously; the compression piston moves toward the regenerator, while the expansion piston moves away from it. So, the volume stays constant. The working fluid is, consequently, transferred through the porous regenerator from compression to expansion space and is heated from $T_{\min}$ to $T_{\max}$. An increase in pressure also takes place between steps 2 and 3. In the expansion step (3 to 4), the expansion piston still moves away from the regenerator, but the compression piston stays idle at an inner dead point. The pressure decreases, and the volume

Hot volume (expansion)   Cold volume (compression)

p_K, T_E p_K, T_K

Piston   Piston

Heater   Regenerator   Cooler

(a)

Close cycle (by regenerator)

From heater

To cooler

(b)   (c)
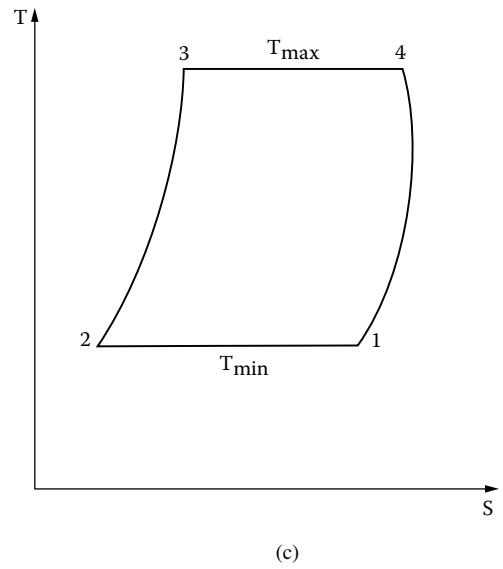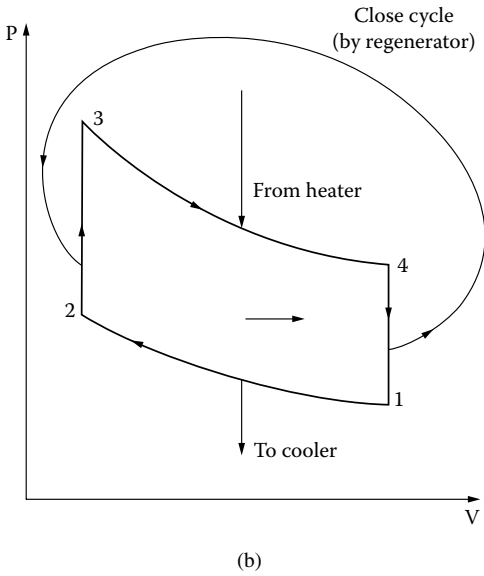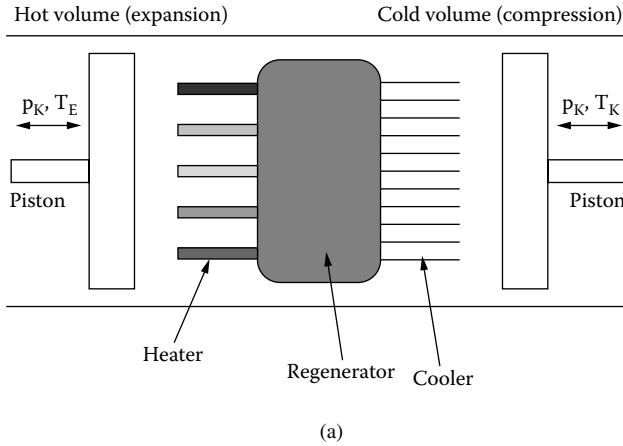
FIGURE 3.27 The Stirling engine: (a) mechanical representation and (b) and (c) the thermal cycle.

increases, but the temperature stays constant, because heat is added from an external source. Then, again, a transfer step (step 4 to step 1) occurs, with both pistons moving simultaneously to transfer the working fluid (at constant volume) through the regenerator from the expansion to the compression space. Heat is transferred from the working fluid to the regenerator, which cools at T_{min} in the compression space.

The ideal thermal efficiency η_{th} is as follows:

$$\eta_{th}^{i} = 1 - \frac{T_{min}}{T_{max}} \tag{3.21}$$

So, it is heavily dependent on the maximum and minimum temperatures, as is the Carnot cycle. Practical Stirling-type cycles depart from the ideal. The practical efficiency of Stirling-cycle engines is much lower: $\eta_{th} < \eta_{th}K_{th}$ ($K_{th} < 0.5$, in general).

Stirling engines may use any heat source and can use various working fuels, such as air, hydrogen, or helium (with hydrogen the best and air the worst). Typical total efficiencies vs. high pressure/liter density
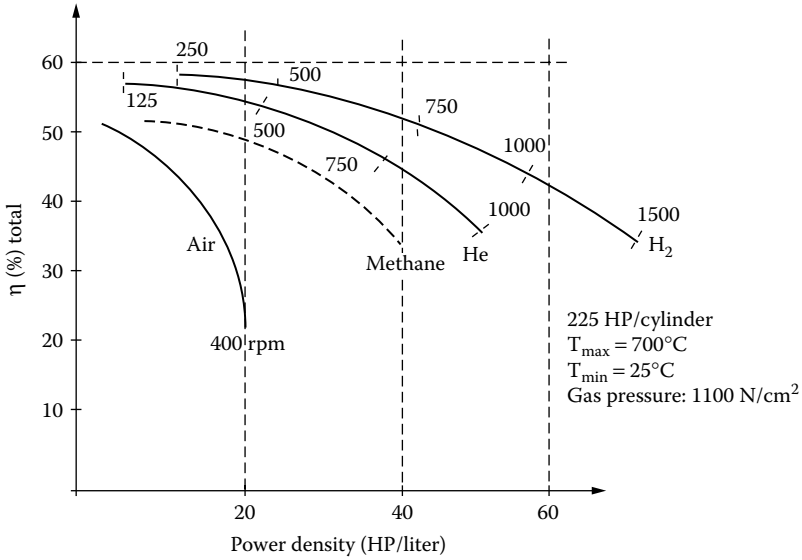
FIGURE 3.28 Efficiency/power density of Stirling engines.
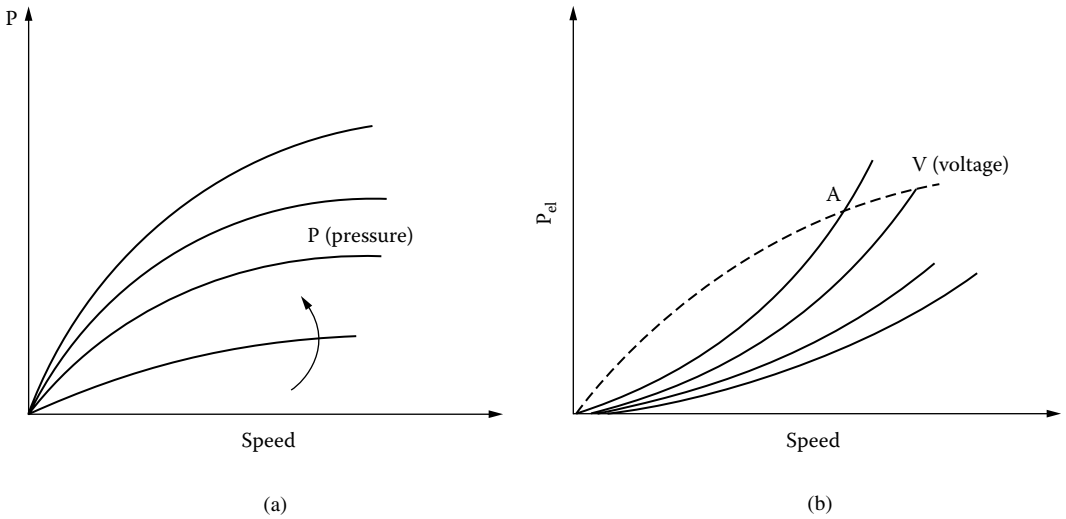
FIGURE 3.29 Power/speed curves: (a) the Stirling engine and (b) the electric generator.

are shown in Figure 3.28 [14] for three working fluids at various speeds. As the power and speed go up, the power density decreases. Methane may be a good replacement for air for better performance.

Typical power/speed curves of Stirling engines with pressure p are shown in Figure 3.29a. And, the power/speed curves of a potential electric generator, with speed, and voltage V as a parameter, appear in Figure 3.29b. The intersection at point A of the Stirling engine and the electric generator power/speed curves looks clearly like a stable steady-state operation point. There are many variants for rotary-motion Stirling engines [14].

3.7.3 Free-Piston Stirling Engines Modeling

Free-piston linear-motion Stirling engines were recently developed (by Sunpower and STC companies) for linear generators for spacecraft or home electricity production (Figure 3.30) [15].
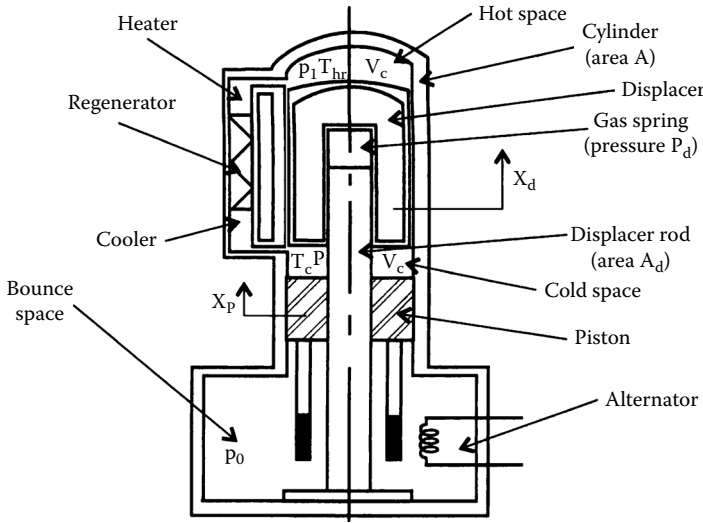
FIGURE 3.30 Linear Stirling engine with free-piston displacer mover.

The dynamic equations of the Stirling engine (Figure 3.30) are as follows:

$$M_d \ddot{X}_d + D_d \dot{X}_d = A_d (P_p - P) \tag{3.22}$$

for the normal displacer, and

$$M_p \ddot{X}_p + D_p \dot{X}_p + F_{elm} + K_p X_p + \left(A - A_d\right)\frac{\partial P}{\partial x_d} X_d = 0 \tag{3.23}$$

for the piston, where
    A_d = the displacer rod area (m²)
    D_d = the displacer damping constant (N/msec)
    P_d = the gas spring pressure (N/m²)
    P = the working gas pressure (N/m²)
    D_p = the piston damping constant (N/msec)
    X_d = the displacer position (m)
    X_p = the power piston position (m)
    A = the cylinder area (m²)
    M_d = the displacer mass (kg)
    M_p = the power piston mass (kg)
    F_{elm} = the electromagnetic force (of linear electric generator) (N)

Equation 3.22 through Equation 3.23 may be linearized as follows:

$$M_d \ddot{X}_d + D_d \dot{X}_d = -K_d X_d - \alpha_p X_p$$

$$M_p \ddot{X}_p + D_p \dot{X}_p + F_{elm} = -K_p X_p - \alpha_T X_d \tag{3.24}$$
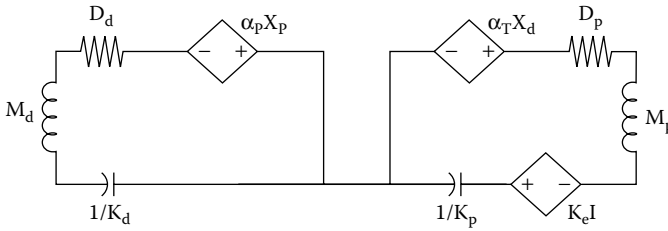
FIGURE 3.31 Free-piston Stirling engine dynamics model.

$$K_d = -A_d \frac{\partial P_d}{\partial X_d} - \frac{\partial P}{\partial X_d}; \alpha_p = \frac{\partial P}{\partial X_d} A_d$$

$$K_p = (A - A_d) \frac{\partial P}{\partial X_p}; \alpha_T = (A - A_d) \frac{\partial P}{\partial X_d}; F_{elm} = K_e I \tag{3.25}$$

where I is the generator current.

The electric circuit correspondent of Equation 3.25 is shown in Figure 3.31.

The free-piston Stirling engine model in Equation 3.25 is a fourth-order system, with $X_d, \dot{X}_d, X_p, \dot{X}_p$ as variables. Its stability when driving a linear permanent magnet (PM) generator will be discussed in Chapter 12 of *Variable Speed Generators*, dedicated to linear reciprocating electric generators. It suffices to say here that at least in the kilowatt range, such a combination was proven stable in stand-alone or power-grid-connected electric generator operation modes.

The merits and demerits of Stirling engines are as follows:

- Independent from heat source: fossil fuels, solar energy
- Very quiet
- High theoretical efficiency; not so large in practice yet, but still 35 to 40% for $T_{max} = 800°C$ and $T_{min} = 40°C$
- Reduced emissions of noxious gases
- High initial costs
- Conduction and storage of heat are difficult to combine in the regenerator
- Materials have to be heat resistant
- Heat exchanger is needed for the cooler for high efficiency
- Not easy to stabilize

A general qualitative comparison of thermal engines is summarized in Table 3.2.

3.8 Hydraulic Turbines

Hydraulic turbines convert the water energy of rivers into mechanical work at the turbine shaft. River water energy and tidal (wave) sea energy are renewable. They are the results of water circuits and are gravitational (tide energy) in nature, respectively. Hydraulic turbines are one of the oldest prime movers used by man.

The energy agent and working fluid is water, in general, the kinetic energy of water (Figure 3.32). Wind turbines are similar, but the wind/air kinetic energy replaces the water kinetic energy. Wind turbines will be treated separately, however, due to their many particularities. Hydraulic turbines are, generally, only prime movers, that is, motors. There are also reversible hydraulic machines that may operate either as turbines or as pumps. They are also called hydraulic turbine pumps. There are hydrodynamic transmissions made of two or more conveniently mounted hydraulic machines in a single frame. They play

TABLE 3.2

Parameter Thermal Engine	Combustion Type	Efficiency	Quietness	Emissions	Fuel Type	Starting	Dynamic Response
Steam turbines	Continuous	Poor	Not so good	Low	Multifuel	Slow	Slow
Gas turbines	Continuous	Good at full loads, low at low load	Good	Reduced	Independent	Easy	Poor
Stirling engines	Continuous	High in theory, lower so far	Very good	Very low	Independent	N/A	Good
Spark-ignition engines	Discontinuous	Moderate	Rather bad	Still large	One type	Fast	Very good
Diesel engines	Discontinuous	Good	Bad	Larger	One type	Rather fast	Good
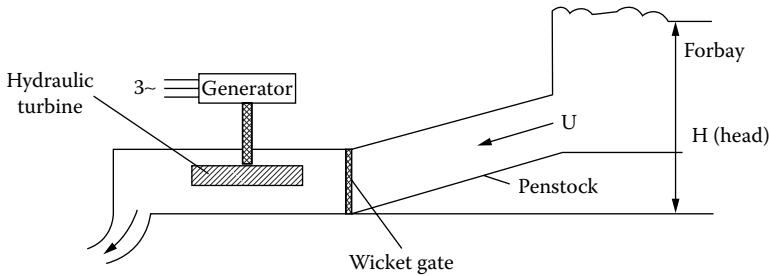
FIGURE 3.32 Hydropower plant schematics.

TABLE 3.3 Hydraulic Turbines

Turbine	Type	Head	Inventor	Trajectory
Tangential	Impulse	>300 m	Pelton (P)	Designed in the transverse plane
Radial-axial	Reaction	<50 m	Francis (F)	Bent into the axial plane
Axial	Reaction (propeller)	<50 m	Kaplan (K), Strafflo (S), Bulb (B)	Bent into the axial plane

the role of mechanical transmissions but have active control. Hydrodynamic transmissions fall beyond our scope here.

There are two main types of hydraulic turbines: impulse turbines for heads above 300 to 400 m, and reaction turbines for heads below 300 m. A more detailed classification is related to the main direction of the water particles in the rotor zone: bent axially or transverse to the rotor axis or related to the inventor (Table 3.3). In impulse turbines, the run is at atmospheric pressure, and all pressure drops occur in the nozzles, where potential energy is turned into kinetic energy of water which hits the runner. In reaction turbines, the pressure in the turbine is above the atmospheric pressure; water supplies energy in both potential and kinetic forms to the runner.

3.8.1 Hydraulic Turbines Basics

The terminology in hydraulic turbines is related to variables and characteristics [16]. The main variables are of geometrical and functional types:

- Rotor diameter: D_r (m)
- General sizes of the turbine

- Turbine gross head: H_T (m)
- Specific energy: $Y_T = gH_T$ (J/kg)
- Turbine input flow rate: Q (m³/sec)
- Turbine shaft torque: T_T (Nm)
- Turbine shaft power: P_T (W [kW, MW])
- Rotor speed: Ω_T (rad/sec)
- Liquid (rotor properties):
  - Density: ρ (kg/m³)
  - Cinematic viscosity: ν (m²/sec)
  - Temperature: T (°C)
  - Elasticity module: E (N/m²)

The main characteristics of a hydraulic turbine are generally as follows:

- Efficiency:

$$\eta_T = \frac{P_T}{P_h} = \frac{T_T \cdot \Omega_r}{\rho g H_T Q} \tag{3.26}$$

- Specific speed n_S:

$$n_S = n \frac{\sqrt{P_T \cdot 0.736}}{H_T^{5/4}}, rpm \tag{3.27}$$

with n equal to rotor speed in revolutions per minute, P_T is measured in kilowatts, and H_T in meters. The specific speed corresponds to a turbine that for a head of 1 m produces 1 HP (0.736 kW).
- Characteristic speed n_C:

$$n_c = \frac{n\sqrt{Q}}{H_T^{3/4}}, rpm \tag{3.28}$$

n equals the rotor speed in revolutions per minute, Q equals the flow rate in cubic meters per second, and H_T is measured in meters.
- Reaction rate γ:

$$\gamma = \frac{p_1 - p_2}{\rho g H_T} \tag{3.29}$$

where p_1, p_2 are the water pressures right before and after the turbine rotor. $\gamma = 0$ for Pelton turbines; ($p_1 = p_2$) for zero-reaction (impulse) turbines; and $0 < \gamma < 1$ for radial–axial and axial turbines (Francis, Kaplan turbines).
- Cavitation coefficient σ_T:

$$\sigma_T = \frac{\Delta h_i}{H_T} \tag{3.30}$$

with Δh_i equal to the net positive suction head.
It is good for σ_t to be small, $\sigma_t = 0.01 - 0.1$. It increases with n_S and decreases with H_T.

• Specific weight G_{sp}:

$$G_{sp} = \frac{G_T}{P_T}, N/kW \tag{3.31}$$

with G_T equal to the turbine mass $\times$ g, in N.
    In general $G_{sp} \approx 70 - 150$ N/kW.

Generally, the rotor diameter $D_r = 0.2 - 12$ m, the head $H_T = 2 - 2000$ m, the efficiency at full load is $\eta_T = 0.8 - 0.96$, the flow rate $Q = 10^{-3} - 10^3$ m³/sec, and rotor speed is $n \approx 50 - 1000$ rpm.

Typical variations of efficiency [16] with load are given in Figure 3.33. The maximum efficiency [16] depends on the specific speed n_S and on the type of turbine (Figure 3.34).

The specific speed is a good indicator of the best type of turbine for a specific hydraulic site. In general, $n_{Sopt} = 2 - 64$ for Pelton turbines, $n_S = 50 - 500$ for Francis turbines, and $n_S = 400 - 1700$ for Kaplan turbines. The specific speed n_S could be changed by changing the rotor speed n, the total power division in multiple turbines rotors or injectors, and the turbine head. The tendency is to increase n_S in order to reduce turbine size, by increasing rotor speed, at the costs of higher cavitation risk.
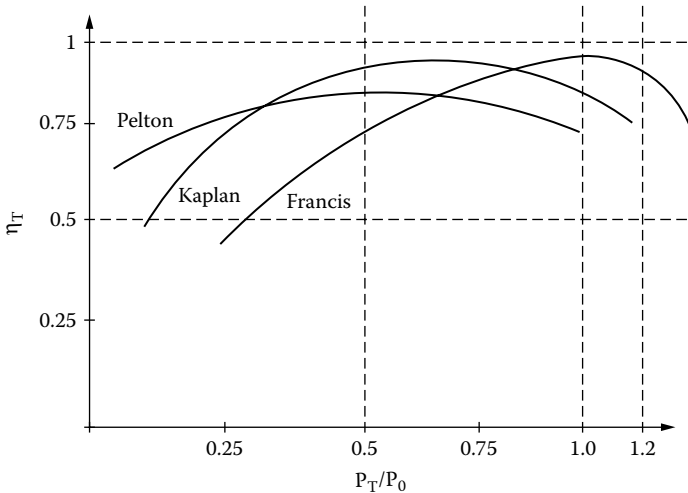
FIGURE 3.33 Typical efficiency/load for Pelton, Kaplan, and Francis turbines.
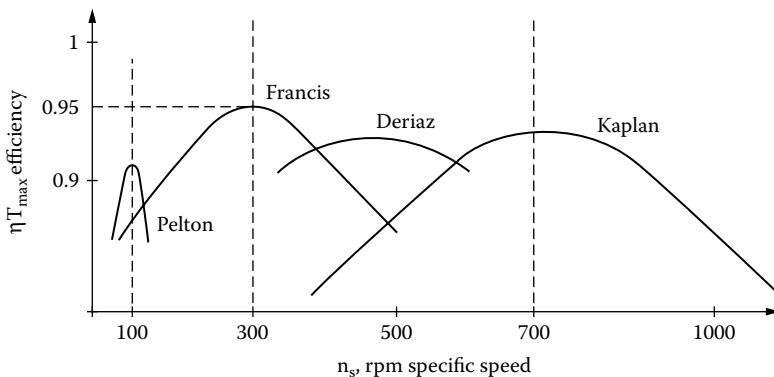
FIGURE 3.34 Maximum efficiency vs. specific speed.
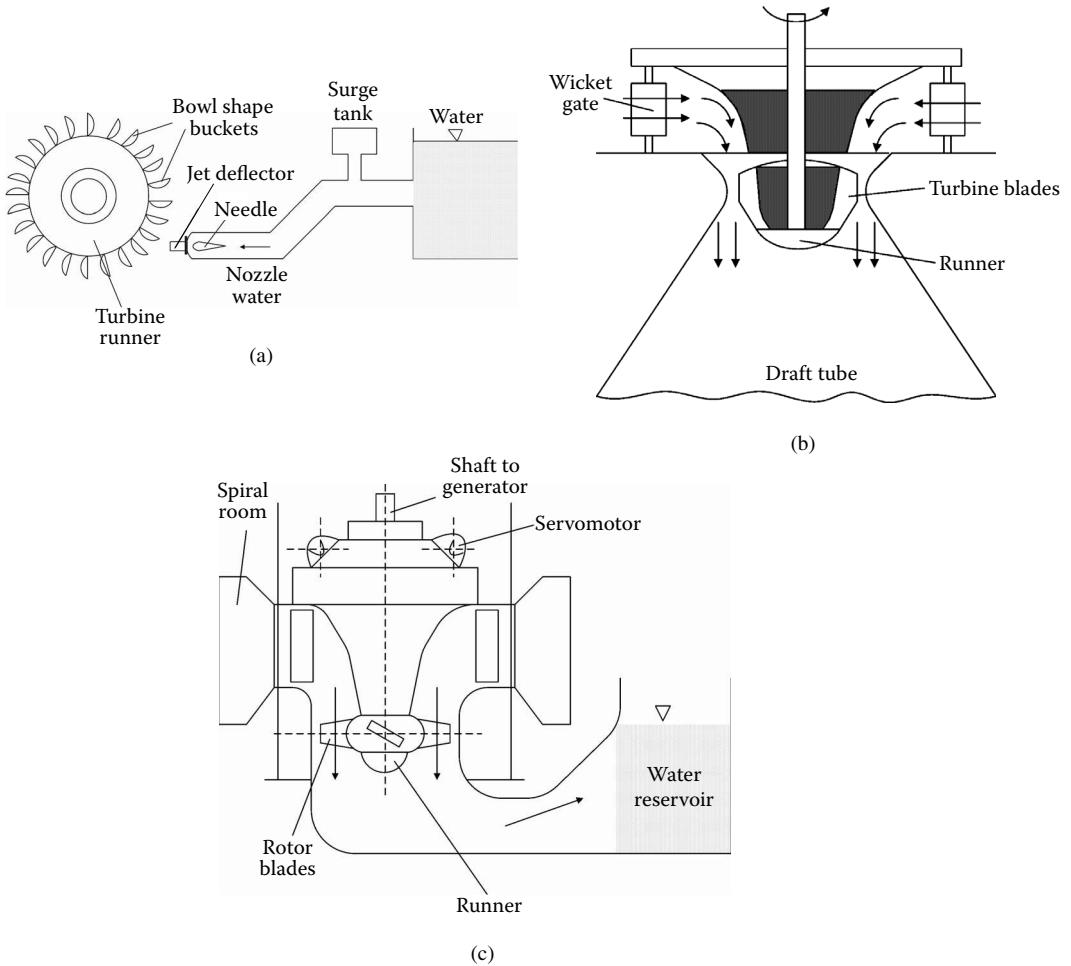
FIGURE 3.35   Hydraulic turbine topology: (a) Pelton type, (b) Francis type, and (c) Kaplan type.

As expected, the efficiency of all hydraulic turbines tends to be high at rated load. At part load, Pelton turbines show better efficiency. The worst at part load is the Francis turbine. It is, thus, the one more suitable for variable speed operation. Basic topologies for Pelton, Francis, and Kaplan turbines are shown in Figure 3.35a through Figure 3.35c.

In the high-head impulse (Pelton) turbine, the high-pressure water is converted into high-velocity water jets by a set of fixed nozzles. The high-speed water jets hit the bowl-shaped buckets placed around the turbine runner, and mechanical torque is produced at the turbine shaft. The area of the jet is controlled by a needle placed in the center of the nozzle. The needle is actuated by the turbine governor (servomotor). In the event of sudden load reduction, the water jet is deflected from the buckets by a jet deflector (Figure 3.35a).

In contrast, reaction (radial–axial) or Francis hydraulic turbines (Figure 3.35b) use lower head and high volumes of water, and run at lower speeds. The water enters the turbine from the intake passage or penstock, goes through a spiral chamber, then passes through the movable wicket gates onto the turbine runner, and then, through the draft tube, goes to the tail water reservoir. The wicket gates have their axes parallel to the turbine axis. In Francis turbines, the upper ends of the rotor blades are tightened to a crown and the lower ends to a band.

At even lower head, in Kaplan hydraulic turbines, the rotor blades are adjustable through an oil servomotor placed within the main turbine shaft.

3.8.2 A First-Order Ideal Model of Hydraulic Turbines

Usually, in system stability studies, with the turbine coupled to an electrical generator connected to a power grid, a simplified (classical) model of the hydraulic turbine is used. Such a model assumes that water is incompressible, the penstock is inelastic, the turbine power is proportional to the product of head and volume flow (volume flow rate), and the velocity of water varies with the gate opening and with the square root of net head [2].

There are three fundamental equations to consider:

- Water velocity u equation in the penstock
- Turbine shaft (mechanical) power equation
- Acceleration of water volume equation

According to the above assumptions, the water velocity in the penstock u is

$$u = K_u G \sqrt{H} \tag{3.32}$$

where

G = the gate opening
H = the net head at the gate

Linearizing this equation and normalizing it to rated quantities ($u_0 = K_u G_0 \sqrt{H_0}$) yields the following:

$$\frac{\Delta U}{U_0} = \frac{\Delta H}{2H_0} + \frac{\Delta G}{G_0} \tag{3.33}$$

The turbine mechanical power P_m is written

$$P_m = K_p H U \tag{3.34}$$

After normalization ($P_{m0} = K_p H_0 U_0$) and linearization, Equation 3.34 becomes

$$\frac{\Delta P_m}{P_0} = \frac{\Delta H}{H_0} + \frac{\Delta U}{U_0} \tag{3.35}$$

Substituting $\dfrac{\Delta H}{H_0}$ or $\dfrac{\Delta U}{U_0}$ from Equation 3.33 into Equation 3.35 yields the following:

$$\frac{\Delta P_m}{P_0} = 1.5\frac{\Delta H}{H_0} + \frac{\Delta G}{G_0} \tag{3.36}$$

and finally,

$$\frac{\Delta P_m}{P_0} = 3\frac{\Delta U}{U_0} - 2\frac{\Delta G}{G_0} \tag{3.37}$$

The water column that accelerates due to change in head at the turbine is described by its motion equation:

$$\rho L A \frac{d\Delta U}{dt} = -A(\rho g)\Delta H \tag{3.38}$$

where

ρ = the mass density
L = the conduit length
A = the pipe area
g = the acceleration of gravity

By normalization, Equation 3.38 becomes

$$T_W \frac{d}{dt}\frac{\Delta U}{U_0} = -\frac{\Delta H}{H_0} \tag{3.39}$$

where

$$T_W = \frac{LU_0}{gH_0} \tag{3.40}$$

is the water starting time. It depends on load, and it is in the order of 0.5 sec to 5 sec for full load.

Replacing d/dt with the Laplace operator, from Equation 3.33 and Equation 3.39, one obtains the following:

$$\frac{\frac{\Delta U}{U_0}}{\frac{\Delta G}{G_0}} = \frac{1}{1+\frac{T_W}{2}s} \tag{3.41}$$

$$\frac{\frac{\Delta P_m}{P_0}}{\frac{\Delta G}{G_0}} = \frac{1-T_W \cdot s}{1+\frac{T_W}{2}s} \tag{3.42}$$

The transfer functions in Equation 3.41 and Equation 3.42 are shown in Figure 3.36. The power/gate opening transfer function (Equation 3.42) has a zero in the right s plane. It is a nonminimum phase system that cannot be identified completely by investigating only its amplitude from its amplitude/frequency curve.

For a step change in gate opening, the initial and final value theorems yield the following:

$$\frac{\Delta P_m}{P_0}(0) = \lim_{s \to \infty} s\frac{1}{s}\frac{1-T_w s}{1+\frac{1}{2}T_w s} = -2 \tag{3.43}$$

$$\frac{\Delta P_m}{P_0}(\infty) = \lim_{s \to 0}\frac{1-T_w s}{1+\frac{1}{2}T_w s} = 1.0 \tag{3.44}$$
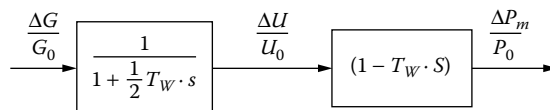
FIGURE 3.36 The linear ideal model of hydraulic turbines in P.U..

The time response to such a gate step opening is

$$\frac{\Delta P_m}{P_0}(t) = \left(1 - 3e^{-2t/T_W}\right)\frac{\Delta G}{G_0} \qquad (3.45)$$

After a unit step increase in gate opening, the mechanical power goes first to a –2 P.U. value and only then increases exponentially to the expected steady state value of 1 P.U. This is due to water inertia.

Practice has shown that this first-order model hardly suffices when the perturbation frequency is higher than 0.5 rad/sec. The answer is to investigate the case of the elastic conduit (penstock) and compressible water where the conduit of the wall stretches at the water wave front.

3.8.3 Second- and Higher-Order Models of Hydraulic Turbines

We start with a slightly more general small deviation (linear) model of the hydraulic turbine [17]:

$$q = a_{11}h + a_{12}n + a_{13}z$$
$$m_t = a_{21}h + a_{22}n + a_{23}z \qquad (3.46)$$

where
> q = the volume flow
> h = the net head
> n = the turbine speed
> z = the gate opening m_t – shaft torque

All variables are measured in P.U. values. As expected, the coefficients a_{11}, a_{12}, a_{13}, a_{21}, a_{22}, a_{23} vary with load and other changes. To a first approximation, $a_{12} \approx a_{22} \approx 0$, and, with constant a_{ij} coefficients, the first-order model is reclaimed.

Now, if the conduit is considered elastic and water as compressible, the wave equation in the conduit may be modeled as an electric transmission line that is open circuited at the turbine end and short-circuited at forebay.

Finally, the incremental head and volume flow rate $h(s)/q(s)$ transfer function of the turbine is as follows [2]:

$$\frac{h(s)}{q(s)} = -\frac{T_w}{T_e}\tanh(T_e \cdot s + F) \qquad (3.47)$$

where
> F = the friction factor
> T_e = the elastic time constant of the conduit

$$T_e = \frac{conduit\_length : L}{wave\_velocity : a}; a = \sqrt{g/\alpha} \qquad (3.48)$$

$$\alpha = \rho g\left(\frac{1}{K} + \frac{D}{Ef}\right) \qquad (3.49)$$

where
> ρ = the water density
> g = the acceleration of gravity

f = the thickness of the conduit wall
D = the conduit diameter
K = the bulk modulus of water compression
E = the Young's modulus of elasticity for the pipe material

Typical values of a are around 1200 m/sec for steel conduits and around 1400 m/sec for rock tunnels. T_e is in the order of fractions of a second and is larger for larger penstocks (Pelton turbines).

If we now introduce Equation 3.41 and Equation 3.42 in Equation 3.47, the power $\Delta P_m(s)$ to gate opening $\Delta z(s)$ in P.U. transfer functions is obtained:

$$G(s) = \frac{\Delta P_m}{\Delta z}(s) = \frac{1 - \frac{T_W}{T_e} \tan h(T_e \cdot s + F)}{1 + \frac{T_W}{2T_e} \tan h(T_e \cdot s + F)} \tag{3.50}$$

Alternatively, from Equation 3.46,

$$G'(s) = \frac{\Delta P_m}{\Delta z}(s) = \frac{1 - q_p - \frac{T_W}{T_e} \tan h(T_e \cdot s + F)}{1 + 0.5 q_p + \frac{T_W}{2T_e} \tan h(T_e \cdot s + F)} \tag{3.51}$$

where q_p accounts for friction.

With $F = q_p = 0$, Equation 3.50 and Equation 3.51 degenerate into the first-order model provided $\tan h\, T_{es} \approx T_{es}$, that is, for very low frequencies:

$$G_1(s) = \frac{1 - T_W \cdot s}{1 + \frac{T_W}{2} \cdot s} \tag{3.52}$$

The frequency response ($s = j\omega$) of Equation 3.50 with $F = 0$ is shown in Figure 3.37.

Now, we may approximate the hyperbolic function with truncated Taylor series [18]:

$$\tan h(T_e \cdot s) = \frac{T_e \cdot s}{1 + \left(\frac{T_e \cdot s}{2}\right)^2} \tag{3.53}$$

$$G_2(s) = \frac{(T_e \cdot s)^2 - 2T_W \cdot s + 2}{(T_e \cdot s)^2 + T_W \cdot s + 2}$$

Figure 3.37 shows comparative results for $G(s)$, $G_1(s)$, and $G_2(s)$ for $T_e = 0.25$ sec and $T_w = 1$ sec.

The second-order transfer function (Figure 3.38) performs quite well to and slightly beyond the first maximum, which occurs in our case at

$$\omega = \frac{\pi}{2T_e} = 6.28 \text{ rad/sec}$$

It is, however, clear that well beyond this frequency, a higher-order approximation is required.
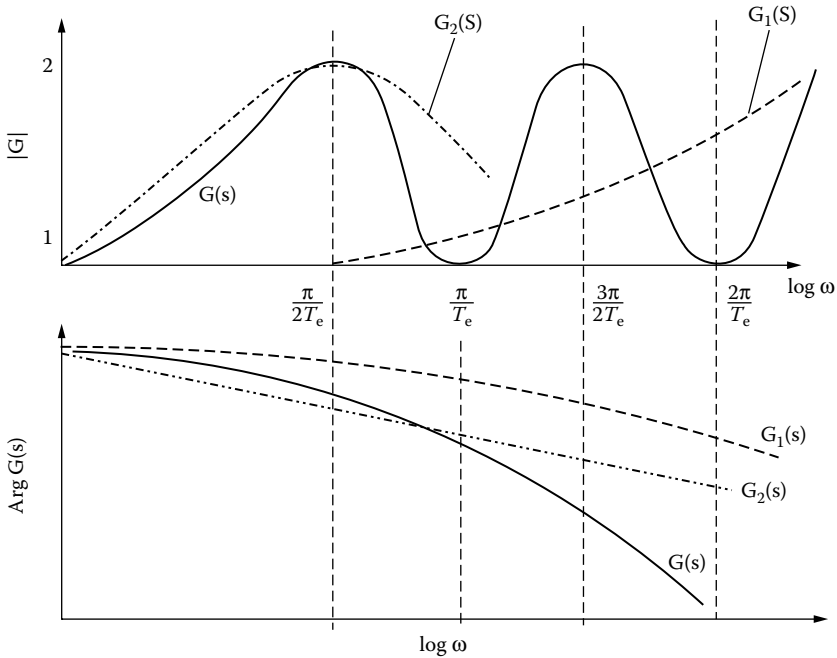
FIGURE 3.37 Higher-order hydraulic turbine frequency response.
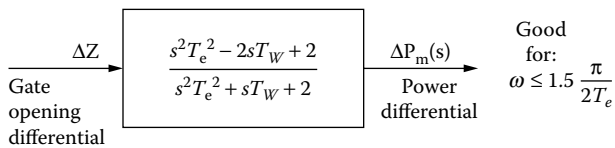
FIGURE 3.38 The second-order model of hydraulic turbines (with zero friction).
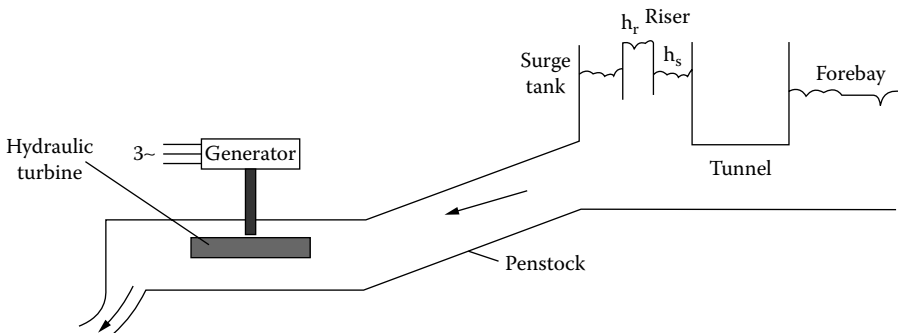
FIGURE 3.39 Hydraulic plant with surge tank.

Such models can be obtained with advanced curve-fitting methods applied to $G_2(s)$ for the frequency range of interest [19,20].

The presence of a surge tank (Figure 3.39) in some hydraulic plants calls for a higher-order model.

The wave (transmission) line equations apply now both for tunnel and penstock. Finally, the tunnel and surge tank can be approximated to $F_1(s)$ [2]:

$$F_1(s) = \frac{q_c + s \cdot T_{WC}}{1 + s \cdot T_s \cdot q_c + s^2 T_{WC} T_S} = -\frac{h_S}{U_p}$$

$$\tanh(T_{ec} \cdot s) = T_{ec} \cdot s \tag{3.54}$$

$$Z_c = \frac{T_{WC}}{T_{ec}}$$

where

T_{ec} = the elastic time constant of the tunnel
T_{WC} = the water starting time in the tunnel
q_c = the surge tank friction coefficient
h_S = the surge tank head
U_p = the upper penstock water speed
T_S = the surge tank riser time ($T_S \approx 600 - 900$ sec)

Now for the penstock, the wave equation yields (in P.U.) the following:

$$h_t = h_r \, \mathrm{sech}(T_{ep} \cdot s) - Z_p U_t \tanh(T_{ep} \cdot s) - q_p U_t$$

$$U_p = U_t \cosh(T_{ep} \cdot s) + \frac{h_t}{Z_p} \sinh(T_{ep} \cdot s) \tag{3.55}$$

where

Z_p = the hydraulic impedance of the penstock $\left(Z_p = \dfrac{T_{Wp}}{T_{ep}} \right)$

q_p = the friction coefficient in the penstock
T_{ep} = the penstock elastic time
T_{Wp} = the penstock water starting time
h_r = the riser head
h_t = the turbine head

The overall water velocity U_p to head at turbine h_t ratio is as follows [2]:

$$F(s) = \frac{U_p}{h_t} = -\frac{\left(1 + F_1(s) \times \tanh(T_{ep} \cdot s)/Z_p\right)}{q_p + F_1(s) + Z_p \tanh(T_{ep} \cdot s)} \tag{3.56}$$

The power differential is written

$$P_m = U_t h_t \text{ in P.U.} \tag{3.57}$$

$F(s)$ now represents the hydraulic turbine with wave (hammer) and surge tank effects considered.

If we add Equation 3.32, which ties the speed at turbine head and gate opening to Equation 3.56 and Equation 3.57, the complete nonlinear model of the hydraulic turbine with penstock and surge tank effects included (Figure 3.40) is obtained.

Notice that g_{fl} and g_{NL} are the full-load and no-load actual gate openings in P.U.

Also, h_0 is the normalized turbine head, U_0 is the normalized water speed at the turbine, U_{NL} is the no-load water speed at the turbine, ω_r is the shaft speed, P_m is the shaft power, and m_t is the shaft torque differential in P.U. values.
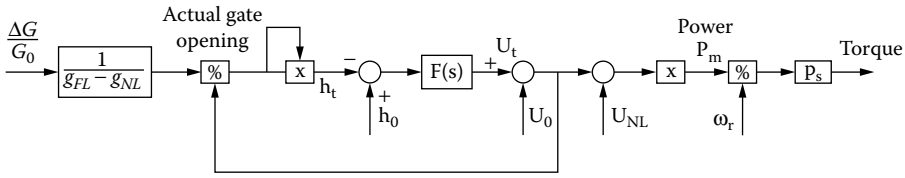
FIGURE 3.40 Nonlinear model of hydraulic turbine with hammer and surge tank effects.

The nonlinear model in Figure 3.40 may be reduced to a high-order (three or more) linear model through various curve fittings applied to the theoretical model with given parameters. Alternatively, frequency response tests may be fitted to a third-order, fourth-order, and so forth, linear system for preferred frequency bands [21].

As the nonlinear complete model is rather involved, the question arises as to when it should be used. Fortunately, only in long-term dynamic studies is it mandatory.

For governor timing studies, as the surge tank natural period (T_s) is of the order of minutes, its consideration is not necessary. Further on, the hammer effect should be considered, but the second-order model suffices.

In transient stability studies, again, the hammer effect should be considered.

For small-signal stability studies, linearization of the turbine penstock model (second-order model) may also be adequate, especially in plants with long penstocks.

3.8.4 Hydraulic Turbine Governors

In principle, hydraulic turbine governors are similar to those used for steam and gas turbines. They are mechanohydraulic or electrohydraulic. In general, for large power levels, they have two stages: a pilot valve servomotor and a larger power gate-servomotor. A classical system with speed control and good performance is shown in Figure 3.41.

T_{PV} = the pilot valve with servomotor time constant (0.05 sec)
T_{GV} = the main (gate) servomotor time constant (0.2 sec)
K_V = the servo (total) gain (5)
$R_{max\ open}$ = the maximum gate opening rate ≈ 0.15 P.U./sec
$R_{max\ close}$ = the maximum closing rate ≈ 0.15 P.U./sec
T_R = the reset time (5 sec)
R_P = the permanent drop (0.04)
R_T = the transient drop (0.4)

Numbers in parentheses above are sample data [2] given only to get a feeling for magnitudes.
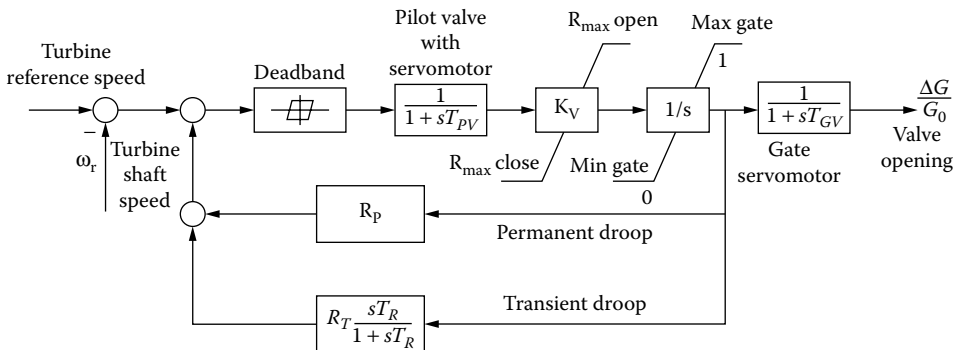
FIGURE 3.41 Typical (classical) governor for hydraulic turbines.

A few remarks on the model in Figure 3.41 are in order:

- The pilot–valve servomotor (lower power stage of governor) may be mechanical or electric; electric servomotors tend to provide faster and more controllable responses.
- Water is not very compressible; thus, the gate motion has to be gradual; near the full closure, even slower motion is required.
- Deadband effects are considered in Figure 3.41, but their identification is not an easy task.
- Stable operation during system islanding (stand-alone operation mode of the turbine–generator system) and acceptable response quickness and robustness under load variations are the main requirements that determine the governor settings.
- The presence of a transient compensation drop is mandatory for stable operation.
- For islanding operation, the choice of temporary drop R_T and reset time T_R is essential; they are related to water starting time constant T_W and mechanical (inertia) time constant of the turbine–generator set T_M. Also, the gain K_V should be high.
  - According to Reference [2],

$$R_T = \left[2.3 - \left(T_W - 1.0 \right) 0.15 \right] \frac{T_W}{T_M}$$

$$T_R = \left[5.0 - \left(T_W - 1.0 \right) 0.5 \right] T_W$$

$$T_M = 2H; \tag{3.58}$$

$$H = \frac{J\omega_0^2}{2S_0}(s)$$

where

$J(\text{kgm}^2)$ = the turbine/generator inertia

ω_0 = the rated angular speed (rad/sec)

S_0 = the rated apparent power (VA) of the electrical generator

- In hydraulic turbines where wicket gates (Figure 3.41) are also used, the governor system has to control their motion also, basing its control on an optimization criterion.

The governing system becomes more involved. The availability of high-performance nonlinear motion controllers (adaptive, variable structure, fuzzy logic, or artificial neural networks) and of various powerful optimization methods [22] puts the governor system control into a new perspective (Figure 3.42).

Though most such advanced controllers have been tried on thermal prime movers and, especially, on power system stabilizers that usually serve only the electric generator excitation, the time for comprehensive digital online control of the whole turbine generator system seems ripe [23, 24]. Still, problems with safety could delay their aggressive deployment; not for a long time, though, we think.

3.8.5 Reversible Hydraulic Machines

Reversible hydraulic machines are, in fact, turbines that work part time as pumps, especially in pump-storage hydropower plants.

Pumping may be required either for land irrigation or for energy storage during off-peak electric energy consumption hours. It is also a safety and stability improvement vehicle in electric power systems in the presence of fast variations of loads over the hours of the day.

As up to 400 MW per unit pump-storage hydraulic turbine pumps are already in operation [25], their "industrial" deployment seems near. Pump-storage plants with synchronous (constant) speed generators (motors) are a well-established technology.
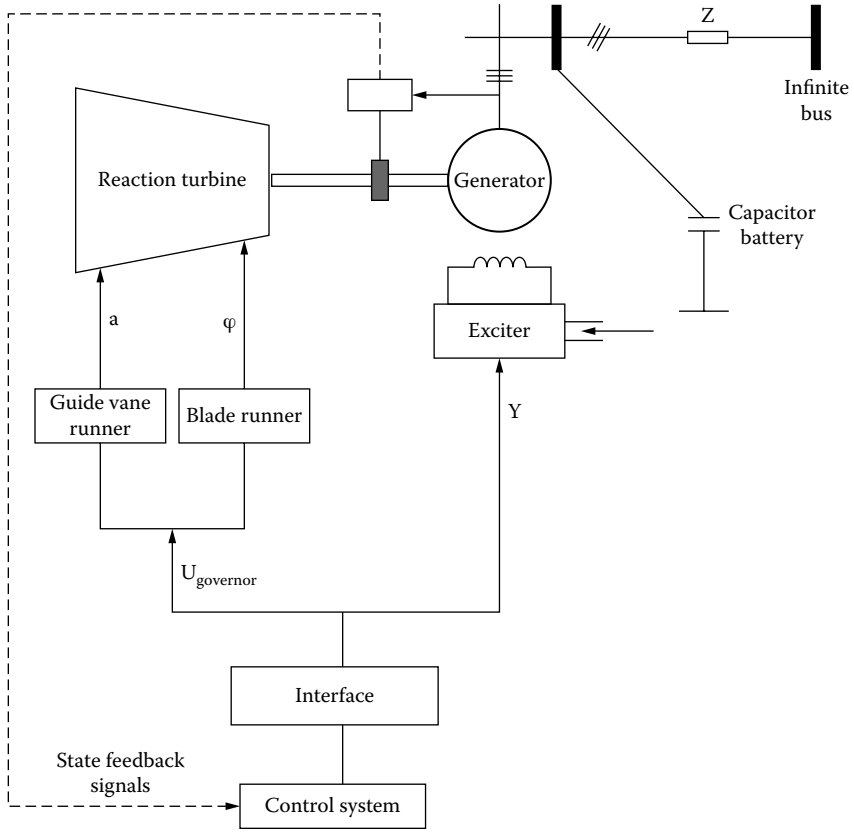
FIGURE 3.42 Coordinated turbine governor–generator–exciter–control system.
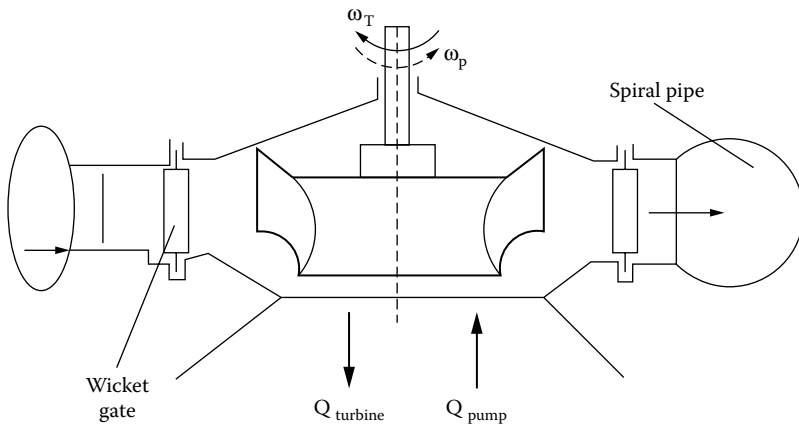
FIGURE 3.43 Radial–axial turbine pump with reversible speed.

A classification of turbine pumps is in order:

- By topology:
  - Radial–axial (Russel Dam) (Figure 3.43)
  - Axial (Annapolis) (Figure 3.44)
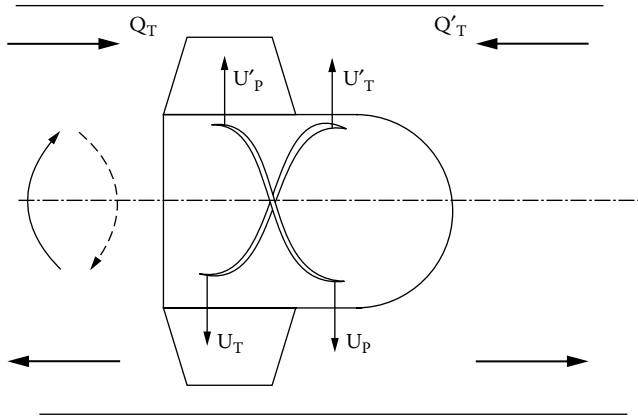
FIGURE 3.44 Axial turbine pump.

- By direction of motion:
  - With speed reversal for pumping (Figure 3.43 and Figure 3.44)
  - Without speed reversal for pumping
- By direction of fluid flow/operation mode:
  - Unidirectional/operation mode (Figure 3.43)
  - Bidirectional/operation mode (Figure 3.44)

There are many topological variations in existing turbine pumps; it is also feasible to design the machine for pumping and then check the performance for turbining, when the direction of motion is reversible.

With pumping and turbining in both directions of fluid flow, the axial turbine pump in Figure 3.44 may be adequate for tidal-wave power plants.

The passing from turbine to pump mode implies the emptying of the turbine chamber before the machine is started by the electric machine as the motor to prepare for pumping. This transition takes time.

More complicated topologies are required to secure unidirectional rotation for both pumping and turbining, though the time to switch from turbining to pumping mode is much shorter.

In order to preserve high efficiency in pumping, the speed in the pumping regime has to be larger than the one for turbining. In effect, the head is larger and the volume flow lower in pumping. A typical ratio for speed would be $\omega_p \approx (1.12 - 1.18)\,\omega_T$. Evidently, such a condition implies adjustable speed and power electronics control on the electric machine side. Typical head/volume flow characteristics [16] for a radial–axial turbine/pump are shown in Figure 3.45. They illustrate the fact that pumping is more efficient at higher speed than turbining and at higher heads, in general. Similar characteristics portray the output power vs. static head for various wicket gate openings [25] (Figure 3.46).

Power increases with speed and higher speeds are typical for pumping. Only wicket gate control by a governor system is used, as adjustable speed is practiced through instantaneous power control in the generator rotor windings, through power electronics.

The turbine governor and electric machine control schemes are specific for generating electric power (turbining) and for pumping [25].

In tidal-wave turbine/pumps, to produce electricity, a special kind of transit takes place from turbining to pumping in one direction of motion and in the other direction of motion in a single day. The static head changes from 0 to 100% and reverses sign (Figure 3.47). These large changes in head are expected to produce large electric power oscillations in the electric power delivered by the generator/motor driven by the turbine pump. Discontinuing operation between pumping and turbining and electric solutions based on energy storage are to be used to improve the quality of power delivered to the electrical power system.
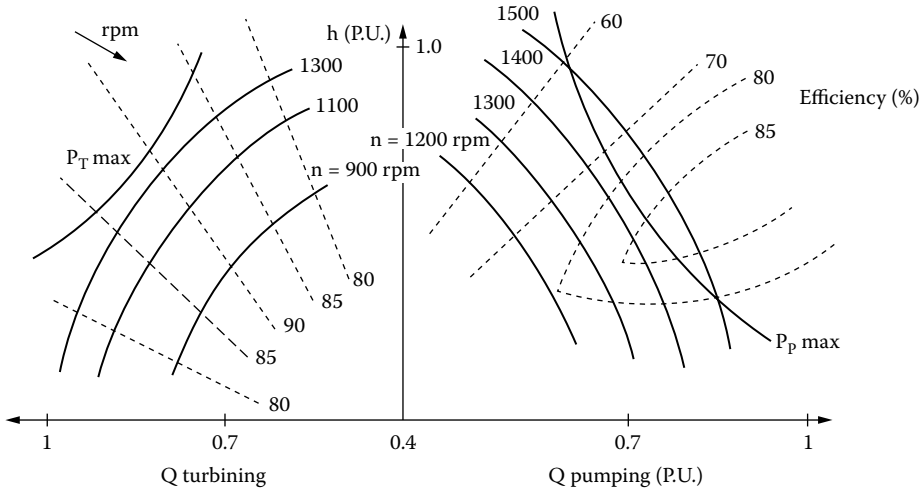
FIGURE 3.45 Typical characteristics of the pumping system of a radial–axial turbine plus pump.
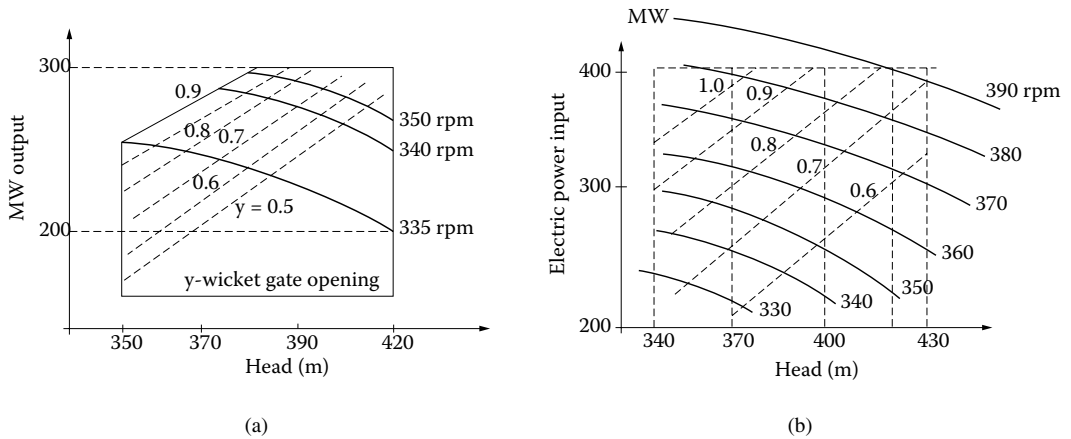
FIGURE 3.46 (a) Turbine/pump system and (b) power/static head curves at various speeds.

3.9 Wind Turbines

Air-pressure gradients along the surface of the Earth produce wind with direction and speed that are highly variable. Uniformity and strength of the wind are dependent on location, height above the ground, and size of local terrain irregularities. In general, wind airflows may be considered turbulent.

In a specific location, the variation of wind speed along the cardinal directions may be shown as in Figure 3.48a. This is important information, as it leads to the optimum directing of the wind turbine, in the sense of extracting the largest energy from wind per year.

Wind speed increases with height (Figure 3.48b) and becomes more uniform. Designs with higher height/turbine diameter lead to more uniform flow and higher energy extraction. These designs come with the price of more expensive towers that are subject to increased structural vibrations.

With constant energy conversion, the turbine power increases approximately with cubic wind speed (u^3) up to a design limit, u_{max}. Above u_{max} (P_{rated}), the power of the turbine is kept constant by some turbine governor control to avoid structural or mechanical inadmissible overload (Figure 3.49).

For a given site, the wind is characterized by the so-called speed deviation (in P.U. per year). For example,
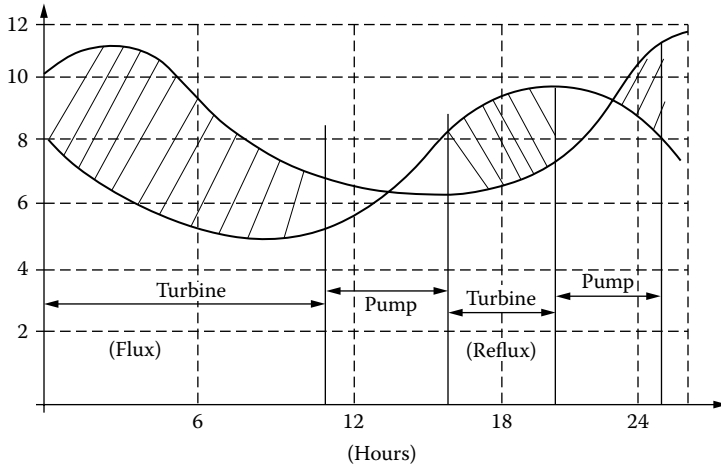
FIGURE 3.47 Head/time of the day in a tidal-wave turbine/pump.
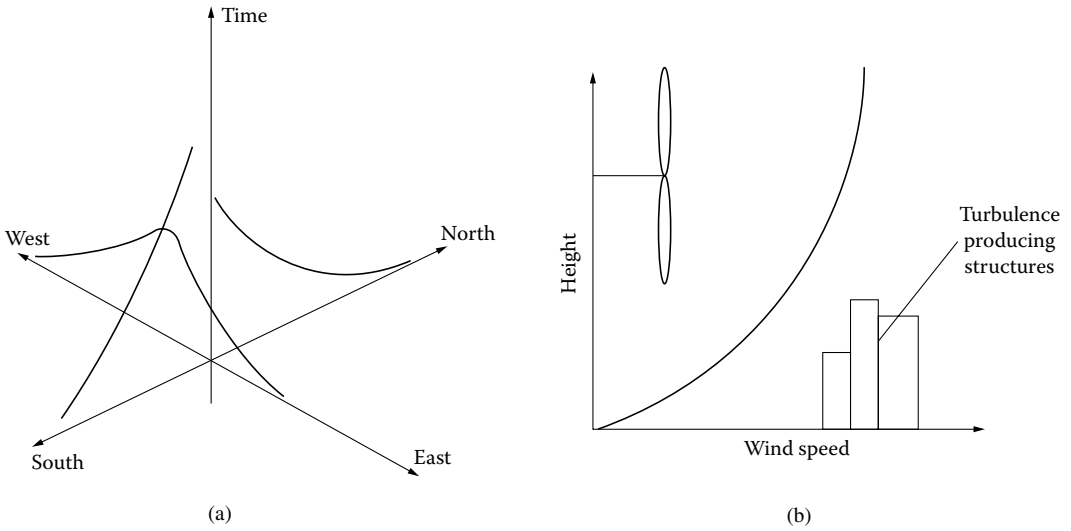
FIGURE 3.48 Wind speed vs. (a) location and (b) height.

$$\frac{t}{t_{max}} = e^{-U^4} \tag{3.59}$$

The slope of this curve is called speed/frequency curve *f*:

$$f(U) = -\frac{d\left(\dfrac{t}{t_{max}}\right)}{dU} \tag{3.60}$$

The speed/time is monotonical (as speed increases, its time occurrence decreases), but the speed/frequency curve generally experiences a maximum. The average speed U_{ave} is defined as follows:
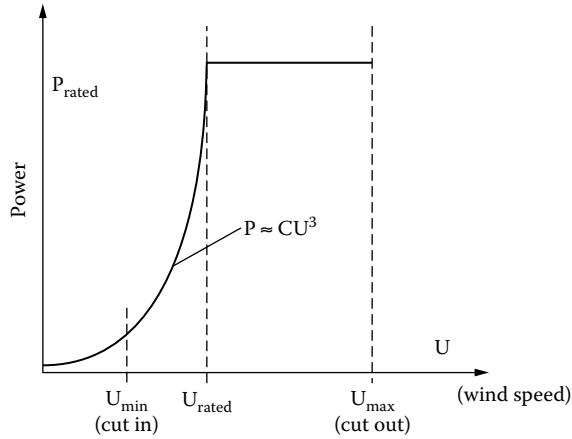
FIGURE 3.49 Wind turbine power vs. wind speed.

$$U_{ave} = \int_0^\infty U f(U) dU \tag{3.61}$$

Other mean speed definitions are also used.

The energy content of the wind E, during t_{max} (1 year) is then obtained from the integral:

$$\frac{Energy\_during\_t_{max}}{\rho \cdot (disc\_area)} = \int_0^\infty U^3 f(U) dU \tag{3.62}$$

with $E(U) = U^3 f(U)$, the energy available at speed U. Figure 3.50 illustrates this line of thinking.

The time average speed falls below the frequency/speed maximum f_{max}, which, in turn, is smaller than the maximum energy per unit speed range E_{max}.

The adequate speed zone for efficient energy extraction is also apparent in Figure 3.50.
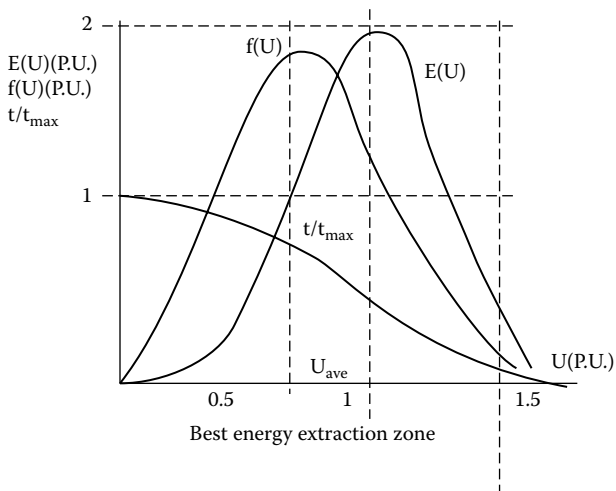
FIGURE 3.50 Sample time/speed, frequency/speed (f), and energy (E)/speed.

It should be borne in mind that these curves, or their approximations, depend heavily on location. In general, inland sites are characterized by large variations of speed over the day and month, while winds from the sea tend to have smaller variations in time.

Good extraction of energy over a rather large speed span, as in Figure 3.50, implies operation of the wind turbine over a pertinent speed range. The electric generator has to be capable of operating at variable speed in such locations.

There are constant-speed and variable-speed wind turbines.

3.9.1 Principles and Efficiency of Wind Turbines

For centuries, windmills operated in countries including Holland, Denmark, Greece, Portugal, and others. The best locations are situated either in the mountains or by the sea or by the ocean shore (or offshore). Wind turbines are characterized by the following:

- Mechanical power P(W)
- Shaft torque (Nm)
- Rotor speed n (rpm) or ω_r (rad/sec)
- Rated wind speed U_R
- Tip speed ratio:

$$\lambda = \frac{\omega_r \cdot D_r / 2}{U} = \frac{rotor\_blade\_tip\_speed}{wind\_speed} \tag{3.63}$$

The tip speed ratio $\lambda < 1$ for slow-speed wind turbines, and $\lambda > 1$ for high-speed wind turbines. The power efficiency coefficient C_p is as follows:

$$C_p = \frac{8P}{\rho \pi D_r^2 \cdot U^3} <> 1 \tag{3.64}$$

In general, C_p is a single maximum function of λ that strongly depends on the type of the turbine. A classification of wind turbines is thus in order:

- Axial (with horizontal shaft)
- Tangential (with vertical shaft)

The axial wind turbines may be slow (Figure 3.51a) and rapid (Figure 3.51b). The shape of the rotor blades and their number are quite different for the two configurations.

The slow axial wind turbines have a good starting torque and the optimum tip speed ratio $\lambda_{opt} \approx 1$, but their maximum power coefficient $C_{pmax}(\lambda_{opt})$ is moderate ($C_{pmax} \approx 0.3$). In contrast, rapid axial wind turbines self-start at higher speeds (above 5 m/sec wind speed), but for an optimum tip speed ratio $\lambda_{opt} \geq 7$, they have a maximum power coefficient $C_{pmax} \approx 0.4$, that is, a higher energy conversion ratio (efficiency).

For each location, the average wind speed U_{ave} is known. The design wind speed U_R is generally around 1.5 U_{ave}. The optimum tip speed ratio λ_{opt} increases as the number of rotor blades Z_1 decreases:

$$(\lambda_{opt}, Z_1) = (1, 8–24; 2, 6–12; 3, 3–6; 4, 2–4; 5, 2–3; >5, 2) \tag{3.65}$$

Three or two blades are typical for rapid axial wind turbines.

The rotor diameter D_r, may be, to a first approximation, calculated from Equation 3.64 for rated (design conditions) — P_{rated}, λ_{opt}, C_{popt}, U_R — with the turbine speed from Equation 3.63.
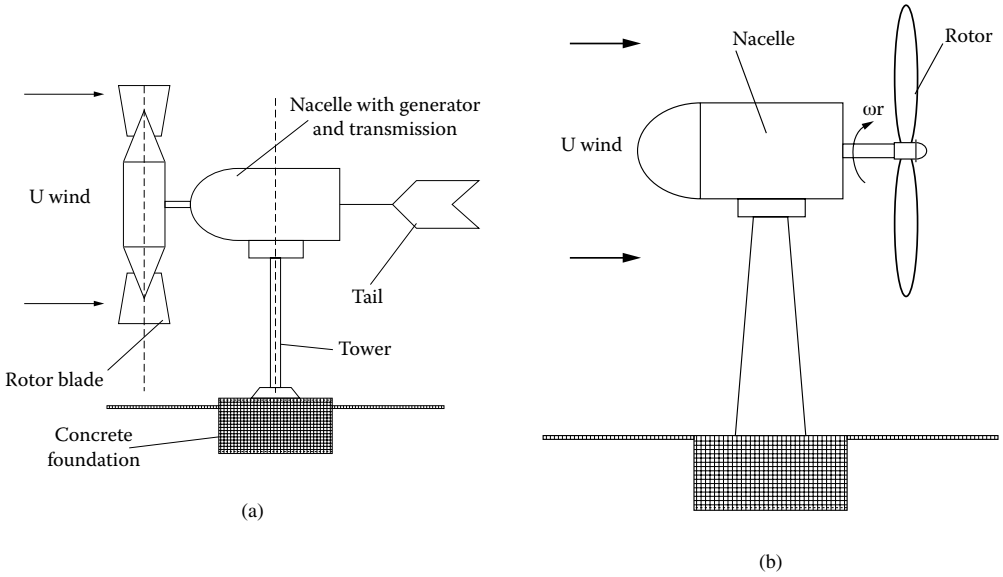
FIGURE 3.51 Axial wind turbines: (a) slow (multiblade) and (b) rapid (propeller).

Tangential (vertical shaft) wind turbines were built in quite a few configurations. They are of two subtypes: drag and lift. The axial (horizontal axis) wind turbines are all of the lift subtype. Some of the tangential wind turbine configurations are shown in Figure 3.52. While the drag subtype (Figure 3.52a) works at slow speeds ($\lambda_{opt} < 1$), the lift subtype (Figure 3.52b) works at high speeds ($\lambda_{opt} > 1$). Slow wind turbines have a higher self-starting torque but a lower power efficiency coefficient C_{pmax}. The efficiency limit (Betz limit) may be calculated by portraying the ideal wind speed and pressure profile before and after the turbine (Figure 3.53, [1]). The wind speed decreases immediately before and after the turbine disk plane, while a pressure differential also takes place. The continuity principle shows that

$$u_1 A_1 = u_\infty A_\infty \tag{3.66}$$

If the speed decreases along the direction of the wind speed, $u_1 > u_\infty$, and thus, $A_1 < A_\infty$.

The wind power P_{wind} in front of the wind turbine is the product of mass flow to speed squared per 2:

$$P_{wind} = \rho U_1 A \cdot \frac{1}{2} \cdot U_1^2 = \frac{1}{2} \rho A U_1^3 \tag{3.67}$$

The power extracted from the wind, $P_{turbine}$ is

$$P_{turbine} = \rho U A \left(\frac{U_1^2}{2} - \frac{U_\infty^2}{2} \right) \tag{3.68}$$

Let us assume

$$U \approx U_1^{-\Delta U_\infty/2}; U_\infty = U_1 - \Delta U_\infty; \Psi = \frac{\Delta U_\infty}{U_1} \tag{3.69}$$

The efficiency limit, η_{ideal}, is as follows:
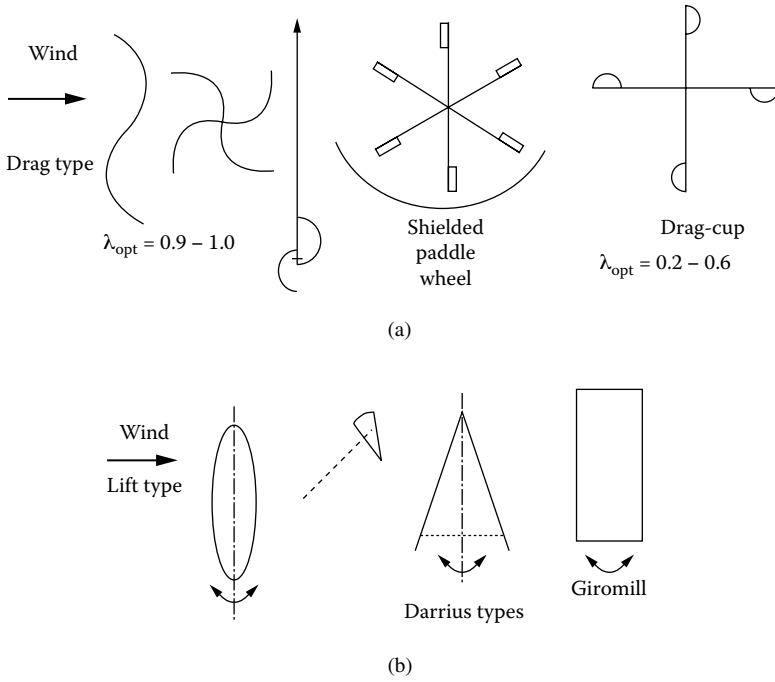
FIGURE 3.52 Tangential (vertical shaft) wind turbines: (a) drag subtype and (b) lift subtype.
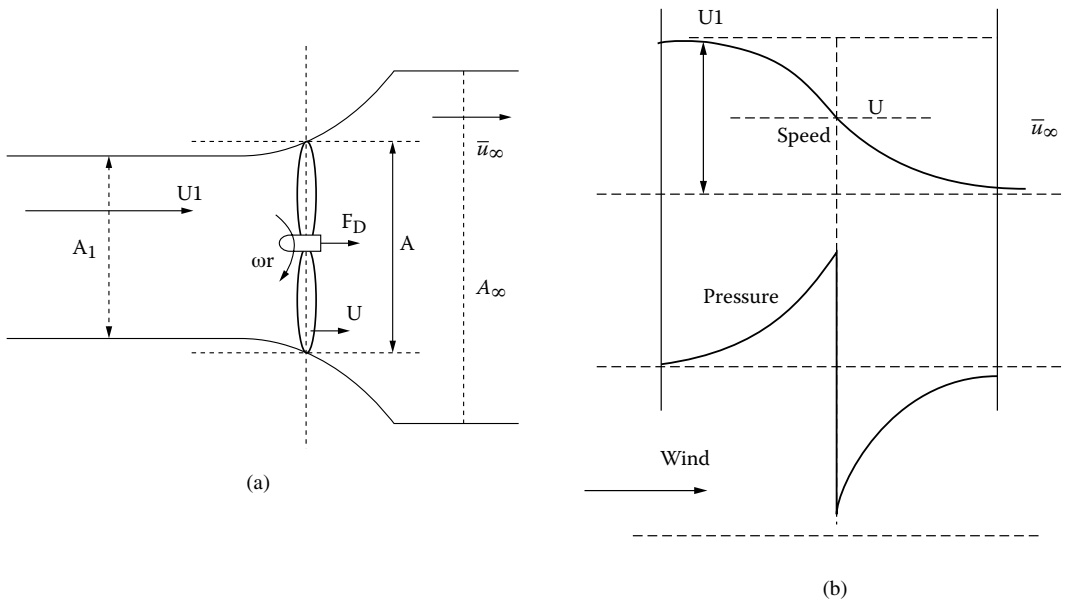
FIGURE 3.53 (a) Basic wind turbine speed and (b) pressure variation.

$$\eta_{ideal} = \frac{P_{turbine}}{P_{wind}} = \frac{\frac{1}{2}\rho U A \left(U_1^2 - U_\infty^2 \right)}{\frac{1}{2}\rho A U_1^3} \tag{3.70}$$

With Equation 3.60, η_{ideal} becomes

$$\eta_{ideal} = \left(1 - \frac{\Psi}{2} \right) \left[1 - \left(1 - \Psi \right)^2 \right] \tag{3.71}$$

The maximum ideal efficiency is obtained for $\partial \eta_i / \partial \Psi = 0$ at $\Psi_{opt} = 2/3$ ($U_\infty/U_1 = 1/3$) with $\eta_{imax} = 0.593$. This ideal maximum efficiency is known as the Betz limit [26].

3.9.2 The Steady-State Model of Wind Turbines

The steady-state behavior of wind turbines is carried out usually through the blade element momentum (BEM) model. The blade is divided into a number of sections with geometrical, mechanical, and aerodynamic properties that are given as functions of the local radius from the hub. At the local radius, the cross-sectional airfoil element of the blade is shown in Figure 3.54.

The local relative velocity $U_{rel}(r)$ is obtained by superimposing the axial velocity $U(1 - a)$ and the rotation velocity $r\omega_r(1 + a')$ at the rotor plane.

xy – Rotor plan

U_{Rel} – Local velocity

U – Undisturbed wind speed

$r\omega_r$ – Tangential velocity of blade section
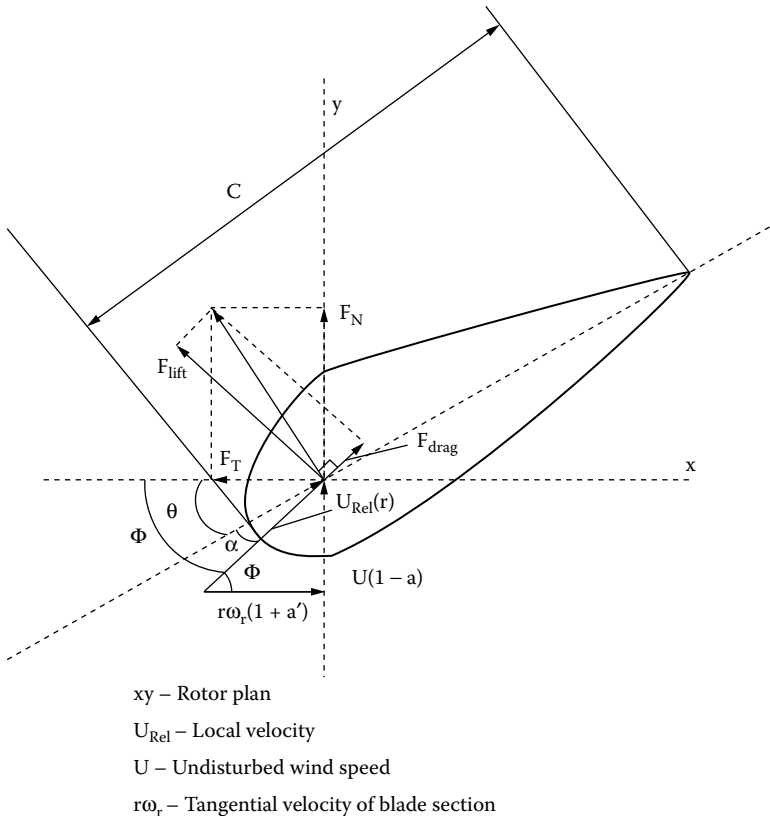
FIGURE 3.54 Blade element with pertinent speed and forces.

The induced velocities ($-aU$ and $a'r\omega_r$) are produced by the vortex system of the machine.
The local attack angle is as follows:

$$\alpha = \phi - \theta \tag{3.72}$$

with

$$\tan \phi = \frac{U(1-a)}{r\omega_r (1+a')} \tag{3.73}$$

The local blade pitch θ is as follows:

$$\theta = \tau + \beta \tag{3.74}$$

with τ the local blade twist angle and β the global pitch angle.

The lift force F_{lift} is rectangular to U_{rel}, while the drag force F_{drag} is parallel to it. The lift and drag forces F_{lift} and F_{drag} may be written as follows:

$$F_{lift} = \frac{1}{2}\rho U_{rel} \cdot C \cdot C_L; \rho = 1.225 \ kg/m^3 \tag{3.75}$$

$$F_{drag} = \frac{1}{2}\rho U_{rel} \cdot C \cdot C_D \tag{3.76}$$

C is the local chord of the blade section and C_L and C_D are lift and drag coefficients, known for a given blade section [26, 27].

From lift and drag forces, the normal force thrust, F_N, and tangential force F_T (along X,Y on the blade section plane) are simply as follows:

$$F_N(r) = F_{lift} \cos\Phi + F_{drag} \sin\Phi \tag{3.77}$$

$$F_T(r) = F_{lift} \sin\Phi - F_{drag} \cos\Phi \tag{3.78}$$

Additional corrections are needed to account for the finite number of blades (B), especially for large values of a (axial induction factor).

Now, the total thrust F_N per turbine is

$$F_T = B \int_0^{Dr/2} F_N(r)dr \tag{3.79}$$

Similarly, the mechanical power P_T is

$$P_T = B \cdot \omega_r \cdot \int_0^{Dr/2} rF_T(r)dr \tag{3.80}$$
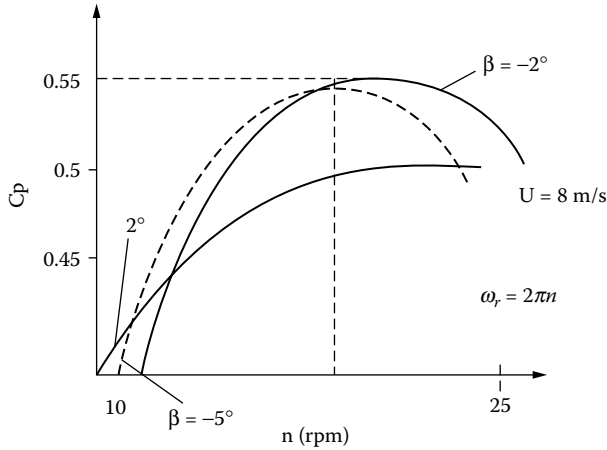
FIGURE 3.55 Typical $C_p - n(\lambda) - \beta$ curves.

Now, with the earlier definition (Equation 3.64), the power efficiency C_p may be calculated. This may be done using a set of airfoil data for the given wind turbine, when a, a', C_L, and C_D are determined first. A family of curves $C_p - \lambda - \beta$ is thus obtained. This, in turn, may be used to investigate the steady-state performance of the wind turbine for various wind speeds U and wind turbine speeds ω_r.

As the influence of blade global pitch angle β is smaller than the influence of tip speed ratio λ in the power efficiency coefficient C_p, we may first keep $\beta = \text{ct.}$ and vary λ for a given turbine. Typical $C_p(\lambda)$ curves are shown in Figure 3.55 for three values of β.

For the time being, let $\beta = \text{ct.}$ and rewrite Equation 3.64 using λ (tip speed ratio):

$$P_M = \frac{1}{2}\rho C_p \pi D_r^2 U^3 = \frac{1}{2}\rho\pi\left(\frac{D_r}{2}\right)^5 \cdot \frac{C_p}{\lambda^3}\omega_r^3 \tag{3.81}$$

Adjusting turbine speed ω_r, that is λ, the optimum value of λ corresponds to the case when C_p is maximum, $C_{p\max}$ (Figure 3.55). Consequently, from Equation 3.81,

$$P_M^{opt} = \frac{1}{2}\rho\pi\left(\frac{D_r}{2}\right)^5 \cdot \frac{C_{p\max}}{\lambda_{opt}^3}\omega_r^3 = K_W\omega_r^3 \tag{3.82}$$

Basically, the optimal turbine power is proportional to the third power of its angular speed (Figure 3.56). Within the optimal power range, the turbine speed ω_r should be proportional to wind speed U as follows:

$$\omega_r = U \cdot \frac{2}{D_r} \cdot \lambda_{opt} \tag{3.83}$$

Above the maximum allowable turbine speed, obtained from mechanical or thermal constraints in the turbine and electric generator, the turbine speed remains constant. As expected, in turbines with constant speed — imposed by the generator to produce constant frequency and voltage power output — the power efficiency constant C_p varies with wind speed ($\omega_r = \text{ct.}$) and less-efficient wind energy extraction is performed. Typical turbine power vs. turbine speed curves are shown in Figure 3.57.

Variable-speed operation — which needs power electronics on the generator side — produces considerably more energy only if the wind speed varies considerably in time (inland sites). This is not
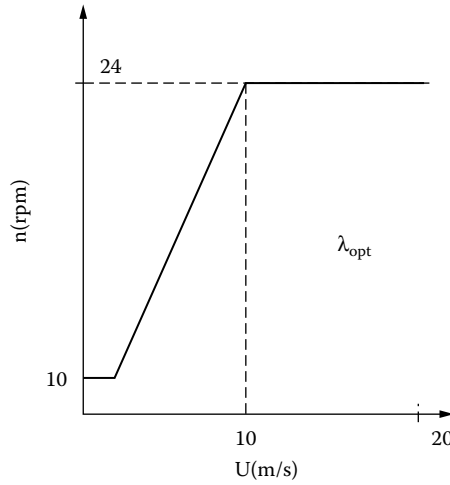
FIGURE 3.56 Typical optimum turbine/wind speed correlation.
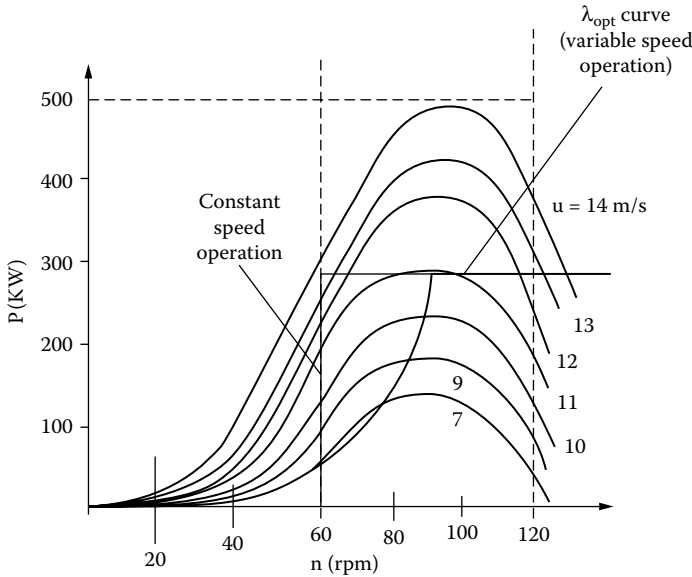
FIGURE 3.57 Turbine power vs. turbine speed for various wind speed u values.

so in on- or offshore sites, where wind speed variations are smaller. However, the flexibility brought by variable speed in terms of electric power control of the generator and its power quality, with a reduction in mechanical stress, in general (especially the thrust and torque reduction), favors variable-speed wind turbines.

There are two methods (Figure 3.58) used to limit power during strong winds ($U > U_{rated}$):

- Stall control
- Pitch control

Stalled blades act as a "wall in the wind." Stall occurs when the angle α between airflow and the blade chord is increased so much that the airflow separates from the airfoil on the suction side to limit the torque-producing force to its rated value. For passive stall, angle β stays constant, as no mechanism to turn the blades is provided. With a mechanism to turn the blades in place above rated wind speed U_{rated},
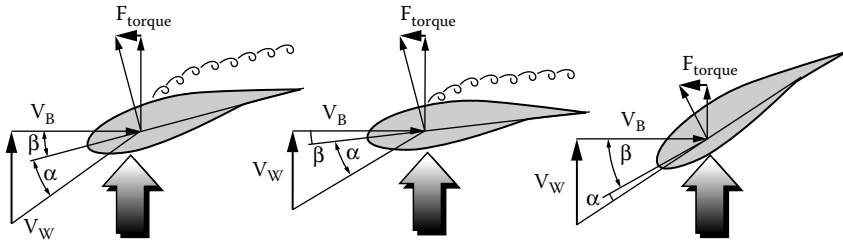
FIGURE 3.58 Stall and pitch control above rated wind speed U_{rated}.

to enforce stall, the angle β is decreased by a small amount. This is the active stall method that may be used at low speeds to increase power extraction by increasing the power efficiency factor C_p (Figure 3.55).

With the pitch control (Figure 3.58), the blades are turned by notably increasing the angle β. The turbine turns to the position of the "flag in the wind" so that aerodynamic forces are reduced. As expected, the servodrive — for pitch control — to change β has to be designed for a higher rating rather than for an active stall.

3.9.3 Wind Turbine Models for Control

Besides slow variations of wind with days or seasons, there are also under 1 Hz and over 1 Hz random wind-speed variations (Figure 3.59) due to turbulence and wind gusts. Axial turbines (with two or three blades) experience two or three speed pulsations per revolution when the blades pass in front of the tower. Tower sideways oscillations also induce shaft speed pulsations. Mechanical transmission and the elasticity of blades, blade fixtures, and couplings produce additional oscillations. The pitch-servo dynamics also has to be considered.

The wind-speed spectrum of a wind turbine located in the wake of a neighboring one in a wind park may also change. Care must be exercised when placing the components of a wind park [29].

Finally, electric load transients or faults produce speed variations.

All of the above clearly indicate intricacy of wind turbine modeling for transients and control.

3.9.3.1 Unsteady Inflow Phenomena in Wind Turbines

The blade element momentum (BEM) model is based in steady state. It presupposes that an instant change of wind profile can take place (Figure 3.59). Transition from state (1) to state (2) in Figure 3.59 corresponds to an increase of global pitch angle β by the pitch-servo.

Experiments have shown that in reality there are at least two time constants that delay the transition: one related to D_r/U and the other related to $2C/(D_r\omega_r)$ [30].

Time lags are related to the axial- and tangential-induced velocities ($-aU$ and $+a'D_r\omega_r/2$).

The inclusion of a lead–lag filter to simulate the inflow phenomena seems insufficient due to considerable uncertainty in the modeling.
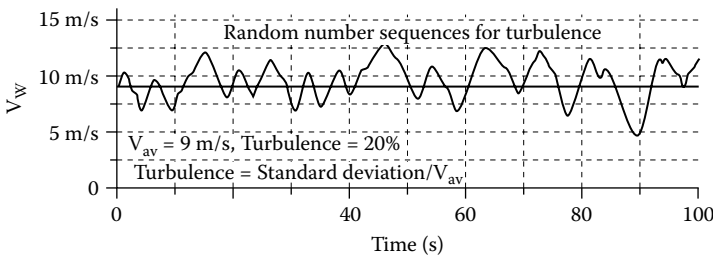
FIGURE 3.59 Typical wind-speed variations with time.

3.9.3.2 The Pitch-Servo and Turbine Model

The pitch-servo is implemented as a mechanical hydraulic or electrohydraulic governor. A first-order (Figure 3.60) or a second-order model could be adopted. In Figure 3.60, the pitch-servo is modeled as a simple delay T_{servo}, while the variation slope is limited between $d\beta_{min}/dt$ and $d\beta_{max}/dt$ (to take care of inflow phenomena). Also, the global attack angle β span is limited from $\beta_{optimum}$ to $\beta_{maximum}$. β_{opt} is obtained from the $C_p - \lambda - \beta$ curve family for C_{pmax} with respect to β (Figure 3.61, [28]).
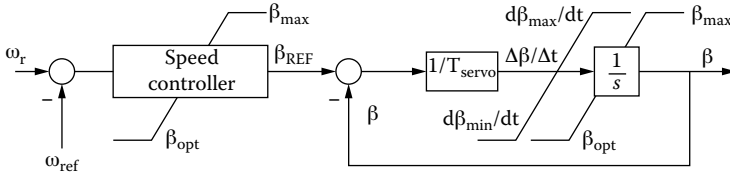
(a)
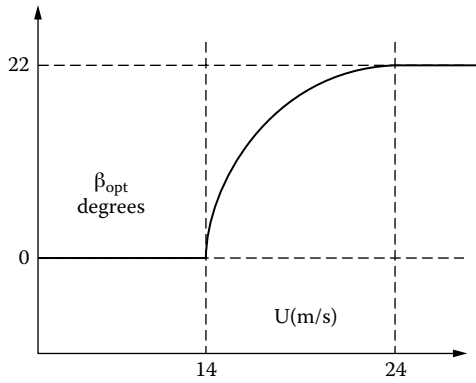
(b)

FIGURE 3.60 Pitch-servo model and (a) control and (b) optimum $\beta(U)$ for variable speed.
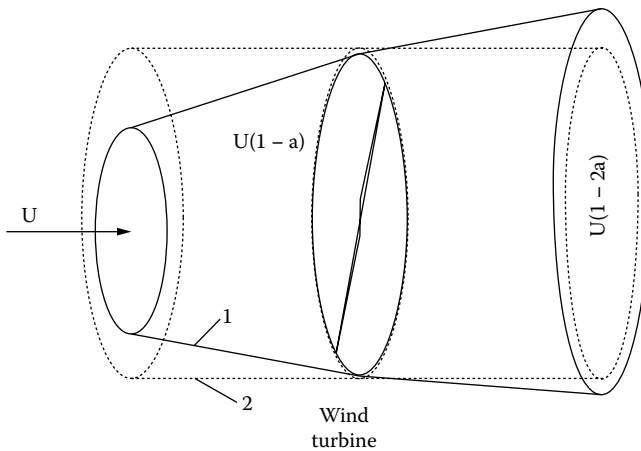
FIGURE 3.61 Wind profile transition from state to state.
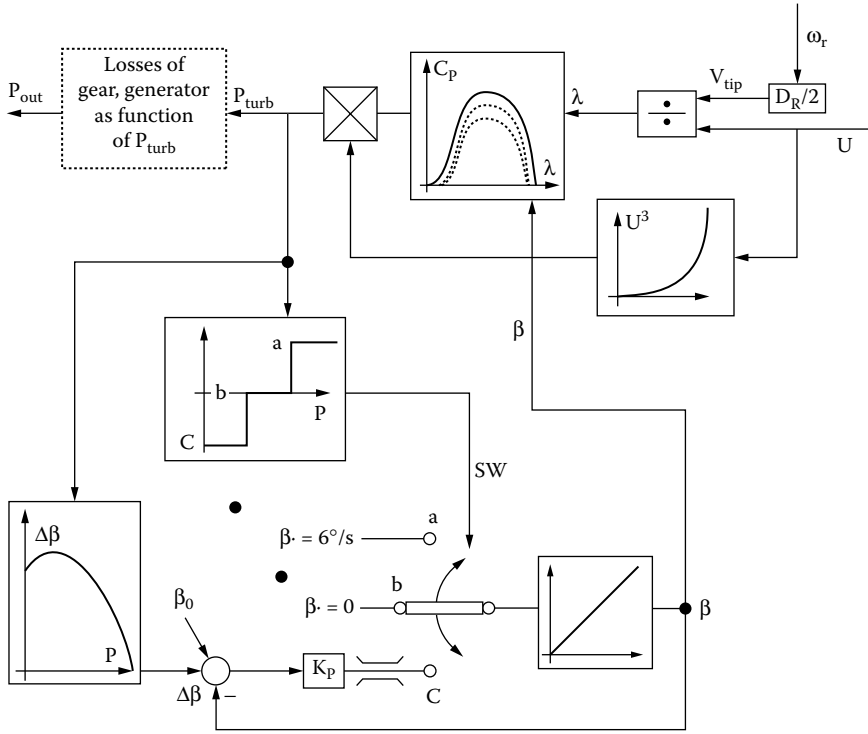
FIGURE 3.62 Simplified structural diagram of the constant speed wind turbine with active stall.

Now, from angle β to output power, the steady-state model of the wind turbine is used (Figure 3.62) for a constant-speed active-stall wind turbine. When the turbine produces more than the rated power, the switch is in position *a*, and the angle β is increased at the rate of 6°/sec to move the blades toward the "flag in the wind" position. When the power is around the rated value, the pitch drive stays idle with $\beta = 0$; thus, β is constant (position b). Below rated power, the switch goes to position "C" and a proportional controller (K_p) produces the desired β. The reference value $\beta^\star$ corresponds to its optimum value as a function of mechanical power, that is, maximum power. This is only a sample of the constant-speed turbine model with pitch-servo control for active stall above rated power and $\beta_{optimization}$ control below rated power.

As can be seen from Figure 3.62, the model is highly nonlinear. Still, because of the delays due to inflow phenomena, the elasticities of various elements of the turbine are not yet included. Also, the model of the pitch-servo is not included. Usually, there is a transmission between the wind turbine and the electric generator. A six-order drive train is shown in Figure 3.63.

Inertias of hub, blades, gearbox, and generator are denoted by H_i. Each part has a spring and a dashpot element. The matrix dynamic equation of the drive train is of the following form [31]:

$$\frac{d}{dt}\begin{bmatrix}|\theta|\\|\omega|\end{bmatrix}=\begin{bmatrix}0 & I\\-\begin{bmatrix}2H^{-1}\end{bmatrix}\begin{bmatrix}C\end{bmatrix} & -\begin{bmatrix}2H^{-1}\end{bmatrix}D\end{bmatrix}\cdot\begin{bmatrix}|\theta|\\|\omega|\end{bmatrix}+\begin{bmatrix}0\\2H^{-1}\end{bmatrix}\begin{bmatrix}T\end{bmatrix} \tag{3.84}$$

A few "real-world" pulsations in speed or electric power may be detected by such models; resonance conditions may be avoided through design or control measures.
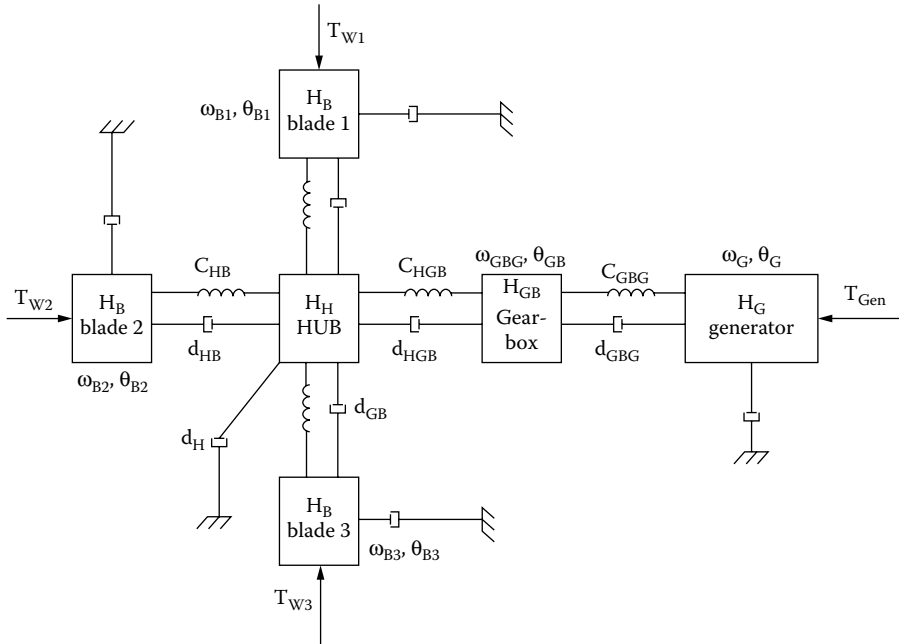
FIGURE 3.63 Six-inertia drive train.

3.10   Summary

- Prime movers are mechanical machines that convert the primary energy of a fuel (or fluid) into mechanical energy.
- Prime movers drive electric generators connected to the power grid or operating in isolation.
- Steam and gas turbines and internal combustion engines (spark-ignited or diesel) are burning fossil fuels to produce mechanical work.
- Steam turbines contain stationary and rotating blades grouped into high-, intermediate-, and low-pressure (HP, IP, LP) sections on the same shaft in tandem-compound and on two shafts in cross-compound configurations.
- Between stages, steam engines use reheaters: single reheat and doubly reheat, at most.
- In steam turbines, typically, the power is divided as follows: 30% in the HP stage, 40% in the IP stage, and 30% in the LP stage.
- Governor valves (GVs) and intercept valves (IVs) are used to control the HP and, respectively, LP stages of the steam flow.
- The steam vessel may be modeled by a first-order delay, while the steam turbine torque is proportional to its steam flow rate.
- Three more delays related to inlet and steam chest, to the reheater, and to the crossover piping may be identified.
- Speed governors for steam turbines include a speed relay with a first-order delay and a hydraulic servomotor characterized by a further delay.
- Gas turbines burn natural gas in combination with air that is compressed in a compressor driven by the gas turbine.
- The 500°C gas exhaust is used to produce steam that drives a steam turbine placed on the same shaft. These combined-cycle unishaft gas turbines are credited with a total efficiency above 55%. Combined-cycle gas turbines at large powers seem to be the way of the future. They are also introduced for cogeneration in high-speed small- and medium-power applications.

- Diesel engines are used from the kilowatt range to the megawatt range power per unit for cogeneration or for standby (emergency) power sets.
- The fuel injection control in diesel engines is performed by a speed governing system.
- The diesel engine model contains a nonconstant gain. The gain depends on the engine equivalence ratio (eer), which, in turn, is governed by the fuel/air ratio; a dead time constant dependent on engine speed is added to complete the diesel engine model.
- Diesel engines are provided with a turbocharger that has a turbine "driven" by the fuel exhaust that drives a compressor, which provides the hot high-pressure air for the air mix of the main engine. The turbocharger runs freely at high speed but is coupled to the engine at low speed.
- Stirling engines are "old" thermal piston engines with continuous heat supply. Their thermal cycles contain two isotherms. In a basic configuration, the engine consists of two opposed pistons and a regenerator in between. The efficiency of the Stirling engine is temperature limited.
- Stirling engines are independent fuel types; they use air, methane, He, or H_2 as working fluids. They did not reach commercial success as a kinetic type due to problems with the regenerator and stabilization.
- Stirling engines with free piston-displacer mover and linear motion recently reached the market in units in the 50 W to a few kilowatts.
- The main merits of Stirling engines are related to their quietness and reduced noxious emissions, but they tend to be expensive and difficult to stabilize.
- Hydraulic turbines convert the water energy of rivers into mechanical work. They are the oldest prime movers.
- Hydraulic turbines are of the impulse type for heads above 300 to 400 m and of reaction type for heads below 300 m. In a more detailed classification, they are tangential (Pelton), radial–axial (Francis), and axial (Kaplan, Bulb, Straflo).
- High head (impulse) turbines use a nozzle with a needle controller, where water is accelerated, and then it impacts the bowl-shaped buckets on the water wheel of the turbine. A jet deflector deflects water from the runner to limit turbine speed when the electric load decreases.
- Reaction turbines — at medium and low head — use wicket gates and rotor blade servomotors to control water flow in the turbine.
- Hydraulic turbines may be modeled by a first-order model if water hammer (wave) and surge effects are neglected. Such a rough approximation does not hold above 0.1 Hz.
- Second-order models for hydraulic turbines with water hammer effect in the penstock are considered valid up to 1 Hz. Higher orders are required above 1 Hz, as the nonlinear model has a gain with amplitude that varies periodically. Second- or third-order models may be identified from tests through adequate curve-fitting methods.
- Hydraulic turbine governors have one or two power levels. The lower power level may be electric, while the larger (upper) power level is a hydraulic servomotor. The speed controller of the governor traditionally has a permanent drop and a transient drop.
- Modern nonlinear control systems may now be used to simultaneously control the guide vane runner and the blade runner.
- Reversible hydraulic machines are used for pump-storage power plants or for tidal-wave power plants. The optimal pumping speed is about 12 to 20% above the optimal turbining speed. Variable-speed operation is required. So, power electronics on the electric side are mandatory.
- Wind turbines use the wind air energy. Nonuniformity and strength vary with location height and terrain irregularities. Wind speed duration vs. speed, speed vs. frequency, and mean (average) speed using Raleigh or Weibull distribution are used to characterize wind at a location in time. The wind-turbine-rated wind speed is generally 150% of mean wind speed.
- Wind turbines can be found in two main types: axial (with horizontal shaft) and tangential (with vertical shaft).

- The main steady-state parameter of wind turbines is the power efficiency coefficient C_p, which is dependent upon blade tip speed $R\omega_r$ to wind speed U (ratio λ). C_p depends on λ and on blade absolute attack angle β.
- The maximum C_p (0.3 to 0.4) is obtained for $\lambda_{opt} \le 1$ for low-speed axial turbines and $\lambda_{opt} \ge 1$ for high-speed turbines.
- The ideal maximum efficiency limit of wind turbines is about 0.6 (Betz limit).
- Wind impacts on the turbine a thrust force and a torque. Only torque is useful. The thrust force and C_p depend on blade absolute attack angle β.
- The optimal power $P_T(\lambda_{opt})$ is proportional to u^3 (u is the wind speed).
- Variable-speed turbines will collect notably more power from a location if the speed varies significantly with time and season, such that λ may be kept optimum. Above the rated wind speed (and power), the power is limited by passive-stall, active-stall, or pitch-servo control.
- Wind turbine steady-state models are highly nonlinear. Unsteady inflow phenomena show up in fast transients and have to be accounted for by more than lead–lag elements.
- Pitch-servo control is becoming more frequently used, even with variable-speed operation, to allow speed limitation during load transients or power grid faults.
- First- or second-order models may be adopted for speed governors. Elastic transmission multimass models have to be added to complete the controlled wind turbine models for transients and control [32].
- Prime-mover models will be used in the following chapters, where electric generator control will be treated in detail.

References

1. R. Decker, *Energy Conversion*, Oxford University Press, Oxford, 1994.
2. P. Kundur, *Power System Stability and Control*, McGraw-Hill, New York, 1994.
3. J. Machowski, J.W. Bialek, and J.R. Bumby, Power System Dynamics and Stability, John Wiley & Sons, New York, 1997.
4. IEEE Working Group Report, Steam models for fossil fueled steam units in power-system studies, *IEEE Trans.*, PWRS-6, 2, 1991, pp. 753–761.
5. S. Yokokawa, Y. Ueki, H. Tanaka, Hi Doi, K. Ueda, and N. Taniguchi, Multivariable adaptive control for a thermal generator, *IEEE Trans.*, EC-3, 3, 1988, pp. 479–486.
6. G.K. Venayagomoorthy, and R.G. Harley, A continually on line trained microcontroller for excitation and turbine control of a turbogenerator, *IEEE Trans.*, EC-16, 3, 2001, pp. 261–269.
7. C.F. Taylor, *The Internal-Combustion Engine in Theory and Practice, vol. II: Combustion, Fuels, Materials, Design*, The MIT Press, Cambridge, MA, 1968.
8. P.M. Anderson, and M. Mirheydar, Analysis of a diesel-engine driven generating unit and the possibility for voltage flicker, *IEEE Trans.*, EC-10, 1, 1995, pp. 37–47.
9. N. Watson, and M.S. Janota, *Turbocharging the Internal Combustion Engine*, Macmillan, New York, 1982.
10. S. Roy, O.P. Malik, and G.S. Hope, Adaptive control of speed and equivalence ratio dynamics of a diesel driven power plant, *IEEE Trans.*, EC-8, 1, 1993, pp. 13–19.
11. A. Kusko, *Emergency Stand-by Power Systems*, McGraw-Hill, New York, 1989.
12. K.E. Yoager, and J.R. Willis, Modelling of emergency diesel generators in an 800 MW nuclear power plant, *IEEE Trans.*, EC-8, 3, 1993, pp. 433–441.
13. U. Kieneke, and L. Nielsen, *Automotive Control Systems*, Springer-Verlag, Heidelberg, 2000.
14. G. Walker, O.R. Fauvel, G. Reader, and E.R. Birgham, *The Stirling Alternative*, Gordon and Breach Science Publishers, London, 1994.
15. R.W. Redlich, and D.W. Berchowitz, Linear dynamics of free piston Stirling engine, *Proc. of Inst. Mech. Eng.*, March 1985, pp. 203–213.

16. M. Barglazan, *Hydraulic Turbines and Hydrodynamic Transmissions*, University Politechnica of Timisoara, Romania, 1999.
17. IEEE Working Group on Prime Mover and Energy Supply, Hydraulic turbine and turbine control models for system stability studies, *IEEE Trans.*, PS-7, 1, 1992, pp. 167–179.
18. C.D. Vournas, Second order hydraulic turbine models for multimachine stability studies, *IEEE Trans.*, EC-5, 2, 1990, pp. 239–244.
19. C.K. Sanathanan, Accurate low order model for hydraulic turbine-penstock, *IEEE Trans.*, EC-2, 2, 1987, pp. 196–200.
20. D.D. Konidaris, and N.A. Tegopoulos, Investigation of oscillatory problems of hydraulic generating units equipped with Francis turbines, *IEEE Trans.*, EC-12, 4, 1997, pp. 419–425.
21. D.J. Trudnowski, and J.C. Agee, Identifying a hydraulic turbine model from measured field data, *IEEE Trans.*, EC-10, 4, 1995, pp. 768–773.
22. J.E. Landsberry, and L. Wozniak, Adaptive hydrogenerator governor tuning with a genetic algorithm, *IEEE Trans.*, EC-9, 1, 1994, pp. 179–185.
23. Y. Zhang, O.P. Malik, G.S. Hope, and G.P. Chen, Application of inverse input/output mapped ANN as a power system stabilizer, *IEEE Trans.*, EC-9, 3, 1994, pp. 433–441.
24. M. Djukanovic, M. Novicevic, D. Dobrijovic, B. Babic, D.J. Sobajic, and Y.H. Pao, Neural-net based coordinated stabilizing control of the exciter and governor loops of low head hydropower plants, *IEEE Trans.*, EC-10, 4, 1995, pp. 760–767.
25. T. Kuwabara, A. Shibuya, M. Furuta, E. Kita, and K. Mitsuhashi, Design and dynamics response characteristics of 400 MW adjustable speed pump storage unit for Obkawachi power station, *IEEE Trans.*, EC-11, 2, 1996, pp. 376–384.
26. L.L. Freris, *Wind Energy Conversion Systems*, Prentice Hall, New York, 1998.
27. V.H. Riziotis, P.K. Chaviaropoulos, and S.G. Voutsinas, Development of the State of the Art Aerolastic Simulator for Horizontal Axis Wind Turbines, Part 2: Aerodynamic Aspects and Application, *Wind Eng.*, 20, 6, 1996, pp. 223–440.
28. V. Akhmatov, Modelling of Variable Speed Turbines with Doubly-Fed Induction Generators in Short-Term Stability Investigations, paper presented at the Third International Workshop on Transmission Networks for Off-Shore Wind Farms, Stockholm, Sweden, April 11–12, 2002.
29. T. Thiringer, and J.A. Dahlberg, Periodic pulsations from a three-bladed wind turbine, *IEEE Trans.*, EC-16, 2, 2001, pp. 128–133.
30. H. Suel, and J.G. Schepers, Engineering models for dynamic inflow phenomena, *J. Wind Eng. Ind. Aerodynamics*, 39, 2, 1992, pp. 267–281.
31. S.A. Papathanassiou, and M.P. Papadopoulos, Mechanical stress in fixed-speed wind turbines due to network disturbances, *IEEE Trans.*, EC-16, 4, 2001, pp. 361–367.
32. S.H. Jangamshatti, and V.G. Rau, Normalized power curves as a tool for identification of optimum wind turbine generator parameters, *IEEE Trans.*, EC-16, 3, 2001, pp. 283–288.

4

Large and Medium Power Synchronous Generators: Topologies and Steady State

4.1   Introduction

By large powers, we mean here powers above 1 MW per unit, where in general, the rotor magnetic field is produced with electromagnetic excitation. There are a few megawatt (MW) power permanent magnet (PM)-rotor synchronous generators (SGs).

   Almost all electric energy generation is performed through SGs with power per unit up to 1500 MVA in thermal power plants and up to 700 MW per unit in hydropower plants. SGs in the MW and tenth of MW range are used in diesel engine power groups for cogeneration and on locomotives and on ships. We will begin with a description of basic configurations, their main components, and principles of operation, and then describe the steady-state operation in detail.

4.2   Construction Elements

The basic parts of an SG are the stator, the rotor, the framing (with cooling system), and the excitation system.

   The stator is provided with a magnetic core made of silicon steel sheets (generally 0.55 mm thick) in which uniform slots are stamped. Single, standard, magnetic sheet steel is produced up to 1 m in diameter in the form of a complete circle (Figure 4.1). Large turbogenerators and most hydrogenerators have stator outer diameters well in excess of 1 m (up to 18 m); thus, the cores are made of 6 to 42 segments per circle (Figure 4.2).
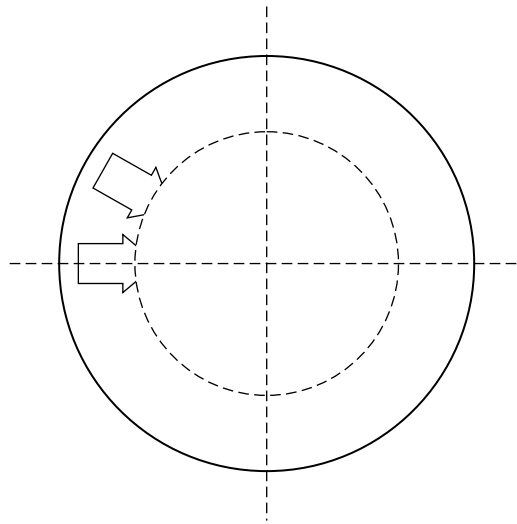
FIGURE 4.1   Single piece stator core.
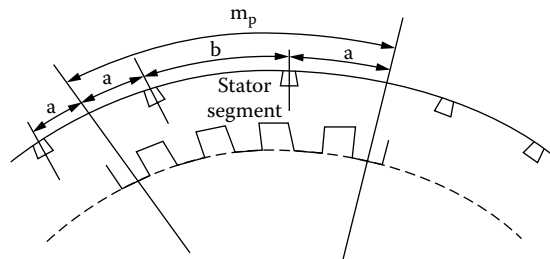
FIGURE 4.2   Divided stator core made of segments.

The stator may also be split radially into two or more sections to allow handling and permit transport with windings in slots. The windings in slots are inserted section by section, and their connection is performed at the power plant site.

When the stator with N_s slots is divided, and the number of slot pitches per segment is m_p, the number of segments m_s is such that

$$N_s = m_s \cdot m_p \tag{4.1}$$

Each segment is attached to the frame through two key-bars or dove-tail wedges that are uniformly distributed along the periphery (Figure 4.2). In two successive layers (laminations), the segments are offset by half a segment. The distance between wedges b is as follows:

$$b = m_p / 2 = 2a \tag{4.2}$$

This distance between wedges allows for offsetting the segments in subsequent layers by half a segment. Also, only one tool for stamping is required, because all segments are identical. To avoid winding damage due to vibration, each segment should start and end in the middle of a tooth and span over an even number of slot pitches.

For the stator divided into S sectors, two types of segments are usually used. One type has m_p slot pitches, and the other has n_p slot pitches, such that

$$\frac{N_s}{S} = K m_p + n_p; n_p < m_p; m_p = 6-13 \tag{4.3}$$

With $n_p = 0$, the first case is obtained, and, in fact, the number of segments per stator sector is an integer. This is not always possible, and thus, two types of segments are required.

The offset of segments in subsequent layers is $m_p/2$ if m_p is even, $(m_p \pm 1)/2$ if m_p is odd, and $m_p/3$ if m_p is divisible by three. In the particular case that $n_p = m_p/2$, we may cut the main segment in two to obtain the second one, which again would require only one stamping tool. For more details, see Reference [1].

The slots of large and medium power SGs are rectangular and open (Figure 4.3a).

The double-layer winding, usually made of magnetic wires with rectangular cross-section, is "kept" inside the open slot by a wedge made of insulator material or from a magnetic material with a low equivalent tangential permeability that is μ_r times larger than that of air. The magnetic wedge may be made of magnetic powders or of laminations, with a rectangular prolonged hole (Figure 4.3b), "glued together" with a thermally and mechanically resilient resin.

4.2.1 The Stator Windings

The stator slots are provided with coils connected to form a three-phase winding. The winding of each phase produces an airgap fixed magnetic field with $2p_1$ half-periods per revolution. With D_{is} as the internal stator diameter, the pole pitch τ, that is the half-period of winding magnetomotive force (mmf), is as follows:

$$\tau = \pi D_{is} / 2 p_1 \tag{4.4}$$

The phase windings are phase shifted by $(2/3)\tau$ along the stator periphery and are symmetric. The average number of slots per pole per phase q is
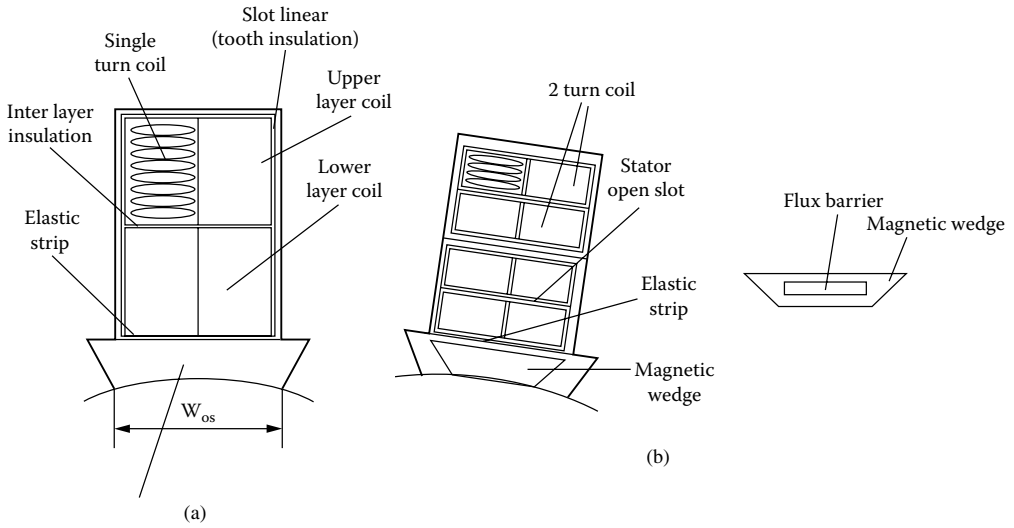
FIGURE 4.3 (a) Stator slotting and (b) magnetic wedge.
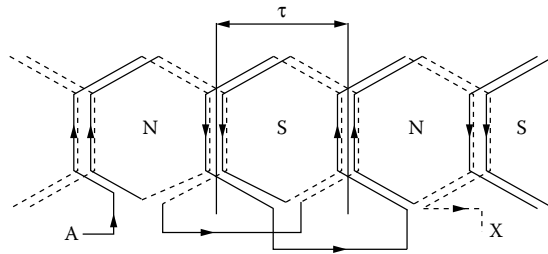
FIGURE 4.4 Lap winding (four poles) with $q = 2$, phase A only.

$$q = \frac{Ns}{2p_1 \cdot 3} \tag{4.5}$$

The number q may be an integer, with a low number of poles ($2p_1 < 8$–10), or it may be a fractionary number:

$$q = a + b/c \tag{4.6}$$

Fractionary q windings are used mainly in SGs with a large number of poles, where a necessarily low integer q ($q \leq 3$) would produce too high a harmonics content in the generator electromagnetic field (emf).

Large and medium power SGs make use of typical lap (multiturn coil) windings (Figure 4.4) or of bar-wave (single-turn coil) windings (Figure 4.5).

The coils of phase A in Figure 4.4 and Figure 4.5 are all in series. A single current path is thus available ($a = 1$). It is feasible to have a current paths in parallel, especially in large power machines (line voltage is generally below 24 kV). With W_{ph} turns in series (per current path), we have the following relationship:

$$N_s = 3 \frac{W_{ph} \cdot a}{n_c} \tag{4.7}$$

with n_c equal to the turns per coil.
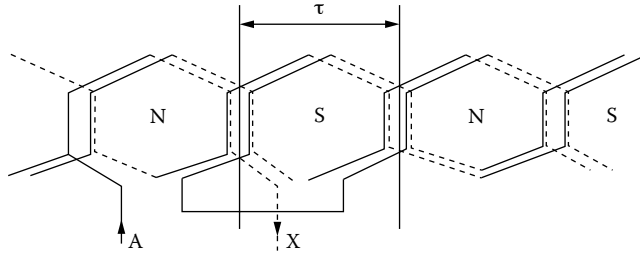
FIGURE 4.5 Basic wave-bar winding with q = 2, phase A only.

The coils may be multiturn lap coils or uniturn (bar) type, in wave coils.

A general comparison between the two types of windings (both with integer or fractionary *q*) reveals the following:

- The multiturn coils ($n_c > 1$) allow for greater flexibility when choosing the number of slots N_s for a given number of current paths *a*.
- Multiturn coils are, however, manufacturing-wise, limited to 0.3 m long lamination stacks and pole pitches $\tau < 0.8$–1 m.
- Multiturn coils need bending flexibility, as they are placed with one side in the bottom layer and with the other one in the top layer; bending needs to be done without damaging the electric insulation, which, in turn, has to be flexible enough for the purpose.
- Bar coils are used for heavy currents (above 1500 A). Wave-bar coils imply a smaller number of connectors (Figure 4.5) and, thus, are less costly. The lap-bar coils allow for short pitching to reduce emf harmonics, while wave-bar coils imply 100% average pitch coils.
- To avoid excessive eddy current (skin) effects in deep coil sides, transposition of individual strands is required. In multiturn coils ($n_c \geq 2$), one semi-Roebel transposition is enough, while in single-bar coils, full Roebel transposition is required.
- Switching or lightning strokes along the transmission lines to the SG produce steep-fronted voltage impulses between neighboring turns in the multiturn coil; thus, additional insulation is required. This is not so for the bar (single-turn) coils, for which only interlayer and slot insulation are provided.
- Accidental short-circuit in multiturn coil windings with $a \geq 2$ current path in parallel produce a circulating current between current paths. This unbalance in path currents may be sufficient to trip the pertinent circuit balance relay. This is not so for the bar coils, where the unbalance is less pronounced.
- Though slightly more expensive, the technical advantages of bar (single-turn) coils should make them the favorite solution in most cases.

Alternating current (AC) windings for SGs may be built not only in two layers, but also in one layer. In this latter case, it will be necessary to use 100% pitch coils that have longer end connections, unless bar coils are used.

Stator end windings have to be mechanically supported so as to avoid mechanical deformation during severe transients, due to electrodynamic large forces between them, and between them as a whole and the rotor excitation end windings. As such forces are generally radial, the support for end windings typically looks as shown in Figure 4.6. Note that more on AC winding specifics are included in Chapter 7, which is dedicated to SG design. Here, we derive only the fundamental mmf wave of three-phase stator windings.

The mmf of a single-phase four-pole winding with 100% pitch coils may be approximated with a step-like periodic function if the slot openings are neglected (Figure 4.7). For the case in Figure 4.7 with *q* = 2 and 100% pitch coils, the mmf distribution is rectangular with only one step per half-period. With chorded coils or *q* > 2, more steps would be visible in the mmf. That is, the distribution then better
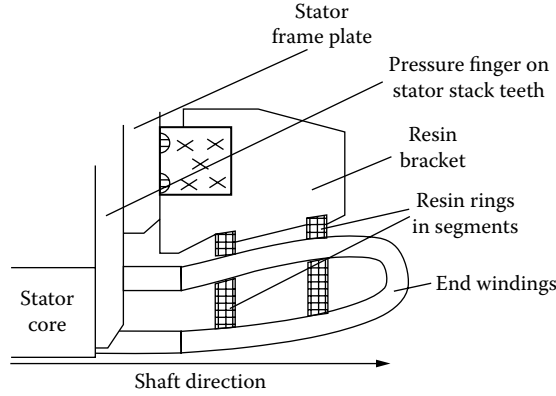
FIGURE 4.6 Typical support system for stator end windings.
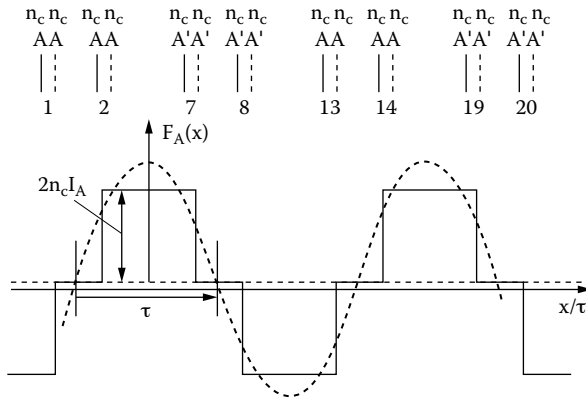
FIGURE 4.7 Stator phase mmf distribution ($2p = 4$, $q = 2$).

approximates a sinusoid waveform. In general, the phase mmf fundamental distribution for steady state may be written as follows:

$$F_{1A}(x,t) = F_{1m} \cdot \cos \frac{\pi}{\tau} x \cdot \cos \omega_1 t \qquad (4.8)$$

$$F_{1m} = 2\sqrt{2} \, \frac{W_1 K_{W1} I}{\pi p_1} \qquad (4.9)$$

where

$\quad W_1$ = the number of turns per phase in series
$\quad\quad I$ = the phase current (RMS)
$\quad p_1$ = the number of pole pairs
$\quad K_{W1}$ = the winding factor:

$$K_{W1} = \frac{\sin \pi/6}{q \cdot \sin \pi/6q} \cdot \sin\left(\frac{y}{\tau} \frac{\pi}{2}\right) \qquad (4.10)$$

with y/τ = coil pitch/pole pitch ($y/\tau > 2/3$).

Equation 4.8 is strictly valid for integer q.

An equation similar to Equation 4.8 may be written for the νth space harmonic:

$$F_{\nu A}(x,t) = F_{\nu m} \cos \nu \frac{\pi}{\tau} x \cos(\omega_1 t)$$

$$F_{\nu m} = \frac{2\sqrt{2}\,W_1 K_{W\nu} I}{\pi p_1 \nu} \tag{4.11}$$

$$K_{W\nu} = \frac{\sin \nu\pi/6}{q \cdot \sin(\nu\pi/6q)} \cdot \sin \frac{y}{\tau} \frac{\nu\pi}{2} \tag{4.12}$$

Phase B and phase C mmf expressions are similar to Equation 4.8 but with $2\pi/3$ space and time lags. Finally, the total mmf (with space harmonics) produced by a three-phase winding is as follows [2]:

$$F_\nu(x,t) = \frac{3W_1 I \sqrt{2} K_{W\nu}}{\pi p_1 \nu}\left[K_{BI} \cos\left(\frac{\nu\pi}{\tau} - \omega_1 t - (\nu-1)\frac{2\pi}{3} \right) - K_{BII} \cos\left(\frac{\nu\pi}{\tau} + \omega_1 t - (\nu+1)\frac{2\pi}{3} \right) \right] \tag{4.13}$$

with

$$K_{BI} = \frac{\sin(\nu-1)\pi}{3 \cdot \sin(\nu-1)\pi/3}$$

$$K_{BII} = \frac{\sin(\nu+1)\pi}{3 \cdot \sin(\nu+1)\pi/3} \tag{4.14}$$

Equation 4.13 is valid for integer q.

For $\nu = 1$, the fundamental is obtained.

Due to full symmetry, with q integer, only odd harmonics exist. For $\nu = 1$, $K_{BI} = 1$, $K_{BII} = 0$, so the mmf fundamental represents a forward-traveling wave with the following peripheral speed:

$$\frac{dx}{dt} = \frac{\tau\omega_1}{\pi} = 2\tau f_1 \tag{4.15}$$

The harmonic orders are $\nu = 3K \pm 1$. For $\nu = 7, 13, 19, \ldots$, $dx/dt = 2\tau f_1/\nu$ and for $\nu = 5, 11, 17, \ldots$, $dx/dt = -2\tau f_1/\nu$. That is, the first ones are direct-traveling waves, while the second ones are backward-traveling waves. Coil chording ($y/\tau < 1$) and increased q may reduce harmonics amplitude (reduced $K_{w\nu}$), but the price is a reduction in the mmf fundamental (K_{W1} decreases).

The rotors of large SGs may be built with salient poles (for $2p_1 > 4$) or with nonsalient poles ($2p_1 = 2, 4$). The solid iron core of the nonsalient pole rotor (Figure 4.8a) is made of 12 to 20 cm thick (axially) rolled steel discs spigoted to each other to form a solid ring by using axial through-bolts. Shaft ends are added (Figure 4.9). Salient poles (Figure 4.8b) may be made of lamination packs tightened axially by through-bolts and end plates and fixed to the rotor pole wheel by hammer-tail key bars.

In general, peripheral speeds around 110 m/sec are feasible only with solid rotors made by forged steel. The field coils in slots (Figure 4.8a) are protected from centrifugal forces by slot wedges that are made either of strong resins or of conducting material (copper), and the end-windings need bandages.
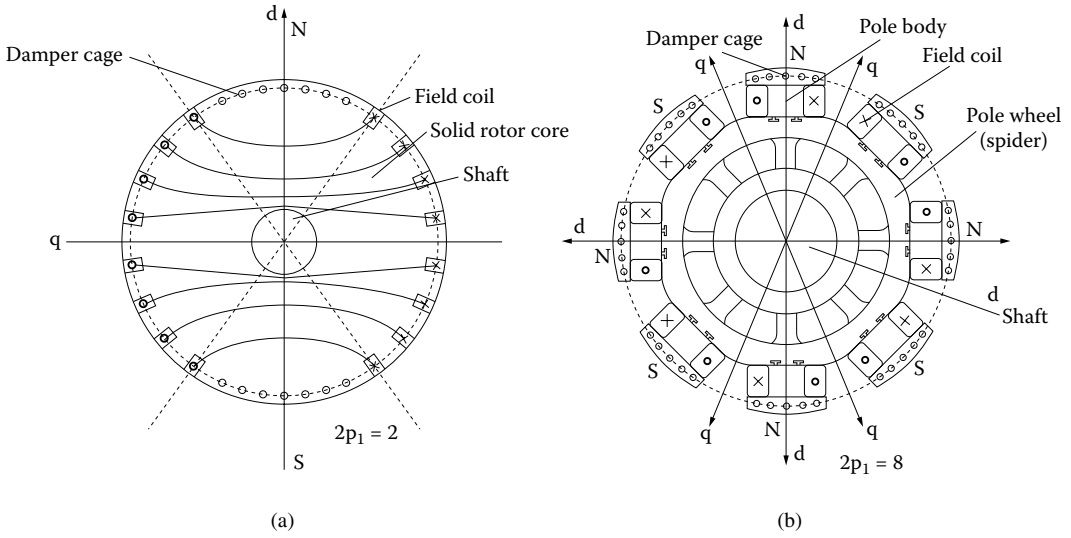
FIGURE 4.8   Rotor configurations: (a) with nonsalient poles $2p_1 = 2$ and (b) with salient poles $2p_1 = 8$.
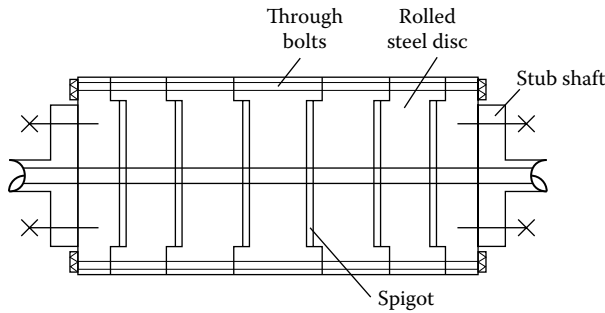
FIGURE 4.9   Solid rotor.

The interpole area in salient pole rotors (Figure 4.8b) is used to mechanically fix the field coil sides so that they do not move or vibrate while the rotor rotates at its maximum allowable speed.

Nonsalient pole (high-speed) rotors show small magnetic anisotropy. That is, the magnetic reluctance of airgap along pole (longitudinal) axis *d*, and along interpole (transverse) axis *q*, is about the same, except for the case of severe magnetic saturation conditions.

In contrast, salient pole rotors experience a rather large (1.5 to 1 and more) magnetic saliency ratio between axis *d* and axis *q*. The damper cage bars placed in special rotor pole slots may be connected together through end rings (Figure 4.10). Such a complete damper cage may be decomposed in two fictitious cages, one with the magnetic axis along the *d* axis and the other along the *q* axis (Figure 4.10), both with partial end rings (Figure 4.10).

4.3   Excitation Magnetic Field

The airgap magnetic field produced by the direct current (DC) field (excitation) coils has a circumferential distribution that depends on the type of the rotor, with salient or nonsalient poles, and on the airgap variation along the rotor pole span. For the time being, let us consider that the airgap is constant under the rotor pole and the presence of stator slot openings is considered through the Carter coefficient K_{C1}, which increases the airgap [2]:
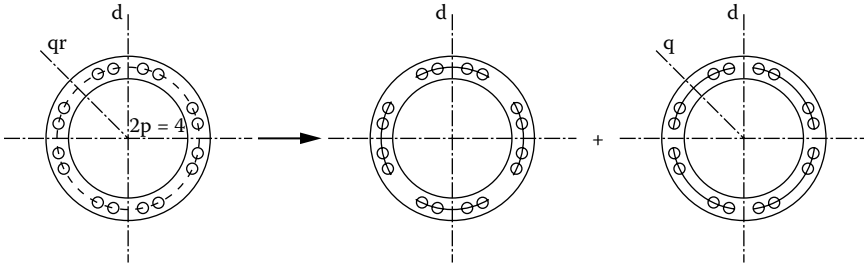
FIGURE 4.10 The damper cage and its *d* axis and *q* axis fictitious components.

$$K_{C1} \approx \frac{\tau_s}{\tau_s - \gamma_1 g} > 1, \tau_s - stone\_slot\_pitch \tag{4.16}$$

$$\gamma_1 = \frac{4}{\pi}\left[\frac{\left(\dfrac{W_{os}}{g}\right)}{\tan\left(\dfrac{W_{os}}{g}\right)} - \ln\sqrt{1+\left(\dfrac{W_{os}}{g}\right)^2}\right] \tag{4.17}$$

with W_{os} equal to the stator slot opening and g equal to the airgap.

The flux lines produced by the field coils (Figure 4.11) resemble the field coil mmfs $F_F(x)$, as the airgap under the pole is considered constant (Figure 4.12). The approximate distribution of no-load or field-winding-produced airgap flux density in Figure 4.12 was obtained through Ampere's law.

For salient poles:

$$B_{gFm} = \frac{\mu_0 W_f I_f}{K_c g(1+K_{S0})}, for : |x| < \frac{\tau_p}{2} \tag{4.18}$$

and $B_{gFm} = 0$ otherwise (Figure 4.12a).
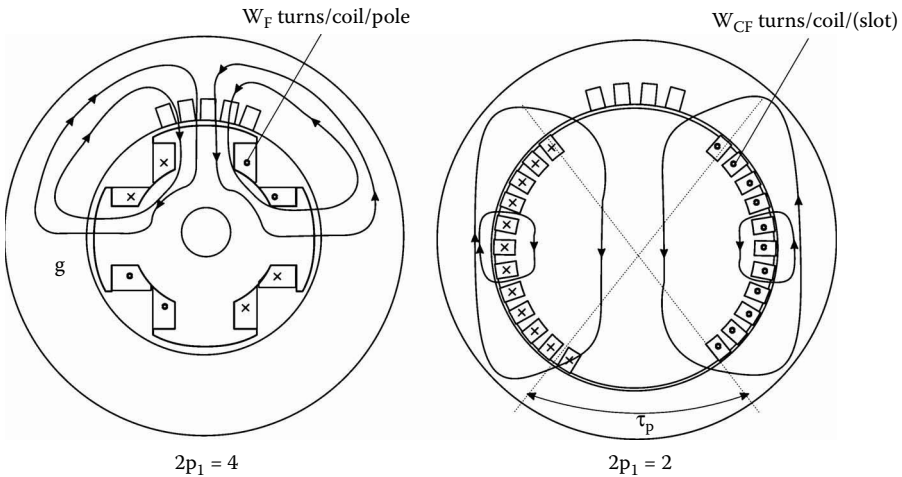
FIGURE 4.11 Basic field-winding flux lines through airgap and stator.

(a)

(b)
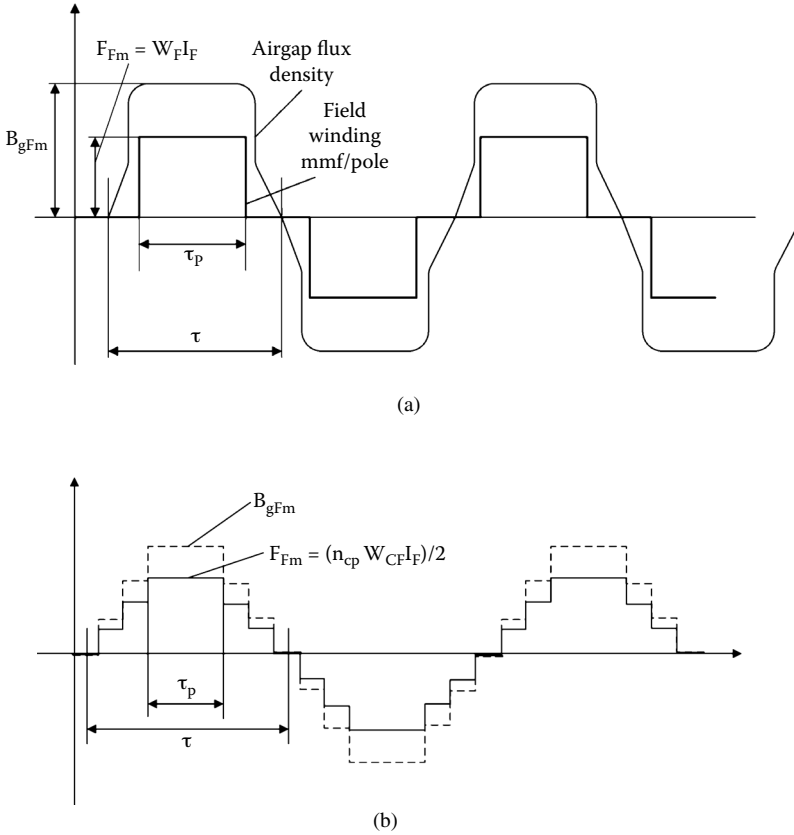
FIGURE 4.12 Field-winding mmf and airgap flux density: (a) salient pole rotor and (b) nonsalient pole rotor.

In practice, $B_{gFm} = 0.6 - 0.8$ T. Fourier decomposition of this rectangular distribution yields the following:

$$B_{gFv}\left(x\right) = K_{Fv} \cdot B_{gFm} \cos \upsilon \frac{\pi}{\tau} x; \quad \upsilon = 1,3,5,... \tag{4.19}$$

$$K_{Fv} = \frac{4}{\pi} \sin \upsilon \frac{\tau_p}{\tau} \frac{\pi}{2} \tag{4.20}$$

Only the fundamental is useful. Both the fundamental distribution ($\nu = 1$) and the space harmonics depend on the ratio τ_p/τ (pole span/pole pitch). In general, $\tau_p/\tau \approx 0.6-0.72$. Also, to reduce the harmonics content, the airgap may be modified (increased), from the pole middle toward the pole ends, as an inverse function of $\cos \pi x/\tau$:

$$g\left(x\right) = \frac{g}{\cos \dfrac{\pi}{\tau} x}, for: \frac{-\tau_p}{2} < x < \frac{\tau_p}{2} \tag{4.21}$$

In practice, Equation 4.21 is not easy to generate, but approximations of it, easy to manufacture, are adopted.

Reducing the no-load airgap flux-density harmonics causes a reduction of time harmonics in the stator emf (or no-load stator phase voltage).

For the nonsalient pole rotor (Figure 4.12b):

$$B_{gFm} = \frac{\mu_0 \frac{n_p}{2} W_{CF} I_f}{K_C g \left(1 + K_{S0}\right)}, \, for : |x| < \frac{\tau_p}{2} \tag{4.22}$$

and stepwise varying otherwise (Figure 4.12b). K_{S0} is the magnetic saturation factor that accounts for stator and rotor iron magnetic reluctance of the field paths; n_p – slots per rotor pole.

$$B_{gF\upsilon}\left(x\right) = K_{F\upsilon} \cdot B_{gFM} \cdot \cos\frac{\upsilon\pi}{\tau} x \tag{4.23}$$

$$K_{F\upsilon} \approx \frac{8}{\upsilon^2 \pi^2} \frac{\cos\upsilon\dfrac{\tau_p}{\tau}\dfrac{\pi}{2}}{\left(1 - \upsilon\dfrac{\tau_p}{\tau}\right)} \tag{4.24}$$

It is obvious that, in this case, the flux density harmonics are lower; thus, constant airgap (cylindrical rotor) is feasible in all practical cases.

Let us consider only the fundamentals of the no-load flux density in the airgap:

$$B_{gF1}\left(x_r\right) = B_{gFm1} \cos\frac{\pi}{\tau} x_r \tag{4.25}$$

For constant rotor speed, the rotor coordinate x_r is related to the stator coordinate x_s as follows:

$$\frac{\pi}{\tau} x_r = \frac{\pi}{\tau} x_s - \omega_r t - \theta_0 \tag{4.26}$$

The rotor rotates at angular speed ω_r (in electrical terms: $\omega_r = p_1 \Omega_r - \Omega_r$ mechanical angular velocity). θ_0 is an arbitrary initial angle; let $\theta_0 = 0$.

With Equation 4.26, Equation 4.25 becomes

$$B_{gF1}\left(x_s, t\right) = B_{gFm1} \cos\left(\frac{\pi}{\tau} x_s - \omega_r t\right) \tag{4.27}$$

So, the excitation airgap flux density represents a forward-traveling wave at rotor speed. This traveling wave moves in front of the stator coils at the tangential velocity u_s:

$$u_s = \frac{dx_s}{dt} = \frac{\tau\omega_r}{\pi} \tag{4.28}$$

It is now evident that, with the rotor driven by a prime mover at speed ω_r, and the stator phases open, the excitation airgap magnetic field induces an emf in the stator windings:

$$E_{A1}(t) = -\frac{d}{dt} W_1 K_{W1} \int_{-\frac{\tau}{2}}^{+\frac{\tau}{2}} l_{stack} B_{gF1}(x_s, t) dx_s \qquad (4.29)$$

and, finally,

$$E_{A1}(t) = E_1 \sqrt{2} \cos \omega_r t \qquad (4.30)$$

$$E_{1m} = \pi \sqrt{2} \left(\frac{\omega_r}{2\pi} \right) B_{gFm1} l_{stack} W_1 K_{W1} \frac{\tau 2}{\pi} \qquad (4.31)$$

with l_{stack} equal to the stator stack length.

As the three phases are fully symmetric, the emfs in them are as follows:

$$E_{A,B,C,1}(t) = E_{1m} \sqrt{2} \cos \left[\omega_r t - (i-1) \frac{2\pi}{3} \right] \qquad (4.32)$$

$$i = 1, 2, 3$$

So, we notice that the excitation coil currents in the rotor are producing at no load (open stator phases) three symmetric emfs with frequency ω_r that is given by the rotor speed $\Omega_r = \omega_r / p_1$.

4.4 The Two-Reaction Principle of Synchronous Generators

Let us now suppose that an excited SG is driven on no load at speed ω_r. When a balanced three-phase load is connected to the stator (Figure 4.13a), the presence of emfs at frequency ω_r will naturally produce currents of the same frequency. The phase shift between the emfs and the phase current ψ is dependent on load nature (power factor) and on machine parameters, not yet mentioned (Figure 4.13b). The sinusoidal emfs and currents are represented as simple phasors in Figure 4.13b. Because of the magnetic anisotropy of the rotor along axes d and q, it helps to decompose each phase current into two components: one in phase with the emf and the other one at 90° with respect to the former: $\underline{I}_{Aq}, \underline{I}_{Bq}, \underline{I}_{Cq}$, and, respectively, $\underline{I}_{Ad}, \underline{I}_{Bd}, \underline{I}_{Cd}$.
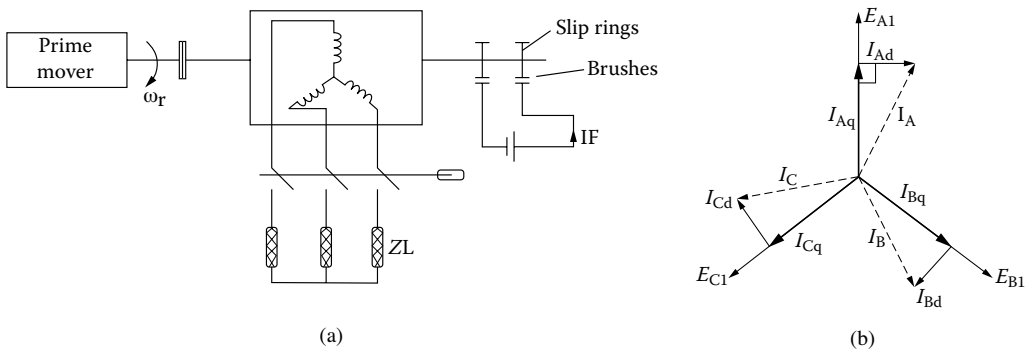
FIGURE 4.13 Illustration of synchronous generator principle: (a) the synchronous generator on load and (b) the emf and current phasors.

As already proven in the paragraph on windings, three-phase symmetric windings flowed by balanced currents of frequency ω_r will produce traveling mmfs (Equation 4.13):

$$F_d(x,t) = -F_{dm} \cos\left(\frac{\pi}{\tau} x_s - \omega_r t\right) \tag{4.33}$$

$$F_{dm} = \frac{3\sqrt{2}\, I_d W_1 K_{W1}}{\pi p_1}; I_d = \left|\underline{I}_{Ad}\right| = \left|\underline{I}_{Bd}\right| = \left|\underline{I}_{Cd}\right| \tag{4.34}$$

$$F_q(x,t) = F_{qm} \cos\left(\frac{\pi}{\tau} x_s - \omega_r t - \frac{\pi}{2}\right) \tag{4.35}$$

$$F_{qm} = \frac{3\sqrt{2}\, I_q W_1 K_{W1}}{\pi p_1}; I_q = \left|\underline{I}_{Aq}\right| = \left|\underline{I}_{Bq}\right| = \left|\underline{I}_{Cq}\right| \tag{4.36}$$

In essence, the *d*-axis stator currents produce an mmf aligned to the excitation airgap flux density wave (Equation 4.26) but opposite in sign (for the situation in Figure 4.13b). This means that the *d*-axis mmf component produces a magnetic field "fixed" to the rotor and flowing along axis *d* as the excitation field does.

In contrast, the *q*-axis stator current components produce an mmf with a magnetic field that is again "fixed" to the rotor but flowing along axis *q*.

The emfs produced by motion in the stator windings might be viewed as produced by a fictitious three-phase AC winding flowed by symmetric currents $\underline{I}_{FA}$, $\underline{I}_{FB}$, $\underline{I}_{FC}$ of frequency ω_r:

$$\underline{E}_{A,B,C} = -j\omega_r M_{FA}\, \underline{I}_{FA,B,C} \tag{4.37}$$

From what we already discussed in this paragraph,

$$E_A(t) = 2\pi \frac{\omega_r}{2\pi} K_{W1} \frac{2}{\pi} l_{stack} \tau \cdot \frac{\mu_0 W_F I_f K_{F1}}{K_c g(1 + K_{S0})} \cos\omega_{1t}$$

$$W_F = \frac{n_p}{2} W_{CF}; \text{for nonsalient pole rotor, see (4.22)} \tag{4.38}$$

The fictitious currents $\underline{I}_{FA}$, $\underline{I}_{FB}$, $\underline{I}_{FC}$ are considered to have the root mean squared (RMS) value of I_f in the real field winding. From Equation 4.37 and Equation 4.38:

$$M_{FA} = \mu_0 \frac{\sqrt{2}}{\pi} \frac{W_1 W_F K_{W1} \tau \cdot l_{stack}}{K_C g\left(1 + K_{S0}\right)} K_{F1} \tag{4.39}$$

M_{FA} is called the mutual rotational inductance between the field and armature (stator) phase windings.

The positioning of the fictitious $\underline{I}_F$ (per phase) in the phasor diagram (according to Equation 4.37) and that of the stator phase current phasor $\underline{I}$ (in the first or second quadrant for generator operation and in the third or fourth quadrant for motor operation) are shown in Figure 4.14.

The generator–motor divide is determined solely by the electromagnetic (active) power:
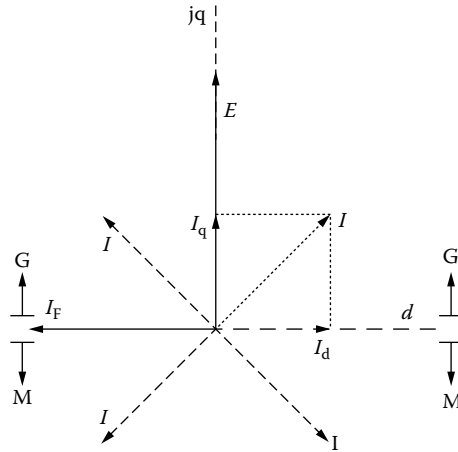
FIGURE 4.14   Generator and motor operation modes.

$$P_{elm} = 3\,\mathrm{Re}\left(\underline{E}\cdot\underline{I}^{*}\right) > 0 \text{ generator}, < 0 \text{ motor} \tag{4.40}$$

The reactive power Q_{elm} is

$$Q_{elm} = 3\,\mathrm{Im}\,ag\left(\underline{E}\cdot\underline{I}^{*}\right) <> 0(\textit{generator}\,/\,\textit{motor}) \tag{4.41}$$

The reactive power may be either positive (delivered) or negative (drawn) for both motor and generator operation.

For reactive power "production," $\underline{I}_d$ should be opposite from $\underline{I}_F$, that is, the longitudinal armature reaction airgap field will oppose the excitation airgap field. It is said that only with demagnetizing longitudinal armature reaction — machine overexcitation — can the generator (motor) "produce" reactive power. So, for constant active power load, the reactive power "produced" by the synchronous machine may be increased by increasing the field current I_F. On the contrary, with underexcitation, the reactive power becomes negative; it is "absorbed." This extraordinary feature of the synchronous machine makes it suitable for voltage control, in power systems, through reactive power control via I_F control. On the other hand, the frequency ω_r, tied to speed, $\Omega_r = \omega_r/p_1$, is controlled through the prime mover governor, as discussed in Chapter 3. For constant frequency power output, speed has to be constant. This is so because the two traveling fields — that of excitation and, respectively, that of armature windings — interact to produce constant (nonzero-average) electromagnetic torque only at standstill with each other.

This is expressed in Equation 4.40 by the condition that the frequency of $\underline{E}_1 - \omega_r -$ be equal to the frequency of stator current $I_1 - \omega_1 = \omega_r -$ to produce nonzero active power. In fact, Equation 4.40 is valid only when $\omega_r = \omega_1$, but in essence, the average instantaneous electromagnetic power is nonzero only in such conditions.

4.5   The Armature Reaction Field and Synchronous Reactances

As during steady state magnetic field waves in the airgap that are produced by the rotor (excitation) and stator (armature) are relatively at standstill, it follows that the stator currents do not induce voltages (currents) in the field coils on the rotor. The armature reaction (stator) field wave travels at rotor speed; the longitudinal $\underline{I}_{aA}$, $\underline{I}_{aB}$, $\underline{I}_{aC}$ and transverse $\underline{I}_{qA}$, $\underline{I}_{qB}$, $\underline{I}_{qC}$ armature current (reaction) fields are fixed to the

rotor: one along axis *d* and the other along axis *q*. So, for these currents, the machine reacts with the magnetization reluctances of the airgap and of stator and rotor iron with no rotor-induced currents.

The trajectories of armature reaction *d* and *q* fields and their distributions are shown in Figure 4.15a, Figure 4.15b, Figure 4.16a, and Figure 4.16b, respectively. The armature reaction mmfs F_{d1} and F_{q1} have a sinusoidal space distribution (only the fundamental reaction is considered), but their airgap flux densities do not have a sinusoidal space distribution. For constant airgap zones, such as it is under the constant airgap salient pole rotors, the airgap flux density is sinusoidal. In the interpole zone of a salient pole machine, the equivalent airgap is large, and the flux density decreases quickly (Figure 4.15 and Figure 4.16).

(a)

(b)
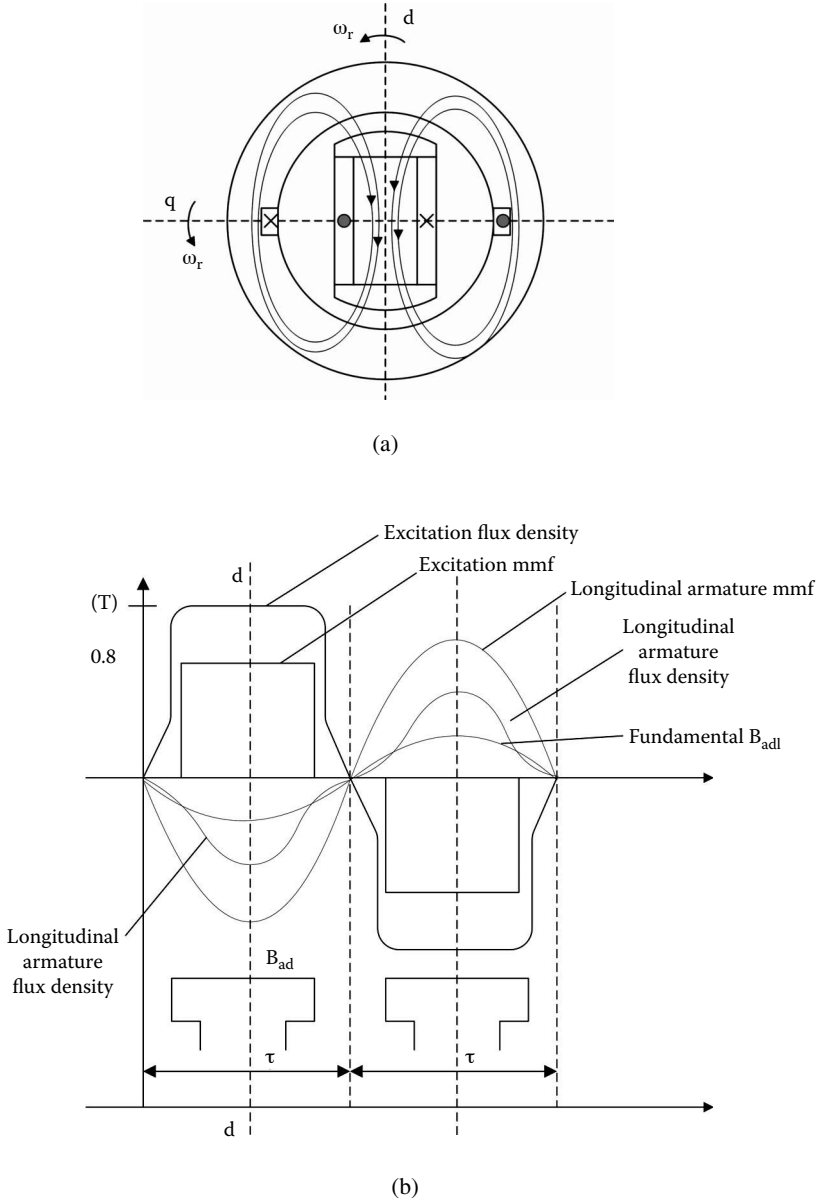
FIGURE 4.15 Longitudinal (*d* axis) armature reaction: (a) armature reaction flux paths and (b) airgap flux density and mmfs.

(a)

(b)
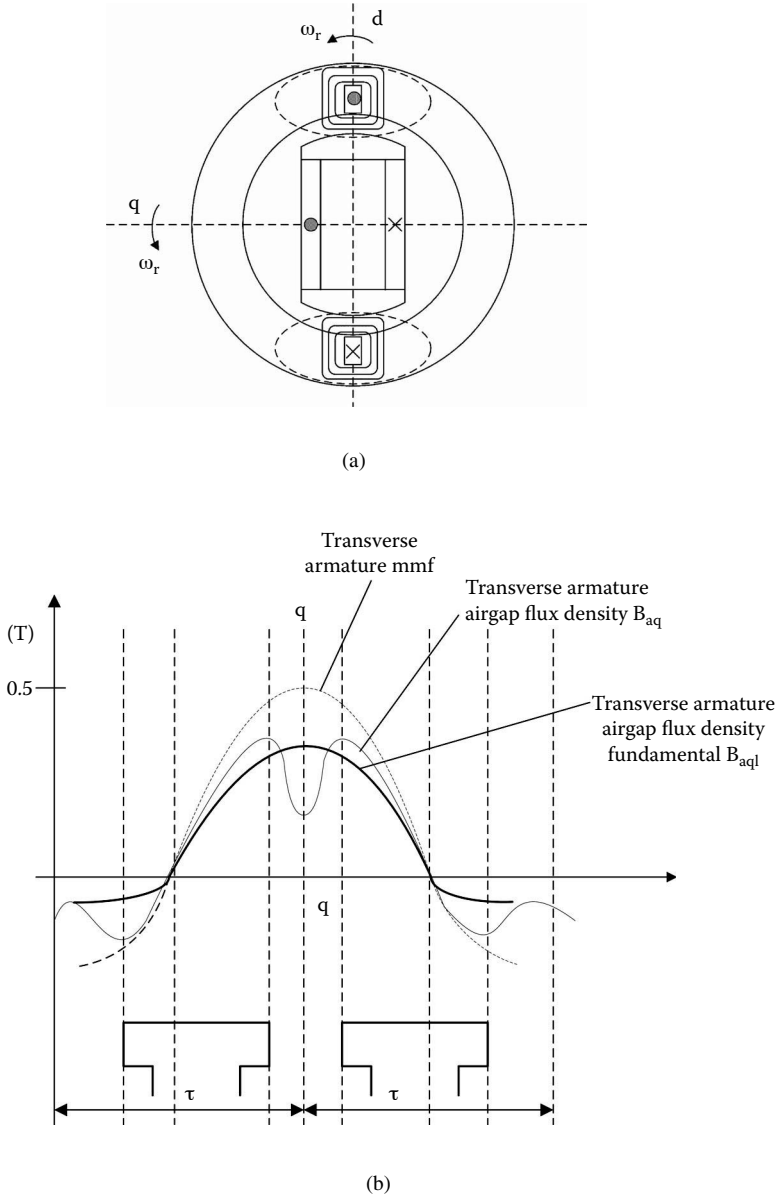
FIGURE 4.16 Transverse (*q* axis) armature reaction: (a) armature reaction flux paths and (b) airgap flux density and mmf.

Only with the finite element method (FEM) can the correct flux density distribution of armature (or excitation, or combined) mmfs be computed. For the time being, let us consider that for the *d* axis mmf, the interpolar airgap is infinite, and for the *q* axis mmf, it is $g_q = 6g$. In axis *q*, the transverse armature mmf is at maximum, and it is not practical to consider that the airgap in that zone is infinite, as that would lead to large errors. This is not so for *d* axis mmf, which is small toward axis *q*, and the infinite airgap approximate is tolerable.

We should notice that the *q*-axis armature reaction field is far from a sinusoid. This is so only for salient pole rotor SGs. Under steady state, however, we operate only with fundamentals, and with respect to them, we define the reactances and other variables. So, we now extract the fundamentals of B_{ad} and B_{aq} to find the B_{ad1} and B_{aq1}:

$$B_{ad1} = \frac{1}{\tau} \int_0^\tau B_{ad}(x_r) \sin\left(\frac{\pi}{\tau} x_r\right) dx_r \tag{4.42}$$

with

$$B_{ad} = 0, \, for : 0 < x_r < \frac{\tau - \tau_p}{2} \, and \, \frac{\tau + \tau_p}{2} < x < \tau$$

$$B_{ad} = \frac{\mu_0 F_{dm} \sin\frac{\pi}{\tau} x_r}{K_c g(1 + K_{sd})} \, for \, \frac{\tau - \tau_p}{2} < x_r < \frac{\tau + \tau_p}{2} \tag{4.43}$$

and finally,

$$B_{ad1} = \frac{\mu_0 F_{dm} K_{d1}}{K_c g(1 + K_{sd})}; K_{d1} \approx \frac{\tau_p}{\tau} + \frac{1}{\pi} \sin\frac{\tau_p}{\tau} \pi \tag{4.44}$$

In a similar way,

$$B_{aq} = \frac{\mu_0 F_{qm} \sin\frac{\pi}{\tau} x_r}{K_c g(1 + K_{sq})}, \, for : 0 \le x_r \le \frac{\tau_p}{2} \, and \, \frac{\tau + \tau_p}{2} < x < \tau$$

$$B_{aq} = \frac{\mu_0 F_{qm} \sin\frac{\pi}{\tau} x_r}{K_c g_q(1 + K_{sq})} \, for \, \frac{\tau_p}{2} < x_r < \frac{\tau + \tau_p}{2} \tag{4.45}$$

$$B_{aq1} = \frac{\mu_0 F_{qm} K_{q1}}{K_c g};$$

$$K_{q1} = \frac{\tau_p}{\tau} - \frac{1}{\pi} \sin\frac{\tau_p}{\tau} \pi + \frac{2}{3\pi} \cos\left(\frac{\tau_p}{\tau} \frac{\pi}{2}\right) \tag{4.46}$$

Notice that the integration variable was x_r, referring to rotor coordinates.

Equation 4.44 and Equation 4.46 warrant the following remarks:

- The fundamental armature reaction flux density in axes *d* and *q* are proportional to the respective stator mmfs and inversely proportional to airgap and magnetic saturation equivalent factors K_{sd} and K_{sq} (typically, $K_{sd} \neq K_{sq}$).
- B_{ad1} and B_{aq1} are also proportional to equivalent armature reaction coefficients K_{d1} and K_{q1}. Both smaller than unity ($K_{d1} < 1, K_{q1} < 1$), they account for airgap nonuniformity (slotting is considered only by the Carter coefficient). Other than that, B_{ad1} and B_{aq1} formulae are similar to the airgap flux density fundamental B_{a1} in an uniform airgap machine with same stator, B_{a1}:

$$B_{a1} = \frac{\mu_0 F_1}{K_c g(1 + K_S)}; F_1 = \frac{3\sqrt{2} W_1 K_{W1} I_1}{\pi p_1} \tag{4.47}$$

The cyclic magnetization inductance X_m of a uniform airgap machine with a three-phase winding is straightforward, as the self-emf in such a winding, E_{a1}, is as follows:

$$E_{a1} = \omega_r W_1 K_{W1} \Phi_{a1}; \Phi_{a1} = \frac{2}{\pi} B_{a1} \tau \cdot l_{stack} \tag{4.48}$$

From Equation 4.47 and Equation 4.48, X_m is

$$X_m = \frac{E_{a1}}{I_1 \sqrt{2}} = \frac{6\mu_0 \omega_r}{\pi^2} \frac{\left(W_1 K_{W1}\right)^2 \tau \cdot l_{stack}}{K_C g (1 + K_S)} \tag{4.49}$$

It follows logically that the so-called cyclic magnetization reactances of synchronous machines X_{dm} and X_{qm} are proportional to their flux density fundamentals:

$$X_{dm} = X_m \frac{B_{ad1}}{B_{a1}} = X_m \cdot K_{d1} \tag{4.50}$$

$$X_{qm} = X_m \frac{B_{aq1}}{B_{a1}} = X_m K_{q1} \tag{4.51}$$

and, $K_{sd} = K_{sq} = K_s$ was implied.

The term "cyclic" comes from the fact that these reactances manifest themselves only with balanced stator currents and symmetric windings and only for steady state. During steady state with balanced load, the stator currents manifest themselves by two distinct magnetization reactances, one for axis d and one for axis q, acted upon by the d and q phase current components. We should add to these the leakage reactance typical to any winding, X_{1l}, to compose the so-called synchronous reactances of the synchronous machine (X_d and X_q):

$$X_d = X_{1\sigma} + X_{dm} \tag{4.52}$$

$$X_q = X_{1\sigma} + X_{qm} \tag{4.53}$$

The damper cage currents are zero during steady state with balanced load, as the armature reaction field components are at standstill with the rotor and have constant amplitudes (due to constant stator current amplitude).

We are now ready to proceed with SG equations for steady state under balanced load.

4.6   Equations for Steady State with Balanced Load

We previously introduced stator fictitious AC three-phase field currents $\underline{I}_{F,A,B,C}$ to emulate the field-winding motion-produced emfs in the stator phases $\underline{E}_{A,B,C}$. The decomposition of each stator phase current $I_{qA,B,C}$, $I_{dA,B,C}$, which then produces the armature reaction field waves at standstill with respect to the excitation field wave, has led to the definition of cyclic synchronous reactances X_d and X_q. Consequently, as our fictitious machine is under steady state with zero rotor currents, the per phase equations in complex (phasors) are simply as follows:

$$\underline{I}_1 R_1 + \underline{V}_1 = \underline{E}_1 - jX_d \underline{I}_d - jX_q \underline{I}_q \tag{4.54}$$

$$\underline{E} = -jX_{Fm} \times \underline{I}_F; \; X_{Fm} = \omega_r M_{FA} \tag{4.55}$$

$$\underline{I}_1 = \underline{I}_d + \underline{I}_q$$

RMS values all over in Equation 4.54 and Equation 4.55.

To secure the correct phasing of currents, let us consider $\underline{I}_F$ along axis d (real). Then, according to Figure 4.13,

$$\underline{I}_q = I_q \times \left(-j \frac{I_F}{I_F} \right); \underline{I}_d = I_d \frac{I_F}{I_F}; I_1 = \sqrt{I_d^2 + I_q^2} \tag{4.56}$$

With $I_F > 0$, I_d is positive for underexcitation ($E_1 < V_1$) and negative for overexcitation ($E_1 > V_1$). Also, I_q in Equation 4.56 is positive for generating and negative for motoring.

The terminal phase voltage $\underline{V}_1$ may represent the power system voltage or an independent load $\underline{Z}_L$:

$$\underline{Z}_L = \frac{\underline{V}_1}{\underline{I}_1} \tag{4.57}$$

A power system may be defined by an equivalent internal emf $\underline{E}_{PS}$ and an internal impedance $\underline{Z}_0$:

$$\underline{V}_1 = \underline{E}_{PS} + \underline{Z}_{PS} \underline{I}_1 \tag{4.58}$$

For an infinite power system, $\left| \underline{Z}_{PS} \right| = 0$ and $\underline{E}_{PS}$ is constant. For a limited power system, either only $\left| \underline{Z}_{PS} \right| \neq 0$, or also E_{PS} varies in amplitude, phase, or frequency. The power system impedance $\underline{Z}_{PS}$ includes the impedance of multiple generators in parallel, of transformers, and of power transmission lines.

The power balance applied to Equation 4.54, after multiplication by $3I_1^*$, yields the following:

$$P_1 + jQ_1 = 3\underline{V}_1 \underline{I}_1^* = 3\underline{E}_1 I_1^* - 3\left(\underline{I}_1 \right)^2 R_1 - 3jX_{1l} \left(\underline{I}_1 \right)^2 - 3j\left(X_{dm} \underline{I}_d + X_{qm} \underline{I}_q \right) \underline{I}_1^* \tag{4.59}$$

The real part represents the active output power P_1, and the imaginary part is the reactive power, both positive if delivered by the SG:

$$P_1 = 3E_1 I_q - 3I_1^2 R_1 + 3(X_{dm} - X_{qm})I_d I_q = 3V_1 I_1 \cos \varphi_1 \tag{4.60}$$

$$Q_1 = -3E_1 I_d - 3I_1^2 X_{sl} - 3(X_{dm} I_d^2 + X_{qm} I_q^2) = 3V_1 I_1 \sin \varphi_1 \tag{4.61}$$

As seen from Equation 4.60 and Equation 4.61, the active power is positive (generating) only with $I_q > 0$. Also, with $X_{dm} \geq X_{qm}$, the anisotropy active power is positive (generating) only with positive I_d (magnetization armature reaction along axis d). But, positive I_d in Equation 4.61 means definitely negative (absorbed) reactive power, and the SG is underexcited.

In general, $X_{dm}/X_{qm} = 1.0–1.7$ for most SGs with electromagnetic excitation. Consequently, the anisotropy electromagnetic power is notably smaller than the interaction electromagnetic power. In nonsalient pole machines, $X_{dm} \approx (1.01–1.05)X_{qm}$ due to the presence of rotor slots in axis q that increase the equivalent airgap (K_C increases due to double slotting). Also, when the SG saturates (magnetically), the level of saturation under load may be, in some regimes, larger than in axis d. In other regimes, when magnetic saturation is larger in axis d, a nonsalient pole rotor may have a slight inverse magnetic saliency ($X_{dm} <$

X_{qm}). As only the stator winding losses have been considered ($3R_1I_1^2$), the total electromagnetic power P_{elm} is as follows:

$$P_{elm} = 3E_1I_q + 3\left(X_{dm} - X_{qm}\right)I_d I_q \tag{4.62}$$

Now, the electromagnetic torque T_e is

$$T_e = \frac{P_{elm}}{\dfrac{\omega_r}{p_1}} = 3p_1\left[M_{fA}I_F I_q + (L_{dm} - L_{qm})I_d I_q\right] \tag{4.63}$$

with

$$L_{dm} = X_{dm}/\omega_r \,; L_{qm} = X_{qm}/\omega_r \tag{4.64}$$

And, from Equation 4.37,

$$E_1 = \omega_r M_{FA} I_F \tag{4.65}$$

We may also separate in the stator phase flux linkage $\underline{\Psi}_1$, the two components Ψ_d and Ψ_q:

$$\begin{aligned} \Psi_d &= M_{FA} + L_d I_d \\ \Psi_q &= L_q I_q \end{aligned} \tag{4.66}$$

$$L_d = \frac{X_d}{\omega_r}\,; L_q = \frac{X_q}{\omega_r} \tag{4.67}$$

The total stator phase flux linkage $\underline{\Psi}_1$ is

$$\Psi_1 = \sqrt{\Psi_d^2 + \Psi_q^2}\,; I_1 = \sqrt{I_d^2 + I_q^2} \tag{4.68}$$

As expected, from Equation 4.63, the electromagnetic torque does not depend on frequency (speed) ω_r, but only on field current and stator current components, besides the machine inductances: the mutual one, M_{FA}, and the magnetization ones L_{dm} and L_{qm}. The currents $\underline{I}_F$, $\underline{I}_d$, $\underline{I}_q$ influence the level of magnetic saturation in stator and rotor cores, and thus M_{FA}, L_{dm}, and L_{qm} are functions of all of them.

Magnetic saturation is an involved phenomenon that will be treated in Chapter 5.

The shaft torque T_a differs from electromagnetic torque T_e by the mechanical power loss (p_{mec}) braking torque:

$$T_a = T_e + \frac{p_{mec}}{\left(\omega_r / p_1\right)} \tag{4.69}$$

For generator operation mode, T_e is positive, and thus, $T_a > T_e$. Still missing are the core losses located mainly in the stator.
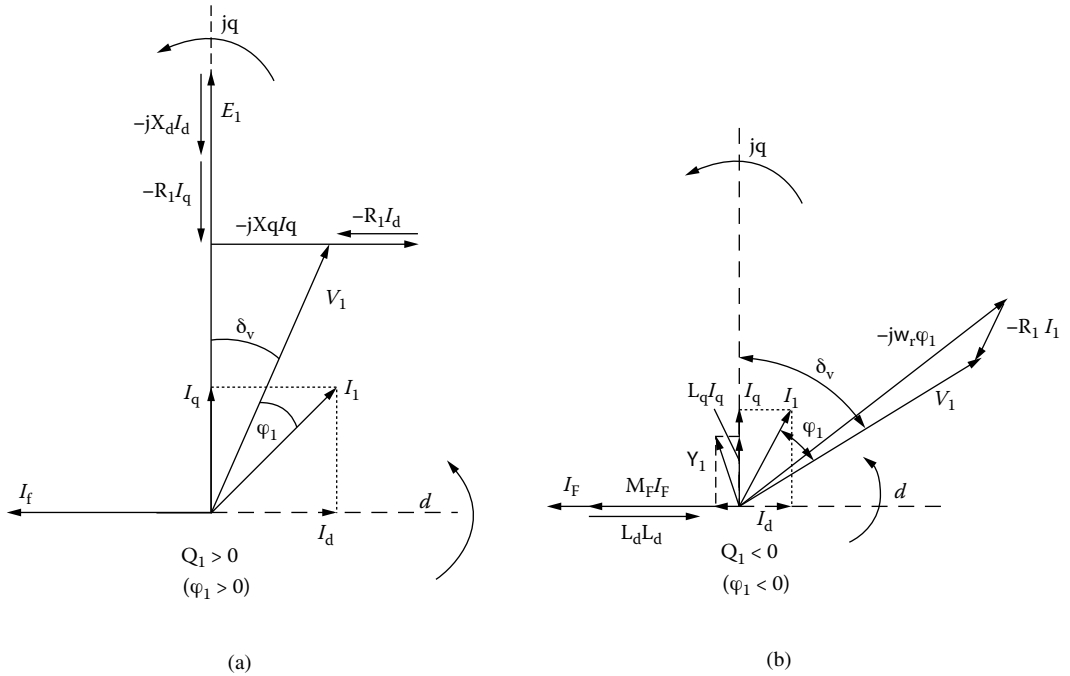
FIGURE 4.17 Phasor diagrams: (a) standard and (b) modified but equivalent.

4.7 The Phasor Diagram

Equation 4.54, Equation 4.55, and Equation 4.66 through Equation 4.68 lead to a new voltage equation:

$$\underline{I}_1 R_1 + \underline{V}_1 = -j\omega_r \underline{\Psi}_1 = \underline{E}_t; \Psi_1 = \Psi_d + j\Psi_q \tag{4.70}$$

where $\underline{E}_t$ is total flux phase emf in the SG. Now, two phasor diagrams, one suggested by Equation 4.54 and one by Equation 4.70 are presented in Figure 4.17a and Figure 4.17b, respectively.

The time phase angle δ_V between the emf $\underline{E}_1$ and the phase voltage $\underline{V}_1$ is traditionally called the internal (power) angle of the SG. As we wrote Equation 4.54 and Equation 4.70 for the generator association of signs, $\delta_V > 0$ for generating ($I_q > 0$) and $\delta_V < 0$ for motoring ($I_q < 0$).

For large SGs, even the stator resistance may be neglected for more clarity in the phasor diagrams, but this is done at the price of "losing" the copper loss consideration.

4.8 Inclusion of Core Losses in the Steady-State Model

The core loss due to the fundamental component of the magnetic field wave produced by both excitation and armature mmf occurs only in the stator. This is so because the two field waves travel at rotor speed. We may consider, to a first approximation, that the core losses are related directly to the main (airgap) magnetic flux linkage $\underline{\Psi}_{1m}$:

$$\underline{\Psi}_{1m} = M_{FA}\underline{I}_F + L_{dm}\underline{I}_d + L_{qm}\underline{I}_q = \Psi_{dm} + j\Psi_{qm} \tag{4.71}$$

$$\Psi_{dm} = M_{FA}I_F + L_{dm}I_d; \Psi_{qm} = L_{qm}I_q \tag{4.72}$$
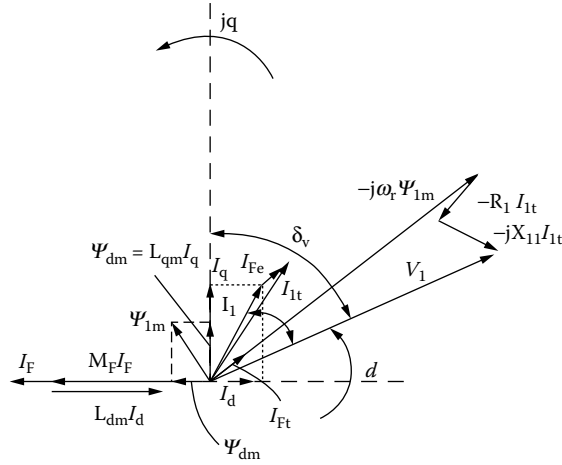
FIGURE 4.18   Phasor diagram with core loss included.

The leakage flux linkage components $L_{sl}\underline{I}_d$ and $L_{sl}\underline{I}_q$ do not produce significant core losses, as $L_{sl}/L_{dm} <$ 0.15 in general, and most of the leakage flux lines flow within air zones (slot, end windings, airgap).

Now, we will consider a fictitious three-phase stator short-circuited resistive-only winding, R_{Fe} which accounts for the core loss. Neglecting the reaction field of core loss currents $\underline{I}_{Fe}$, we have the following:

$$-\frac{d\underline{\Psi}_{1m0}}{dt} = R_{Fe}\,\underline{I}_{Fe} = -\,j\omega_r\,\Psi_{1m0} \tag{4.73}$$

R_{Fe} is thus "connected" in parallel to the main flux emf $(-j\omega_r\underline{\Psi}_{1m})$. The voltage equation then becomes

$$\underline{I}_{1t}\left(R_1 + jX_{sl}\right) + V_1 = -\,j\omega_1\underline{\Psi}_{1m} \tag{4.74}$$

with

$$\underline{I}_{1t} = \underline{I}_d + \underline{I}_q + \underline{I}_{Fe} = \underline{I}_1 + \underline{I}_{Fe} \tag{4.75}$$

The new phasor diagram of Equation 4.74 is shown in Figure 4.18.

Though core losses are small in large SGs and do not change the phasor diagram notably, their inclusion allows for a correct calculation of efficiency (at least at low loads) and of stator currents as the power balance yields the following:

$$P_1 = 3V_1 I_{1t}\cos\varphi_1 = 3\omega_r M_{FA} I_F I_q + 3\omega_r\left(L_{dm} - L_{qm}\right)I_d I_q - 3R_1 I_{1t}^2 - 3\frac{\omega_r^2 \Psi_{1m}^2}{R_{Fe}} \tag{4.76}$$

$$\underline{\Psi}_{1m} = M_{FA} I_f + L_{dm} I_d - jL_{qm} I_q \tag{4.77}$$

$$\underline{I}_{Fe} = \frac{-j\omega_r \underline{\Psi}_{1m}}{R_{Fe}}; \underline{I}_t = \underline{I}_d + \underline{I}_q + \underline{I}_{Fe} \tag{4.78}$$

Once the SG parameters R_1, R_{Fe}, L_{dm}, L_{qm}, M_{FA}, excitation current I_F, speed (frequency) — $\omega_r/p_1 = 2\pi n$ (rps) — are known, the phasor diagram in Figure 4.17 allows for the computation of I_d, I_q, provided the power angle δ_V and the phase voltage V_1 are also given. After that, the active and reactive power delivered by the SG may be computed. Finally, the efficiency η_{SG} is as follows:

$$\eta_{SG} = \frac{P_1}{P_1 + p_{Fe} + p_{copper} + p_{mec} + p_{add}} = \frac{P_{elm} - p_{copper} - p_{Fe} - p_{add}}{P_{elm} + p_{mec}} \tag{4.79}$$

with p_{add} equal to additional losses on load.

Alternatively, with I_F as a parameter, I_d and I_q can be modified (given) such that $\sqrt{I_d^2 + I_q^2} = I_1$ can be given as a fraction of full load current. Note that while decades ago, the phasor diagrams were used for graphical computation of performance, nowadays they are used only to illustrate performance and derive equations for a pertinent computer program to calculate the same performance faster and with increased precision.

Example 4.1

The following data are obtained from a salient pole rotor synchronous hydrogenerator: $S_N = 72$ MVA, $V_{1line} = 13$ kV/star connection, $2p_1 = 90$, $f_1 = 50$ Hz, $q_1 =$ three slots/pole/phase, $I_{1r} = 3000$ A, $R_1 = 0.0125\ \Omega$, $(\eta_r)_{cos1=1} = 0.9926$, and $p_{Fen} = p_{mecn}$. Additional data are as follows: stator interior diameter $D_{is} = 13$ m, stator active stack length $l_{stack} = 1.4$ m, constant airgap under the poles $g = 0.020$ m, Carter coefficient $K_C = 1.15$, and $\tau_p/\tau = 0.72$. The equivalent unique saturation factor $K_s = 0.2$.

The number of turns in series per phase is $W_1 = p_1 q_1 \times$ one turn/coil $= 45 \times 3 \times 1 = 115$ turns/phase.

Let us calculate the following:

1. The stator winding factor K_{W1}
2. The d and q magnetization reactances X_{dm}, X_{qm}
3. X_d, X_q, with $X_{1l} = 0.2 X_{dm}$
4. Rated core and mechanical losses P_{Fen}, p_{mecn}
5. x_d, x_q, r_1 in P.U. with $Z_n = V_{1ph}/I_{1r}$
6. E_1, I_d, I_q, I_1, E_1, P_1, Q_1, by neglecting all losses at $\cos\psi_1 = 1$ and $\delta_v = 30°$
7. The no-load airgap flux density ($K_s = 0.2$) and the corresponding rotor-pole mmf $W_F I_F$

Solution:

1. The winding factor K_{W1} (Equation 4.10) is as follows:

$$K_{W1} = \frac{\sin \pi/6}{3\sin(\pi/6 \cdot 3)} \sin\left(\frac{1}{1} \cdot \frac{\pi}{2}\right) = 0.9598$$

   Full pitch coils are required ($y/\tau = 1$), as the single-layer case is considered.
2. The expressions of X_{dm} and X_{qm} are shown in Equation 4.49 through Equation 4.51:

$$X_{dm} = X_m \cdot K_{d1}$$
$$X_{qm} = X_m \cdot K_{q1}$$

From Equation 4.44,

$$K_{d1} = \frac{\tau_p}{\tau} + \frac{1}{\pi}\sin\frac{\tau_p}{\tau}\pi = 0.72 + \frac{1}{\pi}\sin 0.72\cdot\pi = 0.96538$$

$$K_{q1} = \frac{\tau_p}{\tau} - \frac{1}{\pi}\sin\frac{\tau_p}{\tau}\pi + \frac{2}{3\pi}\cos\frac{\tau_p}{\tau}\frac{\pi}{2} = 0.4776 + 0.0904 = 0.565$$

$$X_m = \frac{6\mu_0}{\pi^2}\omega_r\frac{\left(W_1 K_{W1}\right)^2\cdot\tau\cdot l_{stack}}{K_C g\left(1+K_s\right)p_1}$$

$$with: \tau = \pi D_{is}/2p_1 = \pi\cdot 13/90 = 0.45355\ m$$

$$X_m = \frac{6\cdot 4\pi\times 10^{-7}\cdot 2\pi\cdot 50\cdot\left(115\cdot 0.9598\right)^2\times 0.45355\times 1.4}{\pi^2\times 1.15\times 0.020\left(1+0.2\right)\times 45} = 1.4948\ \Omega$$

$$X_{dm} = 1.4948\times 0.96538 = 1.443\ \Omega$$

$$X_{qm} = 1.4948\times 0.565 = 0.8445\ \Omega$$

3. With $X_{1l} = 0.2\times 1.4948 = 0.2989\ \Omega$, the synchronous reactances X_d and X_q are

$$X_d = X_{1l} + X_{dm} = 0.2989 + 1.443 \approx 1.742\ \Omega$$

$$X_q = X_{1l} + X_{qm} = 0.2989 + 0.8445 = 1.1434\ \Omega$$

4. As the rated efficiency at $\cos\varphi_1 = 1$ is $\eta_r = 0.9926$ and using Equation 4.79,

$$\sum p = p_{copper} + p_{Fen} + p_{mec} = S_n\left(\frac{1}{\eta_r}-1\right) = 72\cdot 10^6\left(\frac{1}{0.9926}-1\right) = 536\cdot 772\ kW$$

The stator winding losses p_{copper} are

$$p_{copper} = 3R_1 I_{1r}^2 = 3\cdot 0.0125\cdot 3000^2 = 337.500\ kW$$

so,

$$p_{Fe} = p_{mec} = \frac{\sum p - p_{copper}}{2} = \frac{536.772 - 337500}{2} = 99.636\ kW$$

5. The normalized impedance Z_n is

$$Z_n = \frac{V_{1ph}}{I_{1r}} = \frac{13\cdot 10^3}{\sqrt{3}\cdot 3000} = 2.5048\ \Omega$$

$$x_d = \frac{X_d}{Z_n} = \frac{1.742}{2.5048} = 0.695$$

$$x_q = \frac{X_q}{Z_n} = \frac{1.1434}{2.5048} = 0.45648$$

$$r_1 = \frac{R_1}{Z_n} = \frac{0.0125}{2.5048} = 4.99\times 10^{-3}$$

6. After neglecting all losses, the phasor diagram in Figure 4.16a, for cos $\varphi_1 = 1$, can be shown.
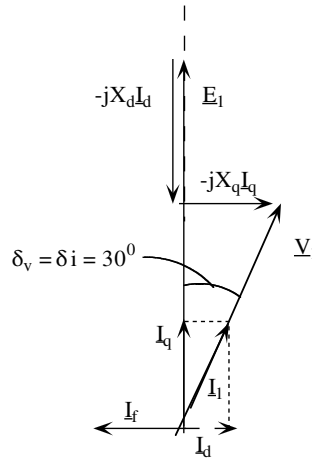
Phasor diagram for cos $\varphi_1 = 1$ and zero losses.

The phasor diagram uses phase quantities in RMS values.

From the adjacent phasor diagram:

$$I_q = \frac{V_1 \sin \delta_V}{X_q} = \frac{13000}{\sqrt{3}} \frac{0.5}{1.1434} = 3286 \ A$$

$$I_d = -I_q \tan 30^0 = -3286 \frac{1}{\sqrt{3}} = -1899.42 \ A$$

$$I_1 = \sqrt{I_d^2 + I_q^2} = 3796 \ A!$$

And, the emf per phase E_1 is

$$E_1 = V_1 \cos \delta_V + X_d |I_d| = \frac{13000}{\sqrt{3}} \cdot \frac{\sqrt{3}}{2} + 1.742 \cdot 1899 = 9.808 \ kV$$

$$P_1 = 3V_1 I_1 \cos \varphi_1 = 3 \cdot \frac{13000}{\sqrt{3}} \cdot 3796 = 85.372 \ MW$$

$$Q_1 = 3V_1 I_1 \sin \varphi_1 = 0$$

It could be inferred that the rated power angle δ_{Vr} is smaller than 30° in this practical example.

7. We may use Equation 4.48 to calculate E_1 at no load:

$$E_1 = \frac{\omega_r}{\sqrt{2}} W_1 K_{W1} \Phi_{pole1}$$

$$\Phi_{pole1} = \frac{2}{\pi} B_{g1} \cdot \tau \cdot l_{stack}$$

Then, from Equation 4.20,

$$B_{g1} = B_{gFM} K_{F1}; K_{F1} = \frac{4}{\pi} \sin \frac{\tau_p}{\tau} \frac{\pi}{2}$$

Also, from Equation 4.78,

$$B_{gFM} = \frac{\mu_0 W_F I_F}{K_C g (1 + K_S)}$$

So, gradually,

$$\Phi_{pole1} = \frac{9808 \times \sqrt{2}}{2\pi 50 \times 115 \times 0.9596} = 0.3991 \; Wb$$

$$B_{g1} = \frac{0.3991 \times 3.14}{2 \times 0.45355 \times 1.4} = 0.9868$$

$$B_{gFM} = \frac{0.9868}{\frac{4}{\pi} \sin 0.72 \cdot \frac{\pi}{2}} = 0.8561 \; T$$

$$W_F I_F = \frac{0.8561 \times 1.15 (1 + 0.2) \times 2 \times 10^{-2}}{1.256 \times 10^{-6}} = 18,812 \; A \; turns / pole$$

Note that the large airgap ($g = 2 \times 10^{-2}$ m) justifies the moderate saturation (iron reluctance) factor $K_S = 0.2$.

The field-winding losses were not considered in the efficiency, as they are covered from a separate power source.

4.9   Autonomous Operation of Synchronous Generators

Autonomous operation of SGs is required by numerous applications. Also, some SG characteristics in autonomous operation, obtained through special tests or by computation, may be used to characterize the SG comprehensively. Typical characteristics at constant speed are as follows:

- No-load saturation curve: $E_1(I_F)$
- Short-circuit saturation curve: $I_{1sc}(I_F)$ for $V_1 = 0$ and $\cos \varphi_1 = $ ct.
- Zero-power factor saturation curve: $V_1(I_1)$; $I_F = $ ct. $\cos \varphi_1 = $ ct.

These curves may be computed or obtained from standard tests.

4.9.1   The No-Load Saturation Curve: $E_1(I_f)$; $n = $ ct., $I_1 = 0$

At zero-load (stator) current, the excited machine is driven at the speed $n_1 = f_1/p_1$ by a smaller power rating motor. The stator no-load voltage, in fact, the emf (per phase or line) E_1 and the field current are measured. The field current is monotonously raised from zero to a positive value I_{Fmax} corresponding to 120 to 150% of rated voltage V_{1r} at rated frequency f_{1r} ($n_{1r} = f_{1r}/p_1$). The experimental arrangement is shown in Figure 4.19a and Figure 4.19b.

At zero-field current, the remanent magnetization of rotor pole iron produces a small emf E_{1r} (2 to 8% of V_{1r}), and the experiments start at point A or A′. The field current is then increased in small increments until the no-load voltage E_1 reaches 120 to 150% of rated voltage (point B, along the trajectory AMB). Then, the field current is decreased steadily to zero in very small steps, and the characteristic evolves along the BNA′ trajectory. It may be that the starting point is A′, and this is confirmed when I_F
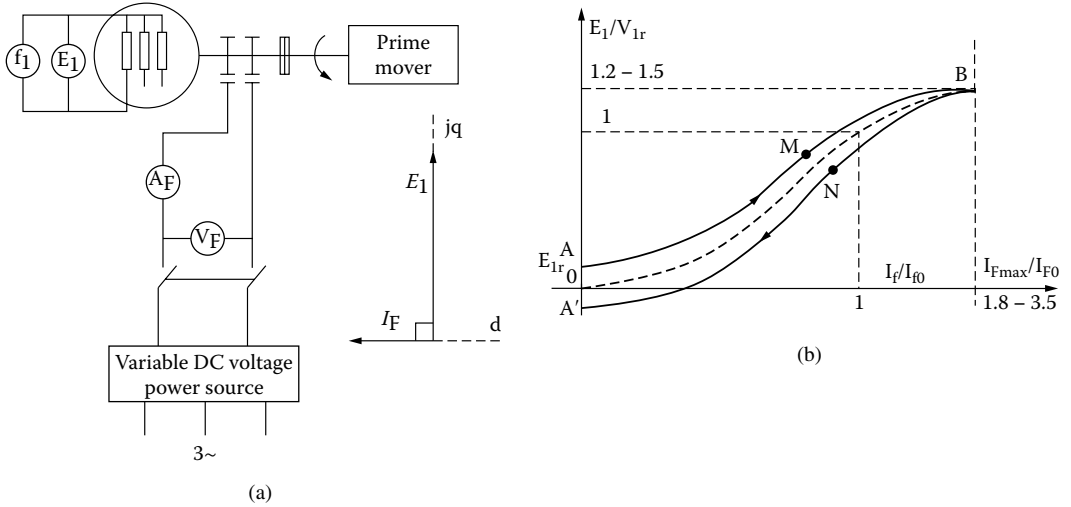
FIGURE 4.19 No-load saturation curve test: (a) the experimental arrangement and (b) the characteristic.

increases from zero, and the emf decreases first and then increases. In this latter case, the characteristic is traveled along the way A'NBMA. The hysteresis phenomenon in the stator and rotor cores is the cause of the difference between the rising and falling sides of the curve. The average curve represents the no-load saturation curve.

The increase in emf well above the rated voltage is required to check the required field current for the lowest design power factor at full load (I_{Fmax}/I_{F0}). This ratio is, in general, $I_{Fmax}/I_{F0} = 1.8$–3.5. The lower the lowest power factor at full load and rated voltage, the larger I_{Fmax}/I_{F0} ratio is. This ratio also varies with the airgap-to-pole-pitch ratio (g/τ) and with the number of pole pairs p_1. It is important to know the corresponding I_{Fmax}/I_{F0} ratio for a proper thermal design of the SG.

The no-load saturation curve may also be computed: either analytically or through finite element method (FEM). As FEM analysis will be dealt with later, here we dwell on the analytical approach. To do so, we draw two typical flux line pairs corresponding to the no-load operation of an SG (Figure 4.20a and Figure 4.20b).

There are two basic analytical approaches of practical interest. Let us call them here the flux-line method and the multiple magnetic circuit method. The simplified flux-line method considers Ampere's law along a basic flux line and applies the flux conservation in the rotor yoke, rotor pole body, and rotor pole shoe, and, respectively, in the stator teeth and yoke.

The magnetic saturation in these regions is considered through a unique (average) flux density and also an average flux line length. It is an approximate method, as the level of magnetic saturation varies tangentially along the rotor-pole body and shoe, in the salient rotor pole, and in the rotor teeth of the nonsalient pole.

The leakage flux lost between the salient rotor pole bodies and their shoes is also approximately considered.

However, if a certain average airgap flux density value B_{gFm} is assigned for start, the rotor pole mmf $W_F I_F$ required to produce it, accounting for magnetic saturation, though approximately, may be computed without any iteration. If the airgap under the rotor salient poles increases from center to pole ends (to produce a more sinusoidal airgap flux density), again, an average value is to be considered to simplify the computation. Once the $B_{gFm}(I_F)$ curve is calculated, the $E_1(I_F)$ curve is straightforward (based on Equation 4.30):

$$E_1(I_F) = \frac{\omega_r}{\sqrt{2}} \times \frac{2}{\pi} \tau B_{gFm}\left(I_f\right) K_{F1} \cdot l_{stack} \cdot W_1 K_{W1}[V(RMS)] \tag{4.80}$$
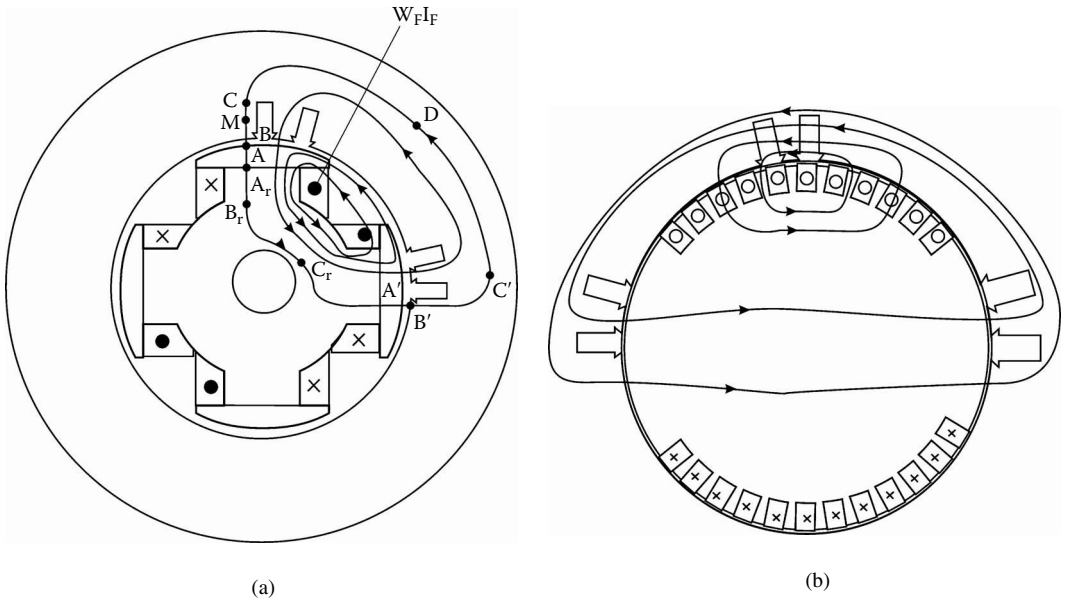
FIGURE 4.20   Flux lines at no load: (a) the salient pole rotor and (b) the nonsalient pole rotor.
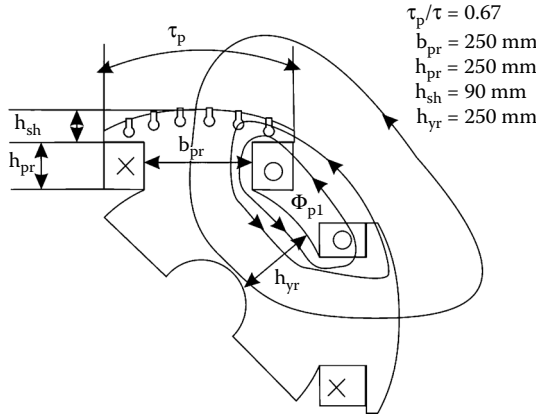
FIGURE 4.21   Rotor geometry and rotor pole leakage flux Φ_{pl}.

The analytical flux-line method is illustrated here through a case study (Example 4.2).

Example 4.2

A three-phase salient pole rotor SG with $S_n = 50$ MVA, $V_1 = 10{,}500$ V, $n_1 = 428$ rpm, and $f_1 = 50$ Hz has the following geometrical data: internal stator diameter $D_r = 3.85$ m, $2p_1 = 14$ poles, $l_{stack} \approx 1.39$ m, pole pitch $\tau = \pi D_r / 2p_1 = 0.864$ m, airgap g (constant) $= 0.021$ m, $q_1 =$ six slots/pole/phase, open stator slots with $h_s = 0.130$ m (total slot height with 0.006 m reserved for the wedge), $Ws = 0.020$ m (slot width), stator yoke $h_{ys} = 0.24$ m, and rotor geometry as in Figure 4.21.

Let us consider only the rated flux density condition, with $B_{gFm1} = 0.850$ T. The stator lamination magnetization curve is given in Table 4.1.

Ampere's law along the contour ABCDC′B′A′ relates the mmf drop from rotor to rotor pole $F_{AA'}$:

TABLE 4.1 The Magnetization Curve $B(H)$ for the Iron Cores

B(T)	0.1	0.2	0.3	0.4	0.5	0.6	0.7	0.8	0.9		
H(A/m)	35	49	65	76	90	106	124	148	177		
B(T)	1	1.1	1.2	1.3	1.4	1.5	1.6	1.7	1.8	1.9	2.0
H(A/m)	220	273	356	482	760	1,340	2,460	4,800	8,240	10,200	34,000
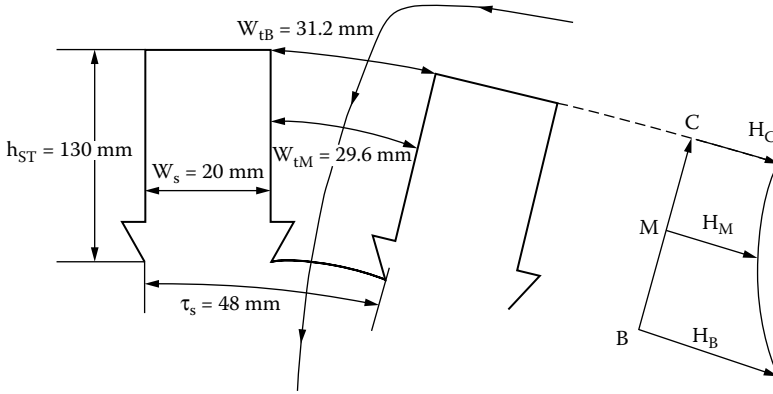
FIGURE 4.22 Stator slot geometry and the no-load magnetic field.

$$F_{AA'} = 2\left(H_{gFm1}gK_c + \frac{1}{6}\left(H_B + 4H_M + H_C\right)h_{st} + H_{YS}l_{YS} \right) \tag{4.81}$$

The airgap magnetic field H_{gFm1} is

$$H_{gFm1} = \frac{B_{gFm1}}{\mu_0} = \frac{0.85}{1.256 \times 10^{-6}} = 0.676 \times 10^6 \; A/m \tag{4.82}$$

The magnetic fields at the stator tooth top, middle, and bottom (H_B, H_M, H_C) are related to Figure 4.22, which shows that the stator tooth is trapezoidal, as the slot is rectangular.

The flux density in the three tooth cross-sections is

$$B_B = B_{gF_m} \cdot \frac{\tau_s}{\tau_s - W_s}; W_S = 0.02 \; m; \tau_S = \frac{\tau}{qm} = \frac{0.8635}{6 \cdot 3} = 0.048 \; m$$

$$B_M = B_B \cdot \frac{\tau - W_S}{W_{tm}}; W_{tm} = \frac{\pi\left(D_{is} + h_{st}\right)}{2pqm} - W_S$$

$$B_C = B_B \cdot \frac{\left(\tau_s - W_S\right)}{W_{tB}}; W_{tB} = \frac{\pi\left(D_{is} + 2h_{st}\right)}{2pqm} - W_S$$

Finally,

$$B_B = 0.85\frac{48}{48 \cdot 20} = 1.457 \; T$$

$$W_{tm} = \frac{\pi(3.85+0.130)}{14\times 6\times 3} - 0.02 = 0.0296 \ m$$

$$B_M = 1.457 \cdot \frac{48-20}{29.6} = 1.378 \ T$$

$$W_{tB} = \frac{\pi(3.85+2\times 0.130)}{14\times 6\times 3} - 0.02 = 0.0312 \ m$$

$$B_C = 1.457 \cdot \frac{(48-20)}{31.2} = 1.307 \ T$$

From the magnetization curve (Table 4.1) through linear interpolation, we obtain the following:

- H_B = 1090.6 A/m
- H_M = 698.84 A/m
- H_C = 501.46 A/m

The maximum flux density in stator yoke B_{ys} is

$$B_{ys} = \frac{\tau}{\pi} \cdot \frac{B_{gFm1}}{h_{ys}} = \frac{0.8635}{\pi} \cdot \frac{0.85}{0.24} = 0.974 \ T$$

From Table 4.1, H_{ys} = 208.82 A/m.

Now, the average length of the flux line in the stator yoke "reduced" to the peak yoke flux density B_{ys}, is approximately

$$l_{ys} \approx \frac{\pi(D_{is}+2h_{st}+h_{ys})}{4p} \cdot K_{ys}; 0.5 < K_{ys} < 1$$

The value of K_{ys} depends on the level of saturation and other variables. FEM digital simulations may be used to find the value of the "fudge" factor K_{ys}. A reasonable value would be $K_{ys} \approx 2/3$. So,

$$l_{ys} = \frac{\pi(3.85+2.013+0.24)}{4\times 7} \times \frac{2}{3} = 0.3252 \ m$$

We may now calculate $F_{AA'}$ from Equation 4.82:

$$F_{AA'} = 2\left(0.676\cdot 10^6 \times 2\cdot 10^{-2} + \frac{1}{6}(1090.6+4\times 698.84+501.46)\right)\cdot 0.130 +$$

$$+208.82\cdot 0.3252 = 27365.93 \ A \ turns$$

Now, the leakage flux Φ_{pl} in the rotor — between rotor poles (Figure 4.21) — is proportional to $F_{AA'}$.

Alternatively, Φ_{pl} may be considered as a fraction of pole flux Φ_p:

$$\Phi_p = \frac{2}{\pi} B_{gFm1} \cdot \tau \cdot l_{stack} = \frac{2}{\pi} 0.85 \cdot 0.8635 \times 0.39 = 0.649 \ Wb$$

$$\Phi_{pl} = K_{sl}\Phi_{pl}; K_{sl} \approx 0.15 - 0.25$$

$$\Phi_{pl} = 0.15 \cdot 0.649 = 0.09747 \ T$$

So, the total flux in the rotor pole Φ_{pr} is

$$\Phi_{pr} = \Phi_p + \Phi_{pl} = 0.649 + 0.09747 = 0.7465 \ Wb$$

The rotor pole shoe is not saturated in the no-load area despite the presence of rotor damper bars, but the pole body and rotor yoke may be saturated. The mmf required to magnetize the rotor F_{rotor} is

$$F_{rotor} = \left(F_{ABr} + F_{BrCr}\right) \times 2 = 2\left(H_{pr} \cdot h_{pr} + H_{yr} \cdot l_{yr}\right) \tag{4.83}$$

With the rotor pole body width $b_{pr} = 0.25$ m, the flux density in the pole body B_{pr} is

$$B_{pr} \approx \frac{\Phi_{pr}}{l_{stack} \cdot b_{pr}} = \frac{0.7465}{1.39 \times 0.25} = 2.148 \ T !!$$

This very large flux density level does not occur along the entire rotor height h_{pr}. At the top of the pole body, approximately, $\Phi_{pr} \approx \Phi_p = 0.649$ Wb.

So,

$$\left(B_{pr}\right)_{Ar} \approx \frac{\Phi_p}{l_{stack}b_{pr}} = \frac{0.649}{1.39 \times 0.25} = 1.8676 \ T !!$$

Consider an average:

$$B_{prav} = \frac{2.148 + 1.8676}{2} = 2T \ !! \ .$$

For this value, in Table 4.1, we can determine that $H_{pr} = 34{,}000$ A/m.

In the rotor yoke, B_{yr} is

$$B_{yr} = \frac{\Phi_{pr}}{2h_{yr} \cdot l_{stack}} = \frac{0.7465}{2 \times 0.25 \times 1.39} = 1.074 \ T !!$$

So, $H_{yr} = 257$ A/m.

The average length of field path in the rotor yoke l_{yr} is

$$l_{yr} \approx \frac{\pi \left(D_{is} - 2g - 2\left(h_{sh} + h_{rp} \right) - h_{yr} \right)}{4p_1} =$$

$$= \frac{\pi \left(3.85 - 2 \cdot 0.02 - 2\left(0.09 + 0.25 \right) - 0.25 \right)}{4 \cdot 7} = 0.32185 \ m$$

So, from Equation 4.83, F_{rotor} is

$$F_{rotor} = 2\left[34,000 \cdot \left(0.09 + 0.25 \right) + 257 \cdot 0.32185 \right] = 23285 \ A \ turns$$

Now, the total mmf per two neighboring poles (corresponding to a complete flux line) $2W_F I_F$ is

$$2 \times W_F I_F = F_{AA'} + F_{rotor} = 27,365 + 23,285 = 50,650 \ A \ turns$$

The airgap mmf requirements are as follows:

$$F_g = 2H_{gFm1} \cdot g = 2 \times 0.676 \times 10^6 + 2 \times 10^{-2} = 27,040 \ A \ turns$$

The contribution of the iron in the mmf requirement, defined as a saturation factor K_s, is

$$1 + K_S = \frac{2W_F I_F}{F_g} = \frac{50,650}{27,040} = 1.8731$$

So, $K_S = 0.8731$.

For the case in point, the main contribution is placed in the rotor pole. This is natural, as the pole body width b_{pr} must have room in which to place the field windings. So, in general, b_{pr} is around $\tau/3$, at most. The above example illustrates the computational procedure for one point of the no-load magnetization curve B_{gFm1} (I_F). Other points may be calculated in a similar way. A more precise solution, at the price of larger computation time, may be obtained through the multiple magnetic circuit method [4], but real precision results require FEM, as shown in Chapter 5.

4.9.2 The Short-Circuit Saturation Curve $I_1 = f(I_f)$; $V_1 = 0$, $n_1 = n_r = ct.$

The short-circuit saturation curve is obtained by driving the excited SG at rated speed n_r with short-circuited stator terminals (Figure 4.23a through Figure 4.23d). The field DC I_F is varied downward gradually, and both I_F and stator current I_{sc} are measured. In general, measurements for 100%, 75%, 50%, and 25% of rated current are necessary to reduce the winding temperature during that test. The results are plotted in Figure 4.23b.

From the voltage equation 4.54 with $V_1 = 0$ and $\underline{I}_1 = \underline{I}_{3sc}$, one obtains the following:

$$\underline{E}_1 \left(I_f \right) = R_1 \underline{I}_{3sc} + jX_d \underline{I}_{dsc} + jX_q \underline{I}_{qsc} \tag{4.84}$$

$$\underline{E}_1 \left(I_f \right) = -jX_F I_F$$

Neglecting stator resistance and observing that, with zero losses, $\underline{I}_{3sc} = \underline{I}_{dsc}$, as $\underline{I}_{qsc} = 0$ (zero torque), we obtain
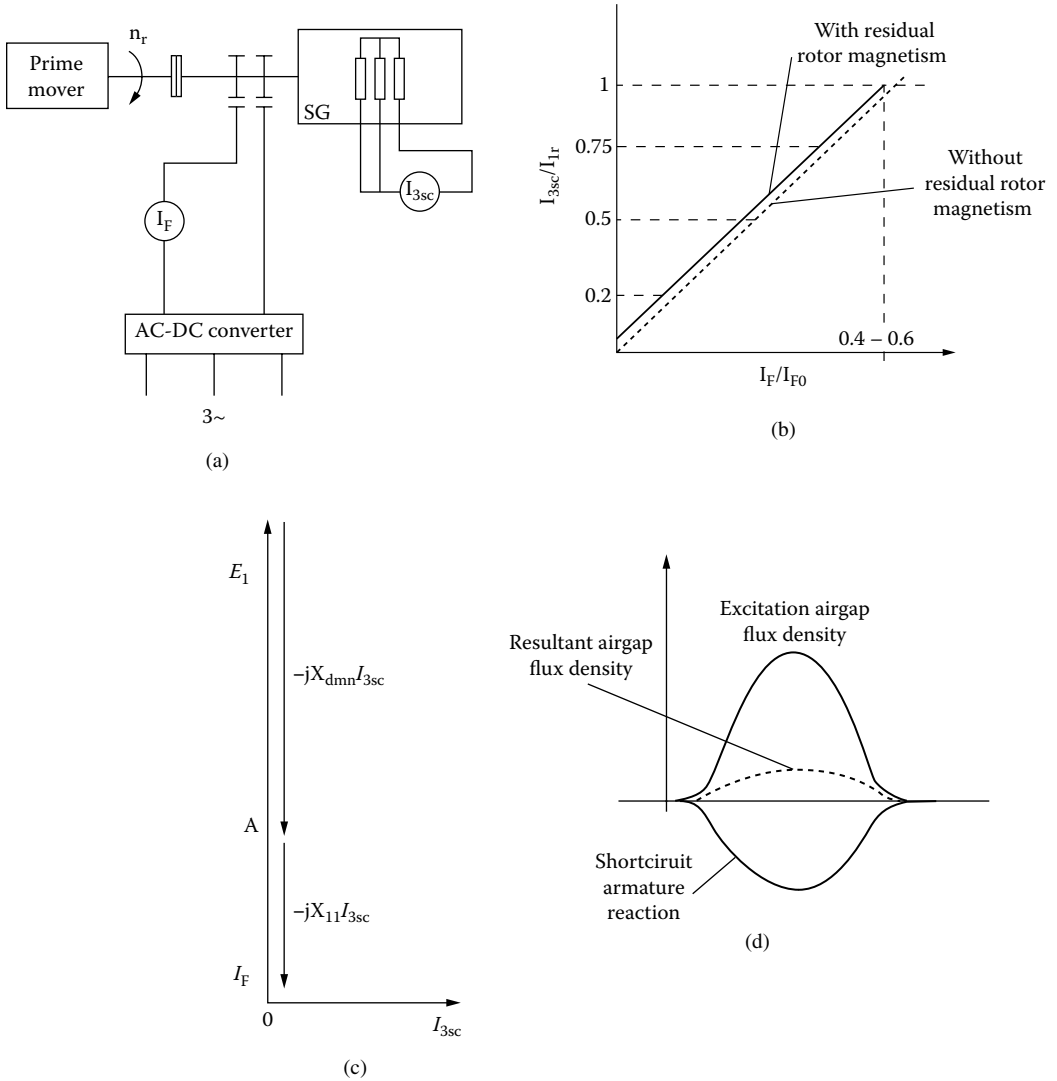
FIGURE 4.23 The short-circuit saturation curve: (a) experimental arrangement, (b) the characteristics, (c) phasor diagram with $R_1 = 0$, and (d) airgap flux density (slotting neglected).

$$\underline{E}_1\left(I_F\right) = j X_d I_{3sc} \tag{4.85}$$

The magnetic circuit is characterized by very low flux density (Figure 4.23d). This is so because the armature reaction strongly reduces the resultant emf E_{1res} to

$$\underline{E}_{1res} = -jX_{1l} \cdot \underline{I}_{3sc} = E_1 - jX_{dm}I_{3sc} \tag{4.86}$$

which represents a low value on the no-load saturation curve, corresponding to an equivalent small field current (Figure 4.24):

$$I_{F0} = I_F - I_{3sc} \cdot \frac{X_{dm}}{X_{FA}} = OA - AC \tag{4.87}$$
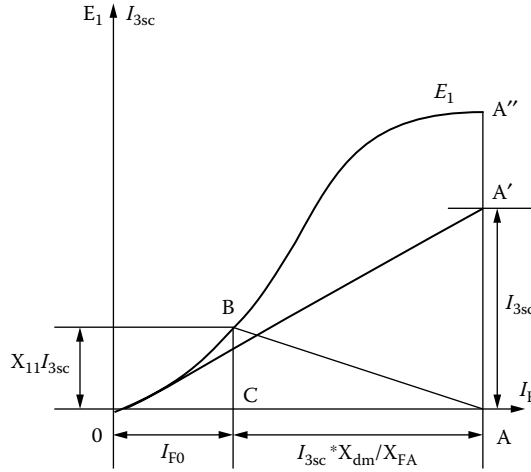
FIGURE 4.24 The short-circuit triangle.

Adding the no-load saturation curve, the short-circuit triangle may be portrayed (Figure 4.24). Its sides are all quasi-proportional to the short-circuit current.

By making use of the no-load and short-circuit saturation curves, saturated values of d axis synchronous reactance may be obtained:

$$X_{ds} = \frac{E_1(I_F)}{I_{3sc}(I_F)} = \frac{\overline{AA''}}{\overline{AA'}} \tag{4.88}$$

Under load, the magnetization state differs from that of the no-load situation, and the value of X_{ds} from Equation 4.88 is of limited practical utilization.

4.9.3 Zero-Power Factor Saturation Curve $V_1(I_F)$; I_1 = ct., $\cos\varphi_1$ = 0, n_1 = n_r

Under zero power factor and zero losses, the voltage Equation 4.54 becomes

$$V_1 = E_1 - jX_d \underline{I}_d; \underline{I}_1 = \underline{I}_d; \underline{I}_q = 0 \tag{4.89}$$

Again, for pure reactive load and zero losses, the electromagnetic torque is zero; and so is I_q.

An underexcited synchronous machine acting as a motor on no load is generally used to represent the reactive load for the SG under zero power factor operation with constant stator current I_d.

The field current of the SG is reduced simultaneously with the increase in field current of the underexcited no-load synchronous motors (SM), to keep the stator current I_d constant (at rated value), while the terminal voltage decreases. In this way, $V_1(I_F)$ for constant I_d is obtained (Figure 4.25a and Figure 4.25b).

The abscissa of the short-circuit triangle OCA is moved at the level of rated voltage, then a parallel 0B′ to 0B is drawn that intersects the no-load curve at B′. The vertical segment 0B′ is defined as follows:

$$X_p I_1 = \overline{B'C} \tag{4.90}$$

Though we started with the short-circuit triangle in our geometrical construction, BC < B′C because magnetic saturation conditions are different. So, in fact, $X_p > X_{1l}$, in general, especially in salient pole rotor SGs.
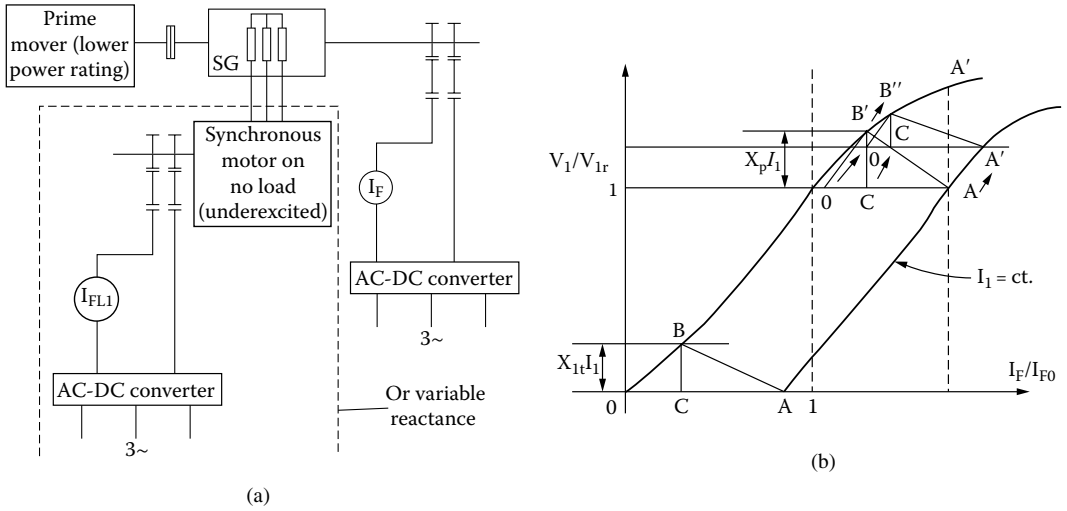
FIGURE 4.25 The zero-power factor saturation curve: (a) the experimental arrangement and (b) the "extraction" of Potier reactance X_p.

The main practical purpose of the zero-power factor saturation curve today would be to determine the leakage reactance and to conduct temperature tests. One way to reduce the value of X_p and thus fall closer to X_{1l} is to raise the terminal voltage above the rated one in the $V_1(I_F)$ curve, thus obtaining the triangle ACB″ with CB″ $\approx X_{1l}I_1$. It is claimed, however, that 115 to 120% voltage is required, which might not be allowed by some manufacturers. Alternative methods for measuring the stator leakage reactance X_{1l} are to be presented in the chapter on the testing of SGs. Zero-power factor load testing may be used for temperature on load estimation without requiring active power full load.

4.9.4 $V_1 - I_1$ Characteristic, I_F = ct., $\cos\varphi_1$ = ct., $n_1 = n_r$ = ct.

The $V_1 - I_1$ characteristic refers to terminal voltage vs. load current I_1, for balanced load at constant field current, load power factor, and speed.

To obtain the $V_1 - I_1$ curve, full real load is necessary, so that it is feasible only on small and medium power autonomous SGs at the manufacturer's site, or the testing may be performed after the commissioning at the user's site.

The voltage equation, phasor diagram, and the no-load saturation curve should provide information so that, with magnetic saturation coarsely accounted for, $V_1(I_1)$ can be calculated for given load impedance per phase $Z_L(Z_L, \varphi_1)$ (Figure 4.26a through Figure 4.26c):

$$\underline{I}_1 R_1 + \underline{Z}_L \underline{I}_1 = \underline{E}_1 - jX_d I_d - jX_q I_q$$

$$\underline{I}_d \left(R_1 + R_L\right) + \underline{I}_q \left(R_1 + R_L\right) + j\left(X_d + X_L\right)I_d + j\left(X_q + X_L\right)I_q = \underline{E}_1 \qquad (4.91)$$

$$\cos\varphi_1 = \frac{R_s}{Z_s}$$

As Figure 4.26b suggests, Equation 4.91 may be divided into two equations:

$$E_1 = I_q\left(R_1 + R_L\right) + \left(X_d + X_L\right)\left(I_d\right); I_d \lessgtr 0$$

$$0 = \left(R_1 + R_L\right)\left(-I_d\right) - \left(X_q + X_L\right)I_q; I_q > 0 \qquad (4.92)$$
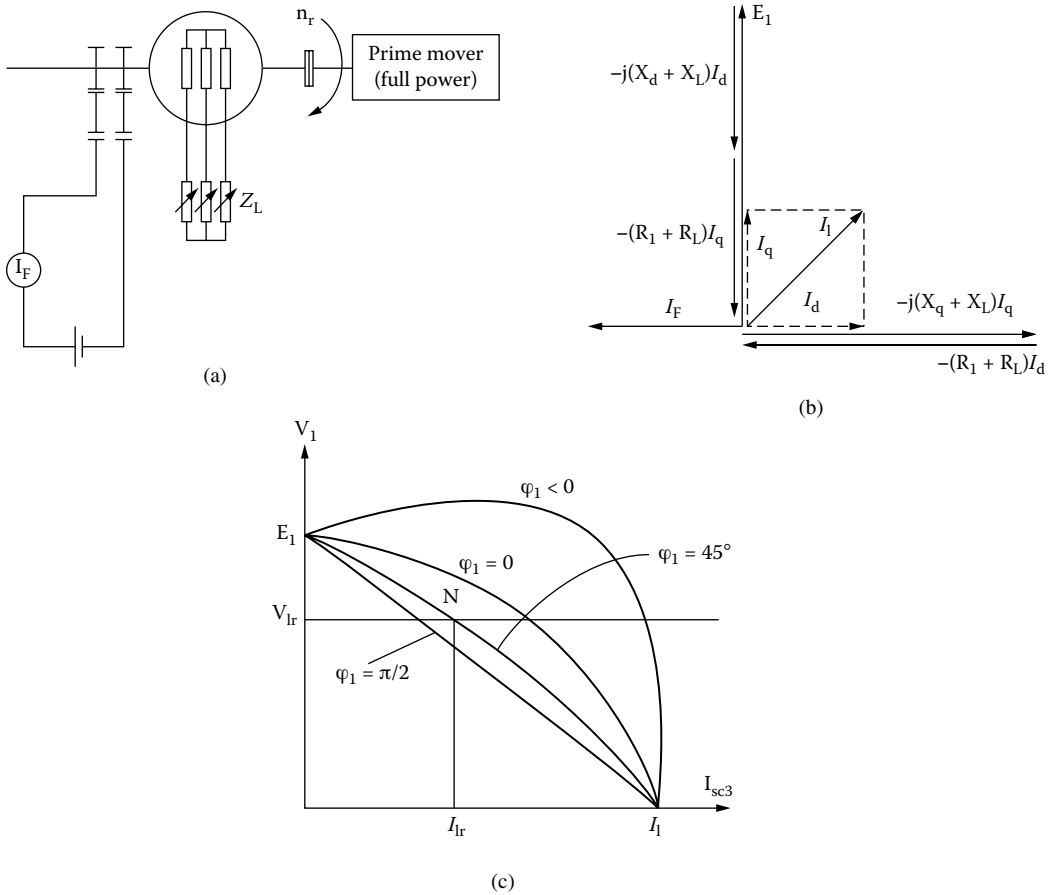
FIGURE 4.26 $V_1 - I_1$ curve: (a) the experimental arrangement, (b) the phasor diagram for load $\underline{Z}_L$, and (c) the curves.

with I_F given, E_1 is extracted from the no-load saturation curve. Then, with $\cos \varphi_1$ given, we may choose to modify R_L (load resistance) only as X_L is

$$X_L = R_L \tan \varphi_1 \tag{4.93}$$

Then, Equation 4.92 can be simply solved to calculate I_d and I_q. The phase current I_1 is

$$I_1 = \sqrt{I_d^2 + I_q^2} \tag{4.94}$$

Finally, the corresponding terminal voltage V_1 is

$$V_1 = \frac{R_L}{\cos \varphi_1} \cdot I_1 \tag{4.95}$$

Typical $V_1(I_1)$ curves are shown in Figure 4.26c. The voltage decreases with load (I_1) for resistive ($\varphi_1 = 0$) and resistive-inductive ($\varphi_1 > 0$) load, and it increases and then decreases for resistive-capacitive load ($\varphi_1 < 0$). Such characteristics may be used to calculate the voltage regulation ΔV_1:

$$\left(\Delta V_1\right)_{I_1/\cos\varphi_1/I_F} = \frac{E_1 - V_1}{E_1} = \frac{no\_load\_voltage - load\_voltage}{no\_load\_voltage} \tag{4.96}$$

Autonomous SGs are designed to provide operation at rated load current and rated voltage and a minimum (lagging) power factor $\cos\varphi_{1min} = 0.6\text{–}0.8$ (point N on Figure 4.26c). It should be evident that I_{1r} should be notably smaller than I_{3sc}.

Consequently,

$$\frac{X_{dsat}}{Z_n} = x_{dsat} < 1; Z_n = \frac{V_N}{I_N} \tag{4.97}$$

The airgap in SGs for autonomous operation has to be large to secure such a condition. Consequently, notable field current mmf is required. Thus, the power loss in the field winding increases. This is one reason to consider permanent magnet rotor SGs for autonomous operation for low to medium power units, even though full-power electronics are needed.

Note that for calculations with errors (below 1 to 2%) when using Equation 4.92, careful consideration of the magnetic saturation level that depends simultaneously on I_F, I_d, I_q must be considered. This subject will be treated in more detail in Chapter 5.

4.10 Synchronous Generator Operation at Power Grid (in Parallel)

SGs in parallel constitute the basis of a regional, national, or continental electric power system (grid). SGs have to be connected to the power grid one by one.

For the time being, we will suppose that the power grid is of infinite power, that is, of fixed voltage, frequency, and phase. In order to connect the SGs to the power grid without large current and power transients, the amplitude, frequency, sequence, and phase of the SG no-load voltages have to coincide with the same parameters of the power grid. As the power switch does not react instantaneously, some transients will always occur. However, they have to be limited. Automatic synchronization of the SG to the power grid is today performed through coordinated speed (frequency and phase) and field current control (Figure 4.27).
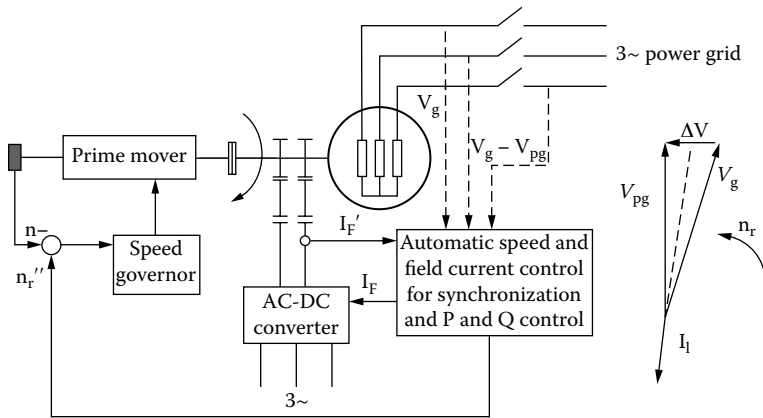
FIGURE 4.27 Synchronous generator connection to the power grid.
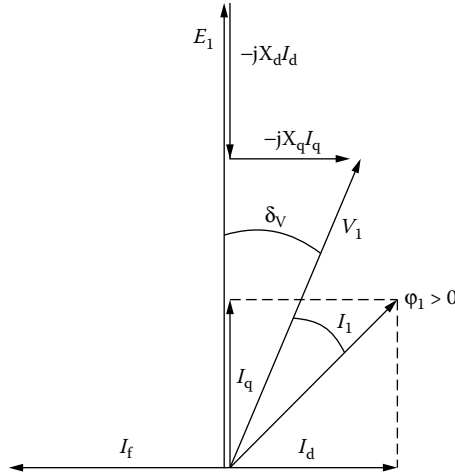
FIGURE 4.28 Synchronous generator phasor diagram (zero losses).

The active power transients during connection to the power grid may be positive (generating) or negative (motoring) (Figure 4.27).

4.10.1 The Power/Angle Characteristic: P_e (δ_V)

The power (internal) angle δ_V is the angle between the terminal voltage V_1 and the field-current-produced emf E_1. This angle may be calculated for the autonomous and for the power-grid-connected generator. Traditionally, the power/angle characteristic is calculated and widely used for power-grid-connected generators, mainly because of stability computation opportunities. For a large power grid, the voltage phasors in the phasor diagram are fixed in amplitude and phase. For clarity, we neglect the losses in the SG. We repeat here the phasor diagram in Figure 4.17a but with $R_1 = 0$ (Figure 4.28).

The active and reactive powers P_1, Q_1 from Equation 4.60 and Equation 4.61 with $R_1 = 0$ become

$$P_1 = 3E_1 I_q + 3(X_{dm} - X_q)I_d I_q \tag{4.98}$$

$$Q_1 = -3E_1 I_d - 3X_d I_d^2 - 3X_q I_q^2 \tag{4.99}$$

From Figure 4.28,

$$I_d = \frac{V_1 \cos \delta_V - E_1}{X_d}; I_q = \frac{V_1 \sin \delta_V}{X_q} \tag{4.100}$$

With Equation 4.100, Equation 4.98 and Equation 4.99 become the following:

$$P_1 = \frac{3E_1 V_1 \sin \delta_V}{X_d} + \frac{3}{2} V_1^2 \left(\frac{1}{X_q} - \frac{1}{X_d} \right) \sin 2\delta_V \tag{4.101}$$

$$Q_1 = \frac{3E_1 V_1 \cos \delta_V}{X_d} - 3V_1^2 \left(\frac{\cos^2 \delta_V}{X_d} + \frac{\sin^2 \delta_V}{X_q} \right)$$

(a)   (b)
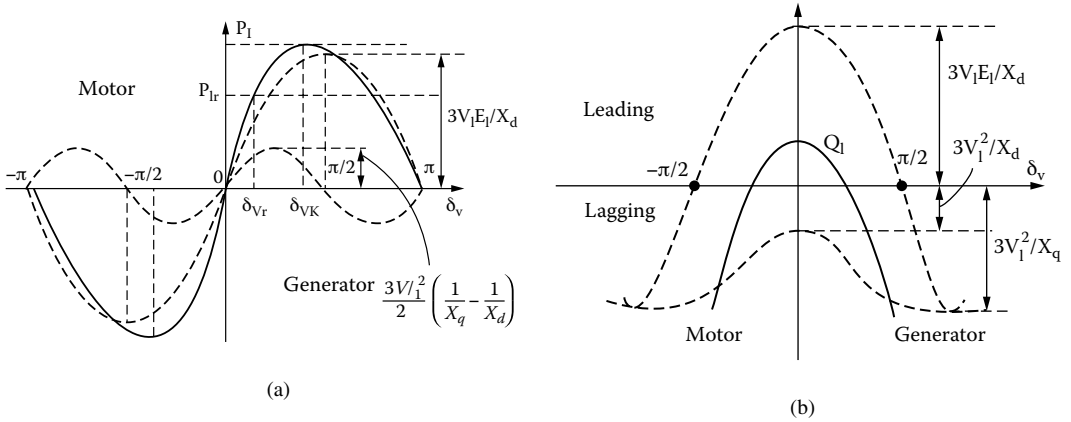
FIGURE 4.29   (a) Active P_1 and (b) reactive Q_1 powers vs. power angle δ_V.

The unity power factor is obtained with $Q_1 = 0$, that is,

$$(E_1)_{Q_1=0} = V_1\left(\cos\delta_V + \frac{X_d}{X_q} \frac{\sin^2\delta_V}{\cos\delta_V} \right) \tag{4.102}$$

For the same power angle δ_V and V_1, E_1 should be larger for the salient pole rotor SG, as $X_d > X_q$. The active power has two components: one due to the interaction of stator and rotor fields, and the second one due to the rotor magnetic saliency ($X_d > X_q$).

As in standard salient pole rotor SGs, $X_d/X_q < 1.7$, the second term in P_e, called here saliency active power, is relatively small unless the SG is severely underexcited: $E_1 \ll V_1$. For given E_1, V_1, the SG reactive and active power delivery depend on the power (internal) angle δ_V (Figure 4.29a and Figure 4.29b).

The graphs in Figure 4.29a and Figure 4.29b warrant the following remarks:

- The generating and motoring modes are characterized (for zero losses) by positive and, respectively, negative power angles.
- As δ_V increases up to the critical value δ_{VK}, which corresponds to maximum active power delivery P_{1K}, the reactive power goes from leading to lagging for given emf E_1, V_1 frequency (speed) ω_1.
- The reactive power is independent of the sign of the power angle δ_V.
- In salient pole rotor SGs, the maximum power P_{1K} for given V_1, E_1 and speed, is obtained for a power angle $\delta_{VK} < 90°$, while for nonsalient pole rotor SGs, $X_d = (1 - 1.05)X_q$, $\delta_{VK} \approx 90°$.
- The rated power angle δ_{Vr} is chosen around 22 to 30° for nonsalient pole rotor SGs and around 30 to 40° for salient pole rotor SGs. The lower speed, higher relative inertia, and stronger damper cage of the latter might secure better stability, which justifies the lower power reserve (or ratio P_{1K}/P_{1r}).

4.10.2   The V-Shaped Curves: $I_1(I_F)$, P_1 = ct., V_1 = ct., n = ct.

The V-shaped curves represent a family of $I_1(I_F)$ curves, drawn at constant V_1, speed (ω_1), with active power P_1 as a parameter. The computation of a V-shaped curve is straightforward once $E_1(I_F)$ — the no-load saturation curve — and X_d and X_q are known. Unfortunately, when I_F varies from low to large values, so does I_1 (that is, I_d, I_q); magnetic saturation varies, despite the fact that, basically, the total flux linkage $\Psi_s \approx V_1/\omega_1$ remains constant. This is due to rotor magnetic saliency ($X_d \neq X_q$), where local saturation conditions vary notably. However, to a first approximation, for constant V_1 and ω_1 (that is
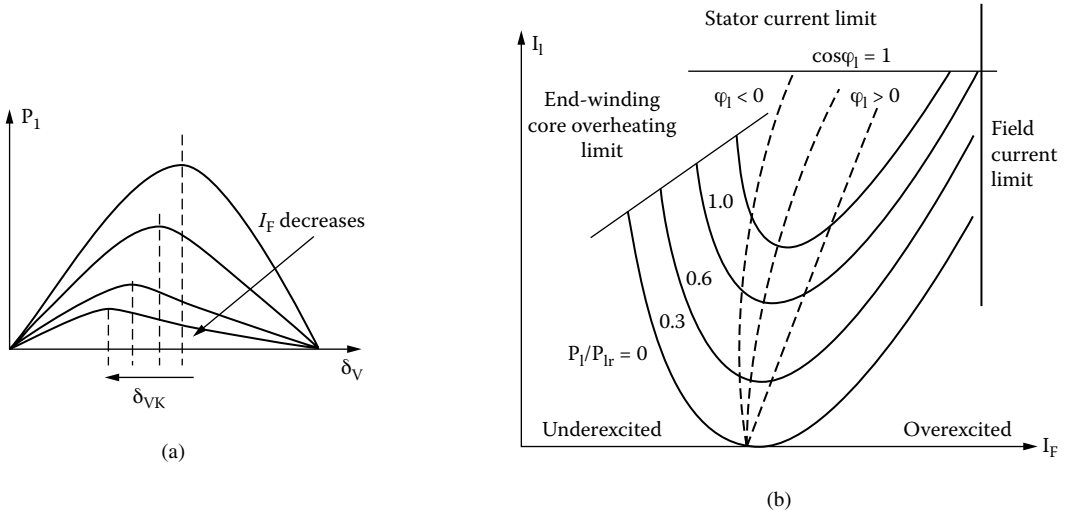
FIGURE 4.30 V-shaped curves: (a) P_1/δ_V assisting curves with I_F as parameter and (b) the $I_1(I_F)$ curves for constant P_1.

Ψ_1), with E_1 calculated at a first fixed total flux, the value of M_{FA} stays constant, and thus, $E_1 \approx M_{FA} \cdot I_F$

$\cdot \omega_r \approx C_{FA} \cdot I_F$; $C_{FA} \approx \dfrac{V_{1r}}{I_{F0}}$. I_{F0} is the field current value that produces $E_1 = V_{1r}$ at no load.

For given I_F, $E_1 = C_{FA} \times I_F$ and P_1 assigned a value from (4.101), we may compute δ_V. Then, from Equation 4.103, the corresponding stator current I_1 can be found:

$$I_1 = \sqrt{I_d^2 + I_q^2} = \sqrt{\left(\frac{-E_1 + V_1 \cos\delta_V}{X_d}\right)^2 + \left(\frac{V_1 \sin\delta_V}{X_q}\right)^2} \qquad (4.103)$$

As expected, for given active delivered power, the minimum value of stator current is obtained for a field current I_F corresponding to unity power factor ($Q_1 = 0$). That is, $(E_1)I_{1min} = (E_1)_{Q1=0}$ may be determined from Equation 4.103 with δ_V already known from Equation 4.101. Then, $I_{fK} = E_1/C_{FA}$. The maximum power angle admitted for a given power P_1 limits the lowest field current admissible for steady state.

Finally, graphs as shown in Figure 4.30a and Figure 4.30b are obtained.

Knowing the field current lower limit, for given active power, is paramount in avoiding an increase in the power angle above δ_{VK}. In fact, δ_{VK} decreases with an increase in P_1.

4.10.3 The Reactive Power Capability Curves

The maximum limitation of I_F is due to thermal reasons. However, the SG heating depends on both I_1 and I_F, as both winding losses are very important. Also, I_1, I_F, and δ_V determine the core losses in the machine at a given speed.

When a reactive power request is increased, the increase in I_F raises the field-winding losses and thus the stator-winding losses (the active power P_1) have to be limited.

The rationale for V-shaped curves may be continued to find the reactive power Q_1 for the given P_1 and I_F. As shown in Figure 4.30, there are three distinct thermal limits: I_F limit (vertical), I_1 limit (horizontal), and the end-winding overheating (inclined) limit at low values of field current. To explain this latest, rather obscure, limitation, refer to Figure 4.31.
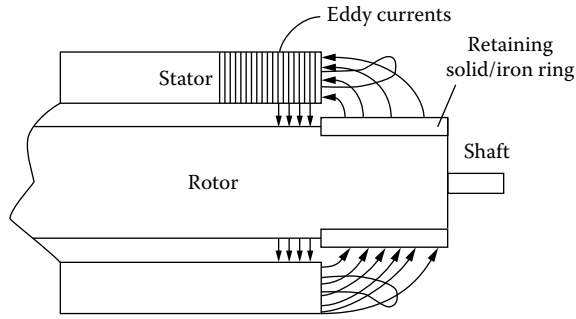
FIGURE 4.31 End-region field path for the underexcited synchronous generator.

For the underexcited SG, the field-current- and armature-current-produced fields have angles smaller than 90° (the angle between I_F and I_1 in the phasor diagram). Consequently, their end-winding fields more or less add to each other. This resultant end-region field enters at 90° the end-region stator laminations and produces severe eddy current losses that thermally limit the SG reactive power absorption ($Q_1 < 0$). This phenomenon is so strong because the retaining ring solid iron eddy currents (produced solely by the stator end-windings currents) are small and thus incapable of attenuating severely the end-region resultant field. This is because the solid iron retaining ring is not saturated magnetically, as the field current is small. When the SG is overexcited, this phenomenon is not important, because the stator and rotor fields are opposite (I_F and I_1 phase-angle shift is above 90°) and the retaining magnetic ring is saturated by the large field current. Consequently, the stator end-windings-current-produced field in the stator penetrates deeply into the retaining rings, producing large eddy currents that further attenuate this resultant field in the end-region zone (the known short-circuit transformer effect on inductance). The $Q_1(P_1)$ curves are shown in Figure 4.32.
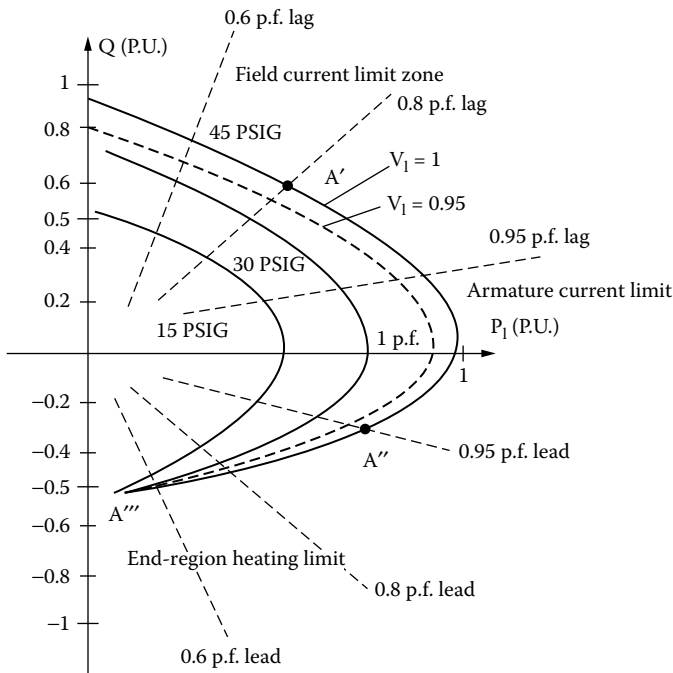
FIGURE 4.32 Reactive power capability curves for a hydrogen-cooled synchronous generator.

The reduction of hydrogen pressure leads to a reduction of reactive and active power capability of the machine.

As expected, the machine reactive power absorption capability ($Q_1 < 0$) is notably smaller than reactive power capability. Both the end-region lamination loss limitation and the rise of the power angle closer to its maximum limitation, seem to be responsible for such asymmetric behavior (Figure 4.32).

4.10.4 Defining Static and Dynamic Stability of Synchronous Generators

The fact that SGs require constant speed to deliver electric power at constant frequency introduces special restrictions and precautionary measures to preserve SG stability, when tied to an electric power system (grid). The problem of stability is complex. To preserve and extend it, active speed and voltage (active and reactive power) closed-loop controls are provided. We will deal in some detail with stability and control in Chapter 6. Here, we introduce the problem in a more phenomenological manner. Two main concepts are standard in defining stability: static stability and dynamic stability.

The static stability is the property of an SG to remain in synchronism to the power grid in the presence of slow variations in the shaft power (output active power, when losses are neglected). According to the rising side of the $P_1(\delta_V)$ curve (Figure 4.28), when the mechanical (shaft) power increases, so does the power angle δ_V, as the rotor slowly advances the phase of E_1, with the phase of $\underline{V}_1$ fixed. When δ_V increases, the active power delivered electrically, by the SG, increases.

In this way, the energy balance is kept, and no important energy increment is accumulated in the inertia of the SG. The speed remains constant, but when P_1 increases, so does δ_V. The SG is statically stable if $\partial P_1/\partial \delta_V > 0$.

We denote by P_{1s} this power derivative with angle and call it synchronization power:

$$P_{1S} = \frac{\partial P_1}{\partial \delta_V} = 3E_1 V_1 \cos\delta_V - 3V_1^2 \left(\frac{1}{X_d} - \frac{1}{X_q} \right) \cos 2\delta_V \tag{4.104}$$

P_{1s} is maximum at $\delta_V = 0$ and decreases to zero when δ_V increases toward δ_{VK}, where $P_{1S} = 0$.

At the extent that the field current decreases, so does δ_{VK}, and thus, the static stability region diminishes. In reality, the SG is allowed to operate at values of δ_V, notably below δ_{VK}, to preserve dynamic stability.

The dynamic stability is the property of the SG to remain in synchronism (with the power grid) in the presence of quick variations of shaft power or of electric load short-circuit. As the combined inertia of SGs and their prime movers is relatively large, the speed and power angle transients are much slower than electrical (current and voltage) transients. So, for example, we can still consider the SG under electromagnetic steady state when the shaft power (water admission in a hydraulic turbine) varies to produce slow-speed and power-angle transients. The electromagnetic torque T_e is thus, approximately,

$$T_e \approx \frac{P_1 \cdot p_1}{\omega_r} = \frac{3p_1}{\omega_r} \left[\frac{E_1 V_1 \sin\delta_V}{X_d} + \frac{V_1^2}{2} \left(\frac{1}{X_q} - \frac{1}{X_d} \right) \sin 2\delta_V \right] \tag{4.105}$$

Consider a step variation of shaft power from P_{sh1} to P_{sh2} (Figure 4.33a and Figure 4.33b) in a lossless SG.

The SG power angle should vary slowly from δ_{V1} to δ_{V2}. In reality, the power angle δ_V will overshoot δ_{V2} and, after a few attenuated oscillations, will settle at δ_{V2} if the machine remains in synchronism.

Neglect the rotor damper cage effects that occur during transients. The motion equation is then written as follows:

$$\frac{J}{p_1} \frac{d\omega_r}{dt} = T_{shaft} - T_e; \omega_r - \omega_{r0} = \frac{d\delta_V}{dt} \tag{4.106}$$

with ω_{r0} equal to the synchronous speed.
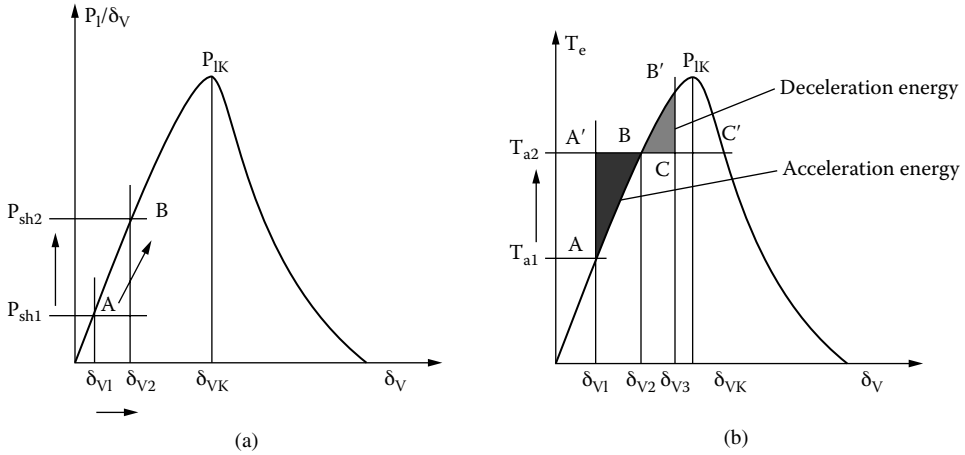
FIGURE 4.33 Dynamic stability: (a) $P_1(\delta_V)$ and (b) the area criterion.

By multiplying Equation 4.106 by $d\delta_V/dt$, one obtains

$$d\left(\frac{J}{2p_1}\left(\frac{d\delta_V}{dt}\right)^2\right) = \left(T_{shaft} - T_e\right)d\delta_V = \Delta T \cdot d\delta_V = dW \qquad (4.107)$$

Equation 4.107 illustrates the variation of kinetic energy of the prime-mover generator set translated in an acceleration area AA′B and a deceleration area BB′C:

$$W_{AB} = area\_of\_AA'B\_triangle = \int_{\delta_{V_1}}^{\delta_{V_2}} \left(T_{shaft} - T_e\right)d\delta_V \qquad (4.108)$$

$$W_{AB'} = area\_of\_BB'C\_triangle = \int_{\delta_{V_2}}^{\delta_{V_3}} \left(T_{shaft} - T_e\right)d\delta_V \qquad (4.109)$$

Only when the two areas are equal to each other is there hope that the SG will come back from B′ to B after a few attenuated oscillations. Attenuation comes from the asynchronous torque of damper cage currents, neglected so far. This is the so-called criterion of areas.

The maximum shaft torque or electric power step variation that can be accepted with the machine still in synchronism is shown in Figure 4.34a and Figure 4.34b and corresponds to the case when point C coincides with C′.

Let us illustrate the dynamic stability with the situation in which there is a loaded SG at power angle δ_{V1}. A three-phase short-circuit occurs at δ_{V1}, with its transients attenuated very quickly such that the electromagnetic torque is zero ($V_1 = 0$, zero losses also). So, the SG starts accelerating until the short-circuit is cleared at δ_{Vsc}, which corresponds to a few tens of a second at most. Then, the electromagnetic torque T_e becomes larger than the shaft torque, and the SG decelerates. Only if

$$Area\_of\_\overline{ABCD} \geq Area\_of\_CB'B'' \qquad (4.110)$$

are there chances for the SG to remain in synchronism, that is, to be dynamically stable.
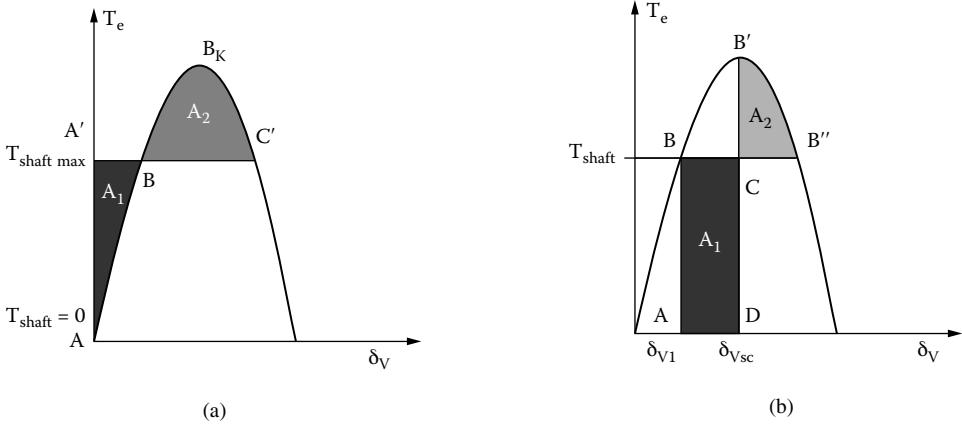
FIGURE 4.34 Dynamic stability ideal limits: (a) maximum shaft torque step variation from zero and (b) maximum short-circuit clearing time (angle: $\delta_{Vsc} - \delta_{V1}$) from load.

4.11   Unbalanced-Load Steady-State Operation

SGs connected to the power grid, but especially those in autonomous applications, often operate on unbalanced three-phase loads. That is, the stator currents in the three phases have different amplitudes, and their phasing differs from 120°:

$$
\begin{aligned}
I_A(t) &= I_1 \cos\left(\omega_1 t - \gamma_1\right) \\[2mm]
I_B(t) &= I_2 \cos\left(\omega_1 t - \frac{2\pi}{3} - \gamma_2\right) \\[2mm]
I_C(t) &= I_3 \cos\left(\omega_1 t + \frac{2\pi}{3} - \gamma_3\right)
\end{aligned}
\tag{4.111}
$$

For balanced load, $I_1 = I_2 = I_3$ and $\gamma_1 = \gamma_2 = \gamma_3$. These phase currents may be decomposed in direct, inverse, and homopolar sets according to Fortesque's transform (Figure 4.35).

$$
\begin{aligned}
\underline{I}_{A+} &= \frac{1}{3}\left(\underline{I}_A + a\underline{I}_B + a^2\underline{I}_C\right); a = e^{j\frac{2\pi}{3}} \\[2mm]
\underline{I}_{A-} &= \frac{1}{3}\left(\underline{I}_A + a^2\underline{I}_B + a\underline{I}_C\right); a^2 = e^{-j\frac{2\pi}{3}} \\[2mm]
\underline{I}_{A0} &= \frac{1}{3}\left(\underline{I}_A + \underline{I}_B + \underline{I}_C\right) \\[2mm]
\underline{I}_{B+} &= a^2\,\underline{I}_{A1}; \\[2mm]
\underline{I}_{C+} &= a\underline{I}_{A1}; \\[2mm]
\underline{I}_{B-} &= a\underline{I}_A; \\[2mm]
\underline{I}_{C-} &= a^2\,\underline{I}_A
\end{aligned}
\tag{4.112}
$$
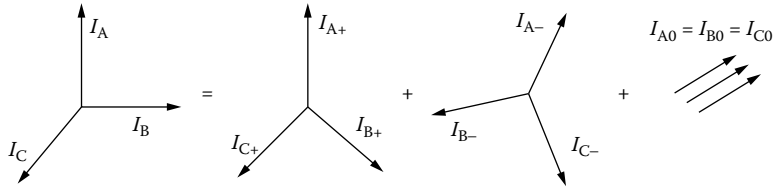
FIGURE 4.35 The symmetrical component sets.

Unfortunately, the superposition of the flux linkages of the current sets is admissible only in the absence of magnetic saturation. Suppose that the SG is nonsaturated and lossless ($R_1 = 0$). For the direct components $\underline{I}_{A1}$, $\underline{I}_{B1}$, $\underline{I}_{C1}$, which produce a forward-traveling mmf at rotor speed, the theory unfolded so far still holds. So, we will write the voltage equation for phase A and direct component of current $\underline{I}_{A1}$:

$$\underline{V}_{A+} = \underline{E}_{A+} - jX_d\,\underline{I}_{dA+} - jX_q\,\underline{I}_{qA+} \tag{4.113}$$

The inverse (negative) components of stator currents $\underline{I}_A^-$, $\underline{I}_B^-$, and $\underline{I}_C^-$ produce an mmf that travels at opposite rotor speed $^-\omega_r$.

The relative angular speed of the inverse mmf with respect to rotor speed is thus $2\omega_r$. Consequently, voltages and currents are induced in the rotor damper windings and in the field winding at $2\omega_r$ frequency, in general. The behavior is similar to an induction machine at slip $S = 2$, but which has nonsymmetrical windings on the rotor and nonuniform airgap. We may approximate the SG behavior with respect to the inverse component as follows:

$$\underline{I}_A \cdot \underline{Z}_- + \underline{U}_{A-} = \underline{E}_{A-}$$
$$Z_- = R_- + jX_- \tag{4.114}$$

Unless the stator windings are not symmetric or some of the field coils have short-circuited turns $\underline{E}_{A-} = 0$. $\underline{Z}_-$ is the inverse impedance of the machine and represents a kind of multiple winding rotor induction machine impedance at $2\omega_r$ frequency.

The homopolar components of currents produce mmfs in the three phases that are phase shifted spatially by 120° and have the same amplitude and time phasing. They produce a zero-traveling field in the airgap and thus do not interact with the rotor in terms of the fundamental component. The corresponding homopolar impedance is $Z_0 \approx R_1 + jX_0$, and

$$X_0 < X_{1l} \tag{4.115}$$

So,

$$X_d > X_q > X_- > X_{1l} > X_0 \tag{4.116}$$

The stator equation for the homopolar set is as follows:

$$j\underline{I}_{A0}X_0 + \underline{V}_{A0} = 0 \tag{4.117}$$

Finally,

$$\underline{V}_A = \underline{V}_{A+} + \underline{V}_{dA-} + \underline{V}_{A0} \tag{4.118}$$

Similar equations are valid for the other two phases. We assimilated here the homopolar with the stator leakage reactance ($X_{1l} \approx X_0$). The truth is that this assertion is not valid if chorded coils are used, when $X_0 < X_{1l}$. It seems that, due to the placement of stator winding in slots, the stator homopolar mmf has a steplike distribution with $\tau/3$ as half-period and does not rotate; it is an AC field. This third–space harmonic-like mmf may be decomposed in a forward and backward wave and move both with respect to rotor and induce eddy currents, at least in the damper cage. Additional losses occur in the rotor. As we are not prepared by now theoretically to calculate Z_- and X_0, we refer to some experiments to measure them so that we get some confidence in using the above theory of symmetrical components.

4.12   Measuring X_d, X_q, Z_-, Z_0

We will treat here some basic measurement procedures for SG reactances: X_d, X_q, Z^-, Z_0. For example, to measure X_d and X_q, the open-field-winding SG, supplied with symmetric forward voltages (ω_{r0}, frequency) through a variable-ratio transformer, is driven at speed ω_r, which is very close to but different from the stator frequency ω_{r0} (Figure 4.36a and Figure 4.36b):

$$\omega_r = \omega_{r0} \cdot \left(1.01 - 1.02\right) \tag{4.119}$$

We need not precisely measure this speed, but notice the slow pulsation in the stator current with frequency $\omega_r - \omega_{r0} \approx (0.01 - 0.02)\omega_{r0}$.

Identifying the maxima and minima in the stator voltage $V_A(t)$ and current $I_A(t)$ leads to approximate values of X_d and X_q:

$$X_d \approx \frac{V_{A\,\max}}{I_{A\,\min}}; X_q = \frac{V_{A\,\min}}{I_{A\,\max}} \tag{4.120}$$

The slip $S = (\omega_r - \omega_{r0})/\omega_{r0}$ has to be very small so that the currents induced in the rotor damper cage may be neglected. If they are not negligible, X_d and X_q are smaller than in reality due to the damper eddy current screening effect.

The saturation level will be medium if currents around or above the rated value are used.

Identifying the voltage and current maxima, even if the voltage and current are digitally acquired and are off-line processed in a computer, is doable with practical precision.

The inverse (negative) sequence impedance Z_- may be measured by driving the rotor, with the field winding short-circuited, at synchronous speed ω_r, while feeding the stator with a purely negative sequence of low-level voltages (Figure 4.37). The power analyzer is used to produce the following:

$$\left|\underline{Z}_-\right| = \frac{V_{A-}}{\underline{I}_{A-}}; R_- = \frac{\left(P_-\right)_{phase}}{I_{A-}^2} \tag{4.121}$$

$$X_- = \sqrt{\left|\underline{Z}_-\right| - \left(R_-\right)^2} \tag{4.122}$$

Again, the frequency of currents induced in the rotor damper and field windings is $2\omega_{r0} = 2\omega_1$, and the corresponding slip is $S = 2.0$. Alternatively, it is possible to AC supply the stator between two phases only:

$$\underline{Z}_- \approx \frac{U_{AB}}{2\underline{I}_A} \tag{4.123}$$
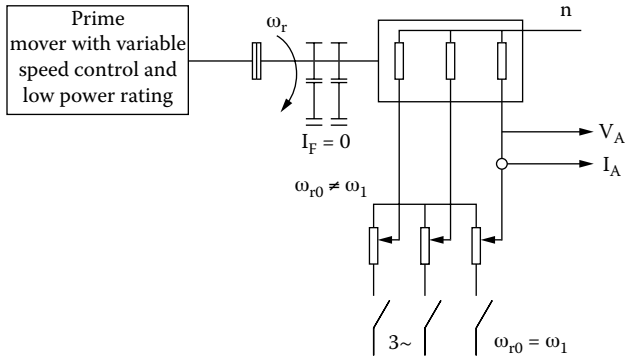
(a)
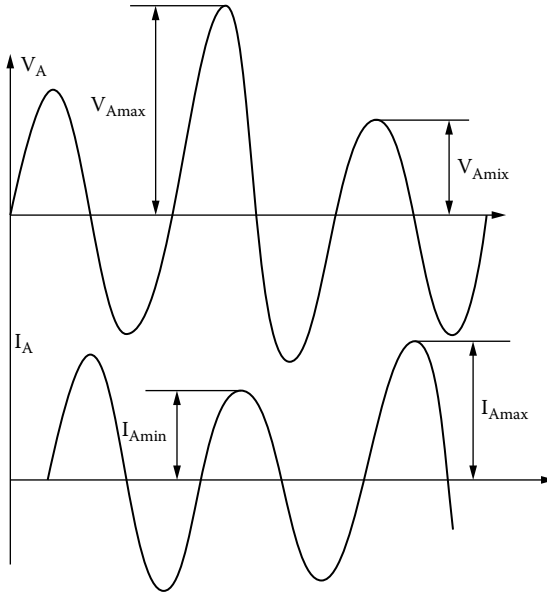
(b)

FIGURE 4.36 Measuring X_d and X_q: (a) the experimental arrangement and (b) the voltage and current waveforms.

This time the torque is zero and thus the SG stays at standstill, but the frequency of currents in the rotor is only $\omega_{r0} = \omega_1$. (The negative sequence impedance will be addressed in detail in Chapter 8 of *Synchronous Generators* on SG testing.) The homopolar impedance $\underline{Z}_0$ may be measured by supplying the stator phases connected in series from a single-phase AC source. The test may be made at zero speed or at rated speed ω_{r0} (Figure 4.38). For the rated speed test, the SG has to be driven at shaft. The power analyzer yields the following:

$$\left|\underline{Z}_0\right| = \frac{3V_{A0}}{3I_{A0}}; R_0 = \frac{P_0}{3I_{A0}^2}; X_0 = \sqrt{\left|\underline{Z}_0\right|^2 - R_0^2} \tag{4.124}$$

A good portion of R_0 is the stator resistance R_1 so $R_0 \approx R_1$.
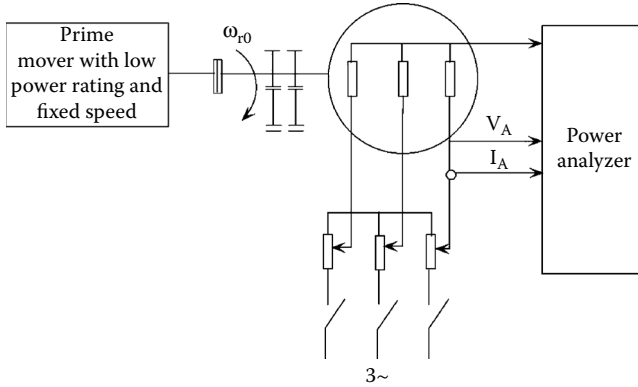
FIGURE 4.37 Negative sequence testing for $\underline{Z}_-$.
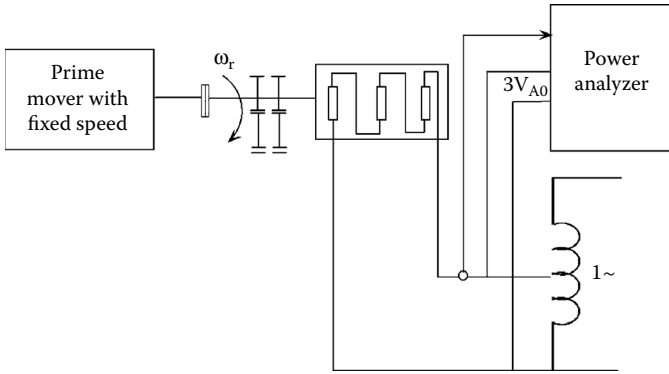
FIGURE 4.38 Measuring homopolar $\underline{Z}_0$.

The voltage in measurements for $\underline{Z}$ and $\underline{Z}_0$ should be made low to avoid high currents.

4.13 The Phase-to-Phase Short-Circuit

The three-phase (balanced) short-circuit was already investigated in a previous paragraph with the current I_{3sc}:

$$I_{3sc} = \frac{E_1}{X_d} \tag{4.125}$$

The phase-to-phase short-circuit is a severe case of unbalanced load. When a short-circuit between two phases occurs, with the third phase open, the currents are related to each other as follows (Figure 4.39a):

$$I_B = -I_C = I_{sc2}; V_B = V_C; I_A = 0 \tag{4.126}$$

From Equation 4.109, the symmetrical components of $\underline{I}_A$ are as follows:

$$\underline{I}_{A+} = \frac{1}{2}\left(a\underline{I}_B + a^2\,\underline{I}_C\right) = \frac{1}{3}\left(a - a^2\right)\underline{I}_{sc2} = \frac{+j}{\sqrt{3}}\underline{I}_{sc2}$$

$$\underline{I}_{A-} = -\underline{I}_{A+}; \underline{I}_{A0} = 0 \tag{4.127}$$
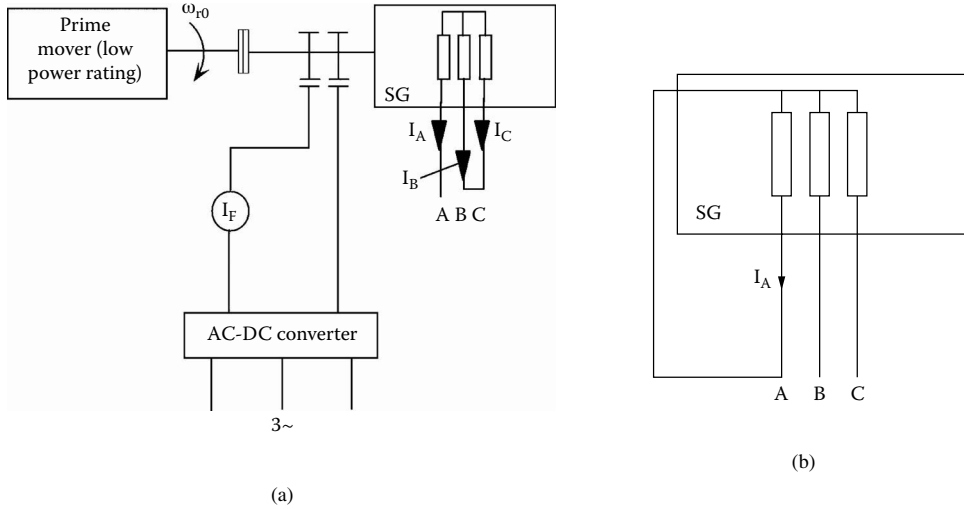
FIGURE 4.39 Unbalanced short-circuit: (a) phase-to-phase and (b) single-phase.

The star connection leads to the absence of zero-sequence current.

The terminal voltage of phase A, V_A, for a nonsalient pole machine ($X_d = X_q = X_+$) is obtained from Equation 4.115 with Equation 4.112 and Equation 4.113:

$$\underline{V}_A = \underline{V}_{A+} + \underline{V}_{A-} + \underline{V}_{A0} = \underline{E}_{A+} - jX_+ \cdot \underline{I}_{A+} - \underline{Z}_- \underline{I}_{A-} =$$

$$= \underline{E}_{A+} - \frac{j}{\sqrt{3}} I_{sc2}\left(jX_+ - Z_-\right) \tag{4.128}$$

In a similar way,

$$\underline{V}_B = a^2 \underline{V}_{A+} + a\underline{V}_{A-} = a^2 \underline{E}_{A+} - \frac{jI_{sc2}}{\sqrt{3}}\left(ja^2 X_+ - a\underline{Z}_-\right)$$

$$\underline{V}_C = a \underline{V}_{A+} + a^2 \underline{V}_{A-} = a\underline{E}_{A+} - \frac{jI_{sc2}}{\sqrt{3}}\left(ajX_+ - a^2 \underline{Z}_-\right) \tag{4.129}$$

But, $\underline{V}_B = \underline{V}_C$ and thus

$$E_{A+} = -\frac{jI_{sc2}}{\sqrt{3}}\left(jX_+ + \underline{Z}_-\right) \tag{4.130}$$

and

$$\underline{V}_A = \frac{2j}{\sqrt{3}} I_{sc2} \underline{Z}_- = -2\underline{V}_B \tag{4.131}$$

Finally,

$$jX_+ + \underline{Z}_- = -j\sqrt{3}\,\frac{E_{A+}(I_F)}{\underline{I}_{sc2}} \tag{4.132}$$

A few remarks are in order:

- Equation 4.132, with the known no-load magnetization curve, and the measured short-circuit current I_{sc2}, apparently allows for the computation of negative impedance if the positive one $jX_+ = jX_d$, for nonsalient pole rotor SG, is given. Unfortunately, the phase shift between $\underline{E}_{A1}$ and $\underline{I}_{sc2}$ is hard to measure. Thus, if we only:

$$Z_- = -jX_- \tag{4.133}$$

Equation 4.132 becomes usable as

$$X_+ + X_- = \frac{E_{A+} \cdot \sqrt{3}}{I_{sc2}} \tag{4.134}$$

RMS values enter Equation 4.134.
- Apparently, Equation 4.131 provides a good way to compute the negative impedance $\underline{Z}_-$ directly, with $\underline{V}_A$ and $\underline{I}_{sc2}$ measured. Their phase shift can be measured if the SG null point is used as common point for $\underline{V}_A$ and $\underline{I}_{2sc}$ measurements.
- During a short-circuit, even in phase to phase, the airgap magnetic flux density is small and distorted. So, it is not easy to verify (Equation 4.131), unless the voltage V_A and current I_{sc2} are first filtered to extract the fundamental.
- Only Equation 4.132 is directly usable to approximate X_-, with X_+ unsaturated known. As $X_+ \gg X_-$ for strong damper cage rotors, the precision of computing X_- from the sum $(X_+ + X_-)$ is not so good
- In a similar way, as above for the single-phase short-circuit (Figure 4.39b),

$$X_+ + X_- + X_0 \approx \frac{3E_{A+}(I_F)}{I_{sc1}} \tag{4.135}$$

with $X_+ > X_- > X_0$.
- To a first approximation,

$$I_{sc3} : I_{sc2} : I_{sc1} \approx 3 : \sqrt{3} : 1 \tag{4.136}$$

for an SG with a strong damper cage rotor.
- E_{A+} should be calculated for the real field current I_F, but, as during short-circuit the real distortion level is low, the unsaturated value of X_{FA} should be used: $E_{A+} = I_f(X_{FA})_{\text{unsaturated}}$.
- Small autonomous SGs may have the null available for single-phase loads; thus, the homopolar component shows up.
- The negative sequence currents in the stator produce double-frequency-induced currents in the rotor damper cage and in the field windings. If the field winding is supplied from a static power converter, the latter prevents the occurrence of AC currents in the field winding. Consequently, notable overvoltages may occur in the latter. They should be considered when designing the field-winding power electronics supply. Also, the double-frequency currents in the damper cage, produced by the negative component set, have to be limited, as they affect the rotor overtemperature. So, the ratio I_-/I_+, that is the level of current unbalance, is limited by standards below 10 to 12%.
- A similar phenomenon occurs in autonomous SGs, where the acceptable level of current unbalance I_-/I_f is given as a specification item and then considered in the thermal design. Finally, experiments are needed to make sure that the SG can really stand the predicted current unbalance.

- The phase-to-phase or single-phase short-circuits are extreme cases of unbalanced load. The symmetrical components method presented here can be used for actual load unbalance situations where the +, −, 0 current components sets may be calculated first. A numerical example follows.

Example 4.3

A three-phase lossless two-pole SG with S_n = 100 KVA, at V_{ll} = 440 V and f_1 = 50 Hz, has the following parameters: $x_+ = x_d = x_q = 0.6$ P.U., $x_- = 0.2$ P.U., $x_0 = 0.12$ P.U. and supplies a single-phase resistive load at rated current. Calculate the load resistance and the phase voltages V_A, V_B, V_C if the no-load voltage E_{ll} = 500 V.

Solution

We start with the computation of symmetrical current components sets (with $I_B = I_C = 0$):

$$I_{A+} = I_{A-} = I_{A0} = I_r/3$$

The rated current for star connection I_r is

$$I_r = \frac{S_n}{\sqrt{3}V_{1l}} = \frac{100000}{\sqrt{3} \cdot 440} \approx 131 \ A$$

The nominal impedance Z_n is

$$Z_n = \frac{U_{1l}}{\sqrt{3}I_r} = \frac{440}{\sqrt{3} \cdot 131} = 1.936 \ \Omega$$

So,

$$X_+ = Z_n x_+ = 1.936 \times 0.6 = 1.1616 \ \Omega$$

$$X_- = Z_n x_- = 1.936 \times 0.2 = 0.5872 \ \Omega$$

$$X_0 = Z_n x_0 = 1.936 \times 0.12 = 0.23232 \ \Omega$$

From Equation 4.112, the positive sequence voltage equation is as follows:

$$\underline{V}_{A+} = \underline{E}_{A+} - jX_+\underline{I}_r / 3$$

From Equation 4.113,

$$\underline{V}_{A-} = -jX_-\underline{I}_r / 3$$

Also, from Equation 4.116,

$$\underline{V}_{A0} = -jX_0\underline{I}_r / 3$$

The phase of voltage $\underline{V}_A$ is the summation of its components:

$$\underline{V}_A = \underline{E}_{A+} - j(X_+ + X_- + X_0)I_r / 3$$
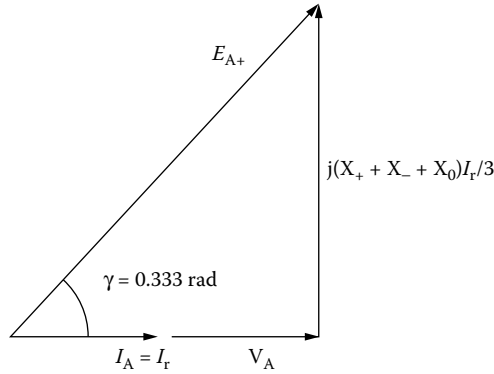
FIGURE 4.40 Phase A phasor diagram.

As the single-phase load was declared as resistive, I_r is in phase with $\underline{V}_A$, and thus,

$$\underline{E}_{A+} = V_{A+} + j\left(X_+ + X_- + X_0\right)\frac{I_r}{3}$$

A phasor diagram could be built as shown in Figure 4.40.

With $E_{A+} = 500$ V/sqrt(3) $= 280$ V and $I_r = 131$ A known, we may calculate the phase voltage of loaded phase, V_A:

$$V_A = \sqrt{E_{A+}^2 - \left[\left(X_+ + X_- + X_0\right)I_r/3\right]^2} = \sqrt{\left(289\right)^2 - \left[\left(1.1616 + 0.3872 + 0.23232\right)\cdot 131/3\right]^2}$$

$$= 278.348\ V$$

The voltages along phases B and C are

$$\underline{V}_B = \underline{E}_{A+}e^{-j\frac{2\pi}{3}} - jX_+\frac{I_r}{3}e^{-j\frac{2\pi}{3}} - jX_-\frac{I_r}{3}e^{+j\frac{2\pi}{3}} - jX_0\frac{I_r}{3} =$$

$$\underline{V}_C = \underline{E}_{A+}e^{+j\frac{2\pi}{3}} - jX_+\frac{I_r}{3}e^{j\frac{2\pi}{3}} - jX_-\frac{I_r}{3}e^{-j\frac{2\pi}{3}} - jX_e\frac{I_r}{3}$$

$$\underline{E}_{A+} = E_{A+}\cdot e^{j\gamma_0}; \gamma_0 = 0.333\ rad$$

The real axis falls along V_A and I_A, in the horizontal direction:

$$\underline{V}_B = -83.87 - j\times 270[V]$$

$$\underline{V}_C = -188.65 + j213.85[V]$$

The phase voltages are no longer symmetric ($V_A = 278$ V, $V_B = 282.67$ V, $V_C = 285$ V). The voltage regulation is not very large, as $x_+ = 0.6$, and the phase voltage unbalance is not large either, because the homopolar reactance is usually small, $x_0 = 0.12$. Also small is X_- due to a strong damper cage on the rotor. A small x_+ presupposes a notably large airgap; thus, the field-winding mmf should be large enough to produce acceptable values of flux density in the airgap on no load ($B_{gFm} = 0.7$–0.75 T) in order to secure a reasonable volume SG.
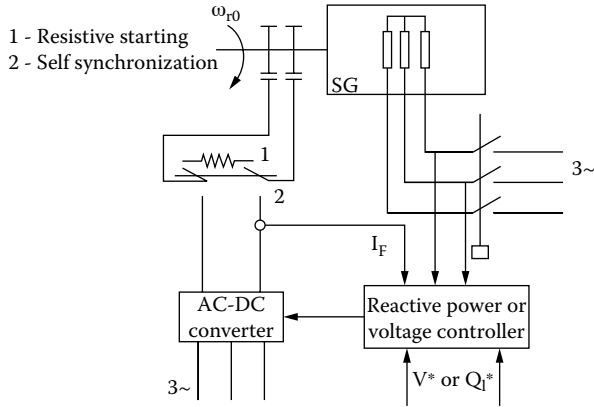
FIGURE 4.41 Synchronous condenser.
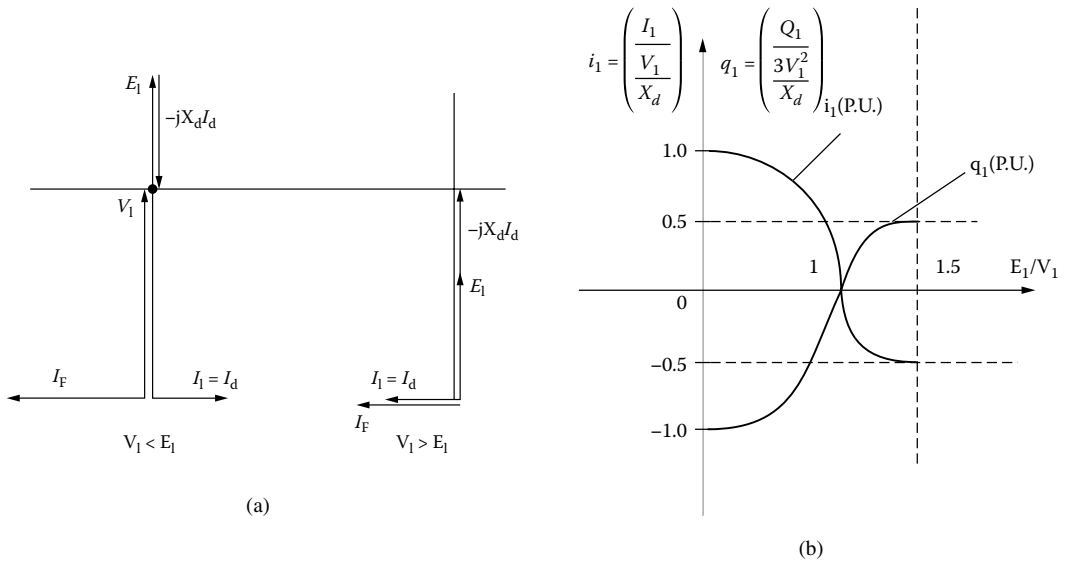
FIGURE 4.42 (a) Phasor diagrams and (b) reactive power of synchronous condenser.

4.14 The Synchronous Condenser

As already pointed out, the reactive power capability of a synchronous machine is basically the same for motor or generating mode (Figure 4.28b). It is thus feasible to use a synchronous machine as a motor without any mechanical load, connected to the local power grid (system), to "deliver" or "drain" reactive power and thus contribute to overall power factor correction or (and) local voltage control. The reactive power flow is controlled through field current control (Figure 4.41).

The phasor diagram (with zero losses) springs from voltage Equation 4.54 with $I_q = 0$ and $R_1 = 0$ (Figure 4.42a and Figure 4.42b):

$$\underline{V}_1 = \underline{E}_1 - jX_d I_d; \underline{I}_1 = \underline{I}_d \tag{4.137}$$

The reactive power Q_1 (Equation 4.102), with $\delta_V = 0$, is

$$Q_1 = 3V_1 \frac{\left(E_1 - V_1\right)}{X_d} = -3V_1 I_d \tag{4.138}$$

$$Q_1 = \frac{3V_1^2}{X}; X = \frac{X_d}{E_1 / V_1 - 1} \tag{4.139}$$

As expected, Q_1 changes sign at $E_1 = V_1$ and so does the current:

$$I_d = \left(V_1 - E_1\right)/X_d; X = \begin{cases} > 0 \ \ for \ E_1/V_1 > 1 \\ < 0 \ \ for \ E_1/V_1 < 1 \end{cases} \tag{4.140}$$

Negative I_d means demagnetizing I_d or $E_1 > V_1$. As magnetic saturation depends on the resultant magnetic field, for constant voltage V_1, the saturation level stays about the same, irrespective of field current I_F. So,

$$E_1 \approx \omega_r \left(M_{FA}\right)_{V_1} \cdot I_F \tag{4.141}$$

Also, X_d should not vary notably for constant voltage V_1. The maximum delivered reactive power depends on I_d, but the thermal design should account for both stator and rotor field-winding losses, together with core losses located in the stator core.

It seems that the synchronous condenser should be designed at maximum delivered (positive) reactive power $Q_{1\max}$:

$$Q_{1\max} = 3\frac{V_1}{X_d}\left[E_{1\max}\left(I_{F\max}\right) - V_1\right]; I_1 = \frac{E_{1\max} - V_1}{X_d} \tag{4.142}$$

To reduce the size of such a machine acting as a no-load motor, two pole rotor configurations seem to be appropriate. The synchronous condenser is, in fact, a positive/negative reactance with continuous control through field current via a low power rating AC–DC converter. It does not introduce significant voltage or current harmonics in the power systems. However, it makes noise, has a sizeable volume, and needs maintenance. These are a few reasons for the increase in use of pulse-width modulator (PWM) converter controlled capacitors in parallel with inductors to control voltage in power systems. Existing synchronous motors are also used whenever possible, to control reactive power and voltage locally while driving their loads.

4.15　Summary

- Large and medium power SGs are built with DC excitation windings on the rotor with either salient or nonsalient poles.
- Salient rotor poles are built for $2p_1 > 4$ poles and nonsalient rotor poles for $2p_1 = 2, 4$.
- The stator core of SGs is made of silicon-steel laminations (generally 0.5 mm thick), with uniform slotting. The slots house the three-phase windings.
- The stator core is made of one piece only if the outer diameter is below 1 m; otherwise, it is made of segments. Sectionable cores are wound section by section, and the wound sections are mounted together at the user's site.
- The slots in SGs are generally open and provided with nonmagnetic or magnetic wedges (to reduce emf harmonic content).

- Stator windings are of single- and double-layer types and are made of lap (multiturn) coils or the bar-wave (single-turn) coils (to reduce the lengthy connections between coils).
- Stator windings are generally built with integer slots/pole/phase q; only for a large number of poles $2p_1 > 16$ to 20, q may be fractionary: 3.5, 4.5 (to reduce the emf harmonics content).
- The symmetric AC currents of stator windings produce a positive mmf wave that travels with the ω_1/p_1 angular speed (with respect to the stator) $\omega_1 = 2\pi f_1$, with f_1 equal to the frequency of currents.
- The core of salient pole rotors is made of a solid iron pole wheel spider on top of which $2p_1$ salient poles usually made of laminations (1 mm thick in general) are placed. The poles are attached to the pole wheel spider through hammer or dove-tail keybars or bolts and screws with end plates.
- Nonsalient pole rotors are made of solid iron with machined radial slots over two thirds of periphery to house distributed field-winding coils. Constrained costs and higher peripheral speeds have led to solid cores for nonsalient poles rotors with $2p_1 = 2$, 4 poles.
- The rotor poles are provided with additional (smaller) slots filled with copper or brass bars short-circuited by partial or total end rings. This is the damper winding.
- The airgap flux density produced by the rotor field windings has a fundamental and space harmonics. They are to be limited in order to reduce the stator emf (no load voltage) harmonics. The larger airgap under the salient poles is used for the scope. Uniform airgap is used for nonsalient poles, because their distributed field coils produce lower harmonics in the airgap flux density. The design airgap flux density flat top value is about 0.7 to 0.8 T in large and medium power SGs. The emf harmonics may be further reduced by the type of stator winding (larger or fractionary q, chorded coils).
- The airgap flux density of the rotor field winding currents is a traveling wave at rotor speed $\Omega_r = \omega_r/p_1$.
- When $\omega_r = \omega_1$, the stator AC current and rotor DC current airgap fields are at standstill with each other. These conditions lead to an interaction between the two fields, with nonzero average electromagnetic torque. This is the speed of synchronism or the synchronous speed.
- When an SG is driven at speed ω_r (electrical rotor angular speed; $\Omega_r = \omega_r/p_1$ is the mechanical rotor speed), the field rotor DC currents produce emfs in the stator windings with frequency ω_1 that is $\omega_1 = \omega_r$. If a balanced three-phase load is connected to the stator terminals, the occuring stator currents will naturally have the same frequency $\omega_1 = \omega_r$; their mmf will, consequently, produce an airgap traveling field at the speed $\omega_1 = \omega_r$. Their phase shift with respect to phase emfs depends on load character (inductive-resistive or capacitive-resistive) and on SG reactances (not yet discussed). This is the principle of the SG.
- The airgap field of stator AC currents is called the armature reaction.
- The phase stator currents may be decomposed in two components (I_d, I_q), one in phase with the emf and the other at 90°. Thus, two mmfs are obtained, with airgap fields that are at standstill with respect to the moving rotor. One along the d (rotor pole) axis, called longitudinal, and the other one along the q axis, called transverse. This decomposition is the core of the two-reaction theory of SGs.
- The two stator mmf fields are tied to rotor d and q axes; thus, their cyclic magnetization reactances X_{dm} and X_{qm} may be easily calculated. Leakage reactances are added to get X_d and X_q, the synchronous reactances. With zero damper currents and DC field currents on the rotor, the steady-state voltage equation is straightforward:

$$\underline{I}_1 R_1 + V_1 = \underline{E}_1 - jX_d\,\underline{I}_d - jX_q\,\underline{I}_q; \underline{I}_1 = \underline{I}_d + \underline{I}_q$$

- The SG "delivers" both active and reactive power, P_1 and Q_1. They both depend on X_d, X_q, and R_1 and on the power angle δ_V, which is the phase angle between the emf and the terminal voltage (phase variables).

- Core losses may be included in the SG equations at steady state as pure resistive short-circuited stator fictitious windings with currents that are produced by the resultant airgap or stator phase linkage.
- The SG loss components are stator winding losses, stator core losses, rotor field-winding losses, additional losses (mainly in the rotor damper cage), and mechanical losses. The efficiency of large SGs is very good (above 98%, total, including field-winding losses).
- The SGs may operate in stand-alone applications or may be connected to the local (or regional) power system. No-load, short-circuit, zero-power factor saturation curves, together with the output $V_1(I_1)$ curve, fully characterize stand-alone operation with balanced load. Voltage regulation tends to be large with SGs as the synchronous reactances in P.U. (x_d or x_q) are larger than 0.5 to 0.6, to limit the rotor field-winding losses.
- Operation of SGs at the power system is characterized by the angular curve $P_1(\delta_V)$, V-shaped curves $I_1(I_F)$ for $P_1 = $ ct., and the reactive power capability $Q_1(P_1)$.
- The $P_1(\delta_V)$ curve shows a single maximum value at $\delta_{VK} \leq 90°$; this critical angle decreases when the field current I_F decreases for constant stator terminal voltage V_1 and speed.
- Static stability is defined as the property of SG to remain at synchronism for slow shaft torque variations. Basically, up to $\delta_V = \delta_{VK}$, the SG is statically stable.
- The dynamic stability is defined as the property of the SG to remain in synchronism for fast shaft torque or electric power (short-circuiting until clearing) transients. The area criterion is used to forecast the reserve of dynamic stability for each transient. Dynamic stability limits the rated power angle 22 to 40°, much less than its maximum value $\delta_{VK} \leq 90°$.
- The stand-alone SG may encounter unbalanced loads. The symmetrical components (Fortesque) method may be applied to describe SG operation under such conditions, provided the saturation level does not change (or is absent). Impedances for the negative and zero components of stator currents, $\underline{Z}_-$ and $\underline{Z}_0$, are defined, and basic methods to measure them are described. In general, $\left| \underline{Z}_+ \right| > \left| \underline{Z}_- \right| > \left| \underline{Z}_0 \right|$, and thus, the stator phase voltage imbalance under unbalanced loads is not very large. However, the negative sequence stator currents induce voltages and produce currents of double stator frequency in the rotor damper cage and field winding. Additional losses are present. They have to be limited to keep rotor temperature within reasonable limits. The maximum I_-/I_+ ratio is standardized (for power system SGs) or specified (for stand-alone SGs).
- The synchronous machine acting as a motor with no shaft load is used for reactive power absorption (I_F small) or delivery (I_F large). This regime is called a synchronous condenser, as the machine is seen by the local power system either as a capacitor (I_F large, overexcited $E_1 > V_1$) or as an inductor (I_F small, underexcited machine $E_1/V_1 < 1$). Its role is to raise or control the local power factor or voltage in the power system.

References

1. R. Richter, *Electrical Machines, vol. 2, Synchronous Machines*, Verlag Birkhauser, Basel, 1954 (in German).
2. J.H. Walker, *Large Synchronous Machines*, Clarendon Press, Oxford, 1981.
3. I. Boldea, and S.A. Nasar, *Induction Machine Handbook*, CRC Press, Boca Raton, Florida, 2001.
4. IEEE Std. 115 – 1995, "Test Procedures for Synchronous Machines."
5. V. Ostovic, *Dynamics of Saturated Electric Machines*, Springer-Verlag, Heidelberg, 1989.
6. M. Kostenko, and L. Piotrovski, *Electrical Machines*, vol. 2, MIR Publishers, Moscow, 1974.
7. C. Concordia, *Synchronous Machines*, John Wiley & Sons, New York, 1951.

5

Synchronous Generators: Modeling for (and) Transients

5.1   Introduction

The previous chapter dealt with the principles of synchronous generators (SGs) and steady state based on the two-reaction theory. In essence, the concept of traveling field (rotor) and stator magnetomotive forces (mmfs) and airgap fields at standstill with each other has been used.

By decomposing each stator phase current under steady state into two components, one in phase with the electromagnetic field (emf) and the other phase shifted by 90°, two stator mmfs, both traveling at rotor speed, were identified. One produces an airgap field with its maximum aligned to the rotor poles (*d* axis), while the other is aligned to the *q* axis (between poles).

The *d* and *q* axes magnetization inductances X_{dm} and X_{qm} are thus defined. The voltage equations with balanced three-phase stator currents under steady state are then obtained.

Further on, this equation will be exploited to derive all performance aspects for steady state when no currents are induced into the rotor damper winding, and the field-winding current is direct. Though unbalanced load steady state was also investigated, the negative sequence impedance $\underline{Z_-}$ could not be explained theoretically; thus, a basic experiment to measure it was described in the previous chapter. Further on, during transients, when the stator current amplitude and frequency, rotor damper and field currents, and speed vary, a more general (advanced) model is required to handle the machine behavior properly.

Advanced models for transients include the following:

- Phase-variable model
- Orthogonal-axis (*d–q*) model
- Finite-element (FE)/circuit model

The first two are essentially lumped circuit models, while the third is a coupled, field (distributed parameter) and circuit, model. Also, the first two are analytical models, while the third is a numerical model. The presence of a solid iron rotor core, damper windings, and distributed field coils on the rotor of nonsalient rotor pole SGs (turbogenerators, $2p_1 = 2,4$), further complicates the FE/circuit model to account for the eddy currents in the solid iron rotor, so influenced by the local magnetic saturation level.

In view of such a complex problem, in this chapter, we are going to start with the phase coordinate model with inductances (some of them) that are dependent on rotor position, that is, on time. To get rid of rotor position dependence on self and mutual (stator/rotor) inductances, the *d–q* model is used. Its derivation is straightforward through the Park matrix transform. The *d–q* model is then exploited to describe the steady state. Further on, the operational parameters are presented and used to portray electromagnetic (constant speed) transients, such as the three-phase sudden short-circuit.

An extended discussion on magnetic saturation inclusion into the *d–q* model is then housed and illustrated for steady state and transients.

The electromechanical transients (speed varies also) are presented for both small perturbations (through linearization) and for large perturbations, respectively. For the latter case, numerical solutions of state-space equations are required and illustrated.

Mechanical (or slow) transients such as SG free or forced "oscillations" are presented for electromagnetic steady state.

Simplified *d–q* models, adequate for power system stability studies, are introduced and justified in some detail. Illustrative examples are worked out. The asynchronous running is also presented, as it is the regime that evidentiates the asynchronous (damping) torque that is so critical to SG stability and control. Though the operational parameters with $s = \omega j$ lead to various SG parameters and time constants, their analytical expressions are given in the design chapter (Chapter 7), and their measurement is presented as part of Chapter 8, on testing.

This chapter ends with some FE/coupled circuit models related to SG steady state and transients.
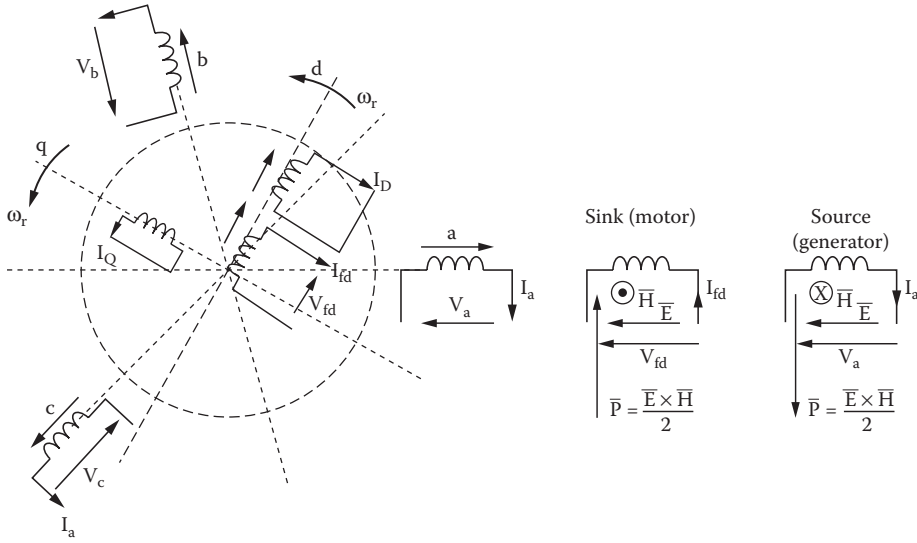
FIGURE 5.1 Phase-variable circuit model with single damper cage.

5.2 The Phase-Variable Model

The phase-variable model is a circuit model. Consequently, the SG is described by a set of three stator circuits coupled through motion with two (or a multiple of two) orthogonally placed (*d* and *q*) damper windings and a field winding (along axis *d*: of largest magnetic permeance; see Figure 5.1). The stator and rotor circuits are magnetically coupled with each other. It should be noticed that the convention of voltage–current signs (directions) is based on the respective circuit nature: source on the stator and sink on the rotor. This is in agreement with Poynting vector direction, toward the circuit for the sink and outward for the source (Figure 5.1).

The phase-voltage equations, in stator coordinates for the stator, and rotor coordinates for the rotor, are simply missing any "apparent" motion-induced voltages:

$$i_A R_s + v_a = -\frac{d\Psi_A}{dt}$$

$$i_B R_S + v_b = -\frac{d\Psi_B}{dt}$$

$$i_C R_S + v_c = -\frac{d\Psi_c}{dt}$$

$$i_D R_D = -\frac{d\Psi_D}{dt} \tag{5.1}$$

$$i_Q R_Q = -\frac{d\Psi_Q}{dt}$$

$$I_f R_f - V_f = -\frac{d\Psi_f}{dt}$$

The rotor quantities are not yet reduced to the stator. The essential parts missing in Equation 5.1 are the flux linkage and current relationships, that is, self- and mutual inductances between the six coupled circuits in Figure. 5.1. For example,

$$\Psi_A = L_{AA}I_a + L_{AB}I_b + L_{AC}I_c + L_{Af}I_f + L_{AD}I_D + L_{AQ}I_Q \qquad (5.2)$$

Let us now define the stator phase self- and mutual inductances L_{AA}, L_{BB}, L_{CC}, L_{AB}, L_{BC}, and L_{CA} for a salient-pole rotor SG. For the time being, consider the stator and rotor magnetic cores to have infinite magnetic permeability. As already demonstrated in Chapter 4, the magnetic permeance of airgap along axes d and q differ (Figure 5.2). The phase A mmf has a sinusoidal space distribution, because all space harmonics are neglected. The magnetic permeance of the airgap is maximum in axis d, P_d, and minimum in axis q and may be approximated to the following:

$$P(\theta_{er}) = P_0 + P_2 \cos 2\theta_{er} = \frac{P_d + P_q}{2} + \left(\frac{P_d - P_q}{2} \right) \cos 2\theta_{er} \qquad (5.3)$$

So, the airgap self-inductance of phase A depends on that of a uniform airgap machine (single-phase fed) and on the ratio of the permeance $P(\theta_{er})/(P_0 + P_2)$ (see Chapter 4):

$$L_{AAg} = \frac{4}{\pi^2} \left(W_1 K_{W1} \right)^2 \left(P_0 + P_2 \cos 2\theta_{er} \right) \qquad (5.4)$$

$$P_0 + P_2 = \frac{\mu_0 \tau l_{stack}}{g_{ed}}; P_0 - P_2 = \frac{\mu_0 \tau l_{stack}}{g_{eq}}; g_{ed} < g_{eq} \qquad (5.5)$$

Also,

$$L_{AAg} = L_0 + L_2 \cos 2\theta_{er} \qquad (5.6)$$

To complete the definition of the self-inductance of phase A, the phase leakage inductance L_{sl} has to be added (the same for all three phases if they are fully symmetric):

$$L_{AA} = L_{sl} + L_0 + L_2 \cos 2\theta_{er} \qquad (5.7)$$

Ideally, for a nonsalient pole rotor SG, $L_2 = 0$ but, in reality, a small saliency still exists due to a more accentuated magnetic saturation level along axis q, where the distributed field coil slots are located.
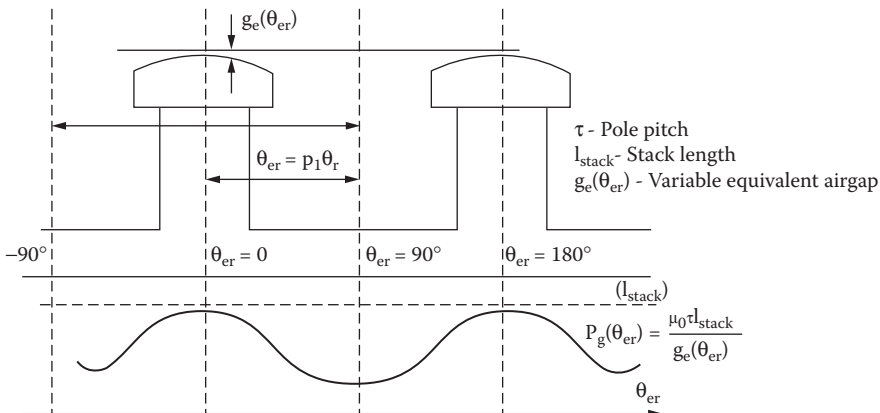
FIGURE 5.2 The airgap permeance per pole versus rotor position.

In a similar way,

$$L_{BB} = L_{sl} + L_0 + L_2 \cos\left(2\theta_{er} + \frac{2\pi}{3}\right) \tag{5.8}$$

$$L_{CC} = L_{sl} + L_0 + L_2 \cos\left(2\theta_{er} - \frac{2\pi}{3}\right) \tag{5.9}$$

The mutual inductance between phases is considered to be only in relation to airgap permeances. It is evident that, with ideally (sinusoidally) distributed windings, $L_{AB}(\theta_{er})$ varies with θ_{er} as L_{CC} and again has two components (to a first approximation):

$$L_{AB} = L_{BA} = L_{AB0} + L_{AB2} \cos\left(2\theta_{er} - \frac{2\pi}{3}\right) \tag{5.10}$$

Now, as phases A and B are 120° phase shifted, it follows that

$$L_{AB0} \approx L_0 \cos\frac{2\pi}{3} = -\frac{L_0}{2} \tag{5.11}$$

The variable part of L_{AB} is similar to that of Equation 5.9 and thus,

$$L_{AB2} = L_2 \tag{5.12}$$

Relationships 5.11 and 5.12 are valid for ideal conditions. In reality, there are some small differences, even for symmetric windings. Further,

$$L_{AC} = L_{CA} = -\frac{L_0}{2} + L_2 \cos\left(2\theta_{er} + \frac{2\pi}{3}\right) \tag{5.13}$$

$$L_{BC} = L_{CB} = -\frac{L_0}{2} + L_2 \cos 2\theta_{er} \tag{5.14}$$

FE analysis of field distribution with only one phase supplied with direct current (DC) could provide ground for more exact approximations of self- and mutual stator inductance dependence on θ_{er}. Based on this, additional terms in $\cos(4\theta_{er})$, even $6\theta_{er}$, may be added. For fractionary q windings, more intricate θ_{er} dependences may be developed.

The mutual inductances between stator phases and rotor circuits are straightforward, as they vary with $\cos(\theta_{er})$ and $\sin(\theta_{er})$.

$$L_{Af} = M_f \cos\theta_{er}$$

$$L_{Bf} = M_f \cos\left(\theta_{er} - \frac{2\pi}{3}\right) \tag{5.15}$$

$$L_{Cf} = M_f \cos\left(\theta_{er} + \frac{2\pi}{3}\right)$$

$$L_{AD} = M_D \cos\theta_{er}$$

$$L_{BD} = M_D \cos\left(\theta_{er} - \frac{2\pi}{3}\right)$$

$$L_{CD} = M_D \cos\left(\theta_{er} + \frac{2\pi}{3}\right)$$

(5.15 cont.)

$$L_{AQ} = -M_Q \sin\theta_{er}$$

$$L_{BQ} = -M_Q \sin\left(\theta_{er} - \frac{2\pi}{3}\right)$$

$$L_{CQ} = -M_Q \sin\left(\theta_{er} + \frac{2\pi}{3}\right)$$

Notice that

$$L_0 = \frac{\left(L_{dm} + L_{qm}\right)}{2}$$

(5.16)

$$L_2 = \frac{\left(L_{dm} - L_{qm}\right)}{2}$$

L_{dm} and L_{qm} were defined in Chapter 4 with all stator phases on, and M_f is the maximum of field/armature inductance also derived in Chapter 4.

We may now define the SG phase-variable 6×6 matrix $\left|L_{ABCfDQ}\left(\theta_{er}\right)\right|$:

	A	B	C	f	D	Q
A	$L_{sl} + L_0 + L_2 \cos 2\theta_{er}$	$-\frac{L_0}{2} + L_2 \cdot \cos\left(2\theta_{er} - \frac{2\pi}{3}\right)$	$-\frac{L_0}{2} + L_2 \cdot \cos\left(2\theta_{er} + \frac{2\pi}{3}\right)$	$M_f \cos\theta_{er}$	$M_D \cos\theta_{er}$	$-M_Q \cos\theta_{er}$
B		$L_{sl} + L_0 + L_2 \cos\left(2\theta_{er} + \frac{2\pi}{3}\right)$	$-\frac{L_0}{2} + L_2 \cdot \cos 2\theta_{er}$	$M_f \cos\left(\theta_{er} - \frac{2\pi}{3}\right)$	$M_D \cos\left(\theta_{er} - \frac{2\pi}{3}\right)$	$-M_Q \sin\left(\theta_{er} - \frac{2\pi}{3}\right)$
C			$L_{sl} + L_0 + L_2 \cos\left(2\theta_{er} + \frac{2\pi}{3}\right)$	$M_f \cos\left(\theta_{er} + \frac{2\pi}{3}\right)$	$M_D \cos\left(\theta_{er} + \frac{2\pi}{3}\right)$	$-M_Q \sin\left(\theta_{er} - \frac{2\pi}{3}\right)$
f				$L_{fl}^r + L_{fm}^r$	M_{fD}^r	0
D					$L_{Dl}^r + L_{Dm}^r$	0
Q				0	0	$L_{Ql}^r + L_{Qm}^r$

$$\left|L_{ABCfDQ}\left(\theta_{er}\right)\right| =$$

(5.17)

A mutual coupling leakage inductance L_{fDl} also occurs between the field winding f and the d-axis cage winding D in salient-pole rotors. The zeroes in Equation 5.17 reflect the zero coupling between orthogonal windings in the absence of magnetic saturation. $L_{fm}^r, L_{Dm}^r, L_{Qm}^r$ are typical main (airgap permeance) self-inductances of rotor circuits. $L_{fl}^r, L_{Dl}^r, L_{Ql}^r$ are the leakage inductances of rotor circuits in axes d and q.

The resistance matrix is of diagonal type:

$$R_{ABCfdq} = Diag\left[R_s, R_r, R_s, R_f^r, R_D^r, R_Q^r \right] \tag{5.18}$$

Provided core losses, space harmonics, magnetic saturation, and frequency (skin) effects in the rotor core and damper cage are all neglected, the voltage/current matrix equation fully represents the SG at constant speed:

$$\left[I_{ABCfDQ} \right]\left[R_{ABCfDQ} \right] + \left[V_{ABCfDQ} \right] = \frac{-d\Psi_{ABCfDQ}}{dt} =$$
$$-\left[L_{ABCfDQ}\left(\theta_{er} \right) \right]\frac{d}{dt}\left[I_{ABCfDQ} \right] - \frac{\partial\left[L_{ABCfDQ} \right]}{\partial\theta_{er}}\frac{d\theta_{er}}{dt}\left[I_{ABCfDQ} \right] \tag{5.19}$$

with

$$V_{ABCfDQ} = \left[+V_A, +V_B, +V_C, -V_f, 0, 0 \right]^T ; \frac{d\theta_{er}}{dt} = \omega_r \tag{5.20}$$

$$\Psi_{ABCfDQ} = \left[\Psi_A, \Psi_B, \Psi_C, \Psi_f^r, \Psi_D^r, \Psi_Q^r \right]^T \tag{5.21}$$

The minus sign for V_f arises from the motor association of signs convention for rotor.

The first term on the right side of Equation 5.19 represents the transformer-induced voltages, and the second term refers to the motion-induced voltages.

Multiplying Equation 5.19 by $[I_{ABCfDQ}]^T$ yields the following:

$$\left[I_{ABCfDQ} \right]^T\left[V_{ABCfDQ} \right] = -\frac{1}{2}\left[I_{ABCfDQ} \right]^T\frac{\partial\left[L_{ABCfDQ}\left(\theta_{er} \right) \right]}{\partial\theta_{er}}\left[I_{ABCfDQ} \right]\cdot\omega_r -$$
$$-\frac{d}{dt}\left[\frac{1}{2}\left[I_{ABCfDQ} \right]^T\cdot L_{ABCfDQ}\left(\theta_{er} \right)\cdot\left[I_{ABCfDQ} \right] \right] - \left[I_{ABCfDQ} \right]^T\left[I_{ABCfDQ} \right]\left[R_{ABCfDQ} \right] \tag{5.22}$$

The instantaneous power balance equation (Equation 5.22) serves to identify the electromagnetic power that is related to the motion-induced voltages:

$$P_{elm} = -\frac{1}{2}\left[I_{ABCfDQ} \right]^T\cdot\frac{\partial}{\partial\theta_{er}}\left[L_{ABCfDQ}\left(\theta_{er} \right) \right]\left[I_{ABCfDQ} \right]\omega_r \tag{5.23}$$

P_{elm} should be positive for the generator regime.

The electromagnetic torque T_e opposes motion when positive (generator model) and is as follows:

$$T_e = \frac{+P_e}{\left(\omega_r / p_1 \right)} = -\frac{p_1}{2}\left[I_{ABCfDQ} \right]^T\frac{\partial\left[L_{ABCfDQ}\left(\theta_{er} \right) \right]}{\delta\theta_{er}}\left[I_{ABCfDQ} \right] \tag{5.24}$$

The equation of motion is

$$\frac{J}{p_1}\frac{d\omega_r}{dt} = T_{shaft} - T_e ; \frac{d\theta_{er}}{dt} = \omega_r \tag{5.25}$$

The phase-variable equations constitute an eighth-order model with time-variable coefficients (inductances). Such a system may be solved as it is either with flux linkages vector as the variable or with the current vector as the variable, together with speed ω_r and rotor position θ_{er} as motion variables.

Numerical methods such as Runge–Kutta–Gill or predictor-corrector may be used to solve the system for various transient or steady-state regimes, once the initial values of all variables are given. Also, the time variations of voltages and of shaft torque have to be known. Inverting the matrix of time-dependent inductances at every time integration step is, however, a tedious job. Moreover, as it is, the phase-variable model offers little in terms of interpreting the various phenomena and operation modes in an intuitive manner.

This is how the *d–q* model was born — out of the necessity to quickly solve various transient operation modes of SGs connected to the power grid (or in parallel).

5.3   The *d–q* Model

The main aim of the *d–q* model is to eliminate the dependence of inductances on rotor position. To do so, the system of coordinates should be attached to the machine part that has magnetic saliency — the rotor for SGs.

The *d–q* model should express both stator and rotor equations in rotor coordinates, aligned to rotor *d* and *q* axes because, at least in the absence of magnetic saturation, there is no coupling between the two axes. The rotor windings *f*, *D*, *Q* are already aligned along *d* and *q* axes. The rotor circuit voltage equations were written in rotor coordinates in Equation 5.1.

It is only the stator voltages, V_A, V_B, V_C, currents I_A, I_B, I_C, and flux linkages Ψ_A, Ψ_B, Ψ_C that have to be transformed to rotor orthogonal coordinates. The transformation of coordinates ABC to *d–q*0, known also as the Park transform, valid for voltages, currents, and flux linkages as well, is as follows:

$$
\left[P\left(\theta_{er}\right) \right] = \frac{2}{3}
\begin{bmatrix}
\cos\left(-\theta_{er}\right) & \cos\left(-\theta_{er} + \dfrac{2\pi}{3}\right) & \cos\left(-\theta_{er} - \dfrac{2\pi}{3}\right) \\[2mm]
\sin\left(-\theta_{er}\right) & \sin\left(-\theta_{er} + \dfrac{2\pi}{3}\right) & \sin\left(-\theta_{er} - \dfrac{2\pi}{3}\right) \\[2mm]
\dfrac{1}{2} & \dfrac{1}{2} & \dfrac{1}{2}
\end{bmatrix}
\tag{5.26}
$$

So,

$$
\begin{vmatrix} V_d \\ V_q \\ V_0 \end{vmatrix} = \left| P\left(\theta_{er}\right) \right| \cdot \begin{vmatrix} V_A \\ V_B \\ V_C \end{vmatrix}
\tag{5.27}
$$

$$
\begin{vmatrix} I_d \\ I_q \\ I_0 \end{vmatrix} = \left| P\left(\theta_{er}\right) \right| \cdot \begin{vmatrix} I_A \\ I_B \\ I_C \end{vmatrix}
\tag{5.28}
$$

$$
\begin{vmatrix} \Psi_d \\ \Psi_q \\ \Psi_0 \end{vmatrix} = \left| P\left(\theta_{er}\right) \right| \cdot \begin{vmatrix} \Psi_A \\ \Psi_B \\ \Psi_C \end{vmatrix}
\tag{5.29}
$$

The inverse transformation that conserves power is

$$\left[P\!\left(\theta_{er}\right)\right]^{-1} = \frac{3}{2}\left[P\!\left(\theta_{er}\right)\right]^{T} \tag{5.30}$$

The expressions of Ψ_A, Ψ_B, Ψ_C from the flux/current matrix are as follows:

$$\left| \Psi_{ABCfDQ}\right| = \left| L_{ABCfDQ}\!\left(\theta_{er}\right)\right|\left| I_{ABCfDQ}\right| \tag{5.31}$$

The phase currents I_A, I_B, I_C are recovered from I_d, I_q, I_0 by

$$\begin{vmatrix} I_A \\ I_B \\ I_C \end{vmatrix} = \frac{3}{2}\left[P\!\left(\theta_{er}\right)\right]^{T} \cdot \begin{vmatrix} I_d \\ I_q \\ I_0 \end{vmatrix} \tag{5.32}$$

An alternative Park transform uses $\sqrt{\dfrac{2}{3}}$ instead of 2/3 for direct and inverse transform. This one is fully orthogonal (power direct conservation).

The rather short and elegant expressions of Ψ_d, Ψ_q, Ψ_0 are obtained as follows:

$$\Psi_d = \left(L_{sl} + L_0 - L_{AB0} + \frac{3}{2}L_2\right) I_d + M_f I_f^r + M_D I_D^r$$

$$\Psi_q = \left(L_{sl} + L_0 - L_{AB0} - \frac{3}{2}L_2\right) I_q + M_Q I_q^r \tag{5.33}$$

$$\Psi_0 = \left(L_{sl} + L_0 + 2L_{AB0}\right) I_0 \,; \; L_{AB0} \approx -L_0/2$$

From Equation 5.16,

$$L_{dm} = \frac{3}{2}\left(L_0 + L_2\right);$$

$$L_{qm} = \frac{3}{2}\left(L_0 - L_2\right) \tag{5.34}$$

are exactly the "cyclic" magnetization inductances along axes d and q as defined in Chapter 4. So, Equation 5.33 becomes

$$\Psi_d = L_d I_d + M_f I_f^r + M_D I_D^r;$$

$$L_d = L_{sl} + L_{dm} \tag{5.35}$$

$$\Psi_q = L_q I_q + M_Q I_Q^r;$$

$$L_q = L_{sl} + L_{qm} \tag{5.36}$$

$$\Psi_0 \approx L_{sl} I_0 \tag{5.37}$$
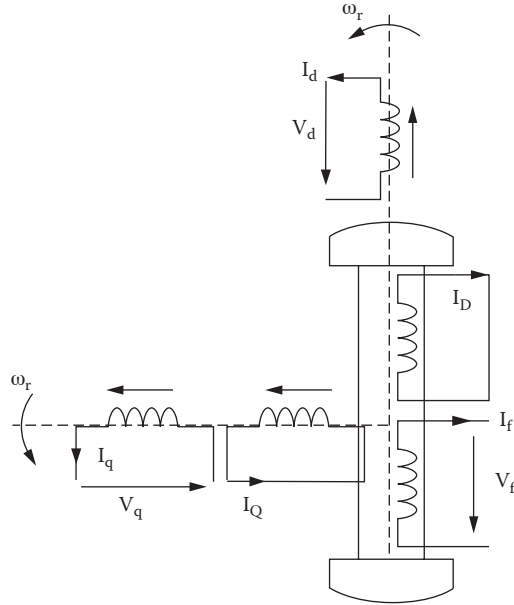
FIGURE 5.3 The *d–q* model of synchronous generators.

In a similar way for the rotor,

$$\Psi^r_f = \left(L^r_{fl} + L_{fm}\right)I^r_f + \frac{3}{2}M_f I_d + M_{fD}I^r_D$$

$$\Psi^r_D = \left(L^r_{Dl} + L_{Dm}\right)I^r_D + \frac{3}{2}M_D I_d + M_{fD}I^r_f \qquad (5.38)$$

$$\Psi^r_Q = \left(L^r_{Ql} + L_{Qm}\right)I^r_Q + \frac{3}{2}M_Q I_q$$

As seen in Equation 5.37, the zero components of stator flux and current Ψ_0, I_0 are related simply by the stator phase leakage inductance L_{sl}; thus, they do not participate in the energy conversion through the fundamental components of mmfs and fields in the SGs.

Thus, it is acceptable to consider it separately. Consequently, the *d–q* transformation may be visualized as representing a fictitious SG with orthogonal stator axes fixed magnetically to the rotor *d–q* axes. The magnetic field axes of the respective stator windings are fixed to the rotor *d–q* axes, but their conductors (coils) are at standstill (Figure 5.3) — fixed to the stator. The *d–q* model equations may be derived directly through the equivalent fictitious orthogonal axis machine (Figure 5.3):

$$I_d R_s + V_d = -\frac{d\Psi_d}{dt} + \omega_r \Psi_q$$

$$\qquad (5.39)$$

$$I_q R_s + V_q = -\frac{d\Psi_q}{dt} - \omega_r \Psi_d$$

The rotor equations are then added:

$$I_f R_f - V_f = -\frac{d\Psi_f}{dt}$$

$$i_D R_D = -\frac{d\Psi_D}{dt} \tag{5.40}$$

$$i_Q R_Q = -\frac{d\Psi_Q}{dt}$$

In Equation 5.39, we assumed that

$$\frac{d\Psi_d}{d\theta_{er}} = -\Psi_q$$

$$\frac{d\Psi_q}{d\theta_{er}} = \Psi_d \tag{5.41}$$

The assumptions are true if the windings *d–q* are sinusoidally distributed and the airgap is constant but with a radial flux barrier along axis *d*. Such a hypothesis is valid for distributed stator windings to a good approximation if only the fundamental airgap flux density is considered. The null (zero) component equation is simply as follows:

$$I_0 R_s + V_0 = -L_{sl} \frac{di_0}{dt} = -\frac{d\Psi_0}{dt};$$

$$I_0 = \frac{(I_A + I_B + I_C)}{3} \tag{5.42}$$

The equivalence between the real three-phase SG and its *d–q* model in terms of instantaneous power, losses, and torque is marked by the 2/3 coefficient in Park's transformation:

$$V_A I_A + V_A I_A + V_A I_A = \frac{3}{2}\left(V_d I_d + V_q I_q + 2V_0 I_0\right)$$

$$T_e = -\frac{3}{2} p_1 \left(\Psi_d I_q - \Psi_q I_d\right) \tag{5.43}$$

$$R_s \left(I_A^2 + I_B^2 + I_C^2\right) = \frac{3}{2} R_s \left(I_d^2 + I_q^2 + 2I_0^2\right) \tag{5.44}$$

The electromagnetic torque, T_e, calculated in Equation 5.43, is considered positive when opposite to motion. Note that for the Park transform with $\sqrt{\frac{2}{3}}$ coefficients, the power, torque, and loss equivalence in Equation 5.43 and Equation 5.44 lack the 3/2 factor. Also, in this case, Equation 5.38 has $\sqrt{\frac{3}{2}}$ instead of 3/2 coefficients.
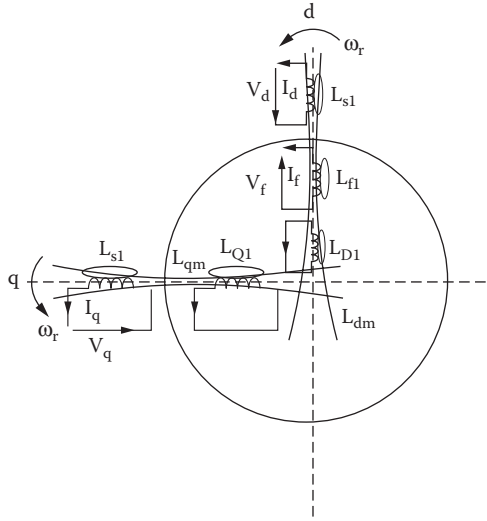
FIGURE 5.4 Inductances of *d–q* model.

The motion equation is as follows:

$$\frac{J}{p_1}\frac{d\omega_r}{dt} = T_{shaft} + \frac{3}{2}p_1\left(\Psi_d I_q - \Psi_d I_q\right) \tag{5.45}$$

Reducing the rotor variables to stator variables is common in order to reduce the number of inductances. But first, the *d–q* model flux/current relations derived directly from Figure 5.4, with rotor variables reduced to stator, would be

$$\Psi_d = L_{sl} I_d + L_{dm}\left(I_d + I_D + I_f\right)$$

$$\Psi_q = L_{sl} I_q + L_{qm}\left(I_q + I_Q\right)$$

$$\Psi_f = L_{fl} I_q + L_{dm}\left(I_d + I_D + I_f\right) \tag{5.46}$$

$$\Psi_D = L_{Dl} I_D + L_{dm}\left(I_d + I_D + I_f\right)$$

$$\Psi_Q = L_{Ql} I_Q + L_{qm}\left(I_q + I_Q\right)$$

The mutual and self-inductances of airgap (main) flux linkage are identical to L_{dm} and L_{qm} after rotor to stator reduction. Comparing Equation 5.38 with Equation 5.46, the following definitions of current reduction coefficients are valid:

$$I_f = I_f^r \cdot K_f$$

$$I_D = I_D^r \cdot K_D$$

$$I_Q = I_Q^r \cdot K_Q \tag{5.47}$$

$$K_f = \frac{M_f}{L_{dm}}$$

$$K_D = \frac{M_D}{L_{dm}}$$

$$K_Q = \frac{M_Q}{L_{Qm}} \qquad \text{(5.47 cont.)}$$

We may now use coefficients in Equation 5.38 to obtain the following:

$$\Psi_f^r \cdot \frac{2}{3} \frac{L_{dm}}{M_f} = \Psi_f = L_{fl} I_f + L_{dm} \left(I_f + I_D + I_d \right) \qquad (5.48)$$

with

$$L_{fl} = \frac{2}{3} L_{fl}^r \cdot \frac{L_{dm}^2}{M_f^2} = L_{fl}^r \frac{2}{3K_f^2}$$

$$L_{fm} \frac{2}{3} \frac{L_{dm}}{M_f^2} \approx 1 \qquad (5.49)$$

$$\frac{2}{3} \frac{L_{dm}}{M_f M_D} \approx 1$$

$$\Psi_D^r \cdot \frac{2}{3} \frac{L_{dm}}{M_D} = \Psi_D = L_{Dl} I_D + L_{dm} \left(I_f + I_D + I_d \right) \qquad (5.50)$$

with

$$L_{Dl} = \frac{2}{3} L_{Dl}^r \frac{L_{dm}^2}{M_D^2} = L_{Dl}^r \cdot \frac{2}{3} \cdot \frac{1}{K_D^2}$$

$$L_{Dm} \cdot \frac{2}{3} \frac{L_{dm}}{M_D^2} \approx 1 \qquad (5.51)$$

$$\Psi_Q^r \frac{2}{3} \frac{L_{qm}}{M_Q} = \Psi_Q = L_{Ql} I_Q + L_{qm} \left(I_q + I_Q \right) \qquad (5.52)$$

with

$$L_{Ql} = \frac{2}{3} L_{Ql}^r \cdot \left(\frac{L_{qm}}{M_Q} \right)^2 = L_{Ql}^r \frac{2}{3} \frac{1}{K_Q^2}$$

$$L_{Qm} \cdot \frac{2}{3} \frac{L_{qm}}{M_Q^2} \approx 1 \qquad (5.53)$$

We still need to reduce the rotor circuit resistances R_f^r, R_D^r, R_Q^r and the field-winding voltage to stator quantities. This may be done by power equivalence as follows:

$$\frac{3}{2} R_f \left(I_f^2 \right) = R_f^r I_f^{r2}$$

$$\frac{3}{2} R_D \left(I_D^2 \right) = R_D^r I_D^{r2} \qquad (5.54)$$

$$\frac{3}{2} R_Q \left(I_Q^2 \right) = R_Q^r I_Q^{r2}$$

$$\frac{3}{2} V_f I_f = V_f^r I_f^r \qquad (5.55)$$

Finally,

$$R_f = R_f^r \frac{2}{3} \frac{1}{K_f^2}$$

$$R_D = R_D^r \frac{2}{3} \frac{1}{K_D^2}$$

$$\qquad (5.56)$$

$$R_Q = R_Q^r \frac{2}{3} \frac{1}{K_Q^2}$$

$$V_f = V_f^r \frac{2}{3} \frac{1}{K_f}$$

Notice that resistances and leakage inductances are reduced by the same coefficients, as expected for power balance.

A few remarks are in order:

- The "physical" *d*–*q* model in Figure 5.4 presupposes that there is a single common (main) flux linkage along each of the two orthogonal axes that embraces all windings along those axes.
- The flux/current relationships (Equation 5.46) for the rotor make use of stator-reduced rotor current, inductances, and flux linkage variables. In order to be valid, the following approximations have to be accepted:

$$L_{fm} L_{dm} \approx \frac{3}{2} M_f^2$$

$$M_{fD} L_{dm} \approx \frac{3}{2} M_f M_D$$

$$\qquad (5.57)$$

$$L_{Dm} L_{dm} \approx \frac{3}{2} M_D^2$$

$$L_{Qm} L_{qm} \approx \frac{3}{2} M_Q^2$$

- The validity of the approximations in Equation 5.57 is related to the condition that airgap field distribution produced by stator and rotor currents, respectively, is the same. As far as the space fundamental is concerned, this condition holds. Once heavy local magnetic saturation conditions occur (Equation 5.57), there is a departure from reality.

- No leakage flux coupling between the d axis damper cage and the field winding ($L_{fDl} = 0$) was considered so far, though in salient-pole rotors, $L_{fDl} \neq 0$ may be needed to properly assess the SG transients, especially in the field winding.
- The coefficients K_f, K_D, K_Q used in the reduction of rotor voltage (V_f^r), currents I_f^r, I_D^r, I_Q^r, leakage inductances L_{fl}^r, L_{Dl}^r, L_{Ql}^r, and resistances R_f^r, R_D^r, R_Q^r, to the stator may be calculated through analytical or numerical (field distribution) methods, and they may also be measured. Care must be exercised, as K_f, K_D, K_Q depend slightly on the saturation level in the machine.
- The reduced number of inductances in Equation 5.46 should be instrumental in their estimation (through experiments).

Note that when $\sqrt{\dfrac{2}{3}}$ is used in the Park transform (matrix), K_f, K_D, K_Q in Equation 5.47 all have to be

multiplied by $\sqrt{\dfrac{3}{2}}$, but the factor 2/3 (or 3/2) disappears completely from Equation 5.48 through Equation 5.57 (see also Reference [1]).

5.4 The per Unit (P.U.) *d–q* Model

Once the rotor variables (V_f^r, I_f^r, I_D^r, I_Q^r, R_f^r, R_D^r, R_Q^r, L_{fl}^r, L_{Dl}^r, L_{Ql}^r) have been reduced to the stator, according to relationships 5.47, 5.54, 5.55, and 5.56, the P.U. *d–q* model requires base quantities only for the stator.

Though the selection of base quantities leaves room for choice, the following set is widely accepted:

$$V_b = V_n \sqrt{2} \quad \text{— peak stator phase nominal voltage} \tag{5.58a}$$

$$I_b = I_n \sqrt{2} \quad \text{— peak stator phase nominal current} \tag{5.58b}$$

$$S_b = 3 V_n I_n \quad \text{— nominal apparent power} \tag{5.59}$$

$$\omega_b = \omega_{rn} \quad \text{— rated electrical angular speed } (\omega_{rn} = p_1 \Omega_{rn}) \tag{5.60}$$

Based on this restricted set, additional base variables are derived:

$$T_{eb} = \frac{S_b \cdot p_1}{\omega_b} \quad \text{— base torque} \tag{5.61}$$

$$\Psi_b = \frac{V_b}{\omega_b} \quad \text{— base flux linkage} \tag{5.62}$$

$$Z_b = \frac{V_b}{I_b} = \frac{V_n}{I_n} \quad \text{— base impedance (valid also for resistances and reactances)} \tag{5.63}$$

$$L_b = \frac{Z_b}{\omega_b} \quad \text{— base inductance} \tag{5.64}$$

Inductances and reactances are the same in P.U. values. Though in some instances time is also provided with a base quantity $t_b = 1/\omega_b$, we chose here to leave time in seconds, as it seems more intuitive.

The inertia is, consequently,

$$H_b = \frac{1}{2} J \left(\frac{\omega_b}{p_1} \right)^2 \cdot \frac{1}{S_b} \tag{5.65}$$

It follows that the time derivative in P.U. terms becomes

$$\frac{d}{dt} \rightarrow \frac{1}{\omega_b} \frac{d}{dt} ; s \rightarrow \frac{s}{\omega_b} \quad \text{(Laplace operator)} \tag{5.66}$$

The P.U. variables and coefficients (inductances, reactances, and resistances) are generally denoted by lowercase letters.

Consequently, the P.U. d–q model equations, extracted from Equation 5.39 through Equation 5.41, Equation 5.43, and Equation 5.46, become

$$\frac{1}{\omega_b} \frac{d}{dt} \psi_d = \omega_r \psi_q - i_d r_s - v_d ; \psi_d = l_{sl} i_d + l_{dm} \left(i_d + i_D + i_f \right)$$

$$\frac{1}{\omega_b} \frac{d}{dt} \psi_q = -\omega_r \psi_d - i_q r_s - v_d ; \psi_q = l_{sl} i_d + l_{qm} \left(i_q + i_Q \right)$$

$$\frac{1}{\omega_b} \frac{d}{dt} \psi_0 = -i_0 r_0 - v_0$$

$$\frac{1}{\omega_b} \frac{d}{dt} \psi_f = -i_f r_f + v_f ; \psi_f = l_{fl} i_f + l_{dm} \left(i_Q + i_D + i_F \right)$$

$$\frac{1}{\omega_b} \frac{d}{dt} \psi_D = -i_D r_D ; \psi_D = l_{Dl} i_D + l_{dm} \left(i_d + i_D + i_F \right) \tag{5.67}$$

$$\frac{1}{\omega_b} \frac{d}{dt} \psi_Q = -i_Q r_Q ; \psi_Q = l_{Ql} i_Q + l_{qm} \left(i_q + i_Q \right)$$

$$2H \frac{d}{dt} \omega_r = t_{shaft} - t_e ; t_{shaft} = \frac{T_{shaft}}{T_{eb}} ; t_e = \frac{T_e}{T_{eb}}$$

$$t_e = -\left(\psi_d i_q - \psi_q i_d \right) ; \frac{1}{\omega_b} \frac{d\theta_{er}}{dt} = \omega_r ; \theta_{er} - in\ radians$$

with t_e equal to the P.U. torque, which is positive when opposite to the direction of motion (generator mode).

The Park transformation (matrix) in P.U. variables basically retains its original form. Its usage is essential in making the transition between the real machine and d–q model voltages (in general). $v_d(t)$, $v_q(t)$, $v_f(t)$, and $t_{shaft}(t)$ are needed to investigate any transient or steady-state regime of the machine. Finally, the stator currents of the d–q model (i_d, i_q) are transformed back into i_A, i_B, i_C so as to find the real machine stator currents behavior for the case in point.

The field-winding current I_f and the damper cage currents I_D, I_Q are the same for the d–q model and the original machine. Notice that all the quantities in Equation 5.67 are reduced to stator and are, thus, directly related in P.U. quantities to stator base quantities.

In Equation 5.67, all quantities but time t and H are in P.U. measurements. (Time t and inertia H are given in seconds, and ω_b is given in rad/sec.) Equation 5.67 represents the d–q model of a three-phase

SG with single damper circuits along rotor orthogonal axes d and q. Also, the coupling of windings along axes d and q, respectively, is taking place only through the main (airgap) flux linkage.

Magnetic saturation is not yet included, and only the fundamental of airgap flux distribution is considered.

Instead of P.U. inductances l_{dm}, l_{qm}, l_{fl}, l_{Dl}, l_{Ql}, the corresponding reactances may be used: x_{dm}, x_{qm}, x_{fl}, x_{Dl}, x_{Ql}, as the two sets are identical (in numbers, in P.U.). Also, $l_d = l_{sl} + l_{dm}$, $x_d = x_{sl} + x_{dm}$, $l_q = l_{sl} + l_{dm}$, $x_q = x_{sl} + x_{qm}$.

5.5 The Steady State via the *d–q* Model

During steady state, the stator voltages and currents are sinusoidal, and the stator frequency ω_1 is equal to rotor electrical speed $\omega_r = \omega_1 =$ constant:

$$V_{A,B,C}(t) = V\sqrt{2}\cos\left[\omega_1 - (i-1)\frac{2\pi}{3}\right]$$

$$I_{A,B,C}(t) = I\sqrt{2}\cos\left[\omega_1 - \varphi_1 - (i-1)\frac{2\pi}{3}\right]$$

$$(5.68)$$

Using the Park transformation with $\theta_{er} = \omega_1 t + \theta_0$ the *d–q* voltages are obtained:

$$V_{d0} = \frac{2}{3}\left(V_A(t)\cos(-\theta_{er}) + V_B(t)\cos\left(-\theta_{er} + \frac{2\pi}{3}\right) + V_C(t)\cos\left(-\theta_{er} - \frac{2\pi}{3}\right)\right)$$

$$V_{q0} = \frac{2}{3}\left(V_A(t)\sin(-\theta_{er}) + V_B(t)\sin\left(-\theta_{er} + \frac{2\pi}{3}\right) + V_C(t)\cos\left(-\theta_{er} - \frac{2\pi}{3}\right)\right)$$

$$(5.69)$$

Making use of Equation 5.68 in Equation 5.69 yields the following:

$$V_{d0} = V\sqrt{2}\cos\theta_0$$

$$V_{q0} = -V\sqrt{2}\sin\theta_0$$

$$(5.70)$$

In a similar way, we obtain the currents I_{d0} and I_{q0}:

$$I_{d0} = I\sqrt{2}\cos(\theta_0 + \varphi_1)$$

$$I_{q0} = -I\sqrt{2}\sin(\theta_0 + \varphi_1)$$

$$(5.71)$$

Under steady state, the *d–q* model stator voltages and currents are DC quantities. Consequently, for steady state, we should consider $d/dt = 0$ in Equation 5.67:

$$V_{d0} = \omega_r \Psi_{q0} - I_{d0}r_s; \Psi_{q0} = l_{sl}I_{q0} + l_{qm}I_{q0}$$

$$V_{q0} = -\omega_r \Psi_{d0} - I_{q0}r_s; \Psi_{d0} = l_{sl}I_{d0} + l_{dm}\left(I_{d0} + I_{f0}\right)$$

$$V_{f0} = r_f I_{f0}; \Psi_{f0} = l_{fl}I_{f0} + l_{dm}\left(I_{d0} + I_{f0}\right)$$

$$I_{D0} = I_{Q0} = 0; \Psi_{D0} = l_{dm}(I_{d0} + I_{f0}); l_d = l_{dm} + l_{sl}$$

$$t_e = -\left(\Psi_{d0}I_{q0} - \Psi_{q0}I_{d0}\right); \Psi_{Q0} = l_{qm}I_{q0}; l_q = l_{qm} + l_{sl}$$

$$(5.72)$$
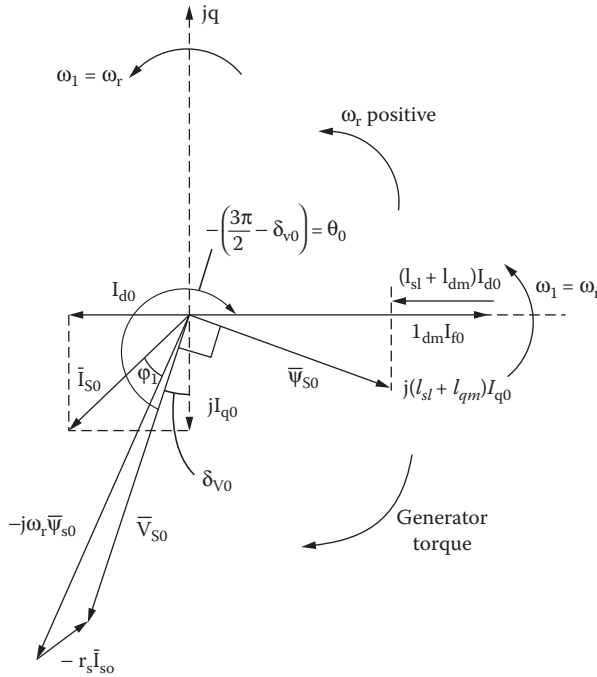
FIGURE 5.5 The space-phasor (vector) diagram of synchronous generators.

We may now introduce space phasors for the stator quantities:

$$\overline{\Psi}_{s0} = \Psi_{d0} + j\Psi_{q0}$$

$$\overline{I}_{s0} = I_{d0} + jI_{q0} \tag{5.73}$$

$$\overline{V}_{s0} = V_{d0} + jV_{q0}$$

The stator equations in Equation 5.72 thus become

$$\overline{V}_{s0} = -r_s\overline{I}_{s0} - j\omega_r\overline{\Psi}_{s0} \tag{5.74}$$

The space-phasor (or vector) diagram corresponding to Equation 5.73 is shown in Figure 5.5. With $\varphi_1 > 0$, both the active and reactive power delivered by the SG are positive. This condition implies that I_{d0} goes against I_{f0} in the vector diagram; also, for generating, I_{q0} falls along the negative direction of axis q. Notice that axis q is ahead of axis d in the direction of motion, and for $\varphi_1 > 0$, $\overline{I}_{s0}$ and $\overline{V}_{s0}$ are contained in the third quadrant. Also, the positive direction of motion is the trigonometric one. The voltage vector $\overline{V}_{s0}$ will stay in the third quadrant (for generating), while $\overline{I}_{s0}$ may be placed either in the third or fourth quadrant. We may use Equation 5.71 to calculate the stator currents I_{d0}, I_{q0} provided that V_{d0}, V_{q0} are known.

The initial angle θ_0 of Park transformation represents, in fact, the angle between the rotor pole (*d* axis) axis and the voltage vector angle. It may be seen from Figure 5.5 that axis *d* is behind V_{s0}, which explains why

$$\theta_0 = -\left(\frac{3\pi}{2} - \delta_{V0}\right) \tag{5.75}$$

Making use of Equation 5.74 in Equation 5.70, we obtain the following:

$$V_{d0} = -V\sqrt{2}\sin\delta_{V0} < 0$$

$$V_{q0} = -V\sqrt{2}\cos\delta_{V0} < 0$$

$$I_{d0} = -I\sqrt{2}\sin(\delta_{V0} + \varphi_1) <> 0 \qquad (5.76)$$

$$I_{q0} = -I\sqrt{2}\cos(\delta_{V0} + \varphi_1) < 0 \quad \textit{for generating}$$

The active and reactive powers P_1 and Q_1 are, as expected,

$$P_1 = \frac{3}{2}\left(V_{d0}I_{d0} + V_{q0}I_{q0}\right) = 3VI\cos\varphi_1$$

$$(5.77)$$

$$Q_1 = \frac{3}{2}\left(V_{d0}I_{q0} - V_{q0}I_{d0}\right) = 3VI\sin\varphi_1$$

In P.U. quantities, $v_{d0} = -v \times \sin\delta_{v0}$, $v_{q0} = -v\cos\delta_{v0}$, $i_{d0} = -i\sin(\delta_{v0} + \varphi_1)$, and $i_{q0} = -i\cos(\delta_{v0} + \varphi_1)$. The no-load regime is obtained with $I_{d0} = I_{q0} = 0$, and thus,

$$V_{d0} = 0$$

$$(5.78)$$

$$V_{q0} = -\omega_r\Psi_{d0} = -\omega_r l_{dm}I_{f0} = -V/\sqrt{2}$$

For no load in Equation 5.74, $\delta_v = 0$ and $I = 0$. V_0 is the no-load phase voltage (RMS value). For the steady-state short-circuit $V_{d0} = V_{q0} = 0$ in Equation 5.72. If, in addition, $r_s \approx 0$, then $I_{qs} = 0$, and

$$I_{d0sc} = \frac{-l_{dm}I_{f0}}{l_d};$$

$$(5.79)$$

$$I_{sc3} = I_{d0sc}/\sqrt{2}$$

where I_{sc3} is the phase short-circuit current (RMS value).

Example 5.1

A hydrogenerator with 200 MVA, 24 kV (star connection), 60 Hz, unity power factor, at 90 rpm has the following P.U. parameters: $l_{dm} = 0.6$, $l_{qm} = 0.4$, $l_{sl} = 0.15$, $r_s = 0.003$, $l_{fl} = 0.165$, and $r_f = 0.006$. The field circuit is supplied at 800 V_{dc}. ($V_f^r = 800$ V).

When the generator works at rated MVA, $\cos\varphi_1 = 1$ and rated terminal voltage, calculate the following:

1. Internal angle δ_{V0}
2. P.U. values of V_{d0}, V_{q0}, I_{d0}, I_{q0}
3. Airgap torque in P.U. quantities and in Nm
4. P.U. field current I_{f0} and its actual value in Amperes

Solution

1. The vector diagram is simplified as $\cos\varphi_1 = 1$ ($\varphi_1 = 0$), but it is worth deriving a formula to directly calculate the power angle δ_{V0}.

Using Equation 5.70 and Equation 5.71 in Equation 5.72 yields the following:

$$\delta_{V0} = \tan^{-1}\left(\frac{\omega_1 l_q I \cos\varphi_1 - r_s I \sin\varphi_1}{V + r_s I \cos\varphi_1 + \omega_1 l_q I \sin\varphi_1}\right)$$

with $\varphi_1 = 0$ and $\omega_1 = 1$, $I = 1$ P.U. (rated current), and $V = 1$ P.U. (rated voltage):

$$\delta_{V0} = \tan^{-1}\frac{1 \times 0.45 \times 1 \times 1 - 0.0}{1 + 0.003 \times 1 \times 1 \times 0} = 24.16^0$$

2. The field current can be calculated from Equation 5.72:

$$i_{f0} = \frac{-V_{q0} - I_{q0}r_s - \omega_r l_d I_{d0}}{\omega_r l_{dm}} = \frac{0.912 + 0.912 \times 0.003 + 1\cdot\left(0.6 + 0.15\right)0.4093}{1.0 \cdot 0.6} = 2.036 \ P.U.$$

The base current is as follows:

$$I_0 = I_n\sqrt{2} = \frac{S_n \cdot \sqrt{2}}{\sqrt{3}V_{nl}} = \frac{200 \cdot 10^6 \cdot \sqrt{2}}{\sqrt{3} \cdot 24000} = 6792 \ A$$

3. The field circuit P.U. resistance $r_f = 0.006$, and thus, the P.U. field circuit voltage, reduced to the stator is as follows:

$$V'_{f0} = r_f \cdot I_{f0} = 2.036 \times 0.006 = 12.216 \times 10^{-3} \ P.U.$$

Now with $V'_f = 800$ V, the reduction to stator coefficient K_f for field current is

$$K_f = \frac{2}{3}\frac{V_f^r}{v_{f0} \cdot V_b} = \frac{2}{3}\frac{800}{12.216 \times 10^{-3} \cdot \frac{24000}{\sqrt{3}} \cdot \sqrt{2}} \approx 2.224$$

Consequently, the field current (in Amperes) I_{f0}^r is

$$I_{f0}^r = \frac{i_{f0} \cdot I_b}{K_f} = \frac{2.036 \cdot 6792}{2.224} = 6218 \ A$$

So, the excitation power: $P_{exc} = V_{f0}^r I_{f0}^r = 800 \times 6218 = 4.9744 \ MW$.

4. The P.U. electromagnetic torque is

$$t_e \approx p_e + r_s I^2 = 1.0 + 0.003 \cdot 1^2 = 1.003$$

The torque in Nm is ($2p_1 = 80$ poles) as follows:

$$T_e = t_e \cdot T_{eb} = 1.003 \times \frac{200 \times 10^6}{2\pi \cdot 60 / 40} = 21.295 \times 10^6 \ Nm(!)$$

5.6 The General Equivalent Circuits

Replace d/dt in the P.U. d–q model (Equation 5.67) by using the Laplace operator s/ω_b, which means that the initial conditions are implicitly zero. If they are not, their values should be added.

The general equivalent circuits illustrate Equation 5.67, with d/dt replaced by s/ω_b after separating the main flux linkage components Ψ_{dm}, Ψ_{qm}:

$$\Psi_d = l_{sl}I_d + \Psi_{dm}; \Psi_q = l_{sl}I_q + \Psi_{qm}$$

$$\Psi_{dm} = l_{dm}\left(I_d + I_D + I_f\right); \Psi_{qm} = l_{qm}\left(I_q + I_Q\right)$$

$$\Psi_f = l_{fl}I_f + \Psi_{dm}; \Psi_D = l_{sl}I_D + \Psi_{dm} \tag{5.80}$$

$$\left(r_0 + \frac{s}{\omega_b}l_0\right)i_0 = -V_0$$

with

$$\left(r_f + \frac{s}{\omega_b}l_{fl}\right)I_f - V_f = -\frac{s}{\omega_b}\Psi_{dm}$$

$$\left(r_D + \frac{s}{\omega_b}l_{Dl}\right)I_D = -\frac{s}{\omega_b}\Psi_{dm}$$

$$\left(r_Q + \frac{s}{\omega_b}l_{Ql}\right)I_Q = -\frac{s}{\omega_b}\Psi_{qm} \tag{5.81}$$

$$\left(r_S + \frac{s}{\omega_b}l_{sl}\right)I_d + V_d - \omega_r\Psi_q = -\frac{s}{\omega_b}\Psi_{dm}$$

$$\left(r_S + \frac{s}{\omega_b}l_{sl}\right)I_q + V_q + \omega_r\Psi_d = -\frac{s}{\omega_b}\Psi_{qm}$$

Equation 5.81 evidentiates three circuits in parallel along axis d and two equivalent circuits along axis q. It is also implicit that the coupling of the circuits along axis d and q is performed only through the main flux components Ψ_{dm} and Ψ_{qm}. Magnetic saturation and frequency effects are not yet considered.

Based on Equation 5.81, the general equivalent circuits of SG are shown in Figure 5.6a and Figure 5.6b. A few remarks on Figure 5.6 are as follows:

- The magnetization current components I_{dm} and I_{qm} are defined as the sum of the d–q model currents:

$$I_{dm} = I_d + I_D + I_f;$$

$$I_{qm} = I_q + I_Q \tag{5.82}$$

- There is no magnetic coupling between the orthogonal axes d and q, because magnetic saturation is either ignored or considered separately along each axis as follows:

$$l_{sl}\left(i_s\right); l_{dm}\left(I_{dm}\right); l_{sl}\left(I_s\right), l_{qm}\left(I_{qm}\right); I_s = \sqrt{I_d^2 + I_q^2}$$
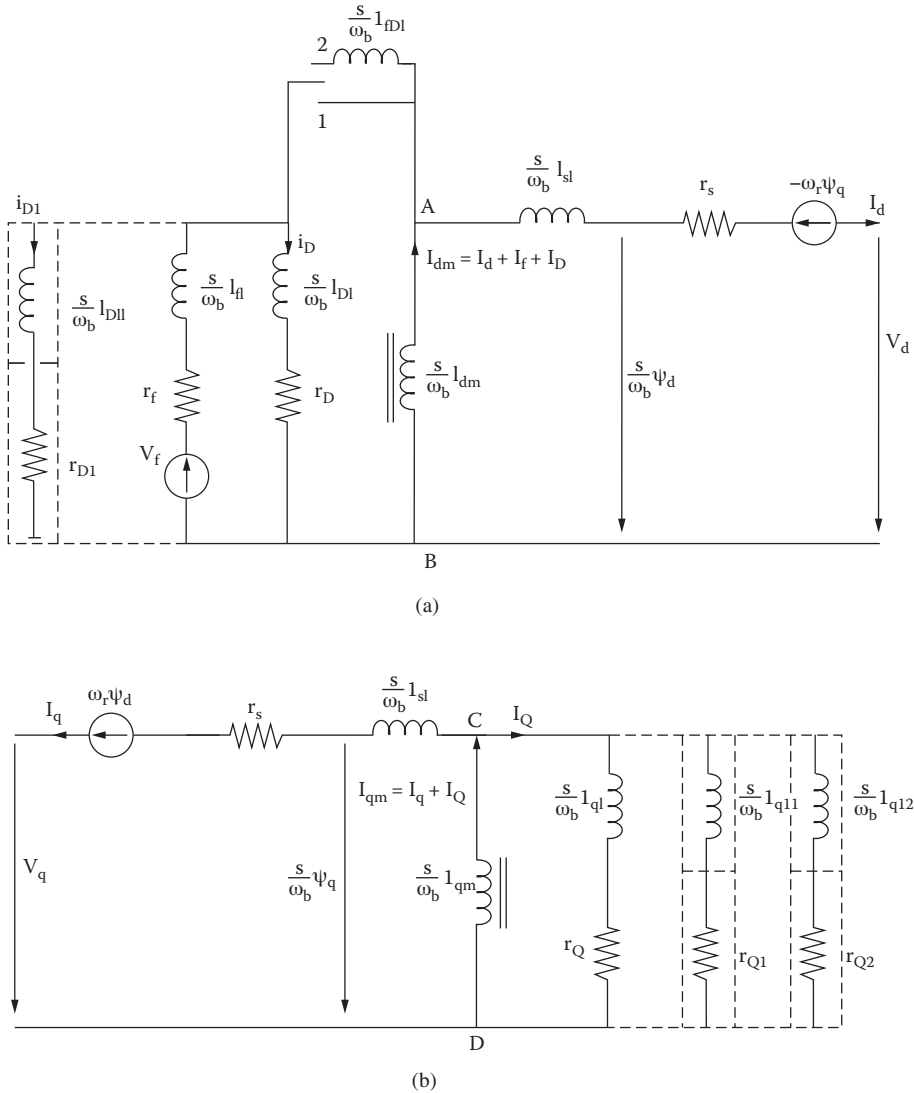
FIGURE 5.6 General equivalent circuits of synchronous generators: (a) along axis d and (b) along axis q.

- Should the frequency (skin) effect be present in the rotor damper cage (or in the rotor pole solid iron), additional rotor circuits are added in parallel. In general, one additional circuit along axis d and two along axis q are sufficient even for solid rotor pole SGs (Figure 5.6a and Figure 5.6b). In these cases, additional equations have to be added to Equation 5.81, but their composure is straightforward.

- Figure 5.6a also exhibits the possibility of considering the additional, leakage type, flux linkage (inductance, l_{fDl}) between the field and damper cage windings, in salient pole rotors. This inductance is considered instrumental when the field-winding parameter identification is checked after the stator parameters were estimated in tests with measured stator variables. Sometimes, l_{fDl} is estimated as negative.

- For steady state, $s = 0$ in the equivalent circuits, and thus, the voltages V_{AB} and V_{CD} are zero. Consequently, $I_{D0} = I_{Q0} = 0$, $V_{f0} = -r_f I_{f0}$ and the steady state d–q model equations may be "read" from Figure 5.6a and Figure 5.6b.

- The null component voltage equation in Equation 5.80:

$$V_0 + \left(r_0 + \frac{s}{\omega_b} l_0 \right) i_0 = 0$$

does not appear, as expected, in the general equivalent circuit because it does not interfere with the main flux fundamental. In reality, the null component may produce some eddy currents in the rotor cage through its third space-harmonic mmf.

5.7   Magnetic Saturation Inclusion in the *d–q* Model

The magnetic saturation level is, in general, different in various regions of an SG cross-section. Also, the distribution of the flux density in the airgap is not quite sinusoidal. However, in the *d–q* model, only the flux-density fundamental is considered. Further, the leakage flux path saturation is influenced by the main flux path saturation. A realistic model of saturation would mean that all leakage and main inductances depend on all currents in the *d–q* model. However, such a model would be too cumbersome to be practical.

Consequently, we will present here only two main approximations of magnetic saturation inclusion in the *d–q* model from the many proposed so far [2–7]. These two appear to us to be representative. Both include cross-coupling between the two orthogonal axes due to main flux path saturation. While the first presupposes the existence of a unique magnetization curve along axes *d* and *q*, respectively, in relation to total mmf ($I_m = \sqrt{I_{dm}^2 + I_{qm}^2}$), the second curve fits the family of curves $\Psi_{dm}^*(I_{dm}, I_{qm}), \Psi_{qm}^*(I_{dm}, I_{qm})$, keeping the dependence on both I_{dm} and I_{qm}.

In both models, the leakage flux path saturation is considered separately by defining transient leakage inductances $l_{sl}^t, l_{Dl}^t, l_{fl}^t$:

$$l_{sl}^t = l_{sl} + \frac{\partial l_{sl}}{\partial i_s} i_s \leq l_{sl}; I_s = \sqrt{I_d^2 + I_q^2}$$

$$l_{Dl}^t = l_{Dl} + \frac{\partial l_{Dl}}{\partial i_D} i_D < l_{Dl}$$

$$l_{fl}^t = l_{fl} + \frac{\partial l_{fl}}{\partial i_f} i_f < l_{fl}$$

(5.83)

$$l_{Ql}^t = l_{Ql} + \frac{\partial l_{Ql}}{\partial i_Q} i_Q < l_{Ql}$$

Each of the transient inductances in Equation 5.83 is considered as being dependent on the respective current.

5.7.1   The Single *d–q* Magnetization Curves Model

According to this model of main flux path saturation, the distinct magnetization curves along axes *d* and *q* depend only on the total magnetization current I_m [2, 3].

$$\Psi_{dm}^*\left(I_m \right) \neq \Psi_{qm}^*\left(I_m \right); I_m = \sqrt{I_{dm}^2 + I_{qm}^2}$$

$$I_{dm} = I_d + I_D + I_f$$

(5.84)

$$I_{qm} = I_q + I_Q$$

Inside figure:
$\psi^{*}{}_{dm}(I_m)$

$\psi^{*}{}_{qm}(I_m)$

$\psi^{*}{}_{dm}$

$\psi^{*}{}_{qm}$

$I_m = \sqrt{(I_d + I_D + I_f)^2 + (I_q + I_Q)^2}$

I_m
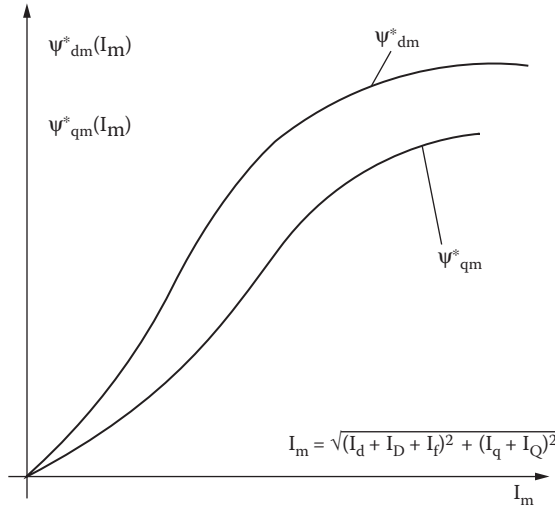
FIGURE 5.7 The unique *d–q* magnetization curves.

Note that the two distinct, but unique, *d* and *q* axes magnetization curves shown in Figure 5.7 represent a disputable approximation. It is only recently that finite element method (FEM) investigations showed that the concept of unique magnetization curves does not hold with the SG for underexcited (draining reactive power) conditions [4]: $I_m < 0.7$ P.U. For $I_m > 0.7$, the model apparently works well for a wide range of active and reactive power load conditions. The magnetization inductances l_{dm} and l_{qm} are also functions of I_m, only

$$\Psi_{dm} = l_{dm}\left(I_m\right) \cdot I_{dm}$$
$$\Psi_{qm} = l_{qm}\left(I_m\right) \cdot I_{qm}$$

(5.85)

with

$$l_{dm}\left(I_m\right) = \frac{\Psi^{*}_{dm}\left(I_m\right)}{I_m}$$

$$l_{qm}\left(I_m\right) = \frac{\Psi^{*}_{qm}\left(I_m\right)}{I_m}$$

(5.86)

Notice that the $\Psi^{*}_{dm}(I_m), \Psi^{*}_{qm}(I_m)$ may be obtained through tests where either only one or both components (I_{dm}, I_{qm}) of magnetization current I_m are present. This detail should not be overlooked if coherent results are to be expected. It is advisable to use a few combinations of I_{dm} and I_{qm} for each axis and use curve-fitting methods to derive the unique magnetization curves $\Psi^{*}_{dm}(I_m), \Psi^{*}_{qm}(I_m)$. Based on Equation 5.85 and Equation 5.86, the main flux time derivatives are obtained:

$$\frac{d\Psi_{dm}}{dt} = \frac{d\Psi^{*}_{qm}}{dI_m}\frac{dI_m}{dt} \cdot \frac{I_{dm}}{I_m} + \frac{\Psi^{*}_{dm}}{I_m^2}\left(I_m \frac{dI_{dm}}{dt} - I_{dm}\frac{dI_m}{dt}\right)$$

$$\frac{d\Psi_{qm}}{dt} = \frac{d\Psi^{*}_{qm}}{dI_m}\frac{dI_m}{dt} \cdot \frac{I_{qm}}{I_m} + \frac{\Psi^{*}_{qm}}{I_m^2}\left(I_m \frac{dI_{qm}}{dt} - I_{qm}\frac{dI_m}{dt}\right)$$

(5.87)

with

$$\frac{dI_m}{dt} = \frac{I_{qm}}{I_m}\frac{dI_{qm}}{dt} + \frac{I_{dm}}{I_m}\frac{dI_{dm}}{dt} \tag{5.88}$$

Finally,

$$\frac{d\Psi_{dm}}{dt} = l_{ddm}\frac{dI_{dm}}{dt} + l_{qdm}\frac{dI_{qm}}{dt}$$
$$\frac{d\Psi_{qm}}{dt} = l_{dqm}\frac{dI_{dm}}{dt} + l_{qqm}\frac{dI_{qm}}{dt} \tag{5.89}$$

$$l_{ddm} = l_{dmt}\frac{I_{dm}^2}{I_m^2} + l_{dm}\frac{I_{qm}^2}{I_m^2}$$
$$l_{qqm} = l_{qmt}\frac{I_{qm}^2}{I_m^2} + l_{qm}\frac{I_{dm}^2}{I_m^2} \tag{5.90}$$

$$l_{dqm} = l_{qdm} = \left(l_{dmt} - l_{dm}\right)I_{dm}\frac{I_{qm}}{I_m^2}$$
$$l_{dmt} - l_{dm} = l_{qmt} - l_{qm} \tag{5.91}$$

$$l_{dmt} = \frac{d\Psi_{dm}^*}{dI_m}$$
$$l_{qmt} = \frac{d\Psi_{qm}^*}{dI_m} \tag{5.92}$$

The equality of coupling transient inductances $l_{dqm} = l_{qdm}$ between the two axes is based on the reciprocity theorem. l_{dmt} and l_{qmt} are the so-called differential d and q axes magnetization inductances, while l_{ddm} and l_{qqm} are the transient magnetization self-inductances with saturation included. All of these inductances depend on both I_{dm} and I_{qm}, while $l_{dm}, l_{dmt}, l_{qm}, l_{qmt}$ depend only on I_m.

For the situation when DC premagnetization occurs, the differential magnetization inductances l_{dmt} and l_{qmt} should be replaced by the so-called incremental inductances l_{dm}^i, l_{qm}^i:

$$l_{dm}^i = \frac{\Delta\Psi_{dm}^*}{\Delta I_m}$$
$$l_{qm}^i = \frac{\Delta\Psi_{qm}^*}{\Delta I_m} \tag{5.93}$$

l_{dm}^i and l_{qm}^i are related to the incremental permeability in the iron core when a superposition of DC and alternating current (AC) magnetization occurs (Figure 5.8).

The normal permeability of iron $\mu_n = B_m/H_m$ is used when calculating the magnetization inductances l_{dm} and l_{qm}: $\mu_d = dB_m/dH_m$ for l_{dm}^t and l_{qm}^t, and $\mu_i = \Delta B_m/\Delta H_m$ (Figure 5.8) for the incremental magnetization inductances l_{md}^i and l_{mq}^i.
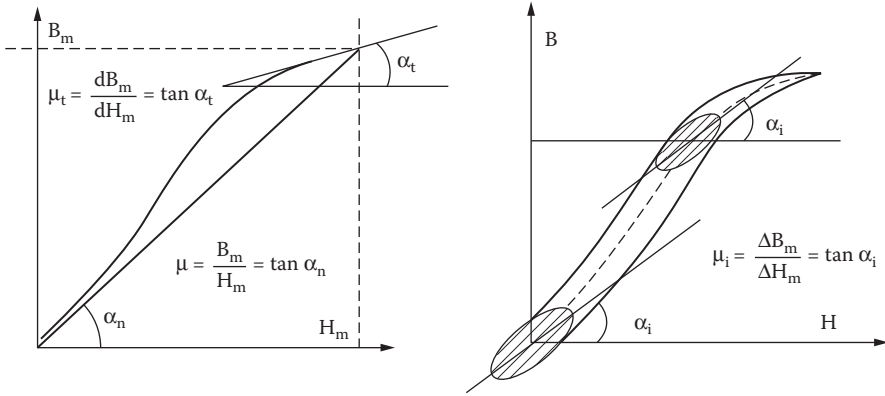
FIGURE 5.8 Iron permeabilities.

For the incremental inductances, the permeability μ_i corresponds to a local small hysteresis cycle (in Figure 5.8), and thus, $\mu_i < \mu_d < \mu_n$. For zero DC premagnetization and small AC voltages (currents) at standstill, for example, $\mu_i \approx (100 - 150)\,\mu_0$, which explains why the magnetization inductances correspond to l_{md}^i and l_{mq}^i rather than to l_{dm} and l_{qm} and are much smaller than the latter (Figure 5.9).

Once $l_{dm}(I_m), l_{qm}(I_m), l_{dm}^t(I_m), l_{qm}^t(I_m), l_{dm}^i(I_m), l_{qm}^i(I_m)$ are determined, either through field analysis or through experiments, then $l_{ddm}(I_{dm}, I_{qm}), l_{qqm}(I_{dm}, I_{qm})$ may be calculated with I_{dm} and I_{qm} given. Interpolation through tables or analytical curve fitting may be applied to produce easy-to-use expressions for digital simulations.

The single unique d–q magnetization curves model included the cross-coupling implicitly in the expressions of Ψ_{dm} and Ψ_{qm}, but it considers it explicitly in the $d\Psi_{dm}/dt$ and $d\Psi_{qm}/dt$ expressions, that is, in the transients. Either with currents $I_{dm}, I_{qm}, I_f, I_D, I_Q, \omega_r, \theta_{er}$ or with flux linkages $\Psi_{dm}, \Psi_{qm}, \Psi_f, \Psi_D, \Psi_Q, \omega_r, \theta_{er}$ (or with quite a few intermediary current, flux-linkage combinations) as variables, models based on the same concepts may be developed and used rather handily for the study of both steady states and transients [5]. The computation of $\Psi_{dm}^*(I_m), \Psi_{qm}^*(I_m)$ functions or their measurement from standstill tests is straightforward.

This tempting simplicity is payed for by the limitation that the unique d–q magnetization curves concept does not seem to hold when the machine is notably underexcited, with the emf lower than the terminal voltage, because the saturation level is smaller despite the fact that I_m is about the same as that for the lagging power factor at constant voltage [4].
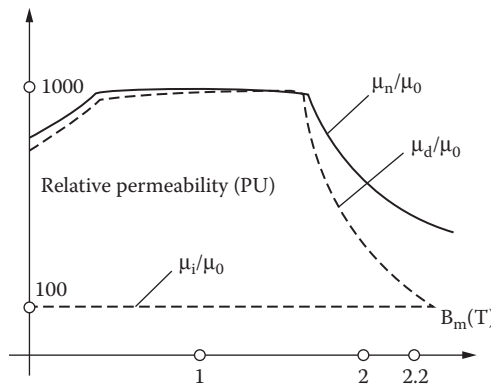
FIGURE 5.9 Typical per unit (P.U.) normal, differential, and incremental permeabilities of silicon laminations.

This limitation justifies the search for a more general model that is valid for the whole range of the active (reactive) power capability envelope of the SG. We call this the multiple magnetization curve model.

5.7.2 The Multiple *d–q* Magnetization Curves Model

This kind of model presupposes that the *d* and *q* axes flux linkages Ψ_d and Ψ_q are explicit functions of I_d, I_q, I_{dm}, I_{qm}:

$$\Psi_d = l_{sl}I_d + l_{dq}\left(I_q + I_Q\right) + l_{dm}\left(I_f + I_D + I_d\right) = l_{sl}I_d + l_{dq}I_{qm} + l_{dms}I_{dm} = l_{sl}I_d + \Psi_{dms}$$

$$\Psi_q = l_{sl}I_d + l_{qm}\left(I_q + I_Q\right) + l_{dq}\left(I_d + I_D + I_f\right) = l_{sl}I_q + l_{qms}I_{qm} + l_{dq}I_{dm} = l_{sl}I_q + \Psi_{qms}$$

$$\Psi_f = l_{fl}I_f + l_{dm}\left(I_f + I_D + I_d\right) + l_{dq}\left(I_q + I_Q\right) = l_{fl}I_f + l_{dms}I_{dm} + l_{dq}I_{qm} = l_{fl}I_f + \Psi_{dms} \tag{5.94}$$

$$\Psi_D = l_{Dl}I_D + l_{dm}\left(I_f + I_D + I_d\right) + l_{dq}\left(I_q + I_Q\right) = l_{Dl}I_D + l_{dms}I_{dm} + l_{dq}I_{qm} = l_{Dl}I_D + \Psi_{dms}.$$

$$\Psi_Q = l_{Ql}I_f + l_{dq}\left(I_f + I_D + I_d\right) + l_{qm}\left(I_q + I_Q\right) = l_{Ql}I_Q + l_{dq}I_{dm} + l_{qms}I_{qm} = l_{Ql}I_Q + \Psi_{qms}$$

Now, l_{dms} and l_{qms} are functions of both I_{dm} and I_{qm}. Conversely, $\Psi_{dms}(I_{dm}, I_{qm})$ and $\Psi_{qms}(I_{dm}, I_{qm})$ are two families of magnetization curves that have to be found either by computation or by experiments.

For steady state, $I_D = I_Q = 0$, but otherwise, Equation 5.94 holds. Basically, the Ψ_{dms} and Ψ_{qms} curves look like as shown in Figure 5.10:

$$\Psi_{dms} = l_{dms}(I_{dm}, I_{qm})I_{dm}$$

$$\Psi_{qms} = l_{qms}(I_{dm}, I_{qm})I_{qm} \tag{5.95}$$

Once this family of curves is acquired (by FEM analysis or by experiments), various analytical approximations may be used to curve-fit them adequately.

Then, with $\Psi_d, \Psi_q, \Psi_f, \Psi_D, \Psi_Q, \omega_r$, and θ_{er} as variables and I_f, I_D, I_Q, I_d, and I_q as dummy variables, the $\Psi_{dms}(I_{dm}, I_{qm}), \Psi_{qms}(I_{dm}, I_{qm})$ functions are used in Equation 5.94 to calculate iteratively each time step, the dummy variables.

When using flux linkages as variables, no additional inductances responsible for cross-coupling magnetic saturation need to be considered. As they are not constant, their introduction does not seem practical. However, such attempts keep reoccurring [6, 7], as the problem seems far from a definitive solution.
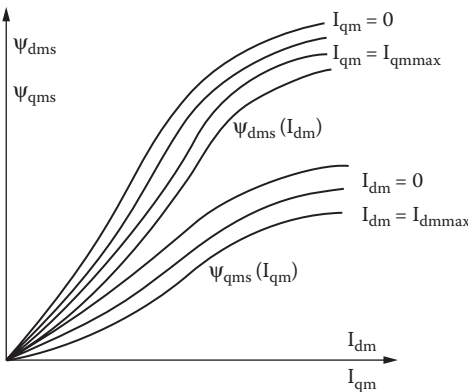
FIGURE 5.10 Family of magnetization curves.

Considering cross-coupling due to magnetic saturation seems to be necessary when calculating the field current, stator current, and power angle, under steady state for given active and reactive power and voltage, with an error less than 2% for the currents and around a 1° error for the power angle [4, 7]. Also, during large disturbance transients, where the main flux varies notably, the cross-coupling saturation effect is to be considered.

Though magnetic saturation is very important for refined steady state and for transient investigations, most of the theory of transients for the control of SGs is developed for constant parameter conditions — operational parameters is such a case.

5.8 The Operational Parameters

In the absence of magnetic saturation variation, the general equivalent circuits of SG (Figure 5.6) lead to the following generic expressions of operational parameters in the Ψ_d and Ψ_q operational expressions:

$$\Psi_d(s) = l_d(s) \cdot I_d(s) + g(s) v_{ex}(s) \ [P.U.]$$
$$\Psi_q(s) = l_q(s) \cdot I_q(s) \tag{5.96}$$

with

$$l_d(s) = \frac{\left(1 + sT_d'\right)\left(1 + sT_d''\right)}{\left(1 + sT_{d0}'\right)\left(1 + sT_{d0}''\right)} \cdot l_d \ [P.U.]$$

$$l_q(s) = \frac{\left(1 + sT_q''\right)}{\left(1 + sT_{q0}''\right)} \cdot l_q \ [P.U.]$$

$$g(s) = \frac{\left(1 + sT_D\right)}{\left(1 + sT_{d0}'\right)\left(1 + sT_{d0}''\right)} \cdot \frac{l_{dm}}{r_f} \left[P.U.\right] \tag{5.97}$$

Sparing the analytical derivations, the time constants $T_d', T_d'', T_{d0}', T_{d0}'', T_q', T_{q0}''$ have the following expressions:

$$T_d' \approx \frac{1}{\omega_b r_f}\left(l_{fl} + l_{fDl} + \frac{l_{dm} l_{sl}}{l_{dm} + l_{sl}}\right); [s]$$

$$T_d'' \approx \frac{1}{\omega_b r_D}\left(l_{Dl} + \frac{l_{dm} l_{fDl} l_{fl} + l_{dm} l_{sl} l_{fl} + l_{sl} l_{fDl} l_{fl}}{l_{dm} l_{fl} + l_{fl} l_{sl} + l_{dm} l_{fDl} + l_{sl} l_{fDl} + l_{fDl} l_{fl} + l_{dm} l_{sl}}\right); [s]$$

$$T_{d0}' \approx \frac{1}{\omega_b r_f}\left(l_{dm} + l_{fDl} + l_{fl}\right); [s] \tag{5.98}$$

$$T_{d0}'' \approx \frac{1}{\omega_b r_D}\left(l_{Dl} + \frac{l_{fl}(l_{dm} + l_{fDl})}{l_{fl} + l_{dm} + l_{fDl}}\right); [s]$$

$$T_q'' \approx \frac{1}{\omega_b r_Q}\left(l_{Ql} + \frac{l_{qm} l_{sl}}{l_{qm} + l_{sl}}\right); [s]$$

$$T_{q0}^{''} \approx \frac{1}{\omega_b r_Q}\left(l_{Ql} + l_{qm}\right); [s]$$

$$T_D \approx \frac{l_{Dl}}{\omega_b r_D}; [s]$$

<div align="right">(5.98 cont.)</div>

As already mentioned, with ω_b measured in rad/sec, the time constants are all in seconds, while all resistances and inductances are in P.U. values. The time constants differ between each other up to more than 100-to-1 ratios. T_{d0}' is of the order of seconds in large SGs, while T_d', T_{d0}'', T_{q0}'' are in the order of a few tenths of a second, T_d'', T_q'' in the order of a few tenths of milliseconds, and T_D in the order of a few milliseconds.

Such a broad spectrum of time constants indicates that the SG equations for transients (Equation 5.81) represent a stiff system. Consequently, the solution through numerical methods needs time integration steps smaller than the lowest time constant in order to correctly portray all occurring transients. The above time constants are catalog data for SGs:

- T_{d0}': d axis open circuit field winding (transient) time constant ($I_d = 0$, $I_D = 0$)
- T_{d0}'': d axis open circuit damper winding (subtransient) time constant ($I_d = 0$)
- T_d: d axis transient time constant ($I_D = 0$) — field-winding time constant with short-circuited stator but with open damper winding
- T_{d0}': d axis subtransient time constant — damper winding time constant with short-circuited field winding and stator
- T_{q0}'': q axis open circuit damper winding (subtransient) time constant ($I_q = 0$)
- T_q'': q axis subtransient time constant (q axis damper winding time constant with short-circuited stator)
- T_D: d axis damper winding self-leakage time constant

In the industrial practice of SGs, the limit — initial and final — values of operational inductances have become catalog data:

$$l_d^{''} = \lim_{\substack{s\to\infty \\ (t\to 0)}} l_d(s) = l_d \cdot \frac{T_d' T_d''}{T_{d0}' T_{d0}''}$$

$$l_d' = \lim_{\substack{s\to\infty \\ T_d''=T_{d0}''=0}} l_d(s) = l_d \cdot \frac{T_d'}{T_{d0}'}$$

$$l_d = \lim_{\substack{s\to 0 \\ t\to\infty}} l_d(s) = l_d \qquad\qquad (5.99)$$

$$l_q^{''} = \lim_{\substack{s\to\infty \\ t\to 0}} l_q(s) = l_q \frac{T_q''}{T_{q0}''}$$

$$l_q = \lim_{\substack{s\to 0 \\ t\to\infty}} l_q(s) = l_q$$

where
l_d'', l_d', l_d = the d axis subtransient, transient, and synchronous inductances
l_q'', l_q = the q axis subtransient and synchronous inductances
l_p = the Potier inductance in P.U. ($l_p \geq l_{sl}$)

Typical values of the time constants (in seconds) and subtransient and transient and synchronous inductances (in P.U.) are shown in Table 5.1.

As Table 5.1 suggests, various inductances and time constants that characterize the SG are constants. In reality, they depend on magnetic saturation and skin effects (in solid rotors), as suggested in previous

TABLE 5.1   Typical Synchronous Generator Parameter Values

Parameter	Two-Pole Turbogenerator	Hydrogenerators
l_d (P.U.)	0.9–1.5	0.6–1.5
l_q (P.U.)	0.85–1.45	0.4–1.0
l_d' (P.U.)	0.12–0.2	0.2–0.5
l_d'' (P.U.)	0.07–0.14	0.13–0.35
l_{fDl} (P.U.)	0.05–+0.05	0.05–+0.05
l_0 (P.U.)	0.02–0.08	0.02–0.2
l_p (P.U.)	0.07–0.14	0.15–0.2
r_s (P.U.)	0.0015–0.005	0.002–0.02
T_{d0}' (sec)	2.8–6.2	1.5–9.5
T_d' (sec)	0.35–0.9	0.5–3.3
T_d'' (sec)	0.02–0.05	0.01–0.05
T_{d0}'' (sec)	0.02–0.15	0.01–0.15
T_q'' (sec)	0.015–0.04	0.02–0.06
T_{q0}'' (sec)	0.04–0.08	0.05–0.09
l_q'' (P.U.)		0.2–0.45

Note: P.U. stands for per unit; sec stands for second(s).

paragraphs. There are, however, transient regimes where the magnetic saturation stays practically the same, as it corresponds to small disturbance transients. On the other hand, in high-frequency transients, the l_d and l_q variation with magnetic saturation level is less important, while the leakage flux paths saturation becomes notable for large values of stator and rotor current (the beginning of a sudden short-circuit transient).

To make the treatment of transients easier to approach, we distinguish here a few types of transients:

- Fast (electromagnetic) transients: speed is constant
- Electromechanical transients: electromagnetic + mechanical transients (speed varies)
- Slow (mechanical) transients: electromagnetic steady state; speed varies

In what follows, we will treat each of these transients in some detail.

5.9   Electromagnetic Transients

In fast (electromagnetic) transients, the speed may be considered constant; thus, the equation of motion is ignored. The stator voltage equations of Equation 5.81 in Laplace form with Equation 5.96 become the following:

$$-v_d(s) = r_s I_d + \frac{s}{\omega_b} l_d(s) I_d - \omega_r l_q(s) I_q + g(s) \frac{s}{\omega_b} v_f(s)$$

$$-v_q(s) = r_s I_q + \frac{s}{\omega_b} l_q(s) I_q + \omega_r \left[l_d(s) I_d + g(s) v_f(s) \right]$$

(5.100)

Note that ω_r is in relative units, and for rated rotor speed, $\omega_r = 1$.

If the initial values I_{d0} and I_{q0} of variables I_d and I_q are known and the time variation of $v_d(t)$, $v_q(t)$, and $v_f(t)$ may be translated into Laplace forms of $v_d(s)$, $v_q(s)$, and $v_f(s)$, then Equation 5.100 may be solved to obtain the $i_d(s)$ and $i_q(s)$:

$$
\begin{vmatrix} -v_d(s) & -g(s)\dfrac{s}{\omega_b}v_f(s) \\ -v_q(s) & -\omega_{r0}g(s)v_f(s) \end{vmatrix}
=
\begin{vmatrix} r_s + \dfrac{sl_d(s)}{\omega_b} & -\omega_{r0}l_q(s) \\ \omega_{r0}l_d(s) & r_s + \dfrac{s}{\omega_b}l_q(s) \end{vmatrix}
\begin{vmatrix} i_d(s) \\ i_q(s) \end{vmatrix}
$$

(5.101)

Though $I_d(s)$ and $I_q(s)$ may be directly derived from Equation 5.101, their expressions are hardly practical in the general case.

However, there are a few particular operation modes where their pursuit is important. The sudden three-phase short-circuit from no load and the step voltage or AC operation at standstill are considered here. To start, the voltage buildup at no load, in the absence of a damper winding, is treated.

Example 5.2: The Voltage Buildup at No Load

Apply Equation 5.101 for the stator voltage buildup at no load in an SG without a damper cage on the rotor when the 100% step DC voltage is applied to the field winding.

Solution

With I_d and I_q being zero, what remains from Equation 5.101 is as follows:

$$-v_d(s) = g(s)\frac{s}{\omega_b}v_f(s)$$

$$-v_q(s) = \omega_r \cdot g(s) \cdot v_f(s)$$

(5.102a)

The Laplace transform of a step function is applied to the field-winding terminals:

$$v_f(s) = \frac{v_f}{s}\omega_b$$

(5.102b)

The transfer function $g(s)$ from Equation 5.97, with $l_{Dl} = l_{fDl} = 0$, $v_D = 0$, and zero stator currents, is as follows:

$$g(s) = \frac{l_{dm}}{r_f} \times \frac{1}{1 + sT'_{d0}}$$

(5.103)

$$T'_{d0} = \frac{l_{dm} + l_{fl}}{r_f \cdot \omega_b}$$

(5.104)

Finally,

$$v_d(t) = -v_f \frac{l_{dm}}{\left(l_{dm} + l_{fl}\right)}e^{-\frac{t}{T'_{d0}}}$$

(5.105)

$$v_q(t) = -v_f \frac{\omega_r l_{dm}}{r_f}e^{-\frac{t}{T''_{d0}}}$$

(5.106)

with $\omega_r = 1$ P.U., $l_{dm} = 1.2$ P.U., $l_{fl} = 0.2$ P.U., $r_f = 0.003$ P.U., $v_{f0} = 0.003$ P.U., and $\omega_b = 2 \times 60 \times \pi$ = 377 rad/sec:

$$T'_{d0} = \frac{1.2 + 0.2}{0.003 \cdot 377} = 1.2378 \text{ sec}$$

$$v_d(t) = -0.003 \frac{1.2}{1.2 + 0.2} e^{-\frac{t}{1.2378}} = -2.5714 \times 10^{-3} \cdot e^{-t/1.2378} \ [P.U.]$$

$$v_q(t) = -0.003 \times 1 \times \frac{1.2}{0.003} \left(1 - e^{-\frac{t}{1.2378}}\right) = -1.2\left(1 - e^{-t/1.2378}\right) \ [P.U.]$$

The phase voltage of phase A is (Equation 5.30)

$$v_A(t) = v_d(t) \cos\omega_b t - v_q(t)\sin\omega_b t =$$

$$= -2.5714 \times 10^{-3} e^{-t/1.2378} \cos(\omega_b t + \theta_0) + 1.2\left(1 - e^{-t/1.2378}\right)\sin(\omega_b t + \theta_0) \ \left[P.U.\right]$$

For no load, from Equation 5.75, with zero power angle ($\delta_{v0} = 0$),

$$\theta_0 = -\frac{3\pi}{2}$$

In a similar way, $v_B(t)$ and $v_C(t)$ are obtained using Park inverse transformation.

The stator symmetrical phase voltages may be expressed simply in volts by multiplying the voltages in P.U. to the base voltage $V_b = V_n \times \sqrt{2}$; V_n is the base RMS phase voltage.

5.10 The Sudden Three-Phase Short-Circuit from No Load

The initial no-load conditions are characterized by $I_{d0} = I_{q0} = 0$. Also, if the field-winding terminal voltage is constant,

$$v_{f0} = I_{f0} \cdot r_f \tag{5.107}$$

From Equation 5.101, this time with $s = 0$ and $I_{d0} = I_{q0} = 0$, it follows that

$$\left(v_{d0}\right)_{s=0} = 0 \tag{5.108}$$

$$\left(v_{q0}\right)_{s=0} = -\omega_{r0} \frac{l_{dm}}{r_f} v_{f0}$$

So, already for the initial conditions, the voltage along axis d, v_{d0}, is zero under no load. For axis q, the no-load voltage occurs. To short-circuit the machine, we simply have to apply along axis q the opposite voltage $- v_{q0}$.

Notice that, as $v_f = v_{f0}$, $v_f(s) = 0$, Equation 5.101 becomes as follows:

$$\begin{vmatrix} 0 \\ -\dfrac{v_{q0} \cdot \omega_b}{s} \end{vmatrix} = \begin{vmatrix} r_s + \dfrac{s}{\omega_b} l_d(s) & -\omega_{r0} l_q(s) \\ \omega_{r0} l_d(s) & r_0 + \dfrac{s}{\omega_b} l_q(s) \end{vmatrix} \cdot \begin{vmatrix} I_d(s) \\ I_q(s) \end{vmatrix} \tag{5.109}$$

The solution of Equation 5.110 is straighforward, with

$$I_d^*(s) = \frac{-v_{q0}\omega_b^3\omega_r}{sl_d(s)\left[\omega_b^2\omega_r^2 + s^2 + sr_s\omega_b\left(\dfrac{1}{l_d(s)} + \dfrac{1}{l_q(s)}\right) + \dfrac{r_s^2\omega_b^2}{l_d(s)\cdot l_q(s)}\right]} \qquad (5.110)$$

As it is, $I_d(s)$ would be difficult to handle, so two approximations are made: the terms in r_s^2 are neglected, and

$$\frac{r_s\omega_b}{2}\left(\frac{1}{l_d(s)} + \frac{1}{l_q(s)}\right) \approx \frac{1}{T_a} = const. \qquad (5.111)$$

with

$$\frac{1}{T_a} \approx \frac{r_s\omega_b}{2}\left(\frac{1}{l_d''} + \frac{1}{l_q''}\right) \qquad (5.112)$$

With Equation 5.111 and Equation 5.112, Equation 5.110′ becomes

$$I_d(s) \approx \frac{-V_{q0}\omega_b^3\omega_r}{s\left(s^2 + \dfrac{2}{T_a}s + \omega_b^2\omega_r^2\right)} \cdot \frac{1}{l_d(s)} \qquad (5.113)$$

$$I_q(s) \approx \frac{-V_{q0}\omega_b^2\omega_r}{\left(s^2 + \dfrac{2}{T_a}s + \omega_b^2\omega_r^2\right)} \cdot \frac{1}{l_q(s)} \qquad (5.114)$$

Making use of Equation 5.96 and Equation 5.97, $1/l_d(s)$ and $1/l_q(s)$ may be expressed as follows:

$$\frac{1}{l_d(s)} = \frac{1}{l_d} + \left(\frac{1}{l_d'} - \frac{1}{l_d}\right)\frac{s}{s + 1/T_d'} + \left(\frac{1}{l_d''} - \frac{1}{l_d'}\right)\frac{s}{s + 1/T_d''} \qquad (5.115)$$

$$\frac{1}{l_q(s)} = \frac{1}{l_q} + \left(\frac{1}{l_q''} - \frac{1}{l_q}\right)\frac{s}{s + 1/T_q''} \qquad (5.116)$$

With T_d', T_q'' larger than $1/\omega_b$ and $\omega_r = 1.0$, after some analytical derivations with approximations, the inverse Laplace transforms of $I_d(s)$ and $I_q(s)$ are obtained:

$$I_d(t) \approx -v_{q0}\left[\frac{1}{l_d} + \left(\frac{1}{l_d'} - \frac{1}{l_d}\right)e^{-t/T_d'} + \left(\frac{1}{l_d''} - \frac{1}{l_d'}\right)e^{-t/T_d''} - \frac{1}{l_d''}e^{-t/T_a}\cos\omega_b t\right]$$

$$I_q(t) \approx -\frac{v_{q0}}{l_q''}e^{-1/T_a}\sin\omega_b t; \qquad (5.117)$$

$$I_d(t) = I_{d0} + I_d(t)$$

$$I_q(t) = I_{q0} + I_q(t)$$

The sudden phase short-circuit current from no load ($I_{d0} = I_{q0} = 0$) is obtained, making use of the following:

$$
\begin{aligned}
I_A(t) &= \left[I_d(t)\cos\left(\omega_b t + \gamma_0\right) - I_q(t)\sin\left(\omega_b t + \gamma_0\right) \right] = \\
&\quad -v_{q0} \left\{ \left[\frac{1}{l_d} + \left(\frac{1}{l_d'} - \frac{1}{l_d} \right) e^{-t/T_d'} + \left(\frac{1}{l_d''} - \frac{1}{l_d'} \right) e^{-t/T_d''} \right] \cos(\omega_b t + \gamma_0) \right. \\
&\quad \left. -\frac{1}{2}\left(\frac{1}{l_d''} - \frac{1}{l_q''} \right) e^{-t/T_a} - \frac{1}{2}\left(\frac{1}{l_d''} - \frac{1}{l_q''} \right) e^{-t/T_a} \cos\left(2\omega_b t + \gamma_0\right) \right\}
\end{aligned}
\tag{5.118}
$$

The relationship between $I_f(s)$ and $I_d(s)$ for the case in point ($v_f(s) = 0$) is

$$
I_f(s) = -g(s)\frac{s}{\omega_b} I_d(s)
\tag{5.119}
$$

Finally,

$$
I_f(t) = I_{f0} + I_{f0} \cdot \frac{\left(l_d - l_d'\right)}{l_d} \left[e^{-t/T_d'} - \left(1 - T_D/T_D''\right) e^{-t/T_d''} - \frac{T_D}{T_d''} e^{-t/T_a} \cos\omega_b t \right]
\tag{5.120}
$$

Typical sudden short-circuit currents are shown in Figure 5.11 (parts a, b, c, and d).
Further, the flux linkages $\Psi_d(s)$, $\Psi_q(s)$ (with $v_f(s) = 0$) are as follows:

$$
\begin{aligned}
\Psi_d(s) &= l_d(s)I_d(s) = \frac{-\omega_b^3 \omega_r^2}{\left(s^2 + \dfrac{2s}{T_a} + \omega_b^2 \omega_r^2 \right)} \cdot \frac{v_{q0}}{s} \\[2ex]
\Psi_q(s) &= l_q(s)I_q(s) = \frac{-\omega_b^2 v_{q0}\omega_r^2}{\left(s^2 + \dfrac{2s}{T_a} + \omega_b^2 \omega_r^2 \right)}
\end{aligned}
\tag{5.121}
$$

With $T_a \gg 1/\omega_b$, the total flux linkage components are approximately as follows:

$$
\begin{aligned}
\Psi_d(t) &= \Psi_{d0} + \Psi_d(t) \approx v_{q0} \times e^{-t/T_a} \times \cos\omega_b t \\
\Psi_q(t) &= 0 + \Psi_q(t) \approx -v_{q0} \times e^{-t/T_a} \times \sin\omega_b t
\end{aligned}
\tag{5.122}
$$

Note that due to various approximations, the final flux linkage in axes *d* and *q* are zero. In reality (with $r_s \neq 0$), none of them is quite zero.

The electromagnetic torque t_e (P.U.) is

$$
t_e(t) = -\left(\Psi_d(t)I_q(t) - \Psi_q(t)I_d(t) \right)
\tag{5.123}
$$

(a)

(b)

(c)

(d)
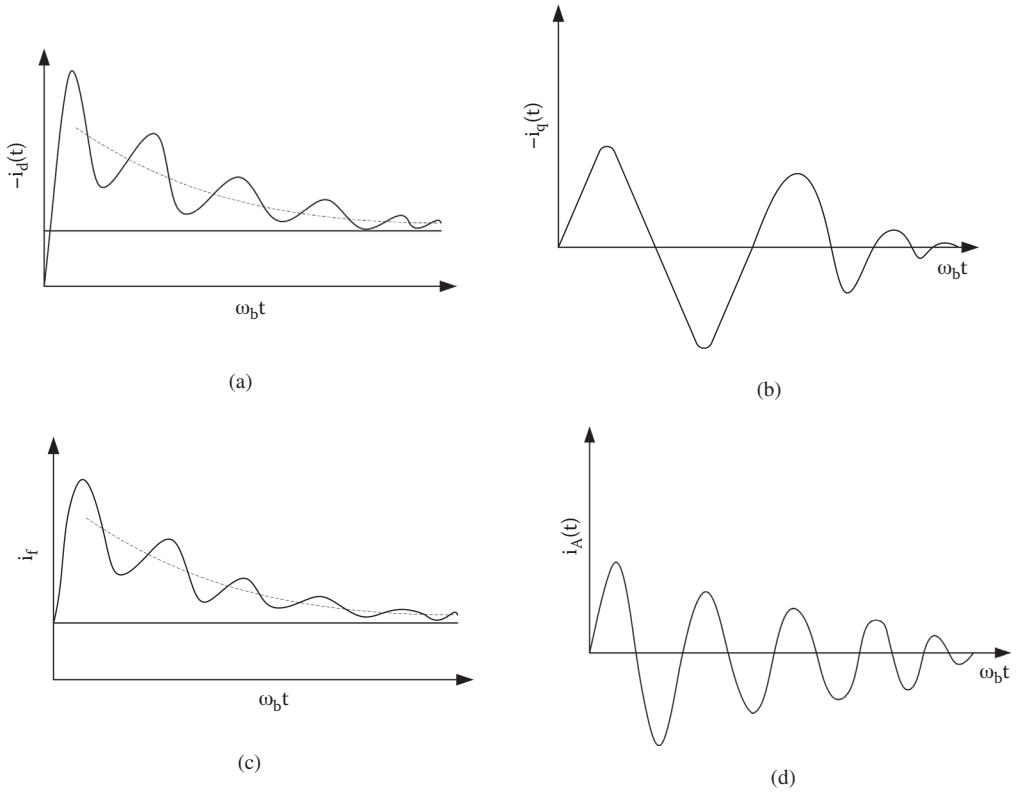
FIGURE 5.11 Sudden short-circuit currents: (a) $I_d(t)$, (b) $I_q(t)$, (c) $I_f(t)$, and (d) $I_A(t)$.

The above approximations ($r_a^2 \approx 0$, $T_a \gg 1/\omega_b$, $\omega_b = ct.$ T_d', $T_{d0}' \gg T_d''$, T_{d0}'', T_a, $r_a < sl_q(s)/\omega_b$) were proven to yield correct results in stator current waveform during unsaturated short-circuit — with given unsaturated values of inductance and time constant terms — within an error below 10%. It may be argued that this is a notable error, but at the same time, we should notice that instrumentation errors are within this range.

The use of Equation 5.118 and Equation 5.120 to estimate the various inductances and time constants, based on measured stator and field current transients during a provoked short-circuit at lower than rated no-load voltage, is included in the standards of both the American National Standards Institute (ANSI) and International Electrotechnical Commission (IEC). Traditionally, grapho-analytical methods of curve fitting were used to estimate the parameters from the sudden three-phase short-circuit. With today's available computing power, various nonlinear programming approaches to SG parameter estimation from short-circuit current versus time curve were proposed [8, 9].

Despite notable progress along this path, there are still uncertainties and notable errors, as both leakage and main flux path magnetic saturation are present and vary during short-circuit transients. In many cases, the speed also varies during short-circuit, while the model assumes it to be constant. To avoid the zero-sequence currents due to nonsimultaneous phase short-circuit, an ungrounded three-phase short-circuit should be performed. Moreover, additional damper cage circuits are to be added for solid rotor pole SGs (turbogenerators) to account for frequency (skin) effects. Sub-subtransient circuits and parameters are introduced to model these effects.

For most large SGs, the sudden three-phase short-circuit test, be it at lower no-load voltage and speed, may be performed only at the user's site, during comissioning, using the turbine as the controlled speed prime mover. This way, the speed during the short-circuit can be kept constant.
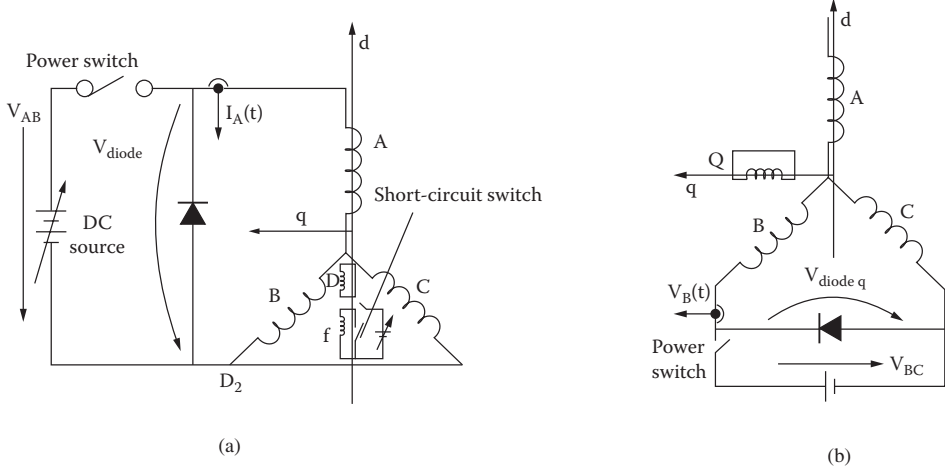
FIGURE 5.12 Arrangement for standstill voltage response transients: (a) axis d and (b) axis q.

5.11 Standstill Time Domain Response Provoked Transients

Flux (current) raise or decay tests may be performed at standstill, with the rotor aligned to axes d and q or for any given rotor position, in order to extract, by curve fitting, the stator current and field current time response for the appropriate SG model. Any voltage-versus-time signal may be applied, but the frequency response standstill tests have recently become accepted worldwide. All of these standstill tests are purely electromagnetic tests, as the speed is kept constant (zero in this case).

The situation in Figure 5.12a corresponds to axis d, while Figure 5.12b refers to axis q.

For axis d,

$$I_A + I_B + I_C = 0; V_B = V_C; V_A + V_B + V_C = 0$$

$$I_d(t) = \frac{2}{3}\left[I_A + I_B \cos\frac{2\pi}{3} + I_C \cos\left(-\frac{2\pi}{3}\right)\right] = I_A(t)$$

$$I_q(t) = 0$$

$$V_d(t) = \frac{2}{3}\left[V_A + V_B \cos\frac{2\pi}{3} + V_C \cos\left(-\frac{2\pi}{3}\right)\right] = V_A(t) \tag{5.124}$$

$$V_q(t) = 0$$

$$V_A - V_B = V_{diode} = V_A - \left(-\frac{V_A}{2}\right) = \frac{3}{2}V_A = \frac{3}{2}V_d(t)$$

$$V_{ABC}/I_A = \frac{3}{2}V_d/I_d$$

For axis q,

$$I_A = 0, I_B = -I_C$$

$$V_q = -\frac{2}{3}\left[V_A \sin(0) + V_B \sin\frac{2\pi}{3} + V_C \sin\left(-\frac{2\pi}{3}\right)\right] = -\frac{2}{3}(V_B - V_C)\cdot\frac{\sqrt{3}}{2} = -(V_B - V_C)/\sqrt{3} \tag{5.125}$$

$$I_q = -\frac{2}{3}\left[I_A \sin(0) + I_B \sin\frac{2\pi}{3} + I_C \sin\left(-\frac{2\pi}{3}\right) \right] = -\frac{2}{3} I_B \sqrt{3} = -2 I_B / \sqrt{3}$$

<div align="right">(5.125 cont.)</div>

$$V_q / I_q = \left(V_B - V_C\right)/2 I_B = \frac{V_{BC}}{2 I_B}; I_d = 0$$

Now, for axis *d*, we simply apply Equation 5.101, with $V_f(s) = 0$, if the field winding is short-circuited, and with $I_q = 0$, $\omega_{r0} = 0$. Also,

$$V_d = +\frac{2}{3} V_{ABC}$$

$$\frac{2}{3} V_{ABC} \cdot \frac{\omega_b}{s} = \left(r_s + \frac{s}{\omega_b} l_d(s) \right) I_d(s); I_d = I_A \tag{5.126}$$

$$I_f(s) = -\frac{s}{\omega_b} g(s) I_d(s)$$

For axis *q*, $I_d = 0$, $\omega_{r0} = 0$:

$$V_q = -\frac{V_{BC}}{\sqrt{3}}$$

$$-\frac{1}{\sqrt{3}} V_{BC} \cdot \frac{\omega_b}{s} = \left(r_s + \frac{s}{\omega_b} l_q(s) \right) I_q(s); \tag{5.127}$$

$$I_q = 2 I_B / \sqrt{3}$$

The standstill time-domain transients may be explored by investigating both the current rise for step voltage application or current decay when the stator is short-circuited through the freewheeling diode, after the stator was disconnected from the power source.

For current decay, the left-hand side of Equation 5.126 and Equation 5.127 should express only –2/3 V_{diode} in axis *d* and $\sqrt{3}\, V_{diode}$ in axis *q*. The diode voltage $V_{diode}(t)$ should be acquired through proper instrumentation.

For the standard equivalent circuits with $l_d(s)$, $l_q(s)$ having Equation 5.96, from Equation 5.126 and Equation 5.127,

$$I_d(s) = \frac{+\dfrac{2}{3} V_{AB0}(s)\omega_b}{s\left[r_s + \dfrac{s}{\omega_b} l_d \dfrac{\left(1+sT_d'\right)\left(1+sT_d''\right)}{\left(1+sT_{d0}'\right)\left(1+sT_{d0}''\right)} \right]} = I_A(s)$$

$$I_f(s) = -\frac{s}{\omega_b} \frac{l_{dm}}{r_f} \frac{1+sT_D}{\left(1+sT_{d0}'\right)\left(1+sT_{d0}''\right)} \cdot I_d(s) \tag{5.128}$$

$$I_q(s) = \frac{-\dfrac{V_{BC}(s)}{\sqrt{3}}\omega_b}{s\left[r_s + \dfrac{s}{\omega_b} l_q \dfrac{\left(1+sT_q''\right)}{\left(1+sT_{q0}''\right)} \right]} = \frac{2 I_B(s)}{\sqrt{3}}$$

With approximations similar to the case of sudden short-circuit transients, expressions of $I_d(t)$ and $I_f(t)$ are obtained. They are simpler, as no interference from axis q occurs.

In a more general case, where additional damper circuits are included to account for skin effects in solid-rotor SG, the identification process of parameters from step voltage responses becomes more involved. Nonlinear programming methods such as the least squared error, maximum likelihood, and the more recent evolutionary methods such as genetic algorithms could be used to identify separately the d and q inductances and time constants from standstill time domain responses.

The starting point of all such "curve-fitting" methods is the fact that the stator current response contains a constant component and a few aperiodic components with time constant close to T_d'', T_d', T_{ad}:

$$\frac{1}{T_{ad}} \approx \frac{r_s}{l_d''}\omega_b \tag{5.129}$$

for axis d, and T_q'' and T_{aq} for axis q:

$$\frac{1}{T_{aq}} \approx \frac{r_s \omega_b}{l_q''} \tag{5.130}$$

When an additional damper circuit is added in axis d, a new time constant T_d''' occurs. Transient and sub-subtransient time constants in axis q (T_q''', T_q') appear when three circuits are considered in axis q:

$$
\begin{aligned}
I_d(t) &= I_{d0} + I_d' e^{-t/T_d'} + I_d'' e^{-t/T_d''} + I_{da} e^{-t/T_{ad}} + I_d''' e^{-t/T_d'''}\\
I_q(t) &= I_{q0} + I_q' e^{-t/T_q'} + I_q'' e^{-t/T_q''} + I_{qa} e^{-t/T_{aq}} + I_q''' e^{-t/T_q'''}\\
I_f(t) &= I_{f0} + I_f' e^{-t/T_d'} + I_f'' e^{-t/T_d''} + I_f''' e^{-t/T_d'''} + I_{f0} e^{-t/T_{ad}}
\end{aligned}
\tag{5.131}
$$

Curve fitting the measured $I_d(t)$ and $I_q(t)$, respectively, with the calculated ones based on Equation 5.131 yields the time constants and l_d''', l_d'', l_d', l_q''', l_q'', l_q'. The main problem with step voltage standstill tests is that they do not properly excite all "frequencies" — time constants — of the machine.

A random cyclic pulse-width modulator (PWM) voltage excitation at standstill seems to be better for parameter identification [11]. Also, for coherency, care must be exercised to set initial (unique) values for stator leakage inductance l_{sl} and for the rotor-to-stator reduction ratio K_f:

$$K_f I_f^r = I_f \tag{5.132}$$

In reality, $I_f^r(t)$ is acquired and processed, not $I_f(t)$. Finally, it is more often suggested, for practicality, to excite (with a random cyclic PWM voltage) the field winding with short-circuited and opened stator windings rather than the stator, at standstill, because higher saturation levels (up to 25%) may be obtained without overheating the machine. Evidently, such tests are feasible only on axis d (Figure 5.13).

Again, $I_d = I_A$, $V_d = V_q = 0$, and $I_q = 0$. So, from Equation 5.101, with $I_q = 0$ and $V_d(s) = 0$, $V_q(s) = 0$:

$$I_d(s) = \frac{-g(s)\dfrac{s}{\omega_b}V_f(s)}{r_s + \dfrac{s}{\omega_b}l_d(s)} \tag{5.133}$$
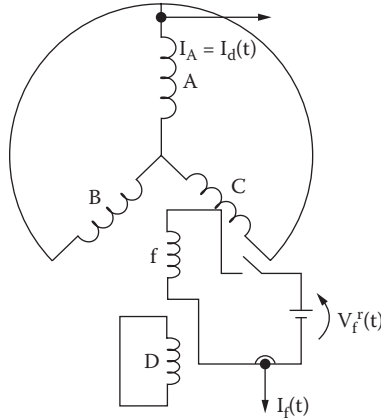
FIGURE 5.13 Field-winding standstill time response test (SSTR) arrangement.

$$I_f(s) = \frac{v_f(s)\left[1 - g(s)\dfrac{s^2}{\omega_b^2}\left(1 - \dfrac{l_{sl}}{r_s + sl_d(s)/\omega_b}\right)\right]}{r_f + \dfrac{s}{\omega_b}l_{fl}}$$

(5.133 cont.)

Again, the voltage and current rotor/stator reduction ratios, which are rather constant, are needed:

$$I_f = K_f I_f^r; V_f = \frac{2}{3K_f}V_f^r; r_f = \frac{2}{3K_f^2}r_f^r$$

(5.134)

To eliminate hysteresis effects (with $V_f(t)$ made from constant height pulses with randomly large timings and zeros) and reach pertinent frequencies, $V_f(t)$ may change polarity cyclically.

The main advantage of standstill time response (SSTR) tests is that the testing time is short.

5.12 Standstill Frequency Response

Another provoked electromagnetic phenomenon at zero speed that is being used to identify SG parameters (inductances and time constants) is the standstill frequency response (SSFR). The SG is supplied in axes d and q, respectively, through a single-phase AC voltage applied to the stator (with the field winding short-circuited) or to the field winding (with the stator short-circuited). The frequency of the applied voltage is varied, in general, from 0.001 Hz to more than 100 Hz, while the voltage is adapted to keep the AC current small enough (below 5% of rated value) to avoid winding overheating. The whole process of raising the frequency level may be mechanized, but considerable testing time is still required. The arrangement is identical to that shown in and Figure 5.13, but now $s = j\omega$, with ω in rad/sec.

Equation 5.128 becomes

$$\frac{V_{ABC}}{I_A} = \frac{3}{2}\left[r_s + j\frac{\omega}{\omega_b}l_d(j\omega)\right] = \frac{3}{2}Z_d(j\omega)$$

$$I_f(j\omega) = -j\frac{\omega}{\omega_b}g(j\omega)\cdot I_d(j\omega)$$

(5.135)

for axis d, and

$$\frac{\underline{V}_{BC}}{\underline{I}_B} = 2\left[r_s + j\frac{\omega}{\omega_b}l_q\left(j\omega\right)\right] = 2\underline{Z}_q\left(j\omega\right)$$

for axis *q*.

Complex number definitions can be used, as a single frequency voltage is applied at any time. The frequency range is large enough to encompass the whole spectrum of electrical time constants that spreads from a few milliseconds to a few seconds.

When the SSFR tests are performed on the field winding (with the stator short-circuited — Figure 5.13), the response in $\underline{I}_A$ and $\underline{I}_f$ is adapted from Equation 5.133 with $s = j\omega$:

$$\underline{I}_d\left(j\omega\right) = \underline{I}_A\left(j\omega\right) = \frac{-g\left(j\omega\right)j\dfrac{\omega}{\omega_b}V_f\left(j\omega\right)}{r_s + j\dfrac{\omega}{\omega_b}l_d\left(j\omega\right)}$$

$$\underline{I}_f\left(j\omega\right) = -v_f\left(j\omega\right)\frac{\left[1 + g\left(j\omega\right)\dfrac{\omega^2}{\omega_b^2}\left(1 - \dfrac{l_{sl}}{\left(rs + j\omega l_d\left(j\omega\right)/\omega_b\right)}\right)\right]}{rf + j\dfrac{\omega}{\omega_b}l_{sl}}$$

(5.136)

The general equivalent circuits emanate $l_d(j\omega)$, $l_q(j\omega)$, and $g(j\omega)$. For the standard case, equivalent circuits of Figure 5.6 and Equation 5.96 and Equation 5.97 are used.

For a better representation of frequency (skin) effects, more damper circuits are added along axis *d* (one, in general; Figure 5.14a) and along axis *q* (two, in general; Figure 5.14b).

The leakage coupling inductance l_{fDl} between the field winding and the damper windings, called also Canay's inductance [14], though generally small (less than stator leakage inductance), proved to be necessary to simultaneously fit the stator current and the field current frequency responses on axis *d*. Adding even one more such a leakage coupling inductance (say between the two damper circuits on the *d* axis) failed, so far, to produce improved results but hampered the convergence of the nonlinear programming estimation method used to identify the SG parameters [15].

The main argument in favor of $l_{fDl} \neq 0$ should be its real physical meaning (Figure 5.15a and Figure 5.15b).

A myriad of mathematical methods were recently proposed to identify the SG parameters from SSFR, with mean squared error [16] and maximum likelihood [17] being some of the most frequently used. A detailed description of such methods is presented in Chapter 8, dedicated to the testing of SGs.

5.13   Asynchronous Running

When the speed $\omega_r \neq \omega_{r0} = \omega_1$, the stator mmf induces currents in the rotor windings, mainly at slip frequency:

$$S = \frac{\omega_1 - \omega_r}{\omega_1}$$

(5.137)

with *S* the slip.

These currents interact with the stator field to produce an asynchronous torque t_{as}, as in an induction machine. For $S > 0$, the torque is motoring; while for $S < 0$, it is generating. As the rotor magnetic and
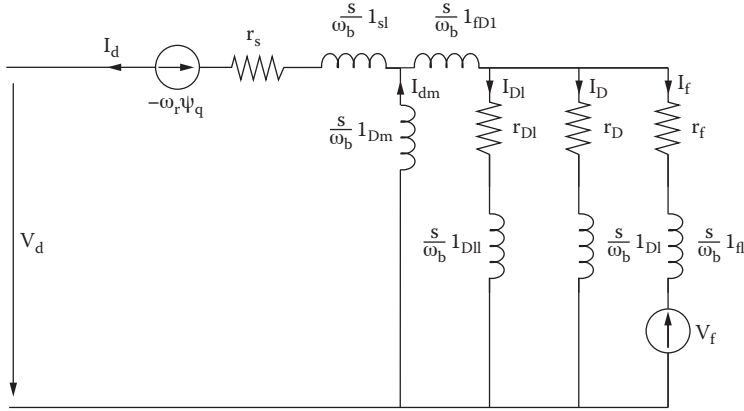
(a)
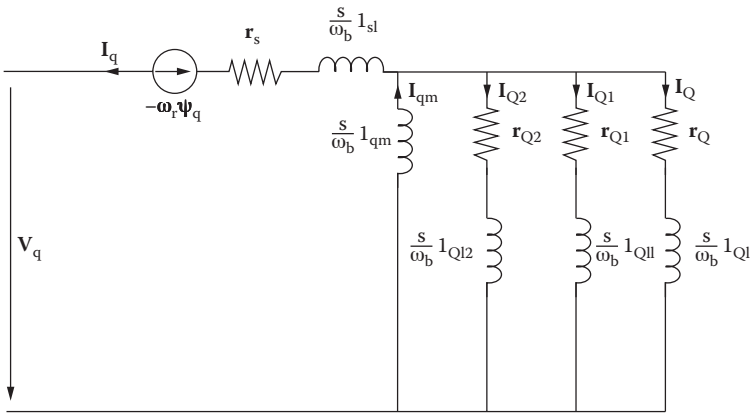
(b)

FIGURE 5.14 Synchronous generator equivalent circuits with three rotor circuits: (a) axis *d* and (b) axis *q*.

electric circuits are not fully symmetric, there will also be asynchronous torque pulsations, even with $\omega_r \neq \omega_1 =$ const. Also, the average synchronous torque t_{eav} is zero as long as $\omega_r \neq \omega_1$.

The *d–q* model can be used directly to handle transients at a speed $\omega_r \neq \omega_1$. Here we use the *d–q* model to calculate the average asynchronous torque and currents, considering that the power source that supplies the field winding has a zero internal impedance. That is, the field winding is short-circuited for asynchronous (AC) currents.

The Park transform may be applied to the symmetrical stator voltages:

$$V_{A,B,C}(t) = V \cos\left(\omega_1 \omega_b t - (i-1)\frac{2\pi}{3} \right); \ [P.U.]$$

$$V_d = -V \cos\left(\omega_1 \omega_b t - \theta_e \right) \tag{5.138}$$

$$V_q = +V \sin\left(\omega_1 \omega_b t - \theta_e \right)$$
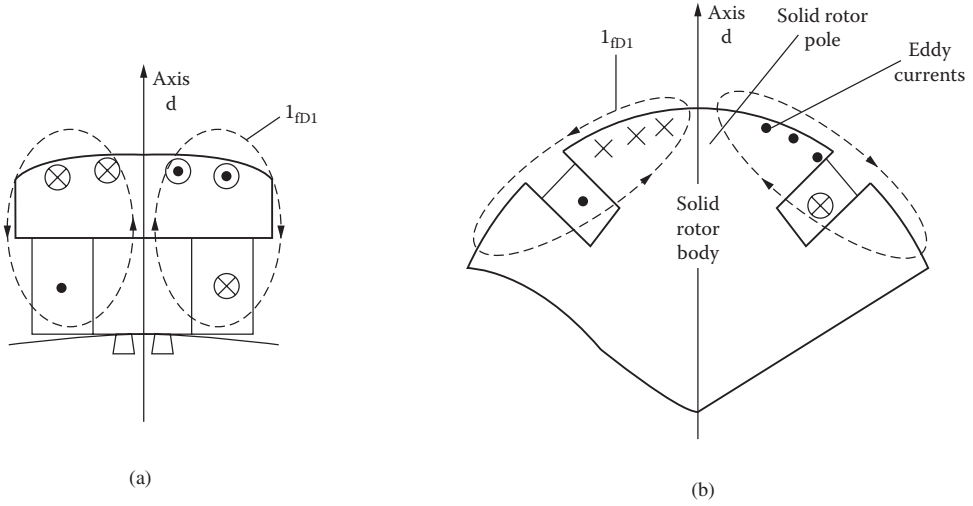
with

FIGURE 5.15 The leakage coupling inductance l_{fDi}: (a) salient-pole and (b) nonsalient-pole solid rotor.

$$\frac{1}{\omega_b}\frac{d\theta_e}{dt} = \omega_r = ct.$$

$$\theta_e = \int \omega_r \omega_b dt + \theta_0$$

with ω_1 in P.U., ω_b in rad/sec, t in seconds, and V in P.U.

We will now introduce complex number symbols:

$$\underline{V}_d = -V$$
$$\underline{V}_q = jV$$
$$(5.139)$$

As the speed is constant, d/dt in the d–q model is replaced by the following:

$$\frac{1}{\omega_b}\frac{d}{dt} \to j\left(\omega_1 - \omega_r\right) = jS\omega_1$$

$$\omega_r = \omega_1\left(1 - S\right)$$
$$(5.140)$$

As the field-winding circuit is short-circuited for the AC current, $\underline{v}_f(jS\omega_1) = 0$.

We will once more use Equation 5.101 in complex numbers and $\omega_r = \omega_1(1 - S)$:

$$\begin{vmatrix} -\underline{V}_d\left(jS\omega_1\omega_b\right) \\ -\underline{V}_q\left(jS\omega_1\omega_b\right) \end{vmatrix} = \begin{vmatrix} r_s + jS\omega_1 l_d\left(jS\omega_1\omega_b\right) & -\omega_1\left(1-S\right)l_q\left(jS\omega_1\omega_b\right) \\ \omega_1\left(1-S\right)l_d\left(jS\omega_1\omega_b\right) & r_s + jS\omega_1 l_q\left(jS\omega_1\omega_b\right) \end{vmatrix} \cdot \begin{vmatrix} \underline{I}_d \\ \underline{I}_q \end{vmatrix} \qquad (5.141)$$

Equation 5.141 may be solved for $\underline{I}_d$ and $\underline{I}_q$ with $\underline{V}_d$ and $\underline{V}_q$ from Equation 5.139. The average torque t_{asav} is

$$t_{asav} = -\operatorname{Re}\left[\underline{\Psi}_d\left(jS\omega_1\omega_b\right)\underline{I}_q^*\left(jS\omega_1\omega_b\right) - \underline{\Psi}_q\left(jS\omega_1\omega_b\right)\underline{I}_d^*\left(jS\omega_1\omega_b\right)\right] \qquad (5.142)$$

with

$$\underline{\Psi}_d \left(jS\omega_1\omega_b \right) = \underline{I}_d l_d \left(jS\omega_1\omega_b \right);$$

$$\underline{\Psi}_q \left(jS\omega_1\omega_b \right) = \underline{I}_q l_q \left(jS\omega_1\omega_b \right)$$

(5.143)

The field-winding AC current $\underline{I}_f$ is obtained from Equation 5.135:

$$\underline{I}_f \left(jS\omega_1\omega_b \right) = -jS\omega_1 g \left(jS\omega_1\omega_b \right) \cdot \underline{I}_d \left(jS\omega_1\omega_b \right)$$

(5.144)

If the stator resistance is neglected in Equation 5.141,

$$\underline{I}_d = \frac{+V}{j\omega_1 l_d \left(jS\omega_1\omega_b \right)}$$

$$\underline{I}_q = \frac{-jV}{j\omega_1 l_q \left(jS\omega_1\omega_b \right)}$$

(5.145)

In such conditions, the average asynchronous torque is

$$t_{asav} \approx -\frac{v^2}{\omega_1^2} \operatorname{Re} \left[\frac{1}{jl_d^* \left(jS\omega_1\omega_b \right)} + \frac{1}{jl_q^* \left(jS\omega_1\omega_b \right)} \right], \; \left[P.U. \right]$$

(5.146)

The torque is positive when generating (opposite the direction of motion). This happens only for $S < 0$ ($\omega_r > \omega_1$). There is a pulsation in the asynchronous torque due to magnetic anisotropy and rotor circuit unsymmetry. Its frequency is $(2S\omega_1\omega_b)$ in rad/sec. The torque pulsations may be evidentiated by switching back from $\underline{I}_d, \underline{I}_q, \underline{\Psi}_d, \underline{\Psi}_q$, complex number form to their instantaneous values:

$$I_d(t) = \operatorname{Re} \left(\underline{I}_d e^{j\left[(S\omega_1\omega_b)t - \theta_0 \right]} \right)$$

$$I_q(t) = \operatorname{Re} \left(\underline{I}_q e^{j\left[(S\omega_1\omega_b)t - \theta_0 \right]} \right)$$

$$\Psi_d(t) = \operatorname{Re} \left(\underline{\Psi}_d e^{j\left[(S\omega_1\omega_b)t - \theta_0 \right]} \right)$$

(5.147)

$$\Psi_q(t) = \operatorname{Re} \left(\underline{\Psi}_q e^{j\left[(S\omega_1\omega_b)t - \theta_0 \right]} \right)$$

$$I_A(t) = I_d(t) \cos \left(\omega_1\omega_b \left(1 - S \right) t + \theta_0 \right) - I_q(t) \sin \left(\omega_1\omega_b \left(1 - S \right) t + \theta_0 \right)$$

$I_d(t)$, $I_q(t)$, $\Psi_d(t)$, $\Psi_q(t)$ will exhibit components solely at slip frequency, while I_A will show the fundamental frequency ω_1(P.U.) and the $\omega_1(1 - 2S)$ component when $r_s \neq 0$.

The instantaneous torque at constant speed in asynchronous running is

$$t_{as}(t) = -\left(\Psi_d(t) I_q(t) - \Psi_q(t) I_d(t) \right); \; \left[P.U. \right]$$

(5.148)

The $2S\omega_1$ P.U. component (pulsation) in t_{as} is thus physically evident from Equation 5.148. This pulsation may run as high as 50% in P.U. The average torque t_{asav} (P.U.) for an SG with the data $V = 1$,
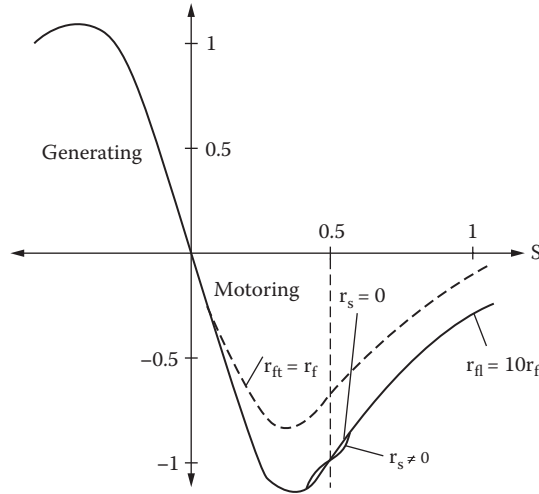
FIGURE 5.16 Asynchronous running of a synchronous generator.

$l_{sl} = 0.15$, $l_{dm} = 1.0$, $l_{fl} = 0.3$, $l_{Dl} = 0.2$, $l_{qm} = 0.6$, $l_{Ql} = 0.12$, $r_s = 0.012$, $r_D = 0.03$, $r_Q = 0.04$, $r_f = 0.03$, and $\underline{V}_f = 0$ is shown in Figure 5.16.

A few remarks are in order:

- The average asynchronous torque may equal or surpass the base torque. As the currents are very large, the machine should not be allowed to work asynchronously for more than 2 min, in general, in order to avoid severe overheating. Also, the SG draws reactive power from the power system while it delivers active power.
- The torque shows a small inflexion around $S = \frac{1}{2}$ when $r_s \neq 0$. This is not present for $r_s \approx 0$.
- With no additional resistance in the field winding ($r_{ft} = r_f$), no inflexion in the torque–speed curve around $S = \frac{1}{2}$ occurs. The average torque is smaller in comparison with the case of $r_{ft} = 10\, r_f$ (additional resistance in the field winding is included).

Example 5.3: Asynchronous Torque Pulsations

For the above data, but with $r_s = 0$ and $\omega_1 = 1$ (rated frequency), derive the formula of instantaneous asynchronous torque.

Solution

From Equation 5.145,

$$\underline{I}_d = \frac{V}{jl_d\left(js\omega_b\right)}$$

$$\underline{I}_q = \frac{-jV}{jl_q\left(jS\omega_b\right)} \qquad (5.149)$$

$$\underline{\Psi}_d = l_d\underline{I}_d = -jV$$

$$\underline{\Psi}_q = l_q\underline{I}_q = -V$$

Also, let us define $l_d(jS\omega_b)$ and $l_q(jS\omega_b)$ as follows:

$$jl_d \left(jS\omega_b \right) = r_d + jl_{dr} = \left| l_d \right| e^{j\varphi_d}$$

$$jl_q \left(jS\omega_b \right) = r_q + jl_{qr} = \left| l_q \right| e^{j\varphi_q}$$

(5.150)

According to Equation 5.147, with $\theta_0 = 0$ (for simplicity), from Equation 5.149,

$$I_d = \frac{V}{\left| l_d \right|} \cos \left(S\omega_b t - \varphi_d \right)$$

$$I_q = + \frac{V}{\left| l_q \right|} \sin \left(S\omega_b t - \varphi_q \right)$$

$$\Psi_d = V \sin \left(S\omega_b t \right)$$

$$\Psi_q = -V \cos \left(S\omega_b t \right)$$

(5.151)

$$t_{as}(t) = -\left(\Psi_d I_q - \Psi_q I_d \right) = \left[-\frac{V^2}{2} \left(\frac{\cos \varphi_d}{\left| l_d \right|} + \frac{\cos \varphi_q}{\left| l_q \right|} \right) + \frac{V^2}{2\left| l_q \right|} \cos \left(2S\omega_b t - \varphi_q \right) - \right.$$

$$\left. -\frac{V^2}{2\left| l_d \right|} \cos \left(2S\omega_b t - \varphi_d \right) \right]$$

(5.152)

The first term in Equation 5.152 represents the average torque, while the last two refer to the pulsating torque. As expected, for a completely symmetric rotor (as that of an induction machine) the pulsating asynchronous torque is zero, because $\left| l_d \right| = \left| l_q \right|, \left| \varphi_d \right| = \left| \varphi_q \right|$ for all slip (speed values).

For motoring ($S > 0$), $\varphi_d, \varphi_q < 90°$ and for generating ($S < 0$), $90° < \varphi_d, \varphi_q < 180°$. For small values of slip, the asynchronous torque versus slip may be approximated to a straight line (see Figure 5.16):

$$t_{asav} \approx -K_{as} S\omega_1 = +K_{as} \left(\omega_r - \omega_1 \right)$$

(5.153)

Equation 5.152 may provide a good basis from which to calculate K_{as} for high-power SGs ($r_s \approx 0$).

Example 5.4: DC Field Current Produced Asynchronous Stator Losses

The DC current in the field winding, if any, produces additional losses in the stator windings through currents at a frequency equal to speed $\omega' = \omega_1(1 - S)$ (P.U.). Calculate these losses and their torque.

Solution

In rotor coordinates, these stator d–q currents I_d', I_q' are DC, at constant speed. To calculate them separately, only the motion-induced voltages are considered, with $V_d' = V_q' = 0$ (the stator is short-circuited, a sign that the power system has a zero internal impedance).

Also, $I_D' = I_Q' = 0$, $I_f = I_{f0}$:

$$0 = -\left(1 - S \right) \omega_1 l_q I_q' + r_s I_d'$$

$$0 = +\left(1 - S \right) \omega_1 \left(l_d I_d + l_{dm} I_{f0} \right) + r_s I_q'$$

(5.154)

From Equation 5.154 and for $\omega_1 = 1$,

$$I'_d = \frac{-l_{dm}I_{F0}(1-S)^2 l_q}{r_s^2 + (1-S)^2 l_d l_q}$$

$$I'_q = \frac{-l_{dm}I_{F0}(1-S)r_s}{r_s^2 + (1-S)^2 l_d l_q}$$

(5.155)

The stator losses P'_{CO} are as follows:

$$P'_{CO} = \frac{3}{2}r_s\left(I_d'^2 + I_q'^2\right)$$

(5.156)

The corresponding braking torque t_{as}' is

$$t'_{as} = \frac{P'_{CO}}{\omega_1(1-S)} > 0$$

(5.157)

The maximum value of t_{as}' occurs at a rather large slip s_K':

$$S'_k \approx 1 - \sqrt{\frac{2l_d l_q - r_s^2}{2l_q^2 + l_d l_q}}$$

(5.158)

The maximum torque $t_{as}'^k$ is as follows:

$$t'^k_{as} \approx t'_{as}\left(S'_K\right)$$

(5.159)

Close to the synchronous speed ($S = 0$), this torque becomes negligible.

5.14   Simplified Models for Power System Studies

The P.U. system of SG equations (Equation 5.67) describes completely the standard machine for any transients. The complexity of such a model makes it less practical for power system stability studies, where tens or hundreds of SGs and consumers are involved and have to be modeled. Simplifications in the SG model are required for such a purpose. Some of them are discussed below, while more information is available in the literature on power system stability and control [1, 17].

5.14.1   Neglecting the Stator Flux Transients

When neglecting the stator transients in the *d–q* model, it means to make $\frac{\partial \Psi d}{\partial t} = \frac{\partial \Psi q}{\partial t} = 0$. It was demonstrated that it is also necessary to simultaneously consider — only in the stator voltage equations — constant (synchronous) speed:

$$V_d = -I_d r_s + \Psi_q \omega_{r0}$$

$$V_q = -I_q r_s - \Psi_d \omega_{r0}$$

$$\frac{1}{\omega_b} \frac{d\Psi_f}{dt} = -I_f r_f + V_f$$

$$\frac{1}{\omega_b} \frac{d\Psi_D}{dt} = -I_D r_D$$

$$\frac{1}{\omega_b} \frac{d\Psi_Q}{dt} = -I_Q r_Q$$

$$\Psi_d = l_{sl} I_d + l_{dm} \left(I_d + I_f + I_D \right)$$

$$\Psi_q = l_{sl} I_q + l_{qm} \left(I_q + I_Q \right) \tag{5.160}$$

$$\Psi_f = l_{fl} I_f + l_{dm} \left(I_d + I_f + I_D \right) + l_{fDl} \left(I_f + I_D \right)$$

$$\Psi_D = l_{fl} I_D + l_{dm} \left(I_d + I_f + I_D \right) + l_{fDl} \left(I_f + I_D \right)$$

$$\Psi_Q = l_{Ql} I_q + l_{qm} \left(I_q + I_Q \right)$$

$$2H \frac{d\omega_r}{dt} = t_{shaft} - t_e ; t_e = \Psi_d I_q - \Psi_q I_d ; \omega_b \frac{d\delta v}{dt} = \omega_r - \omega_0$$

$$\frac{1}{\omega_b} \frac{d\theta_{er}}{dt} = \omega_r ; \left| \begin{matrix} V_d \\ V_q \\ V_0 \end{matrix} \right| = \left| P\left(\theta_{er} \right) \right| \left| \begin{matrix} V_a \\ V_b \\ V_c \end{matrix} \right|$$

The flux and current relationships are the same as in Equation 5.67. The state variables may be I_d, I_q, Ψ_f, Ψ_D, Ψ_Q, ω_r, and θ_{er}. I_d and I_q are calculated from the, now algebraic, equations of stator. The system order was reduced by two units.

As expected, fast 50 (60) Hz frequency transients, occuring in I_d, I_q, and t_e, are eliminated. Only the "average" transient torque is "visible." Allowing for constant (synchronous) speed in the stator equations with $\frac{\partial \Psi d}{\partial t} = \frac{\partial \Psi q}{\partial t} = 0$ counteracts the effects of such an approximation, at least for small signal transients, in terms of speed and angle response [17]. By neglecting stator transients, we are led to steady-state stator voltage equations. Consequently, if the power network transients are neglected, the connection of the SG model to the power network model is rather simple, with steady state all over.

A drastic computation time saving is thus obtained in power system stability studies.

5.14.2 Neglecting the Stator Transients and the Rotor Damper Winding Effects

This time, in addition, the damper winding currents are zero, $I_D = I_Q = 0$, and thus,

$$V_d = -I_d r_s + \Psi_q \omega_{r0}$$

$$V_q = -I_q r_s - \Psi_d \omega_{r0} \tag{5.161}$$

$$\frac{1}{\omega_b}\frac{d\Psi_f}{dt} = -I_f r_f + V_f$$

$$\Psi_d = l_{sl}I_d + l_{dm}\left(I_d + I_f\right)$$

$$\Psi_q = l_{sl}I_q + l_{qm}I_q$$

$$\Psi_f = l_{fl}I_f + l_{dm}\left(I_d + I_f\right) \qquad\qquad \text{(5.161 cont.)}$$

$$2H\frac{d\omega_r}{dt} = t_{shaft} - t_e; t_e = \Psi_d I_q - \Psi_q I_d; \omega_b\frac{d\delta v}{dt} = \omega_r - \omega_{r0}$$

$$\frac{1}{\omega_b}\frac{d\theta_{er}}{dt} = \omega_r; \begin{vmatrix} V_d \\ V_q \\ V_0 \end{vmatrix} = \left|P\left(\theta_{er}\right)\right| \begin{vmatrix} V_A \\ V_B \\ V_C \end{vmatrix}$$

The order of the system was further reduced by two units. An additional computation time saving is obtained, with only one electrical transient left — the one produced by the field winding. The model is adequate for slow transients (seconds and more).

5.14.3 Neglecting All Electrical Transients

The field current is now considered constant. We are dealing with very slow (mechanical) transients:

$$V_d = -I_d r_s + \Psi_q \omega_{r0}$$

$$V_q = -I_q r_s - \Psi_d \omega_{r0}$$

$$I_f = V_f / r_f \qquad\qquad \text{(5.162)}$$

$$2H\frac{d\omega_r}{dt} = t_{shaft} - t_e; t_e = \Psi_d I_q - \Psi_q I_d; \omega_b\frac{d\delta v}{dt} = \omega_r - \omega_{r0}$$

$$\omega_b\frac{d\theta_{er}}{dt} = \omega_r; \begin{vmatrix} V_d \\ V_q \\ V_0 \end{vmatrix} = \left|P\left(\theta_{er}\right)\right| \begin{vmatrix} V_A \\ V_B \\ V_C \end{vmatrix}$$

This time, we start again with initial values of variables: I_{d0}, I_{q0}, I_{f0}, $\omega_r = \omega_{r0}$, $\delta_{V0}(\theta_{er0})$ and V_{d0}, V_{q0}, $t_{e0} = t_{shaft0}$. So, the machine is under steady state electromagnetically, while making use of the motion equation to handle mechanical transients. In very slow transients (tens of seconds), such a model is appropriate. Note that a plethora of constant flux approximate models (with or without rotor damper cage) in use for power system studies [1, 17] are not followed here [17]. Among the simplified models we illustrate here, only the "mechanical" model is followed, as it helps in explaining SG self-synchronization, step shaft torque response, and SG oscillations (free and forced).

5.15 Mechanical Transients

When the prime-mover torque varies in a nonperiodical or periodical fashion, the large inertia of the SG leads to a rather slow speed (power angle δ_V) response. To evidentiate such a response, the electromagnetic transients may be altogether neglected, as suggested by the "mechanical model" presented in the previous paragraph.

As the speed varies, an asynchronous torque t_{as} occurs, besides the synchronous torque. The motion equation becomes (in P.U.) as follows:

$$2H \frac{d\omega_r}{dt} = t_{shaft} - t_e - t_{as} \tag{5.163}$$

with ($r_s = 0$)

$$t_e = e_f \frac{V \sin \delta_V}{l_d} + \frac{V^2}{2} \left(\frac{1}{l_q} - \frac{1}{l_d} \right) \sin 2\delta_V \tag{5.164}$$

$$t_{as} = \frac{K_{as}}{\omega_b} \frac{d\delta_V}{dt}; \tag{5.165}$$

$$\frac{1}{\omega_b} \frac{d\delta_V}{dt} = \omega_r - \omega_1$$

and $e_f = l_{dm}I_f$ represents the no-load voltage for a given field current.

Only the average asynchronous torque is considered here. The model in Equation 5.163 through Equation 5.165 may be solved numerically for ω_r and δ_V as variables once their initial values are given together with the prime-mover torque t_{shaft} versus time or versus speed, with or without a speed governor. For small deviations, Equation 5.163 through Equation 5.165 become

$$\frac{2H}{\omega_b} \frac{d^2 \Delta \delta_V}{dt^2} + \left(\frac{\partial t_e}{\partial \delta_V} \right)_{\delta_{V0}} \cdot \Delta \delta_V + \frac{K_{as}}{\omega_b} \frac{d\Delta \delta_V}{dt} = \Delta t_{shaft} \tag{5.166}$$

$$\left(t_e \right)_{\delta_{V0}} = t_{shaft0}$$

$$\left(\frac{\partial t_e}{\partial \delta_V} \right)_{\delta_{V0}} = t_{es0} \tag{5.167}$$

Equality (Equation 5.167) reflects the starting steady-state conditions at initial power angle δ_{V0}. t_{eso} is the so-called synchronizing torque (as long as $t_{es0} > 0$, static stability is secured).

5.15.1 Response to Step Shaft Torque Input

For step shaft torque input, Equation 5.166 allows for an analytical solution:

$$\Delta \delta_V(t) = \frac{\Delta t_{shaft}}{t_{es0}} + \mathrm{Re} \left[A_1 e^{\underline{\gamma}_1 t} + B_1 e^{\underline{\gamma}_2 t} \right] \tag{5.168}$$

$$\underline{\gamma}_{1,2} = \frac{-\left(K_{as}/\omega_b \right) \pm \sqrt{\left(\dfrac{K_{as}}{\omega_b} \right)^2 - \dfrac{8H \cdot t_{es0}}{\omega_b}}}{4\left(H/\omega_b \right)} = -\frac{1}{T_{as}} \pm j\omega' \tag{5.169}$$

$$\frac{1}{T_{as}} = \frac{K_{as}}{4H};$$

$$\left(\omega'\right)^2 = -\left(\frac{1}{T_{as}}\right)^2 + \omega_0^2; \qquad (5.170)$$

$$\omega_0 = \sqrt{\frac{t_{es0}\omega_b}{2H}}$$

Finally,

$$\Delta\delta_V\left(t\right) = \frac{\Delta t_{shaft}}{t_{es0}}\left[1 - e^{-\frac{t}{T_{as}}}\frac{\sin\left(\omega t + \Psi\right)}{\sin\Psi}\right]$$

The constant Ψ is obtained by assuming initial steady-state conditions:

$$\left(\Delta\delta_V\right)_{t=0} = 0,$$

$$\left(\frac{d\left(\Delta\delta\right)}{dt}\right)_{t=0} = 0 \qquad (5.171)$$

Finally,

$$\tan\Psi = \omega' T_{as} \qquad (5.172)$$

The power angle and speed response for step shaft torque are shown qualitatively in Figure 5.17.

Note that ω_0 (Equation 5.170) is traditionally known as the proper mechanical frequency of the SG. Unfortunately, ω_0 varies with power angle δ_V, field current I_{f0}, and with inertia. It decreases with increasing δ_V and increases with increasing I_{f0}.

In general, $f_0 = \omega_0/2\pi$ varies from less than or about 1 Hz to a few hertz for large and medium power SGs, respectively.
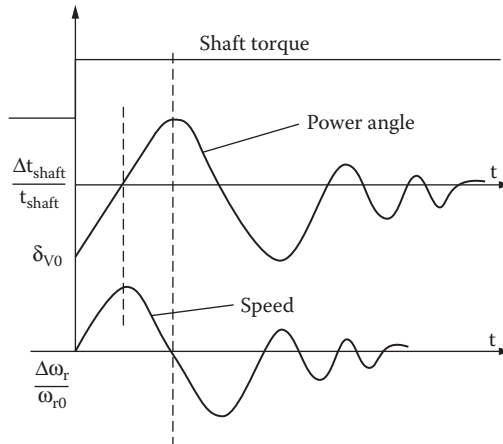
FIGURE 5.17   Power angle and speed responses to step shaft torque input.

5.15.2 Forced Oscillations

Shaft torque oscillations may occur due to various reasons. The diesel engine prime movers are a typical case, as their torque varies with rotor position. The shaft torque oscillations may be written as follows:

$$\Delta t_{shaft} = \sum t_{sh\upsilon} \cos\left(\Omega_{\upsilon}t - \Psi_{\upsilon}\right) \qquad (5.173)$$

with Ω_{υ} in rad/sec.

Consider first an autonomous SG without any asynchronous torque ($K_{as} = 0$). This is the ideal case of free oscillations.

From Equation 5.166,

$$\frac{2H}{\omega_b}\frac{d^2\Delta\delta_V}{dt^2} = \Sigma t_{sh\upsilon}\cos\left(\Omega_{\upsilon}t - \Psi_{\upsilon}\right) \qquad (5.174)$$

The steady-state solution of this equation is straightforward:

$$\Delta\delta_{\upsilon\upsilon}^{a} = -\Delta\delta_{\upsilon\upsilon m}\cos(\Omega_{\upsilon}t - \Psi_{\upsilon})$$

$$-\frac{\omega_b t_{sh\upsilon}}{2H\Omega_{\upsilon}^2} = \Delta\delta_{\upsilon\upsilon m}^{a} \qquad (5.175)$$

The amplitude of this free oscillation (for harmonic υ) is thus inversely proportional to inertia and to the frequency of oscillation squared.

For the SG with rotor damper cage and connected to the power system, both K_{as} and t_{es0} (synchronizing torque) are nonzero; thus, Equation 5.166 has to be solved as it is:

$$\frac{2H}{\omega_b}\frac{d^2\Delta\delta_V}{dt^2} + \frac{K_{as}}{\omega_b}d\frac{\Delta\delta_V}{dt} + t_{es0}\Delta\delta_V = \Sigma\Delta t_{sh\upsilon}\cos\left(\Omega_{\upsilon}t - \Psi_{\upsilon}\right) \qquad (5.176)$$

Again, the steady-state solution is sought:

$$\Delta\delta_{\upsilon\upsilon} = \Delta\delta_{\upsilon\upsilon m}\sin\left(\Omega_{\upsilon}t - \Psi_{\upsilon} - \varphi_{\upsilon}\right) \qquad (5.177)$$

with

$$\Delta\delta_{\upsilon\upsilon m} = \frac{\Delta t_{sh\upsilon}}{\sqrt{\left(\dfrac{2H}{\omega_b}\Omega_{\upsilon}^2 - t_{es0}\right)^2 + \left(\dfrac{K_{as}}{\omega_b}\Omega_{\upsilon}\right)^2}};$$

$$\varphi_{\upsilon} = \tan^{-1}\left(\frac{\left(-\dfrac{2H}{\omega_b}\Omega_{\upsilon}^2 + t_{es0}\right)}{K_{as}\dfrac{\Omega_{\upsilon}}{\omega_b}}\right)^{-1} \qquad (5.178)$$

The ratio of the power angle amplitudes $\Delta\delta_{\upsilon\upsilon m}$ and $\Delta\delta_{\upsilon\upsilon m}^{a}$ of forced and free oscillations, respectively, is called the modulus of mechanical resonance $K_{m\upsilon}$:
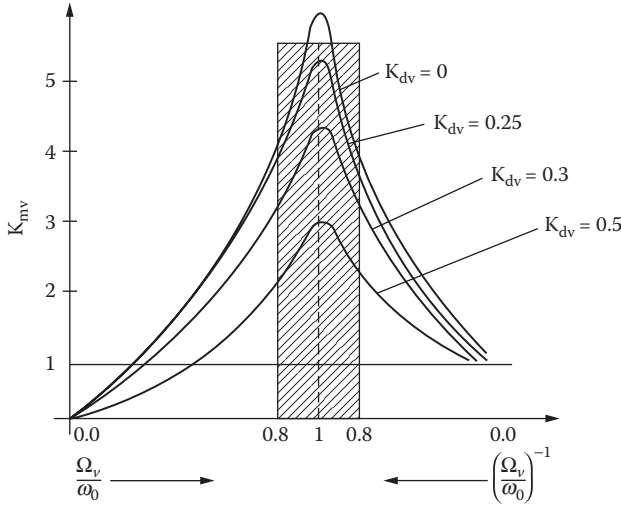
FIGURE 5.18 The modulus of mechanical resonance K_m.

$$K_{mv} = \frac{\Delta \delta_{vvm}}{\Delta \delta_{vvm}^a} = \frac{1}{\sqrt{\left(1 - \frac{\omega_0^2}{\Omega_v^2}\right)^2 + \left(\frac{K_{as}}{2H\Omega_v}\right)^2}} \tag{5.179}$$

The damping coefficient K_{dv} is

$$K_{dv} = \frac{K_{as}}{2H\Omega_v} \tag{5.180}$$

Typical variations of K_{mv} with the ω_0/Ω_v ratio for various K_{dv} values are given in Figure 5.17. The resonance conditions for $\omega_0 = \Omega_v$ are evident. To reduce the amplification effect, K_{dv} is increased, but this is feasible only up to a point by enforcing the damper cage (more copper). So, in general, for all shaft torque frequencies, Ω_v, it is appropriate to fall outside the hatched region in Figure 5.18:

$$1.25 > \frac{\omega_0}{\Omega_v} > 0.8 \tag{5.181}$$

As ω_0 — the proper mechanical frequency (Equation 5.170) — varies with load (δ_v) and with field current for a given machine, the condition in Equation 5.181 is not so easy to fulfill for all shaft torque pulsations. The elasticity of shafts and of mechanical couplings between them in an SG set is a source of additional oscillations to be considered for the constraint in Equation 5.181. The case of the autonomous SG with damper cage rotor requires a separate treatment.

5.16 Small Disturbance Electromechanical Transients

After the investigation of fast (constant speed; electromagnetic) and slow (mechanical) transients, we return to the general case when both electrical and mechanical transients are to be considered.

Electric power load variations typically cause such complex transients.

For multiple SGs and loads, power systems, voltage, and frequency control system design are generally based on small disturbance theories in order to capitalize on the theoretical heritage of linear control systems and reduce digital simulation time.

In essence, the complete (or approximate) *d–q* model (Equation 5.67) of the SG is linearized about a chosen initial steady-state point by using only the first Taylor's series component. The linearized system is written in the state-space form:

$$\Delta \dot{X} = A\Delta X + B\Delta V$$

$$\Delta Y = C\Delta X + D\Delta V$$

(5.182a)

where

ΔX = the state variables vector
ΔV = the input vector
ΔY = the output vector

The voltage and speed controller systems may be included in Equation 5.182; thus, the small disturbance stability of the controlled generator is investigated by the eigenvalue method:

$$\det\left(A - \lambda I\right) = 0$$

(5.182b)

with *I* being the unity diagonal matrix.

The eigenvalues λ may be real or complex numbers. For system stability despite small disturbances, all eigenvalues should have a negative real part.

The unsaturated *d–q* model (Equation 5.87) in P.U. may be linearized as follows:

$$\Delta V_d = -\Delta I_d r_s - \frac{1}{\omega_b} d\left(\frac{\Delta \Psi_d}{dt}\right) + \omega_{r0}\Delta \Psi_q + \Delta \omega_r \Psi_{q0}$$

$$\Delta V_q = -\Delta I_d r_s - \frac{1}{\omega_b} d\left(\frac{\Delta \Psi_q}{dt}\right) - \omega_{r0}\Delta \Psi_d - \Delta \omega_r \Psi_{d0}$$

$$\Delta V_f = \Delta I_f r_f + \frac{1}{\omega_b} d\left(\frac{\Delta \Psi_f}{dt}\right)$$

(5.183)

$$0 = -\Delta I_D r_D - \frac{1}{\omega_b} d\left(\frac{\Delta \Psi_D}{dt}\right)$$

$$0 = -\Delta I_Q r_Q - \frac{1}{\omega_b} d\left(\frac{\Delta \Psi_Q}{dt}\right)$$

$$\Delta t_{shaft} = \Delta t_e + 2H\frac{d}{dt}\left(\Delta \omega_r\right)$$

$$\Delta t_e = -\left(\Psi_{d0}\Delta I_q + I_{q0}\Delta \Psi_{d0} - \Psi_{q0}\Delta I_d - I_{d0}\Delta \Psi_q\right)$$

(5.184)

$$\frac{1}{\omega_b}\frac{d\Delta \delta_V}{dt} = \Delta \omega_r$$

For the initial (steady-state) point,

$$V_{d0} = -I_{d0}r_s + \Psi_{q0}\omega_{r0}$$

$$V_{q0} = -I_{q0}r_s - \Psi_{d0}\omega_{r0}$$

$$\Psi_{d0} = l_{sl}I_{d0} + l_{dm}\left(I_{d0} + I_{f0}\right)$$

$$\Psi_{q0} = \left(l_{sl} + l_{qm}\right)I_{q0} \tag{5.185}$$

$$V_{f0} = I_{f0}r_f\,;\, I_{D0} = I_{Q0} = 0$$

$$t_{e0} = -\left(\Psi_{d0}I_{d0} - \Psi_{q0}I_{q0}\right) = t_{shaft}$$

$$\delta_V = \tan^{-1}\frac{V_{d0}}{V_{q0}}$$

$$V_{d0} = -V_0 \sin\delta_0$$

$$V_{q0} = -V_0 \cos\delta_0$$

$$\Delta V_d \approx -\Delta V \sin\delta_{V0} - V_0 \cos\delta_{V0}\Delta\delta_V$$

$$\Delta V_q \approx -\Delta V \cos\delta_{V0} + V_0 \sin\delta_{V0}\Delta\delta_V$$

$$\Delta\Psi_d = l_{sl}\Delta I_d + l_{dm}\Delta I_{dm}\,;\, \Delta I_{dm} = \Delta I_d + \Delta I_f + \Delta I_D \tag{5.186}$$

$$\Delta\Psi_q = l_{sl}\Delta I_q + l_{qm}\Delta I_{qm}\,;\, \Delta I_{qm} = \Delta I_q + \Delta I_Q$$

$$\Delta\Psi_D = l_{Dl}\Delta I_D + l_{dm}\Delta I_{dm}$$

$$\Delta\Psi_Q = l_{Ql}\Delta I_Q + l_{qm}\Delta I_{qm}$$

Eliminating the flux linkage disturbances in Equation 5.183 and Equation 5.184 by using Equation 5.186 leads to the definition of the following state-space variable vector *X*:

$$\left|\Delta X\right| = \left(\Delta I_{ds}, \Delta I_f, \Delta I_{dm}, \Delta I_{qs}, \Delta I_{qm}, \Delta\omega_r, \Delta\delta_V\right)^t \tag{5.187}$$

The input vector is

$$\left|\Delta V\right| = \left[-\Delta V \sin\delta_0, \Delta V_f, 0, -\Delta V \cos\delta_0, 0, \Delta t_{shaft}, 0\right]^t \tag{5.188}$$

We may now put Equation 5.183 and Equation 5.184 with Equation 5.186 into matrix form as follows:

$$\left|\Delta V\right| = -\left|L\right|\frac{1}{\omega_b}d\frac{(\Delta X)}{dt} - \left|R\right|\Delta X \tag{5.189}$$

with

$$|L| = $$

	1	2	3	4	5	6	7
1	l_{sl}	0	l_{dm}	0	0	0	0
2	0	l_{fl}	l_{dm}	0	0	0	0
3	$-l_{sl}$	$-l_{Dl}$	$l_{dm}+l_{Dl}$	0	0	0	0
4	0	0	0	l_{sl}	l_{qm}	0	0
5	0	0	0	$-l_{Ql}$	$l_{qm}+l_{Ql}$	0	0
6	0	0	0	0	0	-1	0
7	0	0	0	0	0	0	-1

$$|R| = $$

	1	2	3	4	5	6	7
1	r_s	0	0	$-\omega_{r0}l_{sl}$	$-\omega_{r0}l_{qm}$	$-\Psi_{q0}$	$V_0\cos\delta_{V0}$
2	0	r_f	0	0	0	0	0
3	$-r_D$	$-r_D$	$+r_D$	0	0	0	0
4	$\omega_{r0}l_{sl}$	0	$\omega_{r0}l_{dm}$	r_s	0	Ψ_{d0}	$-V_0\sin\delta_{V0}$
5	0	0	0	$-r_Q$	r_Q	0	0
6	$\dfrac{l_{sl}I_{q0}-\Psi_{q0}}{2H\omega_b}$	0	$\dfrac{l_{dm}I_{q0}}{2H\omega_b}$	$\dfrac{\Psi_{d0}-l_{sl}I_{d0}}{2H\omega_b}$	$\dfrac{-l_{dm}I_{d0}}{2H\omega_b}$	-1	0
7	0	0	0	0	0	1	0

Comparing Equation 5.182 with Equation 5.189,

$$A = -|L|^{-1} \cdot |R|;$$
$$B = -\left[L\right]^{-1} \left|1,1,1,1,1,1,1\right|$$

(5.190)

All that remains is calculation of the eigenvalues of matrix A, and thus establishing the small disturbance stability performance of a SG. The choice of I_{dm} and I_{qm} as variables, instead of rotor damper cage currents I_d and I_q, makes [L] more sparse and leaves way to somehow consider magnetic saturation, at least for steady state when the dependences of l_{dm} and l_{qm} on both I_{dm} and I_{qm} (Figure 5.10) may be established in advance by tests or by finite element calculations.

This is easy to apply, as values of I_{dm0} and I_{qm0} are straightforward:

$$I_{dm0} = I_{d0} + I_{f0}$$
$$I_{qm0} = I_{q0}$$

(5.191)

and the level of saturation may be considered "frozen" at the initial conditions (not influenced by small perturbations). Typical critical eigenvalue changes with active power for the I_s, I_f, I_m model above are shown in Figure 5.19 [18].

It is possible to choose the variable vector in different ways by combining various flux linkages and current as variables [18]. There is not much to gain with such choices, unless magnetic saturation is not rigorously considered. It was shown that care must be exercised in representing magnetic saturation by single magnetization curves (dependent on $I_m = \sqrt{I_{dm}^2 + I_{qm}^2}$) in the underexcited regimes of SG when large errors may occur. Using only complete I_{dm} (Ψ_{dm}, Ψ_{qm}), I_{qm} (Ψ_{dm}, Ψ_{qm}) families of saturation curves will lead to good results throughout the whole active and reactive power capability region of the SG.
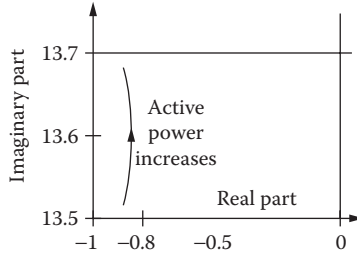
FIGURE 5.19 Critical mode eigenvalues of unsaturated (I_s, I_f, I_m) model when active power rises from 0.8 to 1.2 per unit (P.U.).

As during small perturbation transients the initial steady-state level is paramount, we leave out the transient saturation influence here, to consider it in the study of large disturbance transients when the latter matters notably.

5.17   Large Disturbance Transients Modeling

Large disturbance transients modeling of a single SG should take into account both magnetic saturation and frequency (skin rotor) effects.

To complete a *d*–*q* model, with two *d* axis damper circuits and three *q* axis damper circuits, satisfies such standards, if magnetic saturation is included, even if included separately along each axis (see Figure 5.20a for the *d* axis and Figure 5.20b for the *q* axis). For the sake of completion, all equations of such a model are given in what follows:

$$\Psi_d = l_{sl}I_d + \Psi_{dm}$$

$$\Psi_q = l_{sl}I_q + \Psi_{qm}$$

$$\Psi_f = l_{fl}I_f + \Psi_{dm} + l_{fDl}\left(I_f + I_D + I_{D1}\right)$$

$$\Psi_D = l_{Dl}I_D + \Psi_{dm} + l_{fDl}\left(I_f + I_D + I_{D1}\right)$$

$$\Psi_{D1} = l_{D1l}I_{D1} + \Psi_{dm} + l_{fDl}\left(I_f + I_D + I_{D1}\right)$$

$$\Psi_Q = l_{Ql}I_Q + \Psi_{qm}$$

$$\Psi_{Q1} = l_{Q1l}I_{Q1} + \Psi_{qm}$$

$$\Psi_{Q2} = l_{Q2l}I_{Q2} + \Psi_{qm}$$

$$I_{dm} = I_d + I_D + I_{D1} + I_f$$

$$I_{qm} = I_q + I_Q + I_{Q1} + I_{Q2}$$

(5.192)

$$\Psi_{dm} = l_{dm}(I_{dm}, I_{qm})I_{dm}$$

$$\Psi_{qm} = l_{qm}(I_{dm}, I_{qm})I_{qm}$$

(5.193)

The magnetization curve families in Equation 5.193 have to be obtained either through standstill time response tests or through FEM magnetostatic calculations at standstill. Once analytical polynomial spline
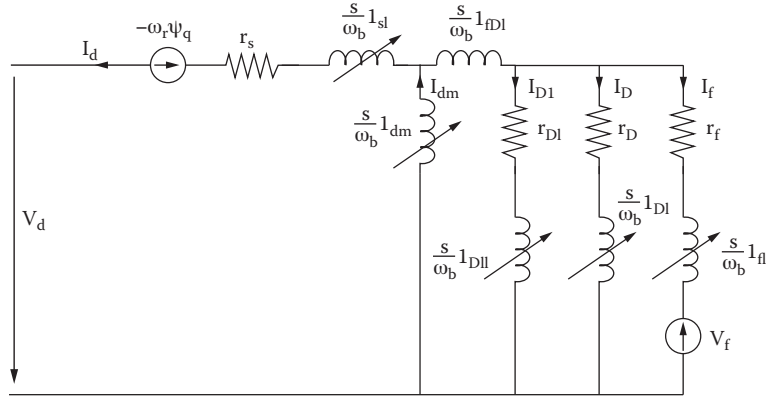
(a)
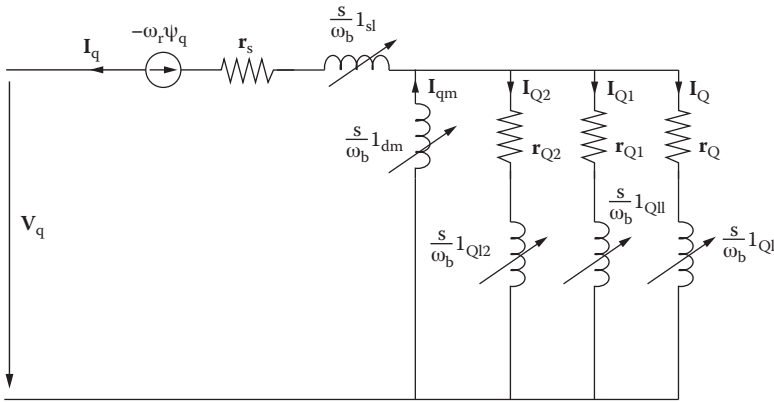
(b)

FIGURE 5.20 Three-circuit synchronous generator model with some variable inductances: (a) axis *d* and (b) axis *q*.

approximation from l_{dm} and l_{qm} functions are obtained, the time derivatives of Ψ_{dm} and Ψ_{qm} may be obtained as follows:

$$\frac{s}{\omega_b}\frac{d\Psi_{dm}}{dt} = L_{ddm}\frac{s}{\omega_b}\frac{dI_{dm}}{dt} + L_{qdm}\frac{s}{\omega_b}\frac{dI_{qm}}{dt}$$

$$\frac{s}{\omega_b}\frac{d\Psi_{qm}}{dt} = L_{dqm}\frac{s}{\omega_b}\frac{dI_{dm}}{dt} + L_{qqm}\frac{s}{\omega_b}\frac{dI_{qm}}{dt}$$

(5.194)

$$l_{ddm} = l_{dm} + \frac{\partial l_{dm}I_{dm}}{\partial I_{dm}} ; l_{qdm} = \frac{\partial l_{dm}I_{dm}}{\partial I_{qm}}$$

$$l_{dqm} = \frac{\partial l_{qm}I_{qm}}{\partial I_{dm}} ; l_{qqm} = l_{qm} + \frac{\partial l_{qm}}{\partial I_{qm}}I_{qm}$$

The leakage saturation occurs only in the field winding and in the stator winding and is considered to depend solely on the respective currents:
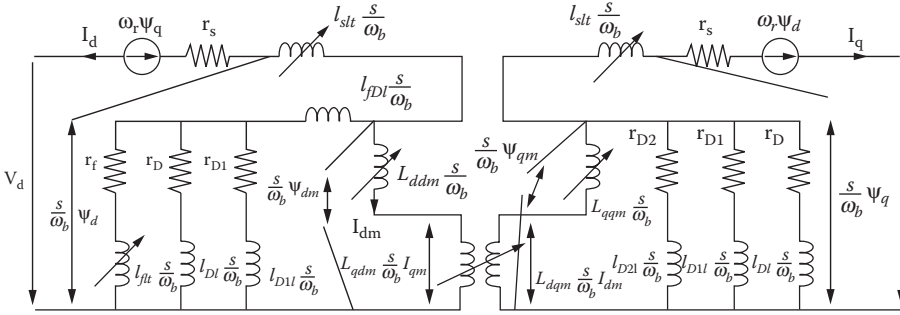
FIGURE 5.21 General three-circuit synchronous generator model with cross-coupling saturation.

$$\frac{s}{\omega_b} l_{sl}(I_s) = \left(l_{sl}(I_s) + \frac{\partial l_{sl}}{\partial I_s} I_s \right) \frac{s}{\omega_b} = l_{slt}(I_s) \frac{s}{\omega_b}$$

$$I(s) = \sqrt{I_d^2 + I_q^2} \qquad\qquad (5.195)$$

$$\frac{s}{\omega_b} l_{fl}(I_f) = \left(l_{fl}(I_f) + \frac{\partial l_{fl}}{\partial I_f} I_f \right) \frac{s}{\omega_b} = l_{flt}(I_f) \frac{s}{\omega_b}$$

So, the leakage inductances of stator and field winding in the equivalent circuit are replaced by their transient value l_{slt}, l_{flt}. However, in the flux–current relationship, their steady-state values l_{sl}, l_{fl} occur. They are all functions of their respective currents. It should be mentioned that only for currents in excess of 2 P.U., is leakage saturation influence worth considering. A sudden short-circuit represents such a transient process.

Equation 5.194 suggests that a cross-coupling between the equivalent circuits of axes d and q is required. This is simple to operate (Figure 5.21). From the reciprocity condition, $l_{dqm} = l_{qdm}$. And the general equivalent circuit may be identified:

- The magnetization curve family (Equation 5.193 and Equation 5.194) and leakage inductance functions $l_{sl}(I_s)$, $l_{fl}(I_f)$ are first determined from time domain standstill tests (or FEM).
- From frequency response at standstill or through FEM, all the other components are calculated.

The dependence of l_{dm} and l_{qm} on both I_{dm} and I_{qm} should lead to model suitability in all magnetization conditions, including the disputed case of underexcited SG when the concept of $l_{dm}(I_m)$, $l_{dm}(I_m)$ unique functions or of total magnetization current (mmf) fails [4].

The machine equations are straightforward from the equivalent scheme and thus are not repeated here. The choice of variables is as in the paragraph on small perturbations. Tedious FEM tests and their processing are required before such a complete circuit model of the SG is established in all rigor.

That the d–q model may be used to investigate various symmetric transients is very clear. The same model may be used in asymmetrical stator connections also, as long as the time functions of V_d and V_q can be obtained. But, $v_d(t)$ and $v_q(t)$ may be defined only if $V_A(t)$, $V_B(t)$, $V_C(t)$ functions are available. Alternatively, the load–voltage–current relationships have to be amenable to the state-space form. Let us illustrate this idea with a few examples.

5.17.1 Line-to-Line Fault

A typical line fault at machine terminals is shown in Figure 5.22.
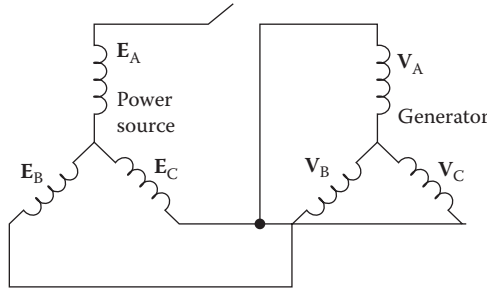
FIGURE 5.22 Line-to-line synchronous generator short-circuit.
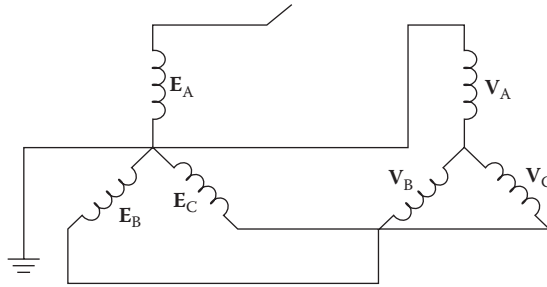
FIGURE 5.23 Line-to-neutral fault.

The power source-generator voltage relationships after the short-circuit are as follows:

$$V_B - V_C = E_B - E_C$$
$$V_A = V_C ; I_A + I_B + I_C = 0, V_0 = 0 \tag{5.196}$$

Consequently,

$$V_C(t) = \frac{1}{3}\left(E_C - E_B\right)$$

$$V_B(t) = -2V_C(t)$$

$$V_A(t) = V_C(t)$$

$$E_{A,B,C}\left(t\right) = V\sqrt{2}\cos\left(\omega_{1t} - \left(i-1\right)\frac{2\pi}{3}\right); i = 1,2,3$$

All stator voltages $V_A(t)$, $V_B(t)$, and $V_C(t)$ may be defined right after the short-circuit.

5.17.2 Line-to-Neutral Fault

In this case, a phase of the synchronous machine is connected to the neutral power system (Figure 5.23), which may or may not be connected to the ground. According to Figure 5.23,

$$V_B - V_C = E_B - E_C$$
$$V_C - V_A = E_C ; V_A + V_B + V_C = 0 \tag{5.197}$$

Consequently,

$$V_A = -\frac{\left(E_C + E_B\right)}{3}$$

$$V_B = V_A + E_B \qquad (5.198)$$

$$V_C = V_A + E_C$$

So, again, provided that E_A, E_B, and E_C are known, time functions $V_A(t)$, $V_B(t)$, and $V_C(t)$ are also known.

5.18 Finite Element SG Modeling

The numerical methods for field distribution calculation in electric machines are by now an established field with a rather long history, even before 1975 when finite difference methods prevailed. Since then, the finite element (integral) methods (FEM) took over to produce revolutionary results.

For the basics of the FEM, see the literature [19]. In 1976, in Reference [20], SG time domain responses at standstill were approached successfully by FEM, making use of the conductivity matrices concept. In 1980, the SG sudden three-phase short-circuit was calculated [21,22] by FEM.

The relative motion between stator and rotor during balanced and unbalanced short-circuit transients was reported in 1987 [23].

In the 1990s, the time stepping and coupled-field and circuit concepts were successfully introduced [24] to eliminate circuit simulation restrictions based in conductivity matrices representations. Typical results related to no-load and steady-state short-circuit curves obtained through FEM for a 150 MVA 13.8 kV SG are shown in Figure 5.24, modeled after Reference [4].

Also for steady state, FEMs were proved to predict correctly (within 1 to 2%) the field current required for various active and reactive power loads over the whole *p–q* capability curve of the same SG [4].

Finally the rotor angle during steady state was predicted within 2° for the whole spectrum of active and reactive power loads (Figure 5.25) [4].
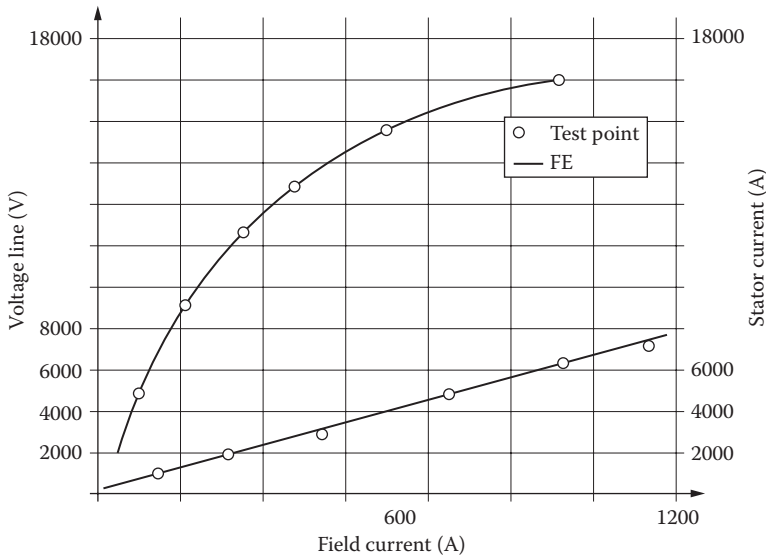
FIGURE 5.24 Open and short-circuit curves of a 150 MVA, 13.8 kV, two-pole synchronous generator.
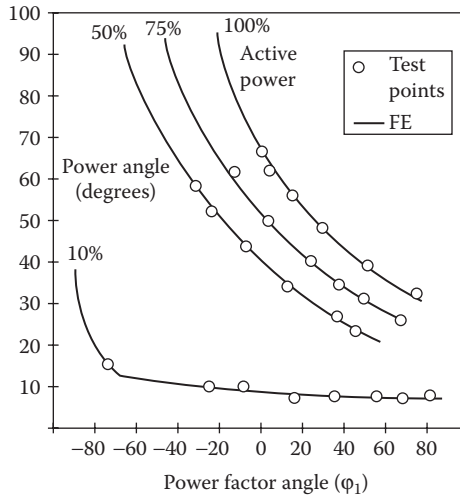
FIGURE 5.25   Power angle δ_V vs. power factor angle φ_1 of a 150 MVA, 13.8 kV, two-pole synchronous generator.

The FEM has also been successful in calculating SG response to standstill time domain and frequency responses, then used to identify the general equivalent circuit elements [25,26].

A complete picture of finite element (FE) flux paths during an ongoing sudden short-circuit process is shown in Figure 5.26 [23]. The traveling field is visible. Also visible is the fact that quite a lot of flux paths cross the slots, as expected.

Finally, FE simulation of a 120 MW, 13.8 kV, 50 Hz SG on load during and after a three-phase fault was successfully conducted [28] (Figure 5.27a through Figure 5.27e).

This is a severe transient, as the power angle reaches over 90° during the transients when notable active power is delivered, as the field current is also large. The plateau in the line voltage recovery from 0.4 to 0.5 sec (Figure 5.27d, Figure 5.27e and Figure 5.27c) is explainable in this way.

It is almost evident that FEM has reached the point of being able to simulate virtually any operation mode in an SG. The only question is the amount of computation time required, not to mention the extraordinary expertise involved in wisely using it. The FEM is the way of the future in SG, but there may be two avenues to that future:

- Use FEM to calculate and store SG lumped parameters for an ever-wider saturation and frequency effect and then use the general equivalent circuits for the study of various transients with the machine alone or incorporated in a power system.
- Use FEM directly to calculate the electromagnetic and mechanical transients through coupled-field circuit models or even through powers, torques, and motion equations.

While the first avenue looks more practical for power system studies, the second may be used for the design refinements of a new SG.

The few existing dedicated FEM software packages are expected to improve further, at reduced additional computation time and costs.

5.19   SG Transient Modeling for Control Design

In Section 5.10, simplified models for power system studies were described. One specific approximation has gained wide acceptance, especially for SG control design. It is related to the neglecting of stator transients, neglecting the damper winding effects altogether (third-order model), or considering one damper winding along axis *q* but no damper winding along axis *d* (fourth-order model).
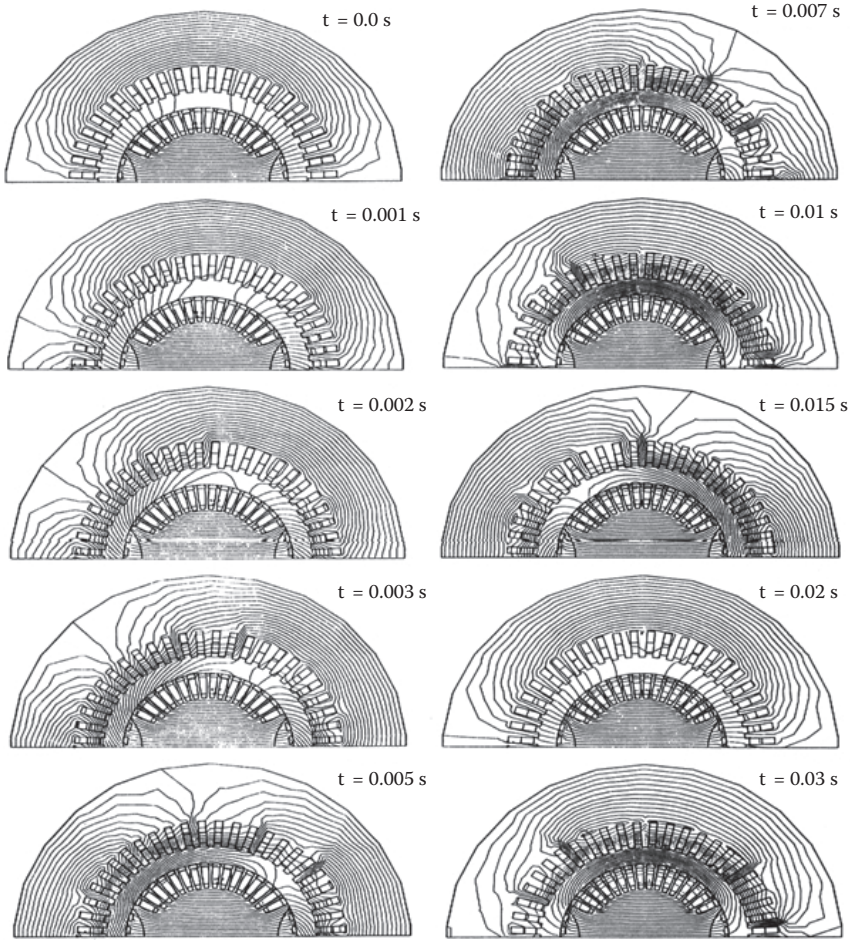
FIGURE 5.26 Flux distribution during a 0.5 per unit (P.U.) balanced short-circuit at a 660 MW synchronous generator terminal (contour intervals are 0.016 Wb/m).

We start with Equation 5.161, the third-order model:

$$V_d = -I_d r_s + \Psi_q \omega_r$$

$$V_q = -I_q r_s - \Psi_d \omega_r$$

$$\begin{vmatrix} \Psi_d \\ \Psi_f \end{vmatrix} = \begin{vmatrix} l_d & l_{dm} \\ l_{dm} & l_f \end{vmatrix} \begin{vmatrix} I_d \\ I_f \end{vmatrix}; \Psi_q = l_q I_q$$

$$\frac{1}{\omega_b} \dot{\Psi}_f = -I_f r_f + v_f \qquad (5.199)$$

$$t_e = -\left(\Psi_d I_q - \Psi_q I_d \right)$$

$$2H \dot{\omega}_r = t_{shaft} - t_e;$$

$$\omega_b \dot{\delta} = \omega_r - \omega_1$$
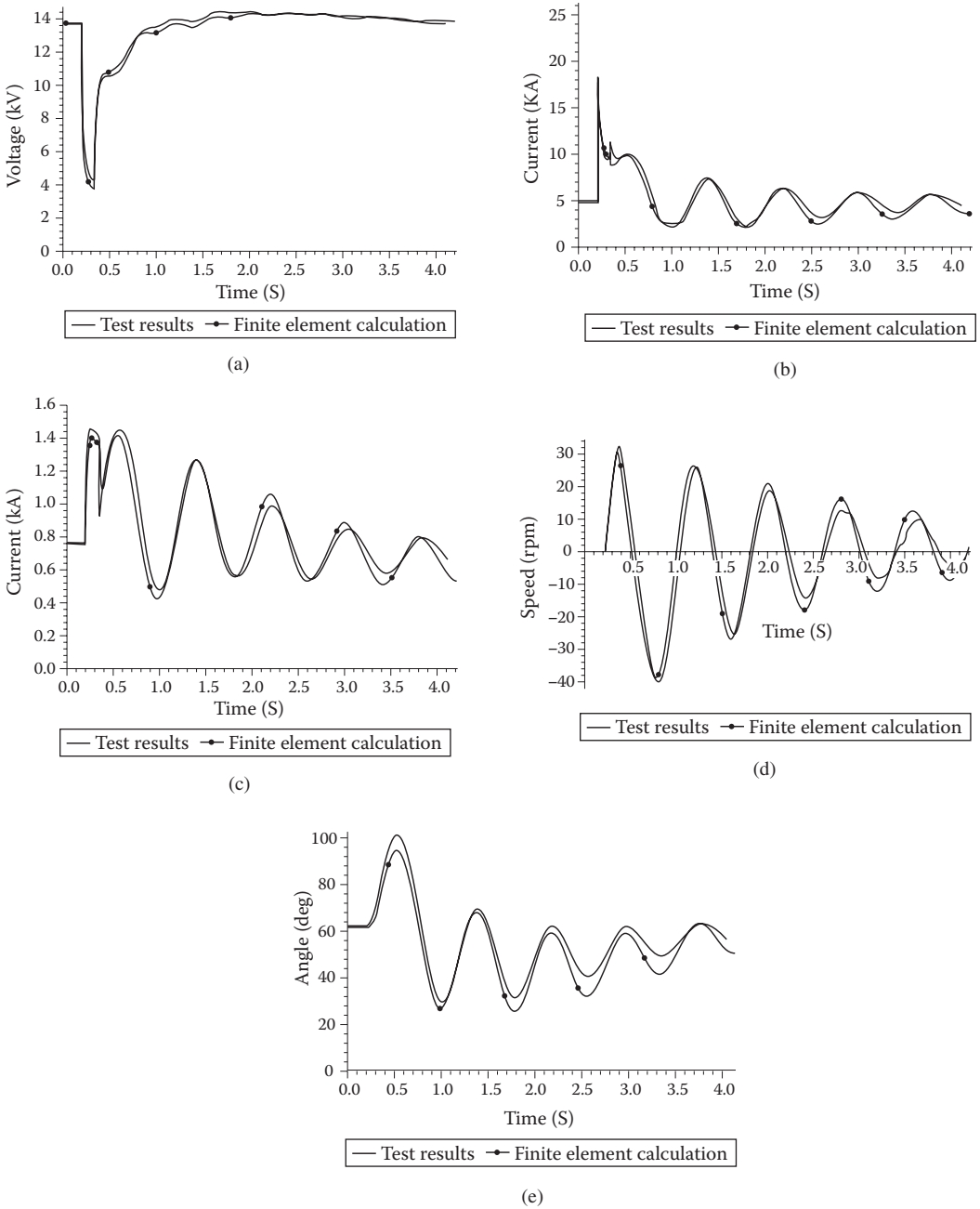
FIGURE 5.27 On-load three-phase fault and recovery transients by finite element and tests: (a) line voltage, (b) line current, (c) field current, (d) rotor speed deviation, and (e) power angle.

Eliminate I_f from the flux–current relationships, and derive the transient emf e_q' as follows:

$$e_q' = +\omega_r \frac{l_{dm}}{l_f} \Psi_f \qquad (5.200)$$

the q – axis stator equation becomes

$$V_q = -r_s I_q - x'_d I_d - e'_q \tag{5.201}$$

where

$$x'_d = \omega_r \left(l_d - \frac{l_{dm}^2}{l_f} \right); \quad l_f = l_{fl} + l_{dm} \tag{5.202}$$

We may now rearrange the field circuit equation in Equation 5.199 with e'_q and x'_d to obtain the following:

$$\dot{e}'_q = \frac{v_f - e'_q + i_d(x_d - x'_d)}{T'_{d0}}; \quad T'_{d0} = \frac{l_f}{r_f} \tag{5.203}$$

By considering a damper winding Q along axis q, an equation similar to Equation 5.200 is obtained, with e'_d as follows:

$$e'_d = \omega_r \frac{l_{qm}}{l_Q} \Psi_Q;$$

$$l_Q = l_{Ql} + l_{qm} \tag{5.204}$$

$$\dot{e}'_d = \frac{-i_q(x_q - x'_q) - e'_d}{T'_{q0}}; \quad T'_{q0} = \frac{l_Q}{r_Q}; \quad x'_q = l_q - \frac{l_{qm}^2}{l_Q} \tag{5.205}$$

$$V_d = -r_s I_d - x'_q I_q - e'_d$$

As expected, in the absence of the rotor q axis damping winding, e'_d is taken as zero, and the third order of the model is restored. x'_d and x'_q are the transient reactances (in P.U.) as defined earlier in this chapter. The two equations of motion in Equation 5.199 and Equation 5.203 and Equation 5.204 have to be added to form the fourth order (transient model) of the SG.

As the transient emf e'_q differential equation includes the field-winding voltage v_f, the application of this model to control is greatly facilitated, as shown in Chapter 6, which is dedicated to the control of SG.

The initial values of transient emfs e'_d and e'_q are calculated from stator equations in Equation 5.201 and Equation 5.204 for steady state:

$$\left(e'_q \right)_{t=0} = \omega_{r0} \left(\frac{l_{dm}}{l_f} \cdot l_f \left(I_f \right)_{t=0} + l_{dm} \left(I_d \right)_{t=0} \right)$$

$$\left(e'_d \right)_{t=0} = \omega_{r0} \frac{l_{qm}^2}{l_Q} \cdot \left(I_q \right)_{t=0} \tag{5.206}$$

In a similar way, a subtransient model may be defined for the first moments after a fast transient process [2]. Such a model is not suitable for control design purposes, where the excitation current control is rather slow anyway. Linearization of the transient model with the rotor speed ω_r as variable (even in the stator equations) proves to be very useful in automatic voltage regulator (AVR) design, as shown in Chapter 6.

5.20   Summary

- SGs undergo transient operation modes when the currents, flux linkages, voltages, load, or speed vary with time. Connection of the SGs to a power system can result in electrical load or shaft torque variations that produce transients. The steady-state, two-reaction, model in Chapter 4, based on traveling fields at standstill to each other, is valid only for steady-state operation.
- The main SG models for transients are as follows:
  - The phase-variable circuit model is based on the SG structure, as multiple electric and magnetic circuits are coupled together electrically and/or magnetically. The stator/rotor circuit mutual inductances always depend on rotor position. In salient-pole rotors, the stator phase self-inductances vary with rotor position, that is, with time. With one damper circuit along each rotor axis, a field winding, and three stator phases, an eighth-order nonlinear system with time-variable coefficients is obtained, when the two equations of motion are added. The basic variables are I_A, I_B, I_C, I_f, I_D, I_Q, ω_r, θ_r.
    - Solving a variable coefficient state-space system requires inversion of a time-variable sixth-order matrix for each integration step time interval. Only numerical methods such as Runge–Kutta–Gill and predictor–corrector can handle the solving of such a stiff state-space high-order system. In addition, the computation time is prohibitive due to the time dependence of inductances. Finally, the complexity of the model leaves little room for intuitive interpretation of phenomena and trends for various transients. And, it is not practical for control design. In conclusion, the phase-variable model should be used only for special situations, such as for highly unbalanced transients or faults.
    - Simpler models are needed to handle transients in a more practical manner.
  - The orthogonal axis (d–q) model is characterized by inductances between windings which are independent from rotor position. The d–q model may be derived from the phase-variable model either through a mathematical change of variables (Park transform) or through a physical orthogonal axis model.
    - The Park transform is an orthogonal change of variables such that to conserve powers, losses, and torque,

$$
\begin{vmatrix} V_d \\ V_q \\ V_0 \end{vmatrix} = \left| P(\theta_{er}) \right| \cdot \begin{vmatrix} V_A \\ V_B \\ V_C \end{vmatrix}
$$

$$
\left| P(\theta_{er}) \right| = \frac{2}{3} \begin{bmatrix} \cos(-\theta_{er}) & \cos\left(-\theta_{er} + \dfrac{2\pi}{3}\right) & \cos\left(-\theta_{er} - \dfrac{2\pi}{3}\right) \\[2mm] \sin(-\theta_{er}) & \sin\left(-\theta_{er} + \dfrac{2\pi}{3}\right) & \sin\left(-\theta_{er} - \dfrac{2\pi}{3}\right) \\[2mm] \dfrac{1}{2} & \dfrac{1}{2} & \dfrac{1}{2} \end{bmatrix} \tag{5.207}
$$

$$
\left| P(\theta_{er}) \right|^{-1} = \frac{3}{2} \left| P(\theta_{er}) \right|^T ; \frac{d\theta_{er}}{dt} = \omega_r
$$

  - The physical d–q model consists of a fictitious machine with the same rotor f, D, Q orthogonal rotor windings as in the actual machine and with two stator windings with magnetic axes (mmfs) that are always fixed to the rotor d and q orthogonal axes. The fact that the rotor d–q axes move at rotor speed and are always aligned with axes d and q secure the independence of the d-q model inductances of rotor position.

- Steady state means DC in the *d–q* model of SG.
- For complete equivalence of the *d-q* model with the real machine, a null component is added. This component does not produce torque through the fundamental, and its current is determined by the stator resistance and leakage inductance:

$$V_0 = -r_s I_0 - l_{sl} \frac{s}{\omega_b} \frac{dI_0}{dt} \qquad (5.208)$$

- The dependence of the *d–q* model parameters on the real machine parameters is rather simple.
- To reduce the number of inductances in the *d–q* model, the rotor quantities are reduced to the stator under the assumption that the airgap main magnetic field couples all windings along axes *d* and *q*, respectively. Thus, the stator–rotor coupling inductances become equal to the stator magnetization inductances l_{dm}, l_{qm}.
- An additional leakage coupling inductance l_{fDl} between the field winding and the *d* axis damper winding is also introduced, as it proves to be useful in providing good results both in the stator and field current transient responses.
- The *d–q* model is generally used in the per unit (P.U.) form to reduce the range of variables during transients from zero to, say, 20 for all transients and all power ranges. The base quantities, voltage, current, and power are rated, in general, but other choices are possible. In this chapter, all variables and parameters are in P.U., but time *t* and inertia *H* are in seconds. In this case, $d/dt \rightarrow s/\omega_b$ in Laplace form (ω_b is equal to the base [rated] angular frequency in rad/sec).
- The rotor-to-stator reduction coefficients conserve losses and power, as expected.
- The *d–q* model equations writing assumes source circuits in the stator and sink circuits in the rotor and the induced voltage $e = -d\Psi / dt$. Also, implicitly, the Poynting vector $\overline{P} = \dfrac{\overline{E} \times \overline{H}}{2}$ enters the sink circuits and exits the source circuits. This way, all flux/current relations contain only positive (+) signs. This choice leads to the fact that while power and torque are positive for generating, the components V_d, V_q, and I_q are always negative for generating. But, I_d can be either negative or positive depending on the load power factor angle. This is valid for the trigonometric positive motion direction.
- The space-vector diagram at steady-state evidentiates the power angle δ_V between the voltage vector and axis *q* in the third quadrant, with $\delta_V > 0$ for generating.
- Based on the *d–q* model, state-space equations in P.U. (Equation 5.81), two distinct general equivalent circuits may be drawn (Figure 5.6). They are very intuitive in the sense that all *d–q* model equations may be derived by inspection. The distinct *d* and *q* equivalent circuits for transients indicate that there is no magnetic coupling between the two orthogonal axes.
- In reality, in heavily saturated SGs, there is a cross-coupling due to magnetic saturation between the two orthogonal axes. Putting this phenomenon into the *d–q* model has received a lot of attention lately, but here, only two representative solutions are described.
- One uses distinct but unique magnetization curves along axes *d* and *q*: $\Psi_{dm}^*(I_m), \Psi_{qm}^*(I_m)$, where I_m is the total magnetization current (or mmf): $I_m = \sqrt{I_{dm}^2 + I_{qm}^2}$. This approximation seems to fail when the SG is "deep" in the leading power factor mode (underexcited, with $I_m < 0.7$ P.U.). However, when $I_m > 0.7$ P.U., it has not yet been proven wrong.
- The second model for saturation presupposes a family of magnetization curves along axis *d* and, respectively, *q*: $\Psi_{dm}^*(I_{dm}, I_{qm}), \Psi_{qm}^*(I_{dm}, I_{qm})$. This model, after adequate analytical approximations of these functions, should not fail over the entire active/reactive power envelope of an SG. But, it requires more computation efforts.
- The magnetization curves along axes *d* and *q* may be obtained either from experiments or through FEM field calculations.

- The cross-coupling magnetic saturation may be handily included in the d–q general equivalent circuit for both axes (Figure 5.21).
- The general equivalent circuits are based on the flux/stator current relationships without rotor currents:

$$\Psi_d\left(s\right) = l_d(s)I_d(s) + g(s)v_f(s)$$
$$\Psi_q\left(s\right) = l_q(s)I_q(s)$$

(5.209)

- $l_d(s)$, $l_q(s)$ and $g(s)$ are known as the operational parameters of the SG (s equals the Laplace operator).
- Operational parameters include the main inductances and time constants that are catalog data of the SG: subtransient, transient, and synchronous inductances l_d'', l_d', l_d, along the d axis and l_q'', l_q' along the q axis. The corresponding time constants are T_d'', T_d', T_{d0}'', T_{d0}', T_q'', T_{q0}'. Additional terms are added when frequency (skin) effect imposes additional fictitious rotor circuits: l_d''', l_q''', l_q', T_d''', T_{q0}'', T_q''', T_{q0}'''.
- Though transients may be handled directly via the complete d–q model through its solving by numerical methods, a few approximations have led to very practical solutions.
- Electromagnetic transients are those that occur at constant speed. The operational calculus may be applied with some elegant analytical approximated solutions as a result. Sudden three-phase short-circuit falls into this category. It is used for unsaturated parameter identification by comparing the measured and calculated current waveforms during a sudden short-circuit. Graphical models (20 years ago) and advanced nonlinear programming methods have been used for curve fitting the theory and tests, with parameter estimation as the main goal.
- Electromagnetic transients may also be provoked at zero speed with the applied voltage vector along axis d or q with or without DC in the other axis. The applied voltage may be DC step voltage or PWM cyclical voltage rich in frequency content. Alternatively, single-frequency voltages may be applied one after the other and the impedance measured (amplitude and phase). Again, a way to estimate the general equivalent circuit parameters was born through standstill electromagnetic transient processing. Alternatively, FEM calculations may replace or accompany tests for the same purpose: parameter estimation.
- For multimachine transient investigation, simpler lower-order d–q models have become standard. One of them is based on neglecting the stator (fast) transients. In this model, the fast-decaying AC components in stator currents and torque are missing. Further, it seems better that in this case, the rotor speed in the stator equations be kept equal to the synchronous speed $\omega_r = \omega_{r0} = \omega_1$. The speed in the model varies as the equation of motion remains in place.
- Gradually, the damper circuit transients may also be neglected ($I_D = I_Q = 0$); thus, only one electrical transient, determined by the field winding, remains. With the two motion equations, this one makes for a third-order system. Finally, all electric transients may be neglected to be left only with the motion equations, for very slow (mechanical) transients.
- Asynchronous running at constant speed may also be tackled as an electromagnetic transient, with $S \rightarrow js\omega_1$; S equals slip; and $S = (\omega_1 - \omega_r)/\omega_1$. An inflexion in the asynchronous torque is detected around $S = \frac{1}{2}$ ($\omega_r = \omega_1/2$). It tends to be small in large machines, as r_s is very small in P.U.
- In close to synchronous speed, $\left| S \right| < 0.05$, the asynchronous torque is proportional to slip speed $S\omega_1$. Also, torque pulsations occur in the asynchronous torque that have to be accounted for during transients, for better precision, as asynchronous torque t_{as} is

$$t_{as} = t_{asav} + t_{asp}\cos\left(2S\omega_1\omega_b + \Psi\right)$$

(5.210)

- Its pulsation frequency is small, because S gets smaller, as it is the case around synchronism ($\left| S \right| < 0.05$, $\omega_r \approx \left(0.95 - 1.05\right)\omega_1$).

- Mechanical (very small) transients may be treated easily with the SG at steady state electromagnetically. Only speed ω_r and power angle δ_v vary in the so-called rotor swing equation. Through numerical methods, the nonlinear model may be solved, but for small perturbations, a simple analytical solution for $\omega_r(t)$ and $\delta_v(t)$ may be found for particular inputs, such as shaft torque step or frequency response.
- For the SG in stand-alone operation without a damper cage, a proper mechanical frequency f_0 is defined. It varies with field current I_f, power angle δ_v, and inertia, but it is generally less than 2 to 3 Hz for large and medium power standard SGs. When an SG is connected to the power grid and the shaft torque presents pulsations at Ω_v, resonance conditions may occur. They are characterized by severe oscillation amplifications (in δ_v) that are tempered by a large inertia and a strong damper cage. Torsional shaft frequencies by the prime-mover shaft and coupling to the SG may also produce resonance mechanical conditions that have to be avoided.
- Electromechanical transients are characterized by both electrical and mechanical transients. For small perturbations, the *d–q* model provides a very good way to investigate the SG stability — without or with voltage and speed control — by the eigenvalue method, after linearization around a steady-state given point.
- For large disturbance transients, the full *d–q* model with magnetic saturation and frequency effects (Figure 5.21) is recommended. Numerical methods may solve the transients, but direct stability methods typical to nonlinear systems may also be used.
- Finite element analysis is widely used to assess various SG steady state and transients through coupled field/circuit models. The computation time is still prohibitive for use in design optimization or for controller design. With the computation power of microcomputers rising by the year, the FEM will become the norm in analyzing the FEM steady-state and transient performance: electromagnetic, thermal, or mechanical.
- Still, the circuit models, with the parameters calculated through FEM and then curve fitted by analytical approximations, will eventually remain the norm for preliminary and optimization design, particular transients, and SG control.
- The approximate (circuit) transient (fourth-order) model of SG is finally given, as it will be used in Chapter 6, which is dedicated to the control of SGs.

References

1. J. Machowski, J.W. Bialek, and J.R. Bumby, *Power System Dynamics and Stability*, John Wiley & Sons, New York, 1997.
2. M. Namba, J. Hosoda, S. Dri, and M. Udo, Development for measurement of operating parameters of synchronous generator and control system, *IEEE Trans.*, PAS-200, 2, 1981, pp. 618–628.
3. I. Boldea, and S.A. Nasar, Unified treatment of core losses and saturation in orthogonal axis model of electrical machines, *IEE Proc.*, 134, 6, 1987, pp. 355–363.
4. N.A. Arjona, and D.C. Macdonald, A new lumped steady-state synchronous machine model derived from finite element analysis, *IEEE Trans.*, EC-14, 1, 1999, pp. 1–7.
5. E. Levi, Saturation modeling in D-Q models of salient pole synchronous machines, *IEEE Trans.*, EC-14, 1, 1999, pp. 44–50.
6. A.M. El-Serafi, and J.Wu, Determination of parameter representing cross-coupling effect in saturated synchronous machines, *IEEE Trans.*, EC-8, 3, 1993, pp. 333–342.
7. K. Ide, S. Wakmi, K. Shima, K. Miyakawa, and Y. Yagi, Analysis of saturated synchronous reactances of large turbine generator by considering cross-magnetizing reactances using finite elements, *IEEE Trans.*, EC-14, 1, 1999, pp. 66–71.
8. I. Kamwa, P. Viarouge, and R. Mahfoudi, Phenomenological models of large synchronous machines from short-circuit tests during commissioning — A classical modern approach, *IEEE Trans.*, EC-9, 1, 1994, pp. 85–97.

9. S.A. Soliman, M.E. El-Hawary, and A.M. Al-Kandari, Synchronous Machine Optimal Parameter Estimation from Digitized Sudden Short-Circuit Armature Current, Record of ICEM-2000, Espoo, Finland.

10. A. Keyhani, H. Tsai, and T. Leksan, Maximum likelihood estimation of synchronous machine parameters from standstill time response data, *IEEE Trans.*, EC-9, 1, 1994, pp. 98–114.

11. I. Kamwa, P. Viarouge, and J. Dickinson, Identification of generalized models of synchronous machines from time domain tests, *IEEE Proc.*, 138, 6, 1991, pp. 485–491.

12. S. Horning, A. Keyhani, and I. Kamwa, On line evaluation of a round rotor synchronous machine parameter set estimated from standstill time domain data, *IEEE Trans.*, EC-12, 4, 1997, pp. 289–296.

13. K. Beya, R. Pintelton, J. Schonkens, B. Mpanda-Maswe, P. Lataire, M. Dehhaye, and P. Guillaume, Identification of synchronous machine parameter, using broadband excitation, *IEEE Trans.*, EC-9, 2, 1994, pp. 270–280.

14. I.M. Canay, Causes of discrepancies in calculation of rotor quantities and exact equivalent diagrams of the synchronous machine, *IEEE Trans.*, PAS-88, 1969, pp. 1114–1120.

15. I. Kamwa, and P. Viarouge, On equivalent circuit structures for empirical modeling of turbine-generators, *IEEE Trans.*, EC-9, 3, 1994, pp. 579–592.

16. P.L. Dandeno, and A.T. Poray, Development of detailed equivalent circuits from standstill frequency response measurements, *IEEE Trans.*, PAS-100, 4, 1981, pp. 1646–1655.

17. A. Keyhani, S. Hao, and R.P. Schultz, Maximum likelihood estimation of generator stability constants using SSFR test data, *IEEE Trans.*, EC-6, 1, 1991, pp. 140–154.

18. P. Kundur, *Power System Stability and Control*, McGraw-Hill, New York, 1993, pp. 169–191.

19. J.V. Milanovic, F. Al-Jowder, and E. Levi, Small Disturbance Stability of Saturated Anisotropic Synchronous Machine Models, Record of ICEM-2000, Espoo, Finland, vol. 2, pp. 898–902.

20. Y. Hanalla, and D.C. Macdonald, Numerical analysis of transient field in electrical machines, *IEE Proc.*, 123, 1976, pp. 183–186.

21. A.Y. Hanalla, and D.C. Macdonald, Sudden 3-phase shortcircuit characteristics of turbine generators from design data using electromagnetic field calculation, *IEE Proc.*, 127, 1980, pp. 213–220.

22. S.C. Tandon, A.F. Armor, and M.V.K. Chari, Nonlinear transient FE field computation for electrical machines and devices, *IEEE Trans.*, PAS-102, 1983, pp. 1089–1095.

23. P.J. Turner, FE simulation of turbine-generator terminal faults and application to machine parameter prediction, *IEEE Trans.*, EC-2, 1, 1987, pp. 122–131.

24. S.I. Nabita, A. Foggia, J.L. Coulomb, and G. Reyne, FE simulation of unbalanced faults in a synchronous machine, *IEEE Trans.*, MAG-32, 1996, pp. 1561–1564.

25. D.K. Sharma, D.H. Baker, J.W. Daugherty, M.D. Kankam, S.H. Miunich, and R.P. Shultz, Generator simulation-model constants by FE comparison with test results, *IEEE Trans.*, PAS-104, 1985, pp. 1812–1821.

26. M.A. Arjona, and D.C. Macdonald, Characterizing the D-axis machine model of a turbogenerator using finite elements, *IEEE Trans.*, EC-14, 3, 1999, pp. 340–346.

27. M.A. Arjona, and D.C. Macdonald, Lumped modeling of open circuit turbogenerator operational parameters, *IEEE Trans.*, EC-14, 3, 1999, pp. 347–353.

28. J. P. Sturgess, M. Zhu, and D.C. Macdonald, Finite element simulation of a generator on load during and after a three phase fault, *IEEE Trans.*, EC-7, 4, 1992, pp. 787–793.

29. T. Laible, *Theory of Synchronous Machines in Transient Regimes*, Springer-Verlag, Heidelberg, 1952.

6

Control of Synchronous Generators in Power Systems

6.1 Introduction

Satisfactory alternating current (AC) power system operation is obtained when frequency and voltage remain nearly constant or vary in a limited and controlled manner when active and reactive loads vary.

Active power flow is related to a prime mover's energy input and, thus, to the speed of the synchronous generator (SG). On the other hand, reactive power control is related to terminal voltage. Too large an electric active power load would lead to speed collapse, while too large a reactive power load would cause voltage collapse.

When a generator acts alone on a load, or it is by far the strongest in an area of a power system, its frequency may be controlled via generator speed, to remain constant with load (isochronous control). On the contrary, when the SG is part of a large power system, and electric generation is shared by two or more SGs, the frequency (speed) cannot be controlled to remain constant because it would forbid generation sharing between various SGs. Control with speed droop is the solution that allows for fair generation sharing.

Automatic generation control (AGC) distributes the generation task between SGs and, based on this as input, the speed control system of each SG controls its speed (frequency) with an adequate speed droop so that generation "desired" sharing is obtained.

By fair sharing, we mean either power delivery proportional to ratings of various SGs or based on some cost function optimization, such as minimum cost of energy.

Speed (frequency) control quality depends on the speed control of the SG and on the other "induced" influences, besides the load dependence on frequency. In addition, torsional shaft oscillations — due to turbine shaft, couplings, generator shaft elasticity, and damping effects — and subsynchronous resonance (due to transmission lines series capacitor compensation to increase transmission power capacity at long distance) influence the quality of speed (active power) control. Measures to counteract such effects are required. Some are presented in this chapter.

In principle, the reactive power flow of an SG may be controlled through SG output voltage control, which, in turn, is performed through excitation (current or voltage) control. SG voltage control quality depends on the SG parameters, excitation power source dynamics with its ceiling voltage, available to "force" the excitation current when needed in order to obtain fast voltage recovery upon severe reactive power load variations. The knowledge of load reactive power dependence on voltage is essential to voltage control system design.

Though active and reactive power control interactions are small in principle, they may influence each other's control stability. To decouple them, power system stabilizers (PSSs) can be added to the automatic voltage regulators (AVRs). PSSs have inputs such as speed or active power deviations and have lately generated extraordinary interest. In addition, various limiters — such as overexcitation (OEL) and underexcitation (UEL) — are required to ensure stability and avoid overheating of the SG. Load shedding and generator tripping are also included to match power demand to offer.

In a phase of the utmost complexity of SG control, with power quality as a paramount objective, SG models, speed governor models (Chapter 3), excitation systems and their control models, and PSSs, were standardized through Institute of Electrical and Electronics Engineers (IEEE) recommendations.

The development of powerful digital signal processing (DSP) systems and of advanced power electronics converters with insulated gate bipolar transistors (IGBTs), gate turn-off or thyristors (GTIs), MOS controlled thyristors (MCTs), together with new nonlinear control systems such as variable structure systems, fuzzy logic neural networks, and self-learning systems, may lead in the near future to the integration of active and reactive power control into unique digital multi-input self-learning control systems. The few attempts made along this path so far are very encouraging.

In what follows, the basics of speed and voltage control are given, while ample reference to the newest solutions is made, with some sample results. For more on power system stability and control see the literature [1–3].

We distinguish in Figure 6.1 the following components:

- Automatic generation control (AGC)
- Automatic reactive power control (AQC)
- Speed/power and the voltage/reactive power droop curves
- Speed governor (Chapter 3) and the excitation system
- Prime mover/turbine (Chapter 3) and SG (Chapter 5)
- Speed, voltage, and current sensors
- Step-up transformer, transmission line (X_T), and the power system electromagnetic field (emf), E_S
- PSS added to the voltage controller input

In the basic SG control system, the active and reactive power control subsystems are independent, with only the PSS as a "weak link" between them.
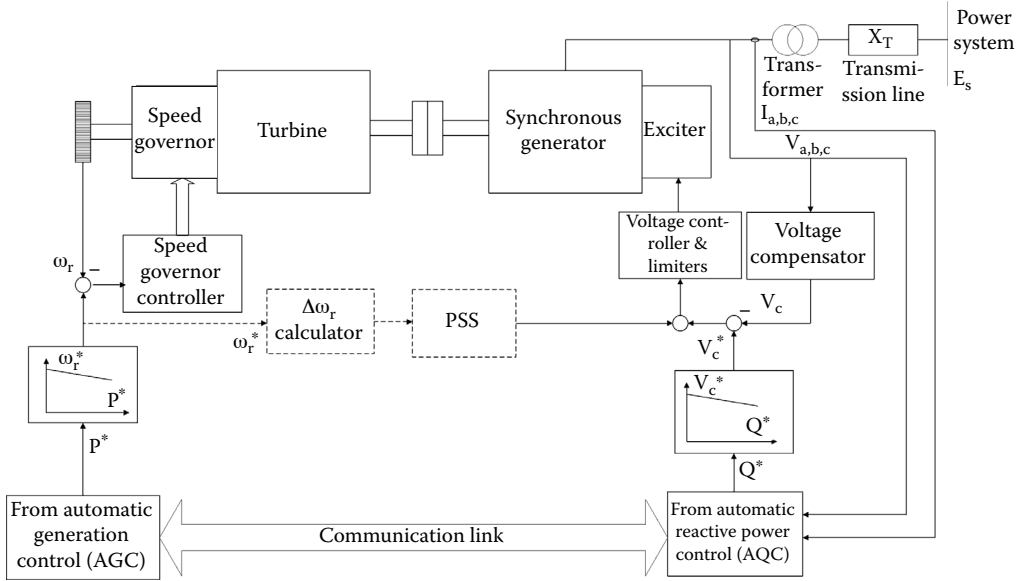
FIGURE 6.1 Generic synchronous generator control system.

The active power reference $P^\star$ is obtained through AGC. A speed (frequency)/power curve (straight line) leads to the speed reference $\omega_r^\star$. The speed error $\omega_r^\star - \omega_r$ then enters a speed governor control system with output that drives the valves and, respectively, the gates of various types of turbine speed-governor servomotors. AGC is part of the load-frequency control of the power system of which the SG belongs. In the so-called supplementary control, AGC moves the ω_r/P curves for desired load sharing between generators. On the other hand, AQC may provide the reactive power reference of the respective generator $Q^\star <> 0$.

A voltage/reactive power curve (straight line) will lead to voltage reference $V_C^\star$. The measured voltage V_G is augmented by an impedance voltage drop $I_G(R_C + jX_C)$ to obtain the compensated voltage V_C. The voltage error $V_C^\star - V_C$ enters the excitation voltage control (AVR) to control the excitation voltage V_f in such a manner that the reference voltage $V_C^\star$ is dynamically maintained.

The PSS adds to the input of AVR a signal that is meant to provide a positive damping effect of AVR upon the speed (active power) low-frequency local pulsations.

The speed governor controller (SGC), the AVR, and the PSS may be implemented in various ways from proportional integral (PI), proportional integral derivative (PID) to variable structure, fuzzy logic, artificial neural networks (ANNs), μ_∞, and so forth. There are also various built-in limiters and protection measures.

In order to design SGC, AVR, PSS, proper turbine, speed governor, and SG simplified models are required. As for large SGs in power systems, the speed and excitation voltage control takes place within a bandwidth of only 3 Hz, and simplified models are feasible.

6.2 Speed Governing Basics

Speed governing is dedicated to generator response to load changes. An isolated SG with a rigid shaft system and its load are considered to illustrate the speed governing concept (Figure 6.2, [1,2]).

The motion equation is as follows:

$$2H \frac{d\omega_r}{dt} = T_m - T_e \tag{6.1}$$
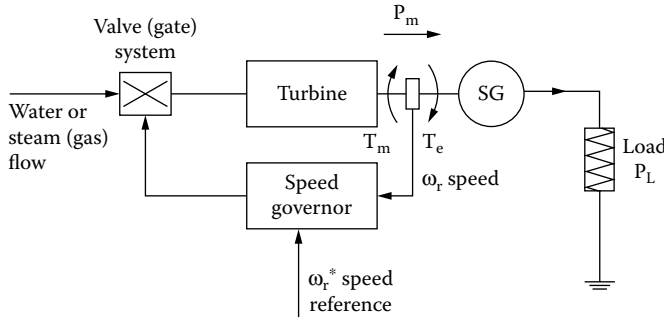
FIGURE 6.2 Synchronous generator with its own load.

where

T_m = the turbine torque (per unit [P.U.])
T_e = the SG torque (P.U.)
H (seconds) = inertia

We may use powers instead of torques in the equation of motion. For small deviations,

$$P = \omega_r T = P_0 + \Delta P$$
$$T_m = T_{m0} + \Delta T_m; T_e = T_{e0} + \Delta T_e \tag{6.2}$$
$$\omega_r = \omega_0 + \Delta \omega_r$$

For steady state, $T_{m0} = T_{en}$; thus, from Equation 6.1 and Equation 6.2,

$$\Delta P_m - \Delta P_e = \omega_0 \left(\Delta T_m - \Delta T_e \right) \tag{6.3}$$

For rated speed $\omega_0 = 1$ (P.U.),

$$2H \frac{d\Delta\omega_r}{dt} = \left(\Delta P_m - \Delta P_e \right)/\omega_0 ; M = 2H\omega_0 \tag{6.4}$$

The transfer function in Equation 6.4 is illustrated in Figure 6.3.

The electromagnetic power P_e is delivered to composite loads. Some loads are frequency independent (lighting and heating loads). In contrast, motor loads depend notably on frequency. Consequently,

$$\Delta P_e = \Delta P_L + D\Delta \omega_r \tag{6.5}$$

where

ΔP_L = the load power change, which is independent of frequency
D = a load damping constant
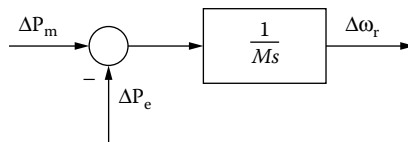
FIGURE 6.3 Power/speed transfer function (in per unit [P.U.] terms).
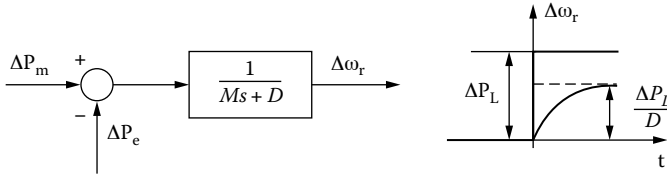
FIGURE 6.4 Power/speed transfer function with load frequency dependence.
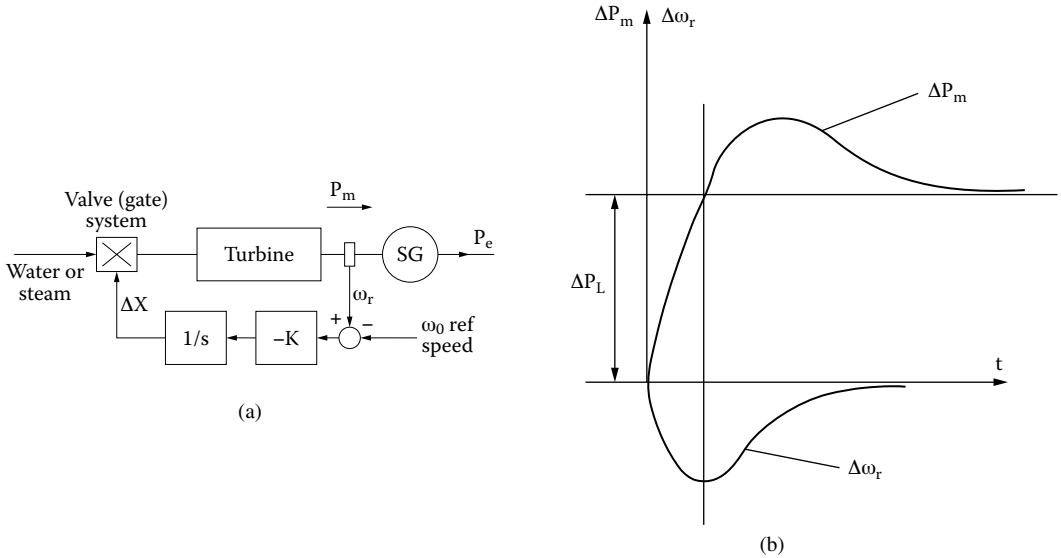
FIGURE 6.5 Isochronous (integral) speed governor: (a) schematics and (b) response to step load increase.

Introducing Equation 6.5 into Equation 6.4 leads to the following:

$$2H\omega_0 d\frac{\Delta\omega_r}{dt} + D\Delta\omega_r = \Delta P_m - \Delta P_L \tag{6.6}$$

The new speed/mechanical power transfer function is as shown in Figure 6.4. The steady-state speed deviation $\Delta\omega_r$, when the load varies, depends on the load frequency sensitivity. For a step variation in load power (ΔP_L), the final speed deviation is $\Delta\omega_r = \Delta P_L/D$ (Figure 6.4). The simplest (primitive) speed governor would be an integrator of speed error that will drive the speed to its reference value in the presence of load torque variations. This is called the isochronous speed governor (Figure 6.5a and Figure 6.5b).

The primitive (isochronous) speed governor cannot be used when more SGs are connected to a power system because it will not allow for load sharing. Speed droop or speed regulation is required: in principle, a steady-state feedback loop in parallel with the integrator (Figure 6.6a and Figure 6.6b) will do. It is basically a proportional speed controller with R providing the steady-state speed vs. load power (Figure 6.6c) straight-line dependence:

$$R = \frac{-\Delta f}{\Delta P_L} \tag{6.7}$$

The time response of a primitive speed-droop governor to a step load increase is characterized now by speed steady-state deviation (Figure 6.6d).
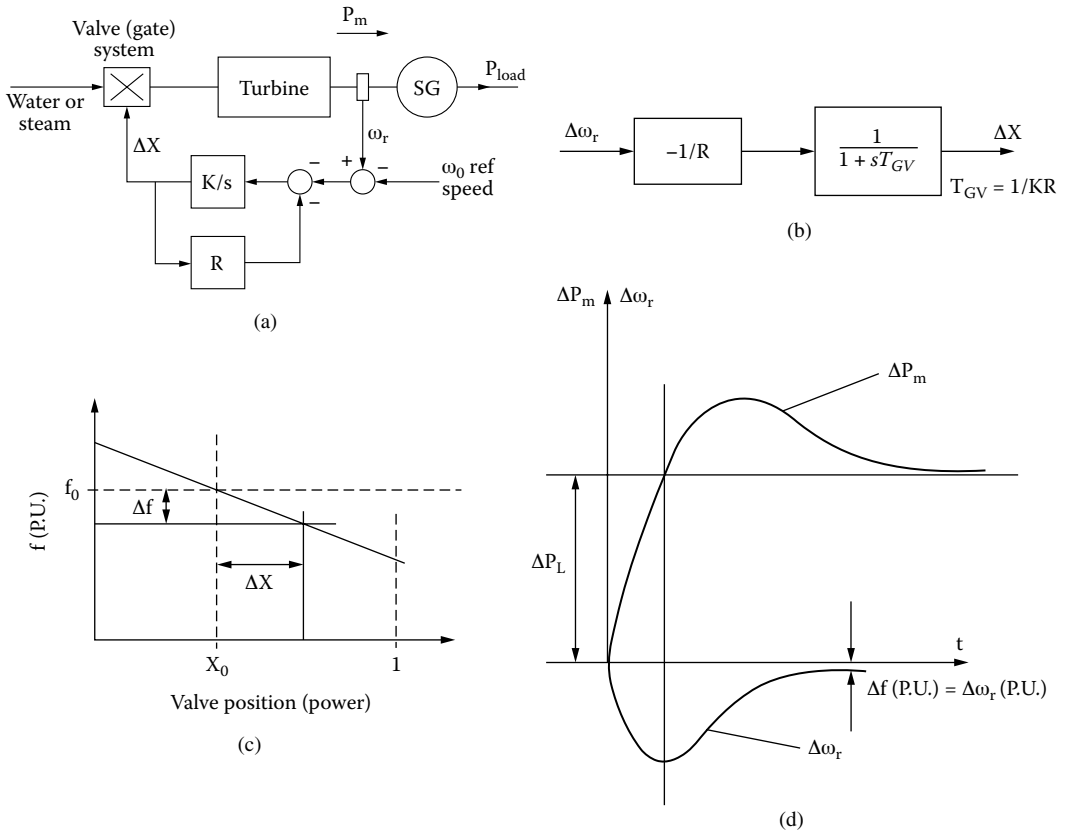
FIGURE 6.6 The primitive speed-droop governor: (a) schematics, (b) reduced structural diagram, (c) frequency/power droop, and (d) response to step load power.

With two (or more) generators in parallel, the frequency will be the same for all of them and, thus, the load sharing depends on their speed-droop characteristics (Figure 6.7). As

$$-\Delta P_1 R_1 = \Delta f\,;$$
$$-\Delta P_2 R_2 = \Delta f \tag{6.8}$$

it follows that

$$\frac{\Delta P_2}{\Delta P_1} = \frac{R_1}{R_2} \tag{6.9}$$

Only if the speed droop is the same ($R_1 = R_2$) are the two SGs loaded proportionally to their rating. The speed/load characteristic may be moved up and down by the load reference set point (Figure 6.8).

By moving the straight line up and down, the power delivered by the SG for a given frequency goes up and down (Figure 6.9). The example in Figure 6.9 is related to a 50 Hz power system. It is similar for 60 Hz power systems. In essence, the same SG may deliver at 50 Hz, zero power (point A), 50% power (point B), and 100% power (point C). In strong power systems, the load reference signal changes the power output and not its speed, as the latter is determined by the strong power system.
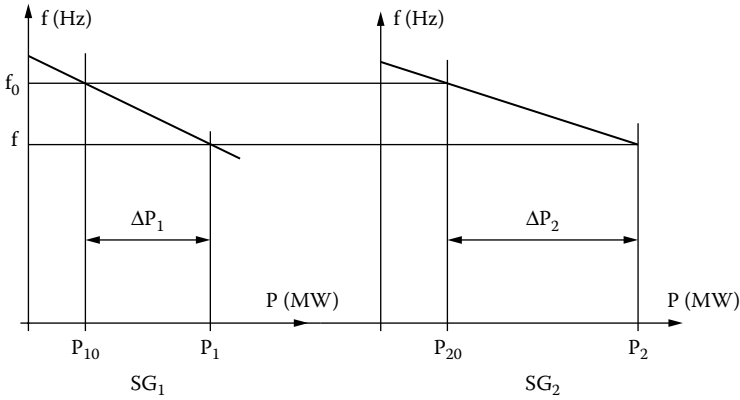
FIGURE 6.7 Load sharing between two synchronous generators with speed-droop governor.
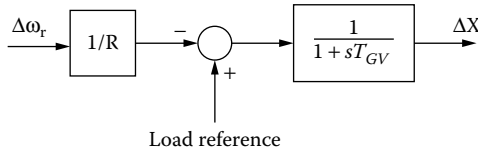
FIGURE 6.8 Speed-droop governor with load reference control.
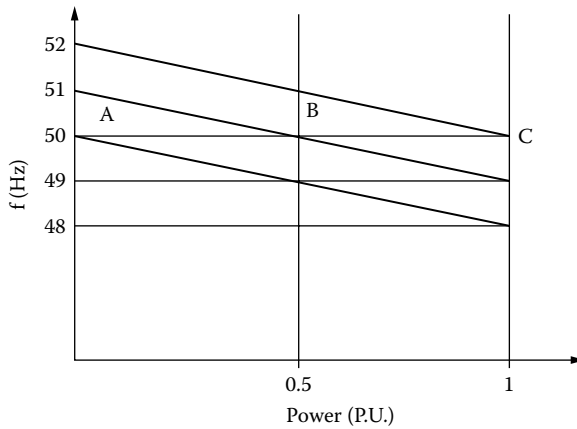
FIGURE 6.9 Moving the frequency (speed)/power characteristics up and down.

It should also be noted that, in reality, the frequency (speed) power characteristics depart from a straight line but still have negative slopes, for stability reasons. This departure is due to valve (gate) nonlinear characteristics; when the latter are linearized, the straight line $f(P)$ is restored.

6.3 Time Response of Speed Governors

In Chapter 3, we introduced models that are typical for steam reheat or nonreheat turbines (Figure 3.9 and Figure 3.10) and hydraulic turbines (Figure 3.40 and Equation 3.42). Here we add them to the speed-droop primitive governor with load reference, as discussed in the previous paragraph (Figure 6.10a and Figure 6.10b):

- T_{CH} is the inlet and steam chest delay (typically: 0.3 sec)
- T_{RH} is the reheater delay (typically: 6 sec)
- F_{HP} is the high pressure (HP) flow fraction (typically: $F_{HP} = 0.3$)

With nonreheater steam turbines: $T_{RH} = 0$.

For hydraulic turbines, the speed governor has to contain transient droop compensation. This is so because a change in the position of the gate, at the foot of the penstock, first produces a short-term turbine power change opposite to the expected one. For stable frequency response, long resetting times are required in stand-alone operation.

A typical such system is shown in Figure 6.10b:

- T_W is the water starting constant (typically: $T_W = 1$ sec)
- R_p is the steady-state speed droop (typically: 0.05)
- T_{GV} is the main gate servomotor time constant (typically: 0.2 sec)
- T_R is the reset time (typically: 5 sec)
- R_T is the transient speed droop (typically: 0.4)
- D is the load damping coefficient (typically: $D = 2$)

Typical responses of the systems in Figure 6.10a and Figure 6.10b to a step load (ΔP_L) increase are shown in Figure 6.11 for speed deviation $\Delta \omega_r$ (in P.U.). As expected, the speed deviation response is rather slow for hydraulic turbines, average with reheat steam turbine generators, and rather fast (but oscillatory) for nonreheat steam turbine generators.
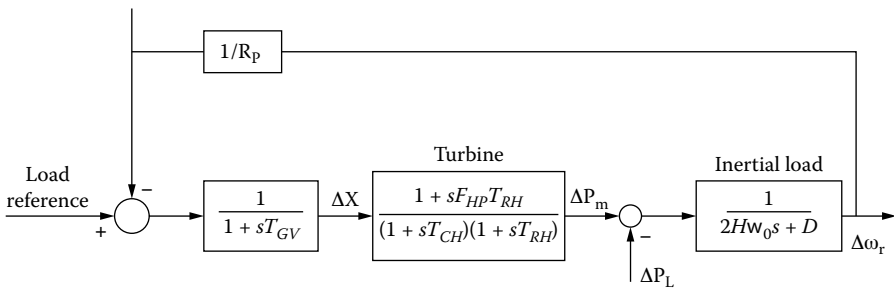
(a)
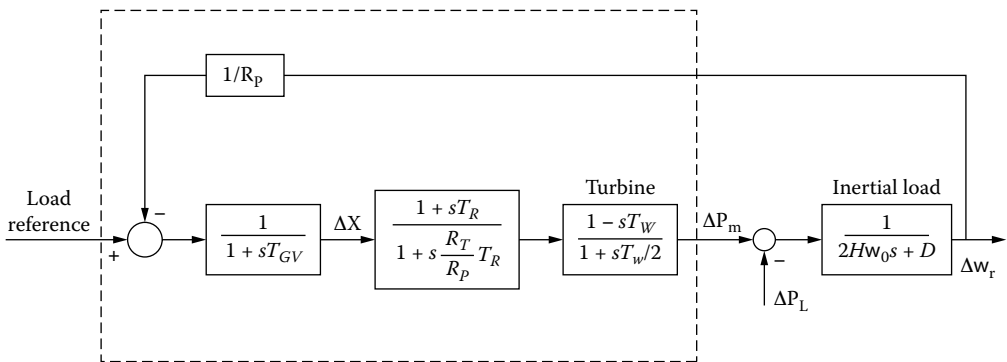
(b)

FIGURE 6.10   (a) Basic speed governor and steam turbine generator; (b) basic speed governor and hydraulic turbine generator.
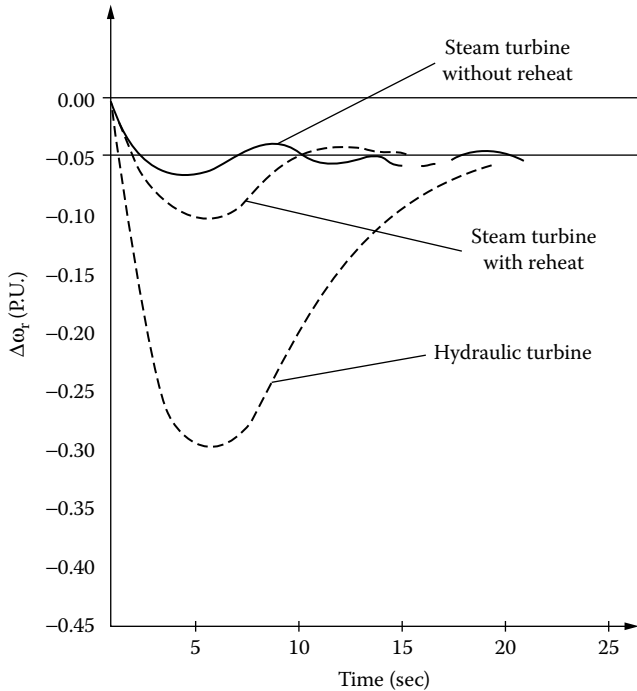
FIGURE 6.11 Speed deviation response of basic speed governor–turbine–generator systems to step load power change.

The speed governor turbine models in Figure 6.10 are standard. More complete (nonlinear) models are closer to reality. Also, nonlinear, more robust speed governor controllers are to be used to improve speed (or power angle) deviation response to various load perturbations (ΔP_L).

6.4 Automatic Generation Control (AGC)

In a power system, when load changes, all SGs contribute to the change in power generation. The restoration of power system frequency requires additional control action that adjusts the load reference set points. Load reference set point modification leads to automatic change of power delivered by each generator.

AGC has three main tasks:

- Regulate frequency to a specified value
- Maintain inter-tie power (exchange between control areas) at scheduled values
- Distribute the required change in power generation among SGs such that the operating costs are minimized

The first two tasks are also called load-frequency control.

In an isolated power system, the function of AGC is to restore frequency, as inter-tie power exchange is not present. This function is performed by adding an integral control on the load reference settings of the speed governors for the SGs with AGC. This way, the steady-state frequency error becomes zero. This integral action is slow and thus overrides the effects of the composite frequency regulation characteristics of the isolated power system (made of all SGs in parallel). Thus, the generation share of SGs that are not under the AGC is restored to scheduled values (Figure 6.12). For an interconnected power system, AGC is accomplished through the so-called tie-line control. And, each subsystem (area) has its own
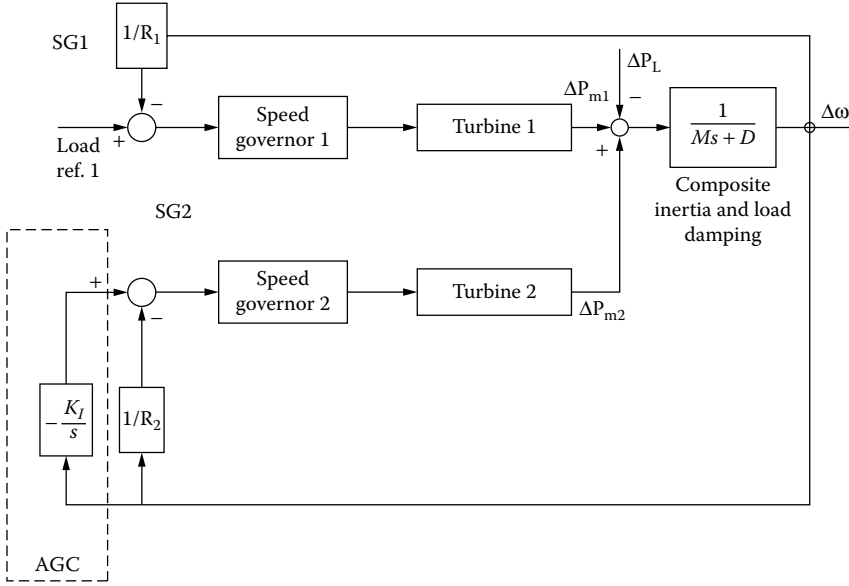
FIGURE 6.12 Automatic generation control of one synchronous generator in a two-synchronous-generator isolated power system.

central regulator (Figure 6.13a). The interconnected power system in Figure 6.13 is in equilibrium if, for each area,

$$P_{Gen} = P_{load} + P_{tie} \tag{6.10}$$

The inter-tie power exchange reference $(P_{tie})_{ref}$ is set at a higher level of power system control, based on economical and safety reasons.

The central subsystem (area) regulator has to maintain frequency at f_{ref} and the net tie-line power (tie-line control) from the subsystem area at a scheduled value P_{tieref}. In fact (Figure 6.13b), the tie-line control changes the power output of the turbines by varying the load reference (P_{ref}) in their speed governor systems. The area control error (ACE) is as follows (Figure 6.13b):

$$ACE = -\Delta P_{tie} - \lambda_R \Delta f \tag{6.11}$$

ACE is aggregated from tie-line power error and frequency error. The frequency error component is amplified by the so-called frequency bias factor λ_R. The frequency bias factor is not easy to adopt, as the power unbalance is not entirely represented by load changes in power demand, but in the tie-line power exchange as well.

A PI controller is applied on ACE to secure zero steady-state error. Other nonlinear (robust) regulators may be used. The regulator output signal is ΔP_{ref}, which is distributed over participating generators with participating factors $\alpha_1, \ldots \alpha_n$. Some participating factors may be zero. The control signal acts upon load reference settings (Figure 6.12).

Inter-tie power exchange and participation factors are allocated based on security assessment and economic dispatch via a central computer.

AGC may be treated as a multilevel control system (Figure 6.14). The primary control level is represented by the speed governors, with their load reference points. Frequency and tie-line control represent secondary control that forces the primary control to bring to zero the frequency and tie-line power deviations.

Economic dispatch with security assessment represents the tertiary control. Tertiary control is the slowest (minutes) of all control stages, as expected.

(a)

(b)
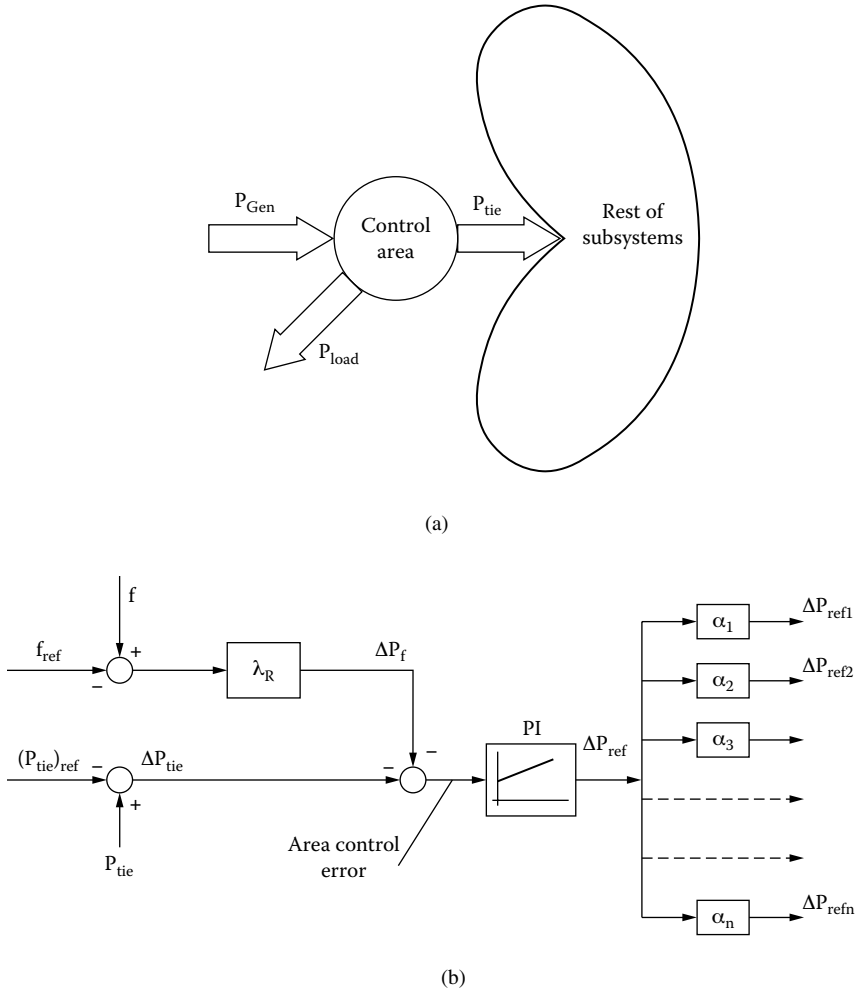
FIGURE 6.13 Central subsystem (tie-line): (a) power balance and (b) structural diagram.

6.5 Time Response of Speed (Frequency) and Power Angle

So far, we described the AGC as containing three control levels in an interconnected power system. Based on this, the response in frequency, power angle, and power of a power system to a power imbalance situation may be approached. If a quantitative investigation is necessary, all the components have to be introduced with their mathematical models. But, if a qualitative analysis is sought, then the automatic voltage regulators are supposed to maintain constant voltage, while electromagnetic transients are neglected. Basically, the power system moves from a steady state to another steady-state regime, while the equation of motion applies to provide the response in speed and power angle.

Power system disturbances are numerous, but consumer load variation and disconnection or connection of an SG from (or to) the power system are representative examples. Four time stages in the response to a power system imbalance may be distinguished:

- Rotor swings in the SGs (the first few seconds)
- Frequency drops (several seconds)
- Primary control by speed governors (several seconds)
- Secondary control by central subsystem (area) regulators (up to one minute)
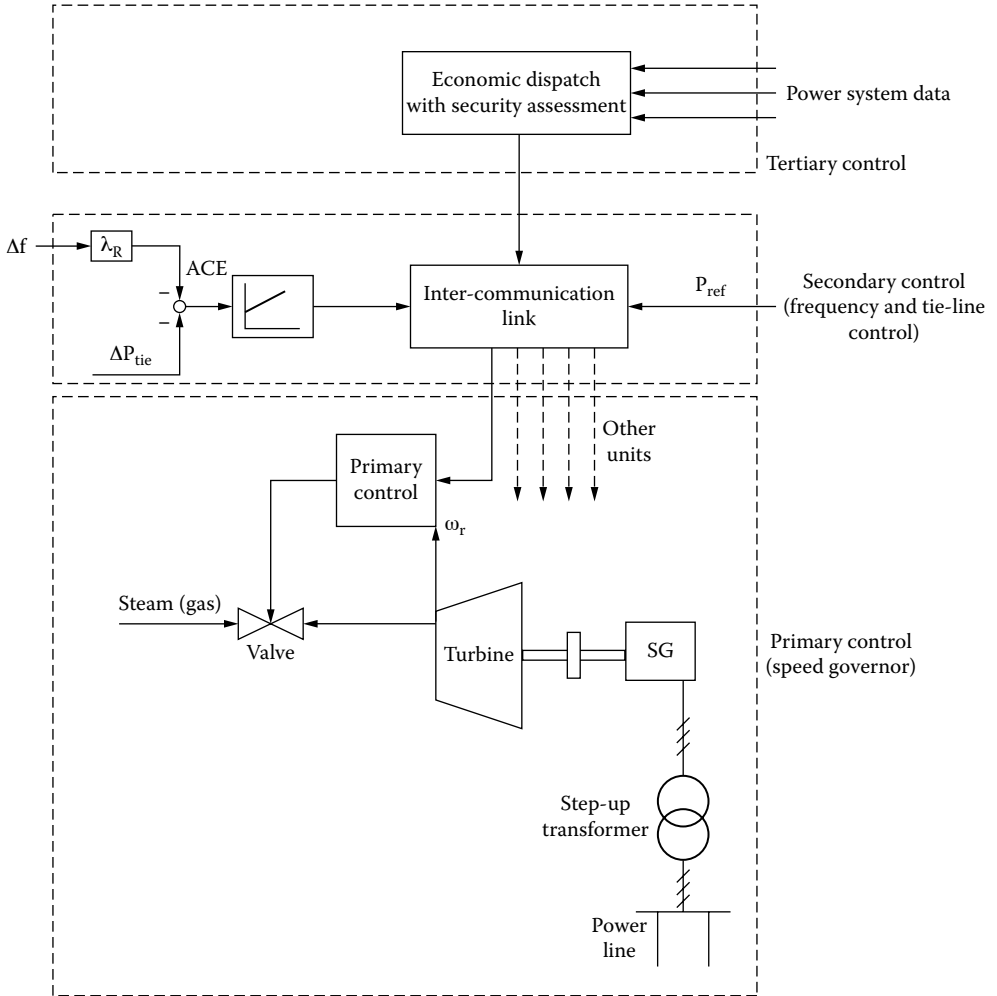
FIGURE 6.14 Automatic generation control as a multilevel control system.

During periodic rotor swings, the mechanical power of the remaining SGs may be considered constant. So, if one generator, out of two, is shut off, the power system mechanical power is reduced twice. The capacity of the remaining generators to deliver power to loads is reduced from the following:

$$P_-\left(\delta_0'\right) = \frac{E'V_S}{\dfrac{X_d' + X_T}{2} + X_S} \sin\delta_0' \qquad (6.12)$$

to

$$P_+\left(\delta\right) = \frac{E'V_S \sin\delta_0'}{X_d' + X_T + X_S}, \ (P.U.) \qquad (6.13)$$

in the first moments after one generator is disconnected. Notice that X_T is the transmission line reactance (there are two lines in parallel) and X_S is the power system reactance. X_d' is the transient reactance of the
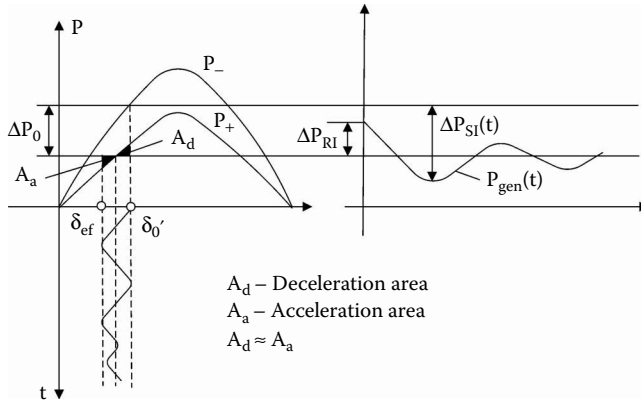
FIGURE 6.15 Rotor swings and power system contributing power change.

generator, E' is the generator transient emf, and V_S is the power system voltage. The situation is illustrated in Figure 6.15.

Notice that the load power has not been changed. Both the remaining generator (ΔP_{RI}) and the power system have to cover for the deficit ΔP_0:

$$\Delta P_{RI} = P_+(\delta') - P_{m+}$$

$$\Delta P_{SI} = \Delta P_0 - \Delta P_{RI}$$

(6.14)

While the motion equation leads to the rotor swings in Figure 6.15, the power system still has to cover for the power $\Delta P_{SI}(t)$. So, the transient response to the power system imbalance (by disconnecting a generator out of two) continues with stage two: frequency control.

Due to the additional power system contribution requirement during this second stage, the generators in the power system slow, and the system frequency drops. During this stage, the share from ΔP_{SI} is determined by the inertia of the generator. The basic element is that the power angle of the studied generator goes further down while the SG is still in synchronism. When this drop in power angle and frequency occurs, we enter stage three, when primary (speed governors) control takes action, based on the frequency/power characteristics.

The increase in mechanical power required from each turbine is, as known, inversely proportional to the droop in the $f(P)$ curve (straight line). When the disconnection of one of the two generators occurred, the $f(P)$ composite curve is changing from P_{T-} to P_{T+} (Figure 6.16).
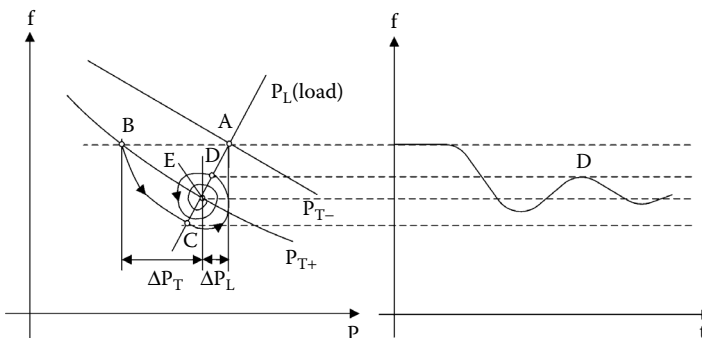
FIGURE 6.16 Frequency response for power imbalance.
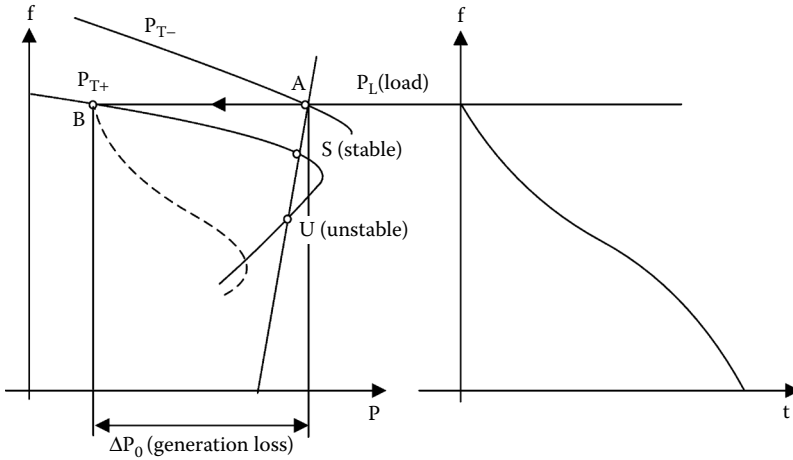
FIGURE 6.17 Extended *f(P)* curves with frequency collapse when large power imbalance occurs.
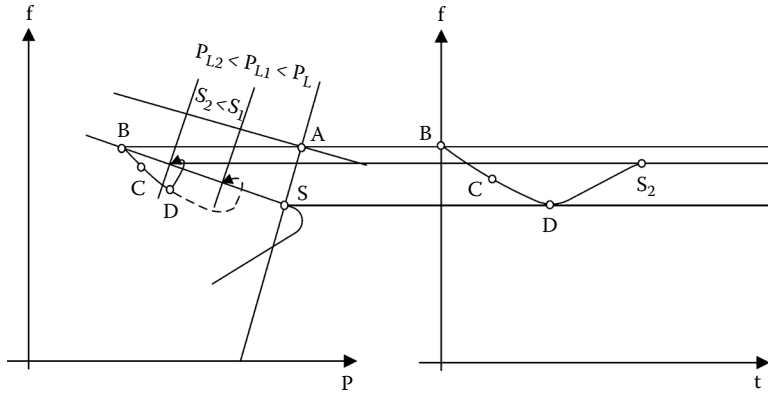
FIGURE 6.18 Frequency restoration via two-stage load shedding.

The operating point moves from A to B as one generator was shut off. The load/frequency characteristic is *f(P_L)* in Figure 6.16. Along the trajectory BC, the SG decelerates until it hits the load curve in C, then accelerates up to D and so on, until it reaches the new stable point E.

The straight-line characteristics *f(P)* will remain valid — power increases with frequency (speed) reduction — up to a certain power when frequency collapses. In general, if enough power (spinning) reserve exists in the system, the straight-line characteristic holds. Spinning reserve is the difference between rated power and load power in the system. Frequency collapse is illustrated in Figure 6.17.

Because of the small spinning reserve, the frequency decreases initially so much that it intercepts the load curve in *U*, an unstable equilibrium point. So, the frequency decreases steadily and finally collapses. To prevent frequency collapsing, load shedding is performed. At a given frequency level, underfrequency relays in substations shut down scheduled loads in two to three steps in an attempt to restore frequency (Figure 6.18).

When frequency reaches point C, the first stage of load (P_{L1}) shedding is operated. The frequency still decreases, but at a slower rate until it reaches level D, when the second load shedding is performed. This time (as D is at the right side of S_2), the generator accelerates and restores frequency at S_2.

In the last stage of response dynamics, frequency and the tie-line power flow control through the AGC take action. In an islanded system, AGC actually moves up stepwise the *f(P)* characteristics of generators

such as to restore frequency to its initial value. Details on frequency dynamics in interconnected power systems can be found in the literature [1, 2].

6.6 Voltage and Reactive Power Control Basics

Dynamically maintaining constant (or controlled) voltage in a power system is a fundamental requirement of power quality. Passive (resistive-inductive, resistive-capacitive) loads and active loads (motors) require both active and reactive power flows in the power system.

While composite load power dependence on frequency is mild, the reactive load power dependency on voltage is very important. Typical shapes of composite load (active and reactive power) dependence on voltage are shown in Figure 6.19.

As loads "require" reactive power, the power system has to provide for it. In essence, reactive power may be provided or absorbed by the following:

- Control of excitation voltage of SGs by automatic voltage regulation (AVR)
- Power-electronics-controlled capacitors and inductors by static voltage controllers (SVCs) placed at various locations in a power system

As voltage control is related to reactive power balance in a power system, to reduce losses due to increased power-line currents, it is appropriate to "produce" the reactive power as close as possible to the place of its "utilization." Decentralized voltage (reactive power) control should thus be favored.

As the voltage variation changes, both the active and reactive power that can be transmitted over a power network vary, and it follows that voltage control interferes with active power (speed) control. The separate treatment of voltage and speed control is based on their weak coupling and on necessity. One way to treat this coupling is to add to the AVR the so-called PSS, with input that is speed or active power deviation.
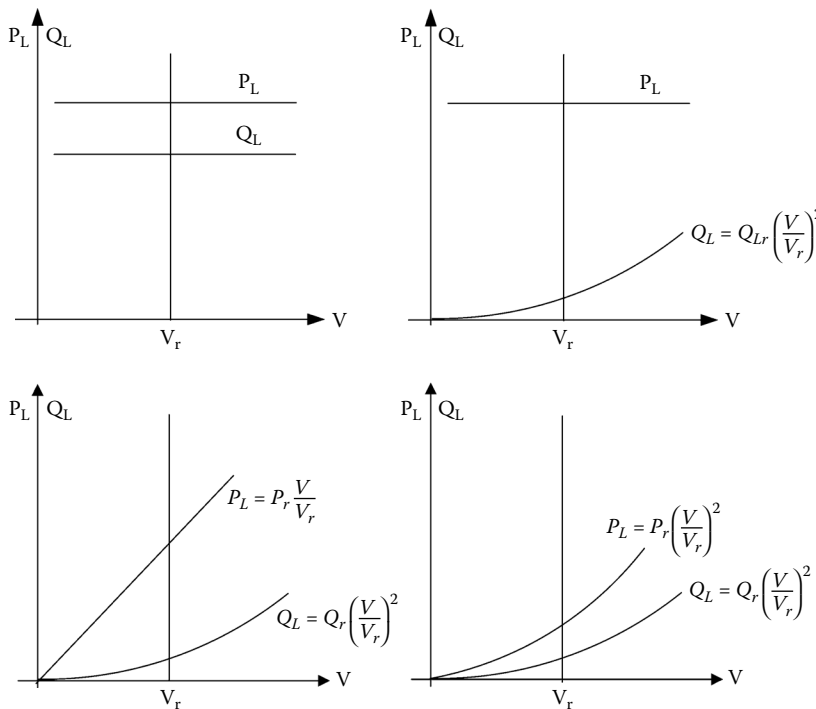
FIGURE 6.19 Typical P_L, Q_L load powers vs. voltage.
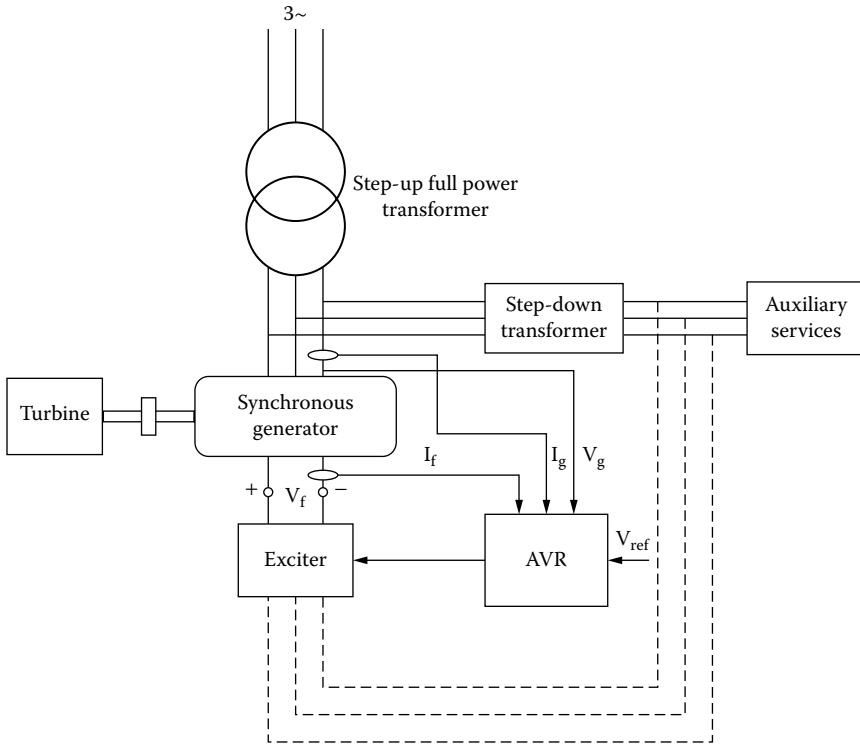
FIGURE 6.20   Exciter with automatic voltage regulator (AVR).

6.7   The Automatic Voltage Regulation (AVR) Concept

AVR acts upon the DC voltage V_f that supplies the excitation winding of SGs. The variation of field current in the SG increases or decreases the emf (no load voltage); thus, finally, for a given load, the generator voltage is controlled as required. The excitation system of an SG contains the exciter and the AVR (Figure 6.20).

The exciter is, in fact, the power supply that delivers controlled power to SG excitation (field) winding. As such, the exciters may be classified into the following:

- DC exciters
- AC exciters
- Static exciters (power electronics)

The DC and AC exciters contain an electric generator placed on the main (turbine-generator) shaft and have low power electronics control of their excitation current. The static exciters take energy from a separate AC source or from a step-down transformer (Figure 6.20) and convert it into DC-controlled power transmitted to the field winding of the SG through slip-rings and brushes.

The AVR collects information on generator current and voltage (V_g, I_g) and on field current, and, based on the voltage error, controls the V_f (the voltage of the field winding) through the control voltage V_{con}, which acts on the controlled variable in the exciter.

6.8   Exciters

As already mentioned, exciters are of three types, each with numerous embodiments in industry.
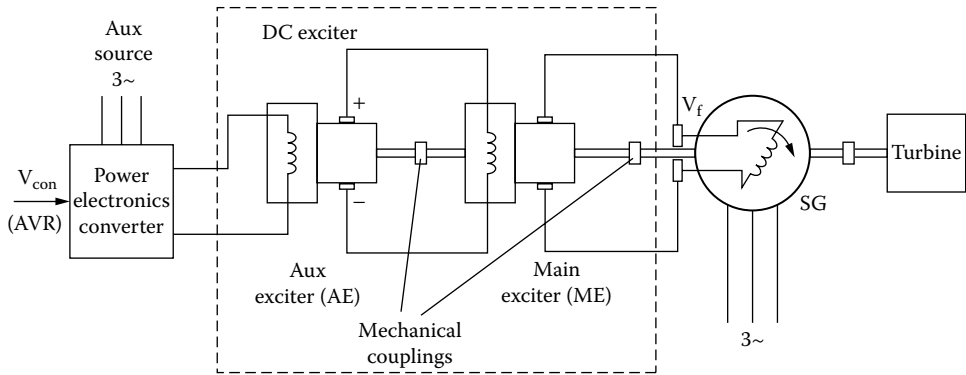
FIGURE 6.21 Typical direct current (DC) exciter.

The DC exciter (Figure 6.21), still in existence for many SGs below 100 MVA per unit, consists of two DC commutator electric generators: the main exciter (ME) and the auxiliary exciter (AE). Both are placed on the SG main shaft. The ME supplies the SG field winding (V_f), while the AE supplies the ME field winding.

Only the field winding of the auxiliary exciter is supplied with the voltage V_{con} controlled by the AVR. The power electronics source required to supply the AE field winding is of very low power rating, as the two DC commutator generators provide a total power amplification ratio around 600/1.

The advantage of a low power electronics external supply required for the scope is paid for by the following:

- A rather slow time response due to the large field-winding time constants of the two excitation circuits plus the moderate time constants of the two armature windings
- Problems with brush wearing in the ME and AE
- Transmission of all excitation power (the peak value may be 4 to 5% of rated SG power) of the SG has to be through the slip-ring brush mechanism
- Flexibility of the exciter shafts and mechanical couplings adds at least one additional shaft torsional frequency to the turbine-generator shaft

Though still present in industry, DC exciters were gradually replaced with AC exciters and static exciters.

6.8.1 AC Exciters

AC exciters basically make use of inside-out synchronous generators with diode rectifiers on their rotors. As both the AC exciter and the SG use the same shaft, the full excitation power diode rectifier is connected directly to the field winding of SG (Figure 6.22). The stator-based field winding of the AC exciter is controlled from the AVR.

The static power converter now has a rating about 1/20(30) of the SG excitation winding power rating, as only one step of power amplification is performed through the AC exciter.

The AC exciter in Figure 6.22 is characterized by the following:

- Absence of electric brushes in the exciter and in the SG
- Addition of a single machine on the main SG-turbine shaft
- Moderate time response in V_f (SG field-winding voltage), as only one (transient) time constant (T_{d0}') delays the response; the static power converter delay is small in comparison
- Addition of one torsional shaft frequency due to the flexibility of the AC exciter machine shaft and mechanical coupling
- Small controlled power in the static power converter: (1/20[30] of the field-winding power rating)
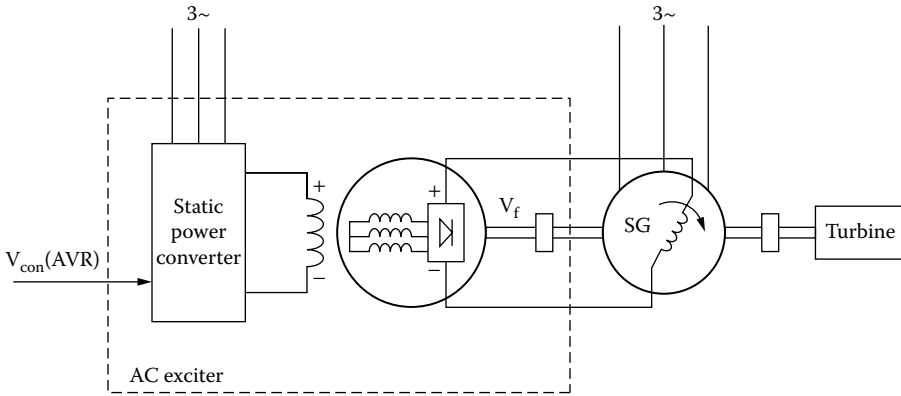
FIGURE 6.22 Alternating current (AC) exciter.

The brushless AC exciter (as in Figure 6.22) is used frequently in industry, even for new SGs, because it does not need an additional sizable power source to supply the exciter's field winding.

6.8.2 Static Exciters

Modern electric power plants are provided with emergency power groups for auxiliary services that may be used to start the former from blackout. So, an auxiliary power system is generally available.

This trend gave way to static exciters, mostly in the form of controlled rectifiers directly supplying the field winding of the SG through slip-rings and brushes (Figure 6.23a and Figure 6.23b). The excitation transformer is required to adapt the voltage from the auxiliary power source or from the SG terminals (Figure 6.23a).

It is also feasible to supply the controlled rectifier from a combined voltage transformer (VT) and current transformer (CT) connected in parallel and in series with the SG stator windings (Figure 6.23b). This solution provides a kind of basic AC voltage stabilization at the rectifier input terminals. This way, short-circuits or short voltage sags at SG terminals do not much influence the excitation voltage ceiling produced by the controlled rectifier.

In order to cope with fast SG excitation current control, the latter has to be forced by an overvoltage available to be applied to the field winding. The voltage ceiling ratio (V_{fmax}/V_{frated}) characterizes the exciter.

Power electronics (static) exciters are characterized by fast voltage response, but still the T_d' time constant of the SG delays the field current response. Consequently, a high-voltage ceiling is required for all exciters.

To exploit with minimum losses the static exciters, two separate controlled rectifiers may be used, one for "steady state" and one for field forcing (Figure 6.24). There is a switch that has to be kept open unless the field-forcing (higher voltage) rectifier has to be put to work. When V_{fmax}/V_{frated} is notably larger than two, such a solution may be considered.

The development of IGBT pulse-width modulator (PWM) converters up to 3 MVA per unit (for electric drives) at low voltages (690 VAC, line voltage) provides for new, efficient, lower-volume static exciters.

The controlled thyristor rectifiers in Figure 6.24 may be replaced by diode rectifiers plus DC–DC IGBT converters (Figure 6.25).

A few such four-quadrant DC–DC converters may be paralleled to fulfill the power level required for the excitation of SGs in the hundreds of MVAs per unit. The transmission of all excitation power through slip-rings and brushes remains a problem. However, with today's doubly fed induction generators at 400 MVA/unit, 30 MVA is transmitted to the rotor through slip-rings and brushes. The solution is, thus, here for the rather lower power ratings of exciters (less than 3 to 4% of SG rating).

The four-quadrant chopper static exciter has the following features:
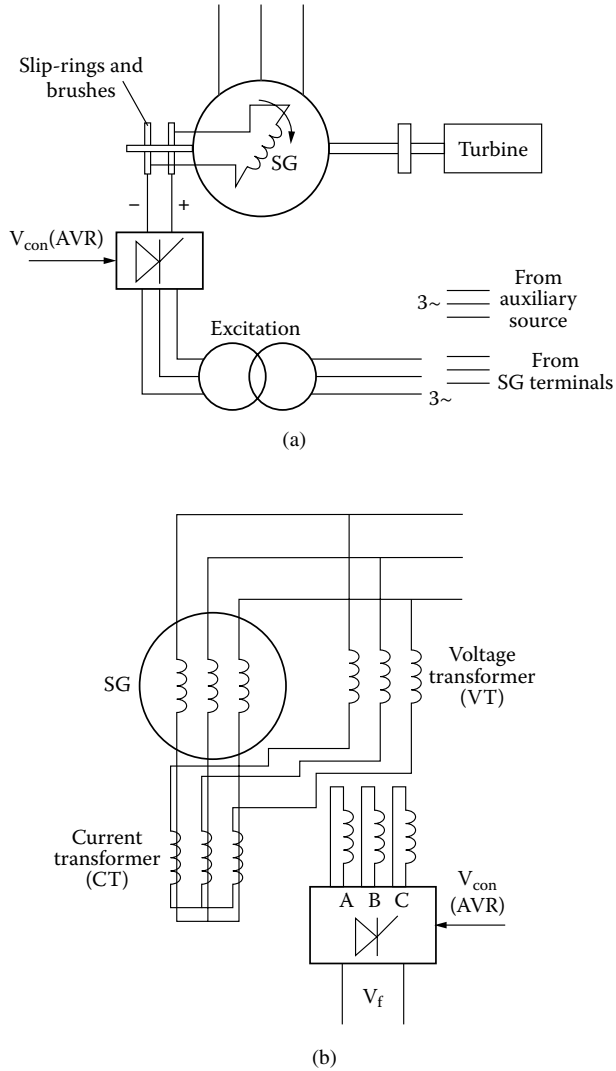
FIGURE 6.23   Static exciter: (a) voltage fed and (b) voltage and current fed.

- It produces fast current response with smaller ripple in the field-winding current of the SG.
- It can handle positive and negative field currents that may occur during transients as a result of stator current transients.
- The AC input currents (in front of the diode rectifier) are almost sinusoidal (with proper filtering), while the power factor is close to unity, irrespective of load (field) current.
- The current response is even faster than that with controlled rectifiers.
- Active front-end IGBT rectifiers may also be used for static exciters.

6.9   Exciter's Modeling

While it is possible to derive complete models for exciters — as they are interconnected electric generators or static power converters — for power system stability studies, simplified models have to be used. The IEEE standard 421.5 from 1992 contains "IEEE Recommended Practice for Excitation System Models for Power Systems."
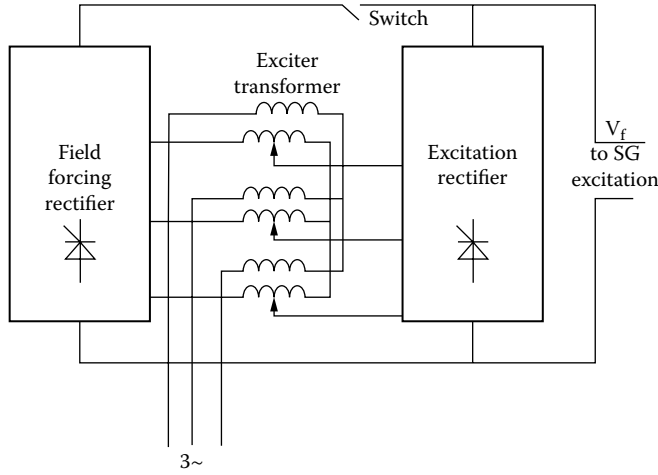
FIGURE 6.24 Dual rectifier static exciter.
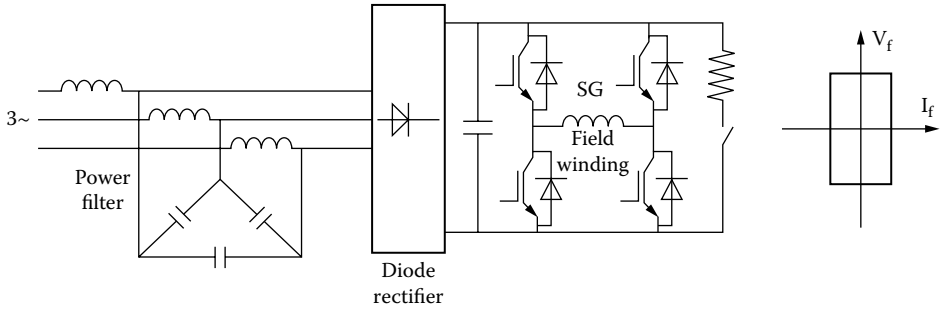
FIGURE 6.25 Diode-rectifier and four-quadrant DC–DC converter as static exciter.

Moreover, "Computer Models for Representation of Digital-Based Excitation Systems" were also recommended by IEEE in 1996.

6.9.1 New P.U. System

The so-called reciprocal P.U. system used for the SG, where the base voltage for the field-winding voltage V_f is the SG terminal rated voltage $V_n \times \sqrt{2}$ leads to a P.U. value of V_f in the range of 0.003 or so. Such values are too small to handle in designing the AVR.

A new, nonreciprocal, P.U. system is now widely used to handle this situation. Within this P.U. system, the base voltage for V_f is V_{fb}, the field-winding voltage required to produce the airgap line (nonsaturated) no-load voltage at the generator terminals. For the SG in P.U., at no load,

$$V_{d0} = +\Psi_{q0} = +L_q I_{q0} = 0$$

$$V_{q0} = -\Psi_{d0} = -L_{dm} I_f \qquad (6.15)$$

$$\left| V_{q0} \right| = V_0 = l_{dm} I_f = 1.0$$

So,

$$I_f = 1/l_{dm}(P.U.) \tag{6.16}$$

The field voltage V_f corresponding to I_f is as follows:

$$V_f = r_f \cdot I_f = \frac{r_f}{l_{dm}}(P.U.) \tag{6.17}$$

This is the reciprocal P.U. system.

In the nonreciprocal P.U. system, the corresponding field current $I_{fb} = 1.0$; thus,

$$I_{fb} = l_{dm}I_f \tag{6.18a}$$

The exciter voltage in the new P.U. system is, thus,

$$V_{fb} = \frac{l_{dm}}{r_f}V_f \tag{6.18b}$$

Using Equation 6.16 in Equation 6.18, we evidently find $V_{fb} = 1.0$, as we are at no-load conditions (Equation 6.15). In Chapter 5, the operational flux Ψ_d at no load was defined as follows:

$$\Delta\Psi_d(s) = \frac{l_{dm}}{r_f} \frac{(1+sT_D)\Delta V_f}{(1+sT'_{d0})(1+sT''_{d0})} \tag{6.19}$$

in the reciprocal P.U. system.

In the new, nonreciprocal, P.U. system, by using Equation 6.18 in Equation 6.19, we obtain the following:

$$\Delta\Psi_{db}(s) = \frac{(1+sT_D)\Delta V_{fb}}{(1+sT'_{d0})(1+sT''_{d0})} \tag{6.20}$$

However, at no load,

$$\Delta\Psi_{db} = \Delta V \tag{6.21}$$

Consequently, with the damping winding eliminated (T''_{d0}, $T_D = 0$),

$$\frac{\Delta V_0(s)}{\Delta V_{fb}(s)} = \frac{1}{1+sT'_{d0}} \tag{6.22}$$

The open-circuit transfer function of the generator has a gain equal to unity and the time constant T'_{d0}:

$$T'_{d0} = \frac{1}{\omega_{base}} \cdot \frac{(l_{fl}+l_{dm})}{r_f} \tag{6.23}$$

Example 6.1

Consider an SG with the following P.U. parameters: $l_{dm} = l_{qm} = 1.6$, $l_{sl} = 0.12$, $l_{fl} = 0.17$, $r_f = 0.0064$.

The rated voltage $V_0 = 24/\sqrt{3}$ kV, $f_1 = 60$ Hz. The field current and voltage required to produce the rated generator voltage at no load on the airgap line are $I_f = 1500$ A, $V_f = 100$ V.

Calculate the following:

1. The base values of V_f and I_f in the reciprocal and nonreciprocal (V_{fb}, I_{fb}) P.U. system
2. The open-circuit generator transfer function $\Delta V_0 / \Delta V_{fb}$

Solution

1. Evidently, $V_{fb} = 100$ V, $I_{fb} = 1500$ A, by definition, in the nonreciprocal P.U. system.

   For the reciprocal P.U. system, we make use of Equation 6.17 and Equation 6.18:

$$I_f = l_{dm} I_{fb} = 1.6 \cdot 1500 = 2400 \ A$$

$$V_f = \frac{l_{dm}}{r_f} V_{fb} = \left(\frac{1.6}{0.0064} \right) \cdot 100 = 250 \ kV$$

2. In the absence of damper winding, only the time constant T'_{d0} remains to be determined (Equation 6.23):

$$T'_{d0} = \frac{1}{2\pi 60} \cdot \frac{(0.17 + 1.6)}{0.0064} = 7.34 \ \text{sec}$$

$$\frac{\Delta V_0(s)}{\Delta V_{fb}(s)} = \frac{1}{1 + 7.34 \times s}$$

   When temperature varies, r_f varies, and thus, all base variables vary. The time constant T'_{d0} also varies.

6.9.2 The DC Exciter Model

Consider the separately excited DC commutator generator exciter (Figure 6.7), with its no-load and on-load saturation curves at constant speed.

Due to magnetic saturation, the relationship between DC exciter field current I_{ef} and the output voltage V_{ex} is nonlinear (Figure 6.26). The airgap line slope in Figure 6.26 is R_g (as in a resistance). In the IEEE standard 451.2, the magnetic saturation is defined by the saturation factor $S_e(V_{ex})$:

$$I_{ef} = \frac{V_{ex}}{R_g} + \Delta I_{ef}$$

$$\Delta I_{ef} = V_{ex} \cdot S_e(V_{ex}) \tag{6.24}$$

The saturation factor is approximated by using an exponential function:

$$S_e(V_{ex}) = \frac{1}{R_g} e^{B_e V_{ex}} \tag{6.25}$$

Other approximations are also feasible.
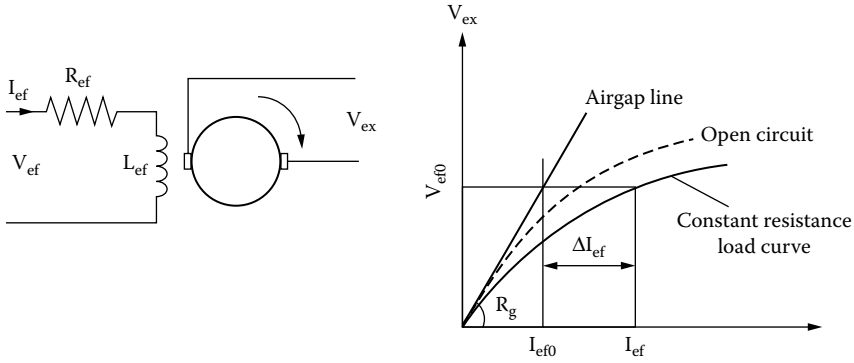
FIGURE 6.26 DC exciter and load-saturation curve.

The no-load DC exciter voltage V_{ex} is proportional to its excitation field Ψ_{ef}. For constant speed,

$$V_{ex} = K_e \cdot \Psi_{ef} = K_e \cdot L_{ef} \cdot I_{ef} \tag{6.26}$$

$$V_{ef} = R_{ef} I_{ef} + \frac{d\Psi_{ef}}{dt} = R_{ef} I_{ef} + L_{ef} \frac{dI_{ef}}{dt} \tag{6.27}$$

With Equation 6.24 through Equation 6.26, Equation 6.27 becomes

$$V_{ef} = \left(\frac{R_{ef}}{R_g} + R_{ef} S_e \left(V_{ex} \right) \right) V_{ex} + \frac{1}{K_e} \frac{dV_{ex}}{dt} \tag{6.28}$$

This is basically the voltage transfer function of the DC exciter on no load, considering magnetic saturation.

Again, P.U. variables are used with base voltage equal to the SG base field voltage V_{fb}:

$$V_{exb} = V_{fb}$$
$$I_{efb} = V_{fb} / R_g ; R_{gb} = R_g \tag{6.29}$$

In P.U., the saturation factor becomes

$$s_e(V_{ex}) = R_g S_e(V_{ex}) \tag{6.30}$$

Finally, Equation 6.28 in P.U. is as follows:

$$V_{ef} = \frac{R_{ef}}{R_g} V_{ex} \left(1 + s_e \left(V_{ex} \right) \right) + \frac{1}{K_e} \frac{dV_{ex}}{dt} \tag{6.31}$$

It is obvious that $1/K_e$ has the dimension of a time constant:

$$\frac{1}{K_e} \approx \frac{L_{ef}}{R_g} \frac{I_{ef0}}{V_{ex0}} = \frac{L_{ef}}{R_g} = T_{ex} \tag{6.32}$$
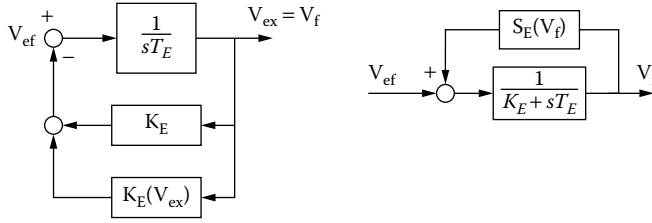
FIGURE 6.27 DC exciter.
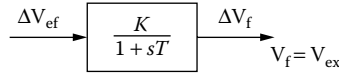
FIGURE 6.28 Small-signal deviation of DC exciters with separate excitation.

The values I_{ef0} and V_{ex0} in P.U., now correspond to a given operating point.
Finally, Equation 6.31 becomes

$$V_{ef} = V_{ex}\left(K_E + S_E\left(V_{ex}\right)\right) + T_E\frac{dV_{ex}}{dt} \tag{6.33}$$

with

$$K_E = \frac{R_{ef}}{R_g};$$

$$S_E\left(V_{ex}\right) = s_e\left(V_{ex}\right)\cdot\frac{R_{ef}}{R_g} \tag{6.34}$$

This is the widely accepted DC exciter model used for AVR design and power system stability studies. It may be expressed in a structural diagram as shown in Figure 6.27.

It is evident that for small-signal analysis, the structural diagram in Figure 6.27 may be simplified to the following:

$$\Delta V_{ef} = \Delta V_f\frac{\left(1 + sT\right)}{K}$$

$$K = \frac{1}{S_E\left(V_{ef0}\right) + K_E};\,T = KT_E \tag{6.35}$$

The corresponding structural diagram is shown in Figure 6.28. As expected, in its most simplified form, for small-signal deviations, the DC exciter is represented by a gain and a single time constant. Both K and T, however, vary with the operating point (V_{f0}). Note that the self-excited DC exciter model is similar, but with $K_E = R_{ef}/R_g - 1$ instead of $K_E = R_{ef}/R_g$. Also, K_E now varies with the operating point.

6.9.3 The AC Exciter

The AC exciter is, in general, a synchronous generator (inside-out for brushless excitation systems). Its control is again through its excitation and, in a way, is similar to the DC exciter. If a diode rectifier is used at the output of the AC exciter, the output DC current I_f is proportional to the armature current, as almost unity power factor operation takes place with diode rectification. What is additional in the AC
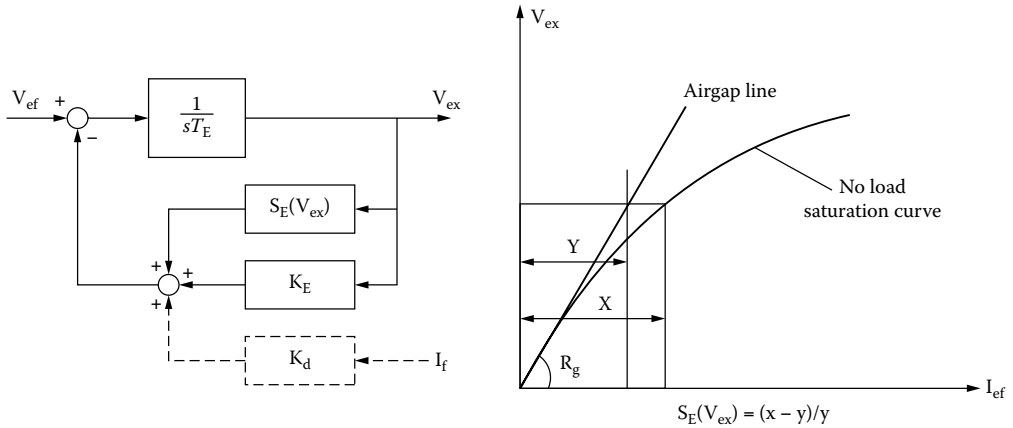
FIGURE 6.29 AC exciter alternator.
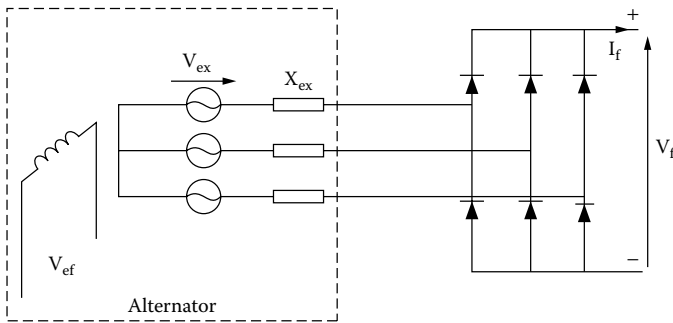
FIGURE 6.30 Diode rectifier plus alternator equals AC exciter.

exciter is a longitudinal demagnetizing armature reaction that tends to reduce the terminal voltage of the AC exciter. Consequently, one more feedback is added to the DC exciter model (Figure 6.29) to obtain the model of the AC exciter.

The saturation factor $S_E(V_f)$ should now be calculated from the no-load saturation curve and the airgap line of the AC exciter. The armature reaction feedback coefficient K_d is related to the d axis coupling inductance of the AC exciter (l_{dm}, when the field winding of the AC exciter is reduced to its armature winding). It is obvious that the influence of armature resistance and damper cage (if any) are neglected, and speed is considered constant. It is V_{ex} and not V_f in Figure 6.29, because a rectifier is used between the AC exciter and the SG field winding to change AC to DC. The uncontrolled rectifier that is part of the AC exciter is shown in Figure 6.30.

The $V_f(I_f)$ output curve of the diode rectifier is, in general, nonlinear and depends on the diode commutation overlapping. The alternator reactance (inductance) x_{ex} plays a key role in the commutation process. Three main operation modes may be identified from no load to short-circuit [5]:

• Stage 1: two diodes conducting before commutation takes place (low load):

$$\frac{V_f}{V_{ex}} = 1 - \frac{1}{\sqrt{3}}\frac{I_f}{I_{sc}} \text{ , for } I_f / I_{sc} < \left(1 - 1/\sqrt{3}\right) \tag{6.36}$$

$$I_{sc} = \frac{V_{ex}\sqrt{2}}{x_{ex}} \tag{6.37}$$
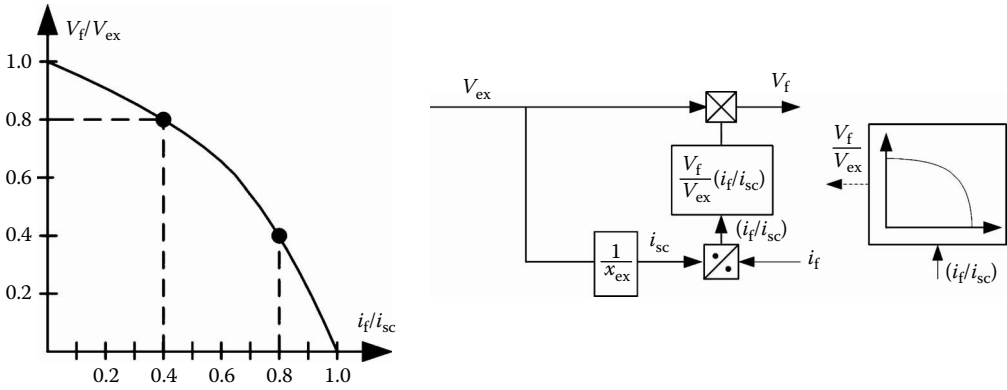
FIGURE 6.31 Diode rectifier voltage/current characteristic and structural diagram.

- Stage 2: when each diode can conduct only when the counterconnected diode of the same phase has ended its conduction interval:

$$\frac{V_f}{V_{ex}} = \sqrt{\frac{3}{4} - \left(\frac{i_f}{i_{sc}}\right)^2};$$

$$1 - 1/\sqrt{3} < \frac{I_f}{I_{sc}} < \frac{3}{4}$$

(6.38)

- Stage 3: four diodes conduct at the same time:

$$\frac{V_f}{V_{ex}} = \sqrt{3}\left(1 - \frac{i_f}{i_{sc}}\right);$$

$$\frac{3}{4} < \frac{i_f}{i_{sc}} < 1$$

(6.39)

The V_f/V_{ex} (i_f/i_{sc}) functions in Equation 6.36, Equation 6.38, and Equation 6.39 are illustrated in Figure 6.31. This is a steady-state characteristic. The response of the rectifier is so fast, in comparison with the alternator or to the SG field current response, that the steady-state characteristic suffices to model the rectifier.

6.9.4   The Static Exciter

Among the static exciter configurations, let us consider here the controlled three-phase rectifier (Figure 6.32).

The average value (steady-state) characteristic represents the output voltage of the V_f as a function of input voltage V_{ex} and the load (I_f) current [5, 6]:

$$V_f = \frac{3\sqrt{2}}{\pi} V_{ex}\sqrt{3}\cos\alpha - \frac{3}{\pi} x_{ex} I_f$$

$$I_{sc} = \frac{V_{ex}\sqrt{2}}{x_{ex}}$$

(6.40)
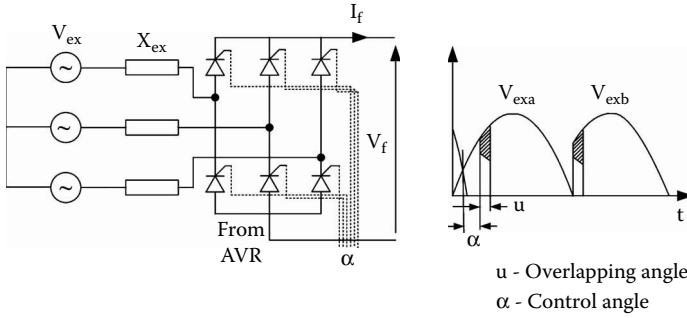
FIGURE 6.32 The controlled rectifier.
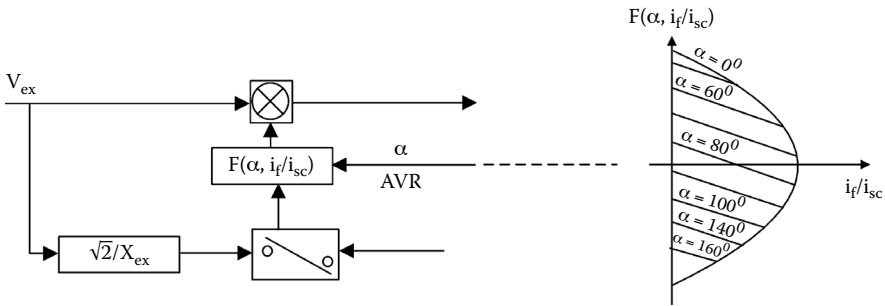
FIGURE 6.33 The structure of a controlled rectifier.

In P.U. values,

$$\frac{V_f}{V_{ex}} = \cos\alpha - \frac{1}{\sqrt{3}} I_f / I_{sc} = F\left(\alpha, i_f / i_{sc}\right) \tag{6.41}$$

The characteristic in Equation 6.41 is similar to the first stage of the diode rectifier characteristic. The structural diagram is also similar (Figure 6.33). For $\alpha = 0$, it degenerates into stage 1 of the diode rectifier case (Equation 6.36).

This time, the voltage V_f applied to the field winding may be either positive or negative, while the field current I_f is always positive. Faster response in I_f is expected, while the control is done through the firing delay angle α.

The power source (a transformer in general) has a rather constant emf V_{ex} and an internal reactance x_{ex}, so $\cos\alpha$ is input to the rectifier and is produced as the output of the AVR.

6.10   Basic AVRs

The basic AVR has to provide close-loop control of the SG terminal voltage by acting upon the exciter input with a voltage, V_{con}. It may have 1,2,3 stabilization loops and additional inputs, besides the reference voltage V_{ref} of SG and its measured value with load compensation V_c:

$$V_c = \left| V_g + \left(r_c + jX_c \right) I_g \right| \cdot \frac{1}{1 + sT_T} \tag{6.42}$$

The load compensator introduces the compensation of generator voltage variation due to load and also the delay T_T due to the voltage sensor. Other than that, a major field-winding voltage V_f loop is

(a)

Typical values:
$K_A = 300$
$T_F = 1.0$ s
$K_E = 1.0$
$T_B = 0$
$T_C = 0$
$T_E = 0.8$
$K_d = 0.4$
$K_F = 0.03$
$V_{rmax} = 7.0$
$V_{rmin} = 6.5$
$V_{amax} = 12.0$
$V_{amin} = -12.0$
$X_{ex} \approx 0.2 = K_C$
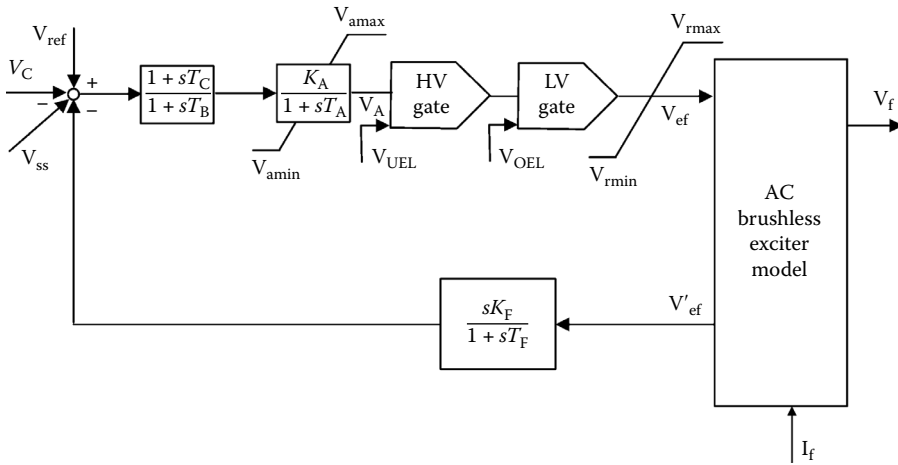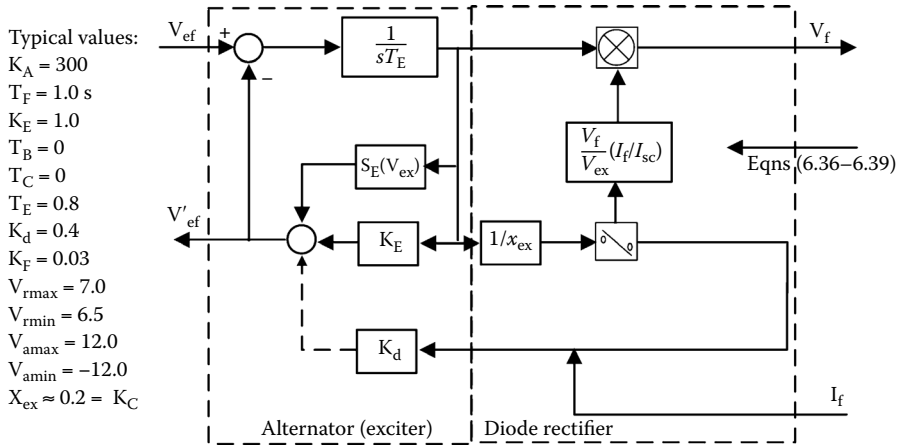
(b)

FIGURE 6.34 (a) IEEE 1992 AC1A (brushless) excitation system and (b) AC exciter with diode rectifier.

introduced. The voltage regulator may be of many types (a lead–lag compensator, for example) with various limiters. Figure 6.34a and Figure 6.34b show the IEEE 1992 AC1A excitation system (with automatic voltage regulator).

A few remarks are in order:

- The feedback loop uses V_{ef}' instead of V_{ex} (exciter's excitation voltage) or SG field-winding V_f.
- A windup limited single constant block with gain K_A is imposed to limit the output variable V_A.
- V_{UEL} is the underexcitation limiter input.
- V_{OEL} is the overexcitation limiter input.
- $(1 + sT_C)/(1 + sT_B)$ is the voltage regulator implemented as a simple lead–lag compensator.
- A non-windup limiter $V_{r\,max}$, $V_{r\,min}$ is applied to the exciter excitation supply voltage.

The IEEE 1992 type ST1A excitation system model is shown in Figure 6.35. It represents a potential source-controlled rectifier. A transformer takes the power from the SG terminals and supplies the controlled rectifier. The exciter ceiling voltage is thus proportional to SG terminal voltage E_t. The rectifier
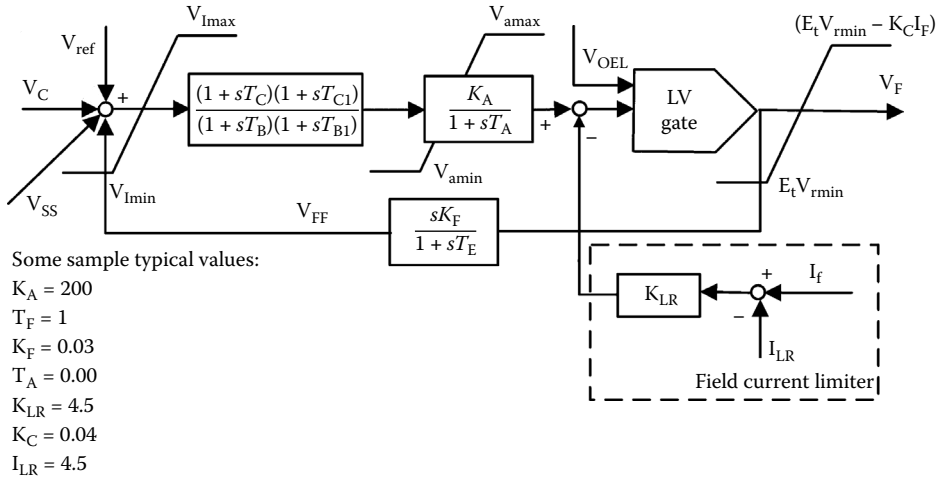
FIGURE 6.35 IEEE 1992 type ST1A excitation system (with automatic voltage regulator [AVR]).

and voltage regulation is represented by K_C ($K_C = x_{ex}$ in previous structural diagrams). The field current I_F is limited through gain K_{LR} at the current limit I_{LR}. Again, non-windup and windup limiters are included, along with underexcitation (V_{UEL}) and overexcitation (V_{OEL}) limiters. The controlled rectifier model is considered only through the non-windup limiter V_{Rmax}, V_{Rmin}.

The IEEE 451.2 standard from 1992 contains a myriad of models for existing excitation systems. More are added in Reference [4].

At the same time, more sophisticated and robust AVRs are presented, proposed, and tested. In what follows, a case study of a digital AVR design is presented.

Example 6.2: Digital Excitation System Design

Let us consider here a PID AVR to be used with a IEEE-1992 standard 421.5, type AC5A alternator and diode rectifier brushless exciter for turbine-SG sets of low to medium power (say up to 50 MW).

Provide a direct design method for the PID-type AVR.

Solution

The IEEE-1992, type AC5A analog excitation system model is modified to introduce the PID-type AVR (Figure 6.36).

The diode rectifier voltage regulation (reduction) with load is neglected here for simplicity.

Although the AVR is to be implemented digitally, the design of the PID controller may be done as if it were continuous, because the sampling frequency is more than 20 times the damped frequency of the closed-loop system.
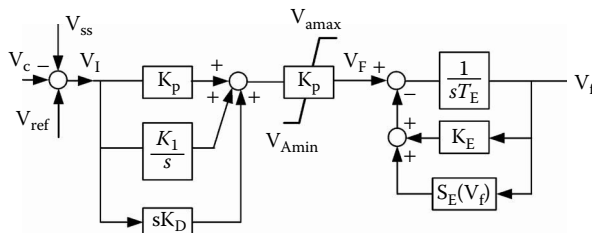
FIGURE 6.36 Simplified AC5A excitation system with PID-type automatic voltage regulator (AVR).

The transfer function of a PID controller is as follows:

$$G_C(s) = K_P + \frac{K_I}{s} + sK_D \qquad (6.43)$$

where

K_P = the proportional gain

K_I = the integral gain

K_D = the derivative gain

Selecting K_P, K_I, and K_D is called controller tuning.

The AC exciter model in Figure 6.36 may be considered a first-order model, at least for small deviations (Figure 6.29). The SG may also be modeled as a first-order system represented by the excitation time constant T'_{d0} at constant speed, in the absence of the damper windings. So, the AC exciter plus the SG may be modeled through a second-order transfer function $G(s)$:

$$G(s) = \frac{l_{dm}/\left(r_f\left(S_E + K_E\right)\right)}{\left(1 + sT'_{d0}\right)\left(1 + sT_e\right)}$$

$$T_e = \frac{1}{\left(S_E + K_E\right)} \cdot T_E \qquad (6.44)$$

$$T'_{d0} = \left(l_{dm} + l_{fl}\right)/\left(\omega_b r_f\right) \qquad (6.45)$$

The closed-loop system characteristic is as follows:

$$G(s)G_C(s) + 1 = 0 \qquad (6.46)$$

Consider, for simplicity,

$$l_{dm}/\left(r_f\left(S_E + K_E\right)\right) = 1$$

With Equation 6.43 and Equation 6.44, Equation 6.46 becomes

$$K_D^2 s^2 + K_P s + K_I = -\left(1 + sT'_{d0}\right)\left(1 + sT_e\right)s \qquad (6.47)$$

It is desirable that the closed-loop system be almost of second order. To do so, select a real negative pole $s_3 = c$ in the far left-half of the plane with the other two as complex conjugates $s_{1,2} = a \pm jb$. The peak overshoot and settling time represent the basis for the pole placement (a,b,c). In this pole placement design method, from three equations, we find three unknowns: K_P, K_I, K_D. The controller settings of K_P, K_I, K_D give rise to two zeros that might be real or complex conjugates. The zeros affect the transient response; thus, some trial and error is required to complete the design. Over-designing the specifications, such as choosing a smaller than desired value to overshoot leads eventually to an adequate design.

For T'_{d0} = 1.5 sec, T_e = 0.3 sec, f_1 = 60 Hz, settling time = 1.5 sec, peak overshoot = 10%, a good analog PID controller gain set is K_P = 39.33, K_I = 76.50, and K_D = 5.4 [7].

The conversion of PID analog settings into discrete form is straightforward with the trapezoidal integration method:

$$s \Rightarrow \frac{\left(1 - z^{-1}\right)}{T};$$

$$\frac{1}{s} \Rightarrow \frac{T}{2} \frac{\left(1 + z^{-1}\right)}{1 - z^{-1}} \tag{6.48}$$

with z^{-1} representing the unit delay.

Consequently, $G_C(t)$ is as follows:

$$G_C(z) = \left[K_{PD} + \frac{K_{ID}}{1 - z^{-1}} + K_{DD}\left(1 - z^{-1}\right) \right] \cdot K_{AA} = \frac{\Delta V_F(z)}{\Delta V_I(z)} \tag{6.49}$$

with

$$K_{PD} = K_P - K_I T / 2$$

$$K_{ID} = K_I T \tag{6.50}$$

$$K_{DD} = K_D / T$$

Again, K_{AA} was added in Equation 6.49. For the case in point, $T = 12.5$ msec, $K_{PD} = 777$, $K_{ID} = 19$, $K_{DD} = 8640$, and $S_E = 7$, for a 75 kVA, 208 V, 0.8 PF lag generator [7].

Using the known property that $Z^{-1}X(K) = X(K-1)$, the expression of $G_C(z)$ may be converted in time discrete form as follows:

$$\Delta F(K) = \Delta F(K-1) + \left(K_{PD} + K_{ID} + K_{DD}\right)\Delta V_I(K) -$$

$$-\left(K_{PD} + 2K_{DD}\right)\Delta V_I(K-1) + K_{DD}\Delta V_I(K-2) \tag{6.51}$$

where ΔV_I is the generator voltage error (Figure 6.36).

A 50 kVAR reactive load application and rejection response is shown in Figure 6.37a, while a step change in voltage set point is presented in Figure 6.37b [7].

The settling time varies between 0.4 to 0.6 sec, while the voltage overshoot is below ±10% (20 V) [7].

6.11   Underexcitation Voltage

The input V_{UEL} in Figure 6.34a signals the presence of the UEL.

The UEL does not interfere with the AVR under normal transient or steady-state conditions, but takes over the AVR control under severe conditions. When the excitation level is too low, UEL boosts excitation, overriding or adding to the AVR.

UEL acts to prevent loss of SG synchronism due to insufficient excitation or to prevent loading to overheating in the stator core end region of the SG, as defined in the leading reactive power zone of the SG capability curve (Chapter 4).

There are many causes for excitation reduction, such as the following:
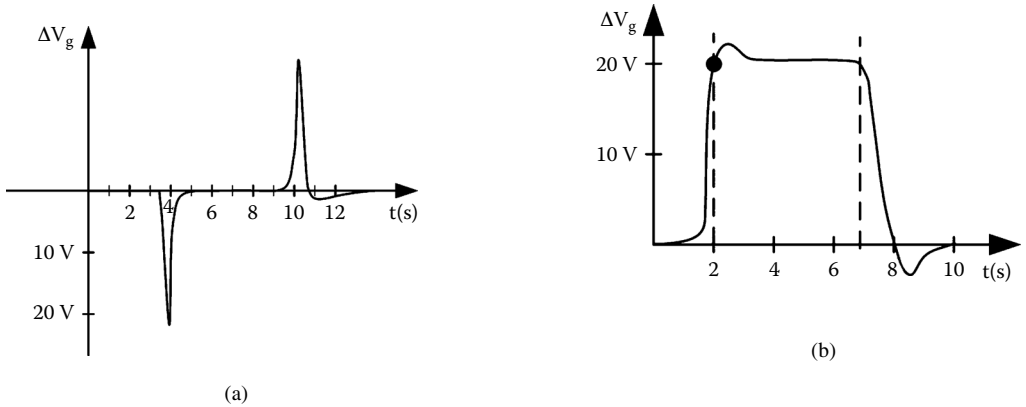
FIGURE 6.37 Generator voltage response: (a) 50 kVAR application and rejection and (b) step change in voltage set point.
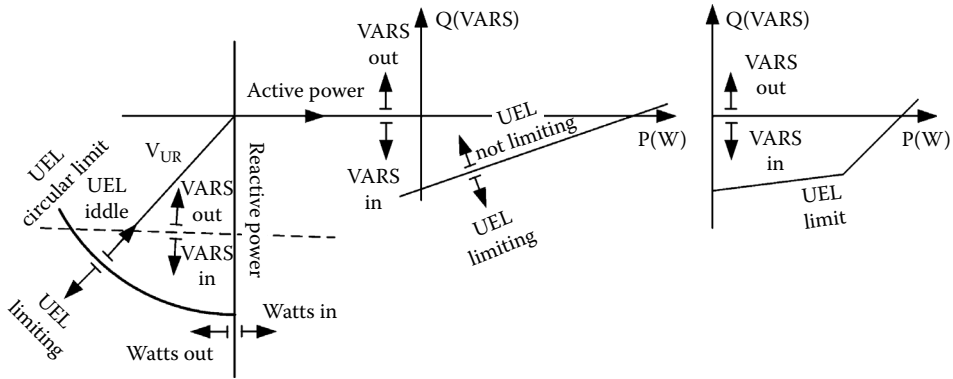
FIGURE 6.38 Underexcitation limiters: circular, straight line, and multisegment.

- Increases in the power system voltage may lead to reduction of SG excitation to keep the voltage at the SG terminals at a preset level by absorbing reactive power (underexcitation)
- Faults in the AVR
- Inadvertent reduction of AVR setting point V_{ref}

When underexcited, the SG absorbs more reactive power, even when the active (turbine) power is maintained constant; thus, the machine stability limit in the $P(\delta_V)$ curve (Chapter 4) is reached, or the SG stator core end region gets overheated.

The UEL may input the AVR either at the generator voltage setting point V_{ref} or after the lead–lag compensator (through a HV gate).

Three main types of UEL models were recommended by IEEE in 1995 (Figure 6.38) [8]:

- Circular type
- Straight-line type
- Multisegment type

A simple digital UEL is presented in Reference [9] and in Figure 6.39, where the limit reactive power from the P–Q capability curves at various voltages is tabled as a function $f(P,V_c)$:

$$Q_{lim} = f(P, V_c) \tag{6.52}$$
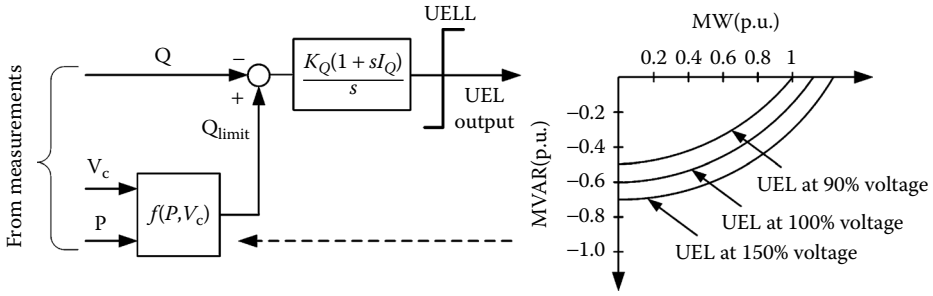
FIGURE 6.39 Simplified underexcitation limiter.

Care must be exercised to prevent UEL side effects on other limiters, such as loss of excitation (LOE) protection, PSSs, or the AVR, overexcitation limiter (OEL), volt/hertz limiters, and overvoltage limiters [10].

6.12 Power System Stabilizers (PSSs)

The field-winding current flux Ψ_f transients may be explored by using the third-order model ($\Delta\Psi_f$, $\Delta\delta$, $\Delta\omega_r$), where the damper cage is eliminated and so are the stator transients (Chapter 4).

After linearization [1],

$$\Delta T_e = K_1\Delta\delta + K_2\Delta\Psi_f \tag{6.53}$$

$$\Delta\Psi_f = \frac{K_3}{1+sT_3}\left(\Delta V_f - K_4\Delta\delta\right) \tag{6.54}$$

where

ΔT_e = the SG torque small deviation
$\Delta\delta$ = the power angle small deviation
$\Delta\Psi_f$ = the SG field-winding flux linkage small deviation

The change $\Delta\Psi_f$ in field flux linkage (Equation 6.54), even for constant field-winding voltage V_f ($\Delta V_f = 0$), is explained by armature reaction contribution change when the power angle changes ($\Delta\delta \neq 0$).

Combining Equation 6.53 and Equation 6.54 yields the following:

$$\Delta T_e = K_1\Delta\delta + \frac{K_3K_2}{1+sT_3}\Delta V_f - \frac{K_2K_3K_4}{1+sT_3}\Delta\delta \tag{6.55}$$

The last term in Equation 6.55 represents the variation of Ψ_f transients caused by the electromagnetic torque, due to power angle variation. At steady state, or low oscillating frequency,

$$\Delta T_e \text{ due to } \Delta\Psi_f \text{ is } (-K_2K_3K_4\Delta\delta); \ \omega << 1/T_3 \tag{6.56}$$

So, the field flux variation produces a negative synchronizing torque component (Equation 6.56). If

$$K_1 \leq K_2K_3K_4 \tag{6.57}$$

the system becomes monotonically unstable.

At higher oscillating frequencies ($\omega >> 1/T_3$) the last term of Equation 6.55 becomes

$$\Delta T_e = \frac{-K_2 K_3 K_4}{1 + j\omega T_3}\Delta\delta \approx \frac{K_2 K_3 K_4}{\omega T_3}\left(j\Delta\delta\right) \qquad (6.58)$$

The airgap torque deviation caused by $\Delta\Psi_f$ is now 90° ahead of power angle deviation and thus in phase with speed deviation $\Delta\omega_r$. Consequently, the field-winding flux linkage deviation $\Delta\Psi_f$ produces a positive damping torque component. At 1 Hz, $\Delta\Psi_f$ produces both a reduction in synchronizing torque and an increase in damping torque of the SG. Moreover, as K_2 and K_3 are positive, in general, K_4 may be positive or negative [1]. With $K_4 < 0$, the synchronizing torque increase produced by $\Delta\Psi_f$ is accompanied by a negative torque damping component. AVRs may introduce similar effects [1].

These two phenomena prompted the addition of PSSs as inputs to the AVRs. Damping the SG rotor oscillations is the main role of PSSs. The most obvious input of PSSs should be the speed deviation $\Delta\omega_r$.

By adding motion Equation 6.1 to Equation 6.43 and Equation 6.44, a simplified model for an AVR–PSS system can be derived, as shown in Figure 6.40. It is based on the small-signal third-order model of SG (Equation 6.43 through Equation 6.45), with the damper windings present only in the motion equation by the asynchronous (damping) torque $K_D\Delta\omega_r$.

The transfer function of the PSS would be a simple gain if the exciter and generator transfer function $\Delta T_e/\Delta V_f$ was a pure gain. In reality, this is not so, and the $G_{PSS}(s)$ has to contain some kind of phase compensation (phase lead) to produce a pure damping torque contribution. A simple such PSS transfer function is shown in Figure 6.41. The frequency range of interest is 1 to 2 Hz, in general. The washout component is a high-pass filter. Without washout contribution, steady-state changes in speed would modify the voltage V_s ($T_w = 1$ to 20 sec). Especially fast response static exciters need PSS contribution to increase damping. A temporary increase of SG excitation current can significantly improve the transient stability, because the synchronizing power (torque) is increased.

The ceiling excitation voltage is limited to 2.5 to 3.0 P.U. in thermal power units. But, fast voltage variations lead to degraded damping as already pointed out. The PSS can improve damping if a terminal voltage limiter is added. This is true for the first positive rotor swing. But, after the first peak of the local swing, the excitation is allowed to decrease before the highest composite peak of the swing is passed by. Keeping excitation at the ceiling value would be useful until this composite swing peak is reached.
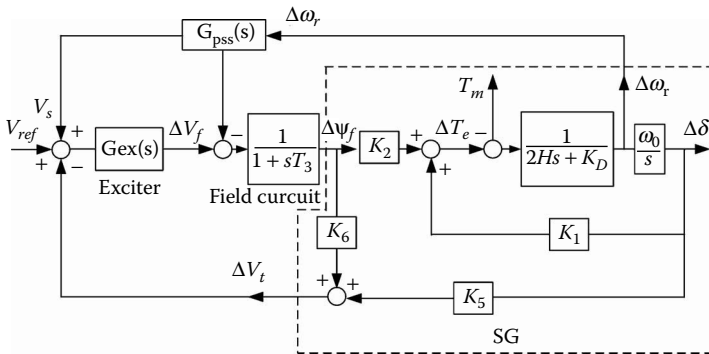
FIGURE 6.40 Automatic voltage regulator (AVR) with power system stabilizer (PSS): the small-signal model.
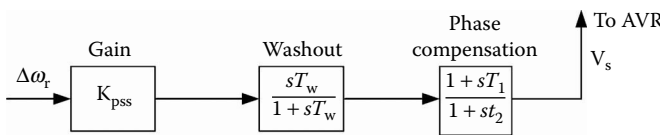
FIGURE 6.41 Basic power system stabilizer (PSS) transfer function.
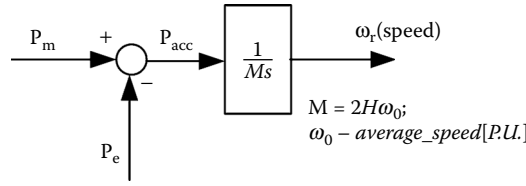
FIGURE 6.42 Accelerating power.
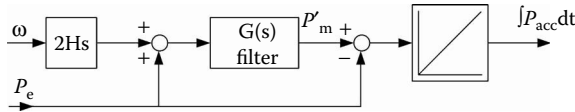
FIGURE 6.43 The integral of accelerating power as input to power system stabilizer (PSS).
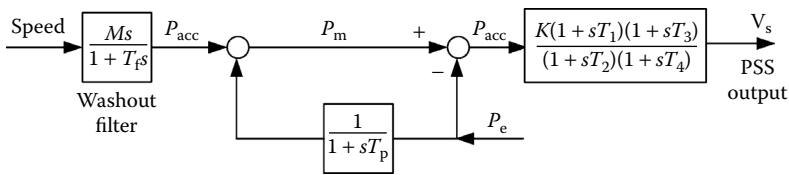
FIGURE 6.44 Accelerating power or speed input power system stabilizer (PSS).

Discontinuous excitation control may be added to the PSS to keep the excitation voltage at its maximum over the entire positive swing of the rotor (around 2 sec or so). This is called transient stability excitation control (TSEC) and is applied, together or in place of other methods such as fast valving or generator tripping, in order to improve power system stability. TSEC imposes smaller duty requirements on the turbine shaft and on the steam supply of the unit.

As PSS should produce electromagnetic torque variations ΔT_e in phase with speed, the measured speed is the obvious input to PSS. But what speed? It could be the turbine measured speed or the generator speed. Both of them are, however, affected by noise. Moreover, the torsional shaft dynamics cause noise that is very important and apparently difficult to filter out from the measured signal.

The search for other more adequate PSS inputs is based on the motion equation in power P.U. terms (Figure 6.3), redrawn here in slightly new denominations (Figure 6.42). It should be noticed that as P_m may not be measured, it could be estimated with ω_r (estimated) and P_e (measured). It is practical to estimate ω_r as the frequency of the generator voltage behind the transient reactance, as it varies slowly enough. This way, the speed sensor signal is not needed. Then, the structural diagram in Figure 6.42 can be manipulated to estimate the mechanical power P_m' and then calculate the accelerating power (Figure 6.43). With a single structure, both speed input and accelerating power input PSS may be investigated [11] (Figure 6.44).

The speed input of PSS may be obtained with $T_p = 0$ and $M = T_f$. For $T_p \neq 0$ and $M = 2H$, the accelerating power PSS is obtained. Accelerating power PSSs are claimed to perform better than speed PSSs in damping local system oscillations in the interval from 0.2 to 5 Hz for 220 MVA turbogenerators [11, 12]. Other inputs such as the electrical power variation, ΔP_e, or frequency may be used with good results [13]. A great deal of attention has attracted the optimization of PSSs with solutions involving fuzzy logic [13, 14], linear optimal PSSs [15], synthesis [16], variable structure control [17], and $H\infty$ [18]. Typical effects of PSSs are shown in Figure 6.45a and Figure 6.45b [12].

The damping of electric power and speed (frequency) oscillations is evident. The excitation system design, including AVR and PSS, today in digital circuitry implementation is a complex enterprise that is beyond our scope here. For details, see the literature [1, 10–18].
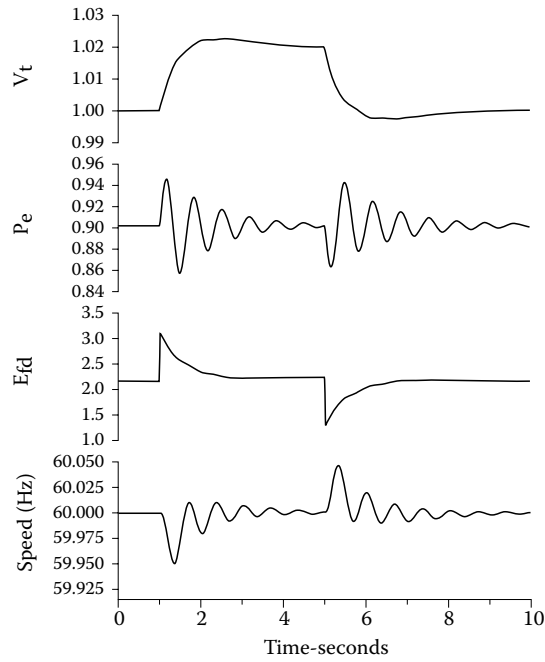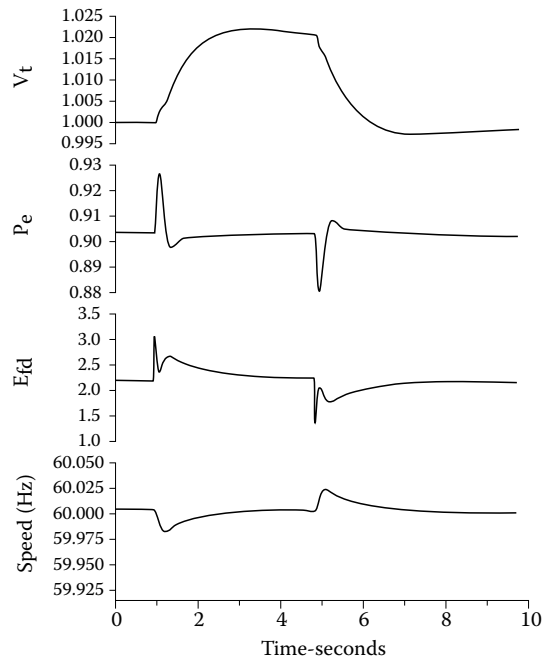
FIGURE 6.45 Simulation response to ±2% step in terminal voltage: (a) no power system stabilizer (PSS) and (b) integral of accelerating power PSS.
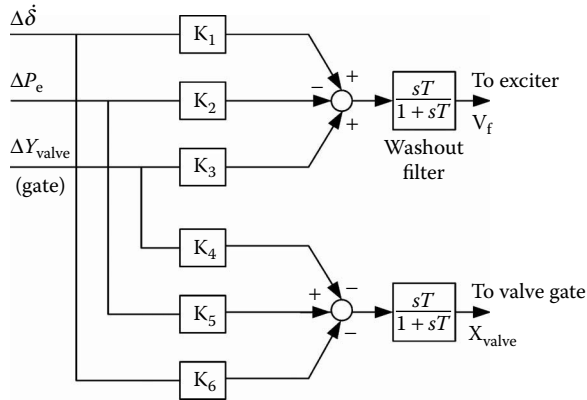
FIGURE 6.46 Primitive coordinated synchronous generator control system.

6.13 Coordinated AVR–PSS and Speed Governor Control

Coordinated voltage and speed control of SGs requires methods of multivariable nonlinear control design. Basically, the SG of interest may be modeled by a third-order model ($\Delta\delta$, $\Delta\omega_r$, or $\Delta\sigma$, $\Delta\Psi_f$), while the power system to which it is connected might be modeled by a dynamic equivalent in order to produce a reduced-order system.

Optimization control methods are to be used to allocate proper weightings to various control variable participation. A primitive such coordinated voltage and speed SG control system is shown in Figure 6.46 [19]. The weights K_1 to K_6 are constants in Figure 6.46, but they may be adaptable. The washout filter also provides for zero steady-state error. A digital embodiment of coordinated exciter-speed-governor control intended for a low-head Kaplan hydroturbine generator is introduced in the literature [20,21].

Given the complexity of coordinated control of SG, continual online trained ANN control systems seem to be adequate [20–22] for the scope of this discussion. Coordinated control of SGs has a long way to go.

6.14 FACTS-Added Control of SG

FACTS stands for flexible AC transmission systems. FACTS contribute voltage and frequency control for enhancing power system stability. By doing so, FACTS intervene in active and reactive power flows in power systems, that is, between SGs and various loads supplied through transmission lines.

Traditionally, only voltage control was available through changing transformer taps or by switching current and adding fixed capacitors or inductors in parallel or in series.

Power electronics (PE) has changed the picture. In the early stages, PE has used back-to-back thyristors in series, which, line commutated, provided for high-voltage and power devices capable of changing the voltage amplitude. The thyristor turns off only when its current goes to zero. This is a great limitation.

The GTO (gate turn-off thyristor) overcame this drawback. MCTs (MOS-controlled thyristor) or insulated-gate thyristors (IGCT) are today the power switches of preference due to a notably larger switching frequency (kHz) for large voltage and power per unit. For the megawatt range, IGBTs are used.

FACTS use power electronics to increase the active and reactive power transmitted over power lines, while maintaining stability. Integrated now in FACTS are the following:

- Static VAR compensators (SVCs)
- Static compensators (STATCOM)
- Thyristor-controlled resistors
- Power-electronics-controlled superconducting energy storage (SMES)
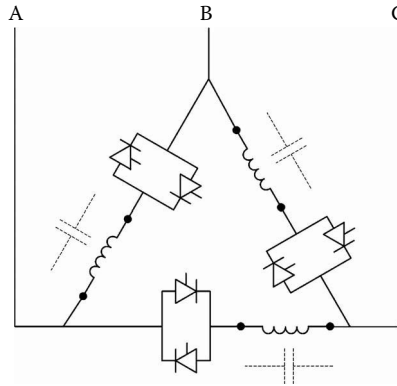
FIGURE 6.47   Basic static VAR compensator (SVC).
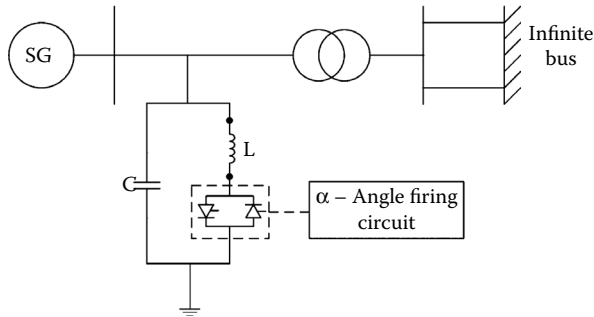
FIGURE 6.48   Synchronous generator with static VAR compensation.

- Series compensators and subsynchronous resonance (SSR) dampers
- Phase-angle regulators
- Unified power flow controller
- High-voltage DC (HVDC) transmission lines

SVCs deliver or drain controlled reactive power according to power system (mainly local) needs. SVCs use basic elements thyristor-controlled inductance or capacitor energy storage elements (Figure 6.47). Adequate control of voltage amplitude on reactor SVCs and capacitor SVCs, connected in parallel to the power system (in power substations), provides for positive or negative reactive power flow and contributes to voltage control.

The presence of SVCs at SG terminals or close to SG influences the reactive power control of the AVR–PSS system. So, a coordination between AVR–PSS and SVC is required [20, 21]. The SVC may enhance the P/Q capability at SG terminals [22] (Figure 6.48). A simplified structure of such a coordinated exciter SVC, based on multivariable control theory, is shown in Figure 6.49a and Figure 6.49b. It uses as variables the speed variation δ, terminal voltage V_t, and active power P_e [23].

A standard solution is here considered in the form of a coordinated exciter–speed governor control system.

The improvement in dynamic stability boundaries is notable (Figure 6.49b) as claimed in Reference [23], with an optimal coordinated controller. STATCOM is an advanced SVC that uses a PWM converter to supply a fixed capacitor. GTOs or MCTs are used, and multilevel configurations are proposed. A step-down transformer is needed (Figure 6.50). The advanced SVC uses an advanced voltage source converter instead of a VARIAC. It is power electronics intensive but more compact and better in power quality.

V_2 may be brought in phase with V_1 by adequate control. If V_2 is made larger than V_1 by larger PWM modulation indexing (more apparent capacitor), the advanced SVC acts as a capacitor at SG terminals.
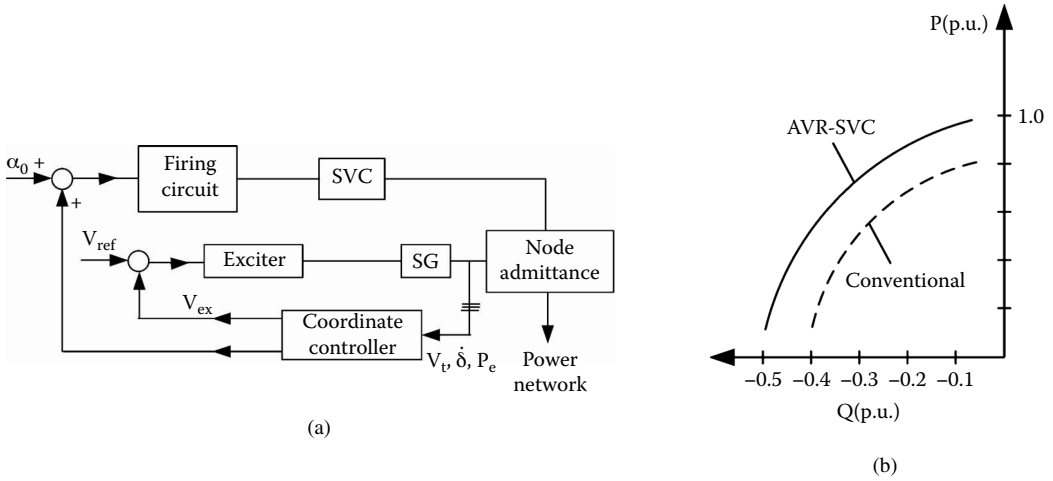
FIGURE 6.49 Coordinated exciter static voltage controller (SVC) control: (a) structural diagram and (b) dynamic stability boundary.
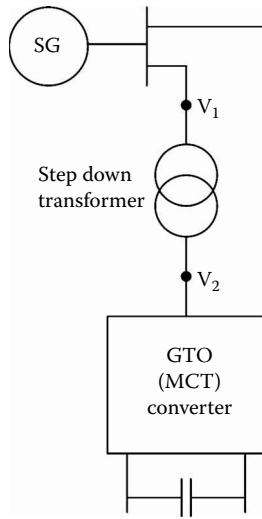
FIGURE 6.50 Advanced static voltage controller (SVC) = STATCOM.

If $V_2 < V_1$, it acts as an inductor. For a transformer reactance of 0.1 P.U., a $\pm10\%$ change in V_2 may produce a $\pm100\%$ P.U. change in the reactive power flow from and to SVC. A parallel-connected thyristor-controlled resistor is used only for transient stability improvement, as it can absorb power from the generator during positive swings, preventing the loss of synchronism.

Note that with SVCs used as reactive power compensators and power factor controllers, the interference with the AVR–PSS controllers has to be carefully assessed, as adverse effects were reported by industry [24]. In essence, the SG voltage-supporting capability may be reduced.

Superconducting magnetic energy storage (SMES) may also be used for energy storage and for damping power system oscillations. The high-temperature superconductors seem to be a potential practical solution. They allow for current density in the superconducting coil wires of 100 A/mm². Losses and volume per MWh stored are reduced, as is the cost.

SMES may be controlled to provide both active and reactive power control, with adequate power electronics. Four-quadrant P, Q operation is feasible (Figure 6.51), as demonstrated in the literature [25, 26].
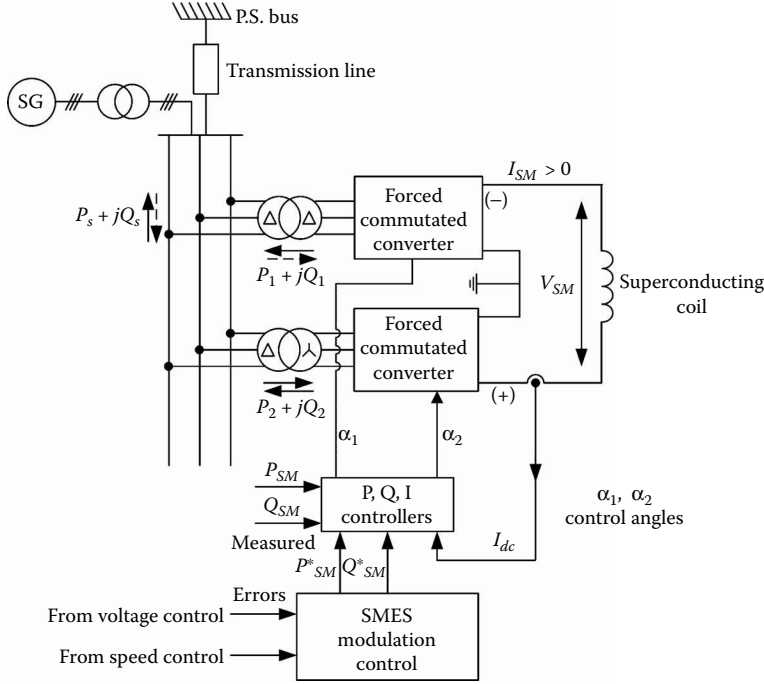
FIGURE 6.51 SMES with double-forced commutated converter for four-quadrant *P, Q* operation.

To investigate the action of SMES, let us consider a single SG connected to the power system (PS) bus by a transmission line. The dual converter impresses $\pm V_{SM}$ volts on the superconducting coil. On the AC side of the converter, the phase angle between the voltage and current may vary from 90° when no energy is transferred from the power system to SMES, to 0° when the SMES is fully charging, and to 180° for maximum discharge of SMES energy into the power system.

The SMES current I_{SM} is not reversible, but the voltage V_{SM} is, and so is the converter output power P_{SM}:

$$P_{SM} = I_{SM} V_{SM}$$

$$V_{SM} \approx K_M V_L \cos \alpha$$

$$V_{SM} \approx L_{ds} \cdot s \cdot I_{SM} \qquad\qquad (6.59)$$

$$P_{SM} = K_M V_L I_{SM} \cos \alpha$$

$$Q_{SM} = K_M V_L I_{SM} \sin \alpha$$

where

$\quad\quad\quad \alpha$ = the converter commutation angle
$\quad\quad K_M$ = the modulation coefficient
$\quad\quad\; V_L$ = the line AC voltage of the converter

For given $P_{SM}{}^{\star}$ and $Q_{SM}{}^{\star}$ demands, unique values of K_M and α are obtained [27].

The DC voltage is controlled by changing the firing angle difference in the two converters: $\alpha_{1,2}$. The transfer function of the converter angle control loop may be written as follows:

$$\Delta V_{SM} = \frac{K_0}{1 + s T_\alpha} \Delta \alpha \qquad\qquad (6.60)$$

The SMES energy stored is

$$W_{SM} = \frac{1}{2} L_d I_{SM0}^2 + \int_{t_0}^{t} P_{SM}(\tau) d\tau \tag{6.61}$$

The SMES power P_{SM} intervenes in the SG motion equations:

$$Ms\Delta\omega_r = \Delta P_m - D\Delta\omega_r - \Delta P_e - \Delta P_{SM};$$

$$M = 2H \tag{6.62}$$

$$s\Delta\delta = \omega_b \cdot \Delta\omega_r \tag{6.63}$$

The power angle δ is now considered as the angle between the no-load voltage of the SG and the voltage V_0 of the PS bus. Essentially, the transmission line parameters r_T and x_T are added to SG stator parameters: D is the damping provided by load frequency dependence and by the SG damper winding; ΔP_m is the turbine power variation; ΔP_e is the electric power variation; and ΔP_{SM} is the SMES power variation, all in P.U. at (around) base speed (frequency) ω_b. The SMES may also influence the reactive power balance by the phase shift between converter AC voltages and currents.

It was shown that optimal multivariable control, with minimum time transition of the whole system from state A to B as the cost function, and $|\Delta\alpha| < \pi/2$ as constraint, may produce speed and voltage stabilization for large PS active power load perturbations or faults (short-circuit) [28]. However, using speed variation $\Delta\omega_r$ as input instead of optimal control to regulate the angle $\Delta\alpha$ loop does not provide satisfactory results [28]. Notable SMES energy exchange within seconds is required for the scope [28].

Besides SG better control, the SMES was also proposed to assist automatic generation control, which deals with inter-area power exchange control [29]. This time, the input of the SMES is proportional to ACE (area control error, see Section 6.4) or is produced by a separate adaptive controller. In both cases, the superconducting inductor current deviation (derivative) is used as negative feedback in order to provide quick restoration of I_{SM} to the set point, following a change in the load demand [30, 31].

The SMES appears to be a very promising emerging technology, but new performance improvements and cost reductions are required before it will be common practice in power systems, together with other forms of energy storage, such as pump storage, batteries, fuel cells, and so forth.

6.14.1 Series Compensators

A transmission line may be modeled as lumped capacitors in series. The line impedance may be varied through thyristor-controlled series capacitors (Figure 6.52a and Figure 6.52b). The capacitor is varied by

(a)

(b)
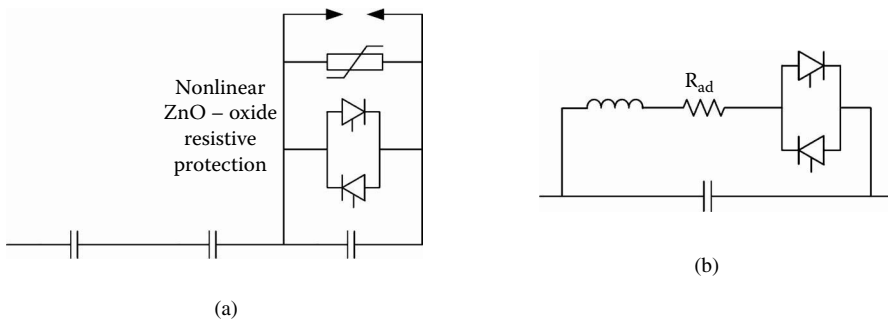
FIGURE 6.52 (a) Series compensator and (b) damper.
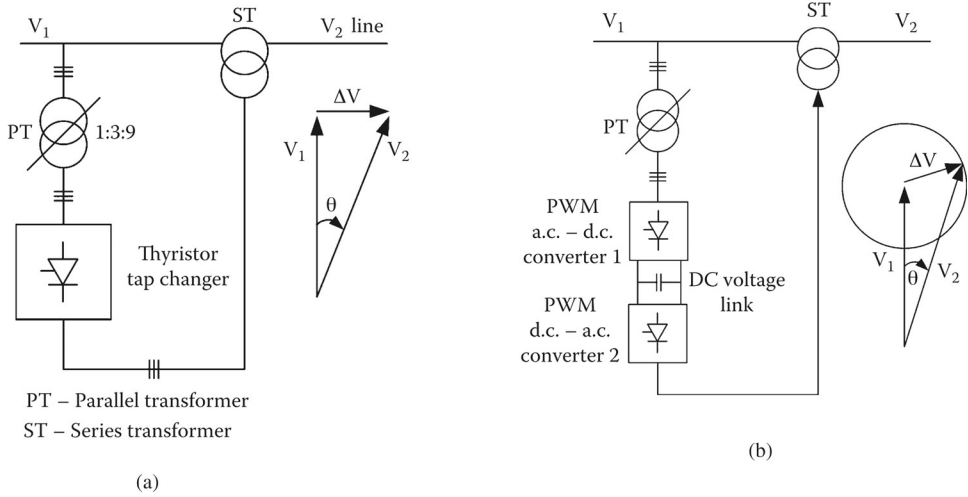
FIGURE 6.53 (a) Phase-angle regulator and (b) unified power flow controller.

PWM short-circuiting it through antiparallel thyristors. Overvoltage protection of thyristors is imperative. Nonlinear zinc-oxide resistors with a paralleled airgap is the standard protection for the scope.

When an additional resistance R_{ad} is added (Figure 6.52b), an oscillation damper is built. Series compensation of long heavily loaded transmission lines might produce oscillations that need attenuation.

6.14.2 Phase-Angle Regulation and Unified Power Flow Control

In-phase and quadrature voltage regulation done traditionally with tap changers in parallel-series transformers may be accomplished by power electronics means (FACTS; see Figure 6.53). The thyristor AC voltage tap changer (Figure 6.53a) performs the variation of ΔV through the ST, while the unified power controller (Figure 6.53b) may vary both the amplitude and the phase of voltage variation ΔV.

The phase-angle regulator may transmit reactive power to increase voltage $V_2 > V_1$, while the unified power flow controller allows for the flow of both active and reactive power, thus allowing for damping electromechanical oscillations.

High voltage direct current (HVDC) transmission systems contain a high-voltage high-power rectifier at the entry and a DC transmission line and an inverter at the end of it [1]. It is power electronics intensive, but it really makes the power transmission system much more flexible. It also interferes with other SG control systems.

As the power electronics SG control systems cost goes down, the few special (cable) or long power transmission lines HVDC, now in existence, will be extended in the near future, as they can do the following:

- Increase transmitted power capability of the transmission lines
- Produce additional electromechanical oscillation damping in the AC system
- Improve the transient stability
- Isolate system disturbances
- Perform frequency control of small isolated systems (by the output inverter)
- Interconnect between power systems of different frequencies (50 Hz or 60 Hz)
- Provide for active power and voltage dynamic support

6.15 Subsynchronous Oscillations

In Chapter 3, dedicated to prime movers, we mentioned the complexity of mechanical shaft, couplings, and mechanical gear in relation to wind turbine generators. In essence, the turbine–generator shaft system consists of several masses (inertias): turbine sections, generator rotor, mechanical couplings, and exciter
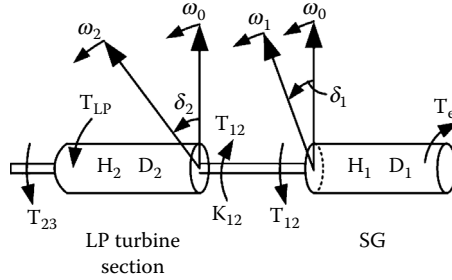
FIGURE 6.54   The two-mass shaft model.

rotor. These masses are connected by shafts of finite rigidity (flexibility). A mechanical perturbation will produce torsional oscillations between various sections of the shaft system that are above 5 to 6 Hz but, in general, below base frequency 50(60) Hz. Hence, the term "subsynchronous oscillations" is used.

The entire turbine-generator rotor oscillates with respect to other generators at a frequency in the range of 0.2 to 2 Hz.

Torsional oscillations may cause the following:

- Torsional interaction with various power system (or SG) controls
- Subsynchronous resonance in series (capacitor) compensated power transmission lines

Torsional characteristics of hydrogenerators units do not pose such severe problems, as the generator inertia is much larger than that in turbine-generator systems with shafts with total lengths up to 50 m.

6.15.1 The Multimass Shaft Model

The various gas or steam turbine sections, such as low pressure (LP), high pressure (HP), intermediate pressure (IP), generator rotor, couplings, and exciter rotor (if any), are elements of a lumped mass model.

Let us consider, for a start, only a two-mass rotor (Figure 6.54).

The motion equation of the generator and LP turbine rotors is as follows:

$$2H_1 \frac{d\left(\Delta\omega_1\right)}{dt} = K_{12}\left(\delta_2 - \delta_1\right) - T_e - D_1\left(\Delta\omega_1\right)$$

$$\frac{d\delta_1}{dt} = \Delta\omega_1 \cdot \omega_0$$

(6.64)

$$2H_2 \frac{d\left(\Delta\omega_2\right)}{dt} = T_{LP} + K_{23}\left(\delta_3 - \delta_2\right) - K_{12}\left(\delta_2 - \delta_1\right) - D_2\left(\Delta\omega_2\right)$$

$$\frac{d\delta_2}{dt} = \Delta\omega_2 \cdot \omega_0$$

(6.65)

ω_0 is the rated electrical speed in rad/sec: 377 rad/sec for 60 Hz and 314 rad/sec for 50 Hz.

For more masses, more equations are added. For a coal-fired turbine generator with HP, IP, and LP sections (and static exciter), two more equations are added:

$$2H_3 \frac{d\left(\Delta\omega_3\right)}{dt} = T_{IP} + K_{34}\left(\delta_4 - \delta_3\right) - K_{23}\left(\delta_3 - \delta_2\right) - D_3\left(\Delta\omega_3\right)$$

$$\frac{d\delta_3}{dt} = \Delta\omega_3 \cdot \omega_0$$

(6.66)

$$2H_4 \frac{d(\Delta\omega_4)}{dt} = T_{HP} - K_{34}(\delta_4 - \delta_3) - D_4(\Delta\omega_4)$$

$$\frac{d\delta_4}{dt} = \Delta\omega_4 \cdot \omega_0$$

(6.67)

Two additional equations are needed for a nuclear power unit with LP_1, LP_2, IP, and HP sections with static exciter.

Example 6.3

Consider a four-mass coal-fired steam turbine generator with HP, IP, and LP sections and a static exciter with inertias: $H_1 = 0.946$ sec, $H_2 = 3.68$ sec, $H_3 = 0.337$ sec, and $H_4 = 0.099$ sec.

The generator is at nominal power and 0.9 PF ($T_e = 0.9$). The stiffness coefficients K_{12}, K_{23}, and K_{34} are: $K_{13} = 82.74$ P.U. torque/rad, $K_{23} = 81.91$, and $K_{34} = 37.95$.

Calculate the steady-state torque and angle of each shaft section if the division of powers is 30% for HP, 40% for IP, and 30% for LP.

Solution

Notice that the damping coefficients (due to blades and shafts materials, hysteresis, friction, etc.) are zero ($D_1 = D_2 = D_3 = D_4 = 0$). The angle by which the LP turbine section leads the generator rotor is as follows (Equation 6.64):

$$\delta_2 - \delta_1 = T_{12} / K_{12}$$

But, $T_{12} = T_e = 0.9$ (from power balance) and, thus,

$$\delta_2 - \delta_1 = 0.9 / 82.74 = 0.010877 \ rad(electrical)$$

The torque between LP and IP shaft sections T_{23} at steady state is

$$T_{23} = T_{12} - T_{LP} = 0.9(1 - 0.3) = 0.54$$

From Equation 6.65,

$$\delta_3 - \delta_2 = T_{23} / K_{23} = 0.54 / 81.91 = 6.5926 \times 10^{-3} \ rad(electrical)$$

Again,

$$T_{34} = T_{23} - T_{IP} = 0.54 - 0.4 \cdot 0.9 = 0.18$$

$$\delta_4 - \delta_3 = T_{34} / K_{34} = \frac{0.18}{37.95} = 4.7431 \times 10^{-3} \ rad(electrical)$$

So, the HP turbine rotor section leads the generator rotor section by $\delta_4 - \delta_1$:

$$\delta_4 - \delta_1 = 0.010877 + 6.5926 \times 10^{-3} + 4.7431 \times 10^{-3}$$

$$= 2.22057 \times 10^{-2}\, rad = 1.273\, \text{deg}$$

at steady state.

6.15.2 Torsional Natural Frequency

The natural frequencies and modal shapes are to be obtained by finding the eigenvalues and vectors of the linearized free system equations from Equation 6.64 through Equation 6.67, with $T_e = K_S \Delta \delta_1$:

$$\Delta \dot{X} = A \Delta X \tag{6.68}$$

and $\Delta T_{\text{HP}} = \Delta T_{\text{LP}} = \Delta T_{\text{IP}} = 0$. With

$$\Delta X = \left[\Delta \omega_1, \Delta \delta_1, \Delta \omega_2, \Delta \delta_2, \Delta \omega_3, \Delta \delta_3, \Delta \omega_4, \Delta \delta_4 \right]^T$$

$$|A| = \begin{array}{c} \\ \Delta \omega_1 \\ \Delta \delta_1 \\ \Delta \omega_2 \\ \Delta \delta_2 \\ \Delta \omega_3 \\ \Delta \delta_3 \\ \Delta \omega_4 \\ \Delta \delta_4 \end{array}
\begin{array}{cccccccc}
\Delta \omega_1 & \Delta \delta_1 & \Delta \omega_2 & \Delta \delta_2 & \Delta \omega_3 & \Delta \delta_3 & \Delta \omega_4 & \Delta \delta_4 \\
-\dfrac{D_1}{2H_1} & -\dfrac{(K_{12}+K_S)}{2H_1} & & \dfrac{K_{12}}{2H_1} & & & & \\
\omega_0 & & & & & & & \\
& \dfrac{K_{12}}{2H_2} & -\dfrac{D_2}{2H_2} & -\dfrac{K_{12}+K_{23}}{2H_2} & & \dfrac{K_{23}}{2H_2} & & \\
& & \omega_0 & & & & & \\
& & & \dfrac{K_{23}}{2H_3} & -\dfrac{D_3}{2H_3} & -\dfrac{(K_{23}+K_{34})}{2H_3} & & \dfrac{K_{34}}{2H_3} \\
& & & & \omega_0 & & & \\
& & & & & \dfrac{K_{34}}{2H_4} & -\dfrac{D_4}{2H_4} & -\dfrac{K_{34}}{2H_4} \\
& & & & & & \omega_0 & \\
\end{array}$$

The natural frequencies are the eigenvalues of $|A|$:

$$|A| - \lambda |I| = 0 \tag{6.69}$$

With zero damping coefficients ($D_i = 0$), the eigenvalues are complex numbers $j\omega_i$ ($i = 0,1,2,3$). The corresponding frequencies for the case in point are 22.4 Hz, 29.6 Hz, and 52.7 Hz. The first, low (system mode) frequency is not included here, as it is the oscillation of the entire rotor against the power system:

$$f_s = \frac{\omega_s}{2\pi} = \frac{\omega_0}{2\pi} \sqrt{\frac{K_s}{2(H_1 + H_2 + H_3 + H_4)}}$$

With $K_s = 1.6$ P.U. torque/rad,

$$f_s = 60 \times \sqrt{\frac{1.6}{2\left(0.946 + 3.68 + 0.33 + 0.049\right) \times 377}} = 1.23 \ Hz$$

The torsional free frequencies are, in general, above 6 to 8 Hz, so they do not interfere, in this case, with the excitation, speed-governor, or inter-tie control (below 3 to 5 Hz).

The PSS may interfere with the high (above 8 Hz) torsional frequencies, as it is designed to provide pure damping (zero phase shift at system frequency f_s = 1.23 Hz in our case). At 22.4 Hz, PSS may produce a large phase lag (well above 20°) and notable negative damping, hence, instability.

To eliminate such a problem, the speed sensor should be placed between LP and IP sections to reduce the torsional mode influence on speed feedback. Another possibility would be a filter with a notch at 22.4 Hz. The terminal voltage limiter may also produce torsional instability. Adequate filter is required here also.

HVDC systems may, in turn, cause torsional instabilities. But, it is the series capacitor compensation of power transmission lines that most probably interacts with the torsional dynamics.

6.16 Subsynchronous Resonance

In a typical (noncompensated) transmission system, transients (or faults) produce DC attenuated 60 (50) Hz and 120 (100) Hz torque components (the latter, for unbalanced loads and faults). Consequently, the torsional frequencies always originate from these two frequencies.

Series compensation is used to bring long power line capacity closer to the thermal rating. In essence, the transmission line total reactance is partially compensated by series capacitors. Consider a simple radial system (Figure 6.55).

The presence of the capacitor eliminates the DC stator current transients, but it introduces offset AC currents at natural frequency of the linductance capacitance (LC) series circuits:

$$\omega_n \approx \frac{1}{\sqrt{LC}} = \omega_0 \sqrt{\frac{X_C}{X_L}} \tag{6.70}$$

with

$$X_L \approx \left(X'' + X_T + X_E\right)\omega_0 \ ; \ X_C = 1/\omega_0 C \tag{6.71}$$

$X'' = (X_d'' + X_q'')/2$ is the subtransient reactance of the SG. The f_n frequency offset stator currents produce rotor currents at slip frequency: 60 (50) − f_n. The subsynchronous resonance frequency f_n may depend solely on the degree of compensation X_C/X_L (Table 6.1).

Shunt compensation (SVC) tends to produce oversynchronous natural frequencies unless the degree of SVC is high and the transmission line is long. There are two situations when series compensation may cause undamped subsynchronous oscillations:

- Self-excitation due to induction generator effect
- Interaction with torsional oscillations
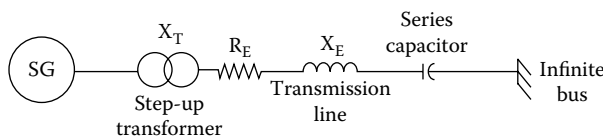
FIGURE 6.55 Radial system with series capacitor compensation.

TABLE 6.1 Subsynchronous Resonance Frequency

Compensation Ratio in % (X_C/X_L)	Natural Frequency f_n (Hz)	Slip Frequency 60-f_n (Hz)
10	18	42
20	26.83	33.17
30	32.86	27.14
40	37.94	22.06
50	42.46	17.54

As $f_n < f_0$, the slip S in the SG is negative. Consequently, with respect to stator currents at frequency f_n, the SG behaves like an induction generator connected to the power system.

The effective synchronous resistance of the SG at $S = (f_n - f_0)/f_0 < 0$, R_{as}, is negative. As such, it may surpass the positive resistance of the transmission line. The latter becomes an LC circuit with negative resistance. Electrical oscillations will self-excite at large levels. A strong damper winding in the SG or an additional resistance in the power line would solve the problem. The phenomenon is independent of torsional dynamics, being purely electromechanical.

If the series compensation slip frequency 60 (50) Hz $- f_n$ is close to one of the torsional-free frequencies of the turbine-generator unit, torsional oscillations are initiated. This is the subsynchronous resonance (SSR). Torsional oscillations buildup may cause shaft fatigue or turbine-generator shaft breaking. In fact, the SSR was "discovered" after two such disastrous events took place in 1970 to 1971.

Some countermeasures to SSR are as follows:

- Damping circuits in parallel with the series compensation capacitors (Figure 6.52b)
- Dynamic filters: the unified power flow controller may be considered for the scope (Figure 6.53b), as it can provide an additional voltage ΔV of such a phase as to compensate the SSR voltage [32]
- Thyristor-controlled shunt reactors or capacitors (SVCs)
- Selected frequency damping in the exciter control [33]
- Superconducting magnetic storage systems: the ability of the SMES to quickly inject or extract from the system active or reactive power by request makes it a very strong candidate to SSR attenuation (about 1 sec attenuation time is claimed in Reference [34])
- Protective relays that trip the unit when SSR is detected in speed by generator current feedback sensors

6.17 Summary

- Control of SGs means basically active power (or speed) and reactive power (or voltage) control.
- Active power (or speed) control of SGs is performed through turbine close-loop speed governing.
- Reactive power (or voltage) control is done through field-winding voltage (current I_f) close-loop control (AVR).
- Though, in principle, weakly coupled, the two controls interact with each other. The main decoupling means used so far is the so-called power system stabilizer (PSS). The PSS input is active power (or speed) deviation. Its output enters the AVR control system with the purpose of increasing the damping torque component.
- When the SG operates in connection with a power system, two more control levels are required besides primary control (speed governing and AVR–PSS). They are automatic generation control (AGC) and economic dispatch with security assessment generation allocation control.
- AGC refers to frequency-load control and inter-tie control.
- Frequency-load control means to allocate frequency (speed)/power characteristics for each SG and move them up and down through area control error (ACE) to determine how much power contribution is asked from each SG.

- ACE is formed by frequency error multiplied by a frequency bias factor λ_R added to inter-tie power error ΔP_{tie}. ACE is then PI controlled to produce load-frequency set points for each SG by allocating pertinent participation factors α_i (some of them may be zero).
- The amount of inter-tie power exchange between different areas of a power system and the participation factors of all SGs are determined in the control computer by the economic dispatch with security assessment, based on lowest operation costs per kilowatt-hour or on other cost functions.
- Primary (speed and voltage) control is the fastest (seconds), while economic dispatch is the slowest (minutes).
- Active and reactive power flow in a power system may be augmented by flexible AC transmission systems (FACTS) that make use of power electronics and of various energy storage elements.
- Primary (speed and voltage) control is slow enough that third- and fourth-order simplified SG models suffice for its investigation.
- Constant speed (frequency) closed loop is feasible only in isolated SGs.
- SGs operating in a power system have speed-droop controllers to allow for power sharing between various units.
- Speed droop is typically 4 to 5%.
- Speed governors require at least second-order models, while for hydraulic turbines, transient speed-droop compensation is required to compensate for the water starting time effect. Speed governors for hydraulic turbines are the slowest in response (up to 20 sec and more for settling time), while steam turbines are faster (especially in fast valving mode), but they show an oscillatory response (settling time is generally less than 10 sec).
- In an isolated power system with a few SGs, automatic generation control means, in fact, adding an integrator to the load-frequency set point of the frequency/power control to keep the frequency constant for that generator.
- AGC in interconnected power systems means introducing the inter-tie power exchange error ΔP_{tie} with frequency error weighted by the frequency bias factor to form the area control error (ACE). ACE contains PI filters to produce ΔP_{ref} that provides the set point level of various generators in each area. Consequently, not only the frequency is controlled but also the inter-tie power exchange, all according to, say, minimum operation costs with security assessment.
- The time response of SG in speed and power angle for various power perturbations is qualitatively divided into four stages: rotor swings, frequency drops, primary control (speed and voltage control), and secondary control (inter-tie control and economic dispatch). The frequency band of speed-governor control in power systems is generally less than 2 Hz.
- Spinning reserve is defined as rated power of all SGs in a system minus the actual power needed in certain conditions.
- If spinning reserve is not large enough, frequency does not recover; it keeps decreasing. To avoid frequency collapse, load is shedded in designated substations in one to three stages until frequency recovers. Underfrequency relays trigger load shedding in substations.
- Active and reactive powers of various loads depend on voltage and frequency to a larger or smaller degree.
- Equilibrium of frequency (speed) is reached for active power balance between offer (SG) and demand (loads).
- Similarly, equilibrium in voltage is reached for balance in reactive power between offer and demand. Again, if not enough reactive power reserve exists, voltage collapse takes place. To avoid voltage collapse, either important reactive loads are shedded or additional reactive power injection from energy storage elements (capacitors) is performed.
- The SG contribution to reactive power (voltage) control is paramount.
- Voltage control at SG terminal AVR is done through field-winding (excitation) voltage V_f, (current I_f) control. The frequency band of automatic voltage regulators (AVR) is within 2 to 3 Hz, in general.

- The DC excitation power for SGs is provided by exciters.
- Exciters may be of three main types: DC exciters, AC exciters, and static exciters.
- DC exciters contain two DC commutator generators mounted on the SG shaft: the auxiliary exciter (AE) and the main exciter (ME). The ME armature supplies the SG excitation through brushes and slip-rings at a full excitation power rating. The AE armature excites the ME. The AE excitation is power electronics controlled at the command (output) of AVR. DC exciters are in existence for SGs up to 100 MW, despite their slow response — due to large time constants of AE and ME — and commutator wear — due to the low control power of AE.
- AC exciters contain an inside-out synchronous generator (ME) with output that is diode-rectified and connected to the SG excitation winding. It is a brushless system, as the ME DC excitation circuit is placed on the stator and is controlled by power electronics at the command (output) of AVR. With only one machine on the SG shaft, the brushless AC exciter is more rugged and almost maintenance free. The control power is 1/20 (1/30) of the SG excitation power rating, but the control is faster, as now only one machine (ME) time constant delay exists.
- Static exciters are placed away from the SG and are connected to the excitation winding of SG through brushes and slip-rings. They are power electronics (static) AC–DC converters with very fast response. Controlled rectifiers are typical, but diode rectifiers with capacitor filters and four-quadrant choppers are also feasible. Static exciters are the way of the future now that slip-ring–brush energy transmission at 30 MW was demonstrated in 400 MVA doubly fed induction generator pump-storage power plants. Also, converters up to this rating are already feasible.
- Exciter modeling requires, for AVR design, a new, nonreciprocal, P.U. system where the base excitation voltage is that which produces no load rated voltage at SG terminals at no load. The corresponding P.U. field current is also unity in this case:

$$I_{fb} = l_{dm} I_f = 1; V_f = I_f r_f$$

$$V_{fb} = \frac{l_{dm}}{r_f} V_f = 1$$

This way, working with P.U. voltages in the range of 10^{-3} is avoided.
- The simplest model of SG excitation is a first-order delay with the transient open-circuit time constant:

$$T'_{d0} = \frac{\left(l_{dm} + l_{lf}\right)}{r_f} \cdot \frac{1}{\omega_0} \quad \text{(seconds)}$$

and a unity P.U. gain (Equation 6.22).
- The DC exciter model (one level; ME or AE), accounting for magnetic saturation, is a nonlinear model that contains a first-order delay and a nonlinear saturation-driven feedback. For small-signal analysis, a first-order model with saturation-variable gain and a time constant is obtained.
- For the AC exciter, the same model may be adopted but with one more feedback proportional to field SG current, to account for a d-axis demagnetizing armature reaction in the ME (alternator).
- The diode rectifier may be represented by its steady-state voltage/current output characteristics. Three diode commutation modes are present from no load to short-circuit. In essence, the diode rectifier characteristic shows a voltage regulation dependent on ME commutation (subtransient) inductance.
- The controlled rectifier may also be modeled by its steady-state voltage/current characteristic with the delay angle α as parameter and control variable.
- The basic AVR acts upon the exciter input and may have one to three stabilizing loops and, eventually, additional inputs. The sensed voltage is corrected by a load compensator.

- A lead–lag compensator constitutes the typical AVR stabilizing loop.
- Various exciters and AVRs are classified in IEEE standard 512.2 of 1992.
- Alternative AVR stabilizer loops such as PID are also practical.
- All AVR systems are provided with underexcitation (UEL) and overexcitation (OEL) limiters.
- Exciter dynamics and AVRs may introduce negative damping generator torques. To counteract such a secondary effect, power system stabilizers (PSSs) were introduced.
- PSSs have speed deviation or accelerating power deviation as input and act as an additional input to AVR.
- The basic PSS contains a gain, a washout (high-pass) filter, and a phase compensator in order to produce torque in phase with speed deviation (positive damping). The role of the washout filter is to avoid PSS output voltage modification due to steady-state changes in speed.
- Accelerating-power-integral input PSSs were proven better than speed or frequency or electric power deviation input PSSs.
- Besides independent speed-governing and AVR–PSS control of SGs, coordinated speed and voltage SG control were introduced through multivariable optimal control methods.
- Advanced nonlinear digital control methods, such as fuzzy logic, ANN, μ synthesis, $H\infty$, and sliding-mode, were proposed for integrated SG generator control.
- Power-electronics-driven active/reactive power flow in power systems may be defined as FACTS (flexible AC transmission systems). FACTS may make use of external energy storage elements such as capacitors, resistors, and inductors (normal or of superconductors material). They also assist in voltage support and regulation.
- FACTS may enhance the dynamic stability limits of SGs but interfere with their speed governing and AVR.
- The steam (or gas) turbines have long multimass shafts of finite rigidity. Their characterization by lumped 4,5 masses is typical.
- Such flexible shaft systems are characterized by torsional natural frequencies above 6 to 8 Hz, in general, for large turbine generators.
- Series compensation by capacitors to increase the transport capacity of long power lines leads to the occurrence of offset AC currents at natural frequency f_n solely dependent on the degree of transmission-line reactance compensation by series capacitors ($X_C/X_L < 0.5$).
- It is the difference $f_0 - f_n$, the slip (rotor) frequency of rotor currents due to this phenomenon that may fall over a torsional free frequency to cause subsynchronous resonance (SSR).
- Subsynchronous resonance may cause shafts to break or, at least, cause their premature wearing.
- The slip frequency currents of frequency $f_0 - f_n$ produced by the series compensation effect, manifest themselves as if the SG were an induction generator connected at the power grid. As slip is negative ($f_n < f_0$), an equivalent negative resistance is seen by the power grid. This negative resistance may overcompensate for the transmission line resistance. With negative overall resistance, the transmission-line reactance plus series compensation capacitor circuit may ignite dangerous torque pulsations. This phenomenon is called induction generator self-excitation and has to be avoided. A way to do it is to use a strong (low resistance) damper cage in SGs.
- Various measures to counteract SSR were proposed. Included among them are the following: damping circuit in parallel with the series capacitor, thyristor-controlled shunt reactors or capacitors, selected frequency damping in AVR, superconducting magnetic energy storage, and protective relays to trip the unit when SSR is detected through generator speed or by current feedback sensors oscillations.
- Coordinated digital control of both active and reactive power with various limiters, by multivariable optimal theory methods with self-learning algorithms, seems to be the way of the future, and much progress in this direction is expected in the near future.
- Emerging silicon-carbide power devices [34] may enable revolutionary changes in high-voltage static power converters for frequency and voltage control in power systems.

References

1. P. Kundur, *Power System Stability and Control*, McGraw-Hill, New York, 1994.
2. J. Machowski, J.W. Bialek, and J.R. Bumby, *Power Systems Dynamics and Stability*, John Wiley & Sons, New York, 1997.
3. L.L. Grigsby, Ed., *Electric Power Engineering Handbook*, CRC Press, Boca Raton, FL, 1998.
4. Task Force, Computer models for representation of digital-based excitation systems, *IEEE Trans.*, EC-11, 3, 1996, pp. 607–615.
5. N. Mohan, T. Undeland, and R. Williams, *Power Electronics*, 3rd ed., John Wiley & Sons, New York, 2002.
6. I. Boldea, and S.A. Nasar, *Electric Drives*, CRC Press, Boca Raton, FL, 1998, chap. 5, pp. 90–91.
7. A. Godhwani, and M.J. Basler, A digital excitation control system for use on brushless excited synchronous generators, *IEEE Trans.*, EC-11, 3, 1996, pp. 616–620.
8. Task Force, Underexcitation limiter models for power system stability studies, *IEEE Trans.*, EC-10, 3, 1995, pp. 524–531.
9. G. Roger Bérubé, Les.M. Hayados, and R.E. Beaulien, A utility perspective on underexcitation limiters, *IEEE Trans.*, EC-10, 3, 1995, pp. 532–537.
10. G.K Girgis, and H.D. Vu, Verification of limiter performance in modern excitation control systems, *IEEE Trans.*, EC-10, 3, 1995, pp. 538–542.
11. H. Vu, and J.C. Agee, Comparison of power system stabilizers for damping local mode oscillations, *IEEE Trans.*, EC-8, 3, 1993, pp. 533–538.
12. A. Murdoch, S. Venkataraman, R.A. Lawson, and W.R. Pearson, Integral of accelerating power type PSS, Part I and II, *IEEE Trans.*, EC-14, 4, 1999, pp. 1658–1672.
13. T. Hiyama, K. Miyazaki, and H. Satoh, A fuzzy logic excitation system for stability enhancement of power systems with multimode oscillations, *IEEE Trans.*, EC-11, 2, 1996, pp. 449–454.
14. P. Hoang, and K. Tomsovic, Design and analysis of an adaptive fuzzy power system stabilizer, *IEEE Trans.*, EC-11, 2, 1996, pp. 455–461.
15. G.P. Chen, O.P. Malik, H.Y. Qim, and G.Y. Xu, Optimization technique for the design of linear optimal power system stabilizer, *IEEE Trans.*, EC-7, 3, 1992, pp. 453–459.
16. S. Chen, and O.P. Malik, Power system stabilizer design using synthesis, *IEEE Trans.*, EC-10, 1, 1995, pp. 175–181.
17. Y. Caoi, L. Jiang, S. Cheng, D. Chen, O.P. Malik, and G.S. Hope, A nonlinear variable structure stabilizer for power system stability, *IEEE Trans.*, EC-9, 3, 1994, pp. 488–495.
18. R. Asgharian, and S.A Tavakoli, A schematic approach to performance weight selection in design of robust H PSS using genetic algorithms, *IEEE Trans.*, EC-11, 1, 1996, pp. 111–117.
19. W.J. Wilson, and J.D. Applevich, Co-ordinated governor exciter stabilizer design in multimachine power systems, *IEEE Trans.*, EC-1, 3, 1986, pp. 61–67.
20. M. Djukanovic, M. Novicevic, D. Dobrojevic, B. Babic, D. Babic, and Y. Pao, Neural-net based coordinated stabilizing control for exciter and governor loops of low head hydroelectric power plants, *IEEE Trans.*, EC-10, 4, 1995, pp. 760–767.
21. M.B. Djukanovic, M.S Calovic, B.V. Vesovic, and D.J. Sobajic, Neuro-fuzzy controller of low head hydropower plants using adaptive-network based fuzzy inference system, *IEEE Trans.*, EC-12, 4, 1997, pp. 375–381.
22. G.K. Venayagamoorthy, and R.G. Herley, A continually online trained neurocontroller for excitation and turbine control of a turbogenerator, *IEEE Trans.*, EC-16, 3, 2001, pp. 261–269.
23. A.R. Mahran, B.W. Hegg, and M.L. El-Sayed, Co-ordinated control of synchronous generator excitation and static VAR compensator, *IEEE Trans.*, EC-7, 2, 1992, pp. 615–622.
24. J.D. Hurley, L.M. Bize, and C.R. Mummart, The adverse effects of excitation system VAR and power factor controllers, *IEEE Trans.*, EC-14, 4, 1999, pp. 1636–1641.
25. T. Ise, Y. Murakami, and K. Tsuji, Simultaneous active and reactive power control of SMES using GTO converters, *IEEE Trans.*, PWRD-1, 1, 1986, pp. 143–150.

26. E. Handschim, and T. Stephanblome, New SMES Strategies as a Link Between Network and Power Plant Control, paper presented at the International IFAC Symposium on Power Plants and Power System Control, Munich, Germany, March 9–11, 1992.

27. Q. Jiang, and M.F. Coulon, The power regulation of a PWM type superconducting magnetic energy storage unit, *IEEE Trans.*, EC-11, 1, 1996, pp. 168–174.

28. A.H.M. Rahim, and A.M. Mohammad, Improvement of synchronous generator damping through superconducting magnetic energy storage systems, *IEEE Trans.*, EC-9, 4, 1996, pp. 736–742.

29. S.C. Tripathy, R. Balasubramanian, and P.S. Nair, Adaptive automatic generation control with superconducting magnetic energy storage in power systems, *IEEE Trans.*, EC-7, 3, 1992, pp. 439–441.

30. S.C. Tripathy, and K.P. Juengst, Sample data automatic generation control with superconducting magnetic energy storage in power systems, *IEEE Trans.*, EC-12, 2, 1997, pp. 187–192.

31. J. Chatelain, and B. Kawkabani, Subsynchronous resonance (SSR) countermeasures applied to the second benchmark model, *EPCS J.*, 21, 1993, pp. 729–739.

32. L. Wang, Damping of torsional oscillations using excitation control of synchronous generator: the IEEE second benchmark model investigation, *IEEE Trans.*, EC-6, 1, 1991, pp. 47–54

33. A.H.M.A. Rahim, A.M. Mohammad, and M.R. Khan, Control of subsynchronous resonant modes in a series compensated system through superconducting magnetic energy storage units, *IEEE Trans.*, EC-11, 1, 1996, pp. 175–180.

34. A. Hefner, R. Singh, and J. Lai, Emerging silicon-carbide power switches enable revolutionary changes in high voltage power conversion, *IEEE Power Electron. Soc. Newsl.*, 16, 4, 2004, pp. 10–13.

7

Design of Synchronous Generators

7.1   Introduction

Most synchronous generator power is transmitted through power systems to various loads, but there are various stand-alone applications, too.

In this chapter, the design of synchronous generators (SGs) connected to a power system is dealt with in some detail.

The successful design and operation of an SG depends heavily on agreement between the SG manufacturer and user in regard to technical requirements (specifications). Published standards such as American National Standards Institute (ANSI) C50.13 and International Electrotechnical Commission (IEC) 34-1 contain these requirements for a broad class of SGs. The Institute of Electrical and Electronics Engineers (IEEE) recently launched two new, consolidated standards for high-power SGs [1]:

   • C50.12 for large salient pole generators
   • C50.13 for cylindrical rotor large generators

The liberalization of electricity markets led, in the past 10 years, to the gradual separation of production, transport, and supply of electrical energy. Consequently, to provide for safe, secure, and reasonable cost supply, formal interface rules — grid codes — were put forward recently by private utilities around the world.

Grid codes do not align in many cases with established standards, such as IEEE and ANSI. Some grid codes exceed the national and international standards "Requirements on Synchronous Generators." Such requirements may impact unnecessarily on generator costs, as they may not produce notable benefits for power system stability [2].

Harmonization of international standards with grid codes becomes necessary, and it is pursued by the joint efforts of SG manufacturers and interconnectors [3] to specify the turbogenerator and hydrogenerator parameters. Generator specifications parameters are, in turn, related to the design principles and, ultimately, to the costs of the generator and of its operation (losses, etc.).

In this chapter, a discussion of turbogenerator specifications as guided by standards and grid codes is presented in relation to fundamental design principles. Hydrogenerators pose similar problems in power systems, but their power share is notably smaller than that of turbogenerators, except for a few countries, such as Norway. Then, the design principles and a methodology for salient pole SGs and for cylindrical rotor generators, respectively, with numerical examples, are presented in considerable detail.

Special design issues related to generator motors for pump-storage plants or self-starting turbogenerators are treated in a dedicated paragraph.

7.2   Specifying Synchronous Generators for Power Systems

The turbogenerators are at the core of electric power systems. Their prime function is to produce the active power. However, they are also required to provide (or absorb) reactive power both, in a refined controlled manner, to maintain frequency and voltage stability in the power system (see Chapter 6). As the control of SGs becomes faster and more robust, with advanced nonlinear digital control methods, the parameter specification is about to change markedly.

7.2.1   The Short-Circuit Ratio (SCR)

The short-circuit ratio (SCR) of a generator is the inverse ratio of saturated direct axis reactance in per unit (P.U.):

$$SCR = \frac{1}{x_{d(sat)}} \tag{7.1}$$

The SCR has a direct impact on the static stability and on the leading (absorbed) reactive power capability of the SG. A larger SCR means a smaller $x_{d(sat)}$ and, almost inevitably, a larger airgap. In turn,

this requires more ampere-turns (magnetomotive force [mmf]) in the field winding to produce the same apparent power.

As the permissible temperature rise is limited by the SG insulation class (class B, in general, $\Delta T = 130°$), more excitation mmf means a larger rotor volume and, thus, a larger SG.

Also, the SCR has an impact on SG efficiency. An increase of SCR from 0.4 to 0.5 tends to produce a 0.02 to 0.04% reduction in efficiency, while it increases the machine volume by 5 to 10% [3].

The impact of SCR on SG static stability may be illustrated by the expression of electromagnetic torque t_e P.U. in a lossless SG connected to a infinite power bus:

$$t_e \approx SCR \cdot E_0 \cdot V_1 \sin\delta \tag{7.2}$$

The larger the SCR, the larger the torque for given no-load voltage (E_0), terminal voltage V_1, and power angle δ (between E_0 and ΔV_1 per phase). If the terminal voltage decreases, a larger SCR would lead to a smaller power angle δ increase for given torque (active power) and given field current.

If the transmission line reactance — including the generator step-up transformer — is x_e, and V_1 is now replaced by the infinite grid voltage V_g behind x_e, the generator torque t_e' is as follows:

$$t_e' = SCR \times E_0 \times V_g \times \frac{\sin\delta'}{\left(1 + x_e / x_d\right)} \tag{7.3}$$

The power angle δ' is the angle between E_0 of the generator and V_g of the infinite power grid. The impact of improvement of a larger SCR on maximum output is diminished as x_e/x_d increases.

Increasing SCR from 0.4 to 0.5 produces the same maximum output if the transmission line reactance ratio x_e/x_d increases from 0.17 to 0.345 at a leading power factor of 0.95 and 85% rated megawatt (MW) output.

Historically, the trend has been toward lower SCRs, from 0.8 to 1.0, 70 years ago, to 0.58 to 0.65 in the 1960s, and to 0.5 to 0.4 today. Modern — fast response — excitation systems compensate for the apparent loss of static stability grounds. The lower SCRs mean lower generator volumes, losses, and costs.

7.2.2 SCR and x_d' Impact on Transient Stability

The critical clearing time of a three-phase fault on the high-voltage side of the SG step-up transformer is a representative performance index for the transient stability limits of the SG tied to an infinite bus bar.

The transient d-axis reactance x_d' (in P.U.) takes the place of x_d in Equation 7.3 to approximate the generator torque transients before the fault clearing. In the case in point, $x_e = x_{Tsc}$ is the short-circuit reactance (in P.U.) of the step-up transformer. A lower x_d' allows for a larger critical clearing time and so does a large inertia. Air-cooled SGs tend to have a larger inertia/MW than hydrogen-cooled SGs, as their rotor size is relatively larger and so is their inertia.

7.2.3 Reactive Power Capability and Rated Power Factor

A typical family of V curves is shown in Figure 7.1. The reactive power capability curve (Figure 7.2) and the V curves are more or less equivalent in reflecting the SG capability to deliver active and reactive power, or to absorb reactive power until the various temperature limitations are met (Chapter 5). The rated power factor determines the delivered/lagging reactive power continuous rating at rated active power of the SG.

The lower the rated (lagging) power factor, the larger the MVA per rated MW. Consequently, the excitation power is increased, and the step-up transformer has to be rated higher. The rated power factor is generally placed in the interval 0.9 to 0.95 (overexcited) as a compromise between generator initial and loss capitalized costs and power system requirements. Lower values down to 0.85 (0.8) may be found
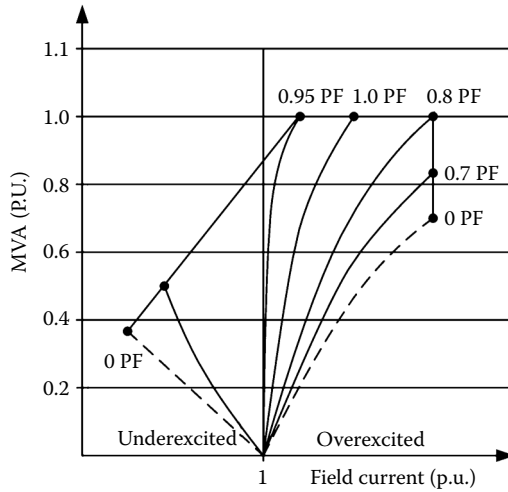
FIGURE 7.1 Typical *V* curve family.
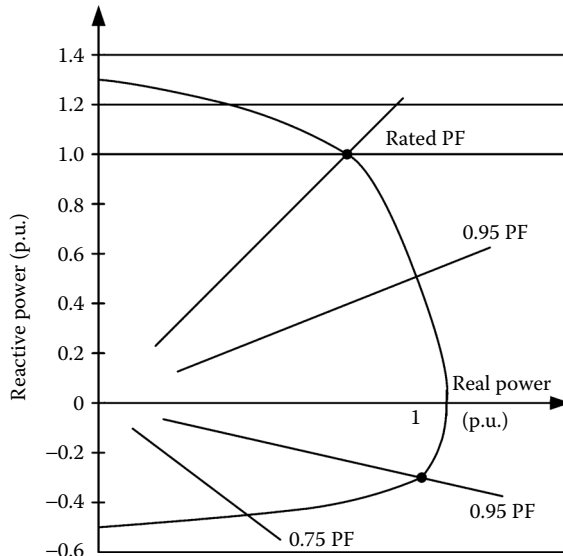
FIGURE 7.2 Reactive power capability curve.

in air (hydrogen)-cooled SGs. The minimum underexcited rated power factor is 0.95 at rated active power. The maximum absorbed (leading) reactive power limit is determined by the SCR and corresponds to maximum power angle and to end stator core overtemperature limit.

7.2.4   Excitation Systems and Their Ceiling Voltage

Fast control of excitation current is needed to preserve SG transient stability and control its voltage. Higher ceiling excitation voltage, corroborated with low electrical time constants in the excitation system, provides for fast excitation current control.

Today's ceiling voltages are in the range of 1.6 to 3.0 P.U. There is a limit here dictated by the effect of magnetic saturation, which makes ceiling voltages above 1.6 to 2.0 P.U. hardly practical. This is more so as higher ceiling voltage means sizing the insulation system of the exciter or the rating of the static exciter voltage for maximum ceiling voltage at notably larger exciter costs.
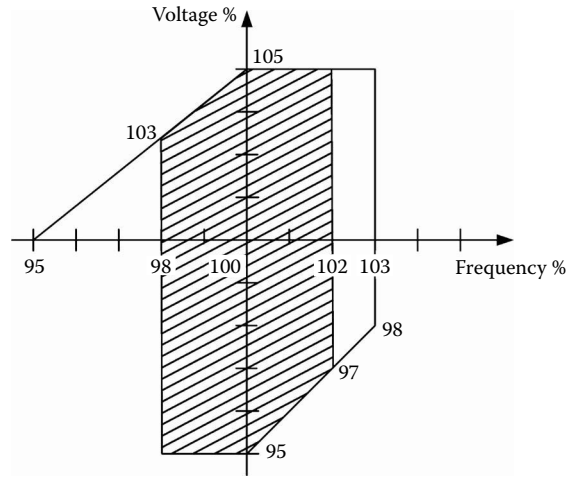
FIGURE 7.3   Voltage/frequency operation.

The debate over which is best — the alternating current (AC) brushless exciter or static exciter (which is specified also with a negative ceiling voltage of –1.2 to 1.5 P.U.) is still not over. A response time of 50 msec in "producing" the maximum ceiling voltage is today fulfilled by the AC brushless exciters, but faster response times are feasible with static exciters. However, during system faults, the AC brushless exciter is not notably disturbed, as it draws its input from the kinetic energy of the turbine-generator unit.

In contrast, the static exciter is fed from the exciter transformer which is connected, in general, at SG terminals, and seldom to a fully independent power source. Consequently, during faults, when the generator terminal voltage decreases, to secure fast, undisturbed excitation current response, a higher voltage ceiling ratio is required. Also, existing static exciters transmit all power through the brush–slip-ring mechanical system, with all the limitations and maintenance incumbent problems.

7.2.4.1   Voltage and Frequency Variation Control

As detailed in Chapter 6, the SG has to deliver active and reactive power with designed speed and voltage variations. The size of the generator is related to the active power (frequency) and reactive power (voltage) requirements. Typical such practical requirements are shown in Figure 7.3.

In general, SGs should be thermally capable of continuous operation within the limits of the P/Q curve (Figure 7.2) over the ranges of ±5% in voltage, but not necessarily at the power level typical for rated frequency and voltage. Voltage increase, accompanied by frequency decrease, means a higher increase in the V/ω ratio.

The total flux in the machine increases. A maximum of flux increase is considered practical and should be there by design. The SG has to be sized to have a reasonable magnetic saturation level (coefficient) such that the field mmf (and losses) and the core loss are not increased so much as to compromise the thermal constraints in the presence of corresponding adjustments of active and reactive power delivery under these conditions.

To avoid oversizing the SG, the continuous operation is guaranteed only in the hatched area, at most, 47.5 to 52 Hz. In general, the 5% overvoltage is allowed only above rated frequency, to limit the flux increase in the machine to a maximum of 5%. The rather large ±5% voltage variation is met by SGs with the use of tap changers on the generator step-up transformer (according to IEC standards).

7.2.4.2   Negative Phase Sequence Voltage and Currents

Grid codes tend to restrict the negative sequence voltage component at 1% (V_2/V_1 in percent). Peaks up to 2% might be accepted for short duration by prior agreement between manufacturer and interconnector.

The SGs should be able to withstand such voltage imbalance, which translates into negative sequence currents in the stator and rotor with negative sequence reactance $x_2 = 0.10$ (the minimum accepted by

the IEC) and a step-up transformer with a reactance $x_T = 0.15$ P.U. Then, the 1% voltage unbalance translates into a negative sequence current i_2 (P.U. in percent) of

$$i_2 = \frac{v_2}{x_2 + x_T} = \frac{0.01}{0.1 + 0.15} = 0.04 \text{ P.U.} = 4\% \tag{7.4}$$

The SG has to be designed to withstand the additional losses in the rotor damper cage, in the excitation winding, and in the stator winding, produced by the negative sequence stator current. Turbogenerators above 700 MV seem to need explicit amortisseur windings for the scope.

7.2.4.3 Harmonic Distribution

Grid codes specify the voltage total harmonic distortion (THD) at 1.5% and 2% in, respectively, near 400 kV and in the near 275 kV power systems. Proposals are made to raise these values to 3 (3.5)% in the voltage THD. The voltage THD may be converted into current THD and then into an equivalent current for each harmonic, considering that the inverse reactance x_2 may be applied for time harmonics as well.

For the fifth time harmonic, for example, a 3% voltage THD corresponds to a current i_5:

$$i_5 = \frac{v_5}{5 \cdot (x_2 + x_T)} = \frac{0.03}{5 \cdot (0.1 + 0.15)} = 0.024 \text{ P.U.} \tag{7.5}$$

7.2.4.4 Temperature Basis for Rating

Observable and hot-spot temperature limits appear in IEEE/ANSI standards, but only the former appears in IEC-60034 standards.

In principle, the observable temperature limits have to be set such that the hot-spot temperatures should not go above 130° for insulation class B and 155° for insulation class F.

In practice, one design could meet observable temperatures (in a few spots in the SG) but exceed the hot-spot limits of the insulation class. Or, we may overrestrict the observable temperature, while the hot spot may be well below the insulation class limit.

Also, the rated cold coolant temperature has to be specified if the hot-spot temperature is maintained constant when the cold coolant temperature varies, as for ambient temperature, following SGs where the observable temperature also varies.

Holding one of the two temperature limits as constant, with the cold coolant (ambient) temperature variable, leads to different SG overrating and underrating (Figure 7.4).

It seems reasonable that we need to fix the observable temperature limit for a single cold coolant temperature and calculate the SG MVA capability for different cold coolant (ambient) and hot-spot temperatures. This way, the SG is exploited optimally, especially for the "ambient-following" operation mode.

7.2.4.5 Ambient-Following Machines

SGs that operate for ambient temperatures between −20° and 50° should have permissible generator output power, variable with cold coolant temperatures. Eventually, peak (short-term) and base MVA capabilities should be set at rated power factor (Figure 7.5).

7.2.4.6 Reactances and Unusual Requirements

The already mentioned d–axis synchronous reactance x_d and d–axis transient reactance x_d' are key factors in defining static and transient stability and maximum leading reactive power rating of SGs. In general practice, x_d and x_d' values are subject to agreement between vendors and purchasers of SGs, based on operating conditions (weak or strong power system area exciter performance, etc.).

To limit the peak short-circuit current and circuit breaker rating, it may be considered as appropriate to specify (or agree upon) a minimum value of the subtransient reactances at the saturation level of rated
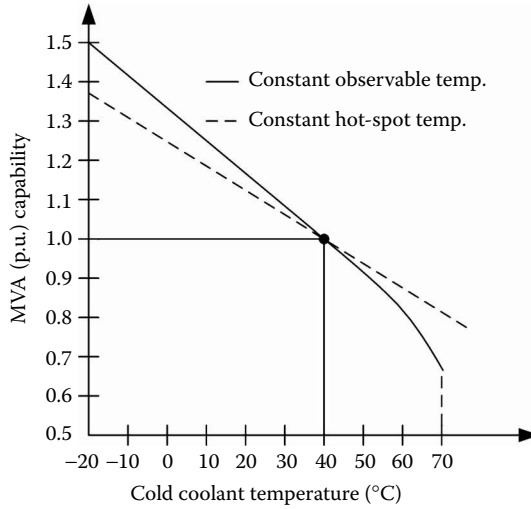
FIGURE 7.4 Synchronous generator millivoltampere rating vs. cold coolant temperature.
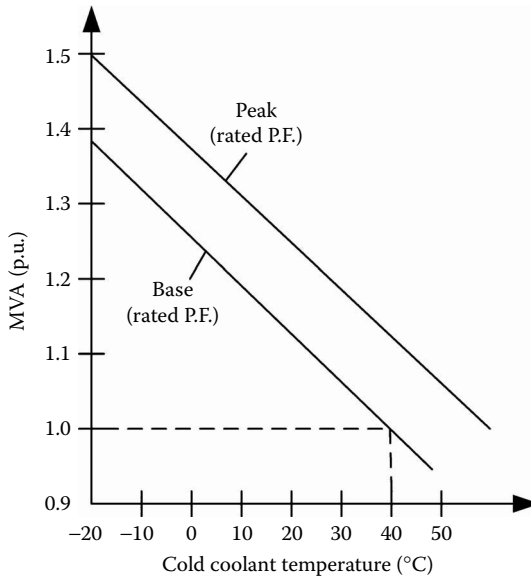
FIGURE 7.5 Ambient following synchronous generator ratings.

voltage. Also, the maximum value of the unsaturated (at rated current) value of transient d axis reactance x_d' may be limited based on unsaturated and saturated subtransient and transient reactances, see IEEE 100 [11].

There should be tolerances for these agreed-upon values of x_d'' and x_d', positive for the first ($20 \div 30\%$) and negative ($-20 \div 30\%$) for the second.

7.2.4.7 Start–Stop Cycles

The total number of starts is important to specify, as the SG should, by design, prevent cyclic fatigue degradation. According to IEC and IEEE and ANSI trends, it seems that the number of starts should be as follows:

- 3000 for base-load SGs
- 10,000 for peak-load SGs or other frequently cycled units [1]

7.2.4.8   Starting and Operation as a Motor

Combustion turbines generator units may be started with the SG as a motor fed from a static power converter of lower rating, in general. Power electronics rating, drive-train losses, inertia, speed vs. time, and restart intervals have to be considered to ensure that the generator temperatures are all within limits.

Pump-storage hydrogenerator units also have to be started as motors on no-load, with power electronics, or back-to-back from a dedicated generator which accelerates simultaneously with the asynchronous motor starting. The pumping action will force the SG to work as a synchronous motor and the hydraulic turbine-pump and generator-motor characteristics have to be optimally matched to best exploit the power unit in both operation modes.

7.2.4.9   Faulty Synchronization

SGs are also designed to survive without repairs after synchronization with ±10° initial power angle. Faulty synchronization (outside ±10°) may cause short-duration current and torque peaks larger than those occurring during sudden short-circuits. As a result, internal damage of the SG may result; therefore, inspection for damage is required. Faulty synchronization at 120° or 180° out of phase with a low system reactance (infinite) bus might require partial rewind of the stator and extensive rotor repairs. Special attention should be paid to these aspects from design stage on.

7.2.4.10   Forces

Forces in an SG occur due to the following:

- System faults
- Thermal expansion cycles
- Double-frequency (electromagnetic) running forces

The relative number of cycles for peaking units (one start per day for 30 yr) is shown in Figure 7.6 [4], together with the force level.

For system faults (short-circuit, faulty, or successful synchronization), forces have the highest level (100:1). The thermal expansion forces have an average level (1:1), while the double-frequency running forces are the smallest in intensity (1:10). A base load unit would encounter a much smaller thermal expansion cycle count.

The mechanical design of an SG should manage all these forces and secure safe operation over the entire anticipated operation life of the SG.
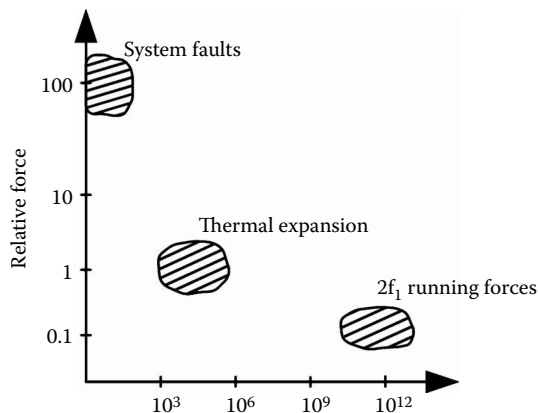
FIGURE 7.6   Forces cycles.

7.2.4.11 Armature Voltage

In principle, the armature voltage may vary in a 2-to-1 ratio without having to change the magnetic flux or the armature reaction mmf, that is, for the same machine geometry.

Choosing the voltage should be the privilege of the manufacturer, to enable him enough freedom to produce the best designs for given constraints. The voltage level determines the insulation between the armature winding and the slot walls in an indirectly cooled SG. This is not so in direct-cooled stator (rotor) windings, where the heat is removed through a cooling channel located in the slots. Consequently, a direct-cooled SG may be designed for higher voltages (say 28 kV instead of 22 kV) without paying a high price in cooling expenses.

However, for air-cooled generators, higher voltage may influence the Corona effect. This is not so in hydrogen-cooled SGs because of the higher Corona start voltage.

7.2.4.12 Runaway Speed

The runaway speed is defined as the speed the prime mover may be allowed to have if it is suddenly unloaded from full (rated) load. Steam (or gas) turbines are, in general, provided with quick-action speed governors set to trip the generator at 1.1 times the rated speed. So, the runaway speed for turbogenerators may be set at 1.25 P.U. speed. For water (hydro) turbines, the runaway speeds are much higher (at full gate opening):

- 1.8 P.U. for Pelton (impulse) turbines (SGs)
- 2.0 to 2.2 P.U. for Francis turbines (SGs)
- 2.5 to 2.8 P.U. for Kaplan (reaction) turbines (SGs)

The SGs are designed to withstand mechanical stress at runaway speeds. The maximum peripheral speed is about 140 to 150 m/sec for salient-pole SGs and 175 to 180 m/sec for turbogenerators. The rotor diameter design is limited by this maximum peripheral speed.

The turbogenerators are built today in only two-pole configurations, either at 50 Hz or at 60 Hz.

7.2.4.13 Design Issues

SG design deals with many issues. Among the most important issues are the following:

- Output coefficient and basic stator geometry
- Number of stator slots
- Design of stator winding
- Design of stator core
- Salient-pole rotor design
- Cylindrical rotor design
- Open-circuit saturation curve
- Field current at full load
- Stator leakage inductance, resistance, and synchronous reactance calculation
- Losses and efficiency calculation
- Calculation of time constant and transient and subtransient reactance
- Cooling system and thermal design
- Design of brushes and slip-rings (if any)
- Design of bearings
- Brakes and jacks design
- Exciter design

Currently, design methodologies of SGs are put in computer codes, and they may contain optimization stages and interface with finite element software for the refined calculation of electromagnetic thermal and mechanical stress, either for verification or for the final geometrical optimization design stage.
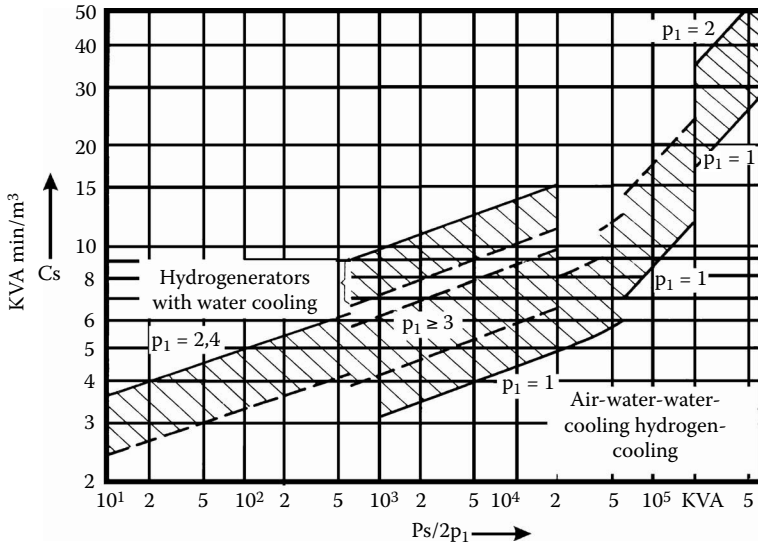
FIGURE 7.7   Output power coefficient for synchronous generators.

7.3   Output Power Coefficient and Basic Stator Geometry

The output coefficient C is defined as the SG kilovoltampere per cubic meter of rotor volume. The value of C (kilovoltampere per cubic meter) depends on machine power/pole, the number of pole pairs p_1, and the type of cooling, and it is often based on past experience (Figure 7.7).

The output power coefficient C may be expressed in terms of machine magnetic and electric loadings, starting from the electromagnetic power P_{elm}:

$$P_{elm} = 3 \cdot \frac{\omega_1}{\sqrt{2}} \cdot \left(W_1 \cdot K_{W1} \right) \cdot \Phi_1 \cdot I_1 \quad ; \quad \omega_1 = 2\pi p_1 \cdot n_n \tag{7.6}$$

The ampereturns per meter, or the electric specific loading (A_1), is as follows:

$$A_1 = \frac{6 \cdot W_1 \cdot I_1}{\pi \cdot D \cdot l_i} \ (\text{A/m}) \quad ; \quad K_{W1} - \text{winding factor} \tag{7.7}$$

with l_i the ideal stator stack length and D the rotor (or stator bore) diameter.

The flux per pole Φ_1 is

$$\Phi_1 = \frac{2}{\pi} \cdot B_{g1} \cdot \frac{\pi \cdot D}{2 p_1} \cdot l_i \tag{7.8}$$

Making use of Equation 7.7 and Equation 7.8 in Equation 7.6 yields

$$P_{elm} = \frac{\pi^2}{\sqrt{2}} \cdot K_{W1} \cdot A_1 \cdot B_{g1} \cdot l_i \cdot n_1 \cdot D^2 = C \cdot D^2 \cdot l_i \cdot n_n \tag{7.9}$$

So,

$$C = \frac{\pi^2}{\sqrt{2}} \cdot K_{W1} \cdot A_1 \cdot B_{g1} \tag{7.10}$$

The airgap flux density B_{g1} relates to magnetic specific loading (saturation level), while A_1 defines the electric specific loading. C is not quite equal to power/rotor volume but is proportional to it. The proportionality coefficient is $\pi/4$.

Going further, we might define the average shear stress on rotor f_t (specific tangential force in Newton per square meter [N/m^2] or Newton per square centimeter [N/cm^2]):

$$f_t = \frac{F_t}{\pi \cdot D \cdot l_i} = \frac{T_{elm} \cdot \left(\dfrac{2}{D}\right)}{\pi \cdot D \cdot l_i} = \frac{P_{elm}}{2\pi n_1 \cdot \pi \cdot \dfrac{D}{2} \cdot D \cdot l_i} = \frac{1}{\pi^2} C \tag{7.11}$$

So, the power output coefficient C is proportional to specific tangential force f_t exerted on the rotor exterior surface by the electromagnetic torque, with C given in voltampere per cubic meter [VA/m^3], f_t comes into Newton per square meter [N/m^2]. In general, C given in kilovoltampere per cubic meter [kVA/m^3].

As seen in Figure 7.7, C is given as a function of power per pole: $P_s/2p_1$ [5]. Direct water cooling in turbogenerators ($2p_1 = 2, 4$) allows for the highest output power coefficient.

The provisional rotor diameter D of SGs is limited by the maximum peripheral speed (140 to 150 m/sec) with 44 to 55 kg/mm^2 yield point, typical rotor core materials. This maximum peripheral speed U_{max} is to be reached at the runaway speed n_{max}, set by design as discussed earlier:

$$U_{max} = \pi \cdot D_{max} \cdot n_n \cdot \frac{n_{max}}{n_n} \tag{7.12}$$

For hydrogenerators n_{max}/n_n is much larger than the value for turbogenerators.

It is imperative that the chosen diameter gives the desired flywheel effect required by the turbine design. As already discussed in Chapter 5, the inertia constant H in seconds is

$$H = \frac{J\left(\omega_1 / p_1\right)^2}{2S_n} \tag{7.13}$$

where

        J = the rotor inertia (in kilogram × square meter)
        S_n = the rated apparent power in voltampere
        H = defined in relation to the maximum speed increase allowed until the speed governor closes
           the fuel (water) input

In general,

$$\frac{\Delta n_{max}}{n_n} \approx \sqrt{\frac{T_{GV}}{H} + 1} \tag{7.14}$$

with T_{GV} equal to the speed governor (gate) time constant in seconds.

For hydrogenerators,

$$\frac{\Delta n_{\max}}{n_n} < 0.3 - 0.4 \qquad (7.15)$$

T_{GV} for hydrogenerators is in the order of 5 to 8 sec. For turbogenerators, T_{GV} and $\Delta n_{\max}/n_n$ are notably smaller (<0.1 to 0.15). H for hydrogenerators varies in the interval from 3 to 8 sec above 1 MVA per unit. H is often stated as GD_{ig}^2 (kg $\cdot$ m²), where D_{ig} is twice the gyration radius of the rotor, and G is the rotor weight in kilogram:

$$H \approx \frac{1.37 \times 10^{-6} GD_{ig}^2 n_n^2}{S_n(\text{kVA})} \quad (\text{kWsec/kVA}) \qquad (7.16)$$

Approximately,

$$GD_{ig}^2 \approx \frac{\pi \gamma_{iron}}{8} \left[1 - \left(\frac{D_{ir}}{D} \right)^2 \right] \cdot D^4 \cdot l_p; \quad l_p - \text{rotor length} \qquad (7.17)$$

where

γ_{iron} = the iron specific weight (kg/m³)
D_{ir} = the interior rotor diameter
D_{ir} = zero in turbogenerators

GD_{ig}^2 may be specified in tonne $\times$ square meter. Alternatively, H in seconds may be specified or calculated from Equation 7.14 with T_{GV} and $\Delta n_{\max}/n_n$ already specified.

With the rotor diameter provisional upper limit from Equation 7.12, the length of the stator core stack l_i may be calculated from Equation 7.9 if P_{elm} is replaced by S_n. Then, with GD_{ig}^2 or H given, from Equation 7.16 and Equation 7.17 and with length $l_p \approx l_i$, the internal rotor interior diameter $D_{ir} < D$ may be calculated.

The pole pitch may also be computed:

$$\tau \approx \frac{\pi D}{2 p_1} \quad ; \quad p_1 = \frac{f_n}{n_n} \qquad (7.18)$$

The ratio l_i/τ has to be placed in a certain interval to secure low enough stator copper losses, as the end-connections length of the stator is proportional to the pole pitch τ. Generally,

$$\lambda = l_i/\tau = 1 \div 4 \quad \text{for } p_1 = 1$$
$$= 0.5 \div 2.5 \text{ for } p_1 > 1 \qquad (7.19)$$

The intervals for λ are rather large, leaving the designer with ample freedom. Though optimization design may be performed, it is good to have a good design start, so λ has to be in the intervals suggested by Equation 7.19.

With the output power coefficient C given by Equation 7.10, and based on past experience, the airgap flux density fundamental B_{g1} is as follows:

- B_{g1} = 0.75 – 1.05 T for cylindrical rotor SGs
- B_{g1} = 0.80 – 1.05 T for salient pole rotor SGs

Correspondingly, with C from Figure 7.7, the linear current loading A (A/m) intervals may be calculated for various cooling methods. The orientative design current densities intervals may also be specified (Table 7.1).

TABLE 7.1 Orientative Electric "Stress" Parameters

	Indirect Air Cooling	Indirect Hydrogen Cooling	Direct Cooling
A (kA/m)	30–80	90–120	160–200
Stator current density j_{cos} (A/mm^2)	3–6	4–7	7–10
			For water
Rotor current density j_{cor} (A/mm^2)	3–5	3–5	6–13
		With stator and rotor direct cooling: (13–18)	
		A/mm^2 and A = (250–300) kA/m	

7.4 Number of Stator Slots

The first requirement in determining the number of stator slots is to produce symmetrical (balanced) three-phase electromagnetic fields (emfs).

For q equal to the integer number of slots per pole and phase, the number of stator slots N_s is

$$N_s = 2p_1 \cdot q \cdot m \quad ; \quad m = 3 \text{ phases;} \quad p_1 - \text{pole pairs} \tag{7.20}$$

A larger integer q is typical for turbogenerators ($2p_1 = 2, 4$): $q > (4 \text{ to } 6)$. For low-speed generators, q may be as low as three but not less. For $q < 3, 4$ and for large power hydrogenerators, a fractionary q winding is adopted:

$$N_s = 2p_1 \cdot \left(b + \frac{c}{d} \right) \cdot 3 \quad ; \quad q = b + \frac{c}{d} \tag{7.21}$$

To secure balanced emfs, the slot pitch number x between the start of phases A and B (C) is such that

$$\frac{2\pi}{N_s} \cdot p_1 \cdot x = K \cdot \frac{2\pi}{3} \quad ; \quad K - \text{integer} \neq 3^p \tag{7.22}$$

Replacing N_s from Equation 7.21 and Equation 7.22 yields the following:

$$\frac{\pi}{3} \cdot \left(\frac{d}{bd+c} \right) \cdot x = K \cdot \frac{2\pi}{3} \quad ; \quad x = 2 \cdot \frac{bd+c}{d} \cdot K \tag{7.23}$$

Now, x has to be an integer, and $2K$ has to be divisible by d. Also, d may not contain a 3^p factor, as this is eliminated from K. For fractionary windings, not only should N_s be a multiple of three, but also the denominator c of q should not contain three as a factor. According to Equation 7.21, if N_s contains a factor of 3^p, then p_1 (pole pairs number) should also contain it, so that it would not appear in c.

In large SGs, the stator core is made of segments (Chapter 4) because the size of the lamination sheets is limited to 1 to 1.1 m in width. The number of slots per segment N_{ss}, for N_c segments, is

$$N_{ss} = \frac{N_s}{N_c} \tag{7.24}$$

For details on stator core segments, revisit Chapter 4. In general, it is advisable that N_{ss} be an even number, so that N_s has to be an even number. But in such cases, apparently, only integer q values are feasible. For fractionary windings, N_{ss} may be an odd number and contain three as a factor. Moreover, large stator bore diameter hydrogenerators have their stator cores made of a few N_K sections that are wound at the
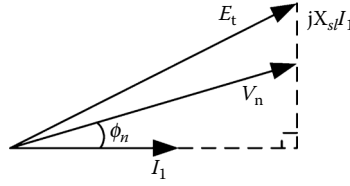
FIGURE 7.8 The total electromagnetic field (emf) $\underline{E}_t$.

manufacturer's site and assembled at the user's site. So, the number of slots N_s has to be divisible by both N_c and N_K.

In large SGs, the stator coil turns are made by transposed copper bars, and generally, there is one turn (bar) per coil. So, the total number of turns for all three phases $(3 \cdot a \cdot W_a)$ is equal to the number of slots N_s:

$$N_s = 3 \cdot a \cdot W_a \tag{7.25}$$

where

  a = the number of current paths in parallel
  W_a = the turns per path/phase

On the other hand, the number of turns W_a per current path is related to the flux per pole and the resultant emf E_t per phase:

$$E_t = \pi\sqrt{2} \cdot f_n \cdot \left(W_a \cdot K_{W1}\right) \cdot \Phi_1 \tag{7.26}$$

$$\Phi_1 = \frac{2}{\pi} \cdot B_{g1} \cdot \tau \cdot l_{Fe} \quad ; \quad \tau \approx \pi D / 2 p_1 \tag{7.27}$$

with τ equal to the pole pitch of stator winding. At this stage, $l_{Fe} \approx l_i$, D, τ and are known, and B_{g1} is the airgap rated flux density that is chosen in the interval given in the previous paragraph. The winding factor K_{W1} is

$$K_{W1} = K_{q_1} K_{y_1} \tag{7.28}$$

$$K_{q_1} \approx \frac{\sin \pi/6}{q \sin \pi/6 q} \quad ; \quad K_{y_1} = \sin \frac{y}{\tau}\frac{\pi}{2} \tag{7.29}$$

with y/τ equal to the coil span/pole pitch. For fractionary $q = (bd + c)/d$, q will be replaced in Equation 7.29 by $bd + c$.

From Figure 7.8, the emf (airgap emf) is

$$E_t \approx V_1\sqrt{1 + x_{sl}(2\sin\varphi_n + x_{sl})} \approx (1.07 - 1.1) \cdot V_n \tag{7.30}$$

The leakage reactance x_{sl} is generally less than 0.15 or

$$x_{sl} \approx x_d' \times (0.35 - 0.4) \tag{7.31}$$

This value of x_{sl} is only orientative and will be recalculated later in the design process.

V_n root mean squared (RMS) is the rated phase voltage of the SG. The rated current I_n is as follows:

$$I_n = \frac{P_n}{3V_n \cos\varphi_n} \tag{7.32}$$

with φ_n equal to the rated power factor angle (specified).

The number of current paths in parallel depends on many factors, such as type of winding (lap or wave), number of stator sectors, and so forth.

With tentative values for a and W_a found from (Equation 7.26 through Equation 7.30) and W_a rounded to a multiple of three (for three phases), the number of slots is calculated from Equation 7.25. Then, it is checked if N_s is divisible by the number of stator sections N_K. The number of stator sections is

$$N_K = 2 \text{ for } D < 4 \text{ m}$$

$$N_K = 4 \text{ for } D = 4 \div 8 \text{ m} \tag{7.33}$$

$$N_K = 6 \text{ (8) for } D > 8 \text{ m}$$

To yield a symmetrical winding for fractionary $q = b + c/d$, we need $2p_1/d$ = integer and, as pointed out above, $d/3 \neq$ integer. With a current paths,

$$d \leq \frac{2p_1}{a} \tag{7.34}$$

It is also appropriate to have a large value for d, so that the distribution factor of higher space harmonics be small, even if, by necessity, $c/d = 1/2$, $b > 3$.

For wave windings, the simplest configuration is obtained for

$$\frac{3c \pm 1}{d} = \text{integer} \tag{7.35}$$

So, the best c/d ratios are as follows:

$$\frac{c}{d} = \frac{2}{5}, \frac{3}{5}, \frac{2}{7}, \frac{5}{7}, \frac{3}{8}, \frac{5}{8}, \frac{3}{10}, \frac{7}{10}, \frac{4}{11}, \frac{7}{11}, \frac{4}{13}, \frac{9}{13} \dots \tag{7.36}$$

For $d = 5, 7, 11, 13, \dots$:

$$\frac{6c \pm 1}{d} = \text{integer} \tag{7.37}$$

with

$$\frac{c}{d} = \frac{1}{5}, \frac{4}{5}, \frac{1}{7}, \frac{6}{7}, \frac{2}{11}, \frac{9}{11}, \frac{2}{13}, \frac{11}{13} \dots \tag{7.38}$$

A low level of noise with fractionary windings requires

$$3 \cdot \left(b + \frac{c}{d} \right) \pm \frac{1}{d} \neq \text{integer} \tag{7.39}$$

With $c/d = 1/2$ ($b > 3$), the subharmonics are cancelled.

More details on choosing the number of slots for hydrogenerators can be found in Reference [6].

7.5   Design of Stator Winding

The main stator winding types for SGs were introduced in Chapter 4. For turbogenerators, with $q > 4$ (5), and integer q, two-layer windings with lap or wave-chorded coils are typical. They are fully symmetric with 60° phase spread per each pole.

Example 7.1: Integer q Turbogenerator Winding

Take a numerical example of a two-pole turbogenerator with an interior stator diameter $D_{is} = 1.0$ m and with a typical slot pitch $\tau_s \approx 60$ to 70 mm. Find an appropriate number of slots for integer q, and then build a two-layer winding for it.

The number of slots N_s is

$$N_s = 2p \cdot q \cdot m \quad ; \quad N_s \cdot \tau_s = \pi \cdot D_{is} \tag{7.40}$$

So,

$$q = \text{integer}\left(\pi \cdot \frac{D_{is}}{\tau_s} \cdot \frac{1}{2p_1 \cdot m} \right) = \text{integer}\left(\frac{\pi \cdot 1.0}{0.07} \cdot \frac{1}{2 \cdot 1 \cdot 3} \right) \tag{7.41}$$

where

$$\tau_s = 0.0654 \text{ m}$$
$$q = 8$$

With a stator stack length $l_{Fe} = 4.5$ m, $B_{g1} = 0.837$ T, $V_A = 12/\sqrt{3}$ kV, $f_n = 60$ Hz, $E_t = 1.10 \, V_n$ (Equation 7.30), and $a = 2$ current paths, the number of turns per current path/phase, W_a, is as follows (Equation 7.26):

$$W_a = \frac{E_t}{\pi\sqrt{2} \cdot f_n \cdot K_{W1} \cdot \Phi_1} \tag{7.42}$$

$$\Phi_1 = \frac{2}{\pi} \cdot B_{g1} \cdot \tau \cdot l_{Fe} = \frac{2}{\pi} \cdot 0.837 \cdot \frac{\pi}{2} \cdot 1 \cdot 4.5 = 3.7674 \text{ Wb/pole} \tag{7.43}$$

$$K_{W1} = \frac{\sin \pi/6}{8 \cdot \sin\left(\pi/(6 \cdot 8)\right)} \times \sin \frac{21}{24} \cdot \frac{\pi}{2} = 0.9556 \times 0.966 = 0.9230 \tag{7.44}$$

So, from Equation 7.42,

$$W_a = \frac{1.07 \times (12/\sqrt{3}) \cdot 10^3}{\pi\sqrt{2} \times 60 \times 0.923 \times 3.7674} = 8.012 \approx 8 = q \tag{7.45}$$

Fortunately, the number of turns per current path, which occupies just one pole of the two, is equal to the value of q. A multiple of q would also be possible. With $W_a = 8$, we have one turn/coil, so the coils are made of single bars aggregated from transposed conductors.

From Equation 7.25, the number of stator slots N_s is

$$N_s = a \times W_a \times 3 = 2 \times 8 \times 3 = 48 \qquad (7.46)$$

The condition $W_a = q$ (or kq) could be fulfilled with modified stator bore diameter or stack length or slot pitch.

In small machines, $W_a = kq$ with $k > 2$.

Building an integer q two-layer winding comprises the following steps:

- The electrical angle of emfs in two adjacent slots α_{es}:

$$\alpha_{es} = \frac{2\pi}{N_s} \cdot p_1 = \frac{2\pi}{48} \cdot 1 = \frac{\pi}{24} \qquad (7.47)$$

- The number t of slots with in-phase emfs:

$$t = \text{largest common divisor} \ (N_s, p_1) = p_1 = 1 \qquad (7.48)$$

- The number of distinct slot emfs:

$$N_s/t = 48/1 = 48 \qquad (7.49)$$

- The angle of neighboring distinct emfs:

$$\alpha_{ef} = \frac{2\pi \cdot t}{N_s} = \frac{2\pi \cdot 1}{48} = \frac{\pi}{24} = \alpha_{es} \qquad (7.50)$$

- Draw the star of slot emfs with $N_s/t = 48$ elements (Figure 7.9).
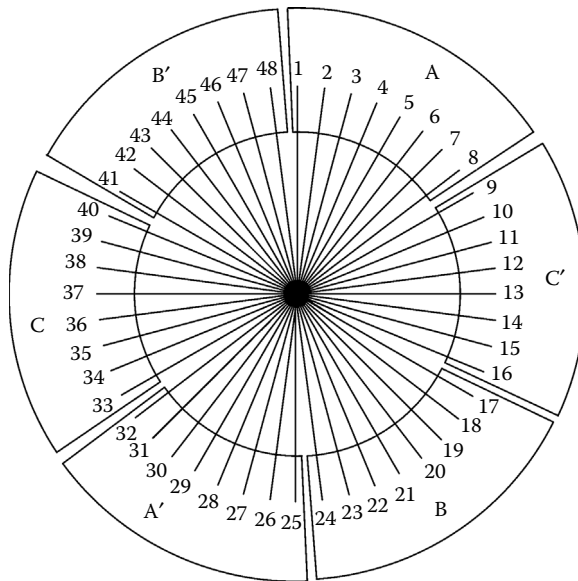
FIGURE 7.9 Electromagnetic field (emf) star for $2p_1 = 2$ and $N_s = 48$.
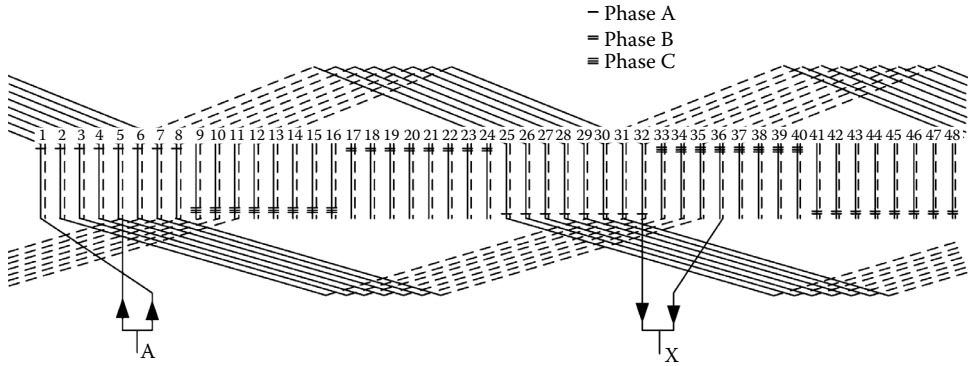
FIGURE 7.10 Two-pole, bar-wave winding with $N_s = 48$ slots, $q = 8$ slot/pole/phase, and $y/\tau = 20/24$.

- Divide the distinct emfs in $2 \times m = 6$ equal zones. Opposite zones represent the in and out slots of a phase in the first layer. The angle between the beginnings of phases A, B, C is $\dfrac{2\pi}{3}$, clockwise.

- From each in-and-out slot phase, coils are initiated in layer one and completed in layer two, from left to right, according to the coil span y: $y = \dfrac{20}{24}\tau = 20$ slot pitches (Figure 7.10).

Making use of bar-wave coils and two current paths in parallel, practically no additional connectors are necessary to complete the phase.

The single-turn bar coils with wave connections are usually used for hydrogenerators ($2p_1 > 4$) to reduce overall connector length — at the price of some additional labor. Here, the very large power of the SG at only 12 kV line voltage imposed a single-turn coil winding.

Doubling the line voltage to 24 kV would lead to a two-turn coil winding, where lap coils are generally preferable.

For the fractionary windings, so typical for hydrogenerators, after setting the most appropriate value of fractionary q in the previous paragraph, an example is worked out here.

Example 7.2: The Fractionary q Winding

Consider the case of a 100 MVA hydrogenerator designed at $V_{nl} = 15,500$ V (RMS line voltage, star connection), $f_n = 50$ Hz, $cos\varphi_n = 0.9$, $n_n = 150$ rpm, and $n_{max} = 250$ rpm.

Calculate the main stator geometry and then with $B_{g1} = 0.9$ T, the number of turns with one current path, and design a single-turn (bar) coil winding with fractionary q.

Solution

For indirect air cooling (see Figure 7.7) with the power per pole,

$$\frac{S_n}{2p_1} = \frac{100 \cdot 10^6}{40} = 2.5 \cdot 10^3 \text{ kVAmin/pole} \tag{7.51}$$

the output power coefficient $C = 9$ kVAmin/m³.

The maximum rotor diameter (Equation 7.12) for $U_{max} = 140$ m/sec:

$$D = \frac{U_{max}}{\pi \cdot n_{max}} = \frac{140 \text{ m/sec}}{\pi \cdot (250/60) \text{ rad/sec}} = 10.70 \text{ m} \tag{7.52}$$

The ideal stack length l_i is calculated from Equation 7.9:

$$l_i \approx \frac{S_n}{C \cdot D^2 \cdot n_n} = \frac{100000 (kVA)}{9 \left(\frac{kVA_{min}}{m^3} \right) (10.70)^2 (m^2) 150 (rpm)} = 0.647 \text{ m} \tag{7.53}$$

The flux per pole Φ_1 (Equation 7.8) is

$$\Phi_1 = \frac{2}{\pi} \cdot B_{g1} \cdot \tau \cdot l_i = \frac{2}{\pi} \cdot 0.9 \cdot \frac{\pi \cdot 10.7}{40} \cdot 0.647 = 0.3115 \text{ Wb/pole} \tag{7.54}$$

With $E_{t1}/V_{nph} = 1.07$ and an assumed winding factor $K_{W1} \approx 0.925$, the number of turns per current path W_a is as follows (Equation 7.26):

$$W_a = \frac{1.1 \cdot V_{nph}}{\pi \sqrt{2} \cdot f_n \cdot K_{W1} \cdot \Phi_1} = \frac{1.07 \times 15500/\sqrt{3}}{\pi \sqrt{2} \cdot 50 \cdot 0.925 \cdot 0.3115} \approx 150 \text{ turns/path/phase} \tag{7.55}$$

For one current path, the total number of turns for all three phases (equal to the number of slots N_s) would be

$$N_s = 3 \cdot a \cdot W_a = 3 \cdot 1 \cdot 150 = 450 \text{ slots} \tag{7.56}$$

A tentative value of q_{ave} would be

$$q_{ave} = \frac{N_s}{2 p_1 \cdot m} = \frac{450}{40 \cdot 3} = \frac{450}{120} = 3\frac{3}{4} \tag{7.57}$$

It is obvious that this value of q is not among those suggested in Equation 7.37 and Equation 7.38, but Equation 7.35 is half fulfilled, as $c = 3$, $d = 4$, and

$$\frac{3c-1}{d} = \frac{3 \cdot 3 - 1}{4} = 2 = \text{integer} \tag{7.58}$$

With 15 slots per segment ($N_{ss} = 15$), the total number of segments N_c per section is

$$N_c = \frac{N_s}{N_{ss} \cdot N_K} = \frac{450}{15 \times 6} = 5 \tag{7.59}$$

So, the total number of segments in the stator core is $N_c \cdot N_K = 5 \cdot 6 = 30$. For a 10.7 m rotor diameter, this is a reasonable value (lamination sheet width is less than 1.1 to 1.2 m).

Though $N_{ss} = 15$ slots/segment is an odd (instead of even) number, it is acceptable.

Finally, we adopt $q_{ave} = 3\frac{3}{4}$ for a 40-pole single-turn bar winding with one current path.
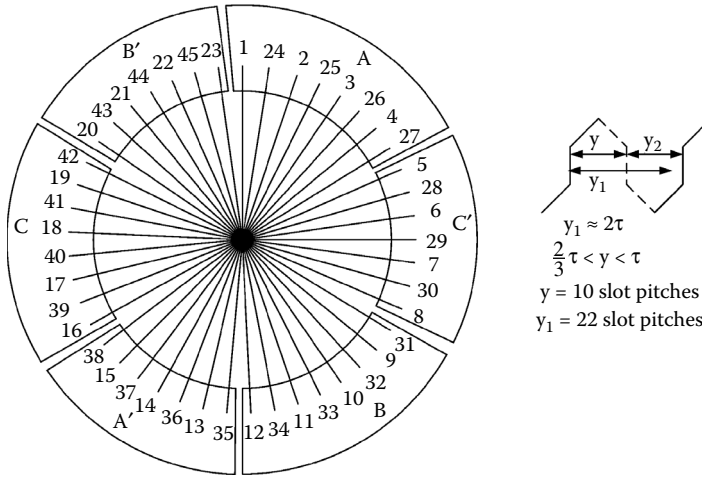
FIGURE 7.11 The electromagnetic force (emf) star for $N_s = 450$ slots, $2p_1 = 40$ poles for the first distinct 45 slots.

To build the winding, we adopt a similar path as for integer q:

- Calculate the slot emf angle: $\alpha_{ec} = \dfrac{2\pi}{N_s} \cdot p_1 = \dfrac{2\pi}{450} \cdot 20 = \dfrac{4\pi}{45}$
- Calculate the highest common divisor t of N_s and p_1: $t = 10 = p_1/2$
- Find the number of distinct slot emfs: $N_s/t = 450/10 = 45$
- Find the angle between neighboring distinct emfs: $\alpha_{et} = \dfrac{2\pi \cdot t}{N_s} = \dfrac{2\pi \cdot 10}{450} = \dfrac{2\pi}{45} = \dfrac{\alpha_{ec}}{2}$
- Draw the emf star, observing that only 45 of them are distinct, and every ten of them overlap each other (Figure 7.11)

As there are only 45 (N_s/t) distinct emfs, it is enough to consider them alone, as the situation repeats itself identically ten times. After four poles ($d = 4$ in $q = b + c/d$), the situation repeats.

- Calculate $\dfrac{N_s/t}{3} = \dfrac{450/10}{3} = 15$, and start by allocating phase A — eight in emfs (slots) and seven out emfs — such that the eight and the seven are in phase opposition as much as possible. In our case, in slots for phase A are (1, 2, 3, 4, 24, 25, 26, 27), and out slots are (13, 14, 15, 35, 36, 37, 38).
- Proceed the same way for phases B and C by allowing groups of eight and seven neighboring slots to alternate. The sequence (clockwise) is A, C′, B, A′, C, B′ to complete the circle.
- The division of slots between the two layers is valid in layer 1; for layer 2, the allocation comes naturally by observing the coil span y:

$$y \le \text{integer}\left(\frac{N_s}{2p_1}\right) = \text{integer}\left(\frac{450}{40}\right) = 11 \text{ slot pitches} \tag{7.60}$$

It is possible to choose $y = 9, 10, 11$, but $y = 10$ seems a good compromise in reducing the fifth and seventh space harmonics while not reducing the emf fundamental too much.

Note that for fractionary q, some of the connections between successive bars of a bar-wave winding have to be made of separate (nonwave) connectors.
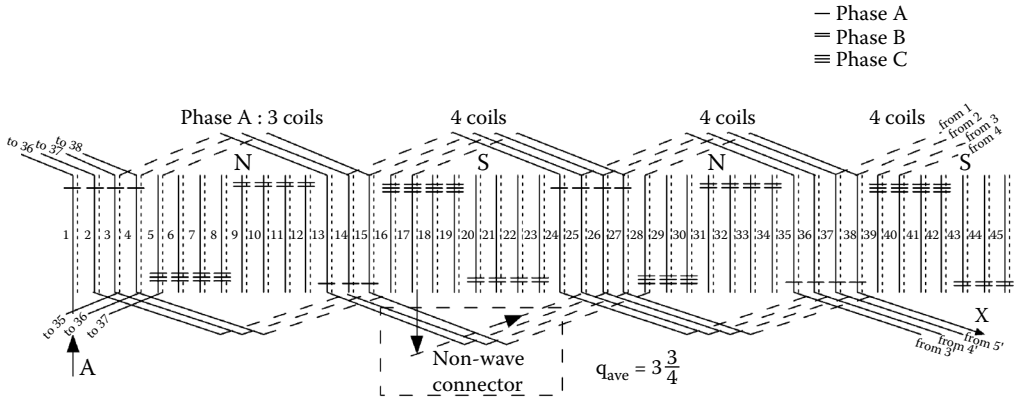
FIGURE 7.12 450-slot, 40-poles, $q = 3\ 3/4$ bar-wave winding/phase A for the first $N_s/t = 45$ slots.

For a minimum number of such additional connectors, y_1 (Figure 7.11) should be as close as possible to two times the pole pitch, and $6q$ equals the integer.

In our case, $6q = 6 \cdot \dfrac{15}{4} = \dfrac{45}{2} \neq$ integer, so the situation is not ideal. But the symmetry of the winding is notable, as there are ten identical zones of the winding, each spanning four poles.

An example of the first 45 slots with all phase allocation completed, but only with phase A coils shown, is given in Figure 7.12.

As Figure 7.12 shows, there is only one nonwave connector per phase for N_s/t section of machine.

A simple rule for allocation of slots per phases is apparent from Figure 7.12.

Based on the sequence A, C′, B, A′, C, B′, …, we allocate for each phase group d slots for b groups and then c slots for one group and repeat this sequence for all the slots of the machine. Again, d should not be divisible by three for symmetry ($q = b + c/d$).

The allocation of slots to phase may also be done through tables [6], but the principle is the same as above.

The emf star has the added advantage of allowing for simple verifications for phase balance by finding the position of the resultant emf of each phase after adding the up (forward) and the opposite of down (backward) emfs.

It is also evident that the distribution factor formula (Equation 7.29) may be adopted for the purpose by noting that the number of vectors included should not be q but the denominator of q, that is, $bd + c$, in our case, $3 \cdot 3 + 3 = 15 = 8 + 7$ vectors:

$$K_{q1} = \frac{\sin \dfrac{\pi}{6}}{(bd + c) \cdot \sin\left(\dfrac{\pi}{6(bd + c)}\right)} \tag{7.61}$$

The chording factor K_{y1} formula (Equation 7.29) still holds.

7.6 Design of Stator Core

By now, in our design process, the rotor diameter D, the stator core ideal length l_i, the pole pitch τ, and the number of slots N_s are already calculated as shown in previous paragraphs.

To design the stator core, the stator bore diameter D_{is} is first required. But to accomplish this, the airgap g has to be calculated first, because

$$D_{is} = D + 2g \tag{7.62}$$

Calculating or choosing the airgap should account for the following:

- Required SCR (or $1/x_d$)
- Reduced airgap flux density harmonics due to slot openings so as to limit the emf time harmonics within standards requirements
- Increased excitation winding losses with larger airgap
- Reduced stator space harmonics losses in the rotor with larger airgap, for a given stator slotting
- Varied mechanical limitation on airgap during operation by at most 10% of its rated value

The trend today is to impose smaller SCR (0.4 to 0.6), that is, smaller airgap, to reduce the excitation winding losses. Transient stability is to be preserved through fast exciter voltage forcing by adequate control. With smaller airgap, care must be exercised in estimating the emf time harmonics and the additional rotor surface (or cage) losses.

So, it seems reasonable to adopt the airgap based on a preliminary calculated value of x_d:

$$x_d = x_{sl} + x_{ad} \tag{7.63}$$

At this point, x_{sl} may be assigned a value $x_{sl} = 0.1 - 0.15$ or $x_{sl} \approx (0.35 - 0.4)x_d'$, when $(x_d')_{\max}$ is imposed as a specification.

The magnetization reactance X_{ad} (in Ω) is

$$X_{ad} = K_{ad} \frac{6\mu_0\omega_1 \left(W_a \cdot K_{W1}\right)^2 \cdot \tau \cdot l_i}{\pi^2 \cdot g \cdot K_C \cdot (1 + K_{sd})} = x_{ad}\left(\frac{V_n}{I_n}\right)_{phase} \tag{7.64}$$

$$\left(I_n\right)_{phase} = \frac{S_n}{3(V_n)_{phase} \cos\varphi_n} \tag{7.65}$$

K_{ad} is a reduction coefficient of d axis magnetizing reactance when a salient pole rotor is used (Chapter 4):

$$K_{ad} \approx \frac{\tau_p}{\tau} + \frac{1}{\pi}\sin\left(\frac{\tau_p}{\tau} \cdot \pi\right) \quad ; \quad \tau_p - \text{rotor pole shoe span} \tag{7.66}$$

Equation 7.66 is valid for constant airgap salient poles. For hydrogenerators, with reduced airgap, the airgap under the salient poles varies to yield a more sinusoidal airgap flux density distribution. With $\tau_p/\tau \approx 0.62 - 0.75$, in general, $K_{ad} > 0.9$ for uniform airgap, but it is lower for increased nonuniform airgap.

The Carter coefficient, K_C, which includes the influence of slot openings and the effect of radial channels in the stator core stack, is also unknown at this stage of the design but, typically, $K_C < 1.15$.

Finally, the magnetic saturation level is not known yet, but it is known to be less than 0.25 ($K_{sd} <$ 0.25). Basically, Equation 7.64 and Equation 7.65, with assigned values of K_{ad}, K_c, and K_{sd} and known winding data W_a, K_{W1} (from the previous paragraph), provide a preliminary value for the airgap to secure the required value of x_d.

A traditional expression for airgap is as follows:

$$g = 4.0 \cdot 10^{-7} \frac{A \cdot \tau}{(x_d - 0.1) B_{g1}} \tag{7.67}$$

where

A = the linear current loading (A/m)
B_{g1} = the design airgap flux density (specified)
τ = the pole pitch $\tau \approx \pi D / 2 p_1$
x_{sl} = 0.1 is the assigned value of stator leakage reactance in P.U.

Knowing the rated current I_n and the number of current path a (current loading), A, is as follows:

$$A \approx \frac{6 \cdot W_a \cdot a \cdot I_{na}}{\pi \cdot D} \tag{7.68}$$

For SCR = 0.5, x_d = 2, and D = 10.7 m, a = 1, W_a = 150, I_{na} = 4000 A (Example 7.2), $2p_1$ = 40 poles, B_{g1} = 0.9 T,

$$g = 4.0 \times 10^{-7} \cdot \frac{6 \cdot W_a \cdot a \cdot I_{na}}{(x_d - 0.1) \cdot 2 p_1 \cdot B_{g1}} = \frac{4 \cdot 10^{-7} \times 6 \times 150 \times 4000}{40 \cdot 0.9 \cdot (2 - 0.1)} = 0.02105 \text{ m} \tag{7.69}$$

Now the pole pitch τ is

$$\tau = \frac{\pi(D + 2g)}{2 p_1} = \frac{\pi(10.7 + 2 \cdot 0.02105)}{40} = 0.8435 \text{ m} \tag{7.70}$$

Note that the rather small specified SCR led to a high $x_d (x_d = 2.0)$ and, thus, to a rather small airgap for this 10.7 m rotor diameter with a 0.8453 m pole pitch.

Turbogenerators are characterized by a larger airgap for the same A, B_{g1}, and SCR, as τ is notably larger. Moreover, the smaller periphery length (smaller diameter) in turbogenerators imposes larger values of A than in hydrogenerators — one more reason for a larger airgap. Airgaps of 60 to 70 mm in two-pole, 1.2 m rotor diameter turbogenerators are not uncommon. This preliminary airgap value is to be modified if the desired x_d is not obtained, or some of the mechanical, emf harmonics or additional losses constraints are not met.

The stator terminal line voltage is chosen based on the following:

- Insulation costs
- Insulation maintenance costs
- Step-up transformer, power switches, and protection costs

Generally, the higher the power, the higher the voltage. Also, the voltage is higher for direct-cooled windings, because the transmission through the conductor and slot insulation to the slot walls is no longer a main constraint.
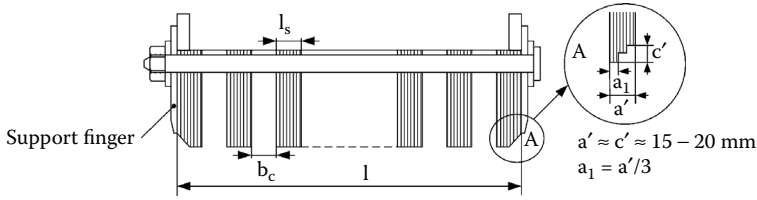
FIGURE 7.13 Stator core with radial channels.

As a starting point,

$$V_{nl} \approx 6 - 7 \text{ kV for } S_n < 20 \text{ MVA}$$

$$10 - 11 \text{ kV for } S_n \approx (20 - 60) \text{ MVA}$$

$$13 - 14 \text{ kV for } S_n \approx (60 - 75) \text{ MVA} \tag{7.71}$$

$$15 - 16 \text{ kV for } S_n \approx (175 - 300) \text{ MVA}$$

$$16 - 28 \text{ kV for } S_n > 300 \text{ MVA}$$

Recently, 56 kV and 100 kV cable-winding SGs were proposed.

7.6.1 Stator Stack Geometry

As radial or radial–axial cooling is used (Figure 7.13), there are n_c radial channels, and each cooling channel is b_c wide. The total iron length l_1 is as follows:

$$l_1 = l - n_c b_c \tag{7.72}$$

The ideal length l_i is approximately

$$l_i = \left[l - n_c \cdot b_c' - 2a' \cdot \left(1 - \frac{g}{g + c'/2} \right) \right] \cdot k_{Fe} \tag{7.73}$$

with b_c' an equivalent cooling channel width that is smaller than b_c and dependent on airgap g. The larger the airgap, the smaller will be b_c'/b_c. Generally, $b_c = 8$ to 12 mm, and the elementary stack width $l_s = 45$ to 60 mm. When the airgap g is larger than b_c, $b_c'/b_c < 0.2 - 0.3$ due to the large fringing flux. K_{Fe} is the iron filling factor that accounts for the existing insulation layer between laminations. For 0.5 mm thick laminations, $K_{Fe} \approx 0.93$ to 0.95.

The open stator slots may house uni-turn (bar) coils (Figure 7.14a) or multiturn (two, in general) coils (Figure 7.14b) placed in two layers. The single- and two-turn coils are made of multiple rectangular cross-sectional conductors in parallel that have to be fully transposed (Figure 7.15a and Figure 7.15b) in large power SGs (Roebel bars). Typically, the elementary conductor height h_c is less than 2.5 mm.

The elementary conductors are transposed to cancel eddy currents induced by each of them in the others, thus reducing drastically the total skin effect AC resistance factor. (More details are presented in the forthcoming paragraph on stator resistance.) The transposition provides for positioning each elementary conductor in all the positions of the other conductors, along the stack length. The transposition step along stack length is above 30 mm, and there should be as many transpositions as there are elementary conductors used to make a turn.
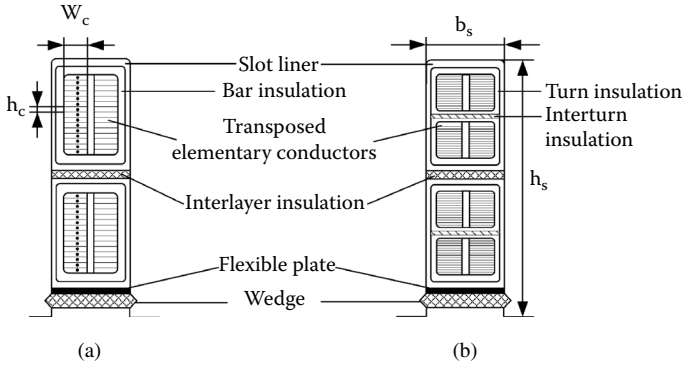
FIGURE 7.14 Stator conductors in slot (indirect cooling): (a) single-turn bar winding and (b) two-turn coil winding.
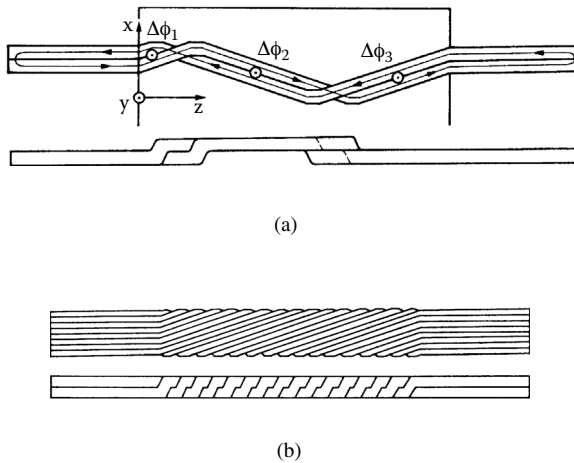
FIGURE 7.15 Roebel bar: (a) two conductors and (b) complete Roebel bar.

The thickness of various insulation layers depends on the terminal voltage and on the number of slots. Generally,

$$\frac{2W_c}{b_s} = \frac{\text{copper width}}{\text{slot width}} \approx 0.6 - 0.7$$

$$\frac{b_s}{\tau_s} = \frac{\text{slot width}}{\text{slot pitch}} \approx 0.35 - 0.55$$

$$\tau_s = \pi \cdot D_{is}/6 p_1 q_1 \tag{7.74}$$

$$\frac{h_s}{b_s} = \frac{\text{slot height}}{\text{slot width}} = 4 - 10$$

For direct cooling, the copper area per slot area is smaller than that for indirect cooling, because each elementary conductor has an interior channel for the coolant.

A single-layer single turn per coil winding, as shown in Figure 7.16, exhibits sequences of two solid elementary conductors followed by a tubular conductor.

It is also possible to use only tubular elementary conductors.
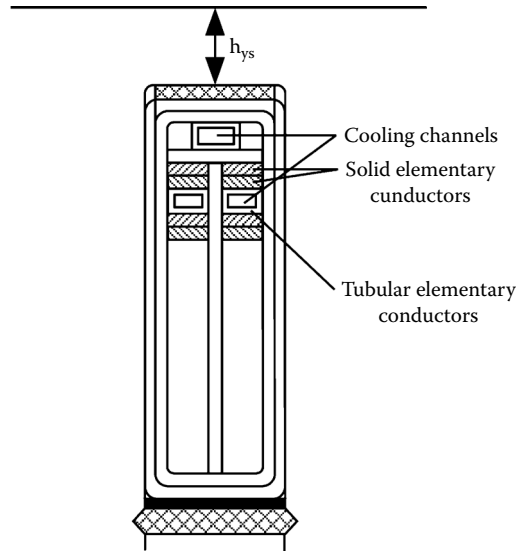
FIGURE 7.16 Single-layer winding with direct cooling.

The slot area A_{slotu} may be calculated by knowing the total current per slot, the design current density j_{cos}, and the total copper filling factor K_{fill}:

$$A_{slotu} = \frac{6 \cdot W_a \cdot I_n}{N_s \cdot K_{fill} \cdot j_{cos}} \quad ; \quad A_{slot} = b_s \cdot h_s \tag{7.75}$$

The output power coefficient secures values of ampere turns per slot that lead to fulfilling constraints (Equation 7.74).

The design current density depends on the adopted cooling system, and for start values, Table 7.1 may be used. It should also be noticed that the terminal voltage impresses lower limits on slot width with orientative values from 15 mm below 6 kV (line voltage) up to 35 to 40 mm at 24 kV. The slot total filling factor goes down from values of up to 0.55 below 6 kV to less than 0.3 to 0.35 at 20 kV and higher, for indirect cooling. Smaller values of K_{fill} are practical for direct cooling windings.

With stator bore diameter D_{is}, number of stator slots N_s, rated path current I_n, number of turns per current paths in parallel W_a, already assigned K_{fill}, j_{cos}, from Equation 7.75 with Equation 7.74, the rectangular stator slot may be sized by calculating h_s and b_s. Finally, all insulation layers are accounted for, and a more exact filling factor is obtained.

The stator yoke height h_{ys} is simply

$$h_{ys} \approx \frac{B_{g1}}{B_{y1}} \cdot \frac{\tau}{\pi} \quad ; \quad B_{y1} = 1.3 - 1.7 \text{ T} \tag{7.76}$$

where

τ = the stator pole pitch
B_{y1} = the design stator yoke flux density

As the slots are rectangular, the teeth are rather trapezoidal, so the tooth flux density B_{t1} varies along the radial direction. The maximum value B_{tmax} occurs approximately at the slot top:

$$B_{t\max} \approx B_{g1} \cdot \frac{\tau_s}{\tau_s - b_s} \approx 1.6 - 2.0 \text{ T} \qquad (7.77)$$

In Equation 7.77, the reduction of tooth flux density due to the fringing flux lines through the slots is neglected.

Example 7.3: Stator Slot and Yoke Sizing

For the same hydrogenerator as discussed in Example 7.2, with S_n = 100 MVA, I_n = 4000 A, U_{nl} = 15 kV, $2p_1$ = 40, D = 10.7 m, l_i = 0.647 m, N_s = 450, airgap $g = 2.1 \times 10^{-2}$ m, B_{g1} = 0.9 T, W_a = 150 turns/current path, and a = 1 current paths, determine (for indirect air cooling), size of the stator slot and yoke, and the stator core outer diameter D_{os}.

Solution

For indirect air cooling, a total slot filling factor is adopted K_{fill} = 0.4.

The current density (Table 7.1) is j_{cos} = 6.0 A/mm².

From Equation 7.75, the slot useful area A_{slotu} is as follows:

$$A_{slotu} = \frac{6 \cdot W_a \cdot I_n}{N_s \cdot K_{fill} \cdot j_{cos}} = \frac{6 \cdot 150 \cdot 4000}{450 \cdot 0.4 \cdot 6 \cdot 10^6} = 3333 \cdot 10^{-6} \text{ m}^2$$

The slot pitch τ_s is

$$\tau_s = \frac{\pi(D + 2g)}{N_s} = \frac{\pi(10.7 + 2 \cdot 0.021)}{450} = 74.95 \cdot 10^{-3} \text{ m}$$

The slot width is selected according to Equation 7.74:

$$b_s = \tau_s \cdot 0.4 = 74.95 \cdot 10^{-3} \approx 30 \cdot 10^{-3} \text{ m}$$

The maximum tooth flux density is as follows:

$$B_{t\max} = B_{g1} \cdot \frac{\tau_s}{\tau_s - b_s} = 0.9 \cdot \frac{74.95}{74.95 - 30} = 1.5 \text{ T}$$

The slot height h_s may now determined from Equation 7.75:

$$h_s \approx \frac{A_{slotu}}{b_s} = \frac{3333 \cdot 10^{-6}}{30 \times 10^{-3}} = 111 \cdot 10^{-3} \text{ m}$$

The ratio $h_s/b_s = 111/30 = 3.7033 < 4$, as suggested in Equation 7.74.

The rather low h_s/b_s ratio tends to produce a low stator slot leakage inductance, that is also a reduction in x'_d. As the maximum value of x'_d is limited for transient stability reasons, it may be adequate to retain this slot geometry.

The moderate $B_{t\max}$ does not account for further reduction of the tooth width in the wedge area.

With stator yoke flux density $B_{ys} = 1.4$ T, the stator yoke height h_{ys} (Equation 7.76) is

$$h_{ys} = \frac{B_{g1}}{B_{ys}} \cdot \frac{\tau}{\pi} = \frac{0.9}{1.4} \cdot 74.95 \times 10^{-3} \cdot \frac{450}{40} \cdot \frac{1}{\pi} = 172.74 \times 10^{-3} \text{ m}$$

The external stator diameter is

$$D_{os} = D + 2g + 2h_s + 2h_{ys} = 10.7 + 2 \cdot 0.0201 + (2 \times 111 + 2 \times 172) \cdot 10^{-3} = 11.309 \text{ m}$$

In general, the stator yoke height h_{ys} should be larger than the slot height h_s to avoid large noise and vibration at $2f_n$ frequency.

7.7   Salient-Pole Rotor Design

Hydrogenerators and most industrial generators make use of salient-pole rotors. They are also found in some wind generators above 2 MW/unit.

The airgap under the rotor pole shoe gets larger toward the pole shoe ends (Figure 7.17).

In general, $g_{max}/g = 1.5$ to 2.5 to make the airgap flux density, produced by the field current, sinusoidal. Ideally,

$$g(\theta) = \frac{g}{\cos(\theta p_1)} \tag{7.78}$$

In reality, the pole shoe may be cut from 1 to 1.8 mm laminations along a circle with radius $R_p < D/2$, where D is the rotor diameter at minimum airgap (g).

The pole shoe b_p per pole pitch τ is a compromise between leaving enough room for field coils and limiting the interpole flux linkage:

$$\alpha_i = \frac{b_p}{\tau} \approx 0.66 - 0.75 \tag{7.79}$$

Generally, α_i increases with the pole pitch τ, reaching 0.75 at $\tau = 0.8$ m. Also, the ratio between the pole shoe span b_p and the stator slot pitch τ_s should be $b_p/\tau_s > 5.5$ to avoid notable pulsations in the emf due to stator slotting. With $q \geq 3$, this condition is met automatically for all values of α_i in Equation 7.79.
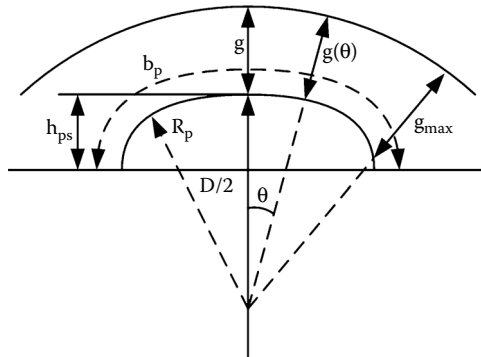
FIGURE 7.17   Variable airgap salient pole.
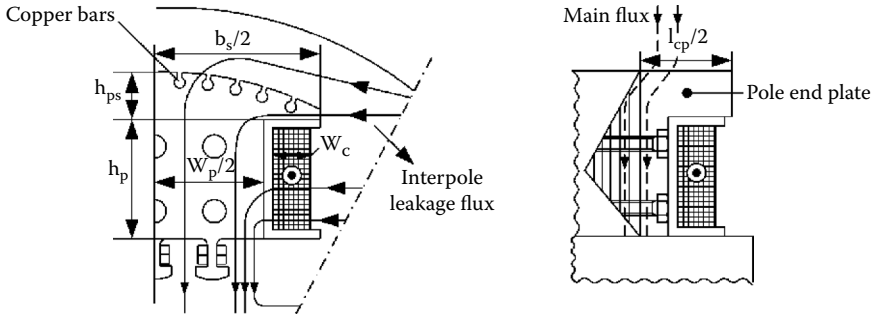
FIGURE 7.18 Salient rotor pole construction.

Given the central and maximum airgaps (g and g_{max}), rotor diameter D, and the pole shoe span b_p, the radius R_p of the pole shoe shape is approximately

$$R_p = \frac{D}{2} \cdot \cfrac{1}{\left(1 + \cfrac{4 \cdot D \cdot (g_{max} - g)}{b_p^2}\right)} < \frac{D}{2} \tag{7.80}$$

The cross-section through a salient rotor pole is shown in Figure 7.18.

The length of pole body (made of 1 to 2 mm thick die-cast laminations) l_p is made smaller than stator core total length l by around 50 to 80 mm, while the end plates (Figure 7.18), l_{ep}, made of solid iron, are l_{ep} = 50 to 120 mm.

So, the total ideal length of rotor pole l_{pi} is as follows:

$$l_{pi} = l - (0.05 \div 0.08) + l_{ep} > l \tag{7.81}$$

The effective iron length of rotor l_{pFe} is

$$l_{pFe} \approx l_{pi} \cdot K_{Fe} \tag{7.82}$$

The lamination filling factor (due to insulation layers) $K_{Fe} \approx 0.95$ to 0.97 for lamination thickness going from 1 to 1.8 mm. The total length of rotor l_{pi} is still larger than the stator stack length l in order to further reduce the flux density in the rotor pole body with width W_p (Figure 7.18) that is, in general,

$$W_p \approx (0.45 - 0.55) \cdot \tau \tag{7.83}$$

The wound rotor pole height h_p per pole τ pitch ratio K_h decreases with the pole pitch τ and with increased average airgap flux density:

$$K_h = \frac{h_p}{\tau} \tag{7.84}$$

In general, for B_{ga} = 0.7 T (B_{gl} = 0.9 T), K_h starts from 0.3 at τ = 0.4 m and ends at 0.1 for τ = 1 m. Higher values of K_h may be used for smaller airgap flux densities.

To design the field winding, the rated, V_{fn}, and peak, V_{fmax}, voltages have to be known, together with field pole mmf $W_f I_f$. By I_{fn}, we mean the excitation current required to produce full voltage at full load and rated power factor. At this stage of the design method, I_{fn} is not known, and it may not be calculated

rigorously, because the rotor pole and yoke design is not finished. But, a preliminary design of rotor pole and yoke is feasible here.

Example 7.4: Salient-Pole Rotor Preliminary Design

For the data in Example 7.3, let us design the salient-pole rotor. The ratio $g_{max}/g = 2.5$.

Solution

Knowing the pole pitch and choosing a conservative $\alpha_i = 0.7$, from Equation 7.79, the pole width b_p is as follows (Example 7.3):

$$b_p \approx \alpha_i \cdot \tau = 0.7 \cdot \frac{\pi(10.7 + 2 \cdot 0.021)}{40} = 0.7 \cdot 0.843 = 0.59 \text{ m}$$

The radius of rotor pole shoe R_p (Equation 7.80) is

$$R_p = \frac{D}{2} \cdot \frac{1}{\left(1 + \dfrac{4 \cdot D \cdot (g_{max} - g)}{b_p^2}\right)} = \frac{10.7}{2} \cdot \frac{1}{1 + \dfrac{4 \cdot 10.7}{0.59^2} \cdot (2.5 - 1) \cdot 2.1 \cdot 10^{-2}} = 1.0978 \text{ m}$$

The rotor pole shoe height at center h_{ps} (Figure 7.17) should be large enough to accommodate the damper winding and is proportional to the pole pitch:

$$\frac{h_{ps}}{\tau} = \quad \approx 0.1 \text{ for } \tau = 0.3 \text{ m}$$

$$\approx 0.2 \text{ for } \tau = 1 \text{ m}$$

The pole body width W_p is chosen from Equation 7.83:

$$W_p = 0.5 \cdot \tau = 0.5 \cdot 0.843 = 0.4215 \text{ m}$$

Consequently, the space left for coil width W_c is

$$W_c = \frac{b_p - W_p}{2} = \frac{0.59 - 0.4215}{2} = 0.08425 \text{ m}$$

The pole body (and coil) height $h_p = K_h \cdot \tau = 0.18 \cdot 0.843 = 0.1517$ m.

So, with a total coil filling $K_{fill} = 0.62$ design current density $j_{cor} = 10$ A/mm², the ampereturns of field coil per pole are as follows:

$$W_F I_{Fn} = j_{cor} \cdot W_c \cdot h_p \cdot K_{fill} = 10 \cdot 151.7 \cdot 84.25 \cdot 0.62 = 79240 \text{ At}$$

On the other hand, the stator rated mmf per pole F_{1n} is

$$F_{1n} = \frac{3\sqrt{2} \cdot W_a \cdot K_{W1} \cdot I_n}{\pi \cdot p_1} = \frac{3\sqrt{2} \cdot 150 \cdot 0.925 \cdot 4000}{\pi \cdot 20} = 37383 \text{ At/pole}$$

As

$$\left(F_{1n}/W_F I_{Fn}\right)^{-1} = \frac{79240}{37383} = 2.12$$

there are chances that the calculated rated field pole mmf $W_F I_{Fn}$ will suffice for rated power, rated voltage, and rated power factor.

However, also notice that the rated current density was raised to 10 A/mm² in the rotor, in contrast to 6 A/mm² in the stator. The much shorter end connections justify this choice. Later in the design, the exact $W_F I_{Fn}$ value will be calculated.

The rotor yoke design is basically similar to the stator yoke design, but there is an additional, leakage (interpole) magnetic flux to consider. Later, it will be calculated in detail, but for now, a 10 to 15% increase in polar flux is enough to allow for preliminary calculation of the rotor yoke radial height h_{yr}:

$$h_{yr} \approx \frac{B_{g1}}{B_{yr}} \cdot \frac{\tau}{\pi}\left(1 + K_{peak}\right) = \frac{0.9}{1.5} \cdot \frac{0.843}{\pi} \cdot \left(1 + 0.12\right) = 0.1804 \text{ m}$$

This is a conservative value.

Though the design methodology can produce a detailed analytical calculation of no-load and on-load magnetization curves, only with the finite element method (FEM) can we provide exact distributions of flux density in the various parts of the machine for given operating conditions.

7.8 Damper Cage Design

Stator space mmf harmonics of order 5, 7, 11, 13, 17, 19,…, as well as airgap permeance harmonics due to slot openings, induce voltages and thus produce currents in the rotor damper winding. These stator mmf aggregated space harmonics are reduced drastically by fractionary windings ($q = b + c/d$), with first slot harmonics that is 6 ($bd + c$) ± 1. When $bd + c > 9$, these harmonics are negligible; thus, it is feasible to use the same slot pitch in the stator τ_s and in the rotor τ_d: $\tau_s = \tau_d$. However, for integer q or $bd + c < 9$ or $q = b + 1/2$:

$$\tau_s \neq \tau_d \tag{7.85}$$

Otherwise, the induced currents in the damper windings by the stator slotting harmonics are augmented when $\tau_s = \tau_r$.

For these cases, it is recommended [7] that

$$\tau_r < \tau_s$$

$$\frac{2\tau}{\tau_r} \geq 6q \pm 1 + c \quad ; \quad c = 0 \text{ for } q = \text{integer} \tag{7.86}$$

$$b_p - 2\tau_r = \frac{2k\tau}{6q+1}$$

In Reference [6], the condition $N_s/p_1 = 2K_1 \pm 1/2$ is demonstrated to lead to the reduction of bar-to-bar currents due to the first slot opening harmonic of the stator. But, the second slot opening harmonic ($\nu = 2$) may violate this condition.
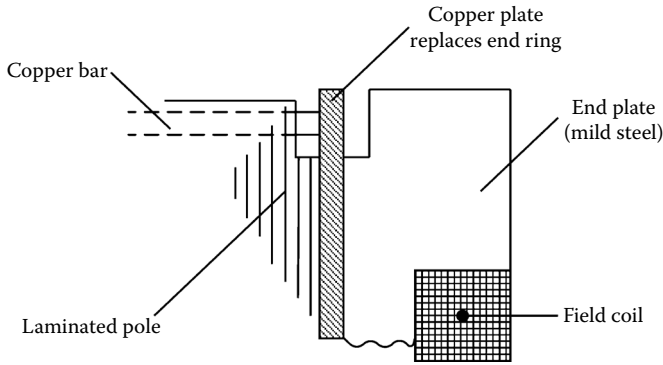
FIGURE 7.19 Copper end plate replaces end ring.

The number of damper bars per pole N_2 is as follows:

$$N_2 \approx \frac{b_p}{\tau_r} - 1 \tag{7.87}$$

In some cases, the damper cage may be left out, but then the pole shoe (at least) should be made of solid mild steel.

The cross-section of the damper cage bars per pole represents a fraction of stator slot area per pole:

$$A_{bar} = \frac{1}{N_2} \cdot (0.15 - 0.3) \cdot \frac{6 \cdot W_a \cdot I_n}{2 p_1 \cdot j_{COs}} \tag{7.88}$$

The cage bars are round and made of copper or brass, so their diameters d_{bar} are standardized:

$$d_{bar} = \sqrt{\frac{4}{\pi} \cdot A_{bar}} \tag{7.89}$$

The cage bars are connected through partial or integral end rings. The cross-section of end ring A_{ring} is about half the cross-sectional area of all bars under a pole:

$$A_{ring} \approx (0.5 - 0.6) \cdot N_2 \cdot A_{bar} \tag{7.90}$$

The complete end rings, though useful in providing $x_d'' \approx x_q''$ and q axis current damping during transients, hamper the free axial circulation of cooling agent between rotor poles. Thus, it is practical to use copper end plates that follow the shape of the poles and extend below the first row of pole bolts. They are located between the laminated rotor pole core and the end plate made of steel (Figure 7.19). For good contact with the copper bars, the copper end plate should have a thickness of about 10 mm [6]. The copper plate plays the role of the complete end ring but without obstructing the cooler axial flow between the rotor poles. Also, it is mechanically more rugged than the latter.

7.9 Design of Cylindrical Rotors

The cylindrical rotor is generally made from solid iron with milled slots over about two thirds of periphery so as to produce $2p_1$ poles with distributed field coils in slots (Chapter 4 and Figure 7.20). Slots are radial
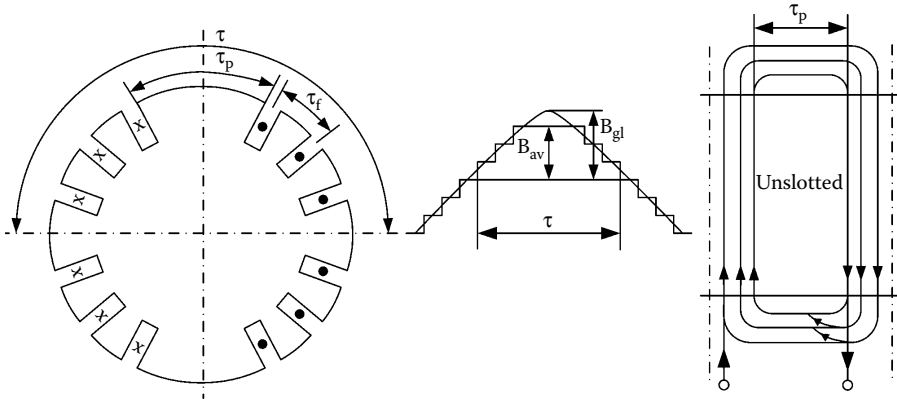
FIGURE 7.20 Two-pole cylindrical rotor with field coils.

and open in Figure 7.20. According to Chapter 4, Equation 4.23, the airgap flux density produced by the distributed field winding is

$$B_{gv}(x) = K_{fv} \cdot B_{gav} \cdot \cos v \frac{\pi}{\tau} x \tag{7.91}$$

in rotor coordinates, with

$$K_{fv} \cong \frac{8}{v^2 \pi^2} \cdot \frac{\cos v \dfrac{\tau_p}{\tau} \cdot \dfrac{\pi}{2}}{1 - v \tau_p / \tau} \tag{7.92}$$

Only odd harmonics are present if all poles are balanced. For the fundamental, the form factor K_{fv} is as follows:

$$\left(K_{f1} \right)_{\frac{\tau_p}{\tau} = \frac{2}{3}} = \frac{8}{\pi^2} \cdot \frac{\cos \dfrac{\tau_p}{\tau} \cdot \dfrac{\pi}{2}}{1 - \tau_p / \tau} = \frac{8}{\pi^2} \cdot \frac{\sqrt{3}/2}{1 - 1/3} = 1.0528 \tag{7.93}$$

The third harmonic is already reduced:

$$\left(K_{f3} \right)_{\frac{\tau_p}{\tau} = \frac{2}{3}} = \frac{8}{9 \cdot \pi^2} \cdot \frac{\cos 3 \dfrac{\tau_p}{\tau} \cdot \dfrac{\pi}{2}}{1 - 3 \tau_p / \tau} = -0.1415 \tag{7.94}$$

The stator and rotor slot opening airgap permeance influence on the excitation airgap flux density harmonics is not considered in Equation 7.92.

The rotor excitation slot pitch τ_f should be chosen in relation to stator slot pitch τ_s, such that the stator emf harmonics and solid rotor eddy current losses are minimized. Further,

$$B_{av} = \frac{\mu_0 \cdot W_{fc} \cdot I_{fa} \times (N_{fp} / 2)}{g \cdot K_c \cdot (1 + K_s)} \tag{7.95}$$

N_{fp} is the number of field-winding slots per rotor pole. K_c is the Carter coefficient accounting for the apparent increase of airgap due to stator and rotor slotting and for the presence of radial cooling channels (if any). Magnetic saturation is accounted for by K_s, with $K_s < 0.2 \div 0.25$.

Example 7.5

Consider a two-pole 30 MVA, 50 Hz, $\cos\varphi_n = 0.9$ lagging turbogenerator. With a stator bore diameter $D_{is} = 0.85$ m, $N_{fp(in\ the\ rotor)} = 12$ slots/pole, $B_{g1} = 0.825$ T, $A = 56{,}000$ A/m, SCR = 0.55, $V_{fn} = 500$ V, and $V_{fmax} = 2\ V_{fn}$.

Design the pertinent field winding after calculating the necessary airgap g.

Solution

The ampereturns per meter A may be turned into mmf per pole F_{1n}:

$$\tau = \pi \cdot D_{is}/2 = \pi \cdot 0.83/2 = 1.303 \ \text{m}$$

$$F_{1n} \approx \frac{A \cdot \tau}{2} = \frac{56000 \cdot 1.303}{2} = 36349 \ \text{At/pole}$$

The no-load equivalent field winding mmf fundamental per pole F_{f10} is

$$F_{f10} \approx SCR \cdot F_{1n} = 0.5 \times 36349 = 18242 \ \text{At/pole}$$

With $K_s = 0.25$, $K_c = 1.1$, and $N_{fp} = 12$, the airgap flux density produced at no load by the field winding is

$$B_{g10} = \frac{\mu_0 \cdot F_{f10}}{g \cdot K_c \cdot (1 + K_s)} \tag{7.96}$$

So, the airgap g becomes

$$g = \frac{1.256 \cdot 10^{-6} \cdot 18242}{1.1 \cdot 1.25 \cdot 0.825} = 20.2 \times 10^{-3} \ \text{m}$$

Consequently, from Equation 7.89 with Equation 7.85 and Equation 7.87, the rotor pole slot mmf $W_{Fc}I_{fo}$ at no load is as follows:

$$I_{fo}W_{fc} = \frac{2}{N_{fp}} \cdot \frac{F_{f10}}{K_{f1}} = \frac{2}{12} \cdot \frac{18242}{1.0528} = 2887.8 \ \text{At/slot} \tag{7.97}$$

At full load and rated power factor, the excitation mmf requirement is about two times larger than that for no load:

$$W_{fc} \cdot I_{fn} = 2W_{fc} \cdot I_{f0} = 5775.7 \ \text{At/slot} \tag{7.98}$$

The slot pitch of rotor slots τ_{fr} is

$$\tau_{fr} = \frac{\pi(D_{is} - 2g) \cdot (1 - \tau_p/\tau)}{2p_1 \cdot N_{fp}} = \frac{\pi(0.83 - 2 \cdot 0.02) \cdot (1 - 0.3)}{2 \cdot 12} = 0.07235 \text{ m}$$

The value of $\tau_p/\tau = 0.3$ is taken to avoid $\tau_{fr} = \tau_s$ (slot pitch in the stator with $q = 6$).

With the slot fill factor $K_{fill} = 0.5$ (profiled conductors), and a design current density $j_{cor} = 6$ A/mm^2, the rotor slot useful area A_{slotr} is as follows:

$$A_{slotr} = \frac{W_{fc}I_{fn}}{j_{cor} \cdot k_{fill}} = \frac{5775.7}{6 \cdot 0.5} = 1925.23 \text{ mm}^2$$

The slot width W_{sr} is

$$W_{sr} = 0.4 \cdot \tau_{fr} = 0.4 \times 0.07235 = 0.02894 \approx 0.029 \text{ m}$$

The slot useful height h_{sr} is

$$h_{sr} = \frac{A_{slotr}}{W_{sr}} = \frac{1925.23 \cdot 10^{-6}}{0.029} = 66.38 \cdot 10^{-3} \text{ m}$$

The aspect ratio of the slot is rather small ($h_{sr}/W_{sr} = 2.289$); therefore, the current density might be reduced or, if needed, higher field mmfs than in Equation 7.98 are feasible.

To finish the design, calculate the number of turns per coil and the conductor cross-section.

The field-circuit rated voltage V_{fn} should be considered when designing the field winding, with the voltage ceiling left for field current forcing during transients to enhance transient stability limits with a small SCR = 0.5.

First, the field-winding resistance per pole R_{fp} has to be calculated:

$$R_{fp} = \rho_{co}\frac{N_{fp} \cdot l_{ave}}{I_{fn}} \cdot W_{fc} \cdot a_p \cdot j_{cor} \tag{7.99}$$

where l_{ave} is the average length of turn. Approximately,

$$l_{ave} \approx 2 \cdot l_{pi} + \pi \cdot K_{av} \cdot \frac{\tau}{2} \quad ; \quad K_{av} \approx 0.5 - 0.7 \tag{7.100}$$

Considering a_p current paths in the rotor, the field voltage equation under steady state is

$$V_{fn} = R_f \cdot I_{fn} \tag{7.101}$$

with

$$R_f = \frac{R_{fp} \times 2p_1}{a_p^2} \tag{7.102}$$

Making use of Equation 7.99 and Equation 7.100 in Equation 7.101 yields the following:

$$V_{fn} = \rho_{co} \cdot \frac{N_{fp} \cdot l_{ave} \cdot j_{cor}}{W_{fc} \cdot (I_{fn}/a_p)} \cdot W_{fc}^2 \times \frac{2p_1}{a_p^2} \cdot I_{fn} = \rho_{co} \cdot N_{fp} \cdot l_{ave} \cdot j_{cor} \frac{2p_1}{a_p} \cdot W_{fc} \qquad (7.103)$$

Equation 7.103 provides for the direct computation of the number of turns per field coil. The copper resistivity should be considered at rated temperature.

Example 7.6: Field Coil Sizing

Calculate, for the rotor in Example 7.5, the number of turns per field coil and the wire cross-section if the stator core total length l is 2.5 m. Also, $I_{fn} W_{fc} = 5775$ At/coil.

Solution

The turn average length is as follows (Equation 7.100):

$$l_{avef} = 2 \cdot \left(2.6 + \pi \cdot 0.6 \cdot \frac{1.303}{2} \right) \cong 7.65 \text{ m}$$

With $\rho_{co} = 2.15 \times 10^{-8}$ Ωm, $j_{cor} = 6$ A/mm^2, $a_p = 2$ current paths in parallel, $2p_1 = 2$, $N_{fp} = 12$ slots/rotor pole, and $V_{fn} = 500$ V, from Equation 7.103, the number of turns per field coil (same for all) W_{fc} is

$$W_{fc} = \frac{V_{fn} \cdot a_p}{\rho_{CO} \cdot N_{fp} \cdot l_{ave} \cdot j_{cor} \cdot 2p_1} = \frac{500 \cdot 2}{2.15 \times 10^{-8} \cdot 12 \cdot 7.65 \cdot 6 \times 10^6 \cdot 2 \cdot 1} = 42.22 \text{ turn/coil}$$

Let us adopt $W_{fc} = 42$ turns/coil.

The total field current I_{fn} comes from the known $I_{fn} W_c$:

$$I_{fn} = \frac{W_{fc} \cdot I_{fn}}{W_{fc}} = \frac{5755}{42} = 137.50 \text{ A}$$

The current per path (in the coils) I_{fna} is

$$I_{fna} = \frac{I_{fn}}{a_p} = \frac{137.5}{2} = 68.75 \text{ A}$$

The copper conductor cross-section A_{co} is

$$A_{co} = \frac{I_{fna}}{j_{cor}} = \frac{68.75}{6 \times 10^6} = 11.458 \cdot 10^{-6} \text{ m}^2$$

A single rectangular cross-section wire may be used.

The total rated power in the excitation winding P_{exn} is

$$P_{exn} = V_{fn} \cdot I_{fn} = 500 \times 137.5 = 68750 \text{ W} \qquad (7.104)$$

For a 30 MW SG, this means only 0.229%.

The rather small airgap ($g = 20 \times 10^{-3}$ m), the moderate rated current density ($j_{cor} = 6 \times 10^6$ A/m^2), and the 2/1 ratio between full load and no-load field mmf may justify the rather small power (0.229%) in the field winding.

7.10   The Open-Circuit Saturation Curve

The open-circuit saturation curve basically represents the no-load generator phase voltage E_{10} as a function of excitation current (or mmf) I_f, at rated frequency:

$$E_{10} = \sqrt{2} \cdot f_n \cdot W_a \cdot K_{W1} \cdot \frac{2}{\pi} \cdot B_{g1} \cdot \tau \cdot l_i = K_E \cdot \Phi_{1g} \tag{7.105}$$

Also at no load, from Equation 7.27, Equation 7.91, and Equation 7.97,

$$\Phi_{1g} = \frac{2}{\pi} \cdot l_i \cdot \tau \cdot B_{g1} \ ; \ B_{g1} = K_{f1} \cdot B_{av} \ ; \ B_{av} = \frac{\mu_0 \left(W_f I_f \right)_{pole}}{g_a K_c \left(1 + K_s \right)} \tag{7.106}$$

The saturation factor K_s depends on I_F, that is, on B_{av} and the machine stator and rotor core geometry and the $B(H)$ curves of stator and rotor core materials. The form factor K_{f1} is as follows (Chapter 4):

$$K_{f1} \approx \frac{4}{\pi} \cdot \sin \frac{\tau_p}{\tau} \cdot \frac{\pi}{2} \quad \text{for salient rotor poles}$$

$$K_{f1} \approx \frac{8}{\pi^2} \cdot \frac{\cos \dfrac{\tau_p}{\tau} \cdot \dfrac{\pi}{2}}{1 - \dfrac{\tau_p}{\tau} \cdot \pi} \quad \text{for cylindrical rotor poles} \tag{7.107}$$

The equivalent stator stack iron length l_i is as follows (Equation 7.73):

$$l_i \approx \left(l - n_c \cdot b_c' - 2a' \cdot \left(1 - \frac{g}{g + c'/2} \right) \right) \tag{7.108}$$

The Carter coefficient K_C is, in general, the product of at least two of three terms:

- K_{C1} — accounting for airgap increase due to stator slot openings
- K_{C2} — accounting for airgap increase due to rotor slotting (caused for damper cage slots or by the field-winding slots)
- K_{C3} — accounting for the airgap increase due to radial channels opening b_c

When the airgap varies under the salient rotor pole shoe from g to g_{max}, in calculating K_{C1}, K_{C2}, and K_{C3}, an average airgap g_a is used:

$$g_a \approx \frac{2}{3} g + \frac{1}{3} g_{max} \tag{7.109}$$
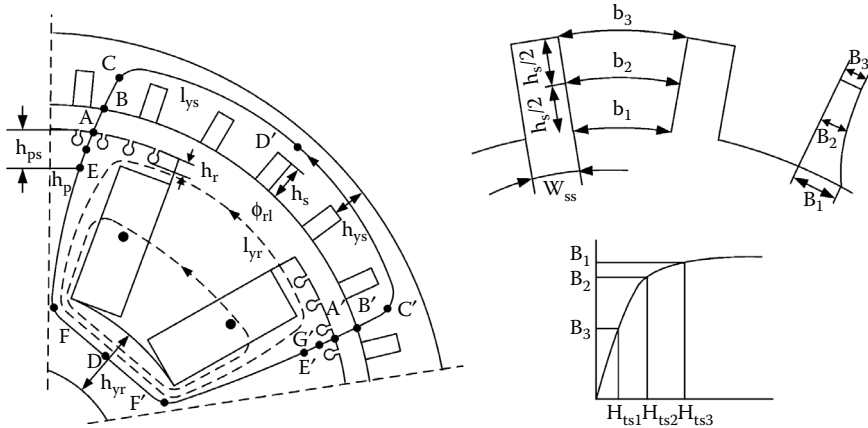
FIGURE 7.21 Average no-load flux path in the synchronous generator.

The literature on induction machines abounds with analytical formulas for Carter coefficients. A simplified practical version is given here:

$$K_{C_1} = \frac{\tau_s + 10 g_a}{(\tau_s - W_{ss}) + 10 g_a} \quad ; \quad W_{ss} - \text{slot opening}, \tau_s - \text{stator slot pitch}$$

$$K_{C_2} = \frac{\tau_r + 10 g_a}{(\tau_r - W_{rr}) + 10 g_a} \quad ; \quad \tau_r - \text{rotor slotting pitch}, W_{rr} - \text{rotor slot opening} \tag{7.110}$$

$$K_{C_3} = \frac{\tau_c + 10 g_a}{(\tau_c - \tau_b) + 10 g_a} \quad ; \quad \tau_c - \text{radial channel average pitch}, b_c - \text{radial channel width}$$

$$K_C = K_{C_1} \cdot K_{C_2} \cdot \left(K_{C_3}\right)^i \tag{7.111}$$

The value of i is $i = 1$ if the radial channels are present only in the stator, but it is $i = 2$ when they are present in both the stator and rotor.

When the airgap is constant (cylindrical rotors), $g_a = g$, as expected.

We will proceed to an analytical calculation of the open-circuit magnetization curve, because we previously defined all the components for given airgap flux density B_{g1} (or B_{av}). Except for one — the interpole rotor leakage flux, Φ_{rl}, which is dependent on the mmf drop along the airgap + stator teeth + yoke: $F_{rl} = F_{AA'}$ (Figure 7.21).

According to Ampere's law, for the average flux line,

$$\left(F_{10}\right)_{pole} = F_g + F_{ts} + F_{ys} + F_{tr} + F_{ps} + F_p + F_{yr} \tag{7.112}$$

$$\text{AB} \quad \text{BC} \quad \text{CD} \quad \text{AG} \quad \text{GE} \quad \text{EF} \quad \text{FD'}$$

Also,

$$F_{rl} = 2 \cdot \left(F_g + F_{ts} + F_{ys}\right) = F_{AA'}$$

$$F_{10} = F_{rl} + F_{rr} \quad ; \quad F_{rr} = 2\left(F_{tr} + F_{ps} + F_p + F_{yr}\right) \tag{7.113}$$

with

$$F_g = \frac{B_{g1}}{\mu_0} \cdot g_a \cdot K_C$$

$$F_{ts} = H_{ts}^{av} \cdot h_s$$

$$F_{ys} = H_{ys}^{av} \cdot l_{ys}^{av}$$

$$F_{tr} = H_{tr}^{av} \cdot h_r \qquad (7.114)$$

$$F_{ps} = H_{ps}^{av} \cdot h_{ps}$$

$$F_p = H_p^{av} \cdot h_p$$

$$F_{yr} = H_{yr}^{av} \cdot l_{yr}^{av}$$

For given B_{g1} and machine geometry, the flux densities in various stator regions may be calculated.

The average value of field H_{ts}^{av} is calculated as follows for the trapezoidal stator teeth:

$$H_{ts}^{av} = \left(H_{ts1} + 4H_{ts2} + H_{ts3} \right)/6 \qquad (7.115)$$

H_{ts1}, H_{ts2}, and H_{ts3} correspond to the tooth flux densities B_1, B_2, and B_3 in the three locations indicated in Figure 7.21:

$$B_1 \approx B_{g1} \cdot \frac{\tau_s}{b_1} \quad ; \quad b_1 = \tau_s - W_{ss}$$

$$B_2 \approx B_1 \cdot \frac{b_1}{b_2} \qquad (7.116)$$

$$B_3 \approx B_1 \cdot \frac{b_1}{b_3}$$

The widths of the stator teeth b_1, b_2, and b_3 at tooth top, middle, and bottom, respectively, are straightforward. From the known lamination magnetization curves, H_{ts1}, H_{ts2}, and H_{ts3}, corresponding to B_1, B_2, and B_3, are obtained. A similar procedure may be used to calculate the mmf drop F_{tr} in the rotor tooth. For the stator yoke, the maximum value of the flux density is used to obtain H_{ys} from the same magnetization curve:

$$B_{ys}^{max} \approx \frac{B_{g1}}{h_{ys}} \cdot \frac{\tau}{\pi} \qquad (7.117)$$

However, to account for the fact that lower flux density levels exist in the yoke and the lengths of various flux lines in this zone are different from each other, flux line length l_{ys}^{av} is to be defined:

$$l_{ys}^{av} \approx K_{ys} \frac{\pi \left(D + 2g + 2h_s + h_{ys} \right)}{4 p_1} \quad ; \quad K_{ys} \approx \left(0.66 - 0.8 \right) \qquad (7.118)$$

Also,

$$l_{ys}^{av} \approx \pi\left(D - 2h_{ps} - 2h_p\right)\big/4\,p_1 \tag{7.119}$$

Realistic values of K_{ys} may be obtained through FEM or multiple magnetic circuit field distribution calculation methods [8,9].

The total pole flux in the rotor also includes the interpole leakage flux Φ_{rl} besides the airgap flux Φ_{1g}:

$$\Phi_{1g} = \frac{2}{\pi} \cdot B_{g1} \cdot \tau \cdot l_i$$

$$\Phi_{1r} = \Phi_{1g} + 2\Phi_{rl} \tag{7.120}$$

Recognize that not all the sections of the rotor pole encounter the entire rotor leakage flux Φ_{rl}, but the rotor yoke does. When calculating the dependence of leakage rotor flux Φ_{rl} on the mmf $1/2\,F_{AB} = F_{rl}$ (Equation 7.113), either analytical or numerical flux distribution investigation is necessary.

However, as the tangential distance between neighboring rotor poles in air is notable, to a first approximation, we have

$$\Phi_{rl} = P_{rl} \cdot F_{rl} \tag{7.121}$$

There are a few analytical approximations for P_r (the permeance of the leakage interpolar flux) [6, 7]. Here, we use the similitude of the interpolar space with a semiclosed slot plus the airgap flux permeance known as zigzag (airgap) leakage [10]:

$$P_{rl} = 2\mu_0 \cdot \left(\lambda_p + \lambda_f\right) \cdot l_{pi} \tag{7.122}$$

$$\lambda_p \approx \frac{h_{ps1}}{\left(b_{r1} + b_{r2}\right)} + \frac{1}{3}\frac{h_{ps2}}{\left(b_{r2} + b_{r3}\right)} + \frac{1}{3}\frac{h_{p1}}{\left(b_{r3} + b_{r4}\right)} \tag{7.123}$$

$$\lambda_f = \frac{5g_a K_c \big/ 2b_{r1}}{5 + \left(4g_a K_c \big/ 2b_{r1}\right)} \tag{7.124}$$

Once the geometry of the rotor is known, all variables in Equation 7.123 and Equation 7.124 are given, and with F_{rl} — the corresponding mmf (Equation 7.113) — also calculated, the interpolar leakage flux is obtained.

Now for the rotor pole shoe, pole body, rotor yoke average flux density B_{ps}^{av}, B_p^{av}, B_{yr} calculations, the leakage flux has to be added to the airgap flux per pole:

$$B_{ps}^{av} \approx \frac{1\big/\pi \cdot B_{g1} \cdot \tau \cdot l_i + C_{ps} \cdot \Phi_{rl}}{l_{pi} \cdot \left(b_p\big/2\right)} \quad ; \quad C_{ps} = 0.3 - 0.5$$

$$B_p^{av} \approx \frac{1\big/\pi \cdot B_{g1} \cdot \tau \cdot l_i + C_p \cdot \Phi_{rl}}{l_{pi} \cdot \left(W_p\big/2\right)} \quad ; \quad C_p \approx 0.75 - 0.85 \tag{7.125}$$

$$B_{yr} \approx \frac{1\big/\pi \cdot B_{g1} \cdot \tau \cdot l_i + \Phi_{rl}}{l_{pi} \cdot h_{yr}}$$
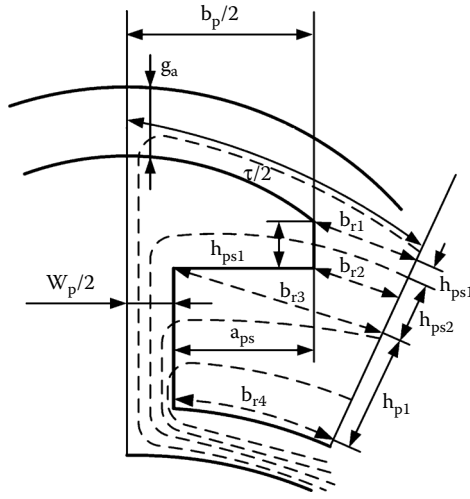
FIGURE 7.22 Rotor leakage flux permeance P_{rl} calculation.

with l_{pi} equal to the total rotor iron length (Equation 7.81) and all other dimensions visible in Figure 7.22. The coefficients C_{ps} and C_p account for the fact that only a part of the leakage flux adds in the pole shoe and in the pole regions.

With the rotor flux densities known, the corresponding rotor mmf F_{ps}, F_p, and F_{yr} per pole may be calculated.

All the terms in Equation 7.112 may be calculated for given fundamental airgap flux density.

Notice that the field pole mmf fundamental F_{10} is related to the field pole mmf $(W_f I_f)_{\text{pole}}$ by

$$F_{10} = K_{f1} \cdot \left(W_f I_f \right)_{pole} \tag{7.126}$$

The translation of this mmf per pole into an equivalent stator mmf per pole F_{1d} is as follows:

$$F_{10} = F_{1d} \cdot K_{ad} = \frac{3\sqrt{2} \cdot W_1 \cdot K_{W1} \cdot I_d}{\pi \cdot p_1} \cdot K_{ad} \tag{7.127}$$

$$K_{ad} \approx \frac{\tau_p}{\tau} + \frac{1}{\pi} \cdot \sin\left(\pi \frac{\tau_p}{\tau} \right) \quad ; \quad 0.8 < K_{ad} < 1.0 \tag{7.128}$$

The *d* axis magnetization reactance reduction coefficient (Chapter 4) accounts for the rotor saliency, and it is equal to unity for a cylindrical rotor.

The whole open-circuit saturation curve may be calculated without any iteration by repeating the above computation sequence for ever-higher values of B_{g1} until the no-load voltage E_1 reaches about 130% of the generator rated terminal phase voltage. The acquired data also allow for the representation of the so-called partial no-load magnetization curves (Figure 7.23).

The partial magnetization curves are generally used to calculate the rated field mmf at rated power and voltage and rated lagging power factor. The no-load magnetization curve is essential in designing and controlling autonomous SGs.

The horizontal variable is either total field mmf F_{10} or the partial stator + airgap mmf, F_{rl}, and, respectively, the rotor mmf F_{rr}. In addition, Φ_{1g} is the airgap flux per pole, $2\Phi_{rl}$ is the total interpolar rotor leakage flux, and Φ_{1r} is the total flux per pole in the rotor ($\Phi_{1r} = 2\Phi_{rl} + \Phi_{1r}$).
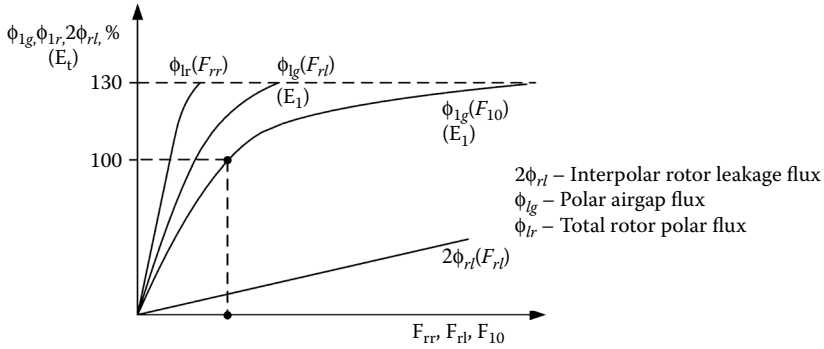
FIGURE 7.23 Partial no-load magnetization curves.

The airgap flux Φ_{lg} is proportional to emf E_1 (Equation 7.105). So, in P.U. values Φ_{lg} and E_1 are superimposed in Figure 7.23.

7.11   The On-Load Excitation mmf F_{1n}

Calculating the on-load excitation F_{1n} per pole is essential in designing the SG in relation to field-winding losses and overtemperatures.

Traditionally, there were two methods used to calculate F_{1n}:

- Potier diagram method
- Partial magnetization curve method

The Potier diagram is meant for cylindrical rotors, while the partial magnetization curve method is necessary for the salient-pole rotor. What is needed in both methods is the rated armature mmf F_{a1}, the rated voltage, and the leakage stator reactance x_{sl}. At this stage in the design, x_{sl} may be calculated.

For now, we consider it known (in general, $x_{sl} = 0.09$ to 0.15 P.U. for all SGs and increases with power). The Potier reactance is as follows:

$$x_p \approx x_{sl} + 0.02 \text{ P.U.} \tag{7.129}$$

7.11.1   Potier Diagram Method

The diagram in Figure 7.24 is drawn in P.U. with rated terminal voltage V_n as the base voltage. Also, the base field mmf corresponds to field mmf at rated voltage under no load. With the rated voltage along the vertical axis and the rated power factor angle, the phase of rated current is visualized. Then, with x_p in P.U., the segment AB — 90° ahead of I_{1n} — the total (airgap) emf at rated load E_t is found:

$$E_t = \sqrt{v_1^2 + x_p^2 i_1^2 + 2 \cdot x_p \cdot i_1 \cdot v_1 \cdot \sin\varphi_n} \text{ (P.U.)} \tag{7.130}$$

Then, the segment CD in the no-load saturation curve represents exactly E_t and OD (the corresponding field mmf).

Now, we only have to add vectorially to $\overline{OD}$ the $\overline{ED}$ in phase with I_{1n} but with its value (in P.U.).

F_{an} is defined as the ratio between the stator pole rated mmf divided by the field mmf, with F_{10n} corresponding to rated voltage $v_n = 1$ (P.U.) at no load.

Rotating $\overline{OE}$ until it reaches the abscissa give $\overline{OF} = \overline{OE} = \overline{F_{1n}}$ — the rated field mmf.

It is well understood that the whole method could be put into algebraic form and integrated into a rather simple computer program that calculates first the no-load saturation curve by advancing in 0.05

FIGURE 7.24 Rated field magnetomotive force (mmf) calculation.

(or so) steps from zero to 130% of rated airgap flux/pole (or no-load voltage). This way, the graphical errors are removed to a great extent.

The vectorial addition of field (OD) and armature (DE) mmfs per pole to reach the resultant mmf is implicitly valid only if the SG rotor has no magnetic saliency. Even the cylindrical rotor, with slots in axis q (only), to house the field coils, has an up to 5% saliency; $x_{dm}/x_{qm} = 1.05$ under full load and rated power factor.

For the salient-pole rotor, the saliency $x_{dm}/x_{qm} = 1.3 \div 1.5$, and such an approximation is no longer practical.

This is how the partial magnetization curve method becomes necessary.

7.11.2 Partial Magnetization Curve Method

Within the frame of this method, the partial no-load magnetization curves (Figure 7.25) are first determined point by point up to 1.3 P.U. voltage or (flux).

FIGURE 7.25 The partial magnetization curves method.

FIGURE 7.26 Saturation coefficients to account for cross-coupling magnetic saturation. (Redrawn from V.V. Dombrowski, A.G. Eremeev, N.P. Ivanov, P.M. Ipatov, M.I. Kaplan, and G.B. Pinskii, *Design of Hydrogenerators*, vols. I and II, Energy Publishers, Moscow, 1965 [in Russian].)

It is well known that magnetic saturation and saliency produce an angle shifting between the resultant airgap flux and armature and resultant mmf. The cross-coupling magnetic saturation is responsible for this phenomenon (Chapter 4). In Reference [11], a rather lucrative procedure to account for this phenomenon is introduced.

Figure 7.25 shows the phasor diagram similar to Figure 7.24, with E_t the rated airgap emf $E_t = \overline{OB'}$ = OB. To E_t, the unsaturated (straight line) $\Phi_{1g} (F_{rl})$ retains the unsaturated B′C′ and saturated B′C″-stator plus airgap mmfs F_{rlu}, F_{rls}:

$$\frac{F_{rlu}}{F_{rls}} = \frac{\overline{B'C'}}{\overline{B'C''}} \tag{7.131}$$

At this ratio, from Figure 7.26 [7], we extract the saturation coefficients K_{sd}, K_{sq}, K_1 for constant airgap ($g_{max} = g$) and K'_{sd}, K'_{sq}, K'_1 for variable airgap ($g_{max}/g = 1.5 - 2.5$).

Then, for rated armature mmf F_{an} (P.U.), Figure 7.24, a q axis equivalent armature reaction occurring for saliency and saturation is calculated:

$$F_{an}^{qs} = F_{an}(\text{P.U.}) \cdot K_{sq} \cdot K_{aq} \tag{7.132}$$

For F_{an}^{qs}, we read on the $\Phi_{1g} (F_{rl})$ curve the fictitious emf $E_{qo} = \overline{HH'}$. E_{qo} is projected as BD along the leakage reactance voltage drop direction (AB). The direction OD corresponds to the q axis. The perpendicular from B to $\overline{OD}$ corresponds to the d axis. The perpendicular from B to $\overline{OD}$ touches the latter in F and $\overline{OF} = E_d$ (resultant emf along axis d).

To E_d, on the $\Phi_{1g} (F_{rl})$ curve, the mmf $\overline{AC''} = \overline{OM}$ corresponds.

The magnetic saturation corresponding effect is considered by an equivalent F_{adq}^s component [9]:

$$F_{adq}^s = K_{sd} \cdot K_{ad} \cdot F_a(\text{P.U.}) \cdot \sin\Psi + K_1 \cdot \frac{\tau_p}{g} \cdot F_a(\text{P.U.}) \cdot \cos\Psi \tag{7.133}$$

for constant airgap, and

$$F_{adq}^s = K_{sd}' \cdot K_{ad} \cdot F_a(\text{P.U.}) \cdot \sin\Psi + K_1' \cdot \frac{\tau_p}{g} \cdot F_a(\text{P.U.}) \cdot \cos\Psi$$

for variable airgap, with K_{sd}, K_{sd}', K_1, K_1' from Figure 7.26. The angle Ψ is the phase angle between the armature current vector and axis q in the d–q model. Equation 7.133 contains the influence of both axes along the axis d.

With F_a (P.U.) known (for rated point, Figure 7.24) and Ψ determined from Figure 7.25, F_{adq}^s is calculated and added to OM along the horizontal axis ($F_{adq}^s = \text{MM}$). Adding the rotor interpole leakage flux per pole ($2\Phi_{lr} = \text{NN}'$), from the Φ_{1r} (F_{rr}) partial magnetization curve, the rotor mmf contribution $F_{rr} = \text{OO}'$, the total on-load excitation mmf is obtained as $\overline{\text{OR}} = F_{1n}$.

Corresponding to F_{1n}, the voltage regulation Δv (P.U.) is also obtained. The graphical procedure seems at first a bit complicated, but it may be acquired after one to two examples. Also, the procedure may be mechanized into a computer program including the calculation of partial magnetization curves.

It may be argued that the whole problem may be solved directly through FEM. To do so, first, E_t must be calculated (from Equation 7.122) and then airgap flux Φ_{1g} can be calculated with given (rated) stator current and assigned values of Ψ, and then Φ_{1g} can be put into P.U. values. The FEM process can then be gone through again with new values of Ψ until Φ_{1g}(P.U.) $= E_t$. The advantage of FEM is the possibility of additionally calculating the slot leakage inductance. In that way, only the end connection leakage inductance is needed in order to obtain an exact value of x_{ls}.

Still, FEM seems practical only in the design refinement stages rather than in the general optimization design process, due to prohibitively high computation times and a lack of generality of results.

Example 7.7

Consider the no-load saturation curves in Figure 7.25 as pertaining to a real SG with a leakage reactance $x_{sl} = 0.11$ and a rated power factor angle $\varphi_n = 20°$.

Also, the no-load excitation mmf F_{10n} that produces the rated voltage at zero load is as follows (from Example 7.5): $F_{10n} = 18242$ At/pole, SCR = 0.7.

Calculate, for a salient pole rotor $\tau_p/\tau = 0.7$, $g/\tau = 0.04$, with constant airgap, the rated load excitation mmf in P.U. and in At/pole.

Solution

First, apply the Potier diagram method, despite the fact that SG has salient poles. From Equation 7.129,

$$x_p \approx x_{sl} + 0.02 = 0.11 + 0.02 = 0.13$$

The airgap emf at full load E_t, for $V_1 = 1$ (P.U.), $i_1 = 1$ (P.U.), is, from Equation 7.130:

$$E_t = \sqrt{1 + 0.13^2 \cdot 1^2 + 2 \cdot 0.13 \cdot 1 \cdot 1 \cdot \sin 20} = 1.0515 \text{ (P.U.)}$$

From Figure 7.24, at scale for $E_t = 1.0515$, from the no-load saturation curve, the resultant mmf OD = 1.3 (due to magnetic saturation).

Now, the rated armature F_{an} is

$$F_{an} = \frac{F_{10n}}{\text{SCR}} = \frac{18242}{0.7} = 26060 \text{ At/pole} = 1.35 \cdot F_{10n}$$

So, in P.U., $F_{an} = 1.35$ (P.U.).

Finally, from Figure 7.24, solving for triangle CDF the total load field mmf $F_{1n} = \overline{OE} = \overline{OF}$ is as follows:

$$F_{1n} = \sqrt{\overline{OD}^2 + \overline{DE}^2 + 2 \cdot \overline{OD} \cdot \overline{DE} \cdot \cos \varphi_n} = \sqrt{1.3^2 + 1.428^2 + 2 \cdot 1.3 \cdot 1.428 \cdot \cos 20} = 2.68 \ (P.U.)$$

The value of field rated mmf is, thus,

$$F_{1n} = F_{1n}(P.U.) \cdot F_{10n} = 2.68 \cdot 18242 = 48876 \ \text{At/pole}$$

As expected, no reference was made to the rotor saliency, as the Potier diagram method was used.

Let us now turn to Figure 7.25 and consider that for E_t, again, the mmf saturation ratio is as follows (Equation 7.131):

$$\frac{F_{qss}}{F_{qsu}} = \frac{\overline{B'C''}}{\overline{B'C'}} = 1.35$$

This saturation ratio corresponds in Figure 7.26, for constant airgap under rotor pole, to

$$K_{sd} = 0.95, \ K_{sq} = 0.46, \ K_1 = 0.55 \times 10^{-2}$$

Now, for the rated mmf F_{an} (1.35 in P.U.), the equivalent armature reaction allowing for saturation and saliency F_{an}^{qs} is as follows (Equation 7.132):

$$F_{an}^{qs} = F_{an}(P.U.) \cdot K_{sq} \cdot K_{aq} = 1.35 \times 0.46 \cdot 0.57 = 0.354 \ (P.U.)$$

The values of K_{ad} and K_{aq} are given in Figure 7.27 for constant and variable airgap under rotor pole, for given τ_p / τ.

For $g/\tau = 0.04$, $\tau_p/\tau = 0.7$, $K_{ad} = 0.84$, and $K_{aq} = 0.57$ (Figure 7.27).
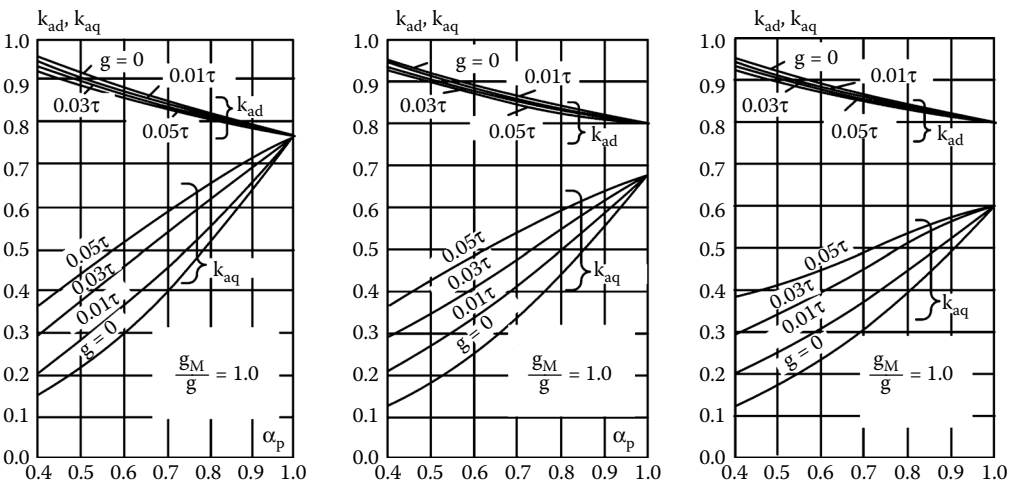
FIGURE 7.27 K_{ad} and K_{aq} (saliency) reactance factors for various τ_p/τ, g_{max}/g, and g/τ values.

For $F_{an}^{qs} = 0.354$, we read from the $\Phi_{1g} (F_{q0})$ the value of emf $E_{q0} = \text{HH}' \approx 0.40 = \overline{\text{BD}}$. From triangle OBD, we determine point F (Figure 7.25); thus, $E_d = \overline{\text{OF}} = \overline{\text{OF}'}$. For E_d, again, from $\Phi_{1g} (F_{rl})$, we determine point M, which corresponds to about 1.15 P.U. (Figure 7.25).

With current angle Ψ to q axis known, we are now able to calculate from Equation 7.133 the cross-coupling global magnetic saturation effect mmf F_{adq}^s:

$$F_{adq}^s = K_{sd} \cdot K_{ad} \cdot F_a(\text{P.U.}) \cdot \sin\Psi + K_1 \cdot \frac{\tau_p}{g} \cdot F_a(\text{P.U.}) \cdot \cos\Psi$$

$$= 0.95 \cdot 0.84 \cdot 1.35 \cdot \sin 45 + 0.55 \cdot 10^{-2} \cdot \frac{2}{3} \cdot \frac{1}{0.04} \cdot 1.3 \cdot \cos 45 = 0.7616 + 0.0834 = 0.845$$

$F_{adq}^s = \overline{\text{MN}}$ along the horizontal axis in Figure 7.25, so the rotor leakage flux $2\Phi_{lr} = \text{NN}'$ that corresponds to it is about 0.35. This value is equal to F'F'' along the vertical axis (F'F'' = 0.35) which, from the $\Phi_{1r} (F_{rr})$ curves, leads to a rotor mmf $F_{rr} \approx 0.30$.

Now, F_{rr} is added along the horizontal axis as $\overline{\text{NR}}$.

The load field mmf is, thus, $F_{1n} = \overline{\text{OR}} = \overline{\text{OM}} + \overline{\text{MN}} + \overline{\text{NR}} = 1.15 + 0.845 + 0.30 = 2.295$.

The obtained value (Equation 2.295) is different from (smaller than) that obtained with the Potier diagram method (Equation 2.68). The three no-load magnetization curves were not calculated point by point, so there is no guarantee of which is better.

However, in terms of precision, it is no doubt that the partial magnetization curves method is better, especially as it accounts for cross-coupling saturation and the magnetic saliency of the rotor.

7.12 Inductances and Resistances

The inductances and resistances of an SG refer to the following:

- Synchronous magnetizing inductances (reactances): $L_{ad} (X_{ad})$, $L_{aq} (X_{aq})$
- Stator phase leakage inductance (reactance): $L_{sl} (X_{sl})$
- Homopolar stator inductance: $L_o (H_o)$
- Stator phase resistance: $R_s [\Omega]$
- Rotor cage leakage inductances (reactances): $L_{Dl} (X_{Dl})$, $L_{Ql} (X_{Ql})$
- Rotor cage resistances: R_D, R_Q
- Excitation leakage inductance (reactance): $L_{fl} (X_{fl})$
- Excitation resistance: R_f

7.12.1 The Magnetization Inductances L_{ad}, L_{aq}

Simplified formulae for L_{ad}, L_{aq} were derived in Chapter 4:

$$L_{ad} = L_m \cdot \frac{\left(K_{ad} \cdot K_f\right)}{1 + K_{sd}^e} \qquad X_{ad} = \omega_1 \cdot L_{ad} \quad ; \quad x_{ad} = X_{dm} \cdot \frac{I_n}{V_n}$$

$$L_{aq} = L_m \cdot \frac{\left(K_{aq} \cdot K_f\right)}{1 + K_{sq}^e} \qquad X_{aq} = \omega_1 \cdot L_{aq} \quad ; \quad x_{aq} = X_{qm} \cdot \frac{I_n}{V_n} \qquad (7.134)$$

$$L_m = \frac{6\mu_0}{\pi^2} \cdot \frac{\tau \cdot l_i \cdot \left(W_1 \cdot K_{W1}\right)^2}{g \cdot K_c} \quad ; \quad K_f - \text{from (7.107)}$$

I_n, V_n are the base (rated) RMS values of SG phase current and voltage. L_m represents the airgap inductance for the uniform airgap machine. The airgap g in L_m expression is the minimum airgap for variable airgap under rotor poles. The saliency coefficients K_{ad} and K_{aq} are given in Figure 7.27. The total magnetic saturation coefficients K_{sd}^e and K_{sq}^e are distinct from those in Figure 7.26, as the latter ones are in relation to the stator plus airgap part of mmf.

K_{sd}^e and K_{sq}^e are both dependent on stator current I_1 and the current angle Ψ with q axis; that is, on both $I_d = I_1 \cdot \sin\Psi$ and $I_q = I_1 \cdot \cos\Psi$. Apparently, only FEM is precise enough for calculating K_{sd}^e, K_{sq}^e family curves, as also pointed out in Chapter 5 on transients. When $I_q = 0$ ($\Psi = 90°$), $K_{sd}^e(I_f)$ may be determined directly from the no-load saturation curve. But this is only a particular case.

From the no-load curve, the magnetization reactances x_{ad}, x_{aq} in P.U. of the direct and quadrature (d–q) axes may be obtained directly from Figure 7.25 as follows:

$$x_{aq} \cdot i \cdot \cos\Psi = \overline{DB}$$

$$x_{ad} \cdot i \cdot \sin\Psi = \overline{FD}$$

(7.135)

As Figure 7.25 may be drawn (or translated in algebraic form) for any value of current i (P.U.) and power factor angle φ_n, the values of x_{ad} and x_{aq} for pairs of i_d, i_q ($i_d = i \cdot \sin\Psi$, $i_q = i \cdot \cos\Psi$) may be obtained for given voltage. From the same rationale, the required excitation mmf may be calculated for each situation, as can the power angle $\delta_v = \Psi - \varphi$.

7.12.2 Stator Leakage Inductance L_{sl}

The stator leakage inductance of SG has four components, as it is the case for induction machines [10]:

$$L_{sl} = L_{ssl} + L_{szl} + L_{sel} + L_{sdl} \quad ; \quad X_{sl} = \omega_1 \cdot L_{sl} \quad ; \quad x_{sl} = L_{sl} \cdot \omega_1 \cdot \frac{I_n}{V_n}$$

(7.136)

where

L_{ssl} = the slot leakage
L_{szl} = the (airgap) leakage
L_{sel} = the end connection leakage
L_{sdl} = the differential (harmonics) leakage

Consider the two-layer winding with rectangular stator slots, which is typical for SGs (Figure 7.28). In general, shorted coils are used; thus, the currents in the upper and lower layer coils are dephased by γ_K (in general, $\gamma_K = 60°$ or zero). The angle γ_K is zero in slots where the same phase occupies both layers.
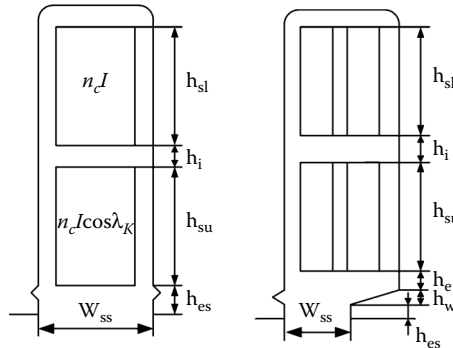
FIGURE 7.28 Typical high- and medium-power synchronous generator stator slots.

As both $\gamma_K = 0°$ and $\gamma_K = 60°$ exist, an average of the slot geometrical permeance is to be used. L_{sl} may be written as follows [10]:

$$L_{sl} \approx 2\mu_0 \cdot \frac{W_1^2 \cdot l}{p_1 \cdot q}\left(\lambda_{ss} + \lambda_{sz} + \lambda_{se} + \lambda_{sd}\right) \tag{7.137}$$

with the slot leakage permeance ratio:

$$\lambda_{ss} = \frac{1}{4}\left[\frac{h_{sl} + h_{su}\cos^2\gamma_K}{3W_{ss}} + \frac{h_{su}}{W_{ss}} + \frac{h_{su}\cos\gamma_K}{W_{ss}} + \frac{h_i}{W_{ss}} + \left(1 + \cos\gamma_K\right)^2\left(\frac{h_{os}}{W_{ss}} + \frac{h_W}{W_{ss}} + \frac{h_o}{W_{ss}}\right)\right] \tag{7.138}$$

When the number of turns per coil is different in the two layers ($n_{cl} \neq n_{cu}$), Equation 7.138 may be corrected by doing the following:

- Replacing $\cos\gamma_K$ by $K\cos\gamma_K$ with $K = n_{cu}/n_{cl}$
- Replacing number 4 by $(1 + K)^2$

For the zigzag (z) permeance ratio λ_{sz}, the so-called Richter formula is applied:

$$\lambda_{sz} \approx \frac{5g \cdot K_c / W_{ss}}{5 + 4g \cdot K_c / W_{ss}}\frac{\left(3\beta_y + 1\right)}{y} \quad ; \quad \beta_y = \frac{y}{\tau} = \text{coil span ratio} \tag{7.139}$$

It is sometimes inferred that the differential (harmonics) permeance ratio λ_{sd} is included in Equation 7.139. The end-connection permeance ratio λ_{se} (for double-layer winding) is as follows:

$$\lambda_{se} \approx 0.34 \cdot \frac{g}{l_i} \cdot \left(l_{ec} - 0.64 \cdot y\right) \quad ; \quad y - \text{coil span} \tag{7.140}$$

with l_{ec} equal to the end-connection length per machine side. A few remarks are in order:

- The total geometrical (rather than iron) length of stator l was used, though it includes the radial channels length, to account for the "slot leakage" of coil parts corresponding to cooling channels. It is an overestimation, and better approximations are welcome.
- Alternative formulae for the z permeance ratio were proposed [11]:

$$\lambda_{sz} = \frac{1}{\pi} \cdot l_{er} \cdot \frac{\sqrt{1 + \left(\frac{2g \cdot K_C}{W_{ss}}\right)^2}}{2} + \frac{g \cdot K_C}{W_{ss}}\left(1 - \frac{2}{\pi} \cdot \tan^{-1}\frac{2 \cdot g \cdot K_C}{W_{ss}}\right) \tag{7.141}$$

Expression 7.141 of λ_{sz} produces large errors for small values of $g \cdot K_C/W_{ss}$, which is not the case, in general, for SG.
- There are reasons to consider separately the differential harmonics permeance ratio λ_{sd}. For standard chorded coil winding [10],

$$\sigma_{dso} \approx \frac{2\pi^2}{9 \cdot K_{W1}^2} \cdot \frac{5g^2 + 1 - \frac{3}{4}\left(1 - \frac{y}{\tau}\right)\left[9q^2\left(1 - \frac{y^2}{\tau^2}\right) + 1\right]}{12q^2} \tag{7.142}$$

$$\lambda_{sd} = \sigma_{dso} \cdot \frac{3}{\pi^2} \cdot \frac{\tau \cdot q}{K_C \cdot g} \cdot \frac{l_i}{l} \tag{7.143}$$

- It should be noticed that, as for induction machines (IMs), the solid rotor or the rotor cage may attenuate the differential leakage coefficient λ_{sd} and σ_{dso} "in exchange" for additional losses in the rotor under SG load.
- However, as the slot pitch is about the same in the rotor cage and in the stator, and the airgap tends to be large, this attenuation is limited. Values of attenuation factor of 0.8 to 0.5 might be expected in special cases.
- The end-connection leakage permeance λ_{se} depends much on the exact shape of end connections, their vicinity to iron (metallic) parts of the frame and to the stator stack end plate, and even on the value of field mmf (the power factor).
- Saturation of stator end core laminations that produces additional losses in the underexcited machine, also causes a reduction in the end-connection leakage permeance ratio λ_{se}, due to induced current effects. And so do the currents induced in the neighboring metallic parts.
- Three-dimensional FEM was used to compute the end-connection leakage flux and losses in the end core and in the metallic parts nearby. The results seem satisfactory for the case in point but lack generality.
- The case of variable airgap above the rotor pole shoe further complicates the computation of both zigzag and differential leakage inductance. As usual, FEM is the solution for refined calculations, but in the preliminary design stages, the above formulae give results with ±10% error, in general, and are fairly reliable.

7.13   Excitation Winding Inductances

As already pointed out in Chapter 4, when reduction to stator is performed, the mutual inductance (reactance) between the field-winding and stator phases, L_{fa} (x_{fa}), equals the d axis magnetization inductance, L_{ad} (x_{ad}). However, in the design and in the testing process, it is useful to first calculate the main and leakage excitation inductance, before the reduction to stator.

The main field inductance L_{fg} and the leakage field inductance L_{fl} make up the excitation total inductance, as seen (or measured) from the rotor:

$$L_f = L_{fg} + L_{fl} \tag{7.144}$$

L_{fg} is simply as follows (as for L_{ad}):

$$L_{fg} = \frac{2\,p_1 \cdot \mu_0 \cdot W_f^2 \cdot \tau \cdot l_i \cdot \dfrac{\tau_p}{\tau}}{g \cdot K_C \cdot \left(1 + K_{sd}\right)} \tag{7.145}$$

The stator reduction coefficient K_{fa} is

$$K_{fa} = \frac{3}{2} \cdot \left(\frac{W_1 \cdot K_{W1}}{2\,p_1 \cdot W_f}\right)^2 \left(\frac{4}{\pi} \cdot K_{ad}\right)^2 \tag{7.146}$$

On the other hand, the actual mutual inductance between the excitation and armature windings, M_{af}, is

$$M_{af} \approx 6 \cdot W_f \cdot W_1 \cdot K_{W1} \cdot K_f \cdot \frac{2\mu_0 \cdot \tau \cdot l_i}{\pi \cdot g \cdot K_C \cdot (1 + K_{sd})} \tag{7.147}$$

The leakage excitation inductance L_{fl} also contains a few terms:

$$L_{fl} = 2 p_1 \cdot \mu_0 \cdot W_f^2 \cdot l_p \cdot \left(\lambda_p + \lambda_{zf} + \lambda_{ef} \right) \tag{7.148}$$

L_{fl} components have similar formulae as those derived for the stator.

The slot leakage permeance ratio λ_p was calculated in Equation 7.138; λ_{zf} was calculated in Equation 7.139. The end-connection permeance ratio λ_{ef} is as follows [11]:

$$\lambda_{ef} \approx 2.55 \cdot \frac{a_{ps}}{l_i} \cdot \ln\left(1 + \frac{\pi}{4} \cdot \frac{\tau_p}{2b_{r1}} \right) \tag{7.149}$$

with b_{r1}, a_{ps} from Figure 7.22.

The reduction of L_{fl} to the stator makes use of K_{fa} of Equation 7.146, while the P.U. translation is done by dividing to $L_B = (V_n / I_n \cdot \omega_1)$:

$$l_{fl} = L_{fl} \cdot K_{fa} / L_B = \frac{L_{ad} \cdot \pi \cdot g \cdot q \cdot K_C}{3 \cdot \mu_0 \cdot K_{W1}^2 \cdot K_{ad} \cdot l_i \cdot \tau} \cdot \left(\lambda_p + \lambda_{zf} + \lambda_{ef} \right) \tag{7.150}$$

Now it is easier to add the differential component missing in Equation 7.148. The differential leakage is similar to the case of stator winding:

$$l_{fl} \rightarrow l_{fl} + l_{ad} \cdot \left(2\frac{\tau_p}{\tau} \cdot \frac{K_{ad}}{K_{f1}^2} - 1 \right) \tag{7.151}$$

K_{f1} was calculated in Equation 7.107 for constant airgap under the pole shoes. It is common practice to express the base inductance (reactance) L_B (X_B) based on the following approximations:

$$V_n \approx \pi\sqrt{2} \cdot f_1 \cdot W_1 \cdot K_{W1} \cdot \Phi_{10} \tag{7.152}$$

with

$$\Phi_{10} = \frac{2}{\pi} \cdot B_{g10} \cdot \tau \cdot l_i$$

B_{g10} corresponds to no-load conditions at rated voltage.

$$F_{an1} = \frac{3\sqrt{2} \cdot W_1 \cdot K_{W1} \cdot I_n}{\pi \cdot p_1} \tag{7.153}$$

as

$$X_b = \frac{V_n}{I_n} = \omega_1 \cdot l_b = \frac{3}{\pi} \cdot \frac{W_1}{p_1} \cdot \frac{\left(W_1 K_{W1}\right)^2}{p_1} \cdot \frac{\Phi_{10}}{F_{an1}} \tag{7.154}$$

By denoting F_{gn}, as the airgap mmf requirement,

$$F_{gn1} = \frac{B_{g1}}{K_{f1}} \cdot \frac{g \cdot K_C}{\mu_0} \tag{7.155}$$

The magnetization reactance x_{ad} and x_{aq} in (P.U.) become

$$x_{ad} = \frac{K_{ad}}{K_{f1}} \cdot \frac{F_{an1}}{F_{gn1}} \tag{7.156}$$

$$x_{aq} = \frac{K_{aq}}{K_{f1}} \cdot \frac{F_{an1}}{F_{gn1}} \tag{7.157}$$

with x_{ad} given in Equation 7.156, together with the airgap flux density B_{g1} and linear current loading $A_n = 3W \cdot I_n/(p_1 \cdot \omega)$, the airgap g may be found:

$$g = \frac{2 \cdot \mu_0 \cdot K_{ad} \cdot K_{W1}}{x_{ad} \cdot K_{f1} \cdot K_C} \cdot \frac{A_n \cdot \tau}{B_{gn1}} \tag{7.158}$$

This expression was used to size the airgap earlier in this chapter (Equation 7.67).

Note that for the cylindrical rotor, the leakage inductance formula is similar to Equation 7.148, but instead of $2 p_1 \cdot W_f^2$, it will be $2 p_1 \cdot N_{fp} \cdot W_{fc}^2$, where W_{fc} is the number of turns per rotor slot, and N_{fp} is the number of field-winding slots per pole in the rotor.

While the slot and zigzag permeances are straightforward, the end-connection permeance ratio λ_{ef} is as follows:

$$\lambda_{ef} \approx \frac{0.2 \times \tau_r}{l_i} \tag{7.159}$$

τ_r = the rotor excitation slot pitch.

7.14   Damper Winding Parameters

The d and q axes damper winding leakage reactances $x_{D\sigma}$ and $x_{Q\sigma}$ in P.U. have expressions similar to those of excitation (l_{fl}) [12,13]:

$$\begin{aligned}
x_{Dl} \approx x_{ad} \cdot \Biggl[&\frac{K_{ad}}{\pi \cdot K_D^2} \frac{\alpha_b \cdot N_2 \cdot \left(1 - K_b\right)}{4 \sin^2 \frac{\alpha_b}{2}} \cdot \left(2 + \frac{\cos N_2 \alpha_b - K_b \cos \alpha_b}{1 - K_b} \right) \cdot \\
&\cdot \left(1 + \frac{2 \cdot \lambda_{De} \cdot g \cdot K_C}{l_i} \right) - 1 + \frac{N_2 \cdot \left(1 - K_b\right) \cdot K_{ad} \cdot l_{pi} \cdot g \cdot K_C}{l_i \cdot \tau \cdot K_D^2} \cdot \left(\lambda_{sD} + \lambda_{zD}\right) \Biggr]
\end{aligned} \tag{7.160}$$

$$\alpha_b = \frac{\pi \cdot \tau_b}{\tau} \quad ; \quad \tau_b - \text{damper bar pitch}$$

$$K_b = \frac{\sin\left(N_2 \alpha_b\right)}{N_2 \sin \alpha_b} \tag{7.161}$$

$$K_D \approx \frac{N_2}{\pi} \cdot \left(1 - K_b\right)$$

with λ_{De} equal to the end-ring permeance ratio. Complete end-ring presence is supposed:

$$\lambda_{De} \approx \frac{3.32}{\pi} \cdot \log \frac{2.35 \cdot D_{ring}}{\left(a + 2b\right)} \tag{7.162}$$

where

D_{ring} = the average ring diameter
a, b = the cross-section ring dimensions: a is radial and b is axial

The zigzag and damper slot permeance ratios λ_{ZD} and λ_{SD} are straightforward.
For axis q,

$$x_{Ql} = x_{ql} \cdot \left\{ \frac{K_{aq}}{\pi K_Q^2} \frac{\alpha_b N_2}{4 \sin^2 \frac{\alpha_b}{2}} \cdot \left[\cos N_2 \alpha_b - K_b \cos \alpha_b + \frac{\alpha_i \pi + \pi\left(1 - \alpha_i\right)\frac{gK_c}{2 g_{max}}}{N_2 \cdot \alpha_b} \times \right. \right.$$

$$\left. \left. \times \left(1 + 2 \cdot \lambda_{De} \cdot \frac{g \cdot K_c}{l_i}\right) \right] - 1 + \frac{N_2 \cdot \left(1 + K_b\right) \cdot K_{aq} \cdot l_{pi} \cdot g \cdot K_c}{l_i \cdot \tau \cdot K_Q^2} \left(\lambda_{SQ} + \lambda_{ZQ}\right) \right\} \tag{7.163}$$

with

$$K_Q \approx \frac{N_2}{\pi} \cdot \left(1 + K_b\right) - \frac{4}{\pi} \cdot \left(1 - \frac{4}{\pi} \frac{\sigma \cdot g \cdot K_c}{g_{max}}\right) \cdot \cos \frac{\alpha_i \cdot \pi}{2} \cdot \frac{\sin\left(\frac{N_2}{2} \cdot \alpha_b\right)}{2 \sin\left(\alpha_b / 2\right)} \tag{7.164}$$

where $\alpha_i = \tau_p/\tau$ is the rotor pole span per pole pitch.
The damper cage resistance in P.U., r_D and r_Q, are as follows:

$$r_D \approx \frac{6\left(W_1 \cdot K_{W1} \cdot K_{ad}\right)^2 \cdot \rho_D \cdot N_2 \cdot \left(1 - K_b\right)}{\pi^2 \cdot p_1 \cdot K_D^2 \cdot X_b} \cdot \left[\frac{l_{pi}}{A_{bar}} + \frac{\alpha_b \cdot \tau}{2\pi \cdot A_{ring} \cdot \sin^2 \frac{\alpha_b}{2}} \times \right.$$

$$\left. \times \left(2 + \frac{\cos N_2 \alpha_b - K_b \cos \alpha_b}{1 - K_b}\right) \right] \tag{7.165}$$

$$r_Q \approx \frac{6\left(W_1 \cdot K_{W1} \cdot K_{aq}\right)^2 \cdot \rho_D \cdot N_2}{\pi^2 \cdot p_1 \cdot K_Q^2 \cdot X_b} \cdot \left\{ \frac{l_{pi}}{A_{bar}}\left(1 + K_b\right) + \frac{\alpha_b \cdot \tau}{2\pi \cdot A_{ring} \cdot \sin^2 \dfrac{\alpha_b}{2}} \times \right.$$

$$\left. \times \left[\cos N_2\alpha_b - K_b \cos\alpha_b + \frac{\pi}{N_2 \cdot \alpha_b} \cdot \left(1 - \cos N_2\alpha_b\right) \right] \right\} \qquad (7.166)$$

Note that for incomplete end-rings, in general,

$$x_{Ql} = \left(2 \div 3\right) x_{Dl} \quad ; \quad R_{Ql} = \left(4 \div 6\right) R_{Dl} \qquad (7.167)$$

where

   ρ_D = the damper cage resistivity (Ωm)
   A_{bar} = the damper bar cross-section (m²)
   A_{ring} = the end-ring cross-section (m²)

The field-winding and stator resistances in P.U. are as follows:

$$r_f = \frac{R_f}{X_b} \cdot \frac{6\left(W_1 \cdot K_{W1} \cdot K_{ad}\right)^2}{\left(\pi \cdot p_1 \cdot W_f \cdot K_{f1}\right)^2} \quad ; \quad R_f = \rho_{cor} \cdot l_f \cdot \frac{W_f}{A_{cof}} \cdot 2p_1 \qquad (7.168)$$

where

   R_f = the actual field-winding resistance (Ω)
   $W_f = N_{fp} \cdot W_{fc}$ for the cylindrical rotor
   l_f = the average field turn length
   A_{cof} = the field turn cross-section

$$r_s = \frac{R_s}{X_b} \quad ; \quad R_s = \rho_{cos} \cdot W_a \cdot \frac{l_{coil} \cdot W_a}{A_{cos} \cdot a} \cdot K_R \qquad (7.169)$$

where

   l_{coil} = the turn length
   A_{cos} = the stator turn cross-section
   K_R = the skin effect coefficient (to be determined in the paragraph on losses)
   a = the stator current paths number
   W_a = the turns/path

7.15   Solid Rotor Parameters

Cylindrical rotors are built of solid iron, and for some salient-pole SGs, solid rotor poles may also be used. The solid iron of the rotor acts as a damper cage with variable resistance and inductance (reactance).

The solid iron parameters depend on the frequency of induced rotor currents — Sf_1 for the fundamental and $2f_1$ for the inverse components.

The presence of field-winding slots in the solid iron poles makes the *d* and *q* axes equivalent parameters of solid iron dampers different from each other and difficult to calculate. Comprehensive analytical formulae with widespread acceptance for r_D, r_Q, l_{Dl}, l_{Ql} for solid iron poles are not yet available, but

$$x_{Dl} \approx 0.6 \cdot r_{Dl} \quad ; \quad x_{Ql} \approx 0.6 \cdot r_{Ql} \qquad (7.170)$$
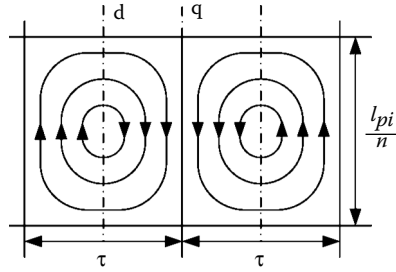
FIGURE 7.29 Solid iron rotor eddy currents trajectory in axis *d*.

The trajectory of eddy currents induced by the mmf space harmonics (Figure 7.29) and stator slot opening airgap conductance harmonics or during transients depends on the pole pitch of the respective harmonics, the frequency as "sensed" by the rotor currents, and level of flux density in the rotor solid iron body.

For the mmf fundamental only, the frequency of rotor-induced currents is $Sf_1 [S = (\omega_1 - \omega_r)/\omega_1]$.

The depth of field penetration for a traveling wave with pole pitch τ is as follows [10]:

$$\delta_1 = \mathrm{Re}\,al \sqrt{\dfrac{1}{\sqrt{\left(\dfrac{\pi}{\tau}\right)^2 + j\mu_{Fe}\sigma_{Fe}\cdot 2\pi\dfrac{Sf_1}{K_t}}}} \tag{7.171}$$

K_t takes into account the conductivity reduction due to the eddy current tangential closure [10] — the so-called transverse cage effect:

$$K_t \approx \dfrac{1}{1 - \left[\tan\left(\dfrac{\pi}{\tau}\cdot\dfrac{l_{pi}}{2\cdot n}\right)\right] \Big/ \dfrac{\pi}{\tau}\cdot\dfrac{l_{pi}}{2\cdot n}} \tag{7.172}$$

n is the number of solid iron rings put together axially to form the rotor.

The iron permeability μ_{Fe} is "dictated" by the "steady-state" conditions. So, the procedures used to calculate the magnetic saturation curves and rated excitation mmf also yield at least an average value for μ_{Fe}. To a first approximation, on the rotor surface, the flux density is, in general, around 1 to 1.2 T in the unslotted region and 1.5 to 1.8 T in the slotted region of cylindrical rotors. Magnetic saturation leads to a decrease in μ_{Fe} and, thus, to a larger field penetration depth. That is, to a smaller equivalent resistance.

For an unslotted rotor, the solid iron resistance reduced to the stator is as follows [10]:

$$R_{Ds} = \dfrac{6\left(W_1\cdot K_{W1}\right)^2\cdot l_{pi}\cdot K_t}{\sigma_{Fe}\cdot p_1\cdot\tau\cdot\delta_1} \quad;\quad r_D = \dfrac{R_{Ds}}{X_B} \tag{7.173}$$

We may, to a first approximation, consider $R_{Ds} = R_{Qs}$, and allow for the airgap leakage:

$$x_{Ds} \approx x_{Qs} \approx 0.6\cdot r_{Ds} + 0.035 \tag{7.174}$$

7.16   SG Transient Parameters and Time Constants

The *d* axis transient reactance x_d' is as follows:

$$x'_d = x_{sl} + \cfrac{1}{\cfrac{1}{x_{ad}} + \cfrac{1}{x_{fl}}} \quad \text{(P.U.)} \tag{7.175}$$

The transient reactance of the d axis damper cage, x'_D, is as follows:

$$x'_D = x_{Dl} + \cfrac{1}{\cfrac{1}{x_{ad}} + \cfrac{1}{x_{fl}}} \quad \text{(P.U.)} \tag{7.176}$$

The subtransient d–q axis reactance x''_d is

$$x''_d = x_{sl} + \cfrac{1}{\cfrac{1}{x_{ad}} + \cfrac{1}{x_{Dl}} + \cfrac{1}{x_{fl}}} \quad \text{(P.U.)} \tag{7.177}$$

For the q axis, x''_q is

$$x''_q = x_{sl} + \cfrac{1}{\cfrac{1}{x_{aq}} + \cfrac{1}{x_{Ql}}} \quad \text{(P.U.)} \tag{7.178}$$

The total excitation time constant T_f is

$$T_f \approx \frac{x_{ad} + x_{fl}}{r_f \cdot \omega_n} \quad \text{(seconds)} \tag{7.179}$$

The transient short-circuit d axis time constant T'_d is

$$T'_d = T_f \cdot \frac{x'_d}{x_d} \quad \text{(seconds)} \; ; \; x_d = x_{sl} + x_{ad} \tag{7.180}$$

The d axis damping time constant T_D, with open stator and short-circuited superconducting ($r_f = 0$) field circuit, is

$$T_D = \frac{x'_D}{r_D \cdot \omega_n} \quad \text{(seconds)} \tag{7.181}$$

The subtransient d axis time constant T''_d is as follows:

$$T''_d = T_D \cdot \frac{x''_d}{x'_d} = \frac{x'_D}{r_D \cdot \omega_n} \cdot \frac{x''_d}{x'_d} \quad \text{(seconds)} \tag{7.182}$$

If the q axis damper winding is considered in isolation, its time constant T_Q is

$$T_Q \approx \frac{x_{Ql} + x_{aq}}{r_Q \cdot \omega_n} \text{ (seconds)} \tag{7.183}$$

The subtransient q axis time constant (the stator and the field windings are short-circuited and superconducting) T_q'' is

$$T_q'' = T_Q \cdot \frac{x_q''}{x_q} = \frac{\left(x_{Ql} + x_{aq}\right)}{\left(x_{sl} + x_{aq}\right)} \cdot \frac{x_q''}{r_Q \cdot \omega_n} \text{ (in seconds)} \tag{7.184}$$

The negative sequence reactance x_2 is

$$x_2 = \frac{x_d'' + x_q''}{2} \tag{7.185}$$

or

$$x_2 = \sqrt{x_d'' \cdot x_q''} \tag{7.186}$$

depending on whether negative sequence voltages or currents are present in the SG stator.

The time constant T_a of the stator currents when all other windings are superconducting and short-circuited is as follows:

$$T_a = \frac{2 x_d'' \cdot x_q''}{r_s \left(x_d'' + x_q''\right) \cdot \omega_n} \tag{7.187}$$

All the above parameters appear in the sudden short-circuit time response. As the sudden three short-circuit is used to measure (estimate) the above parameters, their expressions, as derived in the previous paragraph, serve for checking the design accuracy and predicting the SG transient behavior.

7.16.1 Homopolar Reactance and Resistance

The homopolar sequence (Chapter 4) does not produce interference with the rotor in terms of the fundamental. However, it produces a fixed (AC) magnetic field in the airgap with a pole pitch $\tau_3 = \tau/3$, similar to a third-space harmonic. So, ACs are induced in the rotor cage through this AC third-harmonic field. In general, this effect is neglected, and the homopolar reactance x_o is assimilated to a stator leakage inductance calculated with slot total currents either zero or twice the coil homopolar mmf: $2n_c \cdot I_o$. This is so, as homopolar currents in all phases are the same. To a first approximation,

$$x_o \approx x_{sl} \text{ for diametrical coils}$$

$$x_o \approx 3 \cdot \left(1 - \frac{y}{\tau}\right) \cdot x_{sl} \text{ for chorded coils} \tag{7.188}$$

More complicated expressions are found in the literature [6].

It is evident that Equation 7.188 ignores the damping effect of rotor damper-induced currents produced by the homopolar stator mmf. In such conditions, the homopolar resistance $r_o \approx r_s$.

Example 7.8: The Transient Reactances and Time Constants

A designed salient-pole SG has the following calculated parameters (in P.U.): $r_s = 0.003$, $r_f = 0.006$, $x_{ad} = 1.5$, $x_{aq} = 0.9$, $x_{sl} = 0.12$, $x_{fl} = 0.15$, $x_{Dl} = 0.04$, $x_{Ql} = 0.05$, $r_D = 0.02$, and $r_Q = 0.022$.

Calculate the transient x_d' and subtransient reactances x_d'', x_q'', then $\times 2$ in P.U. and the time constants T_d', T_d'', T_q'', T_a, T_D in seconds for $\omega_r = 2\pi \cdot 60$ rad/sec.

Solution

From Equation 7.175, the subtransient d axis reactance x_d' is as follows:

$$x_d' = x_{sl} + \cfrac{1}{\cfrac{1}{x_{ad}} + \cfrac{1}{x_{fl}}} = 0.12 + \cfrac{1}{\cfrac{1}{1.5} + \cfrac{1}{0.15}} = 0.25636 \text{ P.U.}$$

From Equation 7.177, x_d'' is as follows:

$$x_d'' = x_{sl} + \cfrac{1}{\cfrac{1}{x_{ad}} + \cfrac{1}{x_{Dl}} + \cfrac{1}{x_{fl}}} = 0.12 + \cfrac{1}{\cfrac{1}{1.5} + \cfrac{1}{0.04} + \cfrac{1}{0.15}} = 0.1509 \text{ P.U.}$$

From Equation 7.178,

$$x_q'' = x_{sl} + \cfrac{1}{\cfrac{1}{x_{aq}} + \cfrac{1}{x_{Ql}}} = 0.12 + \cfrac{1}{\cfrac{1}{0.9} + \cfrac{1}{0.05}} = 0.16736 \text{ P.U.}$$

$$x_2 = \frac{x_d'' + x_q''}{2} = \frac{0.1509 + 0.16736}{2} = 0.15913 \text{ P.U.}$$

or

$$x_2 = \sqrt{x_d'' \cdot x_q''} = \sqrt{0.1509 \cdot 0.16736} = 0.158917 \text{ P.U.}$$

The time constants are calculated from Equation 7.180 through Equation 7.184 and Equation 7.187:

$$T_d' = T_f \cdot \frac{x_d'}{x_d} = \frac{1.5 \cdot 0.15}{0.006 \cdot 2\pi \cdot 60} \cdot \frac{0.25636}{(1.5 + 0.12)} = 0.115 \text{ (seconds)}$$

$$T_D = \frac{\left(x_{Dl} + \cfrac{1}{1/x_{ad} + 1/x_{fl}} \right)}{r_D \cdot \omega_n} = \frac{\left(0.05 + \cfrac{1}{1/1.5 + 1/0.15} \right)}{0.02 \cdot 2\pi \cdot 60} = 0.024716 \text{ (seconds)}$$

$$T_d'' = T_D \cdot \frac{x_d''}{x_d'} = 0.024716 \cdot \frac{0.1509}{0.25636} = 0.01458 \text{ (seconds)}$$

$$T_q'' = \frac{\left(x_{Ql} + x_{aq}\right)}{r_Q \cdot \omega_n} \cdot \frac{x_q''}{x_q} = \frac{\left(0.05 + 0.9\right)}{0.022 \cdot 2\pi \cdot 60} \cdot \frac{0.1676}{0.9} = 0.02133 \text{ (seconds)}$$

$$T_a = \frac{2\,x_d'' \cdot x_q''}{r_s\left(x_d'' + x_q''\right) \cdot \omega_n} = \frac{0.1509 \cdot 0.16736}{0.003 \times 0.15913 \cdot 2\pi \cdot 60} = 0.140 \text{ (seconds)}$$

The total no-load excitation time constant T_f (Equation 7.179) is as follows:

$$T_f = \frac{x_{ad} + x_{fl}}{r_f \cdot \omega_n} = \frac{1.5 + 0.15}{0.006 \cdot 2\pi \cdot 60} = 0.7254 \text{ (seconds)}$$

7.17 Electromagnetic Field Time Harmonics

In order to perform well, when connected to the power system, the open-circuit voltage waveform has to be very close to a sine wave. Standards limit the time harmonics, traditionally through the so-called telephonic harmonic factor (THF): 5% up to 1 MW, 3% up to 5 MW, and 1.5% above 5 MW per unit.

Today, "grid codes" specify total harmonic distortion (THD) to 1.5% for SGs in near 400 kV power systems and 2% in near 275 kV power systems. There are proposals to raise these limits to 3% (3.5%).

To analyze possibilities to reduce emf THD, let us start with its expression:

$$E = \omega_1 \cdot \sum_{\nu=1}^{\infty} K_{W_\nu} \cdot W_a \cdot \Phi_\nu$$

$$\Phi_\nu = \frac{2}{\pi} \cdot \frac{\tau}{\nu} \cdot B_{g\nu} \cdot l_i \tag{7.189}$$

$$K_{W\nu} = K_{d\nu} K_{y\nu} = \frac{\sin\left(\upsilon\pi/6\right)}{q \cdot \sin\left(\upsilon\pi/6q\right)} \cdot \sin\left(\frac{\nu \cdot y}{\tau} \cdot \frac{\pi}{2}\right)$$

For fractionary q windings,

$$q = b + c/d = \left(bd + c\right)/d$$

$$K_{d\nu} = \frac{\sin\left(\upsilon\pi/6\right)}{\left(bd + c\right) \cdot \sin\left(\upsilon\pi/6\left(bd + c\right)\right)} \tag{7.190}$$

So, the harmonics occur in the airgap flux density (B_{g1}) first.
They may be reduced by the following:

- Adjusting the ratio of rotor pole shoe span τ_p per pole pitch τ: $\alpha_i = \tau_p/\tau$ in salient pole rotors
- Varying the airgap from g to g_{max} from center to margins in the salient pole rotor shoe
- Adjusting the large (central) tooth τ_p per pole pitch τ ratio in nonsalient pole rotors with uniform airgap

The form (harmonics) coefficients in the excitation airgap flux density for constant airgap are as follows:

$$K_{fv} \approx \frac{4}{\pi \cdot v} \sin\left(v \cdot \frac{\tau_p}{\tau} \cdot \frac{2}{\pi}\right) \quad - \text{salient poles} \qquad (7.191)$$

$$K_{fv} \approx \frac{4}{\pi^2 \cdot v^2} \frac{\cos\left(v \cdot \frac{\tau_p}{\tau} \cdot \frac{2}{\pi}\right)}{1 - v \cdot \frac{\tau_p}{\tau} \cdot \frac{2}{\pi}} \quad - \text{nonsalient poles} \qquad (7.192)$$

It seems that the minimum of harmonics content

$$\frac{\sum\limits_{v>1} E_v^2}{E_1} = \frac{\sum K_{fv}^2}{K_{f1}} \qquad (7.193)$$

caused solely by the airgap flux density harmonics, is obtained in the first case (salient poles) for $\alpha_p =$

$\frac{\tau_p}{\tau} = 0.77 - 0.8$. However, these large values produce too large an interpole excitation flux leakage, and

$\alpha_i \approx 0.7$ is practiced, although occasionally larger.

For the nonsalient poles, $\tau_p/\tau \approx 1/3$ seems adequate, but the precise ratio τ_p/τ may be used to destroy a certain harmonics v:

$$v \cdot \frac{\tau_p}{\tau} \cdot \frac{2}{\pi} = (2K+1) \cdot \frac{\pi}{2} \qquad (7.194)$$

As even harmonics do not normally occur (all pole geometry, airgap, and excitation coils are identical), the harmonics of interest are $v = 3, 5, 7, 9, 11, 13, 15, 17, 19, \ldots$. The first slot-opening-caused harmonic pair $v_c = 6q \pm 1$ may also be the target, especially with integer $q < 5$.

For salient pole machines, the airgap may be varied ideally as follows:

$$\delta(\theta) = \frac{\delta}{\cos p_1 \theta} \qquad (7.195)$$

For such a case,

$$\left(K_{fv}\right)_{g\sin} \approx \frac{2}{\pi} \cdot \left[\frac{\sin(v-1)\alpha_p \pi/2}{v-1} + \frac{\sin(v+1)\alpha_p \pi/2}{v+1}\right] \qquad (7.196)$$

A notable reduction in the fifth and seventh harmonics is obtained (Table 7.2). The augmentation of the third harmonic is not a problem in a three-phase machine.

TABLE 7.2 Airgap Flux Density Harmonics ($\alpha_p = 2/3$)

	K_{f1}	K_{f3}	K_{f5}	K_{f7}
Constant gap	1.105	0	0.221	+0.158
Inverse sine gap	0.941	0.137	0.137	+0.069

In reality, airgap variation under pole shoes is caused by lower radius rotor pole machining. FEM should be used to quantify the "exact" effect on airgap flux harmonics.

The next step in reducing emf harmonics is the proper design of the stator winding. One solution is the reduction of K_{dv} and K_{yv} for key harmonics.

An increase in integer q above five does not produce a notable decrease in $(K_{dv})_{v \geq 5}$, not to mention K_{d3}, which is almost independent of q and large (around 0.67). But, $q = 2, 3$ produces significantly higher harmonics. The worst situation, $K_{dv_c} = 1$, takes place for the slot harmonics $v_c = 6K_q \pm 1$.

Raising the order of the first slot harmonics implies larger integer q ($q \geq 5$) or fractionary $q = b + c/d = (bd + c)/d$. In this case, the first slot harmonic is $v_c = 6 (bd + c) \pm 1$.

One more way to reduce the emf harmonics is to cancel (reduce) the fifth and seventh harmonics by chorded coils two-layer windings:

$$\sin\left(v \cdot \frac{y}{\tau} \cdot \frac{\pi}{2}\right) = 0 \tag{7.197}$$

$$v \cdot \frac{y}{\tau} \cdot \frac{\pi}{2} = K_n \cdot \pi \tag{7.198}$$

For $y/\tau = 0.833 = 5/6$, the best reduction of fifth and seventh harmonics takes place:

$$K_{y5} = \sin\left(5 \cdot 0.833 \cdot \frac{\pi}{2}\right) = 0.256$$

$$K_{y7} = \sin\left(7 \cdot 0.833 \cdot \frac{\pi}{2}\right) = 0.2624$$

A coil chording of about 5/6 may be obtained easily with a large q.

The third harmonic has to be kept below 5% of the fundamental to avoid false tripping of relays for differential protection when an SG is connected or disconnected to a bus bar, with both systems earthed to allow for triple-frequency currents to flow to the ground through neutral points.

It should be mentioned that the stator mmf harmonics due to the location of stator coils in slots produces mmf harmonics of orders $v = 6K \pm 1$, that is, $-5, +7, -11, +13$. These space harmonics do not produce time harmonics in the emf, but produce additional losses in the rotor. This is why they have to be reduced through increased or fractionary q.

7.18   Slot Ripple Time Harmonics

In certain conditions, the airgap permeance variation due to slot openings may produce higher harmonics, known as slot ripple, in the open-circuit emf wave.

The stator slot opening airgap magnetic permeance in interaction with the field mmf fundamental produces the slot ripple emf effect (Figure 7.30):

The excitation (rotor) mmf fundamental F_{f1}, with respect to stator, is written as follows:

$$F_{f1}\left(\theta_s\right) = F_{f1m} \cdot \sin\left(p_1 \cdot \theta_s - \omega_r \cdot t\right) \tag{7.199}$$

The airgap magnetic conductance variation is
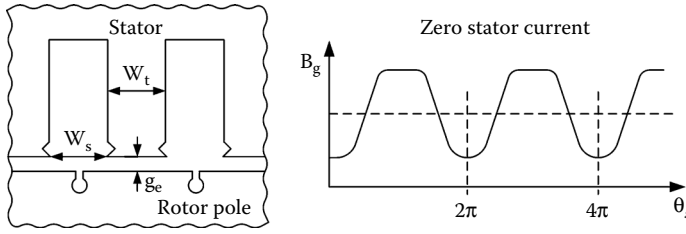
FIGURE 7.30 Slot-opening permeance variation-caused flux density pulsations.

$$P_g = \frac{\mu_0 \cdot K_{fm}}{g} \cdot \sin \nu_1 N_s \theta_s \tag{7.200}$$

The airgap flux density B_g is

$$B_g = P_g \cdot F_{f1} =$$

$$= \frac{\mu_0 \cdot K_{fm}}{g} \cdot F_{f1m} \cdot \left\{ \cos\left[\left(\nu_1 N_s - p_1\right)\theta_s + p_1 \cdot \omega \cdot t \right] - \cos\left[\left(\nu_1 N_s + p_1\right)\theta_s - p_1 \cdot \omega \cdot t \right] \right\} \tag{7.201}$$

For $\nu = 1$, the first airgap permeance harmonic is considered, while for $\nu_1 = 2$, the second one comes into play. Both are important.

If the rotor damper bar pitch τ_d corresponds to a division of circle by $N_s - p_1$ or $N_s + p_1$, then the currents induced by the flux density pulsation due to $\nu_1 = 1$ in the rotor bars are zero. This is why $\tau_s = \tau_r$ (stator slot pitch ≈ damper bar pitch) produces good results.

In addition, with a complete end-ring, rotor-damper-bar-induced currents may flow between adjacent poles if

$$\frac{N_s}{p_1} \pm 1 = 2K_o \pm 1 \tag{7.202}$$

That is, when N_s/p_1 is an even integer number, there will be induced currents in the rotor bars, due to stator slotting, between poles. These rotor-bar-induced interpolar currents produce their own mmfs:

$$F_{1d} = K_{1d} \cdot \left[\cos\left(p_1 \theta_s - \nu_1 N_s \omega t \right) - \cos\left(p_1 \theta_s + \nu_1 N_s \omega t \right) \right] \tag{7.203}$$

This mmf produces its own reaction flux density in the airgap:

$$B_{d1} = K_{1d} \cdot \left[\cos\left(p_1 \theta_s - \left(\nu_1 N_s + p_1\right)\omega t \right) - \cos\left(p_1 \theta_s - \left(\nu_1 N_s - p_1\right)\omega t \right) \right] \tag{7.204}$$

It is now clear that this density produces emf time harmonics of the frequency f':

$$f' = \frac{\omega}{2\pi} \cdot \left(\frac{\nu_1 N_s}{p_1} \pm 1 \right) \tag{7.205}$$

To avoid that such time emf harmonics would, in turn, induce pole-to-pole currents in the rotor cage, we need to fulfill the following condition:

$$\frac{\nu_1 N_s}{p_1} \pm 1 = 2K_o \pm \frac{1}{2} \tag{7.206}$$

Such a condition may be met by displacing the groups of bars on each pole from the center line such that the displacement of cage bars between adjacent poles should be 1/2 stator slot pitch.

Now, if the N_s/p_1 ratio is an odd number, the condition in Equation 7.206 is fulfilled automatically. This is not so for the second slot harmonic ($\nu_1 = 2$) when $2N_s/p_1$ is equal to an even number.

With $W_s/g_e > 2$ and $W_t/W_s > 1.5$, the second permeance harmonic may be large. To avoid the slot ripple mmf for $\nu_1 = 2$, this simply means that in choosing the rotor bar pitch τ_d should be half the stator slot pitch τ_s. As this would seem to be too many rotor bars, skewing the stator slots by one half might be the solution.

Fractionary q tends to eliminate slot ripple influence on the mmf, with $\tau_s \approx \tau_r$.

Note that while the above rationale produces intuitive suggestions to reduce emf time harmonics, their verification is now possible using FEM.

7.19 Losses and Efficiency

Four main categories of losses occur in SGs:

- Winding (copper)
- Core (iron)
- Mechanical
- Brush-ring electrical

The winding (copper) losses include stator winding losses and excitation losses (plus exciter losses if the exciter is mounted on the SG shaft).

Core (iron) losses include the stator core fundamental (50[60] Hz) hysteresis, eddy current losses, and additional core losses.

Additional core losses are produced by the field winding mmf (under no load, also):

- On the rotor surface
- On the stator end laminations stacks, in the tightening plate, and, by the stator mmf space harmonics, again on the rotor core surface

Another way to classify the electromagnetic losses is to consider them as no-load losses and short-circuit losses (at given current). Such a division of losses corresponds to practical tests on SGs, where such losses may be measured.

Despite the fact that there are notable differences between short-circuit and full load in terms of magnetic saturation, the combination of no-load and short-circuit losses proves to be adequate in industry. There are approximate analytical expressions to calculate the various components of no-load and short-circuit losses that have stood the test of time in industry. In parallel, FEM was recently applied to calculate various components of losses in SGs.

At least for rotor surface losses, it was recently proved that analytical methods [14] correlate very well with FEM results [15].

7.19.1 No-Load Core Losses of Excited SGs

The no-load core losses of SG consist of the following:

- Fundamental stator core hysteresis losses, p_h
- Eddy current losses, p_{edo}
- Additional rotor pole shoe losses, p_{pso}
- Additional stator core losses in the lamination stacks p_{eFe10}

There are also additional "core" losses in the stator tightening end plates or pressure fingers and in the axial stator bolts that tighten the stator stack, but these are relatively smaller in a proper design.

The fundamental stator core losses P_{Fe10} are as follows:

$$p_{Fe10} = p_h + p_{edy} = \left[K_h \cdot p_{h0} \cdot \left(\frac{f}{50} \right) + K_{ed} \cdot p_{edo} \cdot \left(\frac{f}{50} \right)^2 \right] \left(\frac{B}{1.0} \right)^2 \cdot G \tag{7.207}$$

where

p_{ho} and p_{edo} = the specific hysteresis and eddy current losses in 1 kg of lamination at 1.0 T and 50 Hz, respectively

G = the weight of laminations material

As known, the flux density B is far from uniform in the stator teeth or yoke. Still, an average has to be considered in Equation 7.207. Even Equation 7.207 is a bit impractical, as it needs separation of hysteresis and eddy current losses, which is not directly available in single frequency tests.

So, in general,

$$p_{Fe10} \approx p_{10} \cdot \left(\frac{f}{50} \right)^{a_f} \cdot \left(\frac{B}{1.0} \right)^{a_b} \cdot G \tag{7.208}$$

where the coefficients a_f and a_b may be found from curve-fitting the losses for a wide range of f (frequency) and B values.

Considering a uniform flux density distribution in stator teeth and yoke, the total stator core losses are as follows:

$$\left(p_{Fe10} \right)_t = p_{10} \cdot \left(\frac{f}{50} \right)^{1.3} \cdot \left[K_{y1} \left(\frac{B_{y1}}{1.0} \right)^2 G_{y1} + K_{t1} \left(\frac{B_{t1/30}}{1.0} \right)^2 G_{t1} \right] \tag{7.209}$$

$B_{t1}/30$ is the tooth flux density at 30% slot height.

K_{y1} and K_{t1} are empirical factors allowing for loss augmentation due to machining the laminations ($K_{y1} \approx 1.3 - 1.6$, $K_{t1} \approx 1.8 - 2.4$). G_{y1}, G_{t1} are the stator yoke and teeth weights. Finally, p_{10} is the specific loss (in watts per kilogram [W/kg]) at 1.0 T and 50 Hz.

When FEM flux distribution is calculated, it is possible to consider the instantaneous values of flux density in each volume element and to add up the losses in these elements. Still, as the machining factors are so important, FEM results in core losses have not yet produced spectacular results in terms of precision over analytical expressions that were corrected over time, based on industrial experience.

Though it is known that for the same frequency and flux density, the specific iron losses (in W/kg) differ in AC and traveling fields, and p_{10} is still obtained from AC field measurements. At least in the stator yoke, the field is mainly of traveling character.

One more question remains here: is it worth it and how do we consider the traveling field and AC field loss regions when determining the stator core losses?

The rotor surface no-load losses p_{pso} are produced by the field-current-caused airgap flux density variation on the rotor pole surface due to stator slot openings.

The frequency of currents induced on the rotor surface is $f_{ps} = N_s \cdot n$, where n is the rotor speed. To reduce these losses, the pole shoes are made, whenever possible, from 1 to 1.8 mm thick laminations.

However, in turbogenerators and in high-speed hydrogenerators, the rotors are made of solid iron. In this case, large airgap g per stator slot opening W_{ss} ratios ($g/W_{ss} \geq 1$) are adopted to secure low flux density pulsations due to slot opening, and thus, moderate pole surface losses result.
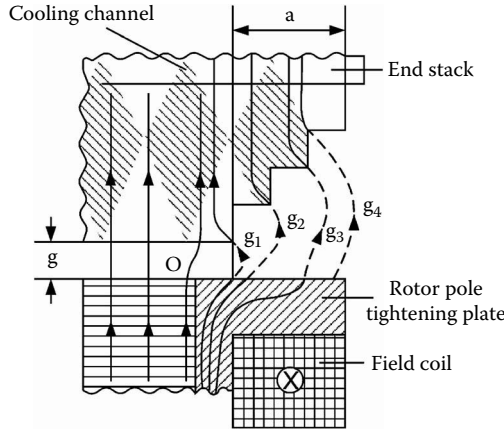
FIGURE 7.31 Excitation flux lines in the end stack of the stator.

Though the situation differs to some extent in salient pole, in contrast to cylindrical pole, rotors, general analytical expressions were produced:

$$p_{pso} = 0.232 \cdot 10^6 \, \Delta \left[\left(K_{C_1} - 1 \right) \cdot B_{go} \cdot \tau_s \right]^2 \cdot 2 p_1 \cdot A_{pole} \cdot \left(N_s \cdot n \right)^{1.5} \qquad (7.210)$$

where

Δ = the lamination thickness in the pole shoe [m]
K_{C1} = the stator slotting Carter coefficient
B_{go} = the no-load airgap flux density [T]
τ_s = the stator slot pitch [m]
A_{pole} = the rotor pole shoe area [m²]
N_s = the number of stator slots
n = the rotor speed in rps

This expression is hardly valid for solid rotor poles, when the depth of field penetration is not only dependent on the frequency ($N_s \cdot n$) but also on flux density level (due to magnetic saturation).

As the stator mmf space harmonics also produce eddy currents on the surfaces of rotor solid poles, we will treat this case in the paragraph on short-circuit (load) losses.

7.19.2 No-Load Losses in the Stator Core End Stacks

As seen in Figure 7.31, a part of airgap excitation flux paths closes through the rotor pole tightening plates. If the latter are long enough, the flux lines meet the end-stack laminations in the stator at 90°. Consequently, the lamination effect does not work anymore, and considerable iron losses are produced in the end stacks. Stepping the airgap in the end stack reduces these losses to some extent.

Considering that the stator and the rotor surfaces are magnetically equipotential, the flux densities B_{g1}, B_{g2}, B_{g3}, corresponding to the airgaps g_1, g_2, g_3 are as follows:

$$B_{g1} = B_{go} \cdot \frac{g \cdot K_c}{g_1}$$

$$B_{g2} = B_{go} \cdot \frac{g \cdot K_c}{g_2} \qquad (7.211)$$

$$B_{g3} = B_{go} \cdot \frac{g \cdot K_c}{g_3}$$

The airgaps g_1, g_2, g_3 are considered half-circles; thus, their lengths are straightforward if the width of end-stack step length a/n is known:

An average axial flux density B_m is

$$B_m = \sqrt{\frac{B_{g1}^2 + 4B_{g2}^2 + B_{g3}^2}{6}} \tag{7.212}$$

The approximate (classical) formula for the end-stack losses in the teeth zone is

$$p_{ezo} \approx \frac{142 \times 10^{-3}}{\rho_{lam}} \cdot \left(B_m \cdot W_{ta}\right)^2 \cdot G_{t1} \tag{7.213}$$

W_{ta} = the width of stator teeth — an average of it.

The teeth may be split in the middle radially, and then $W_{ta} = W_{t1}/2$; thus, the end-stack core losses are notably reduced. The lamination resistivity $\rho_{lam} \approx 0.5 \times 10^{-6}$ Ωm and increases with temperature.

The total no-load core losses p_{Feo} are as follows:

$$p_{Feo} = p_{Fe10} + p_{pso} + p_{ezo} \tag{7.214}$$

7.19.3 Short-Circuit Losses

The short-circuit losses contain quite a few components. The first one is the stator winding loss.

The stator winding (upper) AC resistance loss is as follows:

$$p_{co_{sc}} = 3\left(R_s\right)_{dc} \cdot K_R \cdot I_1^2 \tag{7.215}$$

The coefficient $K_R > 1$ accounts for the frequency (skin) effect on stator resistance.

By design, generally, $K_R < 1.33$, even in large power SGs. In large power SGs, to keep K_R less than 1.33, Roebel bar single-turn windings are used. In Roebel bars, the single turn, divided into many elementary conductors in parallel, uses its transposition along the stack length such that all of the divisions occupy all positions within the turn location; thus, the circulation currents between elementary conductors is zero.

With the circulating currents made zero through transposition, the skin effect coefficient K_R is the same as that for the elementary conductors in series (same current in all):

$$K_{Ra} = \varphi(\xi) + \frac{(n_l^2 - 1)}{3} \cdot \Psi(\xi) \tag{7.216}$$

$$\varphi(\xi) = \xi \cdot \frac{\sinh 2\xi + \sin 2\xi}{\cosh 2\xi - \cos 2\xi} \; ; \; \Psi(\xi) = 2\xi \cdot \frac{\sinh 2 - \sin 2\xi}{\cosh 2\xi - \cos 2\xi} \tag{7.217}$$

$$\xi = \alpha \cdot h_1 \; ; \; \alpha = \sqrt{\pi \cdot f \cdot \mu_0 \cdot \sigma_{co} \cdot \frac{b_1}{W_s}}$$

where

b_1 = the elementary conductor width per layer in slot
n_l = the number of layers in a turn
h_1 = the elementary conductor height
τ_{co} = the copper electrical conductivity

For two-layer winding with chorded coils:

$$K_{Ra} = \varphi(\xi) + \frac{\left(n_l^2 \left(5 + 3\cos\beta \right) - 8 \right)}{24} \cdot \Psi(\xi) \tag{7.218}$$

$\beta = \dfrac{y}{\tau} \cdot \dfrac{\pi}{2}$ is the coil span angle.

With some slots hosting the same phases and some different phases, a kind of average value for K_{Ra} has to be calculated. Notice that for the slots hosting the same phase in both winding layers, the number of elementary conductor layers is $2n_l$ in Equation 7.216.

The skin effect tends to be much smaller in the end connection, and even without transposition in this zone, the skin effect coefficient is smaller than that in the stack (slot) zone.

To secure $K_{Ra} \leq 1.33$, the radial size h_1 of the elementary conductor in the Roebel bar has to be limited.

With the usual number of elementary conductor layers n_l going up to 12 and even more, ξ has to be smaller than unity $\xi < 1$.

For this case,

$$K_{Ra} \approx 1 + \frac{n_l^2}{9} \cdot \xi^4 \cdot \varphi \quad \text{for single-layer winding} \tag{7.219}$$

and, respectively,

$$K_{Ra} = 1 + n_l^2 \cdot \left(\frac{5}{72} + \frac{1}{24}\cos\beta \right) \cdot \xi^4 \quad \text{for double-layer winding} \tag{7.220}$$

where

$\sigma_{co} = 4.8 \cdot 10^7 \ (\Omega m)^{-1}$
$f = 60$ Hz
$b_1/W_s = 0.64$

$$\alpha = \sqrt{\pi \cdot f \cdot \mu_0 \cdot \sigma_{co} \cdot \frac{b_1}{W_s}} = \sqrt{\pi \cdot 60 \cdot 4.8 \cdot 10^7 \cdot 1.256 \cdot 10^{-6} \cdot 0.64} = 85.26 \ (\text{m})^{-1} \tag{7.221}$$

To limit K_{Ra} to 1.33, it may be demonstrated that the maximum elementary conductor height h_1 is as follows [10]:

$$h_1 \approx \frac{15 \text{ mm}}{\sqrt{n_l}} \tag{7.222}$$

The total Roebel bar copper height is $n_l \cdot h_1$:

$$n_l \cdot h_l = h_{bar} \approx 15 \text{ mm} \times \sqrt{n_l} \qquad (7.223)$$

For example, for the number of elementary conductors, $n_l = 16$ per bar, $h_{bar} = 15 \text{ mm} \times \sqrt{16} = 60$ mm, and $h_1 = 15/4 = 3.5$ mm.

With two layers in the windings, the total copper height is $2h_{bar} = 120$ mm. Considering all insulation layers, the total slot height could reach up to 200 mm. As slot width $W_s \leq (30 \text{ to } 40)$ mm, it means that the usual $h_{slot}/W_s < 6.5$.

Most practical cases can be handled by Roebel bars up to highest power per unit (1500 MVA at 28 kV line voltage).

In reality, the number of elementary conductor layers may be increased to 48 when their radial heights go down to almost 2 mm, so even deeper slots may be allowed, once conditions (Equation 7.222 and Equation 7.223) are met.

Note that there are many other formulae corresponding to cases different from Roebel bar (characterized by the zero circulating currents). For example, in the literature [6] for the skin effect losses per coil,

$$K'_{Ra} = \frac{n_l^2 \cdot \xi^2}{9} \cdot n_c^2 \quad \text{for bottom coil side} \qquad (7.224)$$

$$K'_{Ra} = \frac{7 \cdot n_l^2 \cdot \xi^2}{9} \cdot n_c^2 \quad \text{for top coil side} \qquad (7.225)$$

where n_c is equal to turns/coil ($n_c = 1$ for single turn/bar coils).

Besides this, there is an extra loss coefficient due to circulating current K'_{Rc}:

$$K'_{Rc} = \frac{C_e^2 \cdot \xi^4 \cdot n_l^2 \cdot b_e^2}{180} \cdot \left(1 + 15n_c^2\right) \cdot K_{trans} \qquad (7.226)$$

with C_e equal to insulated strand height/bare conductor strand height. Also,

$$b_e = \frac{l - \frac{1}{2}n_c \cdot l_c}{l_{ec}} \qquad (7.227)$$

where
l = the total stator stack length
$1/2 \cdot n_c \cdot l_c$ = half the cooling channel length
l_{ec}–end = connection coil length per machine side

There is no transposition in multiturn coils ($n_c > 1$), and then $K_{trans} = 1$.
For two-turn coils (semi-Roebel transposition), $K_{trans} \approx 0.0784$.
As expected for full Roebel bar transposition, $n_c = 1$ and $K_{trans} = 0$, as discussed earlier in this paragraph.
The total skin effect coefficient K_{Ra} is as follows:

$$K_{Ra} = 1 + K'_{Ra} + K'_{Rc} \qquad (7.228)$$

7.19.4 Third Flux Harmonic Stator Teeth Losses

The third harmonic in airgap flux density, caused jointly by the stator mmf, magnetic saturation, and the field-winding mmf, produces extra iron losses in the stator teeth.

An approximate expression of these losses p_{Fe3} is as follows:

$$p_{Fe3} \approx 10.7 \times p_{10} \left(\frac{f}{50} \right)^2 \cdot \left(\frac{B_{3\sim}}{1} \right)^{1.25} \cdot G_{t1} \tag{7.229}$$

where

p_{10} = the core losses (W/kg) at 1.0 T and 50 Hz
G_{t1} = the stator teeth weight
$B_{3\sim}$ = the third harmonic of airgap flux

To a first approximation, only

$$B_{3\sim} \approx \frac{\left(B_{t1} \right)_{av}}{A_{1s}} \cdot \left(A_{3s} x_d + 1.3 A_{3r} \cdot x_{ad} \right) \tag{7.230}$$

where

$(B_{t1})_{av}$ = the average flux density in the stator teeth
A_{3s} = the third harmonic of stator mmf per pole (A/m)
A_{3r} = the third harmonic of field mmf per pole (A/m)
A_{1s} = the fundamental of stator mmf per pole (A/m)

Still, the magnetic saturation produced third harmonic, in phase with the fundamental, is not included in Equation 7.230. Also, the third flux density harmonic may be damped by the currents induced in the rotor poles or in damper windings. This attention of $B_{3\sim}$ is not considered either.

The slot opening airgap permeance harmonics in the airgap flux density, now produced by the stator mmf, cause rotor surface (and cage) losses p_{pss} (at rated current):

$$p_{pss} \approx K' \cdot \left(\frac{1}{(K_{C1} - 1)} \cdot \frac{2 p_1}{N_s} \cdot x_{ad} \right)^2 \cdot p_{pso} \tag{7.231}$$

where p_{pso} are the same losses but are produced by the excitation mmf (at no load): $K' \approx 0.31$; for $g_{max}/g = 1$; 0.2 for $g_{max}/g = 1.5$; 0.15 for $g_{max}/g = 2.0$; 0.12 for $g_{max}/g = 2.5$. The fifth, seventh, eleventh, thirteenth, and so on, stator mmf space harmonics produce the losses:

$$p_{pss}^a \approx \frac{2.1}{\sqrt[3]{q}} \cdot \left(\frac{x_{ad}}{(K_{C1} - 1)} \cdot K_{ch} \right)^2 \cdot p_{pso} \tag{7.232}$$

where

q = the slots per pole per phase
K_{C1} = the Carter coefficient due to stator slotting
K_{ch} (depending on coil chording) = shown in Figure 7.32

In Reference [15], a more exact analytical approach, now verified by FEM and by some experiments, is given for the no-load and on-load solid rotor surface losses: $(p_{pso}, p_{pss}, p_{pss}^a)$.

We will deal with this approach in some detail here, as it seems to be notable progress in the art.

7.19.5 No-Load and On-Load Solid Rotor Surface Losses

A two-dimensional multilayer field theory was used to develop an analytical formula for solid rotor pole losses in SGs [14]. The losses per unit area of rotor solid pole are as follows:
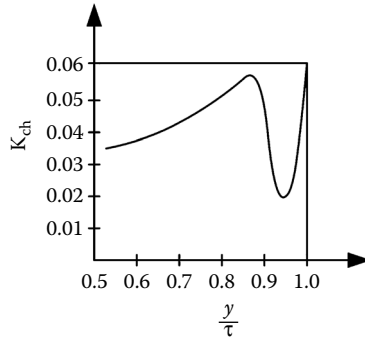
FIGURE 7.32 Coefficient K_{ch} in Equation 7.232.

$$\frac{P_{ps}}{A_{ps}} = \frac{B_{g1p}^2 \cdot \tau_s^2 \cdot f_{el}^2 \cdot \sigma_{Fe}}{4 \cdot \text{Re}(\underline{\gamma}_p)} \cdot K_L \tag{7.233}$$

where B_{g1p} is the first harmonic oscillation flux density in the rotor solid pole. It is a function of airgap no load such as flux density pulsation, B_{g10p}:

$$B_{g1p} = B_{g10p} \cdot \frac{\left[\left(1-\mu_{r3}\right)e^{-\frac{2\pi \cdot g}{\tau_s}}\left(\mu_{r1}-1\right)+\left(1+\mu_{r3}\right)e^{\frac{2\pi \cdot g}{\tau_s}}\left(\mu_{r1}+1\right)\right]}{\left(1-\mu_{r3}\right)e^{-\frac{2\pi \cdot g}{\tau_s}}\left(\mu_{r1}-\frac{\tau_s\left|\underline{\gamma}_p\right|}{2\pi}\right)+\left(1+\mu_{r3}\right)e^{\frac{2\pi \cdot g}{\tau_s}}\left(\mu_{r1}+\frac{\tau_s\left|\underline{\gamma}_p\right|}{2\pi}\right)} \tag{7.234}$$

$$B_{g10p} = \alpha_1 \cdot B_m$$

with

$$\underline{\gamma}_p^2 = \left(\frac{2\pi}{\tau_s}\right)^2 - j \cdot \sigma_{Fe} \cdot 2\pi \cdot f_{el} \cdot \mu_0 \cdot \mu_{r,ab} \tag{7.235}$$

The relative permeabilities μ_{r1}, μ_{r3} refer to rotor pole, and, respectively, to stator core for B_{g10p}. In fact, B_{g1p} replaces B_{g10p} in Equation 7.234 to account for rotor-pole-induced current damping effect.

The ratio K_L is the so-called harmonic factor:

$$K_L = \left(\frac{B_m}{B_{g10p}}\right)^2 \sum_{\nu=1}^{\infty} \frac{1}{\sqrt{\nu}} \cdot \left(\frac{B_{g\nu op}}{B_m}\right)^2 \tag{7.236}$$

where

      α_1 = the flux density oscillation factor (Figure 7.33)
      B_m = the mean flux density in the airgap over one stator slot pitch
      f_{el} = the electrical frequency of induced currents
    $B_{g\nu op}$ = the peak value of the νth harmonic flux density at the rotor pole surface

Typical values for K_L are shown in Figure 7.34 [15].
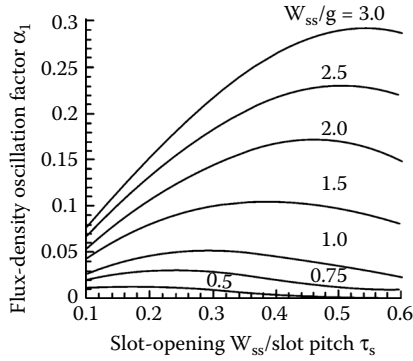
FIGURE 7.33 $\alpha_1 = B_{g10p}/B_m$ ratio: opening/slot.
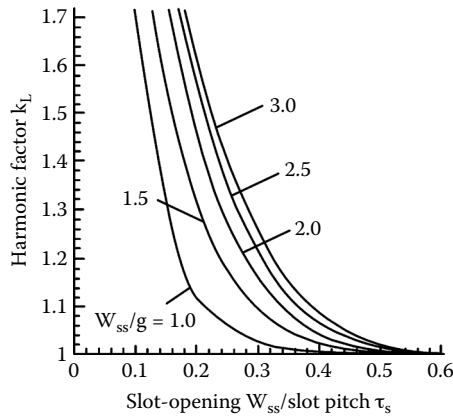
FIGURE 7.34 Harmonic factor K_L vs. slot opening/airgap (W_{ss}/g) and slot pitch W_s/τ_s.

Still, in the inverse of depth of penetration formula (γ_p in 7.235), there is the unique relative permeability of iron $\mu_{r,ab}$, to be determined iteratively from

$$H_o \cdot \sqrt{\mu_0 \cdot \mu_{r,ab}} = \frac{\tau_s}{2\pi} \cdot \left(0.85 \cdot B_{g1p}\right) \cdot \left|\gamma_P\right| \cdot \frac{1}{\sqrt{\mu_0 \cdot \mu_{r,ab}}} \tag{7.237}$$

So, the value of $\mu_{r,ab}(K)$ is calculated for $0.85\, B_{g1p}$, for a given value of B_{g10p}. With this value, from the magnetic material curve B_n/H_n, introduced in the right side of Equation 7.237, a new value $\mu_{r,ab}(K+1)$ is obtained. After a few iterations, with some under relaxation,

$$\mu_{r,ab}(K+1) = \mu_{r,ab}(K) + K_{un}\left[\mu_{r,ab}(K+1) - \mu_{r,ab}(K)\right]$$

$$K_{un} = 0.2 \div 0.3 \tag{7.238}$$

Sufficient convergence is obtained.

It was also shown that the ripple loss per unit area of solid rotor is proportional to the following:

$$\frac{p_{ps}}{A_{ps}} \approx B_{g1p}^2 \cdot \tau_s^2 \cdot f_{el}^{1.5} \cdot K_L \cdot \sqrt{\sigma_{Fe}} \tag{7.239}$$

As the tangential field in the rotor pole dominates, the saturation effect is represented by

$$0.85 \cdot B_{g1p} \cdot \frac{\tau_s}{2\pi} \approx \mu_0 \cdot \mu_{r,ab} \cdot H_o \cdot \frac{1}{\sqrt{\pi \cdot f_{el} \cdot \sigma_{Fe} \cdot \mu_0 \cdot \mu_{r,ab}}}$$

$$H_o \cdot \sqrt{\mu_0 \cdot \mu_{r,ab}} \approx \sqrt{f_{el} \cdot \sigma_{Fe}} \cdot \tau_s \cdot B_{g1p} = S_D \qquad (7.240)$$

In general, the ripple loss per unit area of solid rotor increases linearly with S_D [15].

It is recommended here to check, whenever possible, the flux density values in the airgap and in the solid rotor via FEM eddy current software, in order to secure, by fudge factors, a good estimation level of rotor surface losses.

For special (rated) operation modes, FEM may be used directly.

Additional losses occur in the stator tightening plates made of solid metal and in the teeth pressure fingers. There are again traditional analytical expressions for these losses [6], but, after FEM investigations, it seems that their use should be made with extreme care. The total short-circuit losses p_{sc} are as follows:

$$p_{sc} \approx p_{\cos} + p_{Fe3} + p_{pss} \qquad (7.241)$$

7.19.5.1 Excitation Losses

Basically, the excitation losses contain the following:

- Field winding DC losses:

$$p_{ex} = R_f \cdot I_f^2 \qquad (7.242)$$

- Brush and slip-ring losses (if any):

$$p_b = 2 \cdot \Delta V \cdot I_f \; ; \Delta V < 1\text{V by design} \qquad (7.243)$$

If a machine exciter is used, the total excitation power as seen from the SG, p_{exsh}, is as follows:

$$p_{exsh} = \frac{R_f \cdot I_f^2 + 2 \cdot \Delta V \cdot I_f}{\eta_{ex}} \qquad (7.244)$$

η_{ex} is the total efficiency of the exciter system.

In case of static exciter η_{ex} is the static exciter efficiency. For a brushless exciter, the brush and slip-ring losses are replaced by the rectifier losses, which are, in general, of the same order of magnitudes.

7.19.5.2 Mechanical Losses

Mechanical losses may be approximated to losses at no load, with the SG unexcited ($I_1 = I_f = 0$):

- Bearing losses (axial and guidance bearings in vertical axial SGs)
- Ventilation losses (in the ventilator, its circuit and shaft air friction)

When pumps are used, in direct hydrogen or water cooling, their input power has to be considered.

$$p_{mec} = p_{bear} + p_{vent} + p_{air} \qquad (7.245)$$

Simplified formulae for losses were introduced over the years based on experience.

For air-cooled hydrogenerators with vertical shaft, here are a few such expressions:

- The bearing losses p_{bear} (include both the axial and guidance bearing)

$$p_{bear} = p_{bear}^{axial} + p_{bear}^{guide} \approx \left[9.81 \cdot G_V \cdot U_{bear} + F_m + F_d \cdot U_{bear}^a\right] \cdot \mu_f \tag{7.246}$$

where

G_V = the total vertical mass of turbine and generator rotors plus the axial water–push mass in kilograms

U_{bear} = radial bearing peripheral speed

U_{bear}^a = the axial bearing peripheral speed

F_m = the magnetic pull due to estimated rotor eccentricity

F_d = the mechanical radial force due to eccentricity and mechanical rotational unbalance

$$F_m \approx 0.02 \cdot G_{MT+SG} \cdot 9.81$$

$$F_d \approx 1.256 \times 10^6 \cdot B_{gn}^2 \cdot \alpha_i \cdot D \cdot l_i \cdot \frac{e}{g} \tag{7.247}$$

where

B_{MT+SG} = the turbine plus SG rotor mass

α_i = the ideal rotor pole span ratio

D = the stator bore diameter

l = the stator stack iron length

e = the eccentricity

g = the airgap

B_{gn} = the rated airgap flux density

$e/g \approx 0.1$ to 0.2

The friction coefficient μ_f depends essentially on hydrogenerator speed (in rpm) and on coil temperature at 50°C, $\mu_f = 0.0035$ at $n = 50$ rpm, and $\mu_f = 0.0108$ at $n = 500$ rpm.

- The ventilator plus circuit losses, p_{vent}, may be written as follows:

$$p_{vent} \approx 1.1 \cdot Q_{air} \cdot U_{vent}^2 \tag{7.248}$$

Q_{air} is the airflow rate in cubic meters per second required to evacuate the losses from the SG. U_{vent} is the peripheral average speed of the ventilator.

The rotor air-windage losses p_{air} is as follows:

$$p_{air} \approx C_a \cdot \left(2\pi n\right)^3 \cdot D_r^5 \cdot \left(1 + \frac{5 \cdot l_p}{D_r}\right) \tag{7.249}$$

where

$C_a \approx (1.5 - 3) \cdot 10^{-3}$ = a machine constant depending on rotor smoothness

n = the rotor speed in rps

D_r = the rotor external diameter

l_p = the total length of rotor poles

The total mechanical loss p_{mec} is as follows:

$$p_{mec} = p_{bear} + p_{vent} + p_{air} \tag{7.250}$$

The losses in the machine contain the no-load losses at rated voltage and short-circuit losses at rated current plus the mechanical losses and the excitation losses:

$$\sum losses = p_{Feo} + p_{sc} + p_{mec} + p_{excsh} \tag{7.251}$$

The load losses may be calculated based on no-load and short-circuit losses by adopting an appropriate value for field current I_f, stator current I_1 and the power factor angle φ.

On the other hand, the airflow rate Q_{air} may be calculated from the following:

$$Q_{air} = \frac{\sum losses}{C_a \cdot \Delta T_{air}} \tag{7.252}$$

where

$\sum losses$ = the total SG losses that have to be evacuated by the cooling air
$C_a \approx 1.1 \times 10^3$ Ws/m²C = the heat capacity factor of air
ΔT_{air} = the air warming temperature differential

7.19.5.3 SG Efficiency

The SG efficiency is defined as the output (electrical)/input (mechanical) power:

$$\eta_{SG} = \frac{\left(P_2\right)_{electric}}{\left(P_1\right)_{mechanical}} = \frac{\left(P_2\right)_{electric}}{\left(P_2\right)_{electric} + \sum losses} \tag{7.253}$$

In industry, the efficiency is calculated for five load ratios: 25%, 50%, 75%, 100%, and 125%.

The voltage and speed are constant, so the no-load losses (or iron losses, mainly) p_{Feo} and mechanical losses p_{mec} remain constant. The "on-load" or the "short-circuit" losses p_{sc} are stator current related, and the excitation losses p_{exch} vary with their currents squared:

$$p_{sc} = p_{scn}\left(\frac{I_1}{I_n}\right)^2 \quad ; \quad K_{load} = \frac{I_1}{I_n}$$

$$p_{excsh} = p_{exchn}\left(\frac{I_f}{I_{fn}}\right)^2 + p_{brush} \cdot \left(\frac{I_f}{I_{fn}}\right) \quad ; \quad P_2 = S_n \cdot \frac{I_1}{I_{1n}} \cdot \cos\varphi \tag{7.254}$$

So, the efficiency at part load is

$$\eta_{SG} = \frac{K_{load} \cdot S_n \cdot \cos\varphi}{K_{load} \cdot S_n \cdot \cos\varphi + p_{Feo} + p_{mec} + p_{scn} \cdot K_{load}^2 + p_{exch} \cdot \left(\frac{I_f}{I_{fn}}\right)^2 + p_{brush} \cdot \left(\frac{I_f}{I_{fn}}\right) + p_{stray}} \tag{7.255}$$

Stray load losses are added.

Knowing all steady-state machine parameters, for each value of output power and $\cos\varphi$, stator and field currents may be calculated after the power angle δ_V is determined along the way (Chapter 4). With losses calculated as in previous paragraphs, the total losses and efficiency at different load levels may be predetermined to assess the design goodness from this crucial point of view.

Note that in direct-cooling SGs, the winding losses tend to dominate the losses in the machine, while for indirect cooling, the nonwinding losses tend to be predominant.

It follows that for indirect cooling, the efficiency tends to be maximum above rated load and below rated load for direct cooling.

7.20 Exciter Design Issues

The excitation system supplies the SG field current to control either the terminal voltage or the reactive power to set point.

As already detailed in Chapter 6, the excitation system is provided with protective limiters.

For operation tied to weak power systems, power system stabilizers (PSSs) are used to dampen the oscillations in the range from 0.5 Hz to 2 ÷ 5 Hz.

The specification of excitation systems is guided by IEEE standards 421 [16].There are two key factors that define an excitation system: the transient gain and the ceiling forcing ratio (maximum/rated voltage at SG excitation winding terminal). The transient gain has a direct impact on small signal and dynamic stability. Too small a transient gain may fail to give the desired performance, while too high a transient gain produces faster response but may result in dynamic instability during faults. In this latter case, the PSS may have to be considered. The transient gain refers to frequency of generator oscillations in the range of a few tenths of hertz to a few hertz.

Traditionally, excitation system controllers consisted of a high steady-state gain to secure low steady-state control error and a lag–lead compensator to provide transient gain reduction.

In today's digital control systems PI, PID or more advanced controllers such as Fuzzy Logic, H$_\infty$, sliding-mode, etc. are used.

Steady-state gains of 200 P.U. provide for ±0.5% steady-state regulation.

Transient gains vary, in general, from 20 to 100 with lower values for weak power systems, to avoid local mode power system oscillations (in the 1 to 2 Hz range).

The excitation system ceiling voltage also has an impact on transient stability.

For static excitation systems, 160 to 200% of rated field voltage is set for design to preserve stability after the clearing of a three-phase fault on the higher voltage side of the SG step-up transformer.

As lowering the SCR seems to be the trend in SG design today, to increase SG efficiency, increasing the excitation voltage ceiling becomes the pertinent option to preserve transient stability desired performance.

The three-phase fault clearing critical time (CCT) for constant ceiling forcing decreases when the SCR decreases, both for a lagging and for a leading power factor. For leading power factor, however, the CCT is even smaller.

The required field voltage ceiling ratio has to be specified after critical clearing time limits are checked for lagging and leading power factor for the actual power system area where the SG will work. Such a local system is characterized by the percent reactance looking out from the SG: 10% is a strong system and 40% is already a weak system.

Practical limits of ceiling (maximum) voltage are about 500 V_{dc} in general. But this maximum voltage may correspond to a 3 P.U. ceiling voltage ratio.

AC brushless exciters might allow for a smaller ceiling voltage ratio, as they are less affected by power system faults.

In respect to exciter design, we will treat here only the AC brushless exciter, as it comprises two synchronous generators of smaller power rating.

An alternative brushless exciter, operational from zero speed, is made from a wound rotor induction machine with rotor winding output that is diode rectified and supplies the SG excitation, while its stator winding is supplied at variable (controlled) voltage through a thyristor voltage amplitude controller (Figure 7.35a).

The frequency f_2 of the voltage induced in the AC exciter rotor is $f_2 = f_1 + n \cdot p_{1ex}$ and increases with speed, above $f_1 = 50(60)$ Hz.
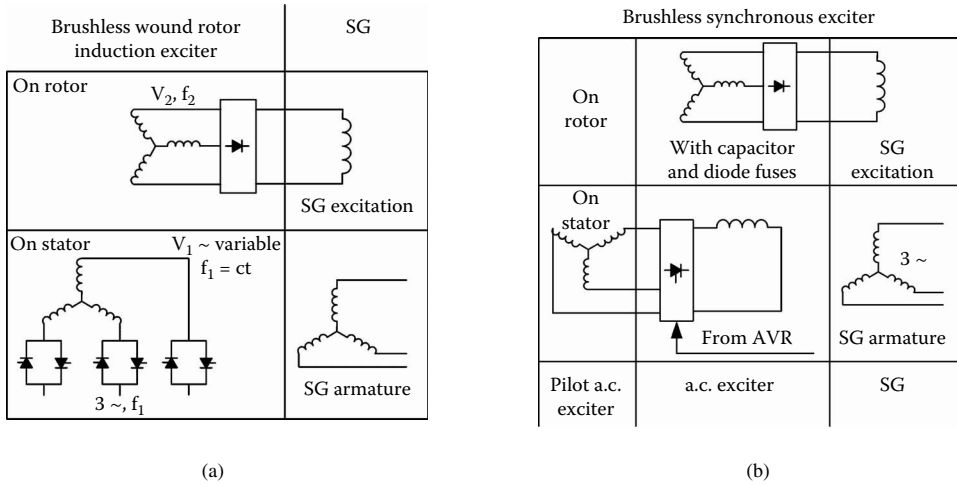
FIGURE 7.35 Brushless alternating current exciter: (a) induction exciter and (b) synchronous exciter.

As the induced rotor voltage amplitude V_2 also tends to increase with f_2, when speed increases, the voltage V_1 in the stator has to be reduced through adequate control.

At zero speed, all the power transmitted to the SG excitation comes from the exciter's stator; it is electrical, in other words.

As the speed increases, more of the excitation power comes from the shaft, especially with increasing the exciter's pole pair number $p_{1exc} > 3$.

The induction exciter voltage response is expected to be rather fast. However, the exciter stator winding has to deliver the whole power of SG excitation, should it be needed at zero speed, as in the case of a pump-storage plant. The induction exciter is also used in industry.

A typical AC brushless exciter contains a PM synchronous pilot exciter with output that is electronically controlled after rectification to supply the DC excitation of the inside–out synchronous exciter with a diode rectified output (with the rectification on the rotor) that is connected directly to the excitation circuit of the SG (Figure 7.35b).

This way, no brushes or an additional power source is involved. However, if faster response is needed, the excitation circuit of the pilot exciter may be supplied directly from a separate power source through power electronics, with a control variable that is the output of the SG excitation control.

The pilot PM alternator is designed for frequencies in the range of 180 to 450 Hz to cut the rectified output voltage pulsations. Also, the AC exciter is designed with a rather large number of poles $2p_1 = 6 - 8$, again to secure a rated armature frequency higher than 100 Hz; thus, low pulsations in the field-winding current and small volume of the AC exciter magnetic circuit (armature yoke, especially) are found.

The relationship between AC exciter phase voltage per phase V_{1s} (RMS value) and the rectified field-winding voltage V_f is as follows:

$$V_{1s} \approx V_f / 2.34 \tag{7.256}$$

$$I_{1s} \approx 0.780 \cdot I_f \tag{7.257}$$

The voltage regulation of the diode rectifier in SG excitation circuit is neglected. If better precision is needed, rectifier voltage regulation has to be considered, as in Chapter 6 (Figure 6.33).

Equation 7.256 and Equation 7.257 imply an ideal (lossless) rectifier.

The AC exciter should be available to produce the ceiling voltage V_{fmax} at the SG excitation terminals, also, during steady state, to allow for the I_{fn} (the rated load excitation current that corresponds to rated SG output power and power factor).
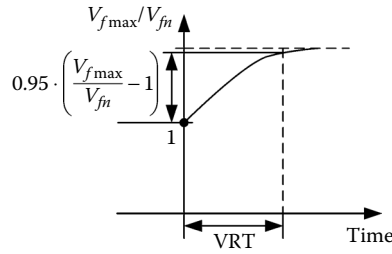
FIGURE 7.36 Voltage response time (VRT).

Besides rated and maximum field voltage and current ratings V_{fn}, I_{fn} for steady state and V_{fmax}, I_{fmax} for transients, the AC exciter has to provide a certain response time in providing the ceiling voltage V_{fmax} from the rated value V_{fn}.

Equally important, the excitation system has to have high efficiency at moderate weight and costs and be reliable. Here, a general design method for a brushless AC exciter is detailed. Optimization design issues will be treated later in this chapter for the SG in general.

7.20.1 Excitation Rating

As already alluded to, the AC exciter rating is given by V_{fn}, I_n for steady state, and V_{fmax}, I_{fmax} for transients.

The exciter response time is also specified. The SG may be required to operate at rated megavoltampere for 105% terminal voltage. As in such a case the magnetic saturation level in the SG increases notably, the continuous power rating of the AC exciter will increase more than 5%. Sometimes, the exciters have redundant circuitry.

The voltage response time (VRT) is the time in seconds for the excitation voltage to travel 95% of the difference between V_{fmax} and V_{fn} (Figure 7.36).

Today's AC exciter systems are required to have VRT < 100 msec under full field current load.

7.20.2 Sizing the Exciter

Sizing the exciter is similar to that process of the main SG, as already developed in this chapter. There are some peculiarities, though [17].

The reduction in voltage response time leads to severe limitation in the AC exciter subtransient reactance x'_d below 0.3. It may also be needed to provide for a rather strong cage in its stator to reduce the commutation reactance $x_c = (x''_d + x''_q)/2$ in the diode rectifier for lower voltage regulation and allowance for higher rated frequency (low yoke height).

As a good part of x'_d is the armature leakage inductance, reducing the latter is paramount. Wide and not so deep armature slots and short end connections (chorded coils) are practical ways to achieve this goal. Also, the leakage inductance of the AC exciter circuit has to be reduced, star connection of AC exciter armature phases is preferred in order to eliminate the third harmonic current and thus avoid limitations on coil span. It also requires a smaller number of slots (with two turns/slot) for the same output DC voltage V_{fn}.

A smaller number of slots means lower manufacturing costs.

Two or more current paths in parallel may be necessary to produce the required V_{fmax} (V_{fn}).

7.20.3 Note on Thermal and Mechanical Design

So far, the various no-load and load losses were calculated. To remove the heat produced by losses, it is necessary to adopt and design appropriate cooling systems.
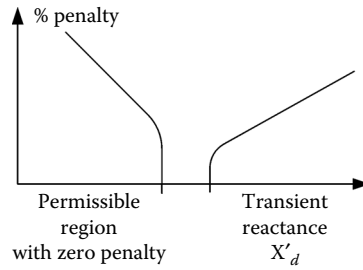
FIGURE 7.37 Penalty function for X_d'.

As already mentioned, SG cooling may be indirect (with air or hydrogen) and direct (with water or hydrogen). Evaporative cooling is gaining in popularity, as well. There are many specific solutions as the power and speed (in rpm) goes up.

Analytical models are generally used for thermal design, but FEM is increasingly used for the scope. The same rationale is valid for the mechanical design.

As the thermal and mechanical limitations observation influences the machine reliability and safety, their summarily treatment is not to be accepted. A detailed such analysis, on the other hand, needs rich space. This is why we stop here, drawing attention to specialized design books [5, 6], while noticing that all manufacturers have their proprietory thermal design methods for SGs.

Forces, noise, and vibration are other important issues in SG design. See, for starters [6, 18].

7.21 Optimization Design Issues

So far, we presented analytical expressions to do the dimensioning of an SG that fulfills given specifications. Also, the computation of resistances, inductances, and losses was investigated. Finally, the cost of active materials may be computed.

This process may be described as the general design, and computer programs may be produced to mechanize it.

The general design produces a realistic (feasible) SG. It is a good starting point for optimization design. Optimization design requires the following:

- An initial practical design
- A machine model to calculate the parameters and performance (and objective functions) for given geometry and various design parameters
- A set of design variables, such as the following:
  - Stator bore diameter is D_{is}
  - Slot width is W_{ss}
  - Slot/tooth width ratio is W_{ss}/W_t
  - A (A/m) is the stator current loading
  - W/m^2 is the stator surface loading
  - Flux density in stator teeth: B_{ts}
  - Flux density in stator yoke: B_{ys}
  - Flux density in the rotor pole body: B_p
  - Thickness of field coil: W_c
  - W/m^2 rotor surface loading

For each variable, minimum and maximum values are set:

- A single or multiple cost function, such that generator costs plus the loss of capitalized costs is a way to accommodate various constraints (such as $X_d' < X_{d\,\max}'$, various temperature limitations, SCR < SCR max, etc.) through penalty terms added to the cost function (Figure 7.37).
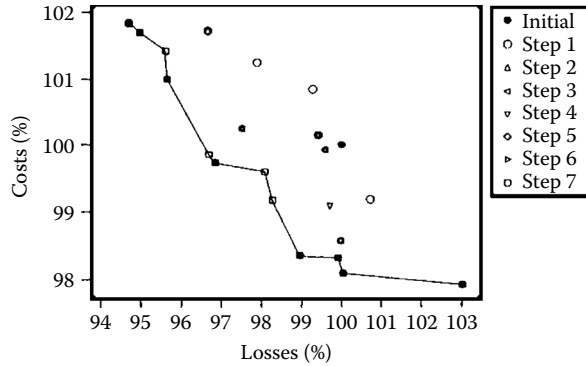
FIGURE 7.38 Pareto front (squares and line) and the initial solution (solid circle).

- A mathematical method (or more) to search for the optimal design [19] that produces the lowest cost function, observing the constraints, and being able to deal with some design variables that are integer numbers (number of slots N_s, number of turns in the coil, etc.).
- There is a plethora of optimization methods of linear and nonlinear programming, indirect and direct, with constraints, deterministic, stochastic, and evolutionary plans.

Such a complete optimization design software, with long use, based on the Monte Carlo optimization method, is described in Reference [20].

More recently, evolution strategies and genetic algorithms (G.A.) were applied to optimize the subdesign of SGs. By subdesign, we mean here a partial problem in design, such as the modification of rotor pole or of stator slot geometry to minimize losses and production costs [21].

When the cost (objective) function may not be stated in terms of a scalar-type function, Pareto optimal sets are used. Pareto sets contain a number of solutions (designs) that are equivalent to each other in terms of trade-offs, that are so common in SG design.

Finding Pareto optimal sets of solutions to the problem, with stator slot and rotor pole dimensions as design variables, and losses and production costs to be simultaneously minimized, constitutes such an optimization subdesign problem in SGs. For such a problem, the design variables could be as follows:

- Geometry and number of copper strands
- Dimensions of rotor pole
- Dimensions of field coil
- Pitch and diameter of damper cage bars
- Airgap

Typical constraints to be inforced through penalty functions are as follows:

- $X_d' < X_{d\,max}'$, $X_d'' > X_{d\,min}''$
- Temperature rise
- Clearance between adjacent field coils
- Mechanical stresses in rotor poles and their dovetails
- Admissible flux density and current density limits

Evolutionary method algorithms of optimization become necessary in nonsmooth and model-based objective (cost) functions. This is the case for SGs.

Figure 7.38 [21] shows the Pareto front (squares and line) with the initial solution (solid circle), while the other points are dominated solutions.

Two simultaneous goals — minimum cost and minimum losses (5000 \$/kW of losses) — were followed in this case.

The G.A. were proven to produce better results [20] than evolutionary strategies.

7.22 Generator/Motor Issues

Pump storage is used in some hydropower plants to replenish the water in the forebay each day and then deliver electric power during the peak demand hours. During the pumping mode, the SG acts as a motor. To start such a large power motor, even on no load, a pony motor was traditionally used. It is also practical to use the back-to-back generator and motor starting when a unit works as a generator and, during its acceleration to speed, it supplies a motor unit and the two advance synchronously to the rated synchronous speed.

A single generator may supply one after the other all pump-storage units. An induction-motor-mode starting with self-synchronization is also feasible, at reduced voltage for large power units.

As the friction torque may be reduced, by refined high-pressure oil bearings, to less than 1% of rated torque, the power required to start the motor, with the waterless turbine — pump, was notably reduced.

It is thus feasible to use a lower relative power rating static power converter to start the motor and disconnect the converter after the motor has been self-synchronized.

An SG designed to be used also as a motor for water pump storage undergoes about one start a day as a motor and one synchronization a day as a generator.

Self-synchronization for motoring and automatic synchronization for generation imply notable transients in currents and torque, and the machine has to be designed to withstand such demanding conditions.

Typically, the direction of motion is changed for motoring as required by the turbine pump. High wicket gate water leakage may cause the "waterless" unit to start rotating still in the generator direction. To avoid the transients that the static power converter would incur in initiating the starting as a motor, the machine has to be stalled before beginning to accelerate it on no load, in the motoring direction.

Asynchronous self-starting is used for low and medium power units, albeit using a step-down autotransformer or a variable reactor to reduce starting currents. For units above 20 MW, pony motor, generator motor back to back, or static power converter starting should be used.

The development of multiple-level voltage source converters with IGBTs (up to 4.5 MW/unit) [22] and with GTOs or MCTs (up to 10 MW/unit and above) [23] might change the picture.

For the low power range (up to 3 MW), it is possible to use a bidirectional voltage source IGBT converter, designed at a generator motor rating, that will not only allow startup for the motoring, but will also provide for generating and motoring at variable speed (to exploit optimally the turbine — pump). It is known that the optimal speed ratio between pumping and turbining is about 1.24. For high power, the multilevel voltage source GTO and MCT converters may replace the controlled — rectifier — current source converters that are used today to accelerate pump-storage units (above 20 MW or so) and then self-synchronize them to the power grid.

The multilevel PWM back-to-back IGBT, GTO, MCT converters provide quality starting while inflicting lower harmonics both on the power line and on the motor side (Figure 7.39a and Figure 7.39b). They are smaller in size and provide controllable (unity) power factor on the line side.

As there is a step-up transformer between the static power converter and the machine, the starting cannot be initiated from zero frequency but instead, from 1 to 2 Hz. This will cause transients that explain the necessary oversizing of the static power converter for the scope.

It goes without saying that to start the motor as a synchronous motor, a static exciter is required, because full excitation is needed from 1 to 2 Hz speed. The static converters might be controlled for asynchronous starting (up to a certain speed), and thus, their kilovoltampere rating has to be increased.

Note that the "ideal" solution for pump storage is the doubly fed induction generator motor that will be studied in *Variable Speed Generators.*

7.23 Summary

- By SG design, we mean here dimensioning to match given specifications of performance with constraints.
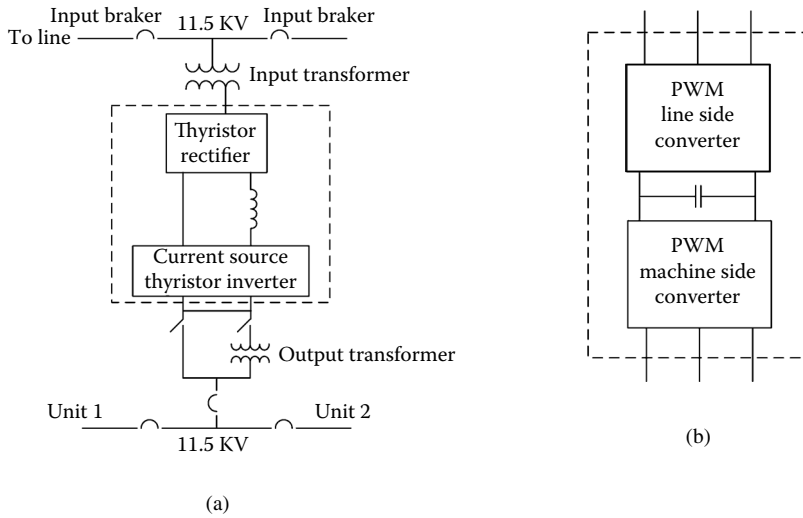
FIGURE 7.39 Static converter starting in pump-storage plants: (a) with rectifier-current (one-phase) source inverter and (b) with voltage source converter.

- Specifying SGs to be connected to a power system is an object of standardization. The proposed consolidated C 50.12, C 50.13 ANSI standards are typical for the scope.
- Besides manufacturers' standards, grid codes have been issued to tailor SG performance to power system typical and extreme operation modes. There may be conflicts between those two kinds of specifications, and mitigation efforts are required to harmonize them.
- The first specification item is the short-circuit ratio (SCR) — the ratio between the short-circuit and rated current or the inverse of d axis synchronous reactance in P.U. ($1/x_{dsat}$). A larger SCR requires a larger airgap and, finally, a larger excitation mmf and losses, while it increases the peak power and thus the static stability. As the transmission line reactive x_c at generator terminal increases, the beneficial effect of a larger SCR on static stability diminishes. A large x_c characterizes a weak power system. Today's trend is to reduce SCR to 0.4 ÷ 0.6, while preserving the static stability by the ever-faster response of contemporary exciter systems.
- The second specification issue is the transient reactance x'_d that influences the transient stability. The smaller x'_d, the better, but there are limits to it due to machine geometry required to produce the design power.
- Rated power factor is essential in SG design: the lower the rated power factor, the larger the excitation power. In general, $\cos\varphi_n$: 0.9 to 0.95 (overexcited).
- The maximum absorbed (leading) reactive power limit is determined by the SCR and corresponds to maximum power angle and to the stator end-core temperature limit.
- Fast control of excitation current is required to preserve SG stability and control the terminal voltage. Today's ceiling voltage ratio for excitation systems is 1.6 to 3.0. The limit is, in fact, determined by the heavy saturation of an SG magnetic circuit. A response time of 50 msec "producing" the maximum ceiling voltage is required to qualify the response of the excitation system as fast. Even with brushless rotary machine configurations, such a response is feasible. Static exciters are much faster.
- Voltage and frequency variations are limited to contain the saturation level in the SG. A ±2 to 3% in both should be provided at rated power. Higher values are to be accepted for a limited amount of time to avoid SG overheating. These requirements are standardized or agreed upon between manufacturers and users.
- Negative phase-sequence voltages and currents are limited by standards to limit rotor damper cage and excitation additional losses (and overtemperatures). Negative sequence voltage is limited to

about 1% ($V_2/V_1\%$), while the current negative sequence i_2/i_1 may reach 4 to 5% and depends on the SG negative sequence reactance x_2 plus the step-up transformer short-circuit reactance x_T.

- Total harmonic distortion (THD) limits are prescribed by grid codes to 1.5 to 2%, with proposals to raise them to 3 to 3.5% in the future.

- The temperature basis for rating power is paramount in SG design. It is between observable and hot-spot temperature. The observable temperature limit is set such that the hot-spot temperature is below 130°C for class B and 155°C for class C insulation systems. The rated coolant temperature also has to be specified. As the cold coolant temperature varies for ambient-following SGs, it seems reasonable to fix the observable temperature limit for a single cold coolant temperature and calculate the SG megavoltampere capability for different ambient temperatures. The hot-spot temperature will also vary. As the ambient temperature goes up, the SG megavoltampere capability goes down.

- Start–stop cycles have to be specified to prevent cyclic fatigue degradation. For base load SGs, 3000 starts are typical, while 10,000 starts are characteristic to peaking load or other frequently cycled units.

- Starting and operating as a motor (in pump-storage units), faulty synchronizations, forces, armature voltage, and runaway speed ratio, have to be specified in a pertinent design.

- The design process consists of sizing the SG in relation to the above-mentioned specifications. The design refers to electromagnetic, thermal, and mechanical aspects. Only electromagnetic design was followed in detail in this chapter. The electromagnetic design essentially comprises the following:
  - The output coefficient stator geometry
  - The selection of number of stator slots
  - The design of the stator core
  - The sizing of salient pole rotors
  - The sizing of cylindrical pole rotors
  - Open-circuit saturation curve computation
  - Stator leakage reactance and resistance computation
  - Field mmf (current) at full load
  - Computation of synchronous reactances x_d, x_q
  - Sizing of damper cage
  - Computation of time constants and transient, subtransient reactances
  - Exciter design
  - Generator/motor design issues
  - Optimization design issues

- The output coefficient C (min kVA/m³) is defined as the SG in kilovoltampere per cubic meter. It is a result of accumulated experience (art) and varies with the power/pole, number of poles pairs, and type of cooling system. The rotor diameter D is computed basically based on runaway speed U_{max}, with given SG synchronous speed and number of pole pairs p_1, for given frequency. The rotor inertia H (in seconds) has to be above a limit value so as to limit the maximum speed of the SG upon loss of electric load, until the speed governor closes the fuel (water) input (unless special fast braking is provided, as is the case of turbogenerators).

- SGs may have integer or fractionary two-layer windings. We refer to q slots/pole/phase as integer or fractionary. Turbogenerators ($2p_1 = 2, 4$) make use of integer q windings in general ($q > 5$ to 6), while hydrogenerators today have fractionary windings. The choice of q determines the number of slots N_s of the stator as $N_s = 6 \cdot p_1 q$. The selection of q also depends on the number of lamination segments N_c that constitute the stator core and on the number of detachable sections N_K in which the core may be divided and wound separately due to the large diameters considered:
  - $N_K = 2$ for $D < 4$ m
  - $N_K = 4$ for $D = 4 \div 8$ m
  - $N_K = 6(8)$ for $D > 8$ m

It is imperative that all N_c segments spread over an integer number of poles N_{ss}. For even N_{ss}, N_s is even and integer q is feasible. For fractionary q, N_{ss} may be an odd number and contain three as a factor.

- For fractionary $q = b + c/d$, symmetrical windings are obtained, in general, for $d/3 \neq$ integer. Windings are made with wave coils and one turn per coil and with lap coils when two or more turns per coil are used.

  - For wave windings,

  $$\frac{3c \pm 1}{d} = \text{integer}$$

  - The noise level is reduced if

  $$3\left(b + \frac{c}{d}\right) \pm \frac{1}{d} \neq \text{integer}$$

  with $c/d = 1/2$ ($b > 3$), the subharmonics are eliminated.

- Apparently, once the value of q is settled, the number of turns per current path is obtained from the stator geometry and the total rated emf $e_t \approx 1.03$ to 1.10 P.U. For one turn (bar) per coil, the number of slots is directly related to the number of turns/path W_a and number of current paths a:

  $$N_s = a \cdot W_a \cdot 3$$

  It is now easy to see how crucial the choice of N_s is as W_a (integer) comes directly from the emf e_t value.

- To size the stator core, the airgap g has to be computed first, as the rotor diameter D_r is already known. Sizing g is directly related to stator-rated linear current loading A, pole pitch τ, airgap flux density fundamental B_{g1}, and the desired x_d (SCR).

- The rated voltage increases with the SG power/unit and is larger for direct cooling. It is, otherwise, decided by the manufacturer. In general, $V_{nline} < 28$ kV, but cable winding 40 to 100 kV SG are in the advance development stage. They lead to the elimination of the step-up transformer that accompanies practically all SGs tied to power systems.

- The salient pole rotors are designed for variable airgap under the pole, to render the airgap flux density more sinusoidal. The maximum to minimum airgap g_{max}/g ratio is up to 2.5. In practice, the radius of the pole shoe shape R_p is notably smaller than rotor radius $D/2$.

- Damper cage design is based on the main assertion that the cage bars total cross area represents 15 to 30% of stator slot area. The damper cage slot pitch τ_d is chosen to reduce losses in the damper cage due to stator mmf space harmonics. For fractionary stator windings ($q = (bd + c)/d$) when $bd + c > q$, it is feasible to chose $\tau_s = \tau_d$ (τ_s, stator slot pitch). For $bd + c < q$ or $q = b + 1/2$, $\tau_s \neq \tau_d$. The damper bars of copper or brass are welded to end-rings with a cross-section that is about half the bars cross-section per rotor pole.

- The cylindrical rotor, made of single or multiple (axially) solid iron rings, is slotted along about two thirds of its periphery to host the field coils. Lower airgap flux harmonics are obtained by placing the field coils in slots, while this is also the only mechanically feasible solution to withstand the centrifugal force stresses. To design the field winding, the rated field mmf is required. As at this stage in design this is not known, a value of 2 to 2.5 times the rated stator mmf per pole is adopted.

- The open-circuit saturation curve may be obtained through an analytical model accounting for magnetic saturation or through FEM.

- The rated field mmf is obtained traditionally through the Potier diagram (Figure 7.24) or through the partial magnetization curves (Figure 7.25). The second method allows for cross-coupling

saturation, while the first one does not and is adequate for cylindrical rotor SGs. Based on the partial magnetization curves method, the synchronous reactances x_d may be determined as functions of i_d and i_q as families of curves. Alternatively, $\Psi_d(i_d,\,i_q)$ and $\Psi_q(i_d,\,i_q)$ may be obtained. Such information is essential in calculating with good precision the rated power angle and steady-state performance of SGs.

- The computation of rotor resistances and various leakage inductances is straightforward if approximate formulae are accepted. They proved adequate in industry, though today, they may be computed by FEM also.
- The solid rotor behaves as an equivalent damper cage with variable parameters. A reliable analytical model to calculate these parameters is presented. This model was recently validated by FEM.
- The various time constants $T'_{do}, T_{do}, T'_d, T''_d, T_a, T_D$ and the transient and subtransient reactances (in P.U.) are straightforward once the synchronous reactance x_d, x_q and all leakage reactances and resistances are defined by analytical expressions. Note that $x'_d < x'_{d\max}$. The negative sequence reactance x_2 is also calculated easily as follows:

$$x_2 = \left(x''_d + x''_q\right)\big/2 \ \ \text{or} \ \ x_2 = \sqrt{x''_d \cdot x''_q}$$

- Emf time harmonics are limited by standards. Higher q, coil chording, and fractionary q are used to reduce emf time harmonics. The variable airgap obtained by shaping the rotor salient poles reduces the fifth and seventh harmonics, while it introduces the third harmonic at the 10 to 14% level.
- The interaction of field mmf fundamental with stator slot openings may produce the so-called slot–ripple emf effect, that is, additional damper cage losses at no load. With N_s/p_1 as an odd number, ideally zero damper cage additional losses at no load occur.
- There are various losses in an SG, but they may be grouped into no-load and short-circuit electromagnetic losses and mechanical losses.
- Analytical formulae are given for most components of losses, and, finally, the efficiency expression is obtained. The designer may thus calculate the total efficiency for various load conditions. Efficiency and losses are paramount performance indexes in an SG.
- Exciter design specifications and issues are treated in some detail for the brushless exciter: note the voltage response time for the excitation voltage to reach 95% of the ceiling (maximum) value (starting from the rated one).
- Once the general design is completed, a sound initial solution exists, and a reliable model of the machine is in place. Optimization design may start, once a set of variables is defined, a cost function is derived, and a mathematical optimization algorithm is chosen. Results with evolutionary and genetic algorithm methods are presented from the literature.
- For generator/motor units, a detailed discussion of motor starting and synchronization methods is given. The unit has to withstand the daily start–stop encountered in generator/motor cycles for pump-storage operation modes.
- Numerical examples are given throughout this chapter to illustrate the various design issues.

References

1. B.E.B. Gott, W.R. Mc Cown, and J.R. Michalec, Progress in Revision of IEEE/ANSI C 50 Series of Standards for Steam and Combustion Turbine Generators and Harmonization with the IEC 60034 Series, Record of IEEE–IEMDC–2001 Conference, MIT.
2. R.J. Nelson, Conflicting Requirements for Turbogenerators from Grid Codes and Relevant Generator Standard, Record of IEEE–IEMDC–2001, Meeting, MIT, pp. 63–68.
3. C.E. Stephan, and Z. Baba, Specifying a Turbogenerator's Electrical Parameters by Standards and Grid Codes, Record of IEEE–IEMDC–2001, Meeting, MIT, pp. 57–62.

4. J.M. Forgarty, Connection Between Generator Specifications and Fundamental Design Principles, Record of IEEE–IEMDC–2001, Meeting, MIT, pp. 51–56.
5. K. Vogt, *Electrical Machines*, VEB Verlag Technik, Berlin, 4th ed., 1988, pp. 416 (in German).
6. J.H. Walker, *Large Synchronous Machines*, Clarendon Press, Oxford, 1981.
7. V.V. Dombrowski, A.G. Eremeev, N.P. Ivanov, P.M. Ipatov, M.I. Kaplan, and G.B. Pinskii, *Design of Hydrogenerators*, vol. I and II, Energy Publishers, Moskow, 1965 (in Russian).
8. V. Ostovic, *Dynamics of Saturated Electric Machines*, Springer-Verlag, Heidelberg, 1989.
9. R. Richter, *Electric Machines*, vol. 2, Verlag Birkhäuser, Basel, Stuttgart, 1963 (in German).
10. I. Boldea, and S.A. Nasar, *The Induction Machine Handbook*, chap. 6, CRC Press, Boca Raton, FL, 2001.
11. A.B. Danilevici, V.V. Dombrovski, and E.I.A. Kazovski, A.C. *Machinery Parameters*, Science Publishers, Moskow, 1965 (in Russian).
12. I.S. Gheorghiu, and A. Fransua, *Treatise of Electric Machines, vol. 4, Synchronous Machine*, Tech. Publ., Bucharest, 1972 (in Romanian).
13. E. Levi, *Polyphase Motors: A Direct Approach to Their Design*, John Wiley & Sons, New York, 1985.
14. K. Oberretl, Eddy current losses in solid pole shoes of synchronous machines at no-load and on load, *IEEE Trans.*, PAS- 91, 1972, pp. 152–160.
15. O. Drubel, and R.L. Stall, Comparison between analytical and numerical methods for calculating tooth ripple losses in salient pole synchronous machines, *IEEE Trans.*, EC-16, 1, 2001, pp. 61–67.
16. A. Murdoch, and M.J. D'Antonio, Generator Excitation Systems — Performance Specification to Meet Interconnection Requirements, Record of IEEE–IEMDC–2001, MIT, June 2001.
17. M. Tartibi, and A. Domijan, Optimizing A.C. Exciter design, *IEEE Trans.*, EC-11, 1, 1996, pp. 16–24.
18. A.M. Knight, N. Karmaker, and K. Weeber, Use of a permeance model to predict force harmonic components and damper winding effect in salient-pole synchronous machines, *IEEE Trans.*, EC-17, 4, 2002, pp. 478–484.
19. S.S. Rao, *Optimization Methods in Engineering*, John Wiley & Sons, New York, 1996.
20. O.W. Andersen, Optimized Design of Salient Pole Synchronous Generators, Record of ICEM–200, Espoo, Finland, August 28–30, 2000, pp. 987–989.
21. E. Schlemmer, W. Harb, G. Lichtenecker, F. Muller, and R. Kleinhaentz, Optimization of Large Salient Pole Generators Using Evolution Strategies and Genetic Algoritms, Record of ICEM–2000, Espoo, Finland, pp. 1030–1034.
22. J. Bäcker, J. Janning, and H. Jebenstreit, High dynamic control of a three-level voltage–source–converter drive for a main strip mill, *IEEE Trans.*, EC-12, 1, 1997, pp. 66–72.
23. T.A. Meynard, H. Foch, P. Thomas, J. Courault, R. Iakob, and M. Mahrstaedt, Multilevel converters: basic concepts and industry applications, *IEEE Trans.*, IE-49, 5, 2002, pp. 955–964.

8

Testing of Synchronous Generators

Testing of synchronous generators (SGs) is performed to obtain the steady-state performance characteristics and the circuit parameters for dynamic (transients) analysis. The testing methods may be divided into standard and research types. Tests of a more general nature are included in standards that are renewed from time to time to include recent well-documented progress in the art. Institute of Electrical and Electronics Engineers (IEEE) standards 115-1995 represent a comprehensive plethora of tests for synchronous machines.

New procedures start as research tests. Some of them end up later as standard tests. Standstill frequency response (SSFR) testing of synchronous generators for parameter estimation is such a happy case. In what follows, a review of standard testing methods and the incumbent theory to calculate the steady-state performance and, respectively, the parameter estimation for dynamics analysis is presented. In addition, a few new (research) testing methods with strong potential to become standards in the future are also treated in some detail.

Note that the term "research testing" may also be used with the meaning "tests to research for new performance features of synchronous generators." Determination of flux density distribution in the airgap via search coil or Hall probes is such an example. We will not dwell on such "research testing methods" in this chapter.

The standard testing methods are divided into the following:

- Acceptance tests
- (Steady-state) performance tests
- Parameter estimation tests (for dynamic analysis)

From the nonstandard research tests, we will treat mainly "standstill step voltage response" and the on-load parameter estimation methods.

8.1   Acceptance Testing

According to IEEE standard 115-1995 SG, acceptance tests are classified as follows:

- A1: insulation resistance testing
- A2: dielectric and partial discharge tests
- A3: resistance measurements
- A4: tests for short-circuited field turns
- A5: polarity test for field insulation
- A6: shaft current and bearing insulation
- A7: phase sequence
- A8: telephone-influence factor (TIF)
- A9: balanced telephone-influence factor
- A10: line to neutral telephone-influence factor
- A11: stator terminal voltage waveform deviation and distortion factors
- A12: overspeed tests
- A13: line charging capacity
- A14: acoustic noise

8.1.1   A1: Insulation Resistance Testing

Testing for insulation resistance, including polarization index, influences of temperature, moisture, and voltage duration are all covered in IEEE standard 43-1974. If the moisture is too high in the windings, the insulation resistance is very low, and the machine has to be dried out before further testing is performed on it.

8.1.2   A2: Dielectric and Partial Discharge Tests

The magnitude, wave shape, and duration of the test voltage are given in American National Standards Institute (ANSI)–National Electrical Manufacturers Association (NEMA) MGI-1978. As the applied voltage is high, procedures to avoid injury to personnel are prescribed in IEEE standard 4-1978. The test voltage is applied to each electrical circuit with all the other circuits and metal parts grounded. During the testing of the field winding, the brushes are lifted. In brushless excitation SGs, the direct current (DC) excitation leads should be disconnected unless the exciter is to be tested simultaneously. The eventual diodes (thyristors) to be tested should be short-circuited but not grounded. The applied voltage may be as follows:

- Alternating voltage at rated frequency
- Direct voltage (1.7 times the rated SG voltage), with the winding thoroughly grounded to dissipate the charge
- Very low frequency voltage 0.1 Hz, 1.63 times the rated SG voltage

8.1.3   A3: Resistance Measurements

DC stator and field-winding resistance measurement procedures are given in IEEE standard 118-1978.

The measured resistance R_{test} at temperature t_{test} may be corrected to a specified temperature t_s:

$$R_s = R_{test} \frac{t_s + k}{t_{test} + k} \tag{8.1}$$

where $k = 234.5$ for pure copper (in °C).

The reference field-winding resistance may be DC measured either at standstill, with the rotor at ambient temperature, and the current applied through clamping rings, or from a running test at normal speed. The brush voltage drop has to be eliminated from voltage measurement.

If the same DC measurement is made at standstill, right after the SG running at rated field current, the result may be used to determine the field-winding temperature at rated conditions, provided the brush voltage drop is eliminated from the measurements.

8.1.4   A4–A5: Tests for Short-Circuited Field Turns and Polarity Test for Field Insulation

The purpose of these tests is to check for field-coil short-circuited turns, for number of turns/coil, or for short-circuit conductor size. Besides tests at standstill, a test at rated speed is required, as short-circuited turns may occur at various speeds. There are DC and alternating current (AC) voltage tests for the scope. The DC or AC voltage drop across each field coil is measured. A more than +2% difference between the coil voltage drop indicates possible short-circuits in the respective coils. The method is adequate for salient-pole rotors. For cylindrical rotors, the DC field-winding resistance is measured and compared with values from previous tests. A smaller resistance indicates that short-circuited turns may be present.

Also, a short-circuited coil with a U-shaped core may be placed to bridge one coil slot. The U-shaped core coil is placed successively on all rotor slots. The field-winding voltage or the impedance of the winding voltage or the impedance of the exciting coil decreases in case there are some short-circuited turns in the respective field coil. Alternatively, a Hall flux probe may be moved in the airgap from pole to pole and measures the flux density value and polarity at standstill, with the field coil DC fed at 5 to 10% of rated current value.

If the flux density amplitude is higher or smaller than that for the neighboring poles, some field coil turns are short-circuited (or the airgap is larger) for the corresponding rotor pole. If the flux density does not switch polarity regularly (after each pole), the field coil connections are not correct.
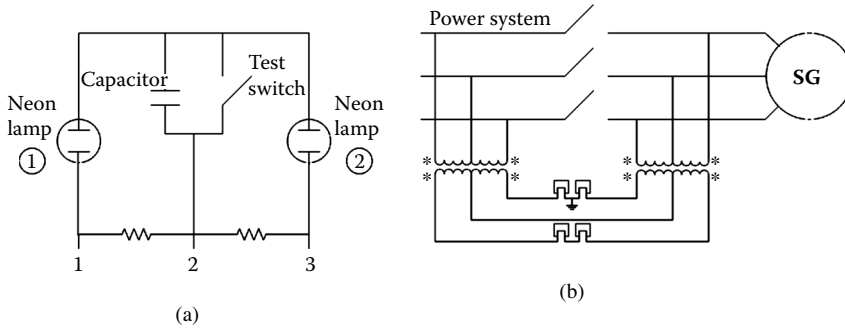
FIGURE 8.1 Phase-sequence indicators: (a) independent (1–2–3 or 1–3–2) and (b) relative to power grid.

8.1.5   A6: Shaft Current and Bearing Insulation

Irregularities in the SG magnetic circuit lead to a small axial flux that links the shaft. A parasitic current occurs in the shaft, bearings, and machine frame, unless the bearings are insulated from stator core or from rotor shaft. The presence of pulse-width modulator (PWM) static converters in the stator (or rotor) of SG augments this phenomenon. The pertinent testing is performed with the machine at no load and rated voltage. The voltage between shaft ends is measured with a high impedance voltmeter. The same current flows through the bearing radially to the stator frame.

The presence of voltage across bearing oil film (in uninsulated bearings) is also an indication of the shaft voltage.

If insulated bearings are used, their effectiveness is checked by shorting the insulation and observing an increased shaft voltage. Shaft voltage above a few volts, with insulated bearings, is considered unacceptable due to bearing in-time damage. Generally, grounded brushes in shaft ends are necessary to prevent it.

8.1.6   A7: Phase Sequence

Phase sequencing is required for securing given rotation direction or for correct phasing of a generator prepared for power bus connection. As known, phase sequencing can be reversed by interchanging any two armature (stator) terminals.

There are a few procedures used to check phase sequence:

- With a phase-sequence indicator (or induction machine)
- With a neon-lamp phase-sequence indicator (Figure 8.1a and Figure 8.1b)
- With the lamp method (Figure 8.1b)

When the SG no-load voltage sequence is 1–2–3 (clockwise), the neon lamp 1 will glow, while for the 1–3–2 sequence, the neon lamp 2 will glow. The test switch is open during these checks. The apparatus works correctly if, when the test switch is closed, both lamps glow with the same intensity (Figure 8.1a).

With four voltage transformers and four lamps (Figure 8.1b), the relative sequence of SG phases to power grid is checked. For direct voltage sequence, all four lamps brighten and dim simultaneously. For the opposite sequence, the two groups of lamps brighten and dim one after the other.

8.1.7   A8: Telephone-Influence Factor (TIF)

TIF is measured for the SG alone, with the excitation supply replaced by a ripple-free supply. The step-up transformers connected to SG terminals are disconnected. TIF is the ratio between the weighted root mean squared (RMS) value of the SG no-load voltage fundamental plus harmonic E_{TIF} and the rms of the fundamental E_{rms}:

$$TIF = \frac{E_{TIF}}{E_{rms}} \quad ; \quad E_{TIF} = \sqrt{\sum_{n=1}^{\infty}\left(T_n E_n\right)} \tag{8.2}$$

T_n is the TIF weighting factor for the nth harmonic. If potential (voltage) transformers are used to reduce the terminal voltage for measurements, care must be exercised to eliminate influences on the harmonics content of the SG no-load voltage.

8.1.8 A9: Balanced Telephone-Influence Factor

For a definition, see IEEE standard 100-1992.

In essence, for a three-phase wye-connected stator, the TIF for two line voltages is measured at rated speed and voltage on no-load conditions. The same factor may be computed (for wye connection) for the line to neutral voltages, excluding the harmonics 3,6,9,12, ….

8.1.9 A10: Line-to-Neutral Telephone-Influence Factor

For machines connected in delta, a corner of delta may be open, at no load, rated speed, and rated voltage. The TIF is calculated across the open delta corner:

$$Residual\ TIF = \frac{E_{TIF(opendelta)}}{3E_{rms(onephase)}} \tag{8.3}$$

Protection from accidental measured overvoltage is necessary, and usage of protection gap and fuses to ground the instruments is recommended.

For machines that cannot be connected in delta, three identical potential transformers connected in wye in the primary are open-delta connected in their secondaries. The neutral of the potential transformer is connected to the SG neutral point.

All measurements are now made as above, but in the open-delta secondary of the potential transformers.

8.1.10 A11: Stator Terminal Voltage Waveform Deviation and Distortion Factors

The line to neutral TIF is measured in the secondary of a potential transformer with its primary that is connected between a SG phase terminal and its neutral points. A check of values balanced, residual, and line to neutral TIFs is obtained from the following:

$$line\ to\ neutral\ TIF = \sqrt{(balanced\ TIF)^2 + (residual\ TIF)^2} \tag{8.4}$$

Definitions of deviation factor and distortion factor are given in IEEE standard 100-1992. In principle, the no-load SG terminal voltage is acquired (recorded) with a digital scope (or digital data acquisition system) at high speed, and only a half-period is retained (Figure 8.2).

The half-period time is divided into J (at least 18) equal parts. The interval j is characterized by E_j. Consequently, the zero-to-peak amplitude of the equivalent sine wave E_{OM} is as follows:

$$E_{OM} = \sqrt{\frac{2}{J}\sum_{j=1}^{J} E_j^{\,2}} \tag{8.5}$$
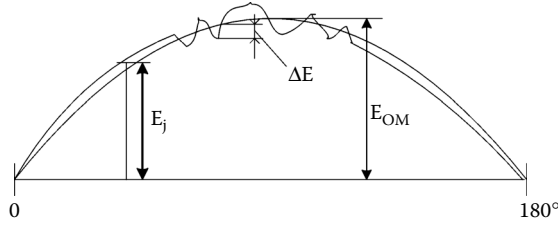
FIGURE 8.2 No-load voltage waveform for deviation factor.

A complete cycle is needed when even harmonics are present (fractionary windings). Waveform analysis may be carried out by software codes to implement the above method. The maximum deviation is ΔE (Figure 8.2). Then, the deviation factor $F_{\Delta EV}$ is as follows:

$$F_{\Delta EV} = \frac{\Delta E}{E_{OM}} \tag{8.6}$$

Any DC component E_o in the terminal voltage waveform has to be eliminated before completing waveform analysis:

$$E_o = \frac{\sum_{i=1}^{N} E_i}{N} \tag{8.7}$$

with N equal to the samples per period.

When subtracting the DC component E_o from the waveform E_i, E_j is obtained:

$$E_j = E_i - E_o \ ; \ j = 1,\dots,N \tag{8.8}$$

The rms value E_{rms} is, thus,

$$E_{rms} = \sqrt{\frac{1}{N} \sum_{j=1}^{n} E_j^{\,2}} \ \ ; \ \ E_{OM} = \sqrt{2} E_{rms} \tag{8.9}$$

The maximum deviation is searched for after the zero crossing points of the actual waveform and of its fundamental are overlapped. A Fourier analysis of the voltage waveform is performed:

$$a_n = \frac{2}{N} \sum_{j=1}^{n} E_j \cos \frac{2\pi nj}{N}$$

$$b_n = \frac{2}{N} \sum_{j=1}^{n} E_j \sin \frac{2\pi nj}{N} \tag{8.10}$$

$$E_n = \sqrt{a_n^{\,2} + b_n^{\,2}}$$

$$\phi_n = \tan^{-1}\left(b_n \,/\, a_n\right) \qquad \text{for } a_n > 0$$

$$\phi_n = \tan^{-1}\left(b_n \,/\, a_n\right) + \pi \quad \text{for } a_n < 0$$

The distortion factor $F_{\Delta i}$ represents the ratio between the RMS harmonic content and the rms fundamental:

$$F_{\Delta i} = \frac{\sqrt{\sum_{n=2}^{\infty} E_n^{\,2}}}{E_{rms}} \tag{8.11}$$

There are harmonic analyzers that directly output the distortion factor $F_{\Delta i}$. It should be mentioned that $F_{\Delta i}$ is limited by standards to rather small values, as detailed in Chapter 7 on SG design.

8.1.12 A12: Overspeed Tests

Overspeed tests are not mandatory but are performed upon request, especially for hydro or thermal turbine-driven generators that experience transient overspeed upon loss of load. The SG has to be carefully checked for mechanical integrity before overspeeding it by a motor (it could be the turbine [prime mover]).

If overspeeding above 115% is required, it is necessary to pause briefly at various speed steps to make sure the machine is still OK. If the machine has to be excited, the level of excitation has to be reduced to limit the terminal voltage at about 105%. Detailed inspection checks of the machine are recommended after overspeeding and before starting it again.

8.1.13 A13: Line Charging Capacity

Line charging represents the SG reactive power capacity when at synchronism, at zero power factor, rated voltage, and zero field current. In other words, the SG behaves as a reluctance generator at no load.

Approximately,

$$Q_{ch\arg e} \approx \frac{3V_{ph}^{\,2}}{X_d} \tag{8.12}$$

where

X_d = the d axis synchronous reactance
V_{ph} = the phase voltage (RMS)

The SG is driven at rated speed, while connected either to a no-load running overexcited synchronous machine or to an infinite power source.

8.1.14 A14: Acoustic Noise

Airborne sound tests are given in IEEE standard 85-1973 and in ANSI standard C50.12-1982. Noise is undesired sound. The duration in hours of human exposure per day to various noise levels is regulated by health administration agencies.

An omnidirectional microphone with amplifier weighting filters, processing electronics, and an indicating dial makes a sound-level measuring device. The ANSI "A" "B" "C" frequency domain is required for noise control and its suppression according to pertinent standards.

8.2   Testing for Performance (Saturation Curves, Segregated Losses, Efficiency)

In large SGs, the efficiency is generally calculated based on segregated losses, measured in special tests that avoid direct loading.

Individual losses are as follows:

- Windage and friction loss
- Core losses (on open circuit)
- Stray-load losses (on short-circuit)
- Stator (armature) winding loss: $3I_s^2R_a$ with R_a calculated at a specified temperature
- Field-winding loss $I_{fd}^2R_{fd}$ with R_{fd} calculated at a specified temperature

Among the widely accepted loss measurement methods, four are mentioned here:

- Separate drive method
- Electric input method
- Deceleration (retardation) method
- Heat transfer method

For the first three methods listed above, two tests are run: one with open circuit and the other with short-circuit at SG terminals. In open-circuit tests, the windage-friction plus core losses plus field-winding losses occur. In short-circuit tests, the stator-winding losses, windage-friction losses, and stray-load losses, besides field-winding losses, are present.

During all these tests, the bearings temperature should be held constant. The coolant temperature, humidity, and gas density should be known, and their appropriate influences on losses should be considered. If a brushless exciter is used, its input power has to be known and subtracted from SG losses. When the SG is driven by a prime mover that may not be uncoupled from the SG, the prime-mover input and losses have to be known. In vertical shaft SGs with hydraulic turbine runners, only the thrust-bearing loss corresponding to SG weight should be attributed to the SG.

Dewatering with runner seal cooling water shutoff of the hydraulic turbine generator is required. Francis and propeller turbines may be dewatered at standstill and, generally, with the manufacturer's approval. To segregate open-circuit and short-circuit loss components, the no-load and short-circuit saturation curves must also be obtained from measurements.

8.2.1   Separate Driving for Saturation Curves and Losses

If the speed can be controlled accurately, the SG prime mover can be used to drive the SG for open-circuit and short-circuit tests, but only to determine the saturation open-circuit and short-circuit curves, not to determine the loss measurements.

In general, a "separate" direct or through-belt gear coupled to the SG motor has to be used. If the exciter is designed to act in this capacity, the best case is met. In general, the driving motor 3 to 5% rating corresponds to the open-circuit test. For small- and medium-power SGs, a dynamometer driver is adequate, as the torque and speed of the latter are measured, and thus, the input power to the tested SG is known.

But today, when the torque and speed are estimated, in commercial direct-torque-controlled (DTC) induction motor (IM) drives with PWM converters, the input to the SG for testing is also known, thereby eliminating the dynamometer and providing for precise speed control (Figure 8.3).

8.2.1.1   The Open-Circuit Saturation Curve

The open-circuit saturation curve is obtained when driving the SG at rated speed, on open circuit, and acquiring the SG terminal voltage, frequency, and field current.
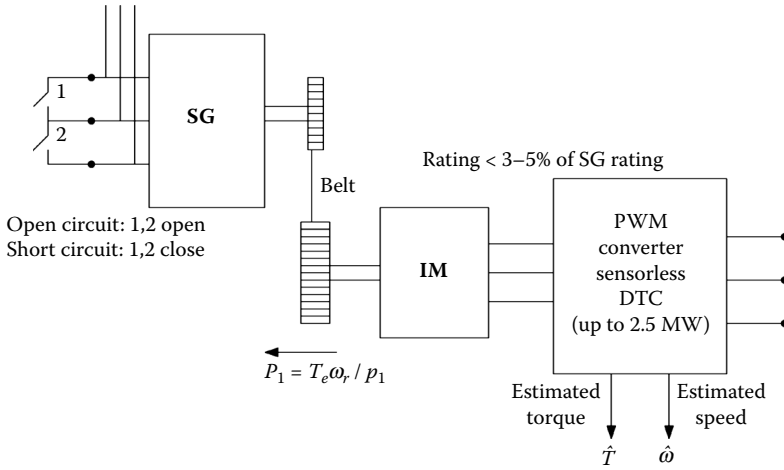
FIGURE 8.3 Driving the synchronous generator for open-circuit and short-circuit tests.
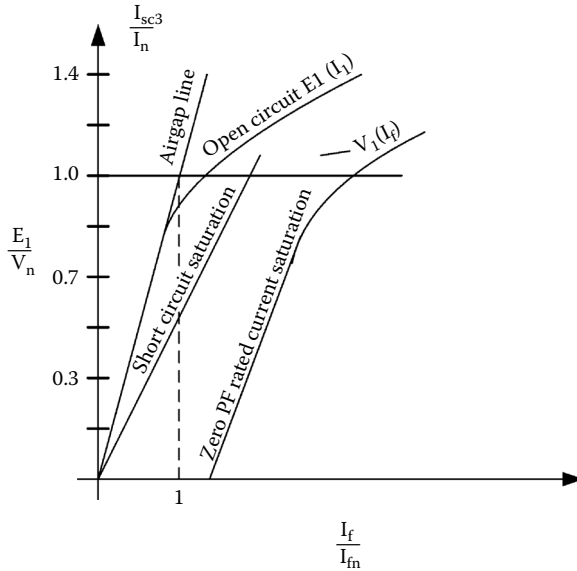
FIGURE 8.4 Saturation curves.

At least six readings below 60%, ten readings from 60 to 110%, two from 110 to 120%, and one at about 120% of rated speed voltage are required. A monotonous increase in field current should be observed. The step-up power transformer at SG terminals should be disconnected to avoid unintended high-voltage operation (and excessive core losses) in the latter.

When the tests are performed at lower than rated speed (such as in hydraulic units), corrections for frequency (speed) have to be made. A typical open-circuit saturation curve is shown in Figure 8.4. The airgap line corresponds to the maximum slope from origin that is tangent to the saturation curve.

8.2.1.2 The Core Friction Windage Losses

The aggregated core, friction, and windage losses may be measured as the input power P_{10} (Figure 8.3) for each open-circuit voltage level reading. As the speed is kept constant, the windage and friction losses
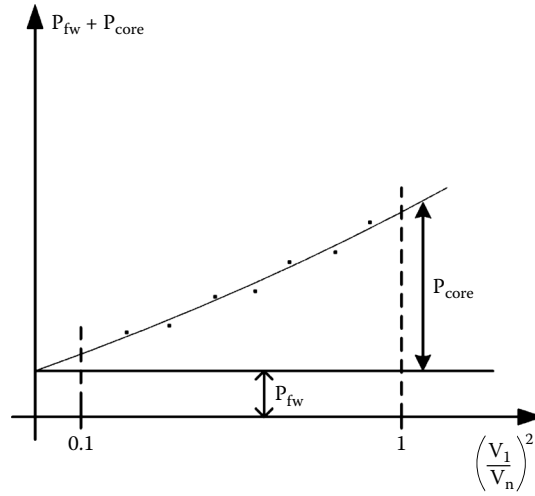
FIGURE 8.5 Core (P_{core}) and friction windage (P_{fw}) losses vs. armature voltage squared at constant speed.

are constant (P_{fw} = constant). Only the core losses P_{core} increase approximately with voltage squared (Figure 8.5).

8.2.1.3   The Short-Circuit Saturation Curve

The SG is driven at rated speed with short-circuited armature, while acquiring the stator and field currents I_{sc} and I_f. Values should be read at rated 25%, 50%, 75%, and 100%. Data at 125% rated current should be given by the manufacturer, to avoid overheating the stator. The high current points should be taken first so that the temperature during testing stays almost constant. The short-circuit saturation curve (Figure 8.4) is a rather straight line, as expected, because the machine is unsaturated during steady-state short-circuit.

8.2.1.4   The Short-Circuit and Strayload Losses

At each value of short-circuit stator current, I_{sc}, the input power to the tested SG (or the output power of the drive motor) P_{1sc} is measured. Their power contains the friction, windage losses, the stator winding DC losses ($3I_{sc3}^2 R_{adc}$), and the strayload loss P_{stray} load (Figure 8.6):

$$P_{isc} = P_{fw} + 3I_{sc3}^2 R_{sdc} + P_{strayload} \tag{8.13}$$

During the tests, it may happen that the friction windage loss is modified because temperature rises. For a specified time interval, an open-circuit test with zero field current is performed, when the whole loss is the friction windage loss ($P_{10} = P_{fw}$). If P_{fw} varies by more than 10%, corrections have to be made for successive tests.

Advantage may be taken of the presence of the driving motor (rated at less than 5% SG ratings) to run zero-power load tests at rated current and measure the field current I_f, terminal voltage V_1; from rated voltage downward.

A variable reactance is required to load the SG at zero power factor. A running, underexcited synchronous machine (SM) may constitute such a reactance, made variable through its field current. Adjusting the field current of the SG and SM leads to voltage increasing points on the zero power factor saturation curve (Figure 8.4).

8.2.2   Electric Input (Idle-Motoring) Method for Saturation Curves and Losses

According to this method, the SG performs as an unloaded synchronous motor supplied from a variable voltage constant frequency power rating supply. Though standards indicate to conduct these tests at rated
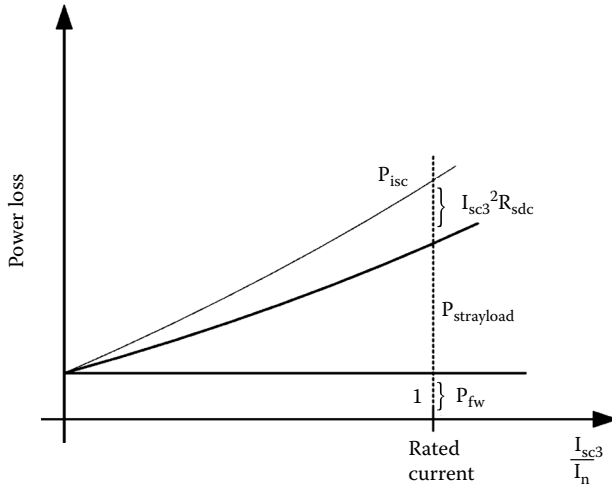
FIGURE 8.6 Short-circuit test losses breakdown.
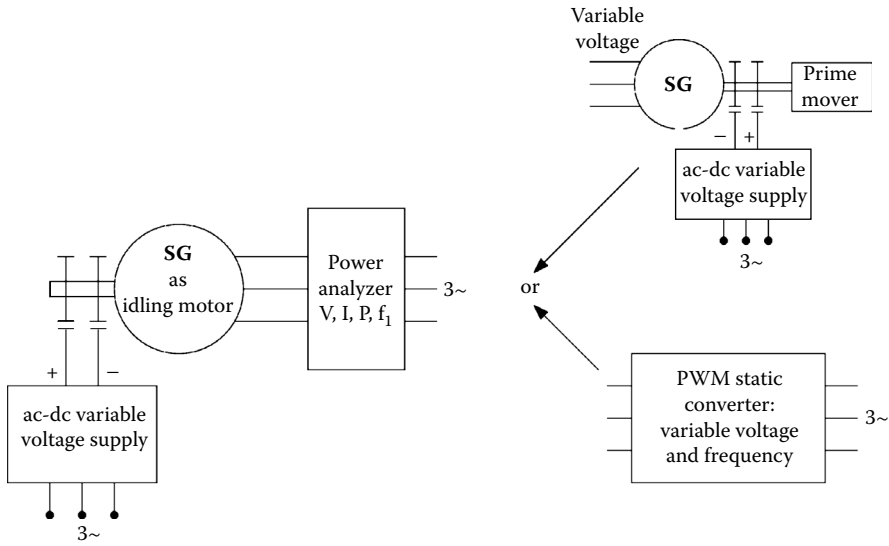
FIGURE 8.7 Idle motoring test for loss segregation and open-circuit saturation curve.

speed only, there are generators that also work as motors. Gas-turbine generators with bidirectional static converters that use variable speed for generation and turbine starting as a motor are a typical example. The availability of PWM static converters with close to sinusoidal current waveforms recommends them for the no-load motoring of SG. Alternatively, a nearly lower rating SG (below 3% of SG rating) may provide for the variable voltage supply.

The testing scheme for the electric input method is described in Figure 8.7.

When supplied from the PWM static converter, the SG acting as an idling motor is accelerated to the desired speed by a sensorless control system. The tested machine is vector controlled; thus, it is "in synchronism" at all speeds.

In contrast, when the power supply is a nearby SG, the tested SG is started either as an asynchronous motor or by accelerating the power supply generator simultaneously with the tested machine. Suppose that the SG was brought to rated speed and acts as a no-load motor. To segregate the no-load loss components, the idling motor is supplied with descending stator voltage and descending field current so
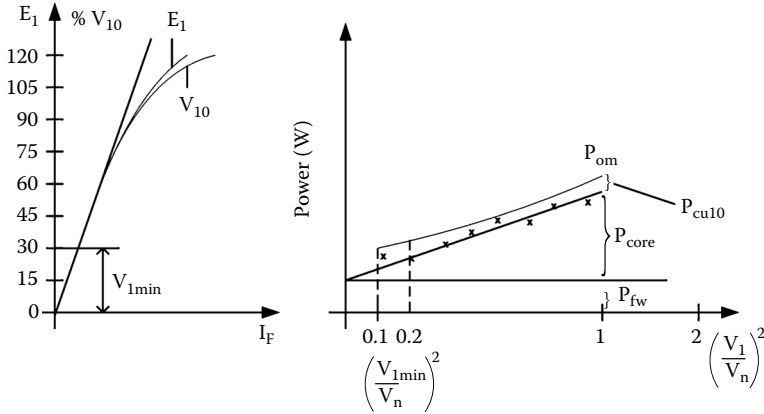
FIGURE 8.8 Loss segregation for idle-running motor testing.

as to keep unity power factor conditions (minimum stator current). The loss components of (input electric power) P_{om} are as follows:

$$P_{om} = P_{cu10} + P_{coreo} + P_{fw} \tag{8.14}$$

The stator winding loss P_{cu10} is

$$P_{cu10} = 3R_{adc}I_o^{\,2} \tag{8.15}$$

and may be subtracted from the electric input P_{om} (Figure 8.8).

There is a minimum stator voltage V_{1min}, at unity power factor, for which the idling synchronous motor remains at synchronism. The difference $P_{om} - P_{cu10}$ is represented in Figure 8.8 as a function of voltage squared to underscore the core loss almost proportionally to voltage squared at given frequency (or to V/f in general) A straight line is obtained through curve fitting. This straight line is prolonged to the vertical axis, and thus, the mechanical loss P_{fw} is obtained. So, the P_{core} and P_{fw} were segregated. The open-circuit saturation curve may be obtained as a bonus (down to 30% rated voltage) by neglecting the voltage drop over the synchronous reactance (current is small) and over the stator resistance, which is even smaller. Moreover, if the synchronous reactance X_s (an "average" of X_d and X_q) is known from design data, at unity power factor, the no-load voltage (the electromagnetic field [emf] E_1) is

$$E_1 \approx \sqrt{\left(V_1 - R_a I_o^{\,2}\right) + X_s^{\,2}I_o^{\,2}} \tag{8.16}$$

The precision in E_1 is thus improved, and the obtained open-circuit saturation curve, $E_1(I_f)$, is more reliable. The initial 30% part of the open-circuit saturation curve is drawn as the airgap line (the tangent through origin to the measured open-circuit magnetic curve section). To determine the short-circuit and strayload losses, the idling motor is left to run at about 30% voltage (and at an even lower value, but for stable operation). By controlling the field current at this low, but constant, voltage, about six current step measurements are made from 125 to 25% of rated stator current. At least two points with very low stator current are also required. Again, total losses for this idling test are

$$\left(P_{om}\right)_{lowvoltage} = P_{fw} + P_{core} + P_{cu1} + P_{strayload} \tag{8.17}$$
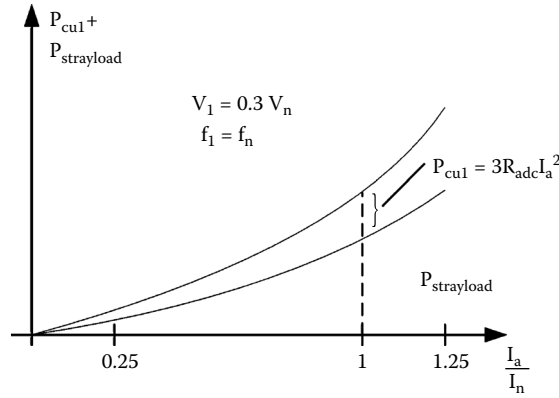
FIGURE 8.9 $P_{cu1} + P_{strayload}$.
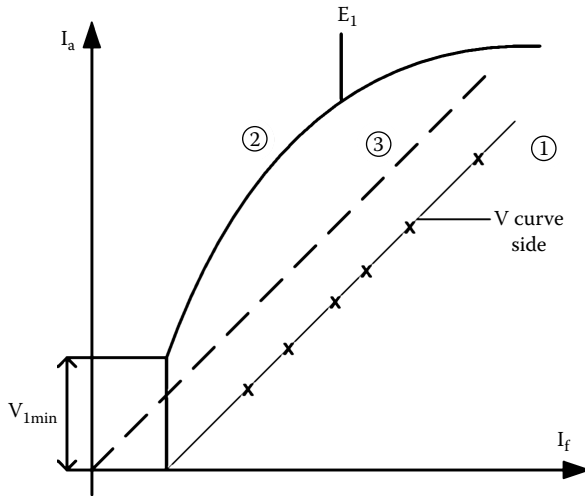
FIGURE 8.10 *V* curve at low voltage V_{1min} (1), open-circuit saturation curve (2), short-circuit saturation curve (3).

This time, the test is done at constant voltage, but the field current is decreased to increase the stator current up to 125%. So, the strayload losses become important. As the field current is reduced, the power factor decreases, so care must be exercised to measure the input electric power with good precision. As the P_{fw} loss is already known from the previous testing, speed is constant, P_{core} is known from the same source at the same low voltage at unity power factor conditions, and only $P_{core} + P_{strayload}$ have to be determined as a function of stator current.

Additionally, the dependence of I_a on I_f may be plotted from this low-voltage test (Figure 8.9). The intersection of this curve side with the abscissa delivers the field current that corresponds to the testing voltage V_{1min} on the open-circuit magnetization curve. The short-circuit saturation curve is just parallel to the *V* curve side $I_a(I_f)$ (see Figure 8.10).

We may conclude that both separate driving and electric power input tests allow for the segregation of all loss components in the machine and thus provide for the SG conventional efficiency computation:

$$\eta_c = \frac{P_1 - \sum P}{P_1}$$

$$\sum P = P_{fw} + P_{core} + P_{cu1}\left(\frac{I_a}{I_n}\right)^2 + P_{strayload}\left(\frac{I_a}{I_n}\right)^2 + R_{fd}I_F \qquad (8.18)$$

The rated stator-winding loss P_{cu1} and the rated stray-load loss $P_{strayload}$ are determined in short-circuit tests at rated current, while P_{core} is determined from the open-circuit test at rated voltage. It is disputable if the core losses calculated in the no-load test and strayload losses from the short-circuit test are the same when the SG operates on loads of various active and reactive power levels.

8.2.3 Retardation (Free Deceleration Tests)

In essence, after the SG operates as an uncoupled motor at steady state to reach normal temperatures, its speed is raised at 110% speed. Evidently, a separate SG supply capable of producing 110% rated frequency is required. Alternatively, a lower rated PWM converter may be used to supply the SG to slowly accelerate the SG as a motor. Then, the source is disconnected. The prime mover of the SG was decoupled or "dewatered."

The deceleration tests are performed with I_f, $I_a = 0$, then with $I_f \neq 0$, $I_a = 0$ (open circuit), and, respectively, for $I_f =$ constant, and $V_1 = 0$ (short-circuit). In the three cases, the motion equation leads to the following:

$$\frac{J}{p_1}\left(\frac{\omega_r}{p_1}\right)\frac{d\omega_r}{dt} = \frac{d}{dt}\left[\frac{J}{2}\left(\frac{\omega_r}{p_1}\right)^2\right] = -P_{fw}(\omega_r)$$

$$= -P_{fw}(\omega_r) - P_{core}(\omega_r) \qquad (8.19)$$

$$= -P_{sc}(I_{sc3}) - P_{fw}(\omega_r)$$

The speed vs. time during deceleration is measured, but its derivation with time has to be estimated through an adequate digital filter to secure a smooth signal.

Provided the inertia J is *a priori* known, at about rated speed, the speed ω_{rn} and its derivative $d\omega_r/dt$ are acquired and used to calculate the losses for that rated speed, as shown on the right side of Equation 8.19 (Figure 8.11).
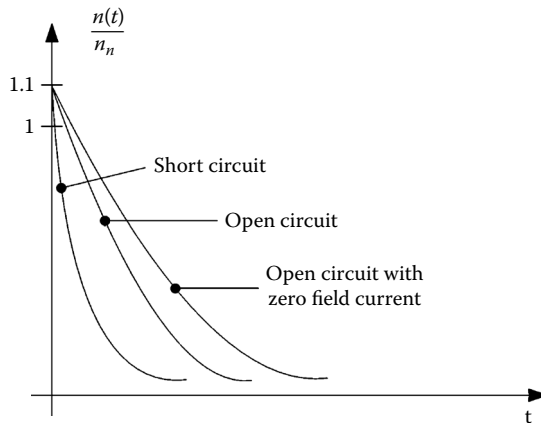

FIGURE 8.11 Retardation tests.

With the retardation tests done at various field current levels, respectively, at different values of short-circuit current, at rated speed, the dependence of $E_1(I_F)$, $P_{core}(I_F)$, and $P_{sc}(I_{sc3})$ may be obtained. Also,

$$P_{sc}\left(I_{sc3}\right) = 3R_{adc}I_{sc3}{}^2 + P_{strayload}\left(I_{sc3}\right) \tag{8.20}$$

In this way, the open-circuit saturation curve $E_1(I_f)$ is obtained, provided the terminal voltage is also acquired. Note that if the SG is excited from its exciter (brushless, in general), care must be exercised to keep the excitation current constant, and the exciter input power should be deducted from losses.

If overspeeding is not permitted, the data are collected at lower than rated speed with the losses corrected to rated speed (frequency). A tachometer, a speed recorder, or a frequency digital electronic detector may be used.

As already pointed out, the inertia J has to be known *a priori* for retardation tests. Inertia may be computed by using a number of methods, including through computation by manufacturer or from Equation 8.19, provided the friction and windage loss at rated speed P_{fw} (ω_{rn}) are already known. With the same test set, the SG is run as an idling motor at rated speed and voltage for unity power factor (minimum current). Subtracting from input powers the stator winding loss, $P_{fw} + P_{core}$, corresponding to no load at the same field current, I_f is obtained. Then, Equation 8.19 is used again to obtain J. Finally, the physical pendulum method may be applied to calculate J (see IEEE standard 115-1995, paragraph 4.4.15).

For SGs with closed-loop water coolers, the calorimetric method may be used to directly measure the losses. Finally, the efficiency may be calculated from the measured output to measured input to SG. This direct approach is suitable for low- and medium-power SGs that can be fully loaded by the manufacturer to directly measure the input and output with good precision (less than 0.1 to 0.2%).

8.3 Excitation Current under Load and Voltage Regulation

The excitation (field) current required to operate the SG at rated steady-state active power, power factor, and voltage is a paramount factor in the thermal design of a machine.

Two essentially graphical methods — the Potier reactance and the partial saturation curves — were introduced in Chapter 7 on design. Here we will treat, basically, in more detail, variants of the Potier reactance method.

To determine the excitation current under specified load conditions, the Potier (or leakage) reactance X_p, the unsaturated d and q reactance X_{du} and X_{qu}, armature resistance R_a, and the open-circuit saturation curve are needed. Methods for determining the Potier and leakage reactance are given first.

8.3.1 The Armature Leakage Reactance

We can safely say that there is not yet a widely accepted (standardized) direct method with which to measure the stator leakage (reactance) of SGs. To the valuable heritage of analytical expressions for the various components of X_l (see Chapter 7), finite element method (FEM) calculation procedures were added [2, 3].

The stator leakage inductance may be calculated by subtracting two measured inductances:

$$L_l = L_{du} - L_{adu} \tag{8.21}$$

$$L_{adu} = L_{afdu} \cdot \frac{2}{3} \cdot \frac{1}{N_{af}} \quad ; \quad L_{afdu} = \frac{V_n\sqrt{2}}{\sqrt{3}\omega_n I_{fdbase}} \tag{8.22}$$

where L_{du} is the unsaturated axis synchronous inductance, and L_{adu} is the stator to field circuit mutual inductance reduced to the stator. L_{afdu} is the same mutual inductance but before reduction to stator. I_{fd} (base value) is the field current that produces, on the airgap straight line, the rated stator voltage on the open stator circuit. Finally, N_{af} is the field-to-armature equivalent turn ratio that may be extracted from design data or measured as shown later in this chapter.

The N_{af} ratio may be directly calculated from design data as follows:

$$N_{af} = \frac{3}{2} \frac{I_{abase}(A)}{i_{fd(base)}(A)} \quad ; \quad i_{fdbase} = I_{fdbase} \cdot l_{adu} \tag{8.23}$$

where i_{fdbase}, I_{fdbase}, and I_{abase} are in amperes, but l_{adu} is in P.U.

A method to directly measure the leakage inductance (reactance) is given in the literature [4]. The reduction of the Potier reactance when the terminal voltage increases is documented in Reference [4]. A simpler approach to estimate X_l would be to average homopolar reactance X_o and reactance of the machine without the rotor in place, X_{lair}:

$$X_l \approx \frac{(X_o + X_{lair})}{2} \tag{8.24}$$

In general, $X_o < X_l$ and $X_{lair} > X_l$, so an average of them seems realistic.

Alternatively,

$$X_l \approx X_{lair} - X_{air} \tag{8.25}$$

X_{air} represents the reactance of the magnetic field that is closed through the stator bore when the rotor is not in place. From two-dimensional field analysis, it was found that X_{air} corresponds to an equivalent airgap of τ/π (axial flux lines are neglected):

$$X_{air} = \frac{6\mu_o \omega_1 (W_1 kw_1)^2 \tau l_i}{\pi^2 p_1 (\tau/\pi)} \cong \frac{\omega_1 L_{adu}}{K_{ad}} \cdot \left(\frac{g\pi K_c}{\tau} \right) \tag{8.26}$$

where

$\quad\quad\quad \tau$ = the pole pitch
$\quad\quad\quad g$ = the airgap
$\quad\quad\quad l_i$ = the stator stack length
$\quad\quad\quad K_{ad} = L_{adu}/L_{mu} > 0.9$ (see Chapter 7)

The measurement of X_o will be presented later in this chapter, while X_{lair} may be measured through a three-phase AC test at a low voltage level, with the rotor out of place. As expected, magnetic saturation is not present when measuring X_o and X_{lair}. In reality, for large values of stator currents and for very high levels of magnetic saturation of stator teeth or rotor pole, the leakage flux paths get saturated, and X_l slightly decreases. FEM inquiries [2, 3] suggest that such a phenomenon is notable.

When identifying the machine model under various conditions, a rather realistic, even though not exact, value of leakage reactance is *a priori* given. The above methods may serve this purpose well, as saturation will be accounted for through other components of the machine model.

8.3.2   The Potier Reactance

Difficulties in measuring the leakage reactance led, shortly after the year 1900, to an introduction by Potier of an alternative reactance (Potier reactance) that can be measured from the zero-power-factor

FIGURE 8.12 Potier reactance from zero power factor saturation curve.

load tests, at given stator voltage. At rated voltage tests, the Potier reactance X_p may be larger than the actual leakage reactance by as much as 20 to 30%.

The open-circuit saturation and zero-power-factor rated current saturation curves are required to determine the value of X_p (Figure 8.12).

At rated voltage level, the segment $a'd' = ad$ is marked. A parallel to the airgap line through a' intersects the open-circuit saturation curve at point b'. The segment $b'c'$ is as follows:

$$\overline{b'c'} = X_p I_a \tag{8.27}$$

It is argued that the value of X_p obtained at rated voltage level may be notably larger than the leakage reactance X_l, at least for salient-pole rotor SGs. A simple way to correct this situation is to apply the same method but at a higher level of voltage, where the level of saturation is higher, and thus, the segment $\overline{b''c''} < \overline{b'c'}$ and $X_p' < X_p$ and, approximately,

$$X_l \approx X_p' \approx \frac{\overline{b''c''}}{I_a} \tag{8.28}$$

It is not yet clear what overvoltage level can be considered, but less than 110% is feasible if the SG may be run at such overvoltage without excessive overheating, even if only for obtaining the zero-power-factor saturation curve up to 110%.

When the synchronous machine is operated as an SG on full load, other methods to calculate X_p from measurements are applicable [1].

8.3.3 Excitation Current for Specified Load

The excitation field current for specified electric load conditions (voltage, current, power factor) may be calculated by using the phasor diagram (Figure 8.13).

For given stator current I_a, terminal voltage E_a, and power factor angle φ, the power angle δ may be calculated from the phasor diagram as follows:
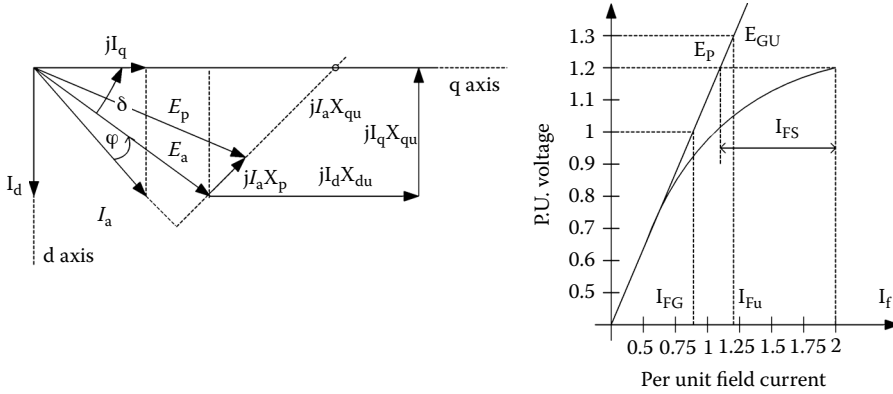
FIGURE 8.13 Phasor diagram with unsaturated reactances X_{du} and X_{qu} and the open-circuit saturation curve. E_a is the terminal phase voltage; δ is the power angle; I_a is the terminal phase current; φ is the power factor angle; E_{as} is the voltage back of X_{qu}; R_a is the stator phase resistance; and E_{Gu} is the voltage back of X_{du}.

$$\delta = \tan^{-1}\left[\frac{I_a R_a \sin\varphi + I_a X_{qu}\cos\varphi}{E_a + I_a R_a \cos\varphi + I_a X_{qu}\sin\varphi}\right] \tag{8.29}$$

$$I_d = I_a \sin(\delta + \varphi) \quad ; \quad I_q = I_a \cos(\delta + \varphi) \tag{8.30}$$

Once the power angle is calculated, for given unsaturated reactances X_{du}, X_{qu} and stator resistance, the computation of voltages E_{QD} and E_{Gu}, with the machine considered as unsaturated, is feasible:

$$\underline{E}_{Gu} = E_a + R_s I_a + jI_q X_{qu} + jX_d X_{du} \tag{8.31}$$

$$E_{Gu} = (E_a + R_a I_a)\cos\delta + X_{du} I_a \sin(\delta + \varphi) \tag{8.32}$$

Corresponding to E_{Gu}, from the open-circuit saturation curve (Figure 8.13), the excitation current I_{FU} is found. The voltage back of Potier reactance E_p is simply as follows (Figure 8.13):

$$\underline{E}_p = \underline{E}_a + R_s \underline{I}_a + jX_p \underline{I}_a$$

$$E_p = \sqrt{(E_a \sin\varphi + I_a X_p)^2 + (E_a \cos\varphi + I_a R_a)^2} \tag{8.33}$$

The excitation current under saturated conditions that produces E_p along the open-circuit saturation curve, is as follows (Figure 8.13):

$$I_F = I_{Fu} + I_{FS} \tag{8.34}$$

The "saturation" field current supplement is I_{FS}. The field current I_F corresponds to the saturated machine and is the excitation current under specified load. This information is crucial for the thermal design of SG. The procedure is similar for the cylindrical rotor machine, where the difference between X_{du} and X_{qu} is small (less than 10%). For variants of this method see Reference [1].

All methods in Reference [1] have in common a critical simplification: the magnetic saturation influence is the same in axes d and q, while the power angle δ calculated with unsaturated reactance X_{qu}
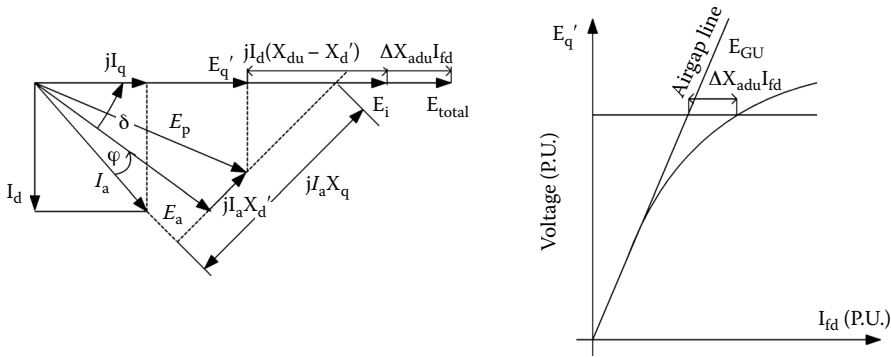
FIGURE 8.14 The transient model phasor diagram.

is considered to hold for all load conditions. The reality of saturation is much more complicated, but these simplifications are still widely accepted, as they apparently allowed for acceptable results so far.

The consideration of different magnetization curves along axes *d* and *q*, even for cylindrical rotors, and the presence of cross-coupling saturation were discussed in Chapter 7 on design, via the partial magnetization curve method. This is not the only approach to the computation of excitation current under load in a saturated SG, and new simplified methods to account for saturation under steady state are being produced [5].

8.3.4 Excitation Current for Stability Studies

When investigating stability, the torque during transients is mandatory. Its formula is still as follows:

$$T_e = \Psi_d I_q - \Psi_q I_d \tag{8.35}$$

When damping windings effects are neglected, the transient model and phasor diagram may be used, with X'_d replacing X_d, while X_q holds steady (Figure 8.14).

As seen from Figure 8.14, the total open-circuit voltage E_{total}, which defines the required field current I_{ftotal}, is

$$E_{total} = E'_q + \left(X_{du} - X'_d\right)I_d + X_{adu}I_{fd} \tag{8.36}$$

$$E'_q = E_a \cos\delta + I_a X'_d \sin\left(\delta + \varphi\right) \tag{8.37}$$

This time, at the level of E'_q (rather than E_p), the saturation increment in excitation (in P.U.), $\Delta X_{adu}{}^*I_{fd}$, is determined from the open-circuit saturation curve (Figure 8.14). The nonreciprocal system (Equation 8.23) is used in P.U. It is again obvious that the difference in saturation levels in the *d* and *q* axes is neglected. The voltage regulation is the relative difference between the no-load voltage E_{total} (Figure 8.14) corresponding to the excitation current under load, and the SG rated terminal voltage E_{an}:

$$voltage\ regulation = \frac{E_{total}}{E_{an}} - 1 \tag{8.38}$$

8.3.5 Temperature Tests

When determining the temperature rise of various points in an SG, it is crucial to check its capability to deliver load power according to specifications. The temperature rise is calculated with respect to a
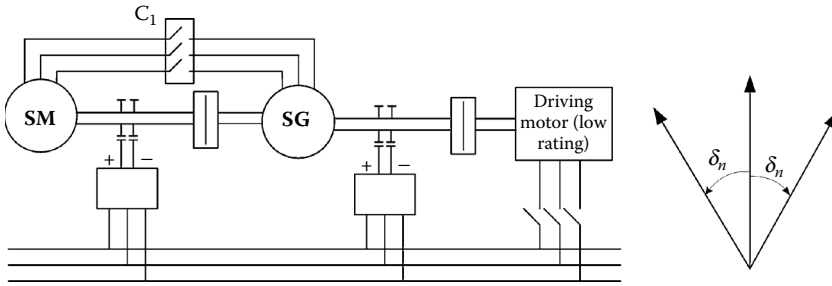
FIGURE 8.15   Back-to-back loading.

reference temperature. Coolant temperature is now a widely accepted reference temperature. A temperature rise at one (rated) or more specified load levels is required from temperature tests. When possible, direct loading should be applied to do temperature testing, either at the manufacturer's or at the user's site. Four common temperature testing methods are described here:

- Conventional (direct) loading
- Synchronous feedback (back-to-back motor [M] + generator [G]) loading
- Zero-power-factor load test
- Open-circuit and short-circuit loading

8.3.5.1   Conventional Loading

The SG is loaded for specified conditions of voltage, frequency, active power, armature current, and field current (the voltage regulator is disengaged). The machine terminal voltage should be maintained within ±2% of rated value. If so, the temperature increases of different parts of the machine may be plotted vs. P.U. squared apparent power $(MVA)^2$. As the voltage-dependent and current-dependent losses are generally unequal, the stator-winding temperature rise may be plotted vs. armature current squared (A^2), while the field-winding temperature can be plotted vs. field-winding dissipated power: $P_{exe} = R_F i_F^2$ (kW). Linear dependencies are expected. If temperature testing is i to be done before commissioning the SG, then the last three methods listed above are to be used.

8.3.5.2   Synchronous Feedback (Back-to-Back) Loading Testing

Two identical SGs are coupled together with their rotor axes shifted with respect to each other by twice the rated power angle $(2\delta_n)$. They are driven to rated speed before connecting their stators (C_1-open) (Figure 8.15).

Then, the excitation of both machines is raised until both SMs show the same rated voltage. With the synchronization conditions met, the power switch C_1 is closed. Further on, the excitation of one of the two identical machines is reduced. That machine becomes a motor and the other a generator. Then, simultaneously, SM excitation current is reduced and that of the SG is increased to keep the terminal voltage at rated value. The current between the two machines increases until the excitation current of the SG reaches its rated value, by now known for rated power, voltage, cos φ. The speed is maintained constant through all these arrangements. The net output power of the driving motor covers the losses of the two identical synchronous machines, $2\Sigma_p$, but the power exchanged between the two machines is the rated power P_n and can be measured. So, even the rated efficiency can be calculated, besides offering adequate loading for temperature tests by taking measurements every half hour until temperatures stabilize.

Two identical machines are required for this arrangement, along with the lower (6%) rating driving motor and its coupling. It is possible to use only the SM and SG, with SM driving the set, but then the local power connectors have to be sized to the full rating of the tested machines.
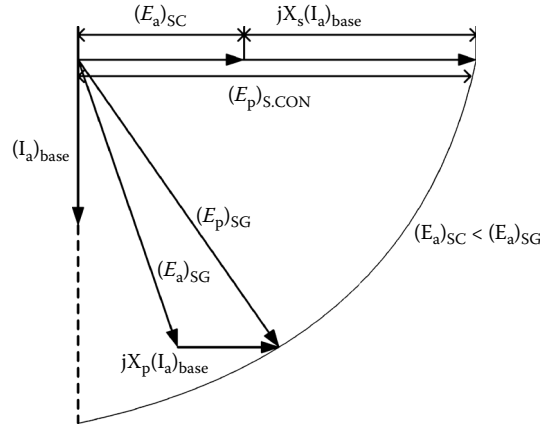
FIGURE 8.16 Equalizing the voltage back of Potier reactance for synchronous condenser and synchronous generator operation modes.

8.3.5.3 Zero-Power-Factor Load Test

The SG works as a synchronous motor uncoupled at the shaft, that is, a synchronous condenser (S.CON). As the active power drawn from the power grid is equal to SM losses, the method is energy efficient. There are, however, two problems:

- Starting and synchronizing the SM to the power source
- Making sure that the losses in the S.CON equal the losses in the SG at specified load conditions

Starting may be done through an existing SG supply that is accelerated in the same time with the SM, up to the rated speed. A synchronous motor starting may be used instead. To adjust the stator winding, core losses, and field-winding losses, for a given speed, and to provide for the rated mechanical losses, the supply voltage $(E_a)_{S.CON}$ and the field current may be adjusted.

In essence, the voltage $(E_p)_{S.CON}$ has to provide the same voltage behind Potier reactance with the S.CON as with the voltage E_a of SG at a specified load (Figure 8.16):

$$\left(E_P\right)_{S.CON} = \left(E_P\right)_{SG} \tag{8.39}$$

There are two more problems with this otherwise good test method for heating. One problem is the necessity of the variable voltage source at the level of the rated current of the SG. The second is related to the danger of too high a temperature in the field winding in SGs designed for larger than 0.9 rated power factor. The high level of E_p in the SG tests claims too large a field current (larger than for the rated load in the SG design).

Other adjustments have to be made for refined loss equivalence, such that the temperature rise is close to that in the actual SG at specified (rated load) conditions.

8.3.5.4 Open-Circuit and Short-Circuit "Loading"

As elaborated upon in Chapter 7 on design, the total loss of the SG under load is obtained by adding the open-circuit losses at rated voltage and the short-circuit loss at rated current and correcting for duplication of heating due to windage losses.

In other words, the open-circuit and short-circuit tests are done sequentially, and the overtemperatures $\Delta t_t = (\Delta t)_{opencircuit}$ and Δt_{sc} are added, while subtracting the additional temperature rise due to duplication of mechanical losses Δt_w:

$$\Delta t_t = \left(\Delta t\right)_{opencircuit} + \left(\Delta t\right)_{shortcircuit} - \left(\Delta t\right)_w \tag{8.40}$$

The temperature rise $(\Delta t)_w$ due to windage losses may be determined by a zero excitation open-circuit run. For more details on practical temperature tests, see Reference [1].

8.4   The Need for Determining Electrical Parameters

Prior to the period from 1945 to 1965, SG transient and subtransient parameters were developed and used to determine balanced and unbalanced fault currents. For stability response, a constant voltage back-transient reactance model was applied in the same period.

The development of power electronics controlled exciters led, after 1965, to high initial excitation response. Considerably more sophisticated SG and excitation control systems models became necessary. Time-domain digital simulation tools were developed, and small-signal linear eigenvalue analysis became the norm in SG stability and control studies. Besides second-order (two rotor circuits in parallel along each orthogonal axis) SG models, third and higher rotor order models were developed to accommodate the wider frequency spectrum encountered by some power electronics excitation systems. These practical requirements led to the IEEE standard 115A-1987 on standstill frequency testing to deal with third rotor order SG model identification.

Tests to determine the SG parameters for steady states and for transients were developed and standardized since 1965 at a rather high pace. Steady-state parameters — X_d, unsaturated (X_{du}) and saturated (X_{ds}), and X_q, unsaturated (X_{qu}) and saturated (X_{qs}) — are required first in order to compute the active and reactive power delivered by the SG at given power angle, voltage, armature current, and field current.

The field current required for given active, reactive powers, power factor, and voltage, as described in previous paragraphs, is necessary in order to calculate the maximum reactive power that the SG can deliver within given (rated) temperature constraints. The line-charging maximum-absorbed reactive power of the SG at zero power factor (zero active power) is also calculated based on steady-state parameters.

Load flow studies are based on steady-state parameters as influenced by magnetic saturation and temperature (resistances R_a and R_f). The subtransient and transient parameters (X_d'', X_d', T_d'', T_d', X_q'', X_q', T_{d0}'', T_{d0}', T_{q0}''), determined by processing the three-phase short-circuit tests, are generally used to study the power system protection and circuit-breaker fault interruption requirements. The magnetic saturation influence on these parameters is also needed for better precision when they are applied at rated voltage and higher current conditions. Empirical corrections for saturation are still the norm.

Standstill frequency response (SSFR) tests are mainly used to determine third-order rotor model sub-subtransient, subtransient, and transient reactances and time constraints at low values of stator current (0.5% of rated current). They may be identified through various regression methods, and some have been shown to fit well the SSFR from 0.001 Hz to 200 Hz. Such a broad frequency spectrum occurs in very few transients. Also, the transients occur at rather high and variable local saturation levels in the SG.

In just how many real-life SG transients are such advanced SSFR methods a must is not yet very clear. However, when lower frequency band response is required, SSFR results may be used to produce the best-fit transient parameters for that limited frequency band, through the same regression methods.

The validation of these advanced third (or higher) rotor order models in most important real-time transients led to the use of similar regression methods to identify the SG transient parameters from online admissible (provoked) transients. Such a transient is a 30% variation of excitation voltage. Limited frequency range oscillations of the exciter's voltage may also be performed to identify SG models valid for on-load transients, *a posteriori*.

The limits of short-circuit tests or SSFR taken separately appear clearly in such situations, and their combination to identify SG models is one more way to better the SG modeling for on-load transients. As all parameter estimation methods use P.U. values, we will revisit them here in the standardized form.

8.5 Per Unit Values

Voltages, currents, powers, torque, reactances, inductances, and resistances are required, in general, to be expressed in per unit (P.U.) values with the inertia and time constants left in seconds. Per-unitization has to be consistent. In general, three base quantities are selected, while the others are derived from the latter. The three commonly used quantities are three-phase base power, $S_{N\Delta}$, line-to-line base terminal voltage $E_{N\Delta}$, and base frequency, f_N.

To express a measurable physical quantity in P.U., its physical value is divided by the pertinent base value expressed in the same units. Conversion of a P.U. quantity to a new base is done by multiplying the old P.U. value by the ratio of the old to the new base quantity. The three-phase power $S_{N\Delta}$ of an SG is taken as its rated kilovoltampere (kVA) (or megavoltampere [MVA]) output (apparent power).

The single-phase base power S_N is $S_N = S_{N\Delta}/3$.

Base voltage is the rated line-to-neutral voltage E_N:

$$E_N = \frac{E_{N\Delta}}{\sqrt{3}} \quad (\text{V,kV}) \quad ; \quad E_{N\Delta} = E_{LL} \tag{8.41}$$

RMS quantities are used.

When sinusoidal balanced operation is considered, the P.U. value of the line-to-line and of the phase-neutral voltages is the same. Baseline current I_N is that value of stator current that corresponds to rated (base) power at rated (base) voltage:

$$I_N = \frac{S_{N\Delta}}{\sqrt{3}V_{N\Delta}} = \frac{S_N}{E_N} \quad (\text{A}) \quad ; \quad S_N = S_{N\Delta}/3 \tag{8.42}$$

For delta-connected SGs, the phase base current $I_{N\Delta}$ is as follows:

$$I_{N\Delta} = \frac{S_{N\Delta}}{3E_{N\Delta}} \quad \text{as} \quad E_{N\Delta} = E_N \tag{8.43}$$

The base impedance Z_N is

$$Z_N = \frac{E_N}{I_N} = \frac{E_N^2}{S_N} = \frac{E_{N\Delta}^2}{S_{N\Delta}} \tag{8.44}$$

The base impedance corresponds to the balanced load phase impedance at SG terminals that requires the rated current I_N at rated (base) line to neutral (base) voltage E_N. Note that, in some cases, the field-circuit-based impedance Z_{fdbase} is defined in a different way (Z_N is abandoned for the field-circuit P.U. quantities):

$$Z_{fbase} = \frac{S_{N\Delta}}{\left(I_{fdbase}\right)} = \frac{3S_N}{\left(I_{fdbase}\right)} \tag{8.45}$$

I_{fdbase} is the field current in amperes required to induce, at stator terminals, on an open-circuit straight line, the P.U. voltage E_a:

$$E_a\left(\text{P.U.}\right) = X_{adu}\left(\text{P.U.}\right)I_a\left(\text{P.U.}\right) \tag{8.46}$$

where

I_a = the P.U. value of stator current I_N

X_{adu} = the mutual P.U. reactance between the armature winding and field winding on the base Z_N

In general,

$$X_{du} = X_{adu} + X_l \tag{8.47}$$

where

X_{du} = the unsaturated d axis reactance

X_l = the leakage reactance

The direct addition of terms in Equation 8.47 indicates that X_{adu} is already reduced to the stator. Rankin [6] designated i_{fdbase} as the reciprocal system.

In the conventional (nonreciprocal) system, the base current of the field winding I_{fdbase} corresponds to the 1.0 P.U. volts E_a on an open-circuit straight line:

$$i_{fdbase} = I_{fdbase} X_{dau} \tag{8.48}$$

The Rankin's system is characterized by equal stator/field and field/stator mutual reactances in P.U. values.

The correspondence between i_{fdbase} and I_{fdbase} is shown graphically in Figure 8.17.

All rotor quantities, such as field-winding voltage, reactance, and resistance, are expressed in P.U. values according to either the conventional (I_{fdbase}) or to the reciprocal (i_{fdbase}) field current base quantity.

The base frequency is the rated frequency f_N. Sometimes, the time also has a base value $t_N = 1/f_N$. The theoretical foundations and the definitions behind expressions of SG parameters for steady-state and transient conditions were described in Chapter 5 and Chapter 6. Here, they will be recalled at the moment of utilization.
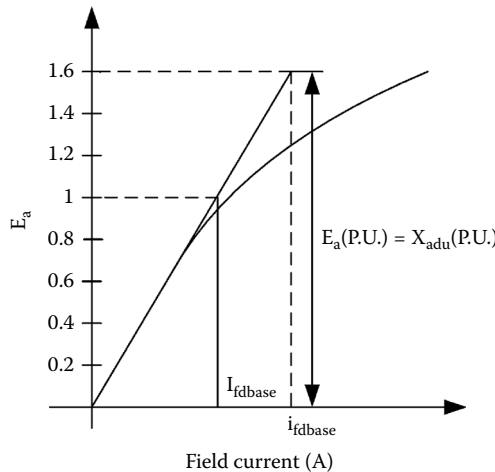

FIGURE 8.17 I_{fdbase} and i_{fdbase} base field current definitions.

8.6 Tests for Parameters under Steady State

Steady-state operation of a three-phase SG usually takes place under balanced load conditions. That is, phase currents are equal in amplitude but dephased by 120° with each other. There are, however, situations when the SG has to operate under unbalanced steady-state conditions. As already detailed in Chapter 5 (on steady-state performance), unbalanced operation may be described through the method of symmetrical components. The steady-state reactances X_d, X_q, or X_l, correspond to positive symmetrical components: X_2 for the negative and X_o for the zero components. Together with direct sequence parameters for transients, X_2 and X_o enter the expressions of generator current under unbalanced transients.

In essence, the tests that follow are designed for three-phase SGs, but with some adaptations, they may also be used for single-phase generators. However, this latter case will be treated separately in Chapter 12 in *Variable Speed Generators*, on small power single-phase linear motion generators.

The parameters to be measured for steady-state modeling of an SG are as follows:

- X_{du} is the unsaturated direct axis reactance
- X_{ds} is the saturated direct axis reactance dependent on SG voltage, power (in MVA), and power factor
- X_{adu} is the unsaturated direct axis mutual (stator to excitation) reactance already reduced to the stator ($X_{du} = X_{adu} + X_l$)
- X_l is the stator leakage reactance
- X_{ads} is the saturated (main flux) direct axis magnetization reactance ($X_{ds} = X_{ads} + X_l$)
- X_{qu} is the unsaturated quadrature axis reactance
- X_{qs} is the saturated quadrature axis reactance
- X_{aqs} is the saturated quadrature axis magnetization reactance
- X_2 is the negative sequence resistance
- X_o is the zero-sequence reactance
- R_o is the zero-sequence resistance
- SCR is the short-circuit ratio ($1/X_{du}$)
- δ is the internal power angle in radians or electrical degrees

All resistances and reactances above are in P.U.

8.6.1 X_{du}, X_{ds} Measurements

The unsaturated direct axis synchronous reactance X_{du} (P.U.) can be calculated as a ratio between two field currents:

$$X_{du} = \frac{I_{FSI}}{I_{FG}} \tag{8.49}$$

where

I_{FSI} = the field current on the short-circuit saturation curve that corresponds to base stator current
I_{FG} = the field current on the open-loop saturation curve that holds for base voltage on the airgap line (Figure 8.18)

Also,

$$X_{du} = X_{adu} + X_l \tag{8.50}$$

When saturation occurs in the main flux path, X_{adu} is replaced by its saturated value X_{ads}:
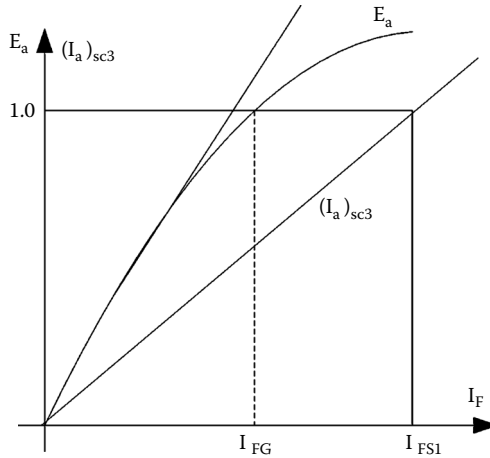
FIGURE 8.18 X_{du} calculation.

$$X_{ds} = X_{ads} + X_l \tag{8.51}$$

As for steady state, the stator current in P.U. is not larger than 1.2 to 1.3 (for short time intervals), the leakage reactance X_l, still to be considered constant through its differential component, may vary with load conditions, as suggested by recent FEM calculations [2, 3].

8.6.2 Quadrature-Axis Magnetic Saturation X_q from Slip Tests

It is known that magnetic saturation influences X_q and, in general,

$$X_{qs} = X_{aqs} + X_l \quad ; \quad X_{qu} = X_{aqu} + X_l \tag{8.52}$$

The slip tests and the maximum lagging current test are considered here for X_q measurements.

8.6.2.1 Slip Test

The SG is driven at very low slip (very close to synchronism) with open field winding. The stator is fed from a three-phase power source at rated frequency. The slip is the ratio of the frequency of the emf of the field winding to the rated frequency. A low-voltage spark gap across the field-winding terminal would protect it from too high accidental emfs. The slip has to be very small to avoid speed pulsations due to damper-induced currents. The SG will pass from positions in direct to positions in quadrature axes, with variations in power source voltage E_a and current I_a from (E_{max}, I_{amin}) to (E_{min}, I_{amax}):

$$X_q = \frac{E_{a\min}}{I_{a\max}} \quad ; \quad X_d = \frac{E_{a\max}}{I_{a\min}} \tag{8.53}$$

The degree of saturation depends on the level of current in the machine. To determine the unsaturated values of X_d and X_q, the voltage of the power source is reduced, generally below 60% of base value V_N.

In principle, at rated voltage, notable saturation occurs, which at least for axis q may be calculated as function of I_q with $I_q = I_{amax}$. In axis d the absence of field current makes X_d ($I_d = I_{amin}$) less representative, though still useful, for saturation consideration.

8.6.2.2 Quadrature Axis (Reactance) X_q from Maximum Lagging Current Test

The SG is run as a synchronous motor with no mechanical load at open-circuit rated voltage field current I_{FG} level, with applied voltages E_a less than 75% of base value E_N. Subsequently, the field current is reduced to zero and reversed in polarity and increased again in small increments with the opposite polarity. During this period of time, the armature current increases slowly until instability occurs at I_{as}. When the field current polarity is changed, the electromagnetic torque (in phase quantities) becomes

$$T_e = 3p_1\left(\Psi_d i_q - \Psi_q i_d\right) = 3p_1\left[-X_{ad}I_F + \left(X_d - X_q\right)i_d\right]i_q \tag{8.54}$$

The ideal maximum negative field current I_F that produces stability is obtained for zero torque:

$$I_F = \left(X_d - X_q\right)\cdot i_d / X_{ad} \tag{8.55}$$

The flux linkages are now as follows:

$$\Psi_d \approx \frac{X_{ad}I_F}{\omega_1} + \frac{X_d}{\omega_1} I_{as} \tag{8.56}$$

With Equation 8.55, Equation 8.56 becomes as follows:

$$\Psi_d = \frac{X_q}{\omega_1} I_{as} \quad ; \quad \Psi_q = \frac{X_q}{\omega_1} I_q \approx 0 \tag{8.57}$$

The phase voltage E_a is

$$E_a = \omega_1 \Psi_s = \omega_1 \Psi_d = X_q I_{as} \tag{8.58}$$

See also Figure 8.19.
Finally,

$$X_q \approx \frac{E_a}{I_{as}} \tag{8.59}$$

Though the expression of X_q is straightforward, running the machine as a motor on no-load is not always feasible. Synchronous condensers, however, are a typical case when such a situation occurs naturally. There is some degree of saturation in the machine, but this is mainly due to *d* axis magnetizing magnetomotive forces (mmfs; produced by excitation plus the armature reaction). Catching the situation when stability is lost requires very small and slow increments in I_F, which requires special equipment.

8.6.3 Negative Sequence Impedance Z_2

Stator current harmonics may change the fundamental negative sequence voltage, but without changes in the fundamental negative sequence current. This phenomenon is more pronounced in salient motor pole machines with an incomplete damper ring or without damper winding, because there is a difference between subtransient reactances X_d'' and X_q''.

Consequently, during tests, sinusoidal negative sequence currents have to be injected into the stator, and the fundamental frequency component of the negative sequence voltage has to be measured for
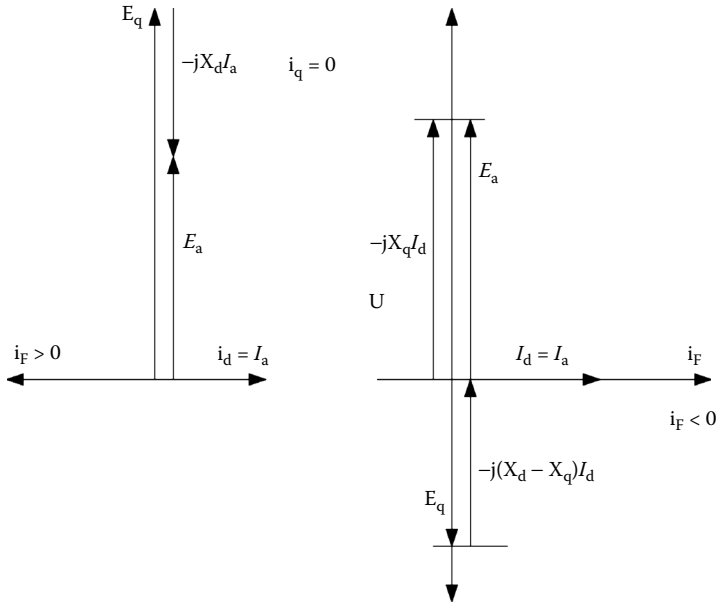
FIGURE 8.19 Phasor diagram for the maximum lagging current tests.

correct estimation of negative sequence impedance Z_2. In general, corrections of the measured Z_2 are operated based on a known value of the subtransient reactance X_d''.

The negative sequence impedance is defined for a negative sequence current equal to rated current. A few steady-state methods to measure X_2 are given here.

8.6.3.1 Applying Negative Sequence Currents

With the field winding short-circuited, the SG is driven at synchronous (rated) speed while being supplied with negative sequence currents in the stator at frequency f_N. Values of currents around rated current are used to run a few tests and then to claim an average Z_2 by measuring input power current and voltage.

To secure sinusoidal currents, with a voltage source, linear reactors are connected in series. The waveform of one stator current should be analyzed. If current harmonics content is above 5%, the test is prone to appreciable errors. The parameters extracted from measuring power, P, voltage (E_a), and current I_a, per phase are as follows:

$$Z_2 = \frac{E_a}{I_a} \quad \text{negative sequence impedance} \tag{8.60}$$

$$R_2 = \frac{P}{I_a^2} \quad \text{negative sequence resistance} \tag{8.61}$$

$$X_2 = \sqrt{Z_2^2 - R_2^2} \quad \text{negative sequence reactance} \tag{8.62}$$

8.6.3.2 Applying Negative Sequence Voltages

This is a variant of the above method suitable for salient-pole rotor SGs that lack damper windings. This time, the power supply has a low impedance to provide for sinusoidal voltage. Eventual harmonics in current or voltage have to be checked and left aside. Corrections to the above value are as follows [1]:

$$X_{2c} = \frac{\left(X_d'\right)^2}{\left(2X_d' - X_2\right)} \tag{8.63}$$

8.6.3.3 Steady-State Line-to-Line Short-Circuit Tests

As shown in Chapter 4, during steady-state line-to-line short-circuit at rated speed, the voltage of the open phase (E_a) is as follows:

$$\left(E_a\right)_{openphase} = \frac{2}{\sqrt{3}} Z_2 \underline{I}_{sc2} \tag{8.64}$$

Harmonics are eliminated from both I_{sc2} and $(E_a)_{openphase}$. Their phase shift φ_{os} is measured:

$$Z_2 = \frac{E_a \sqrt{3}}{2 I_{sc2}} \;\; ; \;\; R_2 = Z_2 \cos\varphi_{os} \tag{8.65}$$

When the stator null point of the windings is not available, the voltage E_{ab} is measured (*bc* line short-circuit). Also, the phase shift φ_{0sc} between $\underline{E}_{ab}$ and $\underline{I}_{sc2}$ is measured. Consequently,

$$Z_2 = \frac{E_{ab}}{\sqrt{3}I_{sc2}} \qquad \text{in } (\Omega)\,; \;\; R_2 = Z_2 \cos\varphi_{osc} \tag{8.66}$$

The presence of the third harmonic in the short-circuit current needs to be addressed [1]. The corrected X_{2c} value of X_2 is

$$X_{2sc} = \frac{X_2^2 + \left(X_d'\right)^2}{2X_d'} \tag{8.67}$$

Both X_2 and X_d'' have to be determined at rated current level. With both E_{ab} and I_{sc2} waveforms acquired during sustained short-circuit tests, only the fundamentals are retained by post-processing; thus, Z_2 and R_2 are determined with good precision.

8.6.4 Zero Sequence Impedance Z_o

With the SG at standstill, and three phases in parallel (Figure 8.20a) or in series (Figure 8.20b), the stator is AC supplied from a single-phase power source. The same tests may also be performed at rated speed.

As an alternative to taking phase-angle φ_o measurements, the input power P_a may be measured:

$$Z_o = \frac{3E_a}{I_a} \;\; \text{for parallel connection} \tag{8.68}$$

$$R_o = \frac{3P_o}{I_a^2} \;\; \text{for parallel connection} \tag{8.69}$$

$$Z_o = \frac{E_a}{3I_a} \;\; \text{for series connection} \tag{8.70}$$
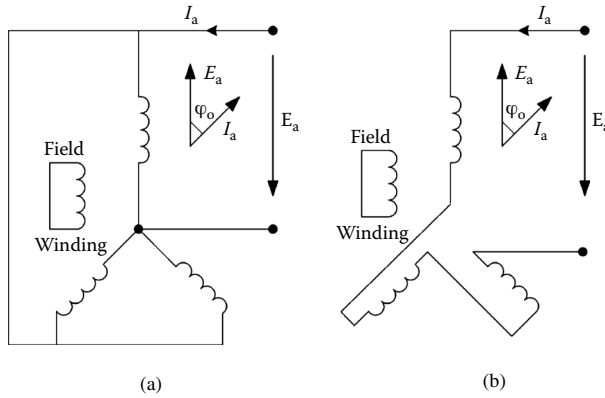
FIGURE 8.20 Single-phase supply tests to determine Z_o.
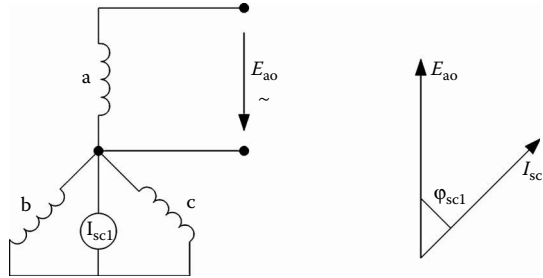

FIGURE 8.21 Sustained two line-to-neutral short-circuit.

$$R_o = \frac{P_o}{3I_a^2} \text{ for series connection} \tag{8.71}$$

Alternatively,

$$R_o = Z_o \cos\varphi_o \qquad X_o = \sqrt{Z_o^2 - R_o^2} \tag{8.72}$$

Among other methods to determine Z_o, we mention here the two line-to-neutral sustained short-circuit (Figure 8.21) methods with the machine at rated speed.

The zero sequence impedance Z_o is simply

$$Z_o = \frac{E_{ao}}{I_{scl}} \tag{8.73}$$

$$R_o = Z_o \cos\varphi_{scl}; \qquad X_o = \sqrt{Z_o^2 - R_o^2} \tag{8.74}$$

In this test, the zero sequence current is, in fact, one third of the neutral current I_{scl}. As Z_o is a small quantity, care must be exercised to reduce the influence of power, voltage, or current devices and of the leads in the measurements for medium and large power SGs.

8.6.5 Short-Circuit Ratio

The SCR is obtained from the open-circuit and short-circuit saturation curves and is defined as in IEEE standard 100-1992:
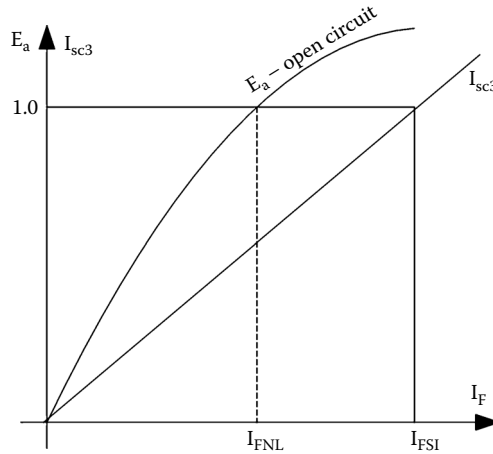
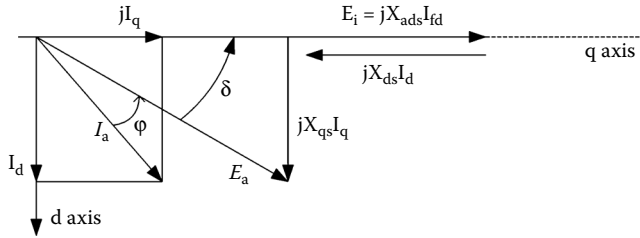**FIGURE 8.22** Extracting the short-circuit ratio (SCR).

FIGURE 8.23 Phasor diagram for zero losses.

$$SCR = \frac{I_{FNL}}{I_{FSI}} \approx \frac{1}{X_d} \quad (P.U.) \tag{8.75}$$

where

I_{FNL} = the field current from the open-circuit saturation curve corresponding to rated voltage at rated frequency

I_{FSI} = the field current for rated armature current from the three-phase short-circuit saturation curve at rated frequency (Figure 8.22)

Though there is some degree of saturation considered in the SCR, it is by no means the same as for rated load conditions; this way, SCR is only a qualitative performance index, required for preliminary design (see Chapter 7).

8.6.6 Angle δ, X_{ds}, X_{qs} Determination from Load Tests

The load angle δ is defined as the angular displacement of the center line of a rotor pole field axis from the axis of stator mmf wave (space vector), for a specified load. In principle δ, may also be measured during transients. When iron loss is neglected δ is the angle between the field-current-produced emf and the phase voltage E_a, as apparent from the phasor diagram (Figure 8.23).

With the machine loaded, if the load angle δ is measured directly by a separate sensor, the steady-state load measurements may be used to determine the steady-state parameters X_{ds} and X_{qs}, with known leakage reactance X_l ($X_{ds} = X_{ads} + X_l$) (Figure 8.21). The load angle δ may be calculated as follows:

$$\delta = \tan^{-1}\left(\frac{I_a X_{qs}\cos\varphi}{E_a + I_a X_{qs}\sin\varphi}\right) \tag{8.76}$$

As δ, I_a, E_a, and φ are measured directly, the saturated reactance X_{qs} may be calculated directly for the actual saturation conditions. The I_d, I_q current components are available:

$$I_d = I_a \sin\left(\varphi + \delta\right) \tag{8.77}$$

$$I_q = I_a \cos\left(\varphi + \delta\right) \tag{8.78}$$

Also, from Figure 8.21,

$$X_{ads} I_{fd} - \left(X_{ads} + X_l\right) I_d = E_a \cos\delta \tag{8.79}$$

As the leakage reactance X_l is considered already known, I_{fd}, E_a, and δ are measured directly (after reduction to stator); I_d is obtained from Equation 8.77; and Equation 8.79 yields the saturated value of the direct-axis reactance $X_{ds} = X_l + X_{ads}$. The load angle may be measured by encoders, by resolvers, or by electronic angle shifting measuring devices [1].

The reduction factor of the directly measured excitation current to the stator from I_f to I_{fd} may be taken from design data or calculated from SSFR tests as shown later in this chapter. If load tests are performed for different currents and power factor angles at constant voltage (P and Q) and δ, I_a, $\cos\varphi$, and I_{fd} are measured, families of curves $X_{ads}(I_d + I_{fd}, I_q)$ and $X_{qs}(I_q, I_d + I_{fd})$ are obtained. Alternatively, the $\Psi_d(I_q, I_d + I_{fd})$ and $\Psi_q(I_q, I_d + I_{fd})$ curve family is obtained:

$$\Psi_d = X_l i_d + X_{ads}\left(i_d + i_{fd}\right) \tag{8.80}$$

$$\Psi_q = X_{qs} i_q \tag{8.81}$$

Based on such data, curve-fitting functions may be built. Same data may be obtained from FEM calculations. Such a confrontation between FEM and direct tests for steady-state parameter saturation curve families (Figure 8.24) for online large SGs is still awaited, while simplified interesting methods to account for steady-state saturation, including cross-coupling effects, are still produced [7, 8].

The saturation curve family, $\Psi_d(I_q, I_d + I_{fd})$ and $\Psi_q(I_q, I_d + I_{fd})$ may be determined as follows from standstill flux decay tests.

8.6.7 Saturated Steady-State Parameters from Standstill Flux Decay Tests

To account for magnetic saturation, high (rated) levels of current in the stator and in the field winding are required. Under standstill conditions, the cooling system of the generator might not permit long time operation. The testing time should be reduced. Further on, with currents in both axes (I_q, $I_d + I_{fd}$), there will be torque, so the machine has to be stalled. Low-speed high-power SGs have large torque, and stalling is not easy.

If the tests are done in axis d or in axis q, there will be no torque, and the cross-coupling saturation (between orthogonal axes) is not present. Flux decay tests consist of first supplying the machine with a small DC voltage with stator phases connected so as to place the stator mmf either along axis d or along axis q. All this time, the field winding may be short-circuited, open, or supplied with a DC current. At a certain moment after the I_{ao}, V_o, and I_{Fo} are measured, the DC circuit is short-circuited by a fast switch
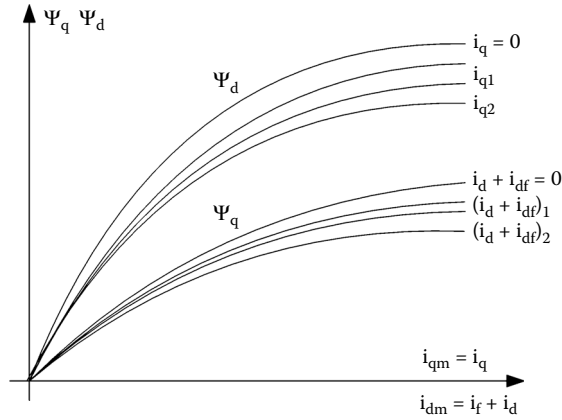
FIGURE 8.24 *d* and *q* axes flux vs. current curves family.

with a very low voltage across it (when closed). A free-wheeling diode may be used instead, but its voltage drop should be recorded and its integral during flux (current) decay time in the stator should be subtracted from the initial flux linkage. The *d* and *q* reactances are then obtained for the initial (DC) situation, corresponding to the initial flux linkage in the machine. The test is repeated with increasing values of initial currents along axes *d* ($i_d + i_{fd}$) and *q* (i_q), and the flux current curve family as in Figure 8.24 is obtained. The same tests may be run on the field winding with an open- or short-circuited stator.

A typical stator connection of phases for *d* axis flux decay tests is shown in Figure 8.25a.

To arrange the SG rotor in axis *d*, the stator windings, connected as in Figure 8.25a, are supplied with a reasonably large DC current with the field winding short-circuited across the free-wheeling diode. If the rotor is heavy and it will not move by itself easily, the stator is fed from an AC source with a small
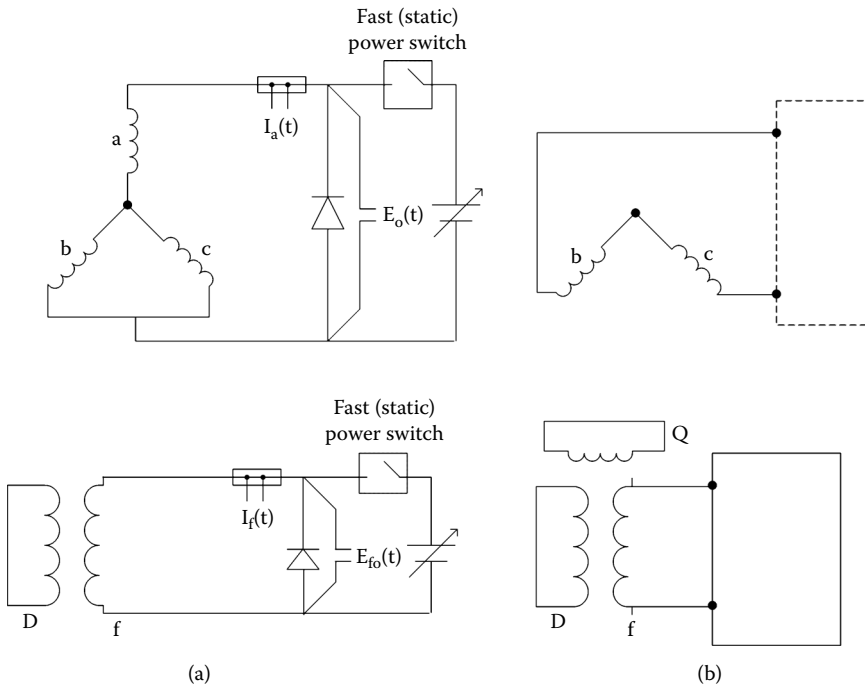

FIGURE 8.25 Flux decay tests: (a) axis *d* and (b) axis *q*.

current, and the rotor is rotated until the AC field-induced current with the free-wheeling diode short-circuited will be at maximum. Alternatively, if phases b and c in series are AC supplied (Figure 8.25b), then the rotor is moved until the AC field-induced current becomes zero. For fractionary stator winding, the position of axis d is not so clear, and measurements in a few closely adjacent positions are required in order to average the results [1].

The SG equations in axes d and q at zero speed are simply

$$I_d R_a - V_d = -\frac{d\Psi_d}{dt} \tag{8.82}$$

$$I_q R_a - V_q = -\frac{d\Psi_q}{dt} \tag{8.83}$$

In axis d (Figure 8.25a),

$$i_d = \frac{2}{3}\left(i_a + i_b \cos\left(\frac{2\pi}{3}\right) + i_c \cos\left(-\frac{2\pi}{3}\right)\right) = i_a \tag{8.84}$$

$$i_q = \frac{2}{3}\left(0 + i_b \sin\left(\frac{2\pi}{3}\right) + i_c \sin\left(-\frac{2\pi}{3}\right)\right) = 0 \quad ; \; i_b = i_c \tag{8.85}$$

The flux in axis q is zero. After short-circuiting the stator ($V_d = 0$) and integrating (8.82),

$$R_a \int_0^\infty I_d dt + K_d \int_0^\infty V_{diode} dt = \left(\Psi_d\right)_{initial} - \left(\Psi_d\right)_{final} \tag{8.86}$$

$$K_d = 2/3 \text{ as } V_d = V_a \text{ and } V_a - V_b = (2/3)V_a \tag{8.87}$$

Equation 8.86 provides the key to determining the initial flux linkage if the final flux linkage is known. The final flux is produced by the excitation current alone and may be obtained from a flux decay test on the excitation, from same initial field current, with the stator open, but this time, recording the stator voltage across the diode $V_o(t) = V_{abc}(t)$ is necessary. As $V_{abc}(t) = (3/2)V_d(t)$,

$$\Psi_{dinitial}\left(i_{fo}\right) = \int_0^\infty \frac{2}{3} V_o\left(t\right) dt; \quad i_a = 0 \tag{8.88}$$

The initial d axis flux $\Psi_{dinitial}$ is as follows:

$$\Psi_{dinitial}\left(i_{fdo} + i_{do}\right) = L_l i_{do} + L_{ad}\left(i_{fdo} + i_{do}\right) \tag{8.89}$$

As i_f and not i_{fd} (reduced to the stator) is measured, the value for the ratio a has to be determined first. It is possible to run a few flux decay tests on the stator, with zero field current, and then in the rotor, with zero stator current, and use the above procedure to calculate the initial flux (final flux is zero). When the initial flux in the stator from both tests is the same (Figure 8.26), then the ratio of the corresponding currents constitutes the reduction (turn ratio) value a:
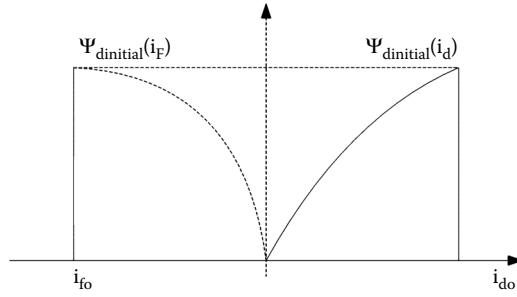
FIGURE 8.26 Turns ratio $a = i_{do}/i_{fo}$.

$$a = \frac{i_{do}}{i_{fo}} \quad i_{fd} = a i_f \tag{8.90}$$

The variation of a with the level of saturation should be small. When the tests are done in axis q (Figure 8.25b),

$$i_d = 0 \quad i_b = -i_c \quad i_a = 0 \tag{8.91}$$

$$i_q = \frac{2}{3}\left(i_b \sin\left(\frac{2\pi}{3}\right) + i_c \sin\left(-\frac{2\pi}{3}\right) \right) = \frac{2}{\sqrt{3}} i_b \tag{8.92}$$

$$V_q = \frac{2}{3}\left(V_a \sin\theta + (V_b - V_c)\sin\frac{2\pi}{3} \right) = \frac{2}{3}(V_b - V_c)\frac{\sqrt{3}}{2} = \frac{V_b - V_c}{\sqrt{3}} \tag{8.93}$$

Under flux decay, from Equation 8.53 with Equation 8.92 and Equation 8.93,

$$\Psi_{qinitial}\left(i_{qo}, i_{fdo}\right) = \frac{2}{\sqrt{3}}\int i_b R_a dt + \frac{1}{\sqrt{3}}\int_0^\infty V_{diode}\, dt \tag{8.94}$$

The final flux in axis q is zero, despite the nonzero field current, because the two axes are orthogonal. Doing the tests for a few values of $i_{fdo}(i_{fo})$ and for specified initial values of $i_{qo} = \frac{2}{\sqrt{3}}i_b$, a family of curves may be obtained:

$$\Psi_{qinitial}\left(i_{qo}, i_{fdo}\right) = L_l I_{qo} + I_{qo} L_{aq}\left(i_{qo}, i_{fdo}\right) \tag{8.95}$$

Considering that the d axis stator current and field current mmfs are almost equivalent, the cross-coupling saturation in axis q is solved for all purposes. This is not so in axis d, where no cross-coupling has been explored. A way out of this situation is to "move" the stator mmf connected as in Figure 8.25 by exchanging phases from a–b and c to b–a and c to c–a and b. This way, the rotor is left in the d axis position corresponding to a–b and c (Figure 8.25). Now, I_d, I_q, V_d, and V_q have to be considered together; thus, both families of curves may be obtained simultaneously, with

$$i_d = \frac{2}{3}\left[i_a \cos\left(-\theta_{er}\right) + i_b \cos\left(-\theta_{er} + \frac{2\pi}{3}\right) + i_c \cos\left(-\theta_{er} - \frac{2\pi}{3}\right) \right] \qquad (8.96)$$

$$i_q = \frac{2}{3}\left[i_a \sin\left(-\theta_{er}\right) + i_b \sin\left(-\theta_{er} + \frac{2\pi}{3}\right) + i_c \sin\left(-\theta_{er} - \frac{2\pi}{3}\right) \right] \qquad (8.97)$$

V_d and V_q are obtained with similar formulae, but notice that $V_b = V_c = -V_a/2$. Then, the flux decay equations after integration are as follows:

$$\Psi_{dinitial} = \Psi_{dfinal} + \int_0^\infty i_d R_a dt + \frac{V_{do}}{V_{abco}} \int_0^\infty V_{diode} dt \qquad (8.98)$$

$$\Psi_{qinitial} = \Psi_{qfinal} + \int_0^\infty i_q R_a dt + \frac{V_{qo}}{V_{abco}} \int_0^\infty V_{diode} dt \qquad (8.99)$$

The final values of flux in the two axes are produced solely by the field current. The flux decay test in the rotor is done again to obtain the following:

$$\Psi_{dinitial}\left(i_{fo}\right) = \int_0^\infty V_d\left(t\right) dt \qquad (8.100)$$

$$\Psi_{qinitial}\left(i_{fo}\right) = \int_0^\infty V_q\left(t\right) dt \qquad (8.101)$$

Placing the rotor in axis d, then in axis q, and then with $\theta_{er} = \frac{\pi}{6}, \frac{2\pi}{3}$ will produce plenty of data to document the flux/current families that characterize the SG (Figure 8.24). Flux decay test results in axis d or axis q in large SGs to determine steady-state parameters as influenced by saturation were published [9], but the procedure — standard in principle — has to be further documented by very neat tests with cross-coupling thoroughly considered, and with hysteresis and temperature influence on results eliminated.

The flux decay tests at nonzero or non-90° electric angle, introduced above, might be the way to obtain the whole flux/current (or flux/mmf) family of curves that characterizes the SG for various loads. Note that it may be argued that, though practically all values of i_d, i_q, and i_{fd} may be produced in flux decay tests, the saturation influence on steady-state parameters may differ under load for the same current triplet. This is true because under load (at rated speed), the stator iron is AC magnetized (at frequency f_N) and not DC magnetized as in flux decay tests.

Direct-load tests or FEM comparisons with these flux decay tests will tell if this is more than an academic issue. The whole process of standstill flux decay tests may be computerized and, thus, mechanized, as static power switches are now available off the shelf. The tests take time, but apparently notably less time than the SSFR test. The two types of tests are, in fact, complementary, as one produces the steady-state (or static) saturated parameters for specified load conditions, while the other estimates the parameters for transients from such initial on-load steady-state states. The standstill flux decay tests were also used to estimate the parameters for transients by curve fitting the current decays vs. time [10, 11].

8.7   Tests To Estimate the Subtransient and Transient Parameters

Subtransient and transient parameters of the SG manifest themselves when sudden changes at or near stator terminals (short-circuits) or at the field current occur. Knowing the sudden balanced and unbalanced short-circuit stator current peak value and evolution in time until steady state is useful in the design of SG protection, calibration of the trip stator and field-current circuit breakers, and calculation of the mechanical stress in the stator end turns. Sudden short-circuit tests from no-load or load operation have been performed for more than 80 years, and, in general, two stages during these transients were traditionally identified.

The first, short in duration, characterized by steep attenuation of stator current I_s, is called the subtransient stage. The second, larger and slower in terms of current decay rate is the so-called transient stage. Phenomenologically, in the transient stage, the transient currents in the rotor damper cage (or solid rotor) are already fully attenuated. Subtransient and transient stages are characterized by time constants: the time elapsed for a current decay to $1/e = 0.368$ from its original value. Based on this observation, graphical methods were developed to identify the subtransient and transient parameters. As short-circuits from no load are typical, only the d axis parameters are obtained in general (X_d'', T_d'', X_d', T_d').

In acquiring the armature and field current during short-circuit, it is important to use a power switch that short-circuits all required phases in the same time. Also, noninductive shunts or Hall probe current sensors with leads kept close together or twisted or via optical fiber cables to reduce the induced parasitic voltages are to be used.

To avoid large errors and high transient voltage in the field circuit, the latter has to be supplied from low-impedance constant voltage supply. For the case of brushless exciters, the field current sensor is placed on the rotor, and its output is transmitted through special slip-rings and brushes placed on purpose there, or through telemetry.

8.7.1   Three-Phase Sudden Short-Circuit Tests

The standard variation of stator terminal RMS AC components of current during a three-phase sudden short-circuit from no load is as follows:

$$I_{ac}(t) = \frac{E}{X_{ds}} + \left(\frac{E}{X_d'} + \frac{E}{X_{ds}} \right) e^{-t/T_d'} + \left(\frac{E}{X_d''} + \frac{E}{X_{ds}'} \right) e^{-t/T_d''} \tag{8.102}$$

where

   $I(t)$ = the AC RMS short-circuit current (P.U.)
   $E(t)$ = the no-load (initial) AC RMS phase voltage (P.U.)

If the test is performed below 0.4 P.U. initial voltage, X_{ds} is replaced by X_{du} (unsaturated), with both taken from the open-circuit saturation curve.

After subtracting the sinusoidal (steady-state) term in Equation 8.93, the second and third terms may be represented in semilogarithmic scales. The rapidly decaying portion of this curve represents the subtransient stage, while the straight line is the transient stage (Equation 8.102).

The extraction of rms values of the stator AC short-circuit current components from its recorded waveform vs. time is now straightforward. If the field current is also acquired, the stator armature time constant T_a may also be determined. The DC decay stator short-circuit current components from all three phases may also be extracted from the recorded (acquired) data.

If a constant-voltage low-impedance supply to the field winding is not feasible, it is possible to simultaneously short-circuit the stator and the field winding. In this case, both the stator current and the field current decay to zero. From the stator point of view, the constant component in Equation 8.102
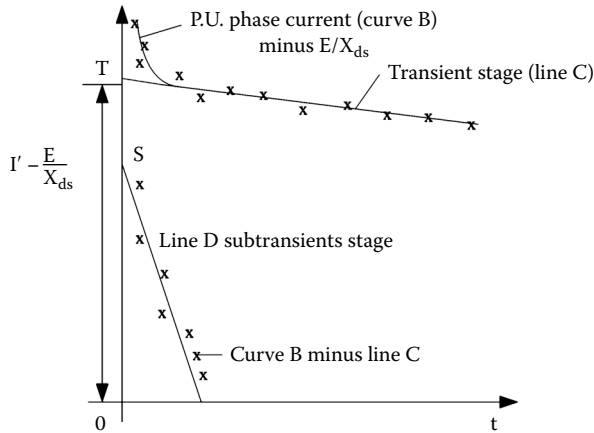
FIGURE 8.27 Analysis of subtransient and transient short-circuit current alternating current components.

has to be eliminated. It is also feasible to reopen the stator circuit (after reaching steady short-circuit) and record the stator voltage recovery.

The transient reactance X_d' is as follows:

$$X_d' = \frac{E}{I'} \qquad (8.103)$$

I' is the initial AC transient current (OT Figure 8.27) plus the steady-state short-circuit current E/X_d.

The subtransient reactance X_d'' is

$$X_d'' = \frac{E}{I''} \qquad (8.104)$$

I'' is the total AC peak at the time of short circuit $I'' = I' + \overline{OS}$ (from Figure 8.27).

The transient reactance is influenced by the saturation level in the machine. If X_d' is to be used to describe transients at rated current, short-circuit tests are to be done for various initial voltages E to plot $X_d'(I')$. The short-circuit time constants T_d' and T_d'' are obtained as the slopes of the straight lines C and D in Figure 8.27.

8.7.2 Field Sudden Short-Circuit Tests with Open Stator Circuit

The sudden short-circuit stator tests can provide values for X_d'', X_d', T_d'', and T_d'. The stator open-circuit subtransient and transient time constants T_{d0}'' and T_{d0}' are, however, required to fully describe the operational impedance X_d. A convenient test to identify T_{d0}' consists of running the machine on armature open circuit with the field circuit provided with a circuit breaker and a field discharge contact with a field discharge resistance (or free-wheeling diode) in series. The field circuit is short-circuited by opening the field circuit breaker (Figure 8.28a).

The field current and stator voltage are acquired and represented in a semilogarithmic scale (Figure 8.28b).

The transient open-circuit time constant T_{d0t}' in Figure 8.28b accounts also for the presence of additional discharge resistance R_D. Consequently, the actual T_{d0}' is as follows:

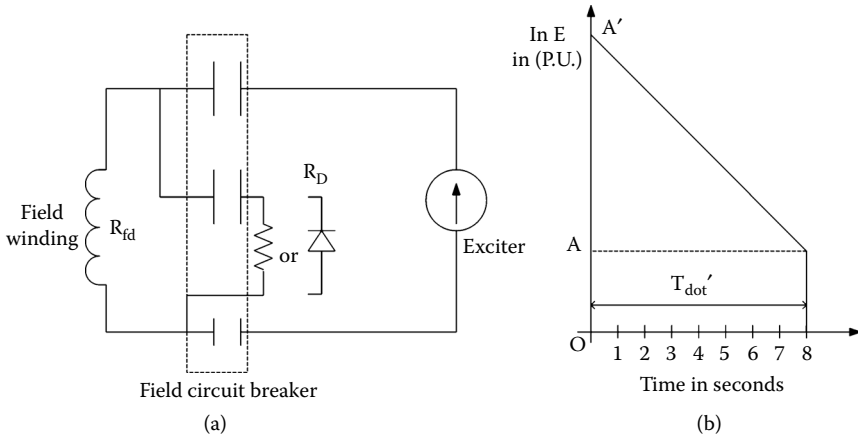$$T_{d0}' = T_{d0t}' \cdot \left(1 + \frac{R_D}{R_{fd}}\right) \qquad (8.105)$$

FIGURE 8.28 Field-circuit short-circuit tests with open armature: (a) the test arrangement and (b) the armature voltage *E* vs. time.
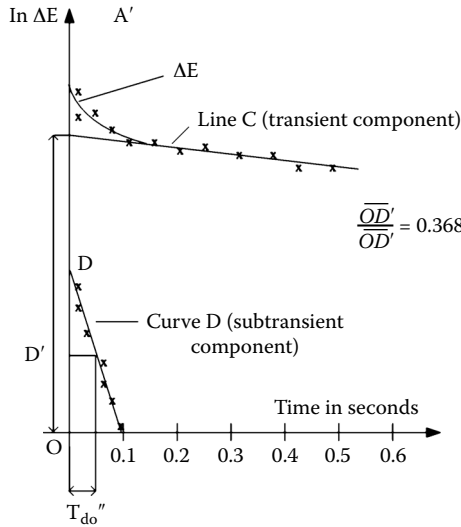

FIGURE 8.29 Difference between recovery voltage and steady-state voltage vs. time.

When a free-wheeling diode is used, R_D may be negligible.

The subtransient open-circuit time constant T_{d0}'' may be obtained after a sudden short-circuit test when the stator armature circuit is suddenly opened and the recovery armature differential voltage is recorded (Figure 8.29). The value of T_{d0}'' is obtained after subtracting the line C (Figure 8.29) from the differential voltage ΔE (recovery RMS voltage minus RMS steady-state voltage) to obtain curve D, approximated to a straight line. Notice that the three-phase short-circuit tests with variants provided only transient and subtransient parameters in axis *d*.

8.7.3 Short-Circuit Armature Time Constant T_a

The stator time constant T_a occurs in the DC component of the three-phase short-circuit current:

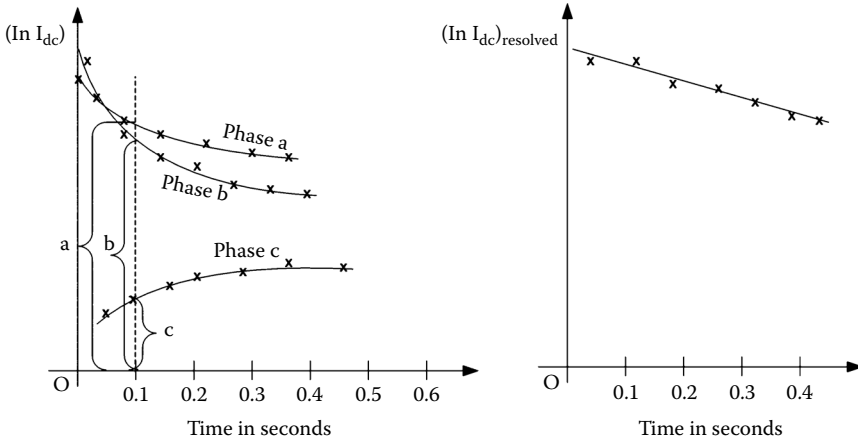$$I_{dc}(t) = \frac{E}{X_d''} e^{-t/T_a} \tag{8.106}$$

FIGURE 8.30 Direct current components of short-circuit currents.

It may be determined by separating the DC components from the short-circuit currents of phases *a*, *b*, and *c* (Figure 8.30).

As can be seen from Figure 8.30, the DC components of short-circuit currents do not vary in time in exactly the same way. A resolved I_{dc} is calculated, from selected values at the same time, as follows [1]:

$$\left(I_{dc}\right)_{resolved} = \left(\sqrt{\left(a^2 + b^2 - ab\right)} + \sqrt{a^2 + c^2 - ac} + \sqrt{b^2 + c^2 - cb}\right)\sqrt{\frac{4}{27}} \qquad (8.107)$$

where *a*, *b*, and *c* are the instantaneous values of I_a, I_b, and I_c for a given value of time with $a > b > c$. Then, from the semilogarithmic graph of (I_{dc}) resolved vs. time, T_a is found as the slope of the straight line.

Note that the above graphical procedure to identify X_d'', X_d', T_d'', T_d', T_a, through balanced short-circuit tests may be computerized to speed up the time to extract these parameters from test data that are currently computer acquired [1].

Various regression methods were also introduced to fit the test data to the SG model.

8.7.4 Transient and Subtransient Parameters from *d* and *q* Axes Flux Decay Test at Standstill

The standstill flux decay tests in axes *d* and *q* provide the variation of $i_d(t)$ and $i_{fd}(t)$ and, respectively, $i_q(t)$ (Figure 8.31). This test was traditionally used to determine — by integration — the initial flux and, thus, the synchronous reactances and the turn ratio *a*. However, the flux decay transient current responses contain all the transient and subtransient parameters. Quite a few methods to process this information and produce X_d'', X_d', X_q'', T_d'', T_d', T_q'' have been proposed. Among them, we mention here the decomposition of recorded current in exponential components [10]:

$$I_{d,q}\left(t\right) = \sum I_j e^{-t/T_j} \qquad (8.108)$$

For the separation of the exponential constants I_j and T_j, a dedicated program based on nonlinear least square analysis may be used. Also, the maximum likelihood (ML) estimation was applied [11] successfully to process the flux decay data — $i_d(t)$, $i_{fd}(t)$ — with two rotor circuits in axes *d* and *q*. To initialize the process, the graphical techniques described in previous paragraphs [12] were also applied for the scope.
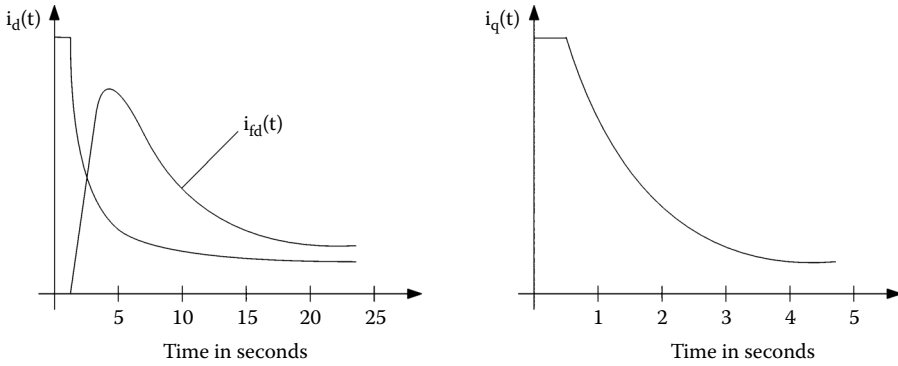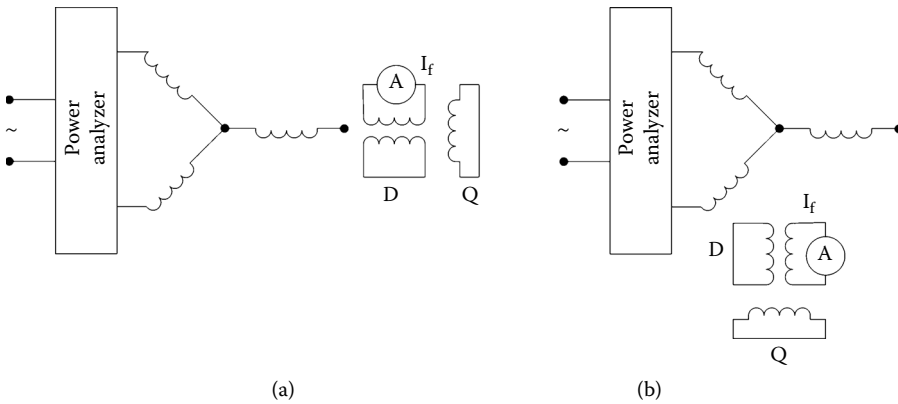
FIGURE 8.31 Flux decay transients at standstill.

FIGURE 8.32 Line-to-line alternating current standstill tests: (a) axis d and (b) axis q.

If the tests are performed for low initial currents, there is no magnetic saturation. On the contrary, for large (rated) values of initial currents, saturation is present.

It may be argued that during the transients in the machine at speed and on load, the frequency content of various rotor currents differs from the case of standstill flux decay transients. In other words, were the transients and the subtransient parameters determined from flux decay tests applied safely? At least they may be safely used to evaluate balanced sudden short-circuit transients.

8.8 Subtransient Reactances from Standstill Single-Frequency AC Tests

The subtransient reactances X_d'' and X_q'' are associated with fast transients or large frequency (Figure 8.32a and Figure 8.32b). Consequently, at standstill when supplying the stator line from a single-phase AC (at rated frequency) source, the rotor circuits (field winding is short-circuited) experience that frequency. The rotor is placed in axis d by noticing the situation when the AC field current is maximum. For axis q, it is zero.

The voltage, current, and power in the stator are measured, and thus,

$$Z_{d,q}'' = \frac{E_{ll}}{2I_a} \tag{8.109}$$

$$R''_{d,q} = \frac{P_a}{2I_a^2} \tag{8.110}$$

$$X''_{d,q} = \sqrt{\left(Z''_{d,q}\right)^2 - \left(R''_{d,q}\right)^2} \tag{8.111}$$

The rated frequency f_N is producing notable skin effects in the solid parts of the rotor or in the damper cage. As for the negative impedance Z_2, the frequency in the rotor $2f_N$, it might be useful to do this test again at $2f_N$ and determine again X''_d $(2f_N)$ and X''_q $(2f_N)$ and then use them to define the following:

$$X_2 = \frac{X''_d\left(2f_N\right) + X''_q\left(2f_N\right)}{2} \tag{8.112}$$

$$R_2 = \frac{R''_d\left(2f_N\right) + R''_q\left(2f_N\right)}{2} \tag{8.113}$$

It should be noticed, however, that the values of X_2 and R_2 are not influenced by DC saturation level in the rotor that is present during SG on load operation. If solid parts are present in the rotor, the skin effect that influences X_2 and R_2 is notably marked, in turn, by the DC saturation level in the machine at load.

8.9   Standstill Frequency Response Tests (SSFRs)

Traditionally, short-circuit tests have been performed to check the SG capability to withstand the corresponding mechanical stresses on one hand, and to provide for subtransient and transient parameter determination to predict transient performance and assist in SG control design, on the other hand. From these tests, two rotor circuit models are identified: the subtransient and transient submodels — a damper plus field winding along the *d* axis and two damper circuits along the *q* axis. As already illustrated in previous paragraphs, sudden short-circuit tests do not generally produce the transient and subtransient parameters in axis *q*.

For today's power system dynamics studies, all parameters along axes *d* and *q* are required.

Identification of the two rotor circuit models in axis *d* and separately in axis *q* may be performed by standstill flux decay tests as illustrated earlier in this chapter.

It seems, however, that both sudden short-circuit tests and standstill flux decay tests do not completely reflect the spectrum of frequencies encountered by an SG under load transients when connected to a power system or in stand-alone mode.

This is how standstill frequency tests have come into play. They are performed separately in axes *d* and *q* for current levels of 0.5% of rated current and for frequencies from 0.001 to 100 Hz and more.

Not all actual transients in an SG span this wide frequency band; thus, the identified model from SSFR tests may be centered on the desired frequency zone.

The frequency effects in solid iron-rotor SGs are very important, and thus, the second-order rotor circuit model may not suffice. A third order in both *d* and *q* axes proved to be better.

As with all standstill tests, the centrifugal effect on the contact resistance of damper bars (or on conducting wedges) to slot walls are not considered, although they may notably influence the identified model. Comparisons between SSFR and on-load frequency response tests for turbogenerators have spotted such differences. The saturation level is very low in SSFR tests, while in real SG transients, the rotor core is strongly DC magnetized, and the additional (transient) frequency currents in the solid iron occur in such an iron core. The field penetration depth is increased by saturation, and the identified model parameters change.

Running SSFR tests in the presence of increasing DC premagnetization through the field current may solve the problem of saturation influences on the identified model. DC premagnetization is required only for frequencies above 1 Hz. Thus, the time to apply large DC currents is somewhat limited, so as to limit the temperature rise during such DC plus SSFR tests. Recently, the researchers in Reference [12] seemed to demonstrate such a claim. So far, however, the pure SSFR tests were investigated in more detail through a very rich literature and were finally standardized [1].

In what follows, the standardized version of SSFR is presented with short notes on the latest publications about the subject [1, 13].

8.9.1 Background

The basic small perturbation transfer function parameters, as developed in Chapter 5, are as follows:

$$\Delta\Psi_d(s) = G(s)\Delta e_{fd}(s) - L_d(s)\Delta i_d(s) \tag{8.114}$$

$$\Delta\Psi_q(s) = -L_q(s)\Delta i_q(s) \tag{8.115}$$

where
$L_d(s)$ = the direct axis operational inductance (the Laplace transform of d axis flux divided by i_d with field-winding short-circuited $\Delta e_{fd} = 0$)
$L_q(s)$ = the quadrature axis operational inductance
$G(s)$ = the armature to field transfer function (Laplace transform of the ratio of d axis flux linkage variation to field voltage variation, when the armature is open circuited)

The "−" signs in Equation 8.114 and Equation 8.115 are common for generators in the United States.
Also,

$$sG(s) = \left(\frac{\Delta i_d(s)}{\Delta i_{fd}(s)}\right)_{\Delta e_{fd}=0} \tag{8.116}$$

Equation 8.116 defines the $G(s)$ for the case when the field winding is short-circuited.
One more transfer function is $Z_{afo}(s)$:

$$Z_{afo}(s) = \left(\frac{\Delta e_{fd}(s)}{\Delta i_d(s)}\right)_{\Delta i_{fd}=0} \tag{8.117}$$

This represents the Laplace transform of the field voltage to d axis current variations when the field winding is open. Originally, the second-order rotor circuit model (Figure 8.33; Chapter 5) was used to fit the SSFR.

The presence of the leakage coupling inductance L_{fld} introduced in Reference [14] to better represent the field-winding transients was found positive in cylindrical solid-iron rotors and negative in salient-pole SGs.

In general, the stator leakage inductance L_l is considered known.

For high-power cylindrical solid-rotor SGs, third-order models were introduced (Figure 8.34). There is still a strong debate over whether one or two leakage inductances are required to fully represent such a machine, where the skin effect in the solid iron (and in the possible copper damper strips placed below the rotor field-winding slot wedges) is notable. Eventually, they lead to rather complex frequency responses (Figure 8.34 and Figure 8.35) [15].
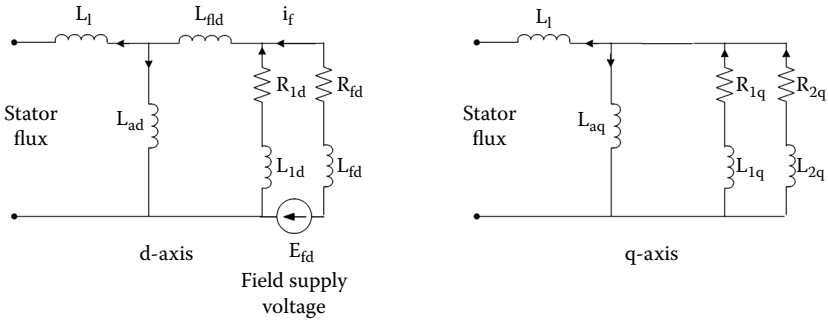
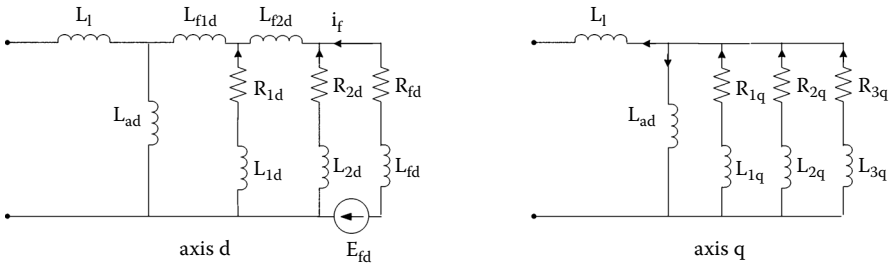**FIGURE 8.33** Second-order synchronous generator model: axis *d* and axis *q*.

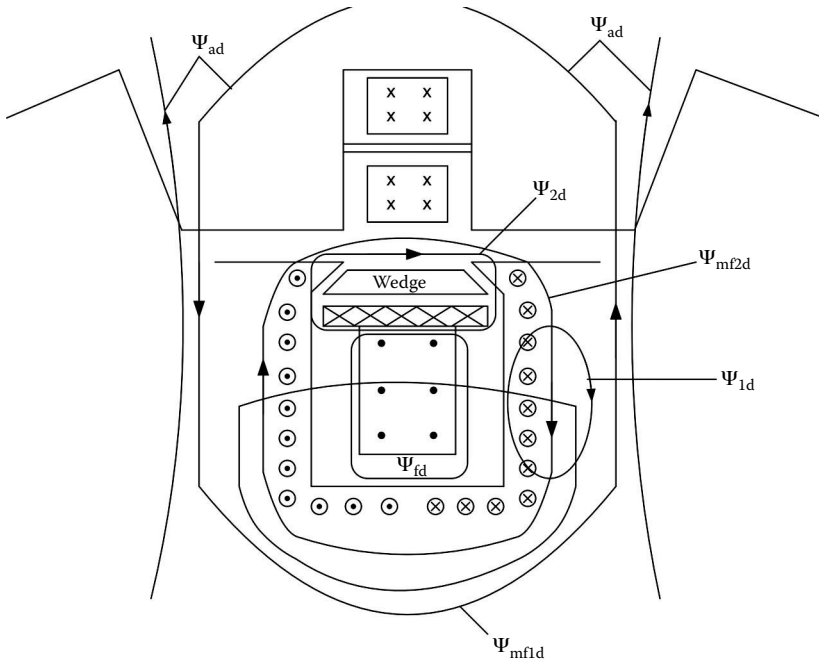

FIGURE 8.34 Third-order model of a synchronous generator.

FIGURE 8.35 Third-order model (axis *d*) with two rotor leakage mutual inductances L_{fl2d} and L_{f2d}.

With the leakage inductance L_l given, it is argued whether both L_{fl2d} and L_{f2d} are necessary to fully represent the actual phenomena in the machine. Though linear circuit theory allows for a few equivalent circuits for the same frequency response over some given frequency bands, it seems natural to follow the physical phenomena flux paths in the machine (Figure 8.35) [15].

Initially, SSFR methods made use of only stator inductances $L_d(\omega)$, $L_q(\omega)$ responses. It was soon realized that, simultaneously, the rotor response transfer function $G(\omega)$ has to be taken into consideration so that the modeling of the transients in the field winding would be adequate. In addition, $Z_{afd}(j\omega)$ is identified in some processes if the frequency range of interest is below 1 Hz.

The magnitudes and the phases of $L_d(j\omega)$, $L_q(j\omega)$, $G(j\omega)$, and $Z_{af0}(j\omega)$ are measured at several frequencies. The smaller the frequencies, the larger the number of measurements per decade (up to 60) required for satisfactory precision [16].

SSFR tests are done at very low current levels (0.5% of base stator current) in order to avoid overheating, as, at least in the low frequency range, data acquisition for two to three periods requires long time intervals ($f = 0.001$ to 1000 Hz).

Although magnetic saturation of the main flux path is avoided, the SSFR makes the stator and rotor-iron magnetization process evolve along low amplitude hysteresis cycles, where the incremental permeability acts $\mu_i = (100$ to $150)\mu_o$. Consequently, L_{ad} and L_{aq} identified from SSFR are not to be used as unsaturated values with the machine at load. The SSFR measurable parameters are as follows:

$$Z_d(j\omega) = \frac{\Delta e_d(j\omega)}{\Delta i_d(j\omega)}\bigg|_{\Delta e_{fd}=0} \tag{8.118}$$

$$Z_q(j\omega) = \frac{\Delta e_q(j\omega)}{\Delta i_q} \tag{8.119}$$

$$G(j\omega) = \frac{\Delta e_d(j\omega)}{j\omega\Delta i_{fd}(j\omega)}\bigg|_{\Delta i_d=0} \tag{8.120}$$

$$j\omega G(j\omega) = \frac{\Delta i_{fd}(j\omega)}{\Delta i_d(j\omega)}\bigg|_{\Delta e_{fd}=0} \tag{8.121}$$

$Z_d(j\omega)$ and $j\omega G(j\omega)$ may be found from the same test (in axis d) by additionally acquiring the field current $i_{fd}(j\omega)$.

The measurable parameter $Z_{af0}(j\omega)$ is as follows:

$$Z_{afo}(j\omega) = \frac{\Delta e_{fd}(j\omega)}{\Delta i_d(j\omega)}\bigg|_{\Delta i_f=0} \tag{8.122}$$

or

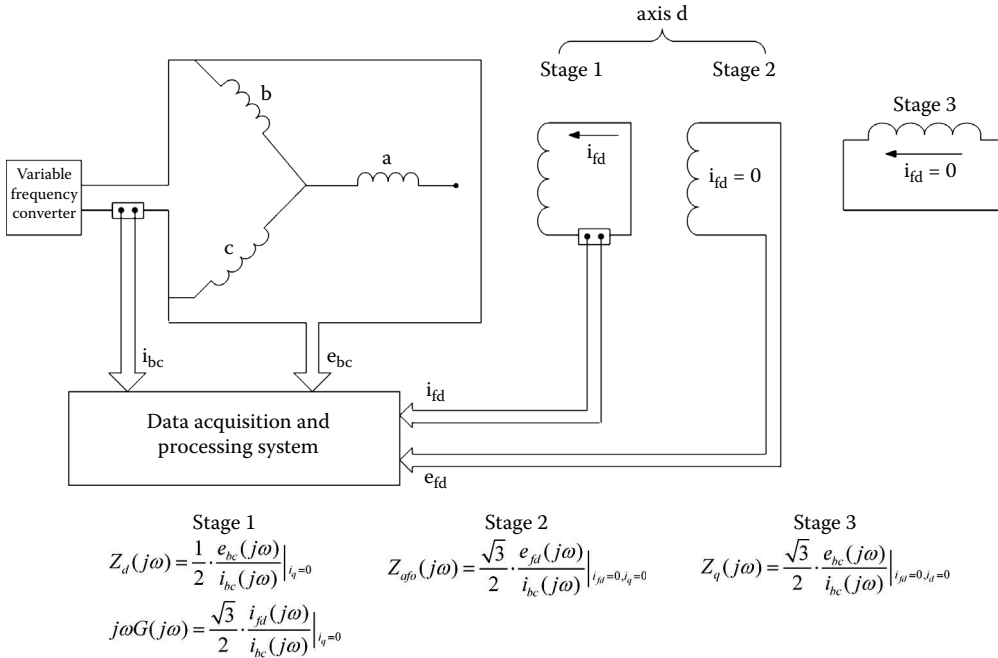$$Z_{afo}(j\omega) = \frac{\Delta e_d(j\omega)}{\Delta i_{fd}(j\omega)}\bigg|_{\Delta i_d=0} \tag{8.123}$$

axis d

Stage 1   Stage 2

Stage 3

i_{fd}

$i_{fd} = 0$

$i_{fd} = 0$

Variable frequency converter

b

a

c

i_{bc} e_{bc}

i_{fd}

Data acquisition and processing system

e_{fd}

Stage 1

$$Z_d(j\omega) = \frac{1}{2} \cdot \frac{e_{bc}(j\omega)}{i_{bc}(j\omega)}\bigg|_{i_q=0}$$

$$j\omega G(j\omega) = \frac{\sqrt{3}}{2} \cdot \frac{i_{fd}(j\omega)}{i_{bc}(j\omega)}\bigg|_{i_q=0}$$

Stage 2

$$Z_{afo}(j\omega) = \frac{\sqrt{3}}{2} \cdot \frac{e_{fd}(j\omega)}{i_{bc}(j\omega)}\bigg|_{i_{fd}=0, i_q=0}$$

Stage 3

$$Z_q(j\omega) = \frac{\sqrt{3}}{2} \cdot \frac{e_{bc}(j\omega)}{i_{bc}(j\omega)}\bigg|_{i_{fd}=0, i_d=0}$$

FIGURE 8.36 Standstill frequency response (SSFR) testing setup stages and computation procedures.

The mutual inductance L_{afd} between the stator and field windings is

$$L_{afd} = \frac{2}{3} \lim_{\omega \to o} \frac{Z_{afo}(j\omega)}{j\omega} \tag{8.124}$$

Alternatively, from Equation 8.121,

$$L_{afd} = \lim_{\omega \to o} \frac{\Delta i_{fd}(j\omega)}{j\omega \cdot \Delta i_d(j\omega)}\bigg|_{\Delta e_{fd}=0} \tag{8.125}$$

Here, R_{fd} is the field resistance plus the shunt and connecting leads.

The typical testing arrangement and sequence are shown in Figure 8.36.

The stator resistance R_a is

$$R_a = \lim_{\omega \to o} \left| Z_d(j\omega) \right| \tag{8.126}$$

Though rather straightforward, Equation 8.126 is prone to large errors unless a resolution of 1/1000 is not available at very low frequencies [1]. Fitting a straight line in the very low frequency range is recommended.

If R_a from Equation 8.126 differs markedly compared to the manufacturer's data, it is better to use the latter value, because the estimation of time constants in $L_d(j\omega)$ would otherwise be compromised:
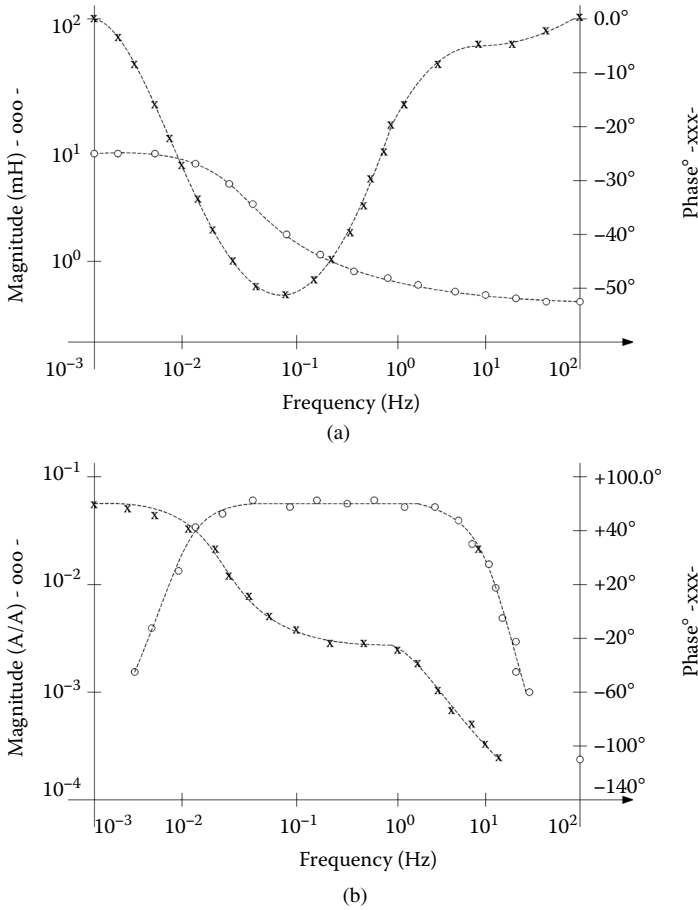
FIGURE 8.37 (a) $L_d(j\omega)$ and (b) $j\omega G(j\omega)$ typical responses.

$$L_d\left(j\omega\right) = \frac{Z_d\left(j\omega\right) - R_a}{j\omega} \tag{8.127}$$

Typical $L_d(j\omega)$ data are shown in Figure 8.37a, and data for $j\omega G(j\omega)$ are shown in Figure 8.37b.

The $Z_{af0}(j\omega)$ function is computed as depicted in . The factor $\sqrt{3}/2$ in both $j\omega G(j\omega)$ and $Z_{af0}(j\omega)$ expressions (Figure 8.36) is due to the fact that stator mmf is produced with only two phases, or because phase *b* is displaced 30° with respect to field axis.

From quadrature tests, again, R_a is calculated as in axis *d*, and finally,

$$L_q\left(j\omega\right) = \frac{Z_q\left(j\omega\right) - R_a}{j\omega} \tag{8.128}$$

A typical $L_q(j\omega)$ dependence on frequency is shown in . Moreover, the test results provide the value of the actual turns ratio $N_{af}(0)$:

$$N_{afo}\left(0\right) = \frac{1}{L_{ad}\left(0\right)} \lim_{\omega \to 0} \left| \frac{Z_{afo}\left(j\omega\right)}{j\omega} \right|_{i_q=0, i_d=0} \tag{8.129}$$

where $L_{ad}(0)$ is

$$L_{ad}(0) = \lim_{\omega \to 0} \left| L_d(j\omega) \right| \tag{8.130}$$

The base N_{af} turns ratio is as follows:

$$N_{af(base)} = \frac{3}{2} \left(\frac{I_{abase}}{I_{fdbase}} \right) = \frac{2p_1 N_f}{N_a} k_{w1} k_{f1} \tag{8.131}$$

where

      p_1 = the pole pairs
      N_f = the turns per field-winding coil
     K_{W1} = the total stator-winding factor
     K_{f1} = the total field form factor
     N_a = turns per stator phase

$N_{af}(0)$ and $N_{af}(base)$ should be very close to each other. The field resistance after reduction to armature winding R_{fd} is as follows:

$$R_{fd} = \frac{\lim\limits_{\omega \to o} \left(j\omega L_{ad} \right)}{\lim\limits_{\omega \to o} \left(\frac{\Delta i_{fd}(j\omega)}{\Delta i_d(j\omega)} \right) \cdot \frac{2}{3} N_{af}(0)} \quad ; \quad (\Omega) \tag{8.132}$$

The directly measured field resistance r_{fd} may be reduced to armature winding to yield R_{fd}:

$$R_{fd} = r_{fd} \cdot \frac{3}{2} \cdot \frac{1}{N_{af}^2(0)} \quad ; \quad (\Omega) \tag{8.133}$$

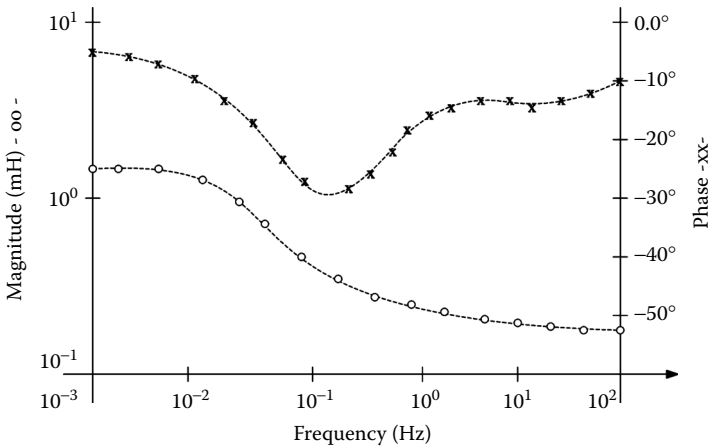Corrections for temperature may be added in Equation 8.133 if necessary.

FIGURE 8.38 Typical $L_q(j\omega)$ response.

The base field current may be calculated from Equation 8.131 if the $N_{af}(0)$ value is used:

$$i_{fd}\left(base\right) = \frac{3}{2} I_a\left(base\right) \cdot \frac{1}{N_{af}\left(0\right)} \quad ; \quad A \ \left(dc\right) \tag{8.134}$$

8.9.2 From SSFR Measurements to Time Constants

In a third-order model, $L_d(j\omega)$ or $L_q(j\omega)$ are of the following form:

$$L_{d,q}\left(j\omega\right) = L_{d,q}\left(0\right) \cdot \frac{\left(1 + j\omega T_{d,q}^{'''}\right)\left(1 + j\omega T_{d,q}^{''}\right)\left(1 + j\omega T_{d,q}^{'}\right)}{\left(1 + j\omega T_{d,qo}^{'''}\right)\left(1 + j\omega T_{d,qo}^{''}\right)\left(1 + j\omega T_{d,qo}^{'}\right)} \tag{8.135}$$

The time constants to be determined through curve fitting, from SSFR tests, are not necessarily the same as those obtained from short-circuit tests (in axis *d*). Numerous methods of curve fitting were proposed [16, 18], some requiring the computation of gradients and some avoiding them, such as the pattern search described in Reference [1].

The direct maximum likelihood method combining field short-circuit open SSFR in axis *d* was shown to produce not only the time constants, but also the parameters of the multiple-order models.

Rather straightforward analytical expressions to calculate the third-order model parameters from the estimated time constants were found for the case in which $L_{f2d} = 0$ (see Figure 8.33) [19]. To shed more light on the phenomenology within the multiple-rotor circuit models, an intuitive method to identify the time constants from SSFR tests, based on phase-response extremes findings [20] is described in what follows.

8.9.3 The SSFR Phase Method

It is widely accepted that second-order circuit models have a bandwidth of up to 5 Hz and can be easily identified from SSFR tests. But even in this case, some simplifications are required to enable us to identify the standard set of short-circuit and open-circuit constants.

With third-order models, such simplifications are not indispensable. While curve-fitting techniques to match SSFR to the identified model are predominant today, they are not free from shortcomings, including the following:

- Define from the start the order for the model
- Initiate the curve fitting with initial estimates of time constants
- Define a cost function and eventually calculate its gradients

Alternatively, it may be possible to identify the time constants pairs $T_1 < T_{10}$, $T_2 < T_{20}$, and $T_3 < T_{30}$ (Equation 8.136) from the operational inductances $L_d(j\omega)$, $L_q(j\omega)$, and $j\omega G(j\omega)$, based on the property of lag circuits [20]:

$$L_d\left(j\omega\right) = L_d \frac{\left(1 + j\omega T_1\right)}{\left(1 + j\omega T_{10}\right)} \cdot \frac{\left(1 + j\omega T_2\right)}{\left(1 + j\omega T_{20}\right)} \cdot \frac{\left(1 + j\omega T_3\right)}{\left(1 + j\omega T_{30}\right)} \tag{8.136}$$

The R–L branches in parallel that appear in the equivalent circuit of SGs, make pairs of zeros and poles when represented in the frequency domain. As each pair of zeros and poles forms a lag circuit ($T_1 < T_{10}$, $T_2 < T_{20}$, $T_3 < T_{30}$), they may be separated one by one from the phase response. Denote $T_1/T_{10} = \alpha < 1$.

The lag circuit main features are as follows:

- It has a maximum phase lag ϕ at the center frequency of the pole zero pair F_c, where

$$\sin\phi = \frac{\alpha-1}{\alpha+1} \tag{8.137}$$

- The overall gain change due to the zero/pole pair is as follows:

$$gain\ change = -20\log\alpha \quad ; \quad \left(dB\right) \tag{8.138}$$

- The two time constants T_{pole} and T_{zero} are as follows:

$$T_{zero} = \frac{T_{pole}}{\alpha} \quad ; \quad T_{pole} = \frac{\sqrt{\alpha}}{2\pi F_c} \tag{8.139}$$

The gain change is, in general, insufficient to be usable in the calculation of α, but Equation 8.137 and Equation 8.139 are sufficient to calculate the zero and pole time constants. Identifying the maximum phase lag points ϕ (at frequency F_c) is first operated by Equation 8.137. Then, T_{pole} and T_{zero} are easily determined from Equation 8.139. The number of maximum phase-lag points in the SSFR frequency corresponds to the order of the equivalent circuit. The process starts by finding the first T_1 and T_{10} pair. Then, the pair is introduced in the experimentally found $L_d(j\omega)$ or $L_q(j\omega)$, and thus eliminated. The order of the circuit is reduced by one unit.

The remainder of the phase will be used to find the second zero-pole pair, and so on, until the phase response left does not contain any maximum.

The order of the equivalent circuit is not given initially but claimed at the end, in accordance with the actual SSFR-phase number of maximum phase-lag points.

The whole process may be computer programmed easily and +/−1 dB gain errors are claimed to be characteristic of this method [20]. To further reduce the errors in determining the value of the maximum phase-lag angle ϕ and the frequency at which it occurs, F_c, sensitivity studies were performed. They showed that an error in F_c produces a significant error in the time constants T_{pole} and T_{zero} α changes the time constants such that ψ varies notably at the same F_c [20].

So, if F_c is varied above and below the firstly identified value F_{ci}, the $L_d(j\omega)$ error varies from positive to negative values. When this error changes sign, the correct value of F_c has been reached (Figure 8.39a). For this "correct" value of F_c, the initially calculated value of α is changed up and down until the error changes sign.

The change in sign of phase error (Figure 8.39b) corresponds to the correct value of α. With these correct values, the final values of two time constants are obtained. A reduction in errors to ±0.5° and, respectively, to ±0.1 dB are claimed by these refinements.

The equivalent rotor circuit resistances may be calculated from the time constants just determined through an analytical solution using a linear transformation [19]. As expected, in such an analytical process, the stator leakage inductance L_l plays an important role. There is a value of L_l above which the rotor circuit leakage inductances become negative. Design values of L_l were shown to produce good results, however.

A few remarks seem to be in order:

- The SSFR phase-lag maxima are used to detect the center frequencies of the zero-pole pairs in the multiple-circuit model of SG.
- The zero-pole pairs are calculated sequentially and then eliminated one by one from the phase response until no maximum phase-lag is apparent. The order of the circuit model appears at the end of the process.
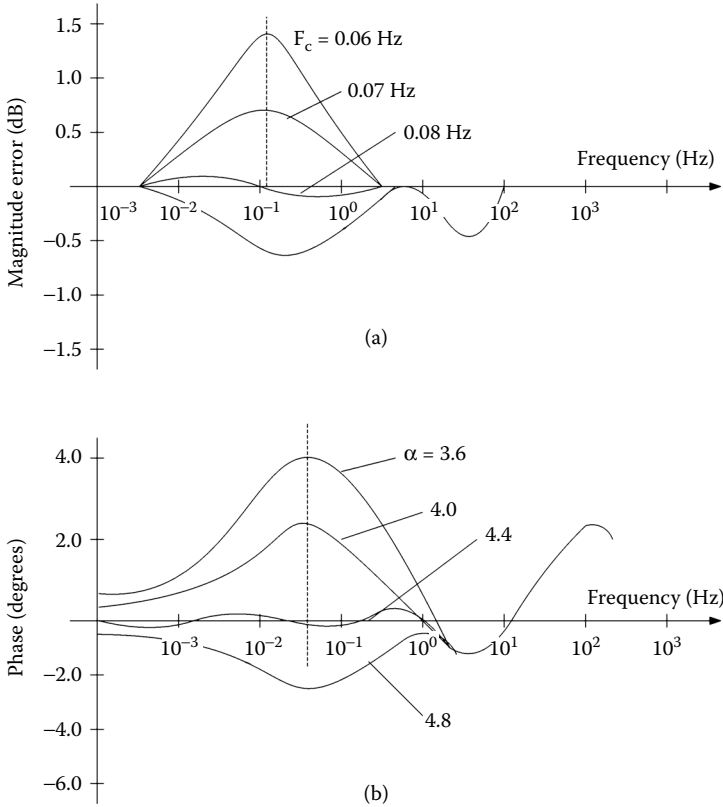
FIGURE 8.39 Variation of errors (a) in amplitude and (b) in phase.

- As the initial values of the time constants are determined from the phase response maxima, the process of optimizing their values as developed above leads to a unique representation of the equivalent circuit.
- It may be argued that the leakage coupling rotor inductances L_{fl1d}, L_{fl2d} are not identified in the process.
- The phase method may be at least used as a very good starting point for the curve-fitting methods to yield more physically representative equivalent circuit parameters of SGs.

8.10   Online Identification of SG Parameters

As today SGs tend to be stressed to the limit, even predictions of +5% additional stability margin will be valuable, as it allows for the delivery of about 5% more power safely. To make such predictions in a tightly designed SG and power system requires the identification of generator parameters from nondangerous online tests, such that a sudden variation of field voltage from one or a few active and reactive power levels [21].

This way, the dynamic parameter identification takes place in conditions closer to those encountered in even larger transients. During a specific on-load large transient, the parameters of the SG equivalent circuit may be considered constant, as identified through an estimation method [22], or variable with the level of magnetic saturation and temperature. Intuitively, it seems more acceptable to assume that magnetic saturation influences some (or all) of the inductances in the model, while the temperature influences the time constants. The frequency effects are considered traditionally by increasing the order of the rotor circuit model (especially for solid rotors). However, in a fast transient, the skin effect in the
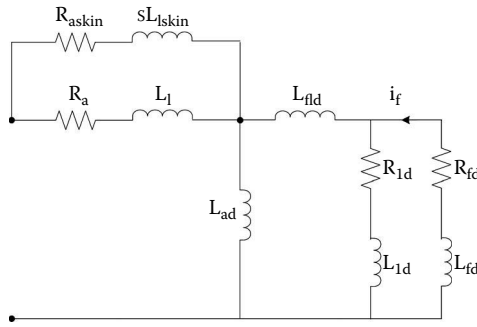
FIGURE 8.40 The addition of a fictitious circuit section to account for stator skin effect during fast transients.

stator winding of a large SG may be considerable. Also, during the first milliseconds of such a transient, the laminated core of stator may enter the model with an additional circuit [23].

When estimating the SG equivalent circuit parameters from rather large online measurements, it may be possible to let the parameters (some of them) vary in time, though in reality, they vary due to the magnetic saturation level that changes in time during transients.

The stator frequency effects may be considered either by adding one cage circuit to a model or by letting the stator resistance R_a vary in time during the process [24]. In the postprocessing stage, the variable parameters may be expressed as a function of, say, field current, power angle, or stator current. Such functions may be used in other online transients. Alternatively, for stator skin effect considerations, an additional fictitious circuit may be connected in parallel with R_a and L_l (Figure 8.40), instead of considering that R_a varies in time during transients. It may also be feasible to adopt a lower-order circuit model (say second order), perform a few representative online tests, and, from all the experimental data, determine the parameters. By making use of the values of these parameters through interpolation (artificial neural networks), for example, new transients may be explored safely [25]. Advanced estimation algorithms, such as using the concept of synthesized information factor (SIF) [24], artificial neural networks [25], constraint conjugate gradient methods [22], and maximum likelihood [26] have all been used for more or less successful validation on large machines under load, via transient responses in power angle, field current, and stator current [24]. The jury is still out, but, perhaps soon, an online measurement field strategy, with a pertinent parameter adaptive estimation scheme, will mature enough to enter the standards.

8.11   Summary

- An almost complete set of testing methods for synchronous generators (SGs) is presented in IEEE standard 115-1995. The International Electrotechnical Commission (IEC) has a similar standard.
- The SG testing methods may be classified into standardized and research types. The standardized tests may be performed for acceptance, performance, or parameters.
- Acceptance testing refers to insulation resistance dielectric and partial discharge, resistance measurements, identifying short-circuited field turns, polarity of field poles, shaft currents and bearing insulation, phase-sequence telephone-influence factor (balanced, residual, line to neutral) stator terminal voltage waveform deviation and distortion factors, overspeed tests, line discharging (maximum absorbed kilovoltampere at zero-power factor with zero field current), acoustic noise. They were presented in similar detail in this chapter following, in general, IEEE standard 115-1996.
- Testing an SG for performance refers to saturation curves, segregated losses, power angle, and efficiency.
- The individual loss components are as follows:
  - Friction and windage loss
  - Core loss (on open circuit)

- Strayload loss (on short-circuit)
- Stator winding loss
- Field winding loss
- To identify the magnetic saturation curves and then segregate the loss components and to finally calculate efficiency under load, four methods have gained wide acceptance:
  - Separate driving method
  - Electric input method
  - Retardation method
  - Heat transfer method
- The separate driving method is based on the concept of driving the SG at precisely controlled (or rated) speed by an external, low rating (<5% of SG rating) motor, or by the exciter (if it contains an electric machine on shaft) or by the prime mover. With the SG driven at rated speed, on open stator circuit, the field current, stator voltage, and the driving motor output are measured for increasing values of field current, until the stator terminal voltage reaches at least 125% of rated value. The open-circuit saturation curve is thus obtained. In addition, as the driving motor output is considered to be known, the field current may be made zero, and thus, the friction and windage losses are measured. From the open-circuit run, where friction and windage and core losses occur, the core loss for various values of terminal voltage is obtained. The same arrangement may be used to determine the short-circuit saturation curve and then the strayload losses for currents levels from 125 to 25% of rated current, if the winding resistance is known from previous measurements. With all loss components known, the efficiency vs. power output may be calculated.
- The electrical input method is similar to the separate driving method, but this time, the SG works as a synchronous motor without a mechanical load.
- In retardation tests, the uncoupled SG is brought at 105 to 110% of rated speed and then left to decelerate in three different situations:
  - Open-circuit stator, zero-field current, to measure friction and windage loss P_{fw}, a.
  - Open-circuit stator, constant field current, to measure friction and windage loss + core loss: $P_{fw} + P_{core}$, b.
  - Short-circuit stator, constant field current, to measure friction and windage + stator winding + strayload losses: $P_{cu1} + P_{strayload} + P_{fw}$, c.

  The inertia may be obtained from run (a), with P_{fw} already known, from the motion equation, by calculating the speed slowing rate around rated speed. Speed has to be recorded. Then, from runs (b) and (c), P_{core} and $P_{strayload}$ may be segregated.
- The other purpose of steady-state tests is to determine the steady-state parameters of SG and the field current under specified load.
- The leakage reactance X_l is approximated usually to the Potier reactance X_p obtained from a rated current zero-power-factor tests at rated voltage. As $X_p > X_l$ at rated voltage, the same test is performed at 110% rated voltage when X_p approaches X_l.
- A procedure to estimate X_l as the average between the zero sequence (homopolar) reactance $X_o(X_o < X_l)$ and the reactance without the rotor inside the stator bore X_{lair}, is introduced. Alternatively, from X_{lair}, the bore air volume reactance X_{air} may be subtracted to obtain the leakage reactance. X_{air} is proportional to the unsaturated uniform airgap reactance X_{adu}; $X_{air} \sim X_{adu} \star gK_c\pi/\tau$: $X_l = X_{lair} - X_{air}$.
- The excitation current at specified load — active and reactive power and voltage — is determined by the Potier diagram method. Magnetic saturation is considered the same in both axes. The power angle is needed for the scope and is computed by using the unsaturated values of quadrature axis reactance, as in Equation 8.29.
- From the simplified transient SG phasor diagram (Figure 8.14), the excitation current for stability studies is obtained.
- Voltage regulation — the difference between no-load voltage and terminal voltage for specified load and same field current — is calculated based on the computed field current at specified load.

- The power angle may be measured by encoders or other mechanical sensors. The power angle is the electrical angle between the terminal voltage and the field-produced emf.
- Temperature tests are required to verify the SG capability to deliver the rated or more power under conditions agreed upon by vendor and buyer. Four methods are described:
  - Conventional (direct) loading
  - Synchronous feedback (back-to-back) loading
  - Zero-power-factor tests
  - Open-circuit running plus short-circuit "loading"
- While direct loading may be done by the manufacturer only for small- and medium-power SGs, the same test may be performed after commissioning, with the machine at the power grid for all power levels.
- Back-to-back loading implies the presence of two coupled identical SGs with their rotors displaced mechanically by $2\delta_N/p_1$. The stator circuits of the two machines are connected together. One machine acts as a motor, the other acts as a generator. If an external low rating motor is driving the MS + SG set, then the former covers the losses in the two machines $2\Sigma P$. Care must be exercised to make the losses fully equivalent with those occurring with the SG under specified load.
- The zero-power-factor load test implies that the SG works as a synchronous condensor (motoring at zero mechanical load). Again, loss equivalence with actual conditions has to be observed.
- The open-circuit stator test for the field current at specified load is run, and the temperature rise until thermal steady state, Δt_{oc}, is measured. Further on, the short-circuit test at rated current is run until new thermal steady state is obtained for a temperature rise of Δt_{sc}. The SG total temperature is $\Delta t_{oc} + \Delta t_{sc}$ minus the temperature differential due to mechanical loss, which is duplicated during the tests.
- All the above tests imply efforts and have shortcomings, but the temperature rise for specified load is so important for SG life that it has to be measured, even if sophisticated FEM thermal-electromagnetic models of SGs are now available.
- Besides steady-state performance, behavior under transient conditions is also important to predict. To this end, the SG parameters for transients have to be identified. Power system stability studies rely on SG parameter knowledge.
- Per unit (P.U.) values are used in parameter definitions to facilitate more generality in results referring to SGs of various power levels. Only three base independent quantities are generally required: voltage, current, and frequency.
- For the rotor, Rankin defined a new base field current $i_{fdbase} = I_{fdbase} {}^* X_{adu}$. I_{fdbase} is the field current (reduced to the stator) that produces the rated voltage on the straight line of the no-load saturation curve. X_{adu} is the unsaturated d axis coupling reactance (in P.U.) between stator and rotor windings. Rankin's reciprocal system produces equal stator-to-field and field-to-stator P.U. reactances.
- The steady-state parameters X_d, X_q may be determined by a few carefully designed tests without loading the SG. Quadrature axis reactance X_q is more difficult to segregate, but pure I_q loading of the machine method provides for the X_q values.
- SGs may work with unbalanced load either when connected to the power system or in stand-alone mode. For steady state, by the method of symmetrical components, the value of $Z_2(X_2)$ may be found from a steady-state line-to-line short-circuit. The elimination of the third harmonics from the measured voltage is crucial in obtaining acceptable precision with this testing method.
- The zero-sequence (homopolar) reactance X_o is measured from a standstill AC test with all stator phases in series or in parallel. In general, $X_o \leq X_l$. A two line to neutral short-circuit test will also provide for X_o.
- The short-circuit ratio (SCR) = $1/X_d = I_{FNL}/I_{FSI}$. I_{FSI} is the field current from the three-phase short-circuit (at rated stator current). I_{FNL} is the field current at rated voltage and open circuit test. SCR today has typical values of 0.4 to 0.6 for high-power SGs.
- Due to magnetic saturation and its cross-coupling effect, all the methods to determine the steady-state parameters so far need special corrections to fit the results from direct on-load measurements.

Families of flux/current curves for axes *d* and *q* are required to be obtained from special operation mode tests, in order to have enough data to cope with on-load various situations.

- Standstill flux decay tests may provide the required flux/current families of curves. They imply short-circuiting the stator or field circuits and recording the currents. The tests are done in axis *d* or *q* or in a given rotor position.

- Integrating the resistive voltage drop in time, the initial (DC) flux linkage is obtained. Care must be exercised to avoid hysteresis-caused errors and to measure the resistance before each new test in order to eliminate temperature rise errors.

- To estimate the transient parameters — X_d'', X_d', T_d'', T_d', X_q'', T_q'', X_q', T_q', T_{do}'', T_{do}', T_{qo}'' — two main types of tests were standardized:
  - Sudden three-phase short-circuit tests
  - Standstill frequency response (SSFR)

- Three-phase sudden short-circuit is used to identify the above parameters of a second-order model of SG in axis *d* and axis *q*. The methods to extract the parameters, from stator phase currents and field current recording, are essentially either graphical with mechanization by computer programs [27] or of regression type.

- Third-order models are required, especially in SGs with solid rotors, due to skin effect strong dependence on frequency in solid bodies.

- Alternatively, there are proposals to determine the parameters for transients from the already mentioned standstill DC flux decay tests, by processing the time variation of currents or voltages during these tests. Though good results were reported, the method has not yet met worldwide acceptance due to insufficient documentation.

- Standstill frequency response tests use similar arrangements as those of the DC flux decay tests. The SG is fed with about 0.5% rated currents at frequencies from 0.001 to 100 Hz and more. The input voltage, stator current, field-current rms values, and phase-lags are measured. The tests take time, as at least two to three periods have to be recorded at all frequencies.

- In general, the amplitude of the operational parameters $L_d(j\omega)$, $L_q(j\omega)$, $G(j\omega)$, and $Z_{afo}(j\omega)$ is used to extract the parameters of the third-order model along axes *d* and *q*: $X_{d,q}'''$, $X_{d,q}''$, $X_{d,q}'$, $I_{d,q}'''$, $T_{d,q}''$, $I_{d,q}'$, $T_{d,qo}'''$, $T_{d,qo}''$, $T_{d,qo}'$, the stator resistance R_a, field-winding resistance R_{fd}, and the turns ratio between rotor and stator *a*. Numerous curve-fitting methods were introduced and improved steadily up to the present time.

- The presence of one or two leakage mutual rotor reactances in the third-order model, with the leakage stator reactance X_l given *a priori*, is still a matter of debate.

- These reactances seem mandatory (at least one of them) to represent correctly, in the same time, the transient behavior of SGs seen from the stator circuit and from the field current side.

- The up to now less favored information from SSFR, the phase response vs. frequency, was recently put to work to identify the third model of SG [20]. The method is based on the observation that the phase response corresponds to zero/pole pairs in the model's transfer function. By using the center frequency F_C and the value of response phase, these maximum phase zero/pole pairs — time constants — are calculated rather simply. They are then corrected until only very low errors persist. After the first pair is identified, its circuits are eliminated from the response. The search for the phase maximum continues until no maximum persists. The model order comes at the end. Determining the resistances and reactances of the SG multiple circuit model, from transient reactances to time constants, may be done by regression methods. Analytical expressions were also found for the third-order models [19].

- Some verifications of the validity of SSFR test results for various large on-load transients were made. Still, this operation seems to be insufficiently documented, especially for solid-rotor SGs.

- On-line SG model identification methods, based on same nondamaging transients on-load (such as up to 30% step field voltage change response at various load conditions), were introduced recently. Artificial neural networks and other learning methods may be used to extend the model thus obtained to new transients, based on a set of representative on-load tests.

- While these complex online adaptive parameter identification methods go on, there are still hopes that simpler methods, such as standstill flux decay tests, standstill DC + SSFR tests, or load recovery tests, may be improved to the point that they become fully reliable for large on-load transients.
- Important developments are expected in SG testing in the near future, as theory, software, and hardware are continuously upgraded through worldwide efforts by industry and academia. These efforts are driven by ever-more demanding power quality standards.

References

1. IEEE standard 115-1995.
2. K. Shima, K. Ide, and M. Takahashi, Finite-element calculation of leakage inductances of a saturated-pole synchronous machine with damper circuits, *IEEE Trans.*, EC-17, 4, 2002, pp. 463–471.
3. K. Shima, K. Ide, and M. Takashashi, Analysis of leakage flux distributions in a salient-pole synchronous machine using finite elements, *IEEE Trans.*, EC-18, 1, 2003, pp. 63–70.
4. A.M. El-Serafi, and J. Wu, A new method for determining the armature leakage reactance of synchronous machines, *IEEE Trans.*, EC-18, 1, 2003, pp. 80–86.
5. A.M. El-Serafi, and N.C. Kar, Methods for determining the Q axis saturation characteristics of salient-pole synchronous machines from the measured D-axis characteristics, *IEEE Trans.*, EC-18, 1, 2003, pp. 80–86.
6. A.W. Rankin, Per unit impedance of synchronous machines, *AIEE Trans.*, 64, pp. 564–572 and 1985, pp. 939–941.
7. S. Tahan, and I. Kamwa, A two factor saturation model for synchronous machine with multiple rotor circuits, *IEEE Trans.*, EC-10, 4, 1995, pp. 609–616.
8. M. Biriescu, and Gh. Liuba, Identification of reactances of synchronous machine including the saturation influence, in *Proceedings of International Conference on Evolution and Modern Aspects of Synchronous Machines*, Zurich, August 27–29, 1991, pp. 55–58.
9. M. Biriescu, G. Liuba, M. Mot, V. Olarescu, and V. Groza, Identification of Synchronous Machine Reactances from Current Decay at Standstill Test, Record of ICEM-2000, Espoo, Finland, pp. 1914–1916.
10. A. Keyhani, S.I. Moon, A. Tumageanian, and T. Leksau, Maximum Likelihood Estimation of Synchronous Machine Parameters from Flux Decay Data, in *Proceedings of ICEM-1992*, vol. 1, Manchester, U.K., 1992, pp. 34–38.
11. N. Dedene, R. Pintelon, and Ph. Lataire, Estimation of global synchronous machine model using a MIMO estimator, *IEEE Trans.*, EC-18, 1, 2003, pp. 11–16.
12. F.P. de Melle, and J.R. Ribeiro, Derivation of synchronous machine parameters from tests, *IEEE Trans.*, PAS-96, 4, 1977, pp. 1211–1218.
13. I.M. Canay, Causes of discrepancies in calculation of rotor quantities and exact equivalent diagrams of the synchronous machine, *IEEE Trans.*, PAS-88, 1969, pp. 114–1120.
14. P.L. Dandeno, Discussion, *IEEE Trans.*, EC-9, 3, 1994, pp. 587–588.
15. I. Kamwa, and P. Viarouge, On equivalent circuit structures for empirical modeling of turbine-generators and discussion, *IEEE Trans.*, EC-9, 3, 1994, pp. 579–592.
16. P.L. Dandeno, and H.C. Karmaker, Experience with standstill frequency response (SSFR) testing and analysis of salient pole synchronous machines, *IEEE Trans.*, EC-14, 4, 1999, pp. 1209–1217.
17. A. Keyhani, and H. Tsai, Identification of high order synchronous generator models from SSFR tests data, *IEEE Trans.*, EC-9, 3, 1994, pp. 593–603.
18. S.D. Umans, I.A. Mallick, and G.L. Wilson, Modelling of solid iron turbogenerators, parts I and II, *IEEE Trans.*, PAS-97, 1, 1978, pp. 269–298.
19. A. Watson, A systematic method to the determination of parameters of synchronous machine from results of frequency response tests, *IEEE Trans.*, EC-15, 4, 2000, pp. 218–223.
20. Z. Zhao, F. Zheng, J. Gao, and L. Xu, A dynamic on-line parameter identification and full system experimental verification for large synchronous machine, *IEEE Trans.*, EC-10, 3, 1995, pp. 392–398.

21. C.T. Huang, Y.F. Chen, C.L. Chang, Ch-Y. Huang, N.D. Chiang, and J. Ch. Wang, On line measurement based model parameter estimation for SG model development and identification schemes, parts I and II, *IEEE Trans.*, EC-9, 2, 1994, pp. 330–343.
22. I. Boldea, and S.A. Nasar, Unified treatment core losses and saturation in the orthogonal axis model of electric machines, *Proc. IEE*, 134-B, 6, 1987, pp. 355–363.
23. Z. Zhao, L. Xu, and J. Jiang, On line estimation of variable parameters of synchronous machines using a novel adaptive algorithm, parts I and II and discussion, *IEEE Trans.*, EC-12, 3, 1997, pp. 193–210.
24. H.B. Karayaka, A. Keyhani, G.T. Heydt, B.L. Agrawal, and D.A. Selin, Neural network based modeling of a large steam turbine-generator rotor body parameters from on-line disturbance data, *IEEE Trans.*, EC-16, 4, 2001, pp. 305–311.
25. R. Wamkeue, I. Kamwa, X. Dai-Do, and A. Keyhani, Iteratively reweighted least squares for maximum likelihood identification of synchronous machine parameters from on line tests, *IEEE Trans.*, EC-14, 2, 1999, pp. 156–166.
26. I. Kamwa, M. Pilote, H. Corle, P. Viarouge, B. Mpanda-Mabwe, and M. Crappe, Computer software to automate the graphical analysis of sudden shortcircuit oscillograms of large synchronous machines, parts I and II, *IEEE Trans.*, EC-10, 3, 1995, pp. 399–414.

The Electric Generators Handbook

SYNCHRONOUS GENERATORS

Published Titles

Electric Drives
Ion Boldea and Syed Nasar

Linear Synchronous Motors:
Transportation and Automation Systems
Jacek Gieras and Jerry Piech

Electromechanical Systems, Electric Machines,
and Applied Mechatronics
Sergey E. Lyshevski

Electrical Energy Systems
Mohamed E. El-Hawary

Distribution System Modeling and Analysis
William H. Kersting

The Induction Machine Handbook
Ion Boldea and Syed Nasar

Power Quality
C. Sankaran

Power System Operations and Electricity Markets
Fred I. Denny and David E. Dismukes

Computational Methods for Electric Power Systems
Mariesa Crow

Electric Power Substations Engineering
John D. McDonald

Electric Power Transformer Engineering
James H. Harlow

Electric Power Distribution Handbook
Tom Short

Synchronous Generators
Ion Boldea

Variable Speed Generators
Ion Boldea

The Electric Generators Handbook

SYNCHRONOUS GENERATORS

Ion Boldea

Polytechnical Institute
Timisoara, Romania

CRC Taylor & Francis
Taylor & Francis Group
Boca Raton   London   New York

Preface

Electric energy is a key ingredient in a community at the civilization level. Natural (fossil) fuels, such as coal, natural gas, and nuclear fuel, are fired to produce heat in a combustor, and then the thermal energy is converted into mechanical energy in a turbine (prime mover). The turbine drives the electric generator to produce electric energy. Water potential and kinetic energy and wind energy are also converted to mechanical energy in a prime mover (turbine) that, in turn, drives an electric generator. All primary energy resources are limited, and they have thermal and chemical (pollutant) effects on the environment.

So far, most electric energy is produced in rather constant-speed-regulated synchronous generators that deliver constant alternating current (AC) voltage and frequency energy into regional and national electric power systems that then transport it and distribute it to various consumers. In an effort to reduce environment effects, electric energy markets were recently made more open, and more flexible, distributed electric power systems emerged. The introduction of distributed power systems is leading to increased diversity and the spread of a wider range of power/unit electric energy suppliers. Stability and quick and efficient delivery and control of electric power in such distributed systems require some degree of power electronics control to allow for lower speed for lower power in the electric generators in order to better tap the primary fuel energy potential and increase efficiency and stability. This is how variable-speed electric generators recently came into play, up to the 400 (300) megavolt ampere (MVA)/unit size, as pump-storage wound-rotor induction generators/motors, which have been at work since 1996 in Japan and since 2004 in Germany.

The present handbook takes an in-depth approach to both constant and variable-speed generator systems that operate in stand-alone and at power grid capacities. From topologies, through steady-state modeling and performance characteristics to transient modeling, control, design, and testing, the most representative standard and recently proposed electric generator systems are treated in dedicated chapters.

This handbook contains most parameter expressions and models required for full modeling, design, and control, with numerous case studies and results from the literature to enforce the assimilation of the art of electric generators by senior undergraduate students, graduate students, faculty, and, especially, by industrial engineers, who investigate, design, control, test, and exploit the latter for higher-energy conversion ratios and better control. This handbook represents a single-author unitary view of the multifaceted world of electric generators, with standard and recent art included. The handbook consists of two volumes: *Synchronous Generators* and *Variable Speed Generators*.

An outline of *Synchronous Generators* follows:

- Chapter 1 introduces energy resources and the main electric energy conversion solutions and presents their merits and demerits in terms of efficiency and environmental touches.
- Chapter 2 displays a broad classification and the principles of various electric generator topologies, with their power ratings and main applications. Constant-speed synchronous generators (SGs) and variable-speed wound rotor induction generators (WRIGs), cage rotor induction generators (CRIGs), claw pole rotor, induction, permanent magnet (PM)-assisted synchronous,

v

switched reluctance generators (SRGs) for vehicular and other applications, PM synchronous generators (PMSGs), transverse flux (TF) and flux reversal (FR) PMSGs, and, finally, linear motion PM alternators, are all included and are dedicated topics in one or more subsequent chapters in the book.

- Chapter 3 covers the main prime movers for electric generators from topologies to basic performance equations and practical dynamic models and transfer functions. Steam, gas, hydraulic, and wind turbines and internal combustion (standard, Stirling, and diesel) engines are dealt with. Their transfer functions are used in subsequent chapters for speed control in corroboration with electric generator power flow control.
- Chapter 4 through Chapter 8 deal with synchronous generator (SG) steady state, transients, control, design, and testing, with plenty of numerical examples and sample results presented so as to comprehensively cover these subjects.

Variable Speed Generators is dedicated to electric machine and power system people and industries as follows:

- Chapter 1 through Chapter 3 deal with the topic of wound rotor induction generators (WRIGs), with information about a bidirectional rotor connected AC–AC partial rating pulse-width modulator (PWM) converter for variable speed operation in stand-alone and power grid modes. Steady-state (Chapter 1) transients and vector and direct power control (Chapter 2) and design and testing (Chapter 3) are treated in detail again, with plenty of application cases and digital simulation and test results to facilitate the in-depth assessment of WRIG systems now built from 1 to 400 MVA per unit.
- Chapter 4 and Chapter 5 address the topic of cage rotor induction generators (CRIGs) in self-excited mode in power grid and stand-alone applications, with small speed regulation by the prime mover (Chapter 4) or with a full rating PWM converter connected to the stator and wide variable speed (Chapter 5) with ±100% active and reactive power control and constant (or controlled) output frequency and voltage, again at the power grid and in stand-alone operation. Chapter 1 through Chapter 5 are targeted to wind, hydro, and, in general, to distributed renewable power system people and industries.
- Chapter 6 through Chapter 9 deal with the most representative electric generator systems recently proposed for integrated starter alternators (ISAs) on automobiles and aircraft, all at variable speed, with full power ratings electronics control. The standard (and recently improved) claw pole rotor alternator (Chapter 6), the induction (Chapter 7), and the PM-assisted synchronous (Chapter 8) and switched reluctance (Chapter 9) ISAs are investigated thoroughly. Again, numerous applications and results are presented, from topologies, steady state, and transient performance to modeling to control design and testing for the very challenging speed range constant power requirements (up to 12 to 1) typical of ISAs. ISAs already reached the markets on a few mass-produced (since 2004) hybrid electric vehicles (HEVs) that feature notably higher gas mileage and emit less pollution for in-town driving. This part of the handbook (Chapter 6 through Chapter 9) is addressed to automotive and aircraft people and industries.
- Chapter 10 deals extensively with radial and axial airgap, surface and interior PM rotor permanent magnet synchronous generators that work at variable speed and make use of full-rating power electronics control. This chapter includes basic topologies, thorough field and circuit modeling, losses, performance characteristics, dynamic models, bidirectional AC–AC PWM power electronics

control at the power grid and in stand-alone applications with constant DC output voltage at variable speed. Design and testing issues are included, and case studies are treated through numerical examples and transient performance illustrations. This chapter is directed to wind and hydraulic energy conversion, generator-set (stand-alone) interested people with power per unit up to 3 to 5 MW (from 10 rpm to 15 krpm) and, respectively, 150 kW at 80 krpm (or more).

- Chapter 11 investigates, with numerous design case studies, two high-torque-density PM SGs (transverse flux [TFG]) and flux reversal [FRG]), introduced in the past two decades to take advantage of multipole stator coils that do not overlap. They are characterized by lower copper losses per Newton mater (Nm) and kilogram per Nm and should be applied to very low-speed (down to 10 rpm or so) wind or hydraulic turbine direct drives or to medium-speed automotive starter-alternators or wind and hydraulic turbine transmission drives.
- Chapter 12 investigates linear reciprocating and linear progressive motion alternators. Linear reciprocating PMSGs (driven by Stirling free piston engines) were introduced (up to 350 W) and used recently for NASA mission generators with 50,000 h or more fail-proof operation; they are also pursued aggressively as electric generators for series (full electric propulsion) vehicles for powers up to 50 kW or more; finally, they are being proposed for combined electric (1 kW or more) and thermal energy production in residencies, with gas as the only prime energy provider.

The author wishes to thank the following:

- The illustrious people who have done research, wrote papers, books, and patents, and built and tested electric generators and their controls over the past decades for providing the author with "the air beneath his wings"
- The author's very able Ph.D. students for computer editing the book
- The highly professional, friendly, and patient editors at Taylor & Francis

Ion Boldea
IEEE Fellow

About the Author

Professor Ion Boldea, Institute of Electrical and Electronics Engineers (IEEE) member since 1977, and Fellow from 1996, worked and published extensively, since 1970, papers (over 120, many within IEEE) and monographs (13) in the United States and the United Kingdom, in the broad field of rotary and linear electric machines modeling, design, power electronics advanced (vector and direct torque [power]) control, design, and testing in various applications, including variable-speed wind and hydraulic generator systems, automotive integrated starter-alternators, magnetically levitated vehicles (MAGLEV), and linear reciprocating motion PM generators. To stress his experience in writing technology books of wide impact, we mention his three latest publications (with S.A. Nasar): *Induction Machine Handbook*, 950 pp., CRC Press, 2001; *Linear Motion Electromagnetic Devices*, 270 pp., Taylor & Francis, 2001; and *Electric Drives*, 430 pp., CD-Interactive, CRC Press, 1998.

He has been a member of IEEE–IAS Industrial Drives and Electric Machines committees since 1990; associate editor of the international journal *Electric Power Components and Systems*, Taylor & Francis, since 1985; co-chairman of the biannual IEEE–IAS technically sponsored International Conference in Electrical Engineering, OPTIM, 1996, 1998, 2000, 2002, 2004, and upcoming in 2006; founding director (since 2001) of the Internet-only *International Journal of Electrical Engineering* (www.jee.ro). Professor Boldea won three IEEE–IAS paper awards (1996–1998) and delivered intensive courses, keynote addresses, invited papers, lectures, and technical consultancy in industry and academia in the United States, Europe, and Asia, and acted as Visiting Scholar in the United States and the United Kingdom for a total of 5 years. His university research power electronics and motion control (PEMC) group has had steady cooperation with a few universities in the United States, Europe, and Asia.

Professor Boldea is a full member of the European Academy of Sciences and Arts at Salzburg and of the Romanian Academy of Technical Sciences.

Contents